MICROMECHANISMS OF CLEAVAGE FRACTURE AT CRYOGENIC TEMPERATURES OF SA-738 GR. B STEEL AND 7% NICKEL STEEL

by

HUIZE FAN

A thesis submitted to the University of Birmingham
for the degree of
DOCTOR OF PHILOSOPHY

School of Metallurgy and Materials
College of Engineering and Physical Sciences
University of Birmingham
June 2023

ACKNOWLEDGEMENT

I would like to thank my supervisor Prof. P. Bowen for his kind encouragement and support during my PhD study, the knowledgeable discussions, and the opportunity of sponsorship. I would also like to thank Baowu Steel for the financial support and the materials provided.

I would like to thank my second supervisor Dr. M. Novovic for his support on my experimental work and the valuable discussions.

I would also like to thank Dr. H. Li for her help and support with fatigue testing.

Many thanks to Mr. D. Price, Dr. T. Dole, and Dr. C. Cooper for their help and advice in mechanical testing labs. Thank for the help and support from Dr. H. Kitaguchi on the SEM techniques.

Special thanks to Yunpeng Gao and Weichen Xu's help on the experimental work together on this liquid nitrogen-involved project, including Charpy, tensile, fracture stress, and fracture toughness tests. I would also like to thank Weichen Xu's fractography analysis.

Thanks to the Fatigue and Fracture group members with their help and interesting discussions related to my study and daily life.

Finally, I would like to thank my parents for supporting me for doing my PhD project, the essential financial support and encouragement with love. Many thanks to my friends, I would not forget the happy time with you. Also, my beloved Liu Yuning, you saved my mental health.

ABSTRACT

This thesis considers a detailed assessment of SA-738 Gr. B steel regarding its mechanical properties and fracture mechanisms at temperatures ranging from −196 to −40ºC. Mechanical testing included hardness test, tensile test, Charpy V-notch test, and fracture toughness tests. A standard heat treatment condition (HT1) was compared with a second heat treatment (HT2) which corresponds to a simulated post-welding heat treatment in order to see the effect of post-welding heat treatment on mechanical properties and microstructure on this steel.

Tensile tests showed that yield stress, tensile strength, Lüders elongation and work hardening exponent were strongly dependent on test temperatures: as the temperature increased, yield stress, tensile strength, and Lüders elongation decreased, while work hardening increased.

The Charpy impact testing results of HT1 and HT2 exhibited closely similar ductile-to-brittle transition behaviour over the temperature range from −100 to −80ºC, with a transition temperature of −91 and −87ºC estimated by tanh-fit curve respectively. The absorbed impact energy had a strong positive linear correlation with lateral expansion and ductile thumbnail extensions. There was a negative linear relationship between impact energy and percentage of cleavage area.

Fracture toughness results for HT1 and HT2 were characterised by the reference temperature T_0 obtained by the Master Curve methodology. The overall application of the Master Curve methodology to estimate the reference temperature of HT1 and HT2 specimens was reliable and gave closely similar reference temperatures of −101 and −97ºC at test temperature of −120ºC respectively.

Detailed fractography of fracture toughness specimens tested at −196 and −170ºC showed that all specimens failed with transgranular cleavage, and eight out of ten cleavage cracks were inclusion-initiated. Nine out of ten specimens had the local fracture initiation sites located at positions consistent with a purely tensile stress-controlled failure criterion.

The local cleavage fracture stresses obtained from sharp-cracked specimens tested at temperatures between −196 to −80ºC were compared to those of blunt-notched specimens tested at temperatures of −196 and −170ºC. The local cleavage fracture stresses appeared to be independent of test temperatures. There was a weak positive relationship between the local

fracture stress and reciprocal square root of the initiating inclusion diameter. Local cleavage fracture stresses were measured as 1678 to 2699MPa.

The study also addresses a 7% nickel steel at temperatures ranging from −196 to −60ºC. Hardness, tensile, Charpy V-notch, slow blunt notch bending, fracture toughness, and fatigue crack growth tests were performed.

In tensile tests, yield stress and tensile strength decreased with increasing test temperature. The work hardening exponent of this 7% nickel steel had a weak positive correlation to test temperature, and total elongation was independent of test temperature. One tensile specimen only, tested at −196ºC, showed some cleavage facets on the fracture surface.

Charpy tests exhibited ductile-to-brittle transition behaviour in the range from −170 to −140ºC. The DBTT was −140ºC estimated by tanh-fit curve. Fractography of specimens tested below −140ºC showed a mixed mode of micro-void coalescence and transgranular cleavage fracture, and as the test temperature increased, the fraction of cleavage area decreased. Slow blunt notch testing of 7% nickel steel showed nonlinearity even at −196ºC. Fractography was mainly transgranular cleavage, with micro-void coalescence located between cleavage facets.

In fracture toughness test of 7% nickel steel tested at −196 to −163ºC, specimens failed by cleavage fracture after some amount of ductile crack growth. The fracture surfaces had a mix of transgranular cleavage facets and micro-void coalescence. K_{Jc} values of specimens tested at −196ºC were in the range of 214 to 291MPam$^{1/2}$, while K_{Jc} values of specimens tested at −170 and −163ºC were in the range of 547 to 726 MPam$^{1/2}$. Values of local cleavage fracture stress for 7% nickel steel were deduced to lie between 2765 to 3501 MPa.

The fatigue crack growth resistance of 7% and 9% nickel steels has also been tested at room temperature and −163ºC.

Contents

CHAPTER 1: INTRODUCTION AND LITERATURE REVIEW

Energies with lower carbon emissions are preferred nowadays for sustainable development, for example, nuclear energy and natural gas are both alternatives for traditional fossil fuels. Nuclear energy is thought to be highly energy-efficient, while natural gas is cleaner with a lower carbon footprint. However, the development of energy is deeply correlated to the acceptance from the public, which is related to the safety concerns behind it, especially nuclear energy always reminds people of the accidents of Chernobyl and Fukushima Daiichi. Natural disasters or mistakes made by the operators seem to be the main causes of energy component failure, but real-life performance and operation life are determined by the properties of the construction materials. Therefore, it is important to investigate the mechanical properties of the construction materials and to find out the possible fracture mechanisms in order to predict the performance of materials and avoid failures under various conditions.

This thesis is part of a development programme of thick-steel plates at Baowu Steel to qualify a range of ferritic steels for use at temperatures as low as −163ºC. It firstly investigates SA-738 Gr. B high-strength low-alloy (HSLA) steel with specimens from two different heat treatments: one underwent a quenching-tempering process, and another one underwent stimulated post-weld heat treatment (SPWHT). SA-738 Gr. B steel is designed for the construction steel of nuclear reactor containment vessels, with a design code specified in ASME SA738/SA738M standard [1]. Although the design code is aimed primarily at applications mostly at ambient temperature, Baowu Steel wished to assess this steel at much lower temperatures. There was also interest in an extended tempering treatment which historically customers had favoured based on the subsequent handling behaviour of these thick plates during secondary processing and working operations. ferritic steel to temperatures and wide application temperature range,

the complex environment and influencing factors inside nuclear power plant including accumulated radiation damage, decrease in temperature, increase in strain rate, etc., special attention should be paid to fracture modes in order to avoid ductile-to-brittle transition. It should be noticed that the carbon content of the steel studied is less than the ASME requirement, with 0.09wt% and 0.20wt% respectively, providing a better weldability, but the mechanical properties of the base material must be affected. Therefore, to secure the safety of the power plant during operation, it is important to investigate the ductile-to-brittle transition region of this SA-738 Gr. B HSLA steel, as well as to identify and understand its fracture mechanisms to obtain a thorough assessment to this specially developed steel.

Secondly, it addresses a development nickel steel with a nickel content of 7%. Such nickel steels are designed for liquefied natural gas storage purposes at a liquefied natural gas temperature of −163ºC. The design code of a 9% nickel steel is specified in ASTM A553/553M [2]. 9% nickel steel has been applied in LNG industry for a long time, but 7% nickel steel does not have a specific standard and its properties require further investigation. Both nickel steels are ferritic steels used for low-temperature applications, facing issues from ductile-to-brittle transition behaviour, and therefore it is important to assess their mechanical properties and failure mechanisms at cryogenic temperatures. Here the thesis concentrates on the assessment of a 7% nickel steel, but opportunity is taken to compare results with a 9% nickel steel.

The aims of this study are:

(a) To investigate micro-mechanisms of cleavage fracture in ferritic steels. In parallel studies on such steels produced by Baowu Steel it was possible to identify dominant sites of fracture initiation-which can greatly aid the interpretation of the underlying

cleavage fracture micro-mechanism. A particular feature of this thesis is to extend such investigations to test temperatures as low as −196ºC;

(b) To investigate whether the Master curve methodology can be applied to the SA-738 Grade steel and whether its application can suggest any differences in reference temperature between two closely similar heat-treated conditions;

(c) To begin the assessment of a 7% nickel steel for use at −163ºC.

This thesis consists of three parts. **This first part** is a review of the previous literature to obtain understanding of the development of fracture mechanisms and concentrates on cleavage fracture micromechanisms at lower shelf and ductile-to-brittle transition region. Linear-elastic and elastic-plastic mechanisms as well as the Master Curve methodology are also reviewed. The background of both SA-738 Gr. B steel and nickel steels are briefly reviewed.

The second part is the study on SA-738 Gr. B steel, and it includes four chapters: Chapter 2 gives the experimental procedures including materials characterisation on microstructure, inclusion distribution, hardness testing, tensile testing, Charpy impact testing, fracture toughness testing, and fractography. The application of the Master Curve methodology in the analysis of fracture toughness data is also described in detail. Chapters 3 and 4 present the results and discussions of the testing presented in Chapter 2, with further investigations on characterising initiation sites of cleavage fracture in fracture toughness specimens tested at lower shelf temperatures, and the local cleavage fracture stresses of fracture toughness specimens based on McMeeking's FEM analysis. Chapter 5 compares and summarises results from HT1 and HT2 and some suggestions are made for the future work of this SA-738 Gr. B steel.

The third part is the work carried out for 7% and 9% nickel steels, and this thesis focuses on 7% nickel steel. 9% nickel steel is included only for comparison. The experimental procedures are described in Chapter 2 together with SA-738 Gr. B steel, as well as fatigue crack growth resistance curves monitored with D.C.P.D. method. Chapters 6 and 7 present the results and discussions of the testing presented in Chapter 2 for 7% and 9% nickel steels. Conclusions are made on Chapter 8. Suggestions on future work of these two nickel steels are made at the end of Chapter 8.

1.1 A Review on Micromechanisms of Fracture

Cleavage fracture is the most unwanted fracture in science and engineering due to its nature of being sudden and catastrophic, especially for large constructions such as nuclear power plants. A decrease in temperature could result in a transition of fracture mode from ductile to brittle. The transition region should be carefully considered for engineering materials to ensure safe use at operation temperatures. The micromechanisms are therefore reviewed to obtain a better understanding behind fracture.

1.1.1 Ductile Fracture

Unlike cleavage fracture, ductile fracture is more stable and predictable, and the crack would not grow continuously without applying a higher load at the crack tip. Figure 1.1 exhibits the stress condition of the crack tip of a ductile material under a load in tension. The stress distribution ahead of the crack is usually not evenly distributed, and the stress at the crack tip is much higher than the applied nominal stress. When the local stress is high enough, the material reaches a yield strength of S_y at a distance of r_y. The distance between r_y and the crack tip ($r = 0$) is plastically deformed, and this deformed region is named the plastic zone. The

factors that influence the size of the plastic zone include the material's yield stress, the applied load, and the local loading conditions. The formation of the plastic zone involves energy absorption and increases the stress needed for crack growth, and as the crack length increases, the required applied stress to grow the crack also increases. The damage tolerance is enhanced as the crack is blunted and difficult to grow to the critical size for failure.

The microscopic cracks are often initiated by dislocation interactions in the plastic zone. The formation and movement of a large number of dislocations entangle and lead to the development of tiny cracks ahead of the main crack, and these cracks link with the main crack to further enhance the fracture process. Formation, growth, and coalescence of micro-voids under stress in plastic region would also advance the fracture process. They usually develop from second phase particles such as inclusions and precipitates. The shape of micro-void coalescence is circular or semicircular, and the semicircular dimples are the results of shear stresses, with parabolic depressions and coalesce in planes of maximum shear stress. The direction of depressions points back to crack origin. The directions of depression on opposing surfaces point in opposite directions. The failure that combines bending and tension also leads to elongated dimples.

Voids that formed due to particles generally have very weak interfacial bonds and the strain could be zero during occurrence, and particles with better bonding would crack and form void nuclei [3]. The voids link with the main crack and the ligaments between would cause ductile tearing. The critical void nucleation stress condition around second phase particles can be expressed as the following equation [4] [5] [6]:

$$\sigma_c = \sigma_m + \sigma_{loc} \tag{1.1}$$

Where σ_c is the critical stress for void nucleation, σ_m is the sum of mean hydrostatic stress, and σ_{loc} is local stress.

The average strain ε_N for void nucleation can be written as:

$$\varepsilon_N{}^{1/2} = H(\sigma_c - \sigma_m) \tag{1.2}$$

where H is an empirical constant.

In order to precisely describe the real condition of void nucleation, Iricibar et al. [4] suggested using particle size and spatial distribution to model the ductile crack nucleation. Rice and Tracey's model [7] for ductile fracture mechanisms is the most widely accepted, the cup-and-cone feature is influenced by the prevailing triaxial stress system. The model replaced the yield stress by effective stress to show the work hardening effect on void growth. This model was further improved by others to include the failure where voids interact and coalesce. Thomason [8] suggested a ductile failure model and he assumed that when the net section between two void reaches a critical stress level $\sigma_{1)}$, the fracture would occur. The ductile crack would be stable when:

$$\sigma_{n(c)} \frac{d}{d+b} > \sigma_1 \tag{1.3}$$

Where 2d is the distance between voids, 2b is the size of void in the direction of maximum principal stress σ_1. If the terms on the left-hand side and the right-hand side of inequality 1.3 are equal, then fracture will occur.

1.1.2 Cleavage Fracture

1.1.2.1 Griffith's Theory

Griffith's energy balance theory [9] is the fundamental to the cleavage fracture mechanism. The Griffith equation suggested that propagation of a crack requires higher energy released from breaking of atomic bonds than the energy needed to create two new surfaces. The equation for fracture stress in plane stress σ_F is given by:

$$\sigma_F = (\frac{2E\gamma_s}{\pi a})^{1/2} \tag{1.4}$$

Where E is the Young's modulus, γ_s is the surface energy per unit area of new crack surface, a is the half length of the crack. For plane strain condition, the equation becomes:

$$\sigma_F = (\frac{2E\gamma_s}{\pi(1-\upsilon^2)a})^{1/2} \tag{1.5}$$

Where υ is Poisson's ratio.

The Griffith equation suits well for brittle materials such as glasses, but for elastic-plastic materials such as metals, the magnitude would be too low to predict the fractur stress. Orowan [10] and Irwin [11] added an extra term γ_p describing the plastic work done around the crack tip prior to fracture in metals:

$$\sigma_F = (\frac{2E(\gamma_s+\gamma_p)}{\pi(1-\upsilon^2)a})^{1/2} \tag{1.6}$$

As γ_p has much greater value than γ_s, the equation could also be written as:

$$\sigma_F = (\frac{2E\gamma_p}{\pi(1-\upsilon^2)a})^{1/2} \quad (1.7)$$

1.1.2.2 Models of Cleavage Fracture

Griffith theory suggested a criterion for the unstable crack growth at a given crack length, but it was not clear for microcrack formation. The tensile results of iron specimens with different grain sizes tested at −196ºC compares the yield stress in compression and fracture stress in tension, as shown in Figure 1.2. Low [12] in his experiment demonstrated that yielding was prior to fracture in fine-grained specimens, whereas in coarse-grained specimens, yielding and fracture happened simultaneously, and this is due to deformation such as twinning or dislocation movement. This experiment proved that the initiation of cleavage microcracks requires prior plastic deformation, but their propagation may require additional loading in fine grain materials. This also suggested the importance of grain size in controlling cleavage fracture.

There were two micromechanisms regarding the formation of microcracks:

Zener/Stroh Micromechanism

Zener [13] suggested the microcracks formed by the coalescence of edge dislocations. Based on this model, Stroh in 1954 [14] found that the dislocation pile-up with stresses around would either result in crack formation or operate a Frank-Read source by pulling it from its locking impurities. At higher temperatures, there is sufficient energy to free the sources locked by impurity atoms, and ductile behaviour is preferred. At lower temperatures, there is no sufficient thermal fluctuation to free the source, it may result in the continuous dislocation pile-up and when it is large enough, a crack is initiated:

$$\tau_{eff} = \tau_y - \tau_i > [\frac{E\,\pi\,\gamma}{4(1-v^2)d}]^{1/2} \quad (1.8)$$

Where τ_{eff} represents the required shear energy, τ_y is the shear stress, τ_I is lattice stress. E is shear modulus, υ is Poisson's ratio, γ is the effective surface energy of ferrite, and d is grain diameter.

The critical stage for Stroh's model is the nucleation of microcrack, providing γ is constant. This criterion focused on the effect of shear stress but ignored propagation control of cleavage demonstrated by Low.

Cottrell's Micromechanism

Cottrell's idea was based on intersecting dislocation pile-ups [15]. In a body-centred cubic iron, the dislocation is glided on intersecting slip planes, as shown in Figure 1.5. A sessile dislocation is formed as the result of dislocation reactions, and Burger's vector is parallel to the cleavage plane. The dislocations sliding on the slip planes attract each other, and the build-up of high-density dislocations result in driving a wedge into the cleavage plane. This model gave a mechanism for the easy nucleation of a micro-crack. This model in combination with the influence of a notch in promoting cleavage fracture, highlighted the importance of tensile stress on cleavage fracture. The critical step of cleavage fracture is thus microcrack propagation rather than microcrack nucleation. Cottrell's model was more widely accepted than Zener/Stroh's model since the latter model could not account for the influence of notches on cleavage fracture. In essence, Stroh would suggest that cleavage fracture resistance would increase at lower temperature since the yield stress would increase.

The effect of carbides on cleavage fracture was investigated by McMahon and Cohen [16] through a series of tensile tests on steel specimens with very low carbon content. The specimens were heat-treated carefully and had similar purely ferrite grain sizes, but the thickness of carbide films located at grain boundary was different. They concluded that specimens with finer and thinner carbides exhibited more ductile behaviour, while specimens with coarser and thicker carbides generated brittle cleavage fracture. Their findings prompted the development of another cleavage microcrack nucleation model based around the failure of carbides, Smith's fracture criterion [17]. It is a propagation-controlled fracture model based on the propagation of a cracked carbide into the ferrite grain:

$$\frac{C_0}{d}{\sigma_F}^2 + {\tau_{eff}}^2[1 + \frac{4}{\pi}\sqrt{(\frac{C_0}{d})}\frac{\tau_i}{\tau_{eff}}]^2 \geq \frac{4E\gamma_p}{\pi(1-\upsilon^2)d} \tag{1.9}$$

where C_0 is the carbide thickness inside a grain with the diameter of d, σ_F is critical tensile stress required for microcrack propagation, τ_{eff} is the effective shear stress, γ_p is the effective surface energy that is required for the microcracked carbide to spread into ferrite matrix.

Smith's criterion does not consider the grain size effect on cleavage fracture. If the term τ_{eff} in Equation 1.9 is replaced with $k_y d^{-1/2}$, where k_y is a constant describing the easiness of unpinning dislocations, and it is independent of the grain size:

$${\sigma_F}^2 + \frac{{k_y}^2}{C_0}\ [1 + \frac{4}{\pi}\sqrt{(C_0)}\frac{\tau_i}{k_y}]^2 \geq \frac{4E\gamma_p}{\pi(1-\upsilon^2)C_0} \tag{1.10}$$

However, Curry and Knott [18] illustrated that the grain size effect in the fracture stress of slow-cooled or normalised mild steel could be represented by the thickness of carbides, as the ratio of carbide thickness to grain size is constant due to the diffusion processes on cooling are similar.

Hence, both parameters were correlated and making it difficult to say which factor is more important. The second term in Equation 1.10 is the dislocation term (initiation) usually accounts for less than 10% of total fracture energy, and if this term is neglected, the equation could be reduced to a Griffith formula:

$$\sigma_F = \left(\frac{2E\gamma_p}{\pi(1-\upsilon^2)r}\right)^{1/2} \tag{1.11}$$

where $C_0 = 2r$.

Cottrell's theory mainly focused on the propagation-controlled fracture rather than nucleation-controlled and this theory continues to be supported.

1.1.2.3 Notched Bar Fracture Mechanical Testing

Tensile tests have limitations on cleavage fracture before necking occurs at temperatures above −196ºC, as the stress conditions are not severe enough, and Orowan [19] assumed the independence of intrinsic microscopic cleavage fracture stress to test temperature. In the early work of Green and Hundy [20], they applied notched bending specimens to determine the minimum depth of notch required to avoid the plastic zone from spreading to the notched surface of the specimens. Knott [21] used bars with various included angles for bending, and the results showed that regardless of test temperatures, the measured maximum principal tensile stress at general yield was equal to the fracture stress. However, as this method used slip line field theory without concerning work hardening, additional tests were required to determine the coincident temperature for fracture and general yield. The maximum principal stress estimation accuracy was also limited by slip line field theory.

1.1.2.4 The Linear Elastic Stress Intensity Factor

Irwin [8] first suggested stress intensity factor K in 1957 to describe a mode I through-thickness crack, with tensile stress perpendicular to the crack, by referring to Westergaard's theory [22] and this was developed as the foundation of linear-elastic fracture mechanics:

$$K = \sigma\sqrt{\pi a} \tag{1.12}$$

Where K is the linear-elastic stress intensity factor, σ is the applied stress, and $\boldsymbol{a}$ is the half size of the micro-crack.

For tests performed at higher temperatures, or the specimens with higher ductility, the plastic deformation is involved at the crack tip. There is a plastic zone developed ahead of the crack tip, and the size of this plastic zone would be too large that linear-elastic stress intensity factor needs some correction.

The size of plastic zone in plane stress condition according to Irwin [11]:

$$r_y = \frac{1}{2\pi}\left(\frac{K}{\sigma_y}\right)^2 \tag{1.13}$$

In plane strain condition:

$$r_y = \frac{1}{4\sqrt{2}\pi}\left(\frac{K}{\sigma_y}\right)^2 \tag{1.14}$$

Where r_y is the plastic zone size. The effective crack length would be a+ r_y.

1.1.2.5 Ritchie, Knott, and Rice (RKR) Model

Ritchie, Knott and Rice [23] investigated the relationship between the microscopic parameter of cleavage fracture stress, σ_F, and the macroscopic parameter of fracture toughness, K_{Ic}. The finite element analysis of the stress field ahead of a blunted crack published by Rice and Johnson [24] was similar to the blunt notch work by Griffith and Owen [25]. The maximum principal tensile stress (σ_{yymax}) is increased by the stress intensification at the crack tip, and when σ_{yymax} is above the microscopic cleavage fracture stress σ_F, unstable fracture was postulated to occur. A characteristic distance, x_c, was introduced into the model for the accuracy in dimensions, this unit is microstructurally dependent, and it was decided to be around two grain diameters. The RKR model can be expressed as:

$$K_{Ic} = \beta^{-(n+1)/2} \sqrt{\frac{x_c}{\frac{\sigma_F^{(n+1)/2}}{\sigma_Y^{(n-1)/2}}}} \tag{1.15}$$

The critical distance and the microscopic cleavage fracture stress (σ_F) are independent of test temperature, and the dependence of K_{Ic} with temperature could be predicted from the material variation in yield stress and work hardening exponent (n) with test temperature.

Curry and Knott verified the RKR model through a series of experimental works by measuring the values of σ_F and fracture toughness K_{Ic} of mild steel with different grain sizes and different carbide sizes [18] [26] [27]. When the grain sizes were above 40μm, the characteristic distance x_c was about 3-4 times the grain size, and for the grain sizes below 40μm, x_c was independent of grain size. For sharp-cracked specimens, the plastic zone size and high stress region are very small, which leads to a steep stress gradient. The carbides of different sizes located within this region compete under varied tensile stress during the nucleation of cleavage crack. For the

blunt-notched specimens, the distance is larger from a micro perspective, the stress gradient is relatively flat. The works from Curry and Knott concluded that the characteristic distance is not correlated to ferrite-carbide microstructure, but related to the probability of finding a microcrack that satisfies the critical size for cleavage fracture propagation from the high stress region ahead of the crack tip. The microscopic cleavage fracture stress is determined according to the largest carbide.

1.1.2.6 Particle-Initiated Cleavage Fracture

Carbides as the initiation point of cleavage microcrack has been widely accepted, while inclusion-initiated cleavage fracture of different steels and weld metals was also found in many other studies [28] [29]. The effect of particle-initiated cleavage fracture was studied by using heterogenous materials containing inclusions [30], and the maximum principal stress of particles is described below:

$$\sigma_1 = \Sigma_1 + k(\Sigma_{eq} - \sigma_0) \tag{1.16}$$

Where Σ_1 is the remote maximum principal stress, Σ_{eq} is the remote von Mises effective stress, σ_0 is the initial yield stress, k is dependent on shape of the particles and loading orientation. As the second term of Equation 1.16 is stress intensification, and thus σ_1 is equal to critical fracture stress σ_{Ic}. As test temperature increased, the yield stress decreased, and thus critical fracture stress increased with test temperature. It should be noticed that this equation does not account the differences between particle cracking or matrix-particle decohesion.

For particle-initiated cleavage failure, the microcrack firstly initiates from a brittle particle such as carbides or inclusions induced by slipping, then crack propagates across particle or particle-matrix interface along (100) cleavage plane of the neighbouring matrix, and then propagates

across grain boundary with grain-sized crack length [31] [32]. The effective surface energy of particle-matrix γ_{pm} is not affected by temperature, but energy stored in matrix-matrix (or boundary energy) γ_{mm} is temperature-dependent, and it will be higher as the temperature increases, and then becomes the dominant controlling factor of cleavage fracture [32]. The ratio between energy stored in matrix and surface energy of the particle at the initiation site is often greater than one as the result of energy dissipation in plastic deformation of the matrix [33].

1.1.3 Elastic-Plastic Fracture Mechanisms

Plastic deformation involvement at the crack tip would blunt the sharp crack, leading to a rapid increase of strains than stresses. Wells in 1961 [34] found that critical stress intensity factor K_{Ic} could not define the fracture resistance of different metals through experiments, and he observed that before fracture, notch has been stretched comparing to the original crack, and the sharp crack tip was blunted. Therefore, the crack opening displacement (COD) or crack-tip opening displacement (CTOD) is introduced as a measurement of fracture resistance. COD is well-related to Griffith energy theory with small-scale plastic deformation by considering plastic zone correction suggested by Irwin and Dugdale-Barenblatt model [35] [36].

Crack blunting is related to the fracture toughness of materials, as plastic work is required for the increase of CTOD. There should be a critical CTOD value, and its relationship with stress intensity factor K_I following linear-elastic fracture mechanics can be presented by:

$$\delta = \frac{{K_I}^2}{nE\sigma_y} \tag{1.17}$$

Where δ is CTOD, n = 1.0 for the plane stress condition, n = 2.0 for the plane strain condition, E is Young's modulus. This approach is still valid for linear-elastic fracture mechanics under

the condition of more plastic deformation at the crack tip. It will be invalid if total yielding occurs.

Rice [37] in 1968 came up with the concept of energetic contour path integral J. J-integral is path-independent, and it is the energy release rate of a nonlinear-elastic body contains a crack. An aerial integral Equation 1.18 can be used to describe J from an arbitrary counter clockwise path, Γ, around the crack tip:

$$J = \int_{\Gamma}(wdy - T_i \frac{\partial u_i}{\partial x} ds) \tag{1.18}$$

Where w is strain energy density, T_i is the outward traction vector components, u_i is the displacement vector components, ds is the increment of length along the contour Γ. Strain energy density is defined as:

$$W = \int_0^{\varepsilon_{ij}} \sigma_{ij} d\varepsilon_{ij} \tag{1.19}$$

Where $T_i = \sigma_{ij} n_j$, and n_j is the unit vector components normal to Γ.

For linear-elastic materials, with accordance to Irwin, energy release rate J and G is related to the stress intensity factor K_I in Mode I loading:

$$J = G = \frac{{K_I}^2}{E} \tag{1.20}$$

Equation 1.21 represents plane stress conditions, and for plane strain conditions:

$$J = G = \frac{{K_I}^2}{E}(1 - v^2) \tag{1.21}$$

The critical J-integral J_{IC} can be used to represent fracture toughness of materials.

Griffith and Owen [25] suggested an advanced elastic-plastic analysis for a bent bar by finite element modelling. A linear work hardening rate was included, and the maximum stress intensification ahead of the notch root for varied load/load at general yield was predictable. The analysis also found that the maximum tensile stress was inside the plastic zone with some distance from the elastic-plastic boundary.

1.1.4 Ductile-to-Brittle Transitions

The above reviews on cleavage fracture suggest that it is more propagation-controlled. Orowan [10] suggested that the cleavage fracture stress is inversely proportional to the square root of the grain size, in accordance with the Griffith theory. It is verified by Petch [38] with experiments. Petch also highlighted the cleavage strength is comparable to the lower yield stress of ferrite. Yielding and the propagation of a Lüders band arise from the shear stresses around the pile-up.

Cottrell's theory [15] focused on the intersection of dislocation pileups. Crack nucleus is formed during the dislocation coalescence on two intersecting {110} slip planes:

$$\frac{1}{2}a[\bar{1}\bar{1}1] + \frac{1}{2}a[111] \rightarrow a[001] \tag{1.22}$$

In which the new dislocation is parallel to the {001} cleavage plane and if let it run, it would form a cleavage crack. If the crack size and slip bands are greater than Griffith value, the crack would continue to grow and results in cleavage fracture, and if the joint value is smaller than Griffith value, the crack would not exceed the critical value and become blunted due to the plastic flow at the crack tip. A transition would occur in grains with the diameter of 2d when the following equation is satisfied:

$$\left(\sigma_i d^{1/2} + k_y\right)k_y = \beta\gamma\mu \tag{1.23}$$

Where σ_i is shear stress, β is a constant related to deformation mode, γ is the surface energy of the crack, μ is shear modulus, k_y is related to Hall-Petch equation with the shear stress for yield σ_y:

$$\sigma_y = \sigma_i + k_y d^{-1/2} \tag{1.24}$$

The value of k_y indicates the stress required to initiate dislocation, σ_i represents the stress hinders the dislocation motions, and this term can be divided into two parts according to Heslop and Petch in 1956 [39]:

$$\sigma_i = \sigma_1 + \sigma_2 \tag{1.25}$$

Where σ_1 is the hardening effect from impurities, precipitates, etc., and σ_2 is the resistance from the lattice. By increasing k_y, σ_i, or d, cleavage fracture would be preferred. Temperature is a factor that affects σ_i of materials with a body-centred cubic (BCC) crystal structure, as BCC crystal structure has 24 slip systems but a lower atomic density compared to face-centred cubic (FCC) crystal structure. The movement of atoms is temperature-sensitive, the decrease in temperature would increase σ_i, resulting in the ductile-to-brittle transition. Other factors such as radiation damage or strain rate can also affect σ_i. Irradiation can increase yield stress with $\Delta\sigma_i$ without affecting cleavage fracture stress [40], while strain rate can affect both σ_y and σ_i. The specimen geometry could affect ductile-to-brittle transition temperature by affecting stress state, and β in Equation 1.23 can incorporate this geometry effect.

For the occurrence of cleavage fracture, a critical stress σ_F should be reached over a critical distance ahead of the crack tip, even though the distance is microstructurally significant. If the

stress is below this critical value, the fibrous fracture would occur, and a stable crack growth would be initiated before final cleavage failure. The reasons for ductile-to-brittle transition are summarised below [41]:

1) The ductile crack growth rate in homogeneous materials increases, and the strain rate at the crack tip also increases, in which the local stress at the crack tip would be raised by the strain rate. Once the stress exceeds the critical cleavage stress, the cleavage fracture would occur. According to Zhang's work of monitoring the ductile crack growth rate of fracture toughness test by potential drop method, the crack growth rate at the first 1.5 to 2mm accelerated until reaching the maximum load, and then the crack growth of the material would drop, and the specimens would fail with plastic collapse.
2) If there is a stress-raising defect exists in a specimen, e.g., a notch or other flaw, another fracture mechanism is possible to take place. The notch could be opened by applying tensile stress, and ductile tearing could start at the root of the notch. A crack could be generated during this ductile tearing formed at this region, in which sharpens the notch, and the stress state would be raised to a level much higher than before. This increased cleavage stress may overpass the critical cleavage fracture stress and induce cleavage fracture.

1.1.5 Master Curve Methodology

Due to the sudden and catastrophic nature of cleavage fracture, ductile-brittle transition should be avoided for the development of engineering materials. Apart from Charpy impact test and drop weight test, the Master Curve methodology was suggested to analyse the behaviour of ferritic material at the transition region.

There is a Wallin, Sarrio and Törrönen (WST) cleavage fracture model developed by Wallin, Sarrio and Törrönen that describes cleavage fracture statistically [42]. According to Griffith instability criteria for a round carbide in the ferritic matrix, WST model gives the relationship between the size of the crack initiators and the local stress that caused failure [43]:

$$r_{CRIT} = \frac{\pi E(\gamma_s + w_p)}{2(1-v^2)\sigma_{yy}^2} \tag{1.26}$$

Where r_{CRIT} is the radius of inclusion that causes cleavage fracture, E is Young's modulus, v is Poisson's ratio, γ_s is the surface energy of the matrix, w_p is the plastic work needed for crack propagation, σ_{yy} is a function of flow properties of the material. If there is an initiator located before the crack tip with a radius exceeding the critical value, cleavage fracture can occur easily. If the size distribution of carbides and the number of carbides per unit volume are known, the probability of fracture can be expressed as [44]:

$$P_f = 1 - \prod_{X=0}^{r_{plastic}} [1 - P(r \geq r_{crit})]^{N \cdot F \cdot B \cdot dX \cdot X \cdot \sin\theta} \tag{1.27}$$

Where P_f is the probability of cleavage fracture, X is the distance at the onset of the crack tip, $r_{plastic}$ is the distance between the crack tip and the interface of elastic and plastic, N is the number of initiation sites of cleavage crack per unit volume, F is the fraction of initiation sites affecting fracture, B is the thickness of specimen, dX is the summation volume width, $X \cdot \sin\theta$ is the summation volume height, θ is the angle that measuring from crack plane in counter-clockwise direction, and this angle is assumed to be constant.

In the 1970s, a PVRC task group collected all valid K_{Ic} (dynamic initiation) and K_{Ia} (crack arrest) fracture toughness data at transition temperature to develop an ASME code as a fracture

mechanics methodology for pressure vessel steels [45]. This methodology also collected drop-weight and Charpy impact test data. All the test temperatures were normalized to a single transition temperature, RT_{NDT}. The plotted underlying curve was defined as the universal lower bound curve for all ferritic pressure vessel steels, and it was applied for thirty years. The RT_{NDT} was originated from an older test method with few direct relationships with fracture mechanics [46].

The data scatter gained more attention when a better refined test method for structural steels was developed. Landes and Schaffer found the size effect for transgranular cleavage failure[47]: smaller specimens tend to have higher fracture toughness than larger specimens. They came up with two possible reasons, the first is that the phenomenon might be due to constraint loss. As the specimen size increases, the plastic zone at the crack tip grows larger, and it is sufficient to have interactions with specimen free surface. Constraint loss would lead to a large increase in deformation, and the driving force to fracture is also enhanced, therefore the toughness value is also elevated. Compared to larger specimens, smaller specimens are more easily affected by loss of constraint, as the plastic zone-free boundary interaction of a small specimen tends to occur at lower deformation levels, which would increase the toughness value. The second one is the fracture initiation site sampling. The toughness value depends on the microstructure of the material and the location of the weakest point along the crack front. The latter may vary from specimen to specimen, and it is more obvious for ferritic steels fractured in a transgranular way. Ferritic steels tested at transition region generally have a very small number of initiation sites, some have single initiation site, which suggests that the toughness behaviours of ferritic steels are controlled by local initiation site.

Landes and Schaffer analysed the data scatter of the multiple test results of a NiMoV generator-rotor steel. The outcome two-parameter Weibull model can be expressed as:

$$P_f = 1 - exp - (\frac{J_C}{\theta})^b \quad (1.28)$$

Where P_f is the probability of cleavage fracture, J_c is the J-integral level at the onset of cleavage fracture for a specially selected specimen, θ is a scale parameter, and b is the Weibull slope of the model. After examining the fracture surfaces of the tested specimens, they found that the distance between the initiation point of cleavage cracks to the initial crack front was related to J_c values and the J-integral at the point of onset of cleavage instability, and therefore they confirmed the data scatter of J_c values and the weakest-link phenomenon, and it was further proven by Heerens and Read in 1991 [48].

The establishment of the weakest-link theory encouraged the future work by Wallin and other co-workers in 1984 [49]. They developed a method to test the cleavage fracture toughness of materials by combining the weakest-link theory with cleavage fracture mechanical model stated by Curry, Knott, etc. The elastic-plastic stress intensity factor, K_{Jc}, can be used to calculate the critical flaw size and the critical stress for a given flaw. Its relationship with J_c is given below[27]:

$$K_{Jc} = (EJ_c)^{1/2} \quad (1.29)$$

The two-parameter Weibull distribution is written as:

$$P_f = 1 - \exp\{-[\frac{K_I}{K_0}]^b\} \quad (1.30)$$

Where K_I is the applied stress, K_0 is a normalization factor. Cleavage initiator distribution does not affect the scatter of fracture toughness values. However, this model gives wide tolerance bounds, and the lower bound is too low. In order to enhance the reliability of this Weibull model, Wallin analysed K_{Ic} data from a set of tests with different sizes of samples by Monte Carlo, and he introduced K_{min} in his 1984's paper, and it is a value of applied stress that is too low for cleavage fracture to occur ($P_f = 0$) as the lower bound value. If the J_c value is zero, then the probability P_f in Equation 1.31 can be finite if there are sufficient amount of data. Below is the new three-parameter Weibull model [42]:

$$P_f = 1 - \exp\{-[\frac{K_{Jc} - K_{min}}{K_0 - K_{min}}]^b\} \quad (1.31)$$

Where K_0 is the toughness that corresponds to a 63.2% probability of failure, and $K_0 - K_{min}$ is the scale parameter. Wallin gave two reasons why K_{min} was not set to zero: 1. With lower values of K_I, cleavage initiator at the crack tip could be larger than that of the volume of material at the crack tip subjecting to plastic flow, which would against the fact that the propagation of cleavage fracture requires the plastic flow [17]. 2. The initiation of cleavage fracture always starts from a pre-existing crack. It was noticeable that if K_{min} was set to be 20MPam$^{1/2}$, then the Weibull slope b was approaching to 4. However, it only happens when there are sufficient number of specimens. This work concluded that comparing to other two scale parameters K_{min} and b, a limited number of data would be enough to treat $K_0 - K_{min}$ as a known constant. Wallin also suggested that the minimum number of specimens required to estimate the data scatter was three. Since then, there were many works surrounding this discovery taking place. The round robin activity was taken place in 18 different laboratories located in different countries, and the material they used is from one single A508 Class 3 pressure vessel steel plate [50]. They took three test temperatures: −50ºC, −75ºC and −100ºC, and for each temperature, five 1T C(T)

specimens were tested. The outcome illustrated that most of the predicted median values of K_{Jc} were close to the combined median value of $K_{Jc.}$ The results also illustrated that despite the different test temperatures, taking K_{min} as 20MPam$^{1/2}$ and b as 4, the three-parameter Weibull distribution model still had a good fit to all test data.

The improved understanding of fracture mechanism and statistical methods gave the emerge of the Master Curve methodology. This methodology contains three characterizations [51]: 1. Ferritic steels with certain microstructures would show data scattering. The data scatter is often fitted by a three-parameter Weibull cumulative probability statistical model. 2. J-integral is calculated and converted into K_{Jc}. The specimens would remain constraint even with 1/40th of the size required for K_{Ic} defined in ASTM Standard E399. 3. The weakest-link theory can explain the specimen size effect, which enables data obtained from one size of specimens convert into another size. Here are some reasons that support the application of this master curve referring to WST statistical model of cleavage fracture [44]:

1. Plastic deformation is required for the occurrence of cleavage fracture. Nearly all the RPV are ferritic steels, and they all have the same BCC crystal structure.
2. The crack tip stress state at failure can be determined if the amount of yielding is small, and initiator distribution of cleavage fracture of a material can affect the median of fracture toughness. However, initiator distribution has no correlations to the scatter of toughness values, and therefore the scatter of toughness values will not be affected by the materials.
3. The cleavage crack initiation sites are distributed randomly throughout the material. The welding may affect the homogeneity of microstructure of material, but for other steels

produced with grain refinement and tempering procedures, they can keep their homogeneity.

All the works above led to the development of ASTM Standard E1921-97 'Test Method for Determination of Reference Temperature, T_0, for Ferritic steels in the Transition Range'. The fracture toughness results of ferritic steel can be plotted against test temperatures to form a 'Master Curve'. In Wallin's paper published in 1993, he suggested the equation for the position of the Master Curve [44]:

$$K_{Jc(median)} = 30 + 70 \cdot \exp\left[0.019(T - T_0)\right] \quad (1.32)$$

Where T is the test temperature, and T_0 is the reference temperature at which the median K_{Jc} values of six or more 1T specimens equals to 100MPam$^{1/2}$. It is a normalized equation showing the shape of the median K_{Jc} for 1T specimens, and the position of this universal curve of cleavage fracture depends on the reference temperature T_0.

ASTM Standard E1921 is applied to all ferritic and bainitic steels with homogeneous microstructures, and it is not limited by the size of the specimens according to the weakest-link theory, which enables the data conversion between different specimens [51]. The test temperature selection is suggested to use the lower part of the ductile-to-brittle transition region in order to get closer to real T_0. The positions of the curve are influenced by the microstructures of different steels with respect to test temperatures [52].

Lots of experimental works have supported this Master Curve methodology. Comparing to the early fracture mechanics ASME K_{Ic} reference curve methodology, the Master Curve method only uses data tested based on fracture mechanism. The Master Curve method is more statistical-based and gives better prediction on the fracture toughness of materials under

cleavage fracture compared to ASME code. The experimental results from the Japanese K_{IR} Project also supported that the reference temperature obtained by the Master Curve method was a stronger indexing parameter than RT_{NDT} in ASME Code [53]. Among all the test specimens stated in ASTM Standard E1921, compact tension specimen is suggested to have a more conservative estimation of T_0 compared to other specimens. The appearance of side grooves may decrease the mean fracture toughness in the upper shelf of the transition region and increase the mean fracture toughness in the lower shelf of the lower transition region. Using CVN test to obtain the value of reference temperature is less reliable compared to using C(T) and SE(B) specimens, as CVN specimens would give much lower reference temperature values than other specimens. The Master Curve method also has limitations. It has the best accuracy for failures occurring under conditions of small-scale yielding only. It is only applicable to homogenous materials, but not to inhomogeneous materials such as heat-affected zone (HAZ). It is also found to be not applicable at temperatures above room temperature [54]. However, this does not affect its effectiveness, and it has been proved to be a valid way to find out the integrity of RPV materials and to ensure the safety of nuclear power plants during the operation time.

1.2 A Brief Review of HSLA Steels Application in Nuclear Industry

1.2.1 Nuclear Power Plant and Material Selection of Containment Structure

Nuclear power has the advantages of very low carbon emission, high energy capacity, very reliable operation, longer operation life, and more cost-effective in the long term than other types of energy sources. It is also more reliable than other green energies as its operation is not as weather-dependent as solar or wind energy. However, safety is always a big concern for

nuclear energy, therefore the construction of nuclear power plants and the selection of nuclear materials should be very careful to avoid any failure.

Containment vessel is the third barrier for radioactive substances and acts as a heat exchanger, and it should be able to withstand internal pressure caused by loss of coolant accident (LOCA) or main steam-line break (MSLB) [55]. Conventional containment structure uses pre-stressed concrete, but AP1000 Advanced Passive Nuclear Power uses steel-made containment and reinforced concrete shield building [56] [57]. AP1000 is a generation III nuclear power plant designed by Westinghouse, and it is a pressurised water reactor [55]. The illustration for AP1000 containment vessel is shown in Figure 1.7.

Containment vessel steel should satisfy the properties of good mechanical properties such as toughness and strength. As large containment vessel is often constructed by welding, vessel steel should also have good weldability to ensure the safety of nuclear power plants during operation. According to the requirement suggested in ASME NE Code 2007 [58], materials with a thickness of more than 44.5mm are required to apply post-welding heat treatment (PWHT), but another ASME CODE case N-841 in 2015 suggested that the PWHT could be exempted if the thickness of the steel plate is in the range of 44.5 to 60mm [59]. The latter case was not approved by the US Nuclear Regulatory Commission due to safety concerns [60]. As an alternative, simulated post-welding heat treatment (SPWHT) is performed on as-delivered steel plates, and it is a preliminary inspection of steel welding ability without doing welding tests on the steel plates.

As a better cost-effective solution than austenitic steels, ferritic/martensitic steels have been widely applied in the nuclear industry, for example, FI ferritic steel is applied as the fuel cladding tubes, A508 Gr. 3 and A533B are used as the reactor pressure vessels. However, apart

from the possible non-homogeneity of the microstructure due to the larger thickness, ferritic/martensitic steel plates are subjected to ductile-to-brittle transition under the effects of decreased temperatures and increased irradiation dose. Their cryogenic properties are mainly achieved with heat treatment in ferrite + austenite region after rolling [61].

1.2.2 High-Strength Low-Alloy Steels and Effects of Alloying Elements

The nuclear structural steels mentioned in the previous section such as A533B and A508 have low alloying element contents. High-strength low-alloy (HSLA) steels are micro-alloyed , and they have a balanced combination of mechanical properties such as strength, toughness, corrosion resistance, weldability, formability, and relatively cheaper production cost, which make them ideal for not only nuclear industry, but other engineering applications such as offshore pipelines and aeronautical components [62].

The alloy element content can affect the mechanical properties of steels via influencing their microstructure. The alloying elements in steels could either be the solid solution of iron, forming inter-metallic compounds with Fe or with each other, forming non-metallic inclusions such as oxides and sulphides, forming carbides, or being in the free state [63]. Oxygen and sulphur have limited solubility in the solid phase of iron and form some oxides and sulphides of iron, such as FeO and FeS. The ductility of steel is decreased with increasing oxides or sulphides. The most detrimental effect on toughness and ductility of steels is the deformation of inclusions within the matrix, therefore the content of these elements and their inclusions are unwanted.

Some elements such as silicon, manganese, and aluminium, they are acceptable for commercial steels due to their affinity nature to oxygen [64]. They act as deoxidizers, and they could form deoxidation products by adding into molten steel. Unlike oxygen, sulphur could not form non-

metallic sulphides with most of the elements, and therefore they should be removed by slag refining and precipitation reactions. In order to prevent the formation of iron sulphide in steels, manganese is often added to form manganese sulphide (MnS), which has a higher melting point, and enhances the hot working of steels.

HSLA steels have a restricted carbon content, with carbon equivalent CE of less than 0.3 [65]. It was found by Irvine and Pickering in 1957 that bainitic/martensitic steels with lower carbon content have better tensile ductility than steels with higher carbon content [66], as carbon content would influence the size and number of carbides: the higher the carbon content, the higher the number of carbides per unit volume in steels. Steels with a higher density of carbide particles would result in a shorter separation distance in fracture due to faster micro-void coalescence, thus the ductility is lowered. A lower carbon content could also avoid the increase in hardness at heat affected zone (HAZ) [67].

The reduced strength in steel due to the reduction of carbon content could be compensated by optimizing the addition of other alloying elements. In the subsequent work from Irvine and Pickering in 1965 [68], they found that the strength of low carbon bainitic steel could be improved by solid solution strengthening. Elements such as Cr, Ni, V, Mo, and Ti can strengthen HSLA steels [69].

The term P_{CM} is defined as the following [67]:

$$P_{CM} = C + \frac{Si}{30} + \frac{Mn}{20} + \frac{Cu}{20} + \frac{Ni}{60} + \frac{Cr}{20} + \frac{Mo}{15} + \frac{V}{10} + 5B \tag{1.33}$$

The value of P_{CM} is weld-crack sensitive, and it includes large temperature softening resistant elements such as Mo, V, Cr, Si, etc [70]. The reduction of phosphorus and sulphur has been

proven to improve the toughness of the base material and suppress the toughness loss of the matrix [67].

The content of manganese in HSLA steel is usually between 0.4-2.0 wt.%. With a higher content of 1.5 to 2.0 wt.% of Mn, acicular ferrite formation or bainitic transformation is promoted, and pearlite reaction slows down greatly. The manganese content of more than 2.5wt.% should be prohibited, as it would cause manganese segregation and thus lead to a brittle banded structure.

The addition of N, Nb, V, and Ti is intended to refine the grain size of steel by changing sulphides from elongated shapes into discrete particles. The addition of calcium could also control the shape of inclusions. N could form carbo nitride in liquid solutions. The recrystallisation and grain size of austenite are restricted by their precipitation as fine dispersions in austenite. At high temperatures, titanium could form stable nitride, which can control the austenite grain size at reheating temperatures below hot working. However, titanium nitride with the properties of high hardness and brittleness, together with its high interfacial bonding with the surrounding matrix, could become the initiator of cleavage fracture.

1.2.3 Microscopic Features of HSLA Steels

HSLA steels are typical ferrous materials with body-centred cubic structure due to their low carbon content. In order to optimise the mechanical properties and the effects from alloying elements, heat treatments are carefully selected. Steels are often treated in a sequence of austenising, quenching, and tempering, and the microstructure can contain martensite, bainite, retained austenite, or ferrite by adjusting cooling rate, tempering temperature, and tempering time. These microscopic features can be either beneficial or detrimental to the mechanical properties of steels.

Martensite

Martensite is formed by fast cooling of austenite, and it is the product of transformation reaction without diffusion. The face-centred crystal (FCC) lattice of austenite is transformed into a distorted BCC lattice. The compositions of steel affect the cooling rate for martensite transformation, and also affect the formation of other non-martensitic transformation products. M_S is defined as the starting temperature of diffusionless transformation.

Prior austenite grain size restricts the size of martensite. Martensite with smaller grain size is preferred due to the small internal stress and isotropic properties. Therefore, any heat treatment that could result in austenite grain growth before cooling below M_S should be avoided.

The martensite is often classified as lath martensite or plate martensite according to the morphology, and the former one is often related to low to medium carbon steels. The lower carbon content (<0.20%) of steel in general has the structure of BCC. There are many dislocations within the lath martensite, as the invariant shear is often undertaken by dislocations. Then these laths form larger packet. For alloys with the M_S below ambient, plate martensite could be found with lenticular shape, and very fine twins could be found within these plates. Twins could also be found in lath martensite, however, according to the TEM result from Tan et al [71].

The transformation of FCC to BCC or body-centred tetragonal (BCT) results in a large number of defects such as substitutional solute atoms, prior austenite grain boundaries, vacant lattice, twins, and dislocations. Steel is often reheated above ambient in order to improve toughness, and thus carbon could be removed from solid solution and precipitates out as carbides. Low-carbon steel is preferred for improved toughness and weldability and a lowered quench-cracking. The embrittlement of tempered martensite can be avoided by adding silicon. Silicon

could prevent the growth of ε carbide and cementite, and maximise the yield strength and notch toughness [72, 73].

Bainite

Bainite was detected by Davenport and Bain in 1929 [74]. Bainite could be formed in steels with a wide range of temperatures during isothermal transformation of austenite or during continuous cooling. Similar to martensite, bainite formation has a displacive mechanism, which can minimise the strain energy associated and makes bainite grow into thin plates. Bainite forms at the temperatures between M_S and ferrite formation temperature, or at the cooling rates which is too fast for diffusion to form other transformation products but insufficient to form martensite.

Bainite mainly divides into two forms: upper bainite and lower bainite. Upper bainite consists of aggregates of ferrite platelets, and each has a thickness of about 0.2μm and a length of 10μm [75]. They are initiated from austenite grain boundaries, and they are in parallel as they have the same crystallographic orientations, with low-angle grain boundaries or thin cementite plates located between the platelets. The clusters formed due to platelet aggregation is called sheaves. During the formation of bainitic ferrite, residual austenite is enriched with carbon, cementite precipitates from the austenite layers, and cementite particles/layers are located within these sheaves, the amount of cementite is related to the carbon content of the steel. When alloying elements such as Al and Si are added, the formation of cementite can be restricted.

Lower bainite has a similar microstructure to upper bainite, the only difference is that the carbides can also precipitate inside the ferrite platelets. The orientations of carbides are related to the ferrite they initiated, and therefore they are in parallel arrays, with 60° to the bainite plate axis, which makes lower bainite different to the tempered martensite. The latter microstructure has carbides precipitate in Widmanstätten arrays. The carbides from lower bainite are fine in

size, with a thickness of a few nanometres, and a length of 500nm. As carbides precipitate within the ferrite platelets, carbon is partitioned into residual austenite, and carbides are further reduced and refined. In this case, lower bainite is often tougher than upper bainite.

Granular bainite has the appearance of equiaxed bainitic ferrite matrix and M-A constituents. It was first found by Habraken [76] in the late 1950s. The formation of granular bainite is at higher temperatures than upper bainite by continuous cooling. A low-carbon content is necessary for the formation of granular bainite to limit the existence of austenite or carbide in sub-unit grains.

Retained Austenite

The formation and influence of retained austenite would be reviewed in detail in the nickel steel section.

1.2.4 SA-738 Gr. B High-Strength Low-Alloy Steel

SA-738 Gr. B steel is a high-strength low-alloy (HSLA) steel under the American Society Mechanical Engineers (ASME) SA738/SA738 M standard [1], and it was preliminary designed as pressure vessel steel for intermediate and low-temperature application, later it is also applied as containment vessel of pressurised water reactors such as AP1000 and CAP1400 [55]. Its heat treatment follows quenching and tempering procedures, and its microstructure varies under different tempering temperatures, according to the experimental work from Li et al. [77]: the microstructure of as-quenched steel was lath martensite, as the tempering temperature increased, M_3C carbides precipitated out and grew, and at the tempering range of 690 to 710ºC, carbides would stop growing as the enrichment of carbon and other alloying elements in austenite. Ferrite became polygonised as tempering temperature increased and fully polygonised after 690ºC. At 670ºC, martensite plates precipitated out and grew along grain during the cooling

process after tempering. The drop in strength and toughness were deeply correlated to the amount of plate martensite as dislocation movements would be hindered and plugged, plate martensite would become stress concentrator, and thus microcrack could be easily initiated and grow at plate martensite or the surrounding matrix of plate martensite, which may cause cleavage fracture.

The work from Li et al. [77] mainly focused on microstructure evolution and the corresponded tensile strength and toughness of SA-738 Gr. B steel. Liu et al. [78] have carried out investigation on mechanical properties of SA-738 Gr. B steel plates with the thickness of 55mm and 103mm at ductile-to-brittle transition region from −100ºC to room temperature, and the properties analysed including tensile strength, impact toughness, fracture toughness, etc. The specimens obtained from the 55mm-thick steel plate had excellent cryogenic properties, regardless of thickness and heat treatment conditions (QT vs. SPWHT), while 130mm-thick steel plate might need further treatment to become more homogeneous to meet the requirement for containment vessel materials. Wang et. al [79] also investigated the weldability of SA-738 Gr. B steel by comparing the mechanical properties and microstructure of as-delivery (QT) specimens and specimens with an additional SPWHT (QT with an additional heating procedure at 600ºC for 10 hours). The tensile tests were carried out at a temperature range of −80 to 20ºC, and CVN tests were carried out at a temperature range of −100 to 20ºC. Their results showed that the carbide size of SPWHT specimens were larger than that of as-delivery specimens, and they concluded that this should be the reason for reduced strength and toughness of SPWHT specimens. Ma et al. [80] investigated the mechanical properties and irradiation behaviours of SA-738 Gr. B steel, and the material exhibited some irradiation resistance with a radiation dose up to 1dpa (displacement per atom), and the maximum neutron dose for normal operation in 60 years is no more than 0.05dpa [81].

The above works are mainly concentrated on mechanical properties of SA-738 Gr. B steel at transition region, while the lower shelf behaviour of this steel was not investigated much. Therefore, it should be worth analysing the mechanical properties and fracture mechanism of this low-temperature steel.

1.3 A Brief Review of Nickel Steels for LNG Industry

1.3.1 Development of LNG Storage

As a relatively clean, non-toxic, non-corrosive, and low-carbon energy, natural gas is preferred to meet the energy demands as well as sustainable development goals. The storage and transportation of liquified natural gas (LNG) saves a volume factor of more than 600 of natural gas, which is more economical than storing natural gas, and LNG is safer in liquid form as it cannot be ignited. However, the very low temperature of LNG is also very challenging for the properties of the storage materials. In 1962, prestressed concrete was verified to be suitable for LNG storage after testing by Linde and the Institute of Gas Technology [82]. In 1964, a 2000m^3 LNG tank was completed by Preload (Cryocrete/Kvaerner) for Gaz de France at Nantes, and it has a prestressed concrete outer layer and Invar membrane inner container. An 80,000 m^3 LNG tank with a prestressed outer layer and flexible inner container was built in Texas Eastern of Staten Island, New York. In the late 1970s, M. W. Kellogg Ltd designed the Full Containment type LNG tanks for Abu Dhabi Gas Liquefaction Co. and Abu Dhabi National Oil Co. The tank has a PC outer wall, 9Ni steel inner wall, and reinforced concrete roof, and the project was completed by CBI in 1985 [83].

The later work started in the early 80s was focused on improving the resistance of the inner tank materials to brittle fracture and using proper welding procedures. Steels with 5-9% nickel

content, especially 9% nickel steel, have been widely used for low-temperature applications such as LNG storage and transportation containment vessels, with the advantages of relatively high yield stress as well as lower cost than stainless steel [84]. 9% nickel steel is proven to have good cryogenic toughness, great strength, good ductility, and good weldability, and it has been widely used in the LNG industry as the inner wall of storage tanks and pipelines.

1.3.2 Nickel Steels and Effects of Nickel Content on Cryogenic Properties

Nickel steels are usually subjected to quenching and tempering (QT) heat treatments, and their microstructure is mainly composed of tempered martensite. During the transformation from FCC to BCC, many defects are formed as a result of strain change. If the carbon content is higher, the primary defects would be internal twins, and they will be too brittle to use. Like other high-strength structural steels, nickel steels have relatively lower carbon contents with the primary defects of dislocations, and the microstructure is mainly lath martensite, which combines good toughness and good strength [85] [86].

Cooling from austenization to room temperature could not transform all the austenite into martensite/bainite completely, especially under lower temperatures, and may results in a portion of retained austenite. Retained austenite has the features of block or film and is located between martensite laths or prior austenite grain boundaries, as grain boundary energy is lower for heterogeneous nucleation [87] [88]. The concentration of carbon as well as other austenite stabilising elements in film austenite is higher than the block austenite, due to the morphology of film austenite is more prone to the segregation of austenite stabilising elements into austenite [89]. Even with a lower carbon concentration, film austenite is more stable than block austenite. This is due to the surrounding matrix of film austenite is martensite, which is stronger than that of block austenite with the surrounding proeutectic ferrite matrix. Film austenite would

experience a higher hydrostatic pressure than block austenite due to the residual stress inside [90]. Film austenite also has better tensile elongation than block austenite [91].

The amount of retained austenite has a positive correlation to nickel content, and the addition of nickel content as well as increasing retained austenite content have proven to enhance the cold resistance of nickel steels, which should be determined by their microstructure. Strife and Passoja [92] compared 5Ni and 9Ni steel, and they found that after QT treatments, 9Ni steel had higher retained austenite content and better cryogenic toughness than 5Ni steel nickel steels, and higher degrees of work hardening in tensile tests as the result of transformation from austenite to martensite at 77K. Wang et al. [93] increased the nickel content of steels from 3wt.% to 9wt.%, and then retained austenite gradually appeared within the matrix and increased with nickel content, while cementite precipitates decreased. The mechanical properties including impact toughness, yield stress and tensile strength increased with the increasing nickel content as well.

Transgranular cleavage fracture is correlated to the block size of the lath martensite in nickel steels. The existence of retained austenite within the martensite lath could hinder the propagation of cleavage cracks, and thus its crystallographic block sizes are refined [94]. Retained austenite is further refined as the nucleation of martensite is restricted. The cleavage fracture stress σ_F is raised due to this refinement, and the toughness of steel is increased [95].

The toughness of nickel steel is also improved through scavenging carbon and other deleterious elements from ferrite by retained austenite, according to Marshall et al [96]. The existence of retained austenite could lead to the depletion of interstitials from the matrix, the resistance to cleavage fracture is enhanced [97] [98]. The carbon content is limited in the matrix as thermally stabilised retained austenite is formed by attracting carbon from the surrounding matrix during

tempering process, which has an inhibiting effect on carbide formation [92] [96] [99]. Cementite precipitation is also eliminated by retained austenite, DBTT is thus lowered, and the impact toughness is improved. The results from Wang et al. [93] exhibit a slow increase in strength when the nickel content increased from 5% to 7%, and this is due to a decrease in cementite content with an increase in nickel content, as cementite could inhibit the movement of dislocations and strengthen the material. A decrease in cementite content will reduce the precipitation strengthening, while increase in nickel content enhances solid solution strengthening as nickel could move towards ferrite matrix and raise the staking fault energy to hinder dislocation movement [100].

The external load can induce the transformation of retained austenite to martensite during deformation at the crack front of 9Ni steel, and this is called transformation-induced toughening (TRIP) [101]. The TRIP effect is correlated to retained austenite content [102]. The volume expansion introduced by this TRIP effect could release local stress concentration [103] [104], and improve crack arrest properties and cleavage fracture stress. The retained austenite could also deform plastically in the vicinity of fracture path under external load, the toughness as well as the fatigue resistance of steel is improved via the crack blunting [105] [106].

Retained austenite could be beneficial if it satisfies a high thermal stability of austenite and a high mechanical stability of austenite. The major stabilising elements are Ni, C, and Mn. High thermal stability of 7% nickel steel is mainly achieved by a higher concentration of Ni and Mn[107], as a decreased M_s temperature [108]. The partitioning of austenite stabilising elements into austenite could also be promoted by heat treatments. During tempering of 9% nickel steel, C is partitioned from martensite to austenite, causing increased content of C in austenite, and thus decreased M_s temperature, and improved TSA of 9Ni steel [109].

In contradiction, retained austenite is sometimes thought to have no effect or even detrimental to the properties of nickel steels. According to Pampillo and Paxton in 1972 [110], retained austenite improves ductility, but it has no correlation to the impact toughness of maraging steels. The results from Hwang et al in 1975 [111] also showed that retained austenite has beneficial effects on the tensile elongation and Charpy impact toughness of fine-grained 12Ni titanium gettered alloys, but a decrease in K_{Ic}. The reduction in hardness of carbon steel is commonly thought to be caused by the presence of retained austenite [85], and which is also correlated to lower yield stress.

1.3.3 QLT Heat Treatment for Nickel Steels

Due to the high price of nickel, for a better cost-effective solution, nickel content is preferred to be lower while good cryogenic properties should be maintained. 5-7% nickel steels were chosen as the substitute for 9% nickel steel.

From Strife and Passoja's work [92], 5Ni steel had an indistinguishable microstructure from 9Ni steel after quenching and tempering, but the maximum retained austenite content was only 3.8wt.%, and relatively poor cryogenic properties compared to 9Ni steel. Strife and Passoja applied a three-step heat treatment to 5Ni steel developed by ARMCO [97] [112]: the specimen was firstly austenised and quenched, and then reheated between Ac1 and Ac3 to form a lamellar structure, followed by water quenching, at last the specimen was heated just above Ac1, followed by air cooling or water quenching. After this three-step heat treatment, they found that the specimen was composed of tempered martensite, ferrite, and retained austenite, and the retained austenite content as well as cryogenic properties of 5Ni steel were significantly enhanced and comparable to 9Ni steel from their research work.

Syn et al. [113] and Kim et al. [114] found a heat treatment procedure called QLT could help with the improvement of the mechanical behaviours of nickel steels, and it consists of direct quenching (Q), secondary quenching at intercritical temperature (L), and tempering (T). By following this treatment, the microstructure of steel was refined, together with the reduction of carbides and carbon content of the matrix, in which could also help with the improvement of toughness behaviours. According to Kim and Morris [115], the carbides within the matrix would be dissolved during the secondary quenching process, and oversaturated ferrite would be diffused during the precipitation of the austenite. The experimental work from Wu et al. [116] exhibited that nickel steel with low carbon content and 4.5% nickel treated with QLT procedure has better ductility than the conventional direct quenching (DQ) and QT treatments. The intercritical temperature of the secondary quenching L could be between Ac1 and Ac3, and some of the martensite from the first quenching could transform into austenite and then transform back to martensite, and the remaining martensite from the first quenching would be decomposed into ferrite and some cementite precipitates. L refined the size of prior austenite and the width of martensite lath. Residual austenite was the untransformed austenite during the first quenching process. The austenite formed during the secondary quenching process L is named reversed austenite, and this reversed austenite has a different shape from retained austenite. By altering the secondary quenching temperature, the amount of reversed austenite could be modified and thus affect the mechanical properties of the steel. The amount of austenite formed during the secondary quenching has a positive correlation with the intercritical temperature. If the intercritical temperature is between Ac1 and Ac3, the austenite formed would be very stable as it would contain many alloying elements partitioned from the ferrite. If the intercritcal temperature is lower and close to Ac1, the amount of austenite would be too low to affect the properties. If the intercritical temperature is close to Ac3, the amount of austenite

would be too high, and the amount of co-exist ferrite is too little, the content of alloying elements of austenite is not high enough and lead to reduced stability of the austenite [117].

The transformation of martensite during the secondary quenching L might lead to the inhomogeneous distribution of the alloying elements. According to Kim et al. [104], the region with higher nickel content would also have a lower Ac1 temperature, and then transform into austenite during the tempering process at suitable temperatures. At higher tempering temperatures, carbides would be preferred to form, particularly for steels with alloying elements such as chromium, molybdenum, vanadium, and titanium. Other microscopic features such as coarsening of carbides, reduction of dislocations and point defects, and disappearance of lath morphology of the martensite and decomposition of retained austenite could also be the results of increasing tempering temperature [116]. The carbon content of the matrix would be reduced due to the formation and coarsening of carbides, and the number of precipitates would drop, but their size would increase. The increasing tempering temperature would lead to a competition between precipitation hardening and the reduction of solid solution strengthening, and there is an optimum tempering temperature for steel to form the maximum content of retained austenite and reach the peak mechanical properties, once the tempering temperature is higher than this value, the retained austenite formed during the secondary quenching process would also start to decompose, and the mechanical properties would also be affected negatively.

CHAPTER 2: EXPERIMENTAL MATERIALS AND PROCEDURES

2.1 Materials

2.1.1 SA-738 Gr. B Steel

The first material investigated in this study is a low-alloy SA-738 Gr. B Steel plate with a thickness of 55mm provided by Baowu Steel, which was produced by rolling of continuous casting slabs. The chemical composition of the low alloy steels is shown in Table 2.1, the chemical composition requirements for this material stated in ASME are listed in the same table as well. The material was subjected to two heat treatment conditions: HT1 condition refers to the low-alloy steel plate that was firstly heated to 900ºC for 2 hours, followed by water quenching process to room temperature, and then tempered at 630ºC for 3 hours. HT2 condition has an additional tempering process at 620ºC for 15 hours than HT1 condition, which is the simulated post-welding heat treatment (SPWHT). The steel plate orientation as well as specimen sampling scheme is shown in Figure 2.1 and Figure 2.2.

2.1.2 7% and 9% Nickel Steels

A 20mm-thick 9% nickel steel plate of production quality was produced by Baowu Steel. The steel is designed for liquefied natural gas (LNG) storage. The steel plate underwent a sequence of heat treatments by firstly heated to 820ºC for 51min, and then tempered at 590ºC for 34min. The chemical composition of the steel is given in Table 2.3. Testing specimens were machined from the quarter thickness of the steel plates, and the sampling scheme is shown in Figure 2.3.

A laboratory development 7% nickel steel plate was also produced by Baowu Steel. It is designed as a substitute of 9% nickel steel for LNG storage purposes. The 20mm-thick steel plate was processed by a QLT treatment: it was firstly heated to 820ºC for 60 minutes, followed by water quenching. After quenching, it was heated to 675ºC for 60 minutes followed once again by water quenching. Then it was tempered at 590ºC for 60 minutes and air-cooled. The chemical composition of 7% nickel steel is given in Table 2.4, and the sampling scheme is the same as 9% nickel steel.

2.2 Microstructure

The specimens were sectioned in longitudinal and transverse planes by the Struer Cutting machine, and then mounted with Bakelite. The mounted samples were ground by SiC abrasive papers with the sequence of grid size from 220, 800, and 1200. The ground surface was carefully washed with soap and cleaned with acetone between each step. After grinding, the samples were polished with 3μm and 1μm diamond suspension, and finished with OP-A and OP-S suspension solutions to reveal grain boundaries.

The inclusion analysis was performed on polished sections by taking back-scattered images using a Jeol 6060 scanning electron microscope. The magnification of the images was 1500 and 2000. The images were processed by ImageJ image analysis software. The locations of inclusions were identified as the dark regions on the BSE image, and therefore the size and number of inclusions could be measured. The dark regions were also analysed by energy dispersive X-ray spectroscopy (EDX) before inclusion analysis to avoid errors.

Electron Backscattered Diffraction (EBSD) analysis was used to examine the grain features as well as the phase information of 9% and 7% nickel steel. It was carried on a Jeol 7000F scanning

electron microscope and a Zeiss EVO15 VP ESEM with Bruker EBSD system. The accelerating voltage was 15V, with a working distance of 19mm and a tilt angle of 70^{o}.

The HT1 and HT2 specimens were etched by 10% Nital to reveal the microstructure, while 7% and 9% nickel steel specimens were etched by 2% Nital solution for 25 seconds. The etched samples were investigated by using a VHX-7000 Digital Keyence Microscope as well as a Zeiss EVO 15 SEM. Linear intercept method was applied to estimate the average grain size of different microstructures.

2.3 Tensile Testing

Tensile testing specimens were machined with the gauge length direction of the tensile specimen parallel to the transverse direction of the SA-738 Gr. B steel and nickel steel plates. The locations and orientations of tensile specimens of SA-738 Gr. B steel are shown in Figure 2.4. The geometry of the tensile specimens had a diameter of 10mm, a reduced parallel section length of 70mm, a gauge length of 50mm, and a total length of 135mm, as illustrated in Figure 2.5. Nickel steel specimens had the same design of gauge, with longer thread ends, and the total length of the individual specimen was 145mm.

The tensile tests were carried out in accordance with ASTM Standard E8/E8M-16a [118] at the temperature range of −196 to −60ºC for SA-738 Gr. B steel, and −196 to −130ºC for 7% and 9% nickel steels. An Instron environmental chamber with an accuracy of ±1°C was attached and connected to a pressurized liquid nitrogen vessel to achieve the desired test temperatures above −170ºC. The load and displacement were recorded using a calibrated load cell with a 100kN capacity on a Denson-Mayes (DMG) screw-driven machine. A low-temperature capable external extensometer was attached to the centre of specimens to monitor the extension of the

specimens, and the gauge length used was 50mm. All tests were carried out in displacement control mode and the crosshead displacement rate was 0.5 mm per minute.

The tensile tests carried out at −196ºC were tested on a Zwick screw-driven machine with a load capacity of 200kN. A heat-isolated tank filled with nitrogen tank (−196ºC) was attached to the machine. The specimens were immersed in liquid nitrogen bath for at least 10 minutes before starting the tests. The obtained load and displacement data were converted into engineering stress-strain curves. No extensometer was attached for tests at −196ºC due to the limited space inside the nitrogen tank.

2.4 Charpy Impact Testing

The Charpy impact specimens were machined following the ASTM Standard E23-16b [119] with a geometry of 10×10mm cross section and 55mm length. The notch was machined in centre with a 2mm-deep "V" notch with a root radius of 0.25mm. The designed geometry and machined Charpy specimen schemes are shown in Figure 2.6 and Figure 2.7 respectively. The Charpy impact tests were carried out on a calibrated Instron-Wolpert impact testing machine with a capacity of 300J, and the test temperatures were ranged from −196 to −40ºC for SA-738 Gr. B steel, and from −196 to −80ºC for 7% nickel steel.

For test temperatures above −100ºC, the desired temperatures were achieved by mixing liquid nitrogen and alcohol. For test temperatures below −100ºC, the temperature was achieved according to time-temperature curves: a 5mm-thick hole was drilled at one surface of a Charpy impact sample, and a type-T thermocouple was inserted to measure the temperature of the sample. The sample together with thermocouple were immersed in liquid nitrogen for at least 20 minutes to reach −196ºC, and then they were taken out and put on a pair of spare anvils that

had the same dimensions as the pair on the impact testing machine. The temperature monitor meter was connected to a computer, and the measured temperature data was converted to voltage and recorded against time. The procedures were repeated for several times to take an average time-temperature curve. Then the test specimen was put on the anvils and then fractured after a certain time intervals according to the obtained time-temperature curve. After reaching the desired test temperature, the specimen was transferred to the anvil within 5 seconds by referring to the ASTM E23.

After fracture, the broken halves were immersed in acetone until they reached room temperature, and then the fracture surfaces were examined by the Keyence digital microscope. The photographs obtained from optical microscope were used to measure the lateral expansion (LE) and percentage of cleavage area.

The absorbed impact energy versus test temperatures were plotted, and tanh curves were fitted for ductile-to-brittle transition temperature estimation. The curve is given by:

$$A + B \times \tanh (T - T_0)/C \qquad (2.1)$$

Where: T is the test temperature.

T_0 is the ductile-to-brittle transition temperature.

A and B are constants, in which A + B = upper shelf temperature, A – B = lower shelf temperature.

C is a further constant and represents the gradient of the curve within the transition region.

2.5 Hardness Tests

The hardness was analysed in transverse-longitudinal (TL) and longitudinal-transverse (LT) directions for HT1 and HT2 of SA-738 Gr. B steel and 7% and 9% nickel steels with Vickers hardness test method. The tests were conducted on a Struers microhardness tester using 5N. The specimens were ground and polished before testing, with a sequence of P220, P800, P1200 SiC papers, 3μm diamond lubricant, and 1μm diamond lubricant. Ten indentations were tested on each specimen, with a separation of 0.6mm between each indentation.

A through-thickness hardness test was conducted on large SENB specimens of nickel steels with a thickness of 16 mm to check the homogeneity of specimens. Five groups were tested on the side of the block along the thickness again using a load of 5N. Each group included 10 hardness indentations evenly distributed along the total thickness (16mm) of the specimen.

2.6 Microscopic Cleavage Fracture Stress Tests

The fracture stress specimens were machined with W = B = 12.7 mm and a length of 80 mm. The root radius was 0.25 mm, the notch included angle was 45º, and the depth of a central notch a was 4.23 mm. Two 1mm-deep notches were machined at a distance of 31.75mm from the centre. The designed geometry and the as-received photos of the fracture stress specimen are shown in Figure 2.8 and Figure 2.9 respectively.

Two fracture stress tests of 7% nickel steel were carried out at −196°C on a Zwick screw-driven machine of 200kN load capacity. The contact roller diameter was 8mm. The loading half-span (the distance between an outer roller and an inner roller), l, was equal to the width, W. The illustration of four-point bending setup is shown in Figure 2.10. The specimens were immersed in liquid nitrogen inside a heat-isolated tank to achieve the testing temperature of −196ºC, and

the immersion time was at least 10 minutes before starting the tests. The tests were set to be stroke-controlled, and the specimen was loaded with the stroke displacement rate of 1mm/min. The experimental setup is shown in Figure 2.11. After fracture, the broken specimens were immersed in acetone after fracture, and then they were dried to observe the fractography.

Finite element analysis (FEM) according to Griffith and Owen [25] of the stress and strain contributions in a local plastic zone ahead of a blunt notch was used to interpret the bend test results, and the nominal stress σ_{nom} was calculated based on the following equation [23]:

$$\sigma_{nom} = \frac{6M}{B(W-a)^2} \tag{2.2}$$

and

$$M = \frac{Pl}{2} \tag{2.3}$$

where M is the bending moment of four-point bending, P is the compressing load, l is the distance between the inner and outer rollers, B is the thickness of the specimen, W is the width of the specimen, and a is the notch depth of the specimen.

The ratio of σ_{nom}/σ_y is defined as the stress intensification factor R, and this ratio can be used to calculate the value of maximum tensile stress σ_{yymax} ahead of the notch root:

$$R\sigma_y = \sigma_{yymax} \tag{2.4}$$

The relationship between R, applied load L/L_{GY}, and nominal stress σ_{nom}/σ_y is shown in Figure 2.12. The applied load was linearly proportional to the nominal stress, and their relationship was expressed as:

$$L/L_{GY} = 0.465\sigma_{nom}/\sigma_y \quad (2.5)$$

For values of $L/L_{GY} \leq 1.065$.

The relationship between stress intensification R and maximum principal stress σ_{yymax} was estimated by Equation 2.6:

$$R = 0.0615+1.8464(\sigma_{nom}/\sigma_y)^{0.4017} \quad (2.6)$$

Griffith and Owen's FEM analysis tells the maximum principal stress available at fracture in a blunt notch test. However, when dominant initiation site could be found from the fracture surface, then the local fracture stress estimation would require measuring the fracture distance X_0 from the fracture surface of specimens, which is the distance between the notch end and the initiation site. The local R-value at the position X_0 was obtained from Griffiths FEM plot, as shown in Figure 2.14. The local cleavage stress $\sigma_f = \sigma(X_0)$. Note some interpolation within the figure may be necessary since local stress distribution are only shown at a limited number of σ_{nom}/σ_y values. The local fracture stress $\sigma(X_0)$ was estimated according to Equation 2.7, where $\sigma(X_0) = \sigma_f$:

$$R = \sigma_f/\sigma_y \quad (2.7)$$

2.7 Fracture Toughness Testing

2.7.1 SA-738 Gr. B Steel

2.7.1.1 Compact Tension Specimens

A total of 32 compact tension (C(T)) specimens with a thickness of 25mm and W = 50mm underwent fracture toughness test, with 16 from HT1 and 16 from HT2 condition respectively.

The test followed the resistance curve procedure in ASTM Standard E1820-17 [120]. The dimensions of C(T) specimens used in the test are shown in Figure 2.15. The specimens were machined with internal knife edges to attach a clip gauge to record the notch mouth opening displacement and the tests were conducted under clip gauge displacement control.

The specimens were fatigue pre-cracked at room temperature (24ºC) using an Amsler Vibrophore machine (Figure 2.17). The maximum stress intensity factor was applied to calculate the maximum load can be used and the ratio of minimum load to maximum load, R, was 0.1. Then compliance method was applied by performing unloading/reloading sequences of the specimen on a DMG screw-driven machine fitted with a 100kN load cell and an environmental chamber at room temperature. A DG-40 clip gauge was attached to measure the crack mouth opening displacement. The compliance data were used to estimate the initial crack length a_0. After pre-cracking and compliance, the environmental chamber was sealed and connected to a liquid nitrogen vessel to cool down and maintain the desired test temperature condition. The experimental setup is shown in Figure 2.18. Most specimens were tested within the ductile-to-brittle transition region of the material (see the following section 2.7.1.2 Master Curve for details). The test temperatures outside the transition region were also selected to investigate the lower shelf toughness behaviours of the material. The test temperatures were ranging from −170 to −80ºC.

The load versus notch mouth opening displacements, which were recorded by the clip gauge attached between the knife edges, were plotted. The reloading/unloading sequences were used to estimate the crack extension during the tests at each sequence. After the data was recorded and tests were stopped, the specimens were then fatigue opened. The original crack length and final crack extension of the opened specimens' halves were measured under a Keyence VHX-

7000 Digital Microscope. The measured actual crack lengths were then used to amend the estimated crack lengths calculated using the reloading/unloading sequences. The values of crack length a_i were calculated according to the ASTM standard E1820 [120], while the conditional values of P_Q, K_Q, and crack tip opening displacement (CTOD) were calculated according to the ASTM standard E399-20a [121]. The validity of K_Q as linear-elastic plane-strain fracture toughness K_{Ic} were checked based on ASTM Standard E399: the ratio of maximum load P_{max} and P_Q should not exceed 1.10, and the value of $2.5(K_Q/\sigma_{YS})^2$ should be less than the ligament size W-a, where σ_{YS} is the 0.2% offset yield strength of the specimen at testing temperature. K_Q is valid as K_{Ic} only if both requirements are satisfied.

2.7.1.2 Master Curve

The fracture toughness results were used to calculate elastic-plastic K_{Jc} in accordance with the Master Curves methodology stated in ASTM Standard E1921-18 [122]. The fracture of ferritic steels within transition temperature region has a statistical nature, and their fracture toughness results show the similar scatter. As a consequence, the fracture toughness results for the same steel can be plotted in one master curve.

The J-integral J_c at the onset of cleavage fracture is given by:

$$J_c = J_e + J_p \tag{2.8}$$

Where J_e is elastic component, and J_p is plastic component.

The elastic-plastic fracture toughness K_{Jc} values are determined by J_c according to the following:

$$K_{Jc} = \sqrt{J_c \frac{E}{1 - v^2}} \tag{2.9}$$

Where E is Young's modulus of the material, ν is the Poisson's ratio and it was taken as 0.3.

The reference temperature T_0 for HT1 and HT2 specimens were calculated using both single-temperature and multiple-temperature test methods to compare the toughness behaviours of specimens in transition region. The single-temperature selection usually falls in ductile-to-brittle transition region, and it was decided by referring to the values of Charpy impact result T_{28J} or T_{41J}:

$$T = T_{CVN} + C \tag{2.10}$$

Where T_{CVN} is the corresponding temperature to Charpy impact energy of 28J or 41J, C is the constant depending on the size of specimen. For C(T) specimens with thickness of 25mm, at least six specimens are required for the Master Curves methodology. The Master Curve was plotted based on the reference temperature, T_0, of specimens, which is defined as the temperature where the median of K_{Jc} equals to 100MPam$^{1/2}$. To calculate T_0 by single temperature analysis, firstly all the K_{Jc} values tested at the same temperature would be substituted into Equation 2.11 to get the Weibull scale parameter, K_0:

$$K_0 = [\sum_{i=1}^{N} \frac{(K_{Jc(i)} - 20)^4}{r}]^{\frac{1}{4}} + 20 \tag{2.11}$$

Where r is the number of uncensored K_{Jc} results, N is the total number of toughness data. The K_{Jc} values obtained from C(T) specimens were within the limit of thickness = 1T, therefore censoring was not needed.

Then $K_{Jc(med)}$ was calculated by putting K_0 into Equation 2.12:

$$K_{Jc(med)} = 20 + (K_0 - 20)[ln2]^{1/4} \quad (2.12)$$

T_0 was then calculated by substituting $K_{Jc(med)}$ into Equation 2.13:

$$T_0 = T - \left(\frac{1}{0.019}\right) \ln \left(\frac{(K_{Jc(med)} - 30}{70}\right) \quad (2.13)$$

Where T is the test temperature.

All fracture toughness data tested at ductile-to-brittle transition region were used to process multiple-temperature test calculation, and in this study, it indicates the fracture toughness specimens tested at a temperature range from −120ºC to −80ºC. The multiple-temperature test method put K_{Jc} results obtained at different temperatures into Equation 2.14 to calculate T_0:

$$\sum_{i=1}^{N} \delta_i \frac{\exp[0.019(T_i\text{-}T_0)]}{11+76.7\exp[0.019(T_i\text{-}T_0)]} - \sum_{i=1}^{N} \frac{(K_{Jc(i)} - 20)^4 \exp[0.019(T_i\text{-}T_0)]}{\{11+76.7\exp[0.019(T_i\text{-}T_0)]\}^5} = 0 \quad (2.14)$$

The equation was solved by iteration.

For the establishment of the Master Curve, the values of K_{Jc} versus test temperatures were plotted, and a curve was plotted according to the following equation:

$$K_{Jc(med)} = 30 + 70 \exp\left[(0.019(T - T_0)\right] \quad (2.15)$$

The upper and lower tolerance bound for the curve was based on the following equation:

$$K_{Jc(0.xx)} = 20 + \left[\ln\left(\frac{1}{1 - 0.xx}\right)\right]^{1/4} \{11 + 77 \exp\left[(0.019(T - T_0)\right]\} \quad (2.16)$$

Where 0.xx refers to the selection of tolerance bound, e.g., for 5% and 1% tolerance, 0.xx would be 0.05 and 0.01 respectively.

2.7.1.3 Single Edge Bending Specimens tested at −196ºC

Primarily to allow testing at −196ºC, single edge bend specimens with W = B = 10mm were machined from broken halves of HT1 specimens, and the specimen notches were machined in both TL and LT directions. The specimens were fatigue pre-cracked to a/W = 0.45 at room temperature by DMG servo hydraulic machine, with R = 0.1. After precracking, three-point bending tests were performed on a Zwick screw-driven machine at −196ºC. The specimens were put inside an insulation tank filled with liquid nitrogen for at least 10 minutes before starting the test.

2.7.2 7% Nickel Steel

2.7.2.1 SENB Specimens with W = 32mm

Fracture toughness tests of 7% nickel steel were also performed using an unloading/reloading elastic compliance method as stated in Section 2.7.1.1. The specimens used were single-edge notched bending (SENB) specimens with W = 32mm, B = 16mm, L = 149mm and a central 12mm deep notch with a notch root radius of 0.08mm in accordance with the sample geometry suggested in ASTM Standard E1820-17. The specimens were machined with internal knife edges to attach a clip gauge to record the notch mouth opening displacement and the tests were conducted under clip gauge displacement control. The designed geometry is shown in Figure 2.19.

The specimens were fatigue pre-cracked on the DMG servo-hydraulic machine under three-point bending, following the resistance curve procedures with unloading/reloading sequences.

The maximum stress intensity factor applied during the final stages of fatigue crack extension did not exceed 25 $MPam^{1/2}$ and the R ratio was 0.1. The fatigue pre-crack length was monitored by the D.C.P.D. method and controlled under a length of 14.4mm (a/W = 0.45). The experimental setup is shown in Figure 2.20.

Based on the Charpy impact testing results and designed application temperature of −163ºC, the three-point bending fracture toughness testing of 7% nickel steel was preliminarily carried out at −163 and −170°C. A total of four three-point bending tests were carried out, with two tests for each test temperature.

The load versus notch mouth opening displacements, which were recorded by the clip gauge attached between the knife edges, were plotted. The reloading/unloading sequences were used to estimate the crack extension during the tests at each sequence. After the data was recorded and tests were stopped, the specimens were then fatigue opened. The original crack length and final crack extension of the opened specimens' halves were measured under a Keyence VHX-7000 Digital Microscope. The measured actual crack lengths were then used to amend the estimated crack lengths calculated using the reloading/unloading sequences. The values of elastic stress intensity factor K_{Jc} were calculated based on ASTM E1921, as stated in Section 2.7.1.2.

2.7.2.2 SENB Specimens with W = 7mm tested at −196ºC

In order to further investigate the toughness behaviours of sharp-notched 7% nickel steel specimens at −196ºC, a total of four smaller bending specimens with W = 7mm, B = 7mm and a span width = 30mm were machined from the broken halves of 7% nickel steel bending specimens to fit the liquid nitrogen tank. Two specimens were machined in T-L direction, and two in L-T direction. All specimens were fatigue pre-cracked at room temperature and the total

crack length was controlled to be under 0.45W. Then the specimens were fractured at −196ºC on a Zwick screw-driven machine with crosshead-controlled compression mode, and the rate of crosshead movement was 0.5mm/min. A heat-isolated tank filled with liquid nitrogen was attached on the screw-driven machine, and specimens were immersed in liquid nitrogen for at least 10 minutes prior to the tests.

After fracture, the specimens were immersed in acetone until their temperature increased to room temperature, and then they were fatigue opened at room temperature. The broken halves were examined by Keyence digital microscope to measure the fatigue pre-crack length as well as ductile crack growth. The values of crack length were measured at nine equally spaced positions, according to ASTM E1820-18. The values of elastic stress intensity factor K_{Jc} were calculated based on ASTM E1921, as stated in Section 2.6.2.

2.8 Fatigue Crack Growth Resistance Curves of Nickel Steels

For the low-temperature fatigue test, a new experimental facility was developed for fatigue crack growth test at University of Birmingham. The fatigue pre-crack and fatigue crack growth rate tests were performed on a Denson-Mayes (DMG) servo-hydraulic machine, and the specimens used was single-edge notched bending (SENB) specimens with dimensions of W = 14 mm, B = 7 mm, L = 66 mm, with a notch length less than 0.25W. The designed geometry is shown in Figure 2.21. They were machined from the broken halves of 9% and 7% nickel steel SENB specimens after fracture toughness testing, with the same notch directions as the original SENB specimen (T-L direction). The reason for machining from the broken halves of big SENB specimens was due to the original SENB specimen was designed for fracture toughness testing, the notch root length limits too short to have a proper monitor on fatigue crack growth rate. An

Instron temperature chamber connecting to a liquid nitrogen pressure vessel was used to achieve the desired test temperatures.

The crack length was monitored by direct current potential drop (D.C.P.D.) method, with two wires spot welded on both sides of the notch. Two copper wires were attached on both ends of the specimens so a current could go through the specimens. The testing setup on the DMG machine is showed in Figure 2.22. An in-house correlation function between V/V_0 and a/W of a bend geometry which could monitor the crack length of specimen during fatigue is shown below:

$$a/W = -0.21395+0.59859(V/V_0)-0.15197(V/V_0)^2+0.01733(V/V_0)^3 \quad (2.17)$$

Where a is crack length; V is the measured P.D. voltage across the specimen; V_0 is the reference crack voltage corresponding to a given initial a/W of the specimen before the fatigue crack growth test.

The fatigue tests were carried out at room temperature, −163ºC, and −170ºC. A 5Hz sinusoidal wave was used with the R ratio of 0.1. A current of 20A was passing through the specimen. The specimens were pre-cracked in three-point bending with a ΔK range of 13-15 $MPam^{1/2}$ at room temperature. After pre-cracking, the specimens were fatigued at a range of ΔK from 30 to 60 MPa√m at the desired test temperatures. The fatigue crack growth was stopped before final failure, and then the specimens were opened by stroke-controlled compression to record the failure load and to calculate the toughness of the specimens. The fracture surfaces were checked by the Keyence Digital microscope to measure the actual fatigue crack length, and this measured crack length was used when necessary to correct the predicted crack length from D.C.P.D. method. The differences between measured crack length and predicted crack length

were in the range from 0.02mm to 0.58mm with 4-5mm of crack growth, regardless of voltage change or test temperatures.

Fatigue crack growth resistance curves generally exhibit three regions: near threshold, steady state region, and acceleration towards fracture. Paris relationship constants, *c* and *m*, are derived from the steady crack growth region and based on the following equation:

$$\frac{da}{dN} = c\Delta K^m \tag{2.18}$$

The ΔK against fatigue crack growth rate, da/dN, of all specimens tested at various temperatures were plotted in the same graph with the log-log scale, and the constant values of c and m could be derived from the fitting line of the steady state region based on the following equation:

$$\log\left(\frac{da}{dN}\right) = \log(c) + m\log\left(\Delta K\right) \tag{2.19}$$

After fatigue crack growth tests, one test-pieces, 7Ni-FCGS4 tested at −170ºC was monotonically loaded at −170ºC till failure, the recorded failure load was 5.9 kN.

2.9 Fractography

2.9.1 SA-738 Gr. B Steel

The fracture surfaces of selected tensile specimens tested at −196 and −120ºC, fracture toughness specimens tested at −196 and −170ºC were investigated. The fractography of tensile, C(T) and SENB specimens was examined by a Jeol 6060 Scanning Electron Microscope at an accelerating voltage of 20 and 30kV. A voltage of 20kV with a spot size between 50 to 60 was used for photographing, while 30kV with a spot size of 70 is used for energy dispersive spectroscopy (EDS) analysis. The location of cleavage initiation site for fracture toughness

specimens was identified to measure the distance between the end of fatigue pre-crack and the initiation site, X_0. For sites initiated from inclusions, the sizes of inclusions and surrounding cleavage facets were also measured, and the chemical compositions of inclusions were analysed by EDX.

2.9.2 7% Nickel Steel

Fracture surfaces of tensile, Charpy impact, fracture stress, fracture toughness, and fatigue crack growth specimens were examined in detail using Jeol 6060 Secondary Electron Microscope, Philips XL30 FEG Secondary Electron Microscope as well as Zeiss EVO 15 with EDS spectrometer built in, under an accelerating voltage of 20 kV and 30 kV. For specimen failing with at least some cleavage fracture, possible initiation sites were investigated. The chemical compositions of some inclusions were identified by EDS.

CHAPTER 3: SA-738 GR. B STEEL RESULTS

3.1 Microstructure

The optical microscope images of the microstructure of HT1 and HT2 revealed after etching are shown in Figure 3.1. The SEM images of HT1 and HT2 are shown in Figure 3.2 to Figure 3.4. According to the features observed, the microstructure of both HT1 and HT2 contains mainly granular bainite, with coarse ferrite plates, and under higher magnification, some lath structure can be observed. There are some small island-like particles located and they are lighter than the ferrite plates, which should be martensite-austenite constituents (M-A). This granular morphology could be granular bainite. The aggregated white dots could be carbide, and they are located at grain boundaries. The SPWHT of HT2 did not change the matrix, but the boundaries and M-A islands of HT2 are slightly coarser than that of HT1.

By line intercept method, the measured average granular bainite grain size of HT1 batch in longitudinal direction was 7.6 μm, with a standard deviation of 1.1 μm. The average grain size of HT1 batch in transverse direction was 6.9 μm, with a standard deviation of 0.6 μm. The average grain size of HT2 batch in longitudinal direction was 9.1 μm, with a standard deviation of 1.2 μm. The average grain size in transverse direction was 8.1μm, with a standard deviation of 0.8 μm.

The inclusion size distribution analysis for HT1 and HT2 is shown in Figure 3.5. A total of 3445 inclusions was counted in the area of 10231 mm^2 for HT1, and 3497 inclusions was counted for HT2 in the area of 10325 mm^2. There were 336 inclusions/mm^2 for HT1, and there were 338 inclusions/mm^2 for HT2. The lower limit of inclusion detection was set to be 0.2μm,

and the smaller inclusions with a diameter below 0.2μm were not counted due to the resolution limit of the analyser.

The inclusions detected from HT1 specimen with the diameter between 0.2μm and 2μm accounted for 88% of the total number of inclusions, while for HT2 specimen, inclusions with the diameter between 0.2μm and 2μm accounted for 84% of total number of inclusions. These inclusions were evenly distributed on the polished surfaces of HT1 and HT2 specimens.

The chemical compositions of inclusions found in HT1 and HT2 were analysed by EDX. Most inclusions contain oxygen, silicon, aluminium, calcium, sulphur, titanium, manganese, carbon, and nickel. The chemical compositions are not affected by the size of inclusions.

3.2 Hardness Testing

The average hardness value for HT1 in longitudinal direction is 191 HV5, with a standard deviation of 2.8 HV5. The average hardness value in transverse direction is 193 HV5, with a standard deviation of 3.6 HV5.

For HT2, the average hardness value in longitudinal direction is 184 HV5, with a standard deviation of 2.7 HV5; while for transverse direction, the average hardness value is 187 HV5, with a standard deviation of 2.7 HV5.

3.3 Tensile Testing

Tensile tests were carried out at −196, −170, −140, −120, −100, −80 and −60ºC. A total of 28 specimens was tested, with 14 from HT1 and 14 from HT2 respectively. The load versus gauge elongation data recorded was converted to engineering stress versus engineering strain curve to evaluate the ultimate tensile strength and yield stress.

All specimens showed necking behaviour before failure, including specimens tested at −196ºC, and the fracture surfaces of specimens tested at −196ºC observed by optical microscope were flat cleavage fracture surfaces. However, many test-pieces also illustrated longitudinal splitting. The stroke-controlled engineering stress-strain curves for HT1 and HT2 are shown in Figure 3.6. Some tensile tests carried out at temperatures from −140 to −60ºC employed an extensometer, and these engineering stress-strain curves are plotted in Figure 3.7. The extensometer output was stopped before the final failure of tensile tests since the overall elongation of specimens exceeded its measuring range. Most tensile curves are prominent, exhibiting a stress drop after reaching the upper yield point, and yield point elongation (Lüders strain) appears before general strain hardening takes place. The amount of elongation decreased with the increasing test temperature, from 5 to 9% at −196ºC, 5% at −170ºC and −140ºC, and 2 to 4% at −120ºC to −60ºC. The values of upper and lower yield stress, tensile strength, and Lüders elongation are summarised in Table 3.3. As the test temperature decreases, the lower yield stress increases from 567 MPa at −60ºC to 928 MPa at −196ºC for HT1, and from 533 MPa at −60ºC to 927 MPa at −196ºC for HT2, while the tensile strength increases from 654 MPa at −60ºC to 952 MPa at −196ºC for HT1, and 640 MPa at −60ºC to 947MPa at −196ºC for HT2 respectively. Any differences between the results of HT1 and HT2 are extremely small.

The yield stress, tensile strength versus test temperatures of HT1 and HT2 from −196 to −60ºC are plotted in Figure 3.9. The differences between the tensile strength and yield stress gradually increase as the test temperature increases, and it indicates more extensive work hardening occurs with increasing temperature.

The uniform plastic deformation of engineering stress versus engineering strain curve was converted to true stress versus true strain curve based on the following equations:

$$\sigma_{true} = \sigma_{eng} \cdot \exp(\varepsilon_{true}) \quad (3.1)$$

and

$$\varepsilon_{true} = \ln(\varepsilon_{eng} + 1) \quad (3.2)$$

where σ_{eng} is engineering stress, ε_{eng} is engineering strain, σ_{true} is true stress, ε_{true} is true strain. The estimation of work hardening exponent n was based on the following equation:

$$\sigma_{true} = k{\varepsilon_{true}}^{n} \quad (3.3)$$

where k is a constant. The true stress-strain curves for HT1 and HT2 are shown in Figure 3.8. The values of work hardening exponent n are summarized in Table 3.3. The work hardening exponent varies from 0.01 to 0.09 for HT1 and from 0.01 to 0.11 for HT2 at the temperature range from −196 to −60ºC. HT1 and HT2 specimens all exhibit lower strain hardening rates at −196ºC than at other test temperatures. At −196ºC, a longer Lüders elongation and smaller differences between the lower yield point and tensile strength are observed.

3.3.1 Fractography

Figure 3.10 and Figure 3.11 illustrate the fractography of tensile specimens HT1-2 and HT2-2 tested at −196ºC. Both specimens exhibited some elongation during necking, and they have a "star" fracture. They show a mixed fracture mode of ductile and cleavage, small cleavage facets are surrounded by micro-void coalescence. Possible initiation sites could be located at the centre of the fracture surfaces by tracing the direction of secondary cracks. Inclusions could be found near the initiation facets, and they contain S or Ca.

Figure 3.12 illustrates the fractography of HT1-10 tested at −120ºC. The specimen was selected to do fractography as it did not fail at the necking region nor in the middle region, and the

fracture surface is mainly transgranular cleavage facets, other features such as tear ridges could be observed as well. The cleavage initiation site is located, and it was inclusion initiated, and it contains O, Al, S, Ca, and Ti.

3.4 Charpy Impact Testing

54 specimens in each of HT1 and HT2 were subjected to CVN testing, and three of each were tested at −196°C, six of each were tested at −120°C, 12 of each were tested at −100°C, nine of each were tested at −90°C and −80°C respectively, six of each were tested at −70°C and −60°C respectively, and three of each were tested at −40°C. The fracture surfaces of specimens are shown in Figure 3.13, and the results of absorbed impact energy, lateral expansion, shear lip extension, percentage of cleavage area, and ductile length are listed in Table 3.4, 3.5, and 3.6.

The results of Charpy impact test indicate that HT1 and HT2 specimens appear to show similar ductile-to-brittle behaviour: when the test temperature was below −100°C, the absorbed impact energy remains relatively low with little scatter, which is only 2 to 9J. At −100°C, the impact energy of specimens increases, and one specimen from HT1 has a relatively higher absorbed impact energy, which is 102J. From −90°C, the absorbed impact energy for specimens from both HT1 and HT2 start to show variations, and the values vary from 12 to 200J for HT1 and from 8.5 to 247.5J for HT2. At −80°C, the values of absorbed impact energy for most specimens are greater than 200J and only one for each heat treatment condition is significantly lower than rest of specimens. At −70°C and temperature above, the absorbed energy values became very high, which are all above 200J.

The impact energy plots are fitted with tanh curves, as shown in Figure 3.14 to Figure 3.16. The transition curve of HT1 is on the left of HT2 transition curve, suggesting that the ductile-to-

brittle transition of HT1 specimens occurs at lower temperature than HT2. The values of estimated transition temperature by fitting tanh curves are −91ºC for HT1 and −87ºC for HT2, respectively. The value of upper shelf energy of the specimens was restricted by the impact machine's maximum load according to the results given by Baowu Steel, as shown in Figure 3.17. The transition temperatures for Baowu results by applying the same tanh-fit estimation gives −70ºC for HT1 and −64ºC for HT2. The tanh fit for HT1 now estimates higher upper shelf energy than HT2.

The plots of absorbed impact energy versus percentage cleavage area of fracture surface, absorbed impact energy versus lateral expansion, absorbed impact energy versus ductile thumbnail extension are shown in Figure 3.18 to Figure 3.26. The fracture surfaces of specimens from upper shelf show 100% of ductile fracture, with a maximum of ductile thumbnail extension of 6.9mm and 7.1mm for HT1 and HT2 respectively, while the specimens from lower shelf exhibit 100% cleavage fracture, with no ductile extension. There is a negative linear relationship between the absorbed impact energy values and the percentage of cleavage area, while there is a positive linear relationship between the absorbed energy and lateral expansion and ductile thumbnail extension. Some specimens do fall out of these trends, but this is not considered in this thesis.

3.5 Fracture Toughness Tests

3.5.1 Compact Tension Specimens

In view of the results displayed in Charpy impact energy tests, T28J and T41J for HT1 are −100ºC and −97ºC respectively; T28J and T41J for HT2 are −97ºC and −95ºC respectively. By referring to Equation 2.10, −120°C that was selected as the test temperature to do fracture

toughness test for the Master Curves single-temperature methodology on HT1 and HT2 steels is. To further analyse the fracture toughness behaviours of HT1 and HT2 steels at ductile-to-brittle transition (DBT) region, −100°C was also selected as the test temperature for single-temperature test.

A total of 24 C(T) specimens with 12 from each condition were tested at −120ºC and −100ºC, and four C(T) specimens in total with two from each condition were tested at −80ºC. Four C(T) specimens in total with two from each condition were tested at −170ºC to investigate the lower shelf toughness behaviour. The load-displacement curves of fracture toughness specimens tested at the temperature range from −170 to −80ºC are shown in Figure 3.27, and the values of P_{max}, P_Q, K_Q, the validity of K_Q as K_{Ic}, K_{Jc}, CTOD of C(T) specimens are summarised in Table 3.7 and Table 3.9. One of HT1 specimens tested at −80°C was excluded from the table as it failed with complete ductile fracture.

Fracture toughness tests on C(T) specimens at −170ºC, −120ºC and −100ºC mostly resulted in catastrophic cleavage fracture with negligible amount of stable crack growth extension. All the specimens tested at −170ºC satisfied the linear-elastic fracture mechanics criteria, with an average fracture toughness value of 47.3 and 43.7 $MPam^{1/2}$ for HT1 and HT2 respectively. Two out of six of the HT1 specimens tested at −120°C satisfied the linear-elastic fracture mechanics criteria for the specimen size exhibiting the fracture toughness values of 54.9 and 55.4 $MPam^{1/2}$ respectively. One of the HT1 specimens and one of the HT2 specimens tested at −100°C satisfied the linear-elastic fracture mechanics criteria, with the fracture toughness values of 64.7 and 58.6 $MPam^{1/2}$ respectively. The validity calculations used the yield stress values obtained in Section 3.3.

From −120ºC, the fracture toughness values show variations due to ductile-to-brittle transitions in micromechanisms of failure. Values of K_Q vary from 54.9 to 94.4 MPam$^{1/2}$ for HT1 and 66.3 to 87.0 MPam$^{1/2}$ for HT2, and the value of K_{Jc} vary from 55.6 to 106.9 MPam$^{1/2}$ for HT1 and 70.1 to 91.4 MPam$^{1/2}$ for HT2 respectively.

As the test temperature increased to −100ºC, the values of K_Q vary from 64.7 to 87.1 MPam$^{1/2}$ for HT1 and 58.6 to 84.8 MPam$^{1/2}$ for HT2, while the values of K_{Jc} vary from 88.3 to 211.7 MPam$^{1/2}$ for HT1 and from 59.6 to 133.3MPam$^{1/2}$ for HT2. The average value of K_Q of HT1 and HT2 tested at −120ºC is 72.9 and 76.3MPam$^{1/2}$ respectively, the average value of K_Q of HT1 and HT2 tested at −100ºC is 79.5 and 75.7MPam$^{1/2}$ respectively.

At −80ºC, the average K_Q value of HT1 and HT2 is 70.9 and 91.3MPam$^{1/2}$ respectively. The values of K_Q and K_{Jc} of C(T) specimens tested at −170 to −80ºC are plotted in Figure 3.29 and Figure 3.30 respectively. K_{Jc} values of specimens exhibit wider scatter than K_Q values as the temperature increases, which is due to that specimens at higher temperatures tend to have more ductile crack growth involved.

3.5.2 Bending Specimens tested at −196ºC

A total of six bending specimens with the width of 10 mm and a span size of 40 mm were machined from the broken C(T) specimens, three of them have a notch machined in TL direction, and other three in LT direction. The load-versus-crosshead displacement curves for bending specimens tested at −196ºC are shown in Figure 3.28. The load and crosshead displacement exhibit linear relationship with sudden load drop after reaching maximum load, which indicates cleavage fracture. Based on the fracture toughness test results of specimens tested at −170ºC, three out of four specimens have the value of P_Q equivalent to the value of P_{max}, and the K_Q values are all valid for K_{Ic}, therefore the test results for the bending specimens

tested at −196ºC could be estimated as $P_{max} = P_Q$, and the values of K_Q should be valid as K_{Ic}, even without the attachment of clip gauge. The average value of K_{Ic} in TL direction is 47.0MPam$^{1/2}$, while for specimens with the notch machined in LT direction, the average K_{Ic} value is 35.5 MPam$^{1/2}$. The results of SENB specimens tested at −196ºC are summarised in Table 3.8.

Size effect according to the weakest-link theory and ASTM E1921:

$$K_{Jc2} = 20 + (\frac{B_1}{B_2})^{\frac{1}{4}} \cdot (K_{Jc1} - 20) \quad (3.4)$$

Where K_{Jc1} is K_{Jc} of specimen with thickness of B_1, and K_{Jc2} is K_{Jc} of specimen with thickness of B_2. The average K_{Ic} value of bending specimens tested at −196ºC is 38MPam$^{1/2}$, and the censored average K_{Ic} value corresponding to C(T) specimen with thickness of 25mm is 31MPam$^{1/2}$. This higher K_{Jc} value from bending specimens is due to that smaller specimens would result in an improvement of heterogeneity and more resistance to fracture.

3.5.3 Master Curve

3.5.3.1 Single Temperature Analysis

For the single temperature analysis of −120°C, the reference temperature T_0 of HT1 is −100.9ºC, which is slightly lower than the reference temperature of HT2 (−96.7°C). The Master Curves in Figure 3.31 shows that K_{Jc} values for HT1 and HT2 tested at −120°C are distributed evenly within 95% and 5% tolerance bounds. K_{Jc} values for HT2 are located closely around the Master Curve, while K_{Jc} values of HT1 show larger scatter.

For HT1 specimens tested at −100°C, the reference temperature is −121.7°C, which is much lower than the reference temperature of HT2 of −96.5°C tested at −100ºC. The Master Curve

established based on single temperature analysis at −100ºC in Figure 3.32 shows that the fracture toughness value of HT1-01 falls out of 99% tolerance bound, HT2 values are mostly distributed evenly within the 95% and 5% tolerance boundaries, with two data points located at the borders of 95% and 5% tolerance bounds.

3.5.3.2 Multiple Temperature Analysis

The reference temperature T_0 calculated by multiple-temperature analysis for HT1 C(T) specimens tested at the temperature range between −120°C and −80°C is −111.9°C. The T_0 obtained by multiple-temperature analysis for HT2 tested at the temperature range of −120 to −80ºC is −100.5°C. The Master Curves based on the multiple-temperature analysis are plotted in Figure 3.33, the figure shows that except HT1-01, the rest of HT1 data fall between 95% and 5% tolerance boundaries. If HT1-01 value is excluded from the analysis, the reference temperature of HT1 calculated by multiple-temperature analysis is −99.9°C, which is close to the T_0 value of HT2 of −100.5°C. The corresponding Master Curves are plotted in Figure 3.34, and the positions of Master Curves as well as the tolerance bounds for HT1 and HT2 mostly overlap.

The reference temperature T_0 calculated by combining all the K_{Jc} values obtained from HT1 and HT2 specimens tested at the temperature range from −120 to −80ºC is −108.6°C, and the corresponding Master Curve is shown in Figure 3.35. The K_{Jc} value of HT1-01 falls far out of 99% tolerance bound. If HT1-01 value is excluded from the calculation, the reference temperature would be −99.14°C, and all the data points fall between 95% and 5% tolerance bounds of the Master Curve, as shown in Figure 3.36.

Referring to ASTM E1921, T_0 is valid within the range of T_{0Q} ±50°C, and this is referring to that the difference between test temperature and calculated T_0 should not exceed 50°C. The

reference temperature values calculated by this Master Curve method meet this requirement. Figure 3.37 shows all the data tested at three different temperatures plotted in the same Weibull coordinates, and the fit lines are based on the rearranged three-parameter Weibull distribution developed by Wallin, as shown in Equation 1.31 in Chapter 1. Equation 1.31 is rearranged as below:

$$ln(1 - P_f) = \{-[\frac{K_{Jc} - K_{min}}{K_0 - K_{min}}]^b\} \tag{3.5}$$

Based on Wallin's method in ASTM Standard E1921, K_{min} is taken as 20MPam$^{1/2}$ and b as 4. Equation 3.5 can be further transformed into Equation 3.6:

$$\ln\left(\ln\left(\frac{1}{1 - P_f}\right)\right) = 4\ln(K_{Jc} - 20) - 4\ln(K_0 - 20) \tag{3.6}$$

P_f is calculated based on the following equation:

$$P_f = \frac{i}{N + 1} \tag{3.7}$$

When N is the total number of uncensored specimens, i is the rank number of fracture toughness values from the lowest to the highest.

The fracture toughness data tested at −120ºC and −80ºC have a good fit by taking K_{min} as 20MPam$^{1/2}$ and b as 4. When HT1-01 is excluded from calculation, the line fits better to data produced at −100ºC.

The fracture toughness results tested at −196ºC and −170ºC were censored and used to calculate the reference temperature T_0 by the Master Curve multiple-temperature analysis. The iterated values of reference temperature were all fell out of the transition range and much smaller than

DBTT, which gives −146ºC for calculations including the results tested at temperatures from −196 to −80ºC, and −180ºC for calculations including the toughness results tested ranging from −170 to −80ºC. This attempt illustrates that the Master Curve methodology is not suitable for specimens tested outside the transition range, even though the yield stress of HT specimens tested at −170ºC is still within the ferritic yield stress range of 275 to 825 MPa stated in ASTM E1921.

3.5.4 Sectioning of HT1-01 Specimen

HT1-01 tested at −100ºC has prior fracture toughness value than other specimens tested at the same temperature of −100ºC, with its K_{Jc} value of 211.7MPam$^{1/2}$ comparing to the mean K_{Jc} value for specimens tested at −100ºC is 117.0MPam$^{1/2}$. One side of the broken halves of HT1-01 was sectioned close to the initiation site, which is also at the mid-thickness of specimen. The sectioned surface was ground, polished and etched, and then investigated by Keyence optical microscope and SEM, as shown in Figure 3.39. A secondary crack path is revealed, and the starting point is close to the fracture surface and deflects towards pre-crack end. The crack path is investigated by using optical microscope and SEM, and the starting point of the path is 765μm from the fatigue pre-crack end. The beginning of the crack path is ductile tearing, followed with transgranular cleavage cracking. The position of this secondary crack is close to the actual fracture distance of the specimen, which is 655μm.

3.5.5 Fractography

Figure 3.38 shows the fracture surface and initiation sites of fracture toughness specimen HT1-01 tested at −100ºC. Figure 3.52 to Figure 3.55 illustrate the fracture surfaces of specimens tested at −170ºC. A very small amount of ductile crack growth could be observed ahead of

fatigue pre-crack, followed by transgranular cleavage fracture. Figure 3.56 to Figure 3.61 illustrate the fracture surfaces and initiation sites of bending specimens tested at −196ºC. As the test temperature decreased to −196ºC, the amount of ductile crack growth ahead of the fatigue pre-crack was negligible, followed by complete transgranular cleavage fracture. Note the analysis in the current thesis concentrates on the fractography of HT fracture toughness specimens tested at lower temperatures at −196 and −170ºC. For C(T) specimens tested at temperatures from −120 to −80ºC, the fractography has been analysed in Weichen Xu's thesis [123] and this is available for comparison.

There are usually multiple inclusion-initiated sites could be found from the fracture surfaces. A global initiation site is often identified from the fracture surface based on the directions of tear ridges, and a non-metallic inclusion could usually be found sitting on the site. The size of inclusions and facets at the initiation site is measured and summarised in Table 3.10.

The cleavage fractures of eight out of ten specimens tested at −196 and −170ºC are inclusion-initiated. The size of inclusions found at initiation sites falls in a range of 0.93 to 3.33μm. By examining the chemical compositions of inclusions located at initiation sites, the inclusions are mainly composed of Mg, Al, S, Ca, and Ti. For the sites containing higher titanium content, the shape of void is cuboidal, and the facet feature is also distinguishable from other facets. The inclusions do not always sit in the centre of the facets. Facets that initiate cleavage fracture have diameters in the range from 42 to 80μm, and their sizes are all larger than the measured grain size of the steel.

The fracture surfaces on both sides of the specimens are checked and analysed by SEM and EDX, and it was found that inclusion-initiated sites could be categorised into two types: some inclusions fail by breaking into two halves, as shown in Figure 3.56, Figure 3.57, Figure 3.58,

Figure 3.60, and Figure 3.61, while some inclusions could only be found on one half of the fracture surface without cracking, and voids are left on the opposite side of the fracture surface, as shown in Figure 3.52, Figure 3.55, and Figure 3.59. These two inclusion-related features are identified as inclusion cracking and inclusion decohesion respectively. For specimens tested at −170ºC, two out of four specimens were failed due to inclusion-initiated cracking and belong to inclusion decohesion. For specimens tested at −196ºC, one out of six specimens were failed due to inclusion decohesion, and five out of six specimens are failed with inclusion cracking. The observation of unique initiation sites combined with the predictions of local tensile stress at these sites, allows an effective surface energy, γ_p, for fracture to be estimated based on a modified Griffith equation stated in Equation 1.11:

$$\sigma_F = \left(\frac{2E\gamma_p}{\pi(1-\upsilon^2)r}\right)^{1/2} \tag{1.11}$$

These effective surface energy values are summarised in Table 3.10 and should be interpreted as the surface energy required to propagate the initial crack from the inclusion into the ferrite grain. Fracture toughness specimens tested at −170ºC have the γ_p values of 5.6 and 8.5Jm^{-2}, and 10.0 to 15.6Jm^{-2} for specimens tested at −196ºC with inclusion diameters <2μm, and 20.3Jm^{-2} for specimen HT1LT-6 tested at −196ºC with an inclusion diameter of 3.3μm.

Not all cleavage fracture is inclusion-initiated. HT1-12 has a higher K_{Ic} value than other specimens tested at −170ºC, and no inclusion was found at the initiation site, and the fracture distance X_0 is also significantly larger than other specimens. However, HT2-15 has a lower K_{Ic} than other specimens tested at −170ºC, the amount of ductile crack growth is smaller than other specimens, as well as its fracture distance. The initiation sites and surrounding matrix are investigated by EDX, and their chemical compositions do not show much difference. The

reason for cleavage fracture of these two specimens is thus unclear but it is not centred on inclusions. It is of interest that this alternative cracking mechanism can produce both higher and lower fracture toughness values compared with cleavage initiation from inclusions.

The fracture distance X_0 is defined as the distances from the fatigue pre-crack end to the front of initiation site, and this value is measured from the fracture surfaces of all the specimens. The values of linear-elastic stress intensity factor K_{Ic} versus fracture distance X_0 for specimens tested at −196ºC and −170ºC are plotted in Figure 3.42. There is a trend for the specimens tested at −170ºC that the fracture distance has a positive correlation to the fracture toughness of the specimen: higher fracture toughness leads to larger initiation site distance. Fracture toughness tests at higher temperatures also exhibit this positive correlation between K_{Jc} and X_0, for example HT1-01 has significantly higher K_{Jc} than other specimens tested at the same temperature, its fracture distance is also significantly higher than other specimens, with 655μm of HT1-01 comparing to the average X_0 of 245μm.

The plastic zone size of specimens tested at −196 and −170ºC is calculated based on Irwin's equation [124]:

$$r_y = \frac{1}{2\pi}\left(\frac{K_I}{\sigma_y}\right)^2 \tag{3.8}$$

Where r_y is the plastic zone size. K_{Ic} values of fracture toughness specimens tested at −196ºC and −170ºC are applied in this equation as K_I. The results are listed in Table 3.11. The results illustrate that the fracture distances are smaller than the plastic zone sizes, which indicates the locations of initiation sites are within the plastic zone and consistent with the widely held concept that local plasticity is a necessary precursor to cleavage fracture.

3.5.6 McMeeking Analysis

The stress analysis on fracture toughness specimens tested at −196 and −170ºC used McMeeking's sharp crack stress distribution analysis. Based on McMeeking's finite element analysis [125], the values of initiation site distance, X_0, and crack-tip opening displacement (CTOD), d, of sharp crack were compared to the stress distribution ahead of the blunted crack-tip.

By referring to McMeeking FEM model, SA-738 Gr. B steel is modelled here with n = 0 and 0.1 as appropriate. The McMeeking plots of stress and plastic strain around the blunted notch are shown in Figure 3.40 and 3.41 [125], where $\sigma_{\theta\theta}$ is the true stress, σ_0 is the yield stress, R and θ are undeformed position of the material. For fracture toughness specimens tested at −196 and −170ºC, the specimens are subjected to a mode I type when θ = 0, and R is the measured distance from pre-crack end to initiation site of fractured specimens, X_0, and b is the crack-tip opening displacement (CTOD). The values of R/b are calculated, and the corresponded $\sigma_{\theta\theta}/\sigma_0$ values are found from McMeeking's plots.

The results of R/b, $\sigma_{\theta\theta}/\sigma_y$, $\sigma_{\theta\theta}$, maximum principal stress σ_{max} and the corresponding fracture distance X_{max}, and the percentage of $\sigma_{\theta\theta}/\sigma_{max}$ are summarised in Table 3.11 with n = 0. The yield stress values are taken from the results obtained in Section 3.3, and the yield stress notation σ_0 in Figure 3.40 and 3.41 is presented as σ_y in table to prevent confusion. One out of four C(T) specimen tested at −170ºC and two out of six bending specimens tested at −196ºC have the values of R/b exceeding 10, which is the maximum x-axis value of McMeeking's plots, the corresponded $\sigma_{\theta\theta}$ values of these specimens are therefore estimated by extrapolating the plots. As the extrapolation is carried where the slope of the curve is relatively shallow and thus some confidence can be attached even to those extrapolated values.

The local cleavage stress versus fracture distance X_0 for specimens tested at −196 and −170°C with n = 0 is plotted in Figure 3.43. Most specimens failed with fracture distances within 50μm. One out of four C(T) specimens tested at −170°C have values of fracture distance of more than 50μm, which is HT1-12. Two out of six bending specimens tested at −196°C have values of fracture distance more than 50μm.

The cleavage fracture behaviour of specimens is analysed by comparing the local cleavage stress to maximum principal stress obtained from blunted crack tip, as shown in Figure 3.44 with n = 0, the values of ratio of local cleavage stress versus maximum principal stress, $\sigma_{\theta\theta}/\sigma_{max}$, are ranging from 71% to 97%. By referring to the estimated values of fracture distance with maximum principal stress, X_{max} listed in Table 3.11, except HT1-12 tested at −170ºC, the real fracture distances X_0 of the rest of specimens tested from −196 to −170ºC are beyond X_{max}.

The plots of local cleavage stress versus test temperature based on McMeeking FEM analysis with n = 0 is shown in Figure 3.45. There is a weak tendency of increasing of test temperatures would lead to a decrease in local cleavage stress values.

One out of four C(T) specimens tested at −170ºC has R/b ratio before the position of maximum stress, which is from HT2 condition, while all bending specimens tested at −196ºC have R/b values beyond the maximum principal stress position. According to McMeeking's plot of stress and plastic strain around the blunted notch in Figure 3.40, plastic strain decreases drastically as the stress increases, and therefore specimens are mostly stress-controlled.

The local cleavage stress versus reciprocal square root of inclusion diameter plots based on McMeeking FEM of n = 0 is shown in Figure 3.46, and they have a weak positive correlation. The local cleavage stress based on McMeeking FEM of n = 0 versus reciprocal square root of

facet diameter is plotted in Figure 3.47. The figures show that facet sizes of specimens have little impact on their local cleavage stresses.

The local cleavage stress obtained according to McMeeking FEM analysis against fracture distance of fracture toughness specimens tested at −120 and −100ºC are plotted together with fracture toughness specimens tested at −196 and −170ºC, as shown in Figure 3.48, and the values of local cleavage fracture stress of sharp-cracked specimens are estimated according to McMeeking's finite element analysis of n = 0 for specimens tested at −196 and −170ºC, and n = 0.1 for specimens tested from −120 to −80ºC, respectively. The local cleavage fracture stresses obtained from blunt-notched fracture stress specimens tested at −196 and −170ºC according to Griffiths and Owen's FEM analysis are also plotted in the same figure with these sharp-cracked specimen data. The fracture distances of blunt-notched specimens are larger than that of sharp-cracked specimens tested at the same temperatures, but with lower local cleavage stresses than sharp-cracked specimens.

The values of local cleavage stress estimated according to McMeeking FEM analysis versus test temperature of fracture toughness specimens tested at −120 and −100ºC (with n = 0.1) are plotted together with fracture toughness specimens tested at −196 and −170ºC (with n = 0), as shown in Figure 3.49. The local cleavage stress values of both sharp-cracked specimens and blunt-notched specimens show little dependence with test temperatures. However, this figure again shows that some of the sharp-cracked specimens have larger local cleavage fracture stresses than those of blunt-notched specimens tested at the same temperatures.

The values of local cleavage stress versus the reciprocal square root of inclusion diameter of both sharp-cracked specimens tested from −196 to −80ºC and blunt-notched specimens tested at −196 and −170ºC, are plotted in Figure 3.51, with local cleavage stress of sharp-cracked

specimens obtained according to McMeeking FEM of n = 0 (−196 and −170ºC) and n = 0.1 (−120 to −80ºC), respectively. The values of local cleavage stress exhibit variation, and there is a weak positive correlation between local cleavage stress and reciprocal square root of inclusion diameter.

CHAPTER 4: SA-738 GR. B STEEL DISCUSSION

4.1 Microstructure

After a stimulated post-weld heat treatment, the microstructure of HT1 changed only very slightly to HT2: boundaries seemed to etch a little deeper and some hint of precipitate coarsening was suggested. However, overall any changes were minimal. became coarsened, and precipitates were coarsened as well. Grain coarsening of HT2 after SPWHT would affect tensile and toughness behaviours in a negative way, so does impact toughness.

4.2 Tensile Testing

The engineering stress-strain curves of SA-738 Gr. B steel specimens show typical mild steel behaviour: it starts with a linear-elastic behaviour until reaching the upper yield point of the specimen, followed with the plastic deformation. The stress drops to the lower yield point, the straining of material continues, and it enters the relatively flat Lüders region. At the end of this region, the stress increases again till ultimate tensile strength.

The yield stress is the point where the material would be deformed permanently. The formation of upper yield stress is often raised by interstitial contaminations such as carbon and nitrogen, these molecules could lock the disengagement. Low temperatures would further hinder the unlocking process, and more stress would be needed, this should explain why yield stress increases with decreasing temperatures. Once the interlocking is opened, the stress would drop to a lower stress level, which is the so-called lower yield stress.

Lüders strain happens due to the inhomogeneous plastic flow contained within the specimens as the result of unpinned dislocations from nitrogen and carbon [126]. The nucleation of local

yielding occurs when a certain stress is achieved. These yielding regions exceed the cross-section of the specimen, and then the upper yield stress drops to a lower stress which maintains the growth of yield bands (Lüders bands), and the propagation direction is in the same direction as the loading directions of tensile tests. After the Lüders strain, the deformation occurs at higher strains and stress becomes homogeneous again [127].

According to Butler [128], the Lüders elongation is related to factors such as grain size, strain rate, and test temperature. As summarised in Table 3.3, the results of HT1 and HT2 tensile specimens show the increase of the Lüders elongation as the temperature drops, as at lower temperatures, yield stress increases and strain rate decreases. The grain sizes of HT1 and HT2 specimens are very similar, and thus their Lüders elongation tested at the same temperature did not show much difference.

Ultimate tensile strength is the maximum stress the material can withstand before necking, and it is a measure of how ductile the material is. The toughness behaviour of HSLA steels with BCC crystal structure is sensitive to temperatures, and the steel would have higher plastic deformation as the temperature increases, leading to a decrease in yield stress in particular. According to Table 3.3 and Figure 3.9, the yield stress and ultimate tensile strength of HT1 are closely similar to that of HT2, noting very similar grain sizes and hardness between HT1 and HT2: the hardness of HT2 is slightly smaller than that of HT1 in both longitudinal and transverse directions in a magnitude of 6-7 HV5, reflecting a relatively higher yield stress and tensile strength of HT1.

During the calculations of the values of work hardening exponent n, it was found that n is sensitively influenced by the gauge length value used for calculation and the data selected from the true stress-strain curve. The work hardening exponent that is estimated by converting the

whole engineering stress-strain curve would result in much higher work hardening exponent value. Obviously, it is better to use an extensometer with the test-piece's own defined gauge length of 50mm, and if it is not available, here I have carefully measured the parallel length of the standard tensile test-piece geometry used and it is 70mm. By using this value, I have been able to obtain closely similar values for tests where I can compare the results with extensometer and without extensometer. For example, the work hardening exponent of HT1-10 tested at −120ºC is 0.059 with extensometer attachment, and 0.061 without extensometer, respectively. The non-uniform Lüders elongation does create some interpretation difficulties with the simple fitting of a true stress-true strain curve. Here we set the strain at the end of the Lüders elongation to be defined by the lower yield stress divided by the Young's modulus. This becomes our starting value of strain for the uniform work-hardening region which follows. As the work hardening exponent is determined by the uniform elongation, it can reflect the material's embrittlement [129]: a lower work hardening exponent would lead to the build-up of local stress within the specimen, and the moment redistribution is also decreased, leading to a poor resistance of the specimen to deformation.

Apart from the work hardening exponent, the ratio between yield stress and tensile strength, yield ratio (YR), can also suggest the deformability of materials [129]. YR has an inverse relationship to the uniform elongation.

4.3 Charpy Impact Testing

According to the absorbed impact energy versus test temperature plot in Figure 3.16, HT1 and HT2 specimens exhibit ductile-to-brittle transitions. The impact toughness values of HT1 and HT2 are very similar, and both conditions exhibit narrow ductile-to-brittle transition regions between −100 and −80ºC, with few data points falling within this transition range. At −100ºC,

the majority of specimens fall on the lower shelf, and as the test temperature increased to −80ºC, most specimens were distributed close to the upper shelf, and only one out of nine specimens had a lower impact energy. HT2 had more evenly distributed impact energy values at −90ºC. The narrow transition region and the resulting steep tanh curve gradient here are deduced to be both the cleanliness of the steels and the fact that the inclusions are observed initiate both cleavage fracture and micro-void coalescence mechanisms of fracture. The steels appear to be clean from the inclusion size distributions shown in Figure 3.5, where sizes of the larger inclusions range from 2 to 7μm account for 12 to 15% of the total number of inclusions identified. In addition, the same population of inclusions triggers both cleavage (if they crack or decohere), and micro-void coalescence.

According to the ASME Code [1], the minimum value of the required Charpy impact energy for SA-738 Gr. B steel plate with a thickness between 38.1 and 63.5mm at −60ºC should be greater than or equal to 48J, and the average impact energy at −60ºC should be greater than or equal to 55J. By referring to the results of Charpy impact tests of HT1 and HT2 in Table 3.4, the minimum absorbed impact energy for both HT1 and HT2 is 237.0J, which fully satisfies the ASME Code.

The upper shelf energy could not be estimated as the maximum capacity of the impact tester used in testing was 300J, and the upper shelf energy of some specimens is close to or exceeds the maximum capacity of the tester. The impact test results of the same material conducted on an impact tester with the maximum capacity of 350J provided by Baowu Steel are plotted in Figure 3.17. According to Baowu's results, the upper shelf energy of HT specimens is around 320J.

By referring to the fracture surface examination results under optical microscope, the surface features are related to the absorbed impact energy. Percentage of cleavage area is negatively related to the absorbed impact energy, and lateral expansion is positively correlated to the absorbed impact energy, as shown in Figure 3.20 and Figure 3.23 respectively. The fracture surface changes from 100% ductile fracture at the upper shelf to 100% cleavage fracture at the lower shelf, and the absorbed impact energy also changes as the temperature drops. The specimens that failed within the transition region exhibit both cleavage and ductile features on the fracture surface: the ductile crack initiates and grows at the notch root until cleavage fracture occurs to cause final failure, and the length of the ductile thumbnail is positively correlated with the absorbed impact energy, as shown in Figure 3.26. There are relatively few data points fall in the region between the upper shelf and the lower shelf of the plots mentioned above, which should be due to similar reasons as the narrow transition region of HT1 and HT2. Cleavage fracture does not absorb much energy and would not cause too much deformation. The cleanliness of the material would lead to either high fraction of cleavage fracture initiated close to the notch root or high fraction of ductile crack growth at the notch root followed by cleavage fracture, as few inclusions would trigger cleavage fracture [130]. According to Zhang's work on SA-738 Gr. B steel, further heat treatment could lead to recovery and recrystallisation process, and more carbides precipitate along boundaries, and the carbide sites could reduce grain boundary's cohesive energy and enhance embrittlement [131]. Other phenomena that would increase DBTT includes carbide coarsening and phosphorus segregation during aging [132]. However, here HT1 and HT2 are closely similar in impact transition behaviour- consistent with their closely similar microstructure and inclusion distribution.

Tanh curves were fitted to absorbed energy versus test temperature plots, as shown in Figure 3.14 to Figure 3.16, and the values of DBTT for HT1 and HT2 are −91 and −87ºC respectively.

Both DBTTs are well below the designed application temperature of nuclear containment vessel plate. Although the upper shelf energy used was 300J when fitting the transition curves, there are enough data points falling at the transition region to locate the position of transition curve from lower shelf to upper shelf. Master Curve methodology in Section 2.6.2 estimated the values of T_{41J}, according to the transition curves in Figure 3.14 and Figure 3.15, and the results in Section 3.5.3 prove the reliability of these ductile-to-brittle transition curves. Although there are some limitations for the tanh fitting method, its symmetrical nature is not a necessary property for the impact transition data scatter. The shape of the curve is also limited, and it is lacking some flexibility. Special care is often needed to be taken to choose the constant values to set the position of the curve. However, this tanh fitting method works very well in this work.

4.4 Fracture Toughness Testing

The K_{Jc} value describes the local effective stress intensity, whereas K_Q describes the local constraint. Local constraint is affected by local effective stress intensity, and local stress intensity is affected by any ductile tearing that occurs before cleavage initiation. It is straightforward to compare the values of K_Q and K_{Jc} tested at the range from −196 to −80ºC in Figure 3.29 and 3.30: the larger the difference, the more the ductile crack growth involved due to the increment of J-integral at the onset of cleavage fracture J_c. As test temperature increases, more specimens tend to have higher K_{Jc} values as the results of increased plastic mode and J_c values. At temperatures of −120ºC and below, smaller differences between K_Q and K_{Jc} suggest that specimens were fractured mainly with cleavage. The average K_Q values of specimens tested at −196 and −170ºC are significantly less than specimens tested at or above −120ºC due to that the specimens were fractured at lower shelf temperatures, and their results are all valid as linear-elastic K_{Ic} with little or no ductile crack growth at the pre-crack front.

According to the load-displacement curves of fracture toughness specimens, the specimens tested at the ductile-to-brittle transition region failed after reaching the plateau of maximum load, and ductile crack propagated. In general, specimens fail by general yielding (plastic collapse) after passing maximum load, but fractography shows that specimens cleave after some amount of ductile crack growth. This could be due to the increase in yield stress at the lower shelf temperature than at higher temperatures, the maximum tensile stress for cleavage fracture becomes lower with temperature increase. In order to fracture by cleavage with a lower maximum local tensile stress available, the crack continues to grow in a ductile manner, and the maximum tensile stress position also moves further until a potent initiation site is met, and thus cleavage fracture occurs.

The transition behaviour of fracture toughness tests started at a lower test temperature of −120ºC compared to the transition behaviours of CVN tests starting at −100ºC, but at −80ºC, the scattering of fracture toughness data still existed, and wider than the scattering of Charpy impact test data [133]. The phenomenon is due to that there are some differences between Charpy impact test and fracture toughness test. Firstly, the strain rate of Charpy tests is much faster than that of fracture toughness tests [134]. Apart from strain rate, two specimens have different constraint levels: both Charpy impact test specimens and fracture toughness specimens have machined notches, and the notches of fracture toughness specimens are fatigue pre-cracked to form sharp notches, the crack notch of fracture toughness specimens are gradually blunted during loading. The shallow notch of CVN specimens together with a faster loading rate would result in a rapid loss of constraint, and the crack resistance is thus enhanced. The Charpy impact specimen shows a higher fracture toughness, which enhances the apparent crack resistance curve in comparison to a plane strain quasi-static condition.

4.4.1 Master Curve Methodology

The application of the Master Curve methodology to estimate reference temperature T_0 of SA-738 Gr. B steel is proved to be a valid way to analyse the toughness behaviours of this HSLA steel at the transition range. Both single temperature analysis and multiple-temperature analysis estimated that the temperature at which the median elastic-plastic K_{Jc} equals 100MPam$^{1/2}$ is around −100ºC. HT1 and HT2 specimens exhibited similar toughness behaviours at a temperature range from −120 to −80ºC, except HT1-01 tested at −100ºC, and there is a difference of ~ 10ºC between the calculated values of reference temperature T_0 when including HT1-01 and excluding HT1-01, by comparing the Master Curves plotted in Figure 3.35 and Figure 3.36. The fracture surface of HT1-01 shows that it has a longer region of stable crack growth, according to Figure 3.38(b). The crack side path of HT1-01 also reveals the appearance of secondary crack and the ductile crack initiated and grew at the beginning, followed by transgranular cleavage. Higher failure load, more unloading/reloading cycles, larger ductile crack length, and larger CTOD indicate higher stress intensity and more plasticity involved during fracture, the existence of secondary crack also took the compliance of fracture. The above factors all contribute to a larger K_{Jc} and thus bring down the reference temperature.

Estimation of the reference temperature by using the Master Curve methodology is invalid when using the fracture toughness results of specimens tested at lower shelf temperatures of −196ºC and −170ºC. The reference temperature value should satisfy $T_0 \pm 50$ºC, which suggests for specimens tested at −196 to −80ºC, T_0 = −146ºC is only valid for specimens tested at the range from −196ºC to −96ºC, and for specimens tested at −170 to −80ºC, T_0 = −180ºC is only valid for specimens tested at the range from −230 to −130ºC. These attempts prove that the Master Curve methodology is not suitable to analyse toughness behaviours of specimens tested

outside the transition range, even though the yield strength of HT specimens tested at −170ºC is still within the ferritic yield strength range of 275 to 825 MPa as stated in ASTM E1921.

The selection of single temperature analysis for the estimation of reference temperature was based on the results of T_{28J} and T_{41J} obtained from the tanh-fit transition curve from Charpy V-notch tests. Although the CVN specimens have higher impact energy exceeding the impact tester energy limit, there are enough data points lie at the lower shelf and ductile-to-brittle transition region to ensure the tanh curves fit well with the data points, and the fracture toughness test results also verified the position of the curve is reliable.

4.4.2 Fractography of Specimens tested at Lower Shelf Temperatures

Fractography analysis was mainly focused on fracture toughness specimens tested at −196 and −170ºC, which are the lower shelf temperatures. As mentioned above, local K_Q is affected by any ductile tearing occurs prior to cleavage initiation. Referring to the fractography of specimens tested at −170ºC, they exhibit a small amount of ductile crack growth before cleavage, while for specimens tested at −196ºC, ductile extension is negligible. According to the results of linear-elastic K_{Ic} and fracture distance X_0 of fracture toughness testing at −196 and −170ºC as plotted in Figure 3.42, the distribution of toughness values does not have a strong correlation to the fracture distance. According to Landes [135], cleavage fracture is initiated from the weakest point of microstructure, and this weakest point is randomly located along the crack front.

Referring to the local cleavage stresses based on McMeeking FEM analysis of n = 0 (Figure 3.40), one out of nine specimens, HT2-15 tested at −170ºC, failed from a site at R/b = 1.2, which is **before** the maximum stress position of R/b = 2.9. Failure before the position of maximum stress is not consistent with a purely tensile stress-controlled failure condition. This

site will have seen this level of tensile stress at a lower applied CTOD value, but it did not fail until the local strain at this position built up with increasing applied CTOD. However, nine out of ten sites do fail at sites where R/b > 2.9, thus they do support a purely tensile stress-controlled failure criterion combined with some variability due to sampling weakest link theory. Most specimens tested at −196 and −170ºC have fracture distances of less than 100μm, and referring to Figure 3.48, many fracture toughness specimens tested at −120, −100 and −80ºC have fracture distances of less than 200μm, and this will be discussed in later sections.

The plastic zone is assumed to be a circular region around the crack tip, and the estimations of plastic zone size have shown that the initiation sites of fracture toughness specimens cleaved at −196 and −170ºC are located within the plastic zone, and according to Xu's analysis on the plastic zone size of SA-738 Gr. B steel specimens tested at transition region from −120 to −80ºC[123], the initiation sites are also located within the plastic zone. It is almost routine, and prior plasticity long been recognised as essential pre-requisite for cleavage.

Eight out of ten cleavage fracture initiation sites are identified as inclusion-initiated for fracture toughness specimens tested at −196 and −170ºC, as summarised in Table 3.10. Most initiating inclusions have the size between 1 to 2μm, one out of eight have a diameter below 1μm with inclusion decohesion, and one out of eight has the diameter above 3μm with inclusion cracking. According to the inclusion size distribution as shown in Figure 3.5 obtained by analysing polished surfaces of HT1 and HT2 Charpy V-notch specimens in longitudinal direction, the size of most initiating inclusions falls in the more frequent categories, but the number of inclusions with diameter of more than 3μm is much less.

HT1TL-E tested at −196ºC with a smaller fracture distance of 21μm has the highest local cleavage stress of 2699MPa among all specimens plotted in Figure 3.48. HT1TL-E has the

initiator diameter of 1.2μm with cubic shape containing Mg, Al, Ca, Ti, Nb, O, S, these sharp edges of inclusion could easily become stress concentrator and lead to cleavage fracture comparing to other circular inclusions.

Referring to Figure 3.46, there is a weak positive linear relationship between local cleavage stress and reciprocal of reciprocal square root of inclusion diameter, and it matches with the modified Griffith equation of a penny-shaped crack in the material, where the initiator size is thought to be the critical crack length.

Two out of two inclusion-initiated fractures are caused by inclusion decohesion for specimens tested at −170ºC, while one out of six inclusion-initiated fractures tested at −196ºC failed by inclusion decohering. Other five inclusion-initiated fractures are caused by inclusion cracking, which reflects that inclusion cracking is more preferred at −196ºC, and less energy and stress is required to break open a crack than inclusion decohering from the surrounding matrix. However, the local cleavage stresses are not affected at these two similar lower shelf temperatures as shown in Figure 3.45.

According to the results of EDX analysis, the chemical compositions of inclusions found on the fracture surfaces contain oxides or sulphides with Mg, Al, Ca, Ti. This is due to that the second-phase particle is originated from a single oxide, and this original oxide plays as the core and nucleation point for the formation of complex oxide. There are some limitations for EDX analysis, as the beams could only detect chemical compositions of surface region of the selected area, which may not be able to analyse the whole 3D inclusions, and the results cannot be avoided to include the chemical compositions from the surrounding matrix.

The surface energy of the initiating particles γ_p was not influenced by test temperatures, and this was in agreement to the previous literatures [136, 137].

4.4.3 Comparisons Between Sharp-Cracked and Blunt-Notched Specimens

4.4.3.1 Local Cleavage Stress and Fracture Distance

The local cleavage stress versus fracture distance of both sharp-cracked specimens tested at the range from −196 to −80ºC and blunt-notched specimens tested at −196ºC and −170ºC are plotted together in Figure 3.48. Sharp-cracked specimens have fracture distances ranging from 6 to 657μm, and their local cleavage stresses vary from 1716 to 2699 MPa. For blunt-notched specimens, the fracture distances are ranging from 220 to 400 μm, and their local cleavage stresses vary from 1678 to 2039MPa. The average value of local cleavage stresses for blunt-notched specimens and sharp-cracked specimens is 2176 MPa, with a standard deviation of 240 MPa. Many sharp-cracked specimens have fracture distances of less than 200 μm, and these specimens have higher local cleavage stress than blunt-notched specimens. The sharp-cracked specimens with fracture distances of less than 200μm have higher local cleavage stress than those with fracture distances of more than 200μm. The average cleavage stress for sharp-cracked specimens with fracture distances of less than 200μm is 2316 MPa, and the standard deviation is 169 MPa. The blunt-notched specimens were tested at lower shelf temperatures of −196ºC and −170ºC, and they have lower local cleavage fracture stresses than sharp-cracked specimens tested at the same temperatures, and this should be due to that sharp crack has higher stress concentration at the crack tip than the blunted notch, in which cleavage initiation would be easier to occur at shorter fracture distances. Both Griffiths and Owen FEM analysis and McMeeking FEM analysis plots exhibit that specimen fails with larger fracture distance would result in lower local cleavage stress.

For the occurrence of cleavage fracture, a critical local stress should be reached, and otherwise ductile crack will result. Three criteria should be satisfied simultaneously: 1. $\epsilon_p \geq \epsilon_{pc}$ for the initiation of a crack nucleus; 2. $\sigma_m/\sigma_e \geq T_c$ for the prevention of crack tip blunting; and 3. $\sigma_{yy} \geq \sigma_F$ for the propagation of the crack, where ϵ_p is plastic strain, ϵ_{pc} is fracture plastic strain, σ_m is the mean stress, σ_e is the equivalent stress, σ_m/σ_e is stress triaxiality, T_c is the critical stress triaxiality, σ_{yy} is the normal tensile stress perpendicular to the surface of cracking, and σ_F is the local cleavage fracture stress [138]. Chen and other co-workers did their experimental work on C-Mn ferritic steels at temperatures from the lower shelf region to the transition region, and they compared the results with the FEM analysis. For specimens tested at lower shelf temperatures, the cleavage fracture was triggered either by second-phase particles or inside the ferrite matrix. The specimens that failed inside the ferrite matrix have a negligible amount of fracture distances, and by referring to their FEM analysis, the nucleation of crack inside ferrite matrix was induced by a high strain, and the crack nucleated by second-phase particles has a higher stress and little strain [137, 139]. The strain-induced crack nucleation is related to the high yield stress at low temperatures.

For specimens tested at moderately low temperatures (transition region), the results suggested that the tip of fatigue pre-crack in a quasi-cleavage material might be blunted due to the residual tensile plastic strain, this strain is sufficient for the initiation of a crack nucleus. When the applied load is too small, the stress triaxiality is not high enough to prevent samples from blunting, and failure stress is not high enough for propagation. If the load is increased, three criteria for cleavage fracture can be satisfied, and cleavage fracture can be triggered if a second-phase particle is presented, and the scatter of the toughness data tested at moderately low temperatures is due to the various locations of the second-phase particles [139].

The local cleavage stress levels of sharp-cracked specimens with fracture distances exceeding 200μm are similar to those of blunt-notched specimens, and they have an average local cleavage stress of 1941MPa, with a standard deviation of 132 MPa. At higher temperatures, the yield stress decreases, and as a result, fracture stress σ_{yy} also decreases. To compensate for this reduction, fracture plastic strain increases, and the work hardening also increases, and the above can be satisfied by increasing the applied load. However, the maximum value of stress is limited, according to Rice and Johnson [24]. $\sigma_{yyt} > \sigma_{F(c)}$ is the criteria for crack propagation under this condition, where σ_{yyt} represents the driving force for propagation, and this term includes normal tensile stress σ_{yy} produced by the applied load and the dislocation pileup σ_L. When the test temperatures increased further and entered the upper end of the lower shelf, the fracture surfaces of the tested specimens exhibit a short fibrous crack extension before cleavage fracture. The measured average values of σ_{yyt} are close to the specimens tested at the lower region of the lower shelf. However, the measured average values of σ_{yy} was lower than that of specimens tested at lower temperatures, and σ_{yy} determines the critical event of microcracking is most likely to be the propagation of a grain-sized crack rather than the propagation of a particle-sized crack. At higher temperatures, yield stress σ_y would be further decreased, but $\sigma_{yy} \geq \sigma_F$ is the critical requirement for the propagation of a grain-sized crack into contiguous grains, and the value of σ_f is stable and temperature-independent. If σ_{yy} is reduced as the result of the reduction in yield strength, and it may not be high enough to propagate the crack, the crack would be hindered by the grain boundaries. In order to trigger the cleavage fracture, σ_{yy} should keep the same value in both lower and higher division of the lower shelf. The differences in the value of σ_{yy} between two regions should be due to the presence of fibrous crack after blunting of the notch [137].

The ductile extension of the specimen would move the peak of the normal stress σ_{yy} closer to the pre-crack tip, and the criteria of cleavage fracture nucleation and propagation could be satisfied [137]. The works from Dodds et al. [140], O'Dowd et al. [141], and Ostby et al. [142] all showed the above phenomenon, and the peak value of σ_{yy} would also increase.

It may suggest that when sharp-cracked specimens have fracture distances exceeding 200μm, they would have similar local stress conditions with blunt-notched specimens, regardless of their test temperatures or specimen geometry.

4.4.3.2 Local Cleavage Stress and Test Temperature

According to Figure 3.49, the local cleavage stresses of blunt-notched specimens tested at −196 and −170ºC based on Griffiths and Owen FEM, as well as the local cleavage stress of sharp-cracked specimens tested from −196 to −80ºC based on McMeeking FEM, are comparable, and they have quite close lower bound values, with 1777, 1716, 1954, 1870, and 1992MPa for sharp-cracked specimens tested at −196, −170, −120, −100 and −80ºC. For blunt-notched specimens tested at −196 and −170ºC, their lower bound values of local cleavage stress are 1678 and 1915MPa respectively. The local cleavage stresses are thus considered to be independent of test temperature.

4.4.3.3 Local Cleavage Stress and Maximum Principal Stress

The maximum stress is achieved when R/b = 2.96 and 2.17, for n = 0 and 0.1 respectively. The local fracture stress versus the maximum principal stress of all sharp-cracked specimens together with blunt-notched fracture stress specimens is plotted in Figure 3.50. For the fracture stress values of sharp-notched specimens tested at −196 and −170ºC estimated based on n = 0, there is one out of ten specimen failed with CTOD before the maximum principal stress, and

for the fracture stress values of sharp-notched specimens tested at −120 to −80ºC estimated based on n = 0.1, two out of 28 specimens failed with R/b before the maximum principal stress, the failures for these specimens are not purely tensile stress-controlled, but with the involvement of tensile strain. For specimens failed with R/b corresponding to the position beyond the maximum principal stress, the peak stress should have promoted the occurrence of cleavage fracture. Sites occur when they first hit the local tensile stress to achieve failure.

4.4.3.4 Local Cleavage Stress and Surface Energy Estimates

According to the modified Griffith's equation, there should be a linear relationship between local cleavage stress $\sigma(X_0)$ and the reciprocal of inclusion diameter. In current work, there is a weak positive correlation between the local cleavage stress of sharp-cracked specimens as well as the blunt-notched specimens tested at −196 and −170ºC and the reciprocal of inclusion diameter, as shown in Figure 3.46 and Figure 3.51. Analysis suggests a γ_p value of 5.6 and 8.5Jm^{-2} for fracture toughness specimens tested at −170ºC, and 10.0 to 15.6Jm^{-2} for specimens tested at −196ºC with inclusion diameters of less than 2μm, 20.3Jm^{-2} for specimen HT1LT-6 tested at −196ºC with inclusion diameter of 3.3μm. According to Xu's works on sharp-notched specimens tested at temperatures from −120 to −80ºC, however, the correlation of the local cleavage stresses calculated according to McMeeking FEM analysis versus the reciprocal of inclusion diameter is very poor, with variations from 7.2 to 33.5Jm^{-2} at −120ºC and 7.4 to 30.0Jm^{-2} at −100ºC. The values of effective surface energy estimated from the fracture of these cracked inclusions are independent of test temperature, and this is in agreement to many other works [31] [143].

4.5 Comparisons to other SA-738 Gr. B Steel

Wang et. al [79] conducted a series of mechanical tests on SA-738 Gr. B steel with similar chemical compositions and quenching-tempering heat treatment conditions to the SA-738 Gr. B steel studied in this thesis. The results from Wang et. al showed that the yield stress and tensile strength of QT specimens were higher than that of specimens with an additional SPWHT process. The tensile results were higher than the ASME requirement, and similar to the tensile results obtained in this thesis. The impact test results, however, exhibited a smoother transition from the lower shelf to upper shelf.

The carbon content of SA-738 Gr. B steel plate tested by Zhang et al. [144] was similar to that of SA-738 Gr. B steel plate tested in this study, and the thickness of their steel plate was 60mm. The upper shelf energy obtained from their CVN test was about 400J, and transition temperature values of T_{28J} and T_{41J} were about −120ºC and −113ºC, while their yield stress and tensile strength values at −120ºC were higher than that of steel plate investigated in this thesis. The yield stress of 66mm steel plate at −110ºC was higher than that of both HT1 and HT2 tested at −100ºC in this thesis, but the tensile strength of this 66mm steel plate at −110ºC was lower than that of HT1 and HT2 tested at −100ºC. Zhang et al. also showed that the Master Curve methodology was not applicable to their fracture toughness due to inhomogeneity of their steel plate. Overall, the experimental works from different project group have proved the reliability of the experimental procedures and processing in this thesis.

CHAPTER 5: SA-738 GR. B STEEL CONCLUSIONS

1. The experimental programme of SA-738 Gr. B steel manufactured by Baowu Steel focused on two heat treatment conditions, HT1 and HT2. One objective of this thesis was to compare these two heat treatment conditions based on their mechanical testing results and fractography. The test results show that specimens of both HT1 and HT2 have similar grain size, hardness, tensile, impact toughness, and fracture toughness properties.
2. The yield stress and tensile strength of HT1 and HT2 show strong dependency on test temperatures, as the temperature increased, yield stress and tensile strength both decreased- differences between tensile strength and yield stress however increased, defining more extensive work hardening with temperature increase.
3. The engineering stress-strain curves exhibit Lüders elongation after passing lower yield point, and the amount of Lüders elongation increased as the temperature decreased. The work hardening exponents are increased with increasing temperatures, and the n values vary from 0.01 to 0.11 at test temperatures ranging from −196 to −60ºC.
4. The Charpy impact testing results of HT1 and HT2 exhibit clear lower shelf and upper shelf behaviour, with failure from 2J to close to 300J. The ductile-to-brittle transition occurred at the temperature range from −100 to −80ºC. According to the fitted tanh curves to absorbed energy versus test temperature plots: HT1 has the DBTT of −91ºC, while HT2 has the DBTT of −87ºC. The upper shelf energies of both HT1 and HT2 are above 300J, and the lower shelf energies of both HT1 and HT2 are about 2-5J.
5. The absorbed impact energy has a strong positive linear correlation with lateral expansions and ductile thumbnail extension. There is also a negative linear relationship between impact energy and percentage of cleavage area. The crystallinity of fracture surface varied from 100% cleavage at lower shelf and 100% ductile at upper shelf.

6. The fracture toughness results on HT1 and HT2 results exhibited ductile-to-brittle transition behaviour. The number of unloading compliance cycles during testing, the values of K_Q, and K_{Jc} increased as the test temperatures increased- indicating more ductile crack growth involved during the fracture process, and it is confirmed by fractography.
7. The reference temperature T_0 of specimens from HT1 and HT2 condition obtained by the Master Curve methodology are consistent at −120ºC, with the K_{Jc} data distributed evenly within 95% and 5% tolerance bounds. The reference temperature HT2 tested at −100°C remain to be around −100ºC, but the abnormally higher fracture toughness value of HT1-01 lowers the reference temperature of HT1 condition obtained at −100°C and at multiple-temperature analysis, due to the involvement of more ductile crack extension and a major secondary crack within the test-piece. The behaviour of this individual test is thus different. The overall application of the Master Curve methodology to estimate the reference temperature of HT1 and HT2 specimens is reliable.
8. Fractography of fracture toughness specimens tested at −196 and −170ºC showed that all specimens failed with transgranular cleavage, and eight out of ten cleavage cracks were initiated from inclusions. In five out of eight test-pieces, these inclusions were cracked, and three out of eight inclusions were decohered. There is also a weak positive correlation between local cleavage stress and the reciprocal square root of inclusion diameter according to the modified Griffith equation. Values of γ_p vary from 5.6 to 20.3 Jm^{-2}. For specimens tested at −196 and −170ºC, the locations of initiation sites show a variation from 6 to 221 μm, but this limited variation does not produce a consistent change in fracture toughness. According to the McMeeking's FEM analysis on the ratio of fracture distance and CTOD, R/b, nine out of ten specimens have the local fracture initiation sites located at positions consistent with a pure tensile stress-controlled failure criterion, with only one failure

deduced to be under mixed tensile stress/strain control. The results also showed the independence of local cleavage fracture stress over a very wide range of test temperatures from −196 to −80ºC. This is consistent with a classical mechanism for the ductile-brittle transition region, as progressively increased stress concentration is needed to achieve the local cleavage fracture stress with temperature increase, with a concomitant reduction in yield stress.

9. The local cleavage fracture stresses of both sharp-cracked specimens and blunt-notched specimens analysed by McMeeeking and Griffith and Owen's FEM respectively are independent of test temperatures. There is a weak positive relationship between the local fracture stress of blunt-notched specimens and reciprocal square root of initiating inclusion diameter. The locations of initiation sites of these specimens all sit within the plastic zone, and close to the position of the maximum principal stress.
10. The mechanical behaviour of HT1 and HT2 is identical.

Future Work

The splitting of tensile specimens on longitudinal direction has driven interest on the low-temperature toughness behaviour of this 20mm-thick SA-738 Gr. B steel in this specific direction. Specimens of CVN, fracture stress, and fracture toughness could be machined with the notch direction of STL to further investigate the mechanical performance and micromechanism of the steel.

Griffiths and Owen and McMeeking FEM analysis of fracture stress used in this thesis were established in 1970s. The work hardening exponents of SA-738 Gr. B steel plate studied vary from 0.01 to 0.11, and it is perhaps worth developing a specific finite element analysis for this material.

According to the fractography analysis of initiation sites of cleavage fracture in section 3.5.5, most initiators are non-metallic inclusions, but other sites could be initiated from microstructure features such as carbides or M-A constituents. It is also difficult to tell the differences between granular bainitic and irregular ferrite region. Further investigations could be carried out to address such sites further.

CHAPTER 6: 7% AND 9% NICKEL STEELS: RESULTS

6.1 Microstructure

The microstructure images of 9% and 7% nickel steels taken by both optical microscopy and SEM are shown in Figure 6.1 and Figure 6.2. The SEM micrographs and electron backscattered maps of 7% and 9% nickel steels are shown in Figure 6.3, and the grains are coloured according to the orientations based on inverse-pole figure (IPF). The microstructure of 9% nickel steel is mainly composed of tempered martensite. The phase maps obtained by EBSD analysis are shown in Figure 6.3(c) and (d) for 7% nickel steel and 9% nickel steel. The phase for 7% nickel steel is mostly BCC by EBSD analysis, and no FCC content could be identified. For 9% nickel steel, the identified phase is mostly BCC, with 4% FCC content, which is considered to be retained austenite, and they can be seen to be mainly located at the grain boundaries. The average martensitic block size for 9% nickel steel was measured by lineal intercept procedure stated in ASTM Standard E112-13, which gives 9.8μm, with a standard deviation of 2.1μm. The block size was also measured automatically by Bruker's EBSD analysis function according to the orientation of packets within the blocks, the total number of grains counted was 3531, with an average block size of 9.3μm, and the median size was 6.7μm. The grains identified as FCC have much smaller size, and the average prior-austenite grain size is 1.6μm.

The 7% nickel steel is considered to be mainly contains tempered martensite, with distinct block boundaries. The average martensitic block size for 7% nickel steel was 22.5μm by lineal intercept procedure. The average prior austenite grain size among 2410 grains was 16.2μm according to the EBSD analysis of Bruker, and the median grain size was 12.2μm. Figure 6.4 and Figure 6.5 show the distribution of misorientation angles of 9% and 7% nickel steel grains. For both nickel steels, most grains have high-angle misorientation (>15^{o}).

The inclusion size distribution of 9% and 7% nickel steels is shown in Figure 6.6. The results exhibit a 2D modal for both steels. The lower limit of detection was set to be 0.2μm due to the image resolution. For 9% nickel steel, a total of 6080 inclusions in the area of 10267 mm^2 was counted, and it gives 593 inclusions/mm^2. For 7% nickel steel, a total of 10427 inclusions was counted in the area of 11035 mm^2, and it gives 945 inclusions/mm^2. Both nickel steels have 96% of inclusions with inclusion size between 0.2μm and 3μm.

6.2 Hardness Testing

The mean hardness value along longitudinal direction of 9% nickel steel was 255 HV5, with a standard deviation of 4 HV5. For transverse direction, the mean hardness value was 254 HV5, with a standard deviation of 2 HV5.

The through-thickness hardness was tested along the thickness of 16mm-thick 9% nickel steel SENB sample. The hardness values of 9% nickel steel are listed in Table 6.1. The results show an average hardness of 256 HV5 and a standard deviation of 3 HV5.

The mean hardness value at longitudinal direction of 7% nickel steel was 254 HV5, with a standard deviation of 5 HV5. For transverse direction, the mean hardness value was 256 HV5, with a standard deviation of 2 HV5.

The through-thickness hardness was tested along the thickness of 16mm-thick 7% nickel steel SENB sample, which is also the transverse direction. The hardness values of 7% nickel steel are illustrated in Table 6.2. The results give an average hardness of 228 HV5 and a standard deviation of 4 HV5.

6.3 Tensile Testing

The tensile tests for nickel steels focused on the temperature range from −196 to −130°C, to span the suggested material service temperature of −163°C. For 7% nickel steel, a total of eight specimens has been tested, with two specimens tested at each of the −196, −170, −150 and −130°C test temperatures. The measured diameters of 7% nickel steel tensile specimens are summarised in Table 6.3. The broken halves of the tested specimens at each temperature are shown in Figure 6.9. Most specimens failed with micro-void coalescence with some splits observed at the fracture surface. However, 7Ni-9 tested at −196ºC has some different fracture feature- the specimen failed with longitudinal fragmentation and details of a side view of 7Ni-9 are shown in Figure 6.10. The tip of the fracture surface is about 53º to the main longitudinal fracture surface. There is a crack extending along loading direction towards the grip section, and then crack moved away from the loading direction at an angle of 45º. Necking before failure was observed for all specimens, and it is worth noting that for most of the tensile specimens, the first crack observed during necking before final failure is parallel to the loading direction.

The engineering stress-strain curves of 7% nickel steel tested at temperatures from −196 to −130°C based on crosshead displacement records are shown in Figure 6.12. The calculation of engineering strain used a parallel length of 70mm. These graphs indicate the characteristic definite yield point behaviour at these test temperatures, and the stresses decrease ~20MPa. At −196°C and −170°C, the curves enter the flat Lüders region before the rise of stress till tensile strength, while specimens tested at temperatures above −170°C do not exhibit the same way, and the stress increased directly from the lower yield point. The engineering stress-strain curves based on extensometer records are shown in Figure 6.13, the recordings were interrupted before final failure as the total plastic strain exceeded the measuring range of extensometer.

The tensile testing results of 7% nickel steel are summarised in Table 6.4, including the upper and lower yield stress, ultimate tensile strength, and total plastic strain. The yield stress increases from an average of 879 MPa at −130°C to an average of 1052 MPa at −196°C while the tensile strength increases from an average of 932 MPa at −130°C to an average of 1094MPa at −196°C. The values of total plastic strain for 7% nickel steel according to the engineering stress-strain curves varied from 19.3% to 21.0% at the test temperatures range from −196 to −130ºC. The elongation of specimens appears to be independent of test temperatures.

True stress-strain curves of 7% nickel steel tested at the temperature range from −196 to −130ºC are plotted by taking logarithm of engineering stress and strain values, including the region from lower yield stress to ultimate tensile strength, as shown in Figure 6.14. The conversion method is the same as the one used for SA-738 Gr. B steel in Section 3.3. The Lüders regions of 7% nickel steel specimens tested at −196 and −170ºC were excluded from the calculation of work hardening exponent n due to their inhomogeneous nature. The work hardening exponent values of 7% nickel steel are summarised in Table 6.4, they have a weak positive relationship with the test temperatures: the lower the test temperature, the lower the value of work hardening exponent. The values of work hardening exponent at temperatures from −196 to −130ºC range from 0.03 to 0.06.

Referring to the previous tensile tests for Baowu 9% nickel steel listed in Table 6.5, the 0.2% proof stress of Baowu 9% nickel steel increases from an average of 812 MPa at −130ºC to an average of 1071 MPa at −196ºC, while the tensile strength increases from an average of 1009 MPa at −130ºC to an average of 1166 MPa at −196ºC. The results of UTS and yield stress of 7% nickel steel and 9% nickel steel are plotted together in Figure 6.17. Comparing to 7% nickel steel, 9% nickel steel has lower values of yield stress (0.2% proof), but higher values of tensile

strength. The stress-strain curves of 9% nickel steel tested at −196°C as shown in Figure 6.16 do not have Lüders elongation, and the stresses decrease slightly after reaching the upper yield point and starts the strain hardening process till tensile strength. The values of total elongation of two 9% nickel steel specimens tested at −196ºC are 25.0% and 25.1% respectively, and the values of work hardening exponent n are both 0.14. 9% nickel steel exhibits larger total plastic strain and higher work hardening exponent than 7% nickel steel even at −196ºC.

6.3.1 Fractography of Tensile Specimens

The total fracture surfaces and detail of the fracture surfaces observed under higher magnification of selected 7% nickel steel tensile specimens tested at the range from −196 to −130°C are shown in Figure 6.18. Most tensile specimens failed with micro-void coalescence, and the splits are all located in the middle of the fracture surfaces, with smaller splits extending from centre to the border of fracture surfaces. Many even smaller splits are in parallel to the main split. The presence of micro-void coalescence on fracture surfaces indicates the ductile mode of failure of these specimens. The torn dimple features suggested shear fracture existed during fracture.

The fracture of 7Ni-Tensile-9 tested at −196ºC behaves differently to other specimens, with crack growing along the plane parallel to the loading direction, results in fragmentation of the specimen, as shown in Figure 6.19a. The fracture surface which is parallel to the loading direction has a woody appearance, which should be the side view of micro-void coalescence. There are some cleavage facets at the tip of the fracture surface, and this tip surface is about 45º to the loading direction. There is also crack path perpendicular to loading direction on the fracture surface around necking. There are full of dimples inside the crack path that is perpendicular to the loading direction. The cleavage facets only exist at the front of

fragmentation with an angle of 53º to the loading direction. The 7Ni-Tensile-9 was cut to view the fractography in loading direction, as shown in Figure 6.19b. Cleavage facets as well as micro-void coalescence could be observed from the fracture surface, and according to the tear ridges, there is a possible initiation site for cleavage. It is worth noting that in Figure 6.19b, the fracture surface close to the cut is 53º to the loading direction, according to the side view of fractured specimens as shown in Figure 6.10. The possible fracture process might be that the crack in longitudinal direction firstly appeared after necking, and the crack in loading direction was also growing due to shear stress. The specimen was continuously loaded in tension, and once the critical load was reached, as the crack was long enough and the specimen was immersed in liquid nitrogen, cleavage fracture was initiated at the shear plane. The final failure is mixed with micro-void coalescence and cleavage facets.

As a comparison, the fractography of 9Ni-Tensile 1 tested at −196ºC is shown in Figure 6.20. The specimen was failed with micro-void coalescence, and some splits exist at the edge of the fracture surface, and the roughness in centre might be undeveloped splitting. For other 9% nickel steel tensile specimens, splitting also occurred as shown in Figure 6.11, from −196 to −130ºC. There are more limited splits in 9% nickel steel comparing to 7% nickel steel.

6.4 Charpy Impact Testing of 7% Nickel Steel

15 of 7% nickel steel CVN specimens were tested at the temperature range from −196 to −80°C to evaluate the variability of the results. Three tests were carried out at −196ºC, one test at −180ºC, three tests at −170ºC, two tests at −160ºC, two tests at −150ºC, one test at −140ºC, one at −130ºC, two tests at −100ºC, and one test at −80ºC. Except a few CVN specimens tested at −196 and −180ºC separated into two pieces, others are unbroken specimens. The images of fracture surfaces taken by the Keyence digital microscope are shown in Figure 6.21. The

absorbed impact energy, the lateral expansion as well as percentage of cleavage fracture of all specimens are listed in Table 6.6. The impact behaviour of 7% nickel steel exhibits a clear ductile-to-brittle transition as the test temperature drops. The values of absorbed Charpy impact energy range from 38 J to 238 J, and ductile-to-brittle transition occurred between −170 and −140ºC, the impact energy varied from 72 J to 123 J. An absorbed impact energy versus test temperature curve was plotted, and the transition temperature was estimated by fitting a tanh curve, as shown in Figure 6.22, and the estimated ductile-to-brittle transition temperature (DBTT) is −165ºC. The sample with the lowest impact energy of 38J, and the smallest lateral expansion of 0.40mm, which is still within the material requirement stated in ASTM Standard A553/A553M [2] for LE of not less than 0.381mm, and the longitudinal Charpy V-notch impact toughness shall not be less than 34J.

The 7% Ni specimens from the lower shelf did not show a 100% cleavage failure, and the fraction of cleavage area is higher than 70%. There is some small amount of ductile crack growth at the root of the notch end, followed with cleavage. The specimen tested at −140ºC with a high absorbed impact energy of 223J still shows 3.6% cleavage area. The specimens start to show fully ductile at −130ºC and the test temperatures above.

A graph of absorbed impact energy against lateral expansion is exhibited in Figure 6.23, which displays a strong positive linear correlation. Another graph of absorbed impact energy against percentage of cleavage area is exhibited in Figure 6.24, and it shows a negative linear relationship.

6.4.1 Fractography of CVN Specimens

Fractography of the selected Charpy impact test specimens of 7% nickel steel tested from −196 to −80ºC is presented in Figure 6.25. Lateral expansion, shear lip, and ductile thumbnail all

increase in size with the increase of test temperature, meanwhile the cleavage area decreases with increasing temperature.

The fracture surfaces of specimens tested at temperatures from −196 to −170ºC are mainly cleavage-dominated fracture. Large cleavage facets are observed, and ductile crack growth region can still be observed from the notch root of the specimens, and there are full of dimples at tear ridges and stable crack growth regions. Cleavage initiation sites are hard to find due to the rough fracture surfaces. Possible initiation sites of cleavage fracture are shown in Figure 6.26 to Figure 6.30 tested from −196 to −170ºC, but initiating particles could not always be found. The failure might be caused by matrix cracking. The fracture distance from notch root to the front of initiation site, X_0, was measured, and values of absorbed impact energy versus X_0 of CVN specimens are plotted in Figure 6.31, and they show a positive trend. Figure 6.32 exhibits the negative relationship between absorbed impact energy and the distance from the ductile end to initiation site. This plot shows that the increase of impact energy is clearly correlated to the increase of ductile crack extension.

Tear ridges are formed during the cleavage fracture process in the shear lip zone, which enable part of the energy to be released. The highest temperature for the observation of cleavage facets is 7NiCVN12 tested at −140ºC, with the absorbed impact energy of 223J. Referring the optical images of Charpy specimens, the fracture surfaces of 7Ni-CVN7, 7Ni-CVN15 tested at −160ºC, and 7Ni-12 tested at −140ºC contain splits, and the splits extend in the longitudinal direction of the steel plate. At the locations at the edges of the splits and inside the splits, cleavage facets could be observed, and dimples around the splits.

At temperatures above −140ºC, no cleavage facets could be found from the fracture surfaces, and there are full of dimples, some with inclusions sit in the voids. The chemical compositions

of these inclusions are analysed by EDX, and they contain O, Al, S, some contain Mg, Ca. One of the inclusions found from specimen 7Ni-CVN13 tested at −180ºC is shown in figure 6.34(e), was analysed by EDX mapping as shown in Figure 6.42. In EDX map, the higher the contrast, the higher the element content. Fe could not be identified from the inclusion, and elements like C, Cr, Mn, and Ni, they are evenly dispersed on the fracture surface, and higher content of O, Al, S, and Mn is detected from the inclusion. Referring to the overlapped areas of (a). O and Al, and (b). S and Mn, the inclusion should contain both alumina and manganese sulphide.

6.5 Fracture Stress Tests on 7% Nickel Steel

Four-point bending tests of 7% nickel Steel were carried out on the specimens to preliminarily evaluate the intrinsic resistance of material to cleavage fracture by finite element analysis (FEM). The slow blunt notch bend testing has been employed as an attempt to evaluate the intrinsic resistance to cleavage fracture of the 7% nickel Steel. Two fracture stress tests were carried out at −196°C in four-point bending loading. Both specimens failed at ~102 kN. The corresponding load-displacement curves exhibit nonlinearity, which indicate the involvement of plastic deformation, as shown in Figure 6.45. A large percentage of cleavage area could be observed from the fracture surfaces under optical microscope, but lateral expansion, as well as ductile crack extension, also exist, as shown in Figure 6.44. The length of ductile extension of 7Ni-FS2 and 7Ni-FS3 is 0.27mm and 0.30mm respectively.

The results of four-point bending tests were summarised in Table 6.7, and both specimens of 7% nickel steel tested at −196ºC have a σ_{nom}/σ_y ratio from 4.04 to 4.08, which exceeds the maximum ratio of 2.292 in the Griffiths and Owen FEM analysis, as shown in Figure 2.13. The values of stress intensification factor R are 3.30J and 3.31J respectively, and both values exceed the maximum stress intensification of 2.62 in the Griffiths and Owen FEM analysis. The results

are thus invalid for microscopic cleavage fracture stress analysis even at −196°C. The local values of nominal stress are 4251 and 4290 MPa respectively, with an average value of 4271 MPa. The maximum principal stress predicted by the Griffiths and Owen FEM analysis ($2.62\sigma_y$) is 2756 MPa. A lower bound value to the local cleavage fracture stress is therefore deduced to be at least 2756 MPa for this 7% nickel steel.

6.5.1 Fractography of Fracture Stress Specimens

The fractography of fracture stress tests is shown in Figure 6.46 to Figure 6.48. The fracture surfaces of two fracture stress samples tested at −196ºC are mainly cleavage facets, but the onset of the cleavage is from the ductile regions near the notch root. The initiation sites of cleavage fracture are difficult to locate. Some single cleavage facets are surrounded by ductile voids, and these non-metallic inclusions are located in a cleavage facet near the ductile region. The inclusion found is globular shape, and they are Al-rich, with S presented in the chemical compositions. The inclusions sit on the cleavage facets do not break into halves, which should be inclusion decohesion.

Unlike 7% nickel steel, 9% nickel steel did not cleave at −196ºC, and micro-void coalescence alone is seen on the fracture surfaces of 9% nickel steel specimens.

6.6 Fracture Toughness Testing of 7% Nickel Steel

6.6.1 SENB Specimens with W = 32mm

Charpy impact tests reveal the ductile-to-brittle transition behaviour exist in 7%Ni steel, and the value of DBTT of −165ºC is close to the aimed service temperature of −163ºC. Therefore, the fracture toughness tests were conducted at the designed application temperature of −163ºC

and a slightly lower temperature to −170ºC. A total of four SENB samples were tested, with two at each test temperature.

The fracture surfaces under optical microscopy are shown in Figure 6.49. The illustration of the method for measuring the length of fatigue pre-crack and stable crack extension is shown in Figure 6.50. The load versus notch-mouth opening displacement curves are shown in Figure 6.51. As shown in the curves, multiple unloading/reloading sequences were performed during the tests. All four samples went for stable crack growth after precracking, and after reaching the maximum load of ~50kN, 7Ni-SENB1 tested at −163ºC and two specimens tested at −170ºC cleaved quickly after a few unloading/reloading cycles, while for 7Ni-SENB2 tested at −163ºC, load dropped gradually with more unloading/reloading cycles than other specimens and cleaved afterwards. These specimens did not have a catastrophic failure after cleavage. The values of crack extension Δa, J_c, K_Q, K_{Jc} were calculated and summarised in Table 6.8, regarding ASTM Standard E399-20 and ASTM Standard E1921-18. Values of K_Q, K_{Jc} and J_c for specimens tested at −163ºC are all higher than the specimens tested at −170ºC: K_Q values vary from 89.0 to 103.8MPam$^{1/2}$, K_{Jc} values vary from 547 to 726 MPam$^{1/2}$, the large differences between K_Q and K_{Jc} indicating more plastic deformation and ductile crack growth was involved during the fracture process, and J_c values are in agreement to it: they vary from 1206 to 2195 kJm^{-2}.

7Ni-SENB1 tested at −163ºC has higher but close values of K_Q, K_{Jc} and J_c to SENB specimens tested at −170ºC: the values are 96.6 MPam$^{1/2}$, 568 MPam$^{1/2}$, and 1315 kJm^{-2} respectively comparing to the average values of K_Q, K_{Jc} and J_c for specimens tested at −170ºC: 89 MPam$^{1/2}$, 548 MPam$^{1/2}$, 1208 kJm^{-2} respectively, indicating similar plastic deformation and ductile crack growth: their ductile crack lengths are 1.1 mm for 7Ni-SENB and 1.0 mm for SENB specimens tested at −170ºC. However, as shown in the load-displacement curve from Figure 6.51, 7Ni-

SENB2 tested at −163ºC has more unloading/reloading cycles than other three SENB specimens, suggesting more ductile crack growth was involved during the test: 7Ni-SENB2 has K_Q, K_{Jc} and J_c value of 104 $MPam^{1/2}$, 726 $MPam^{1/2}$ and 2195 Jm^{-2} respectively, with a ductile crack length of 1.9mm, comparing to the average value of K_Q, K_{Jc} and J_c for other three SENB specimens with 92 $MPam^{1/2}$, 555 $MPam^{1/2}$, and 1244 Jm^{-2} respectively, with the average ductile crack length of 1.0mm.

6.6.2 SENB Specimens with W = 7mm

The machined small bending specimens with the width W of 7mm and a span width S of 30mm were tested in liquid nitrogen bath at −196ºC, with two machined in T-L direction and two machined in L-T direction. The load versus load line displacement curves are shown in Figure 6.53. The curves at the start of tests exhibit some linearity, then the increment of loads slows down and approaches to the maximum load, followed with sudden load drop. The specimens did not show catastrophic failure after the load drop.

The opened fracture surfaces were observed under the Keyence digital microscope as shown in Figure 6.52, and they reveal some short ductile crack growth at the onset of fatigue precrack, from 0.03 to 0.2 mm, followed with cleavage fracture. Values of Δa, P_{max}, J_c, K_Q, K_{Jc} are summarised in Table 6.9. The validity of K_Q as K_{Ic} was also checked according to ASTM E399, and none of the specimens meet the requirements, indicates elastic-plastic fracture occurred. The average load for specimens in L-T direction is 5.3kN, while for specimens machined in T-L direction, the average load is 5.8kN. The values of K_Q, J_c, and K_{Jc} of specimens in T-L direction are similar to specimens in L-T direction.

The values of K_Q and K_{Jc} of all fracture toughness specimens tested at −196, −170 and −163ºC are plotted in Figure 6.54. The average value of K_Q increases from 77.4$MPam^{1/2}$ to

100.2MPam$^{1/2}$. Due to the size differences between specimens tested at different temperatures, the fracture toughness values of these small specimens are converted to specimens with W =32, based on Equation 3.1 from the ASTM Standard E1921, and the resulting K_{Jc} values tested at −196ºC are in the range of 41 to 50MPam$^{1/2}$. As the temperature increases, the K_{Jc} values also increase, suggesting more plastic deformation is involved. The variation of K_{Jc} values in the plot shows the test temperatures could affect the amount of plastic deformation in 7% nickel steel specimens, as the test temperature increases, the amount of ductile crack growth would also increase.

6.6.3 Fractography of Fracture Toughness Specimens

The fractography of fracture toughness tests for all 7% nickel steel SENB samples with W = 32mm show ductile crack growth before the onset of cleavage fracture, as shown in Figure 6.55 to Figure 6.58. 7Ni-SENB2 tested at −163ºC exhibited wider crack extension zone than another specimen tested at −163ºC, 7Ni-SENB1, and 7Ni-SENB1 has similar width of crack extension zone to other two specimens tested at −170ºC. These observations could refer to the ductile crack length measured from optical images in Figure 6.50: the average value of maximum ductile crack extension for 7Ni-SENB1 tested at −163ºC and other two SENB specimens tested at −170ºC is 1.3mm, while the maximum ductile crack extension for 7Ni-SENB2 is 3.81mm.

The cleavage regions of specimens are rough, with ductile dimples locate between cleavage facets. At lower magnification of SEM, there is a possible cleavage initiation site by tracing back the tear ridges from the fracture surface, but nothing could be found at higher zoomed magnification. It is difficult to locate initiation site for cleavage fracture. Local cleavage fracture stress based on McMeeking's FEM analysis could be estimated based on the distance ahead the ductile crack, for example 7Ni-SENB1 tested at −163ºC. Referring to the tensile specimens

tested at −170 and −150ºC, they have the work hardening exponents ranging from 0.03 to 0.06 as listed in Table 6.4, estimations are done for local cleavage fracture stress based on McMeeking analysis with n = 0 and n = 0.1. The maximum local tensile stress available is 2765 to 3501 MPa.

The fracture surfaces of smaller SENB specimens with W = 7mm tested at −196ºC under SEM are shown in Figure 6.58 to Figure 6.64. There is small amount of ductile crack growth from the fatigue pre-crack, followed by transgranular cleavage. Shear lips with dimples could be observed from the fracture surfaces, and pop-in feature could be observed. Due to the rough cleavage region, it is unable to locate the cleavage fracture initiation sites. The cleavage facets are separated by narrow dimple regions.

The non-initiating inclusions that have been observed on the fracture surfaces of samples have been analysed by using EDX analysis. The shape of the observed inclusions was primarily polyhedral or spherical, as shown in Figure 6.59 and Figure 6.60. The majority of inclusions are Al-rich in compositions, some inclusions contain Mg, S, Ti, or Mn.

6.7 Fatigue Crack Growth Tests of 7% and 9% Nickel Steel

Fatigue crack growth tests were performed at −170ºC, −163ºC and room temperature (~24ºC). The fatigue crack lengths of all tested specimens were measured using Keyence digital optical microscope. Values of crack length estimated by the D.C.P.D. method were corrected as required based on the actual measured crack length, and the corrected da/dN versus ΔK curves were plotted for all fatigue tests on a log-log scale, as shown in Figure 6.65.

The crack growth curves obtained at different temperatures within the steady crack growth region are relatively parallel (the gradients of the curves are similar). It is worth noting that the

tails at the lower end of crack growth rate curves bending towards the x-axis were not related to the fatigue threshold but were the consequence of the crack growth rate of specimens under the influence of previous loading and/or temperature history of pre-cracking and the geometry of the notch of the specimens. The values of C and m obtained from the plots are listed in Table 6.10. From Figure 6.65, m values (gradient of the plots) appear to be similar, and they are calculated to range from 2.2 to 2.8, referring to Table 6.10. It shows that at −170 and −163ºC, the plots of da/dN versus ΔK are on the right side of the plots for fatigue crack growth test at room temperature, which indicate that the fatigue crack growth rates at cryogenic temperatures are lower than that tested at room temperature under the same applied stress intensity. 7% nickel steel and 9% nickel steel tested at room temperature have similar C values, from 9.2×10^{-9} to 1.9×10^{-8}mm/cycle. At −163ºC, the fatigue crack growth rate of 7% nickel steel is slightly faster than 9% nickel steel, with C values of 4.5×10^{-9} and 4.1×10^{-9}mm/cycle respectively. At −170ºC, C values for two 7% nickel steel specimens are 1.5×10^{-8} and 4.0×10^{-8}mm/cycle respectively, but they have the lowest m values of 2.2 and 2.4 respectively.

6.7.1 Fractography of Fatigue Crack Growth Specimens

Fractography of cracks growing at rates within the Paris regime was investigated under SEM. The fatigue crack propagation region of 7Ni-FCGS2 tested at −170ºC is shown in Figure 6.66. The fatigue striations are the result of cyclic loading, and the striation distance reflects the rate of fatigue crack growth. The wider the striation distance, the faster the fatigue crack growth.

Secondary cracks and tear ridges could also be observed from this propagation region, which suggests that the fatigue crack propagation is prone to deflection against loading direction, resulting in a rough fatigue crack propagation surface. Figure 6.66a and 6.66b are the near-end of pre-crack at room temperature and the beginning of fatigue crack propagation at −170ºC,

respectively. As the crack length increases, the stress intensity factor range ΔK increases, and number of tear ridges also increases as well, and the surface become rougher.

Striations could be observed from the fractography of fatigue crack growth region. The measured average striation distance at a stress intensity range of approximately 50MPam$^{1/2}$ for 7Ni-FCG3 tested at room temperature is 2.4×10^{-4} mm per cycle, comparing to the predicted da/dN is 2.3×10^{-4} mm per cycle; while the measured average striation distance for 7Ni-FCG2 tested at −170ºC is 4.4×10^{-4} mm per cycle at a stress intensity range of 60 MPam$^{1/2}$, the predicted da/dN is 4.3×10^{-4} mm per cycle. Thus, the estimated crack growth rate by D.C.P.D. method thus matches quite well with the actual striation distance, and it suggests reliability of D.C.P.D. monitoring method in cryogenic temperatures down to −170ºC.

The overall fracture surfaces of 7% and 9% nickel steel fatigue specimens are shown in Figure 6.67 to Figure 6.69. The fracture surfaces of both materials exhibit mainly micro-void coalescence. For 7Ni-FCGS4 tested at −163ºC in Figure 6.68, there are some cleavage facets at the ductile region and a burst of cleavage close to the final fracture, and it suggests that the specimen is difficult to cleave at −163ºC, which should be even harder to get cleavage facets in fatigue crack growth region II.

CHAPTER 7: 7% AND 9% NICKEL STEELS: DISCUSSION

7.1 Microstructure

9% nickel steel has a smaller average martensitic block size than 7% nickel steel, which is 9.3μm compared to 16.2μm, but these two steels with different grain sizes have similar hardness profiles: their average hardness values are 255 and 254 HV5, respectively. This could be due to the differences in the chemical contents of these two nickel steels: higher manganese content as well as the additional secondary hardening elements such as chromium and molybdenum in 7% nickel steel [145]. The presence of retained austenite in 9% nickel steel could be another reason as there is some softening effect from austenite. The hardness values between these two nickel steels do not show much difference in agreement with previous experiments [146].

The content of retained austenite was analysed by X-ray diffraction method as well as EBSD. For the XRD results, however, the content of retained austenite detected from the same specimen varied from 0-4% by using the same X-ray diffractometer. Retained austenite contents were detected by two different SEM, Jeol 7000F SEM with Oxford EBSD system, and Zeiss EVO15 VP ESEM with Bruker EBSD system, both scanning electron microscopies gave the results of ~4% FCC phase from 9% nickel steel and little or no FCC phase from 7% nickel steel. The higher retained austenite content in 9% nickel steel should be a result of its higher nickel content than 7% nickel steel. As mentioned in the literature [95], nickel acts as the austenite stabilising element to increase the toughness of steel, and therefore 9% nickel steel are expected to have better low-temperature properties than 7% nickel steel as discussed in a later section. Grain boundary misorientation can be a factor that affects the properties of a steel.

As the grain boundaries of both nickel steels are mainly high angle grain boundaries, while HAGBs have higher grain boundary energy than LAGBs due to higher fraction of atom deviation from the equilibrium position [147, 148]. The propagation energy of crack is dissipated and therefore hinders the crack propagation, and HAGBs become the obstacle of cleavage fracture [149] [150]. As the result, the toughness of material is enhanced, and DBTT is lowered.

7.2 Tensile Testing

Both 7% and 9% nickel steel specimens tested at −196ºC showed necking before final failure, and except for 7Ni-09 which has some cleavage facets on its fragments, only micro-void coalescence could be observed from fracture surfaces of other specimens of these two nickel steels. The engineering stress-strain curves of 9% nickel steel behave differently to the engineering stress-strain curves of 7% nickel steel: even at −196ºC, the yield stress of 9% nickel steel specimens did not decrease too much, and there were no Lüders elongations before reaching the ultimate tensile stress. The work hardening exponents and total elongations of 9% nickel steel specimens tested at −196ºC are all higher than that of 7% nickel steel. By referring to Figure 6.17, 7% nickel steel has higher yield stress than 9% nickel steel at the temperature ranges from −196 to −130ºC, but lower values of ultimate tensile strength than 9% nickel steel specimens. The higher elongations and n values, larger differences between ultimate tensile stress and yield stress, suggesting better ductility of 9% nickel steel than 7% nickel steel. The existence of retained austenite in 9% nickel steel could bring down its yield stress due to the softness of austenite, the harder phase starts to deform after the strain hardening of the softer phase [91] [151] [152]. The lower yield stress is also due to the internal strain caused by the displacive transformation and resultant mobile dislocations [68].

Splits could be observed from the fracture surfaces of 7% nickel steel specimens at temperatures of −196 to −130ºC, and they often occurred after necking. This splitting phenomenon is often parallel to the rolling direction, which might be related to specimen geometry and test temperature. Necking gives the notch as stress/strain concentrations and followed with cracking. This additional fracture mode within the necked region in materials with high ductility could be caused by the large radial and hoop stresses developed during necking, and this is often happened because of the high level of plastic deformation involved. Tensile results of other mild steels have showed that the yield stress and tensile strength of specimens with loading direction of 45º to the rolling direction was slightly higher than specimens loaded in rolling/transverse direction, but with lower ductility. This could explain the cleavage facets on 45º, but ductile features such as micro-void coalescence and elongated dimples on loading direction, and cleavage only occurred at −196ºC. The splitting in loading direction also acts as a sharp-crack, which could perhaps also explain the later appearance of cleavage facets on fractured surfaces by referring to the cleavage fractures of other notched specimens (i.e., Charpy, fracture stress, fracture toughness) of 7% nickel steel tested at −196ºC. This splitting phenomenon will be discussed in a later section.

Lüders elongations only appeared in 7% nickel steel specimens tested at −196ºC and −170ºC. Jaoul [153] concluded that the formation of Lüders bands is the combination effect of high yield stress, less slip system, and low work hardening. Therefore, factors such as grain size, strain rate, and carbon content which affect the yield stress would also affect Lüders band. The results of 7% nickel steel show that the Lüders elongation increases as the yield stress increases, which agrees with the experimental results from N. Tsuchida et al [154]. The impact of grain size on Lüders elongation could be explained by the Hall-Patch relationship.

7.3 Charpy Impact Testing

The estimated ductile-to-brittle transition temperature for 7% nickel steel by the tanh-fitting curve is −165ºC. Ductile-to-brittle transition behaviours occurred at temperatures ranging from −170 to −140ºC, and the lower shelf and upper shelf energies vary from 38J to 238J. Scatter can be observed in the transition region, suggesting varied amounts of ductile crack growth. The designed service temperature (−163ºC) of this steel falls in the transition region.

Specimens failed with ~80% cleavage area at lower shelf temperatures, with lateral expansions higher than that of the minimum lateral expansion requirements of ASTM A553/A553M [2]. There is also ductile crack growth at the onset of notch root before transgranular cleavage, and suggest plastic deformation involved during fracture. At upper shelf temperatures, the specimens show 100% ductile failure with micro-void coalescence full of the fracture surfaces. The percentage of crystallinity decreases as the absorbed energy increases, while lateral expansion as well as fracture distance increases with the increase of absorbed energy.

As a comparison, all six Charpy specimens of 9% nickel steel tested at −196ºC exhibited complete upper shelf behaviour: the test-pieces did not break into two parts after hitting by the impact tester pendulum, and the fracture surfaces of 9% nickel steel specimens are fully ductile, with ductile crack extension and micro-void coalescence according to fractography analysis under SEM. The better impact toughness could be related to the smaller prior-austenite grain sizes and higher nickel content in 9% nickel steel.

The average value of absorbed impact energies for 9% nickel steel specimens is 260J, which is slightly higher than that of 7% nickel steel at upper shelf temperatures (238J), and thus 9% nickel steel might be able to absorb more energy per unit of crack extension than 7% nickel

steel. As the absorbed impact energy is correlated to the plastic deformation of the materials, factors such as yield stress, ductility, and work hardening of materials could all affect the amount of absorbed energy. 9% nickel steel has lower yield stress, better ductility and higher work hardening exponent than 7% nickel steel, and these may account for higher upper shelf energy of 9% nickel steel.

The fractography of 7% nickel steel Charpy specimens tested at lower shelf temperatures could also be compared to that of SA-738 Gr. B steel in Section 3.4. Referring to the fractography of SA-738 Gr. B steel Charpy specimens observed by Xu [123] under SEM, 7% nickel steel specimens have longer ductile crack growth extension and rougher fracture surface under the same test temperatures, which suggests more ductile fracture was involved in 7% nickel steel at lower shelf. This could be the result of their different microstructure. The microstructure of SA-738 Gr. B steel is mainly composed of granular bainite, and full of irregular ferrite and irregular grain boundaries. For heavy steel plates like SA-738 Gr. B steel, the welding properties are the priority for the manufacturers, and fine-grained microstructure such as quasi-polygonal ferrite, lath bainite, lath austenite, and acicular ferrite are more preferred, as they would bring a combination of good toughness and strength [155]. Granular bainite is often thought to be harmful to the cryogenic properties of the materials due to the existence of M-A constituents, as microcracks often nucleate and propagate around these constituents [156-159]. The coarsened grains of granular bainite could also be detrimental.

Nickel steels tend to have a microstructure of tempered martensite, with martensite lath and carbides. The formation of retained austenite can absorb carbon, and thus reduce the carbon content of the matrix and prohibit the precipitation of cementite. Retained austenite can hinder the crack propagation process [93]. The transformation from austenite to martensite can occur

during the impact test as the stress concentration increases suddenly, and this 'TRIP' effect can also enhance the toughness of 7% nickel steel [103] [104]. The tiny amount of austenite found from 7% nickel steel by EBSD analysis might also improve its mechanical properties. Apart from the increased RA content, 9% nickel steel has finer block size than that of 7% nickel steel, and Pickering et al. [160] previously addressed the relationship between DBTT and block width:

$$DBTT = A - K \cdot \ln d^{-1/2} \tag{7.1}$$

where d is block width, A and K are constants. This relationship suggests that DBTT can be reduced by the refinement of block size of steel, which explains the better impact toughness of 9% nickel steel.

7.4 Microscopic Cleavage Fracture Stress Tests

All fracture stress tests were performed at −196ºC, which is the lower shelf temperature of 7% nickel steel according to Charpy impact test results. Similar to CVN specimens tested at −196ºC, the fracture surfaces of 7% nickel steel fracture stress specimens do not show 100% crystallinity, but ductile crack region developed below the notch root, followed with very rough cleavage region. In this point of view, the calculation of microscopic cleavage fracture stress σ_f is affected, as the ductile crack growth changes the stress field ahead of the notch (i.e., sharpen the notch), which is beyond the limit of the Griffiths and Owen FEM analysis. The FEM analysis is designed for cleavage fracture stress, the microscopic cleavage fracture stress of 7% nickel steel specimens with an altered stress profile by ductile crack growth is not suitable for this method. The estimated fracture stress values of 7% nickel steel and non-linearity of load-displacement curves also prove its excellent intrinsic cleavage fracture resistance.

The fracture surfaces of these fracture stress specimens have very high fraction of transgranular cleavage, but the surfaces are rough with micro-void coalescence, and no initiation sites could be observed by SEM. The fractography again proves the involvement of plastic deformation during bending.

For 9% nickel steel fracture stress tests performed at −196ºC, specimens did not break during the test and were interrupted at ~80kN, and the corresponding load-displacement curves exhibit more nonlinearity than that of 7% nickel steel. 9% nickel steel specimens are too ductile to analyse by the Griffiths and Owen FEM analysis. 9% nickel steel specimens are deduced to have better cleavage fracture resistance than 7% nickel steel.

7.5 Fracture Toughness Tests

All 7% nickel steel specimens tested at the temperature range of −196 to −163ºC have a certain amount of ductile crack growth after the pre-crack and prior to failure, and they did not break into two halves after cleaving. Referring to Table 6.8, the maximum load P_{max} of 7NiSENB2 specimens tested at −163ºC does not have much difference to other large SENB specimens tested at −170 and −163ºC, but stable crack extension, K_Q, K_{Jc}, and J_c values of 7NiSENB2 are higher than other three specimens, in which suggested more ductile crack growth occurs prior to fracture. The result of 7NiSENB2 is caused by the ductile-to-brittle transition behaviour of 7% nickel steel- the fracture toughness results tested at this temperature range show larger variation. According to Figure 6.54, fracture toughness specimens tested at same temperatures tend to have similar K_Q values, while K_{Jc} values show scattering. The higher the test temperatures, the larger the differences between K_Q and K_{Jc} as plasticity involved during fracture increases.

It is clear to find out that specimens have longer fatigue pre-crack length would have smaller value of maximum load, according to Table 6.8 and Table 6.9, and except 7NiSENB2, specimens with longer fatigue pre-crack would also have less ductile crack extension. Longer initial crack length would limit the amount of ductile crack growth of test-pieces before the ligament could no longer take the applied load.

Fractography of fracture toughness specimens tested at the range from −196 to −163ºC shows ductile crack extension after the fatigue pre-crack, followed with mixed regions having both cleavage facets and micro-void coalescence. Cleaving did not propagate through the whole thickness of specimens, but slowed down, in which corresponded to the "popping" feature of load drop of the load-displacement curves. The fractography of fracture toughness specimens is different to the blunt notch specimens of Charpy and fracture stress tests tested at −196 to −170ºC with very high fractions of cleavage area. The McMeeking analysis gives the fracture stress falling within 2765 to 3501 MPa, which gives a good resistance to cleavage fracture.

Two SENB specimens of 9% nickel steel with W×B×L = 32×16×140mm were also tested by using unloading elastic compliance method at −170ºC. The ratio between initial crack length and width a_0/W is 0.58-0.59 for these two 9Ni-SENB specimens, which is larger than that of 7% nickel steel specimens of 0.44-0.46. However, the amount of ductile crack growth was longer than that of 7% nickel steel specimens tested at same temperature, with 1.3 and 1.6mm respectively comparing to 1.0mm approximately, as shown in Table 6.8. The load-displacement curves also have more unloading/reloading cycles. With sharp crack tip and fatigue pre-crack cleaved at −163ºC after stable crack growth. The cleavage regions of 9% nickel steel specimens are rougher than 7% nickel steel specimens, with a mixed mode of cleavage facets coexist with ductile dimples. Rougher fracture surfaces and smaller sizes of cleavage facets are seen for 9%

nickel steel. Since cleavage is still seen in these fracture toughness tests for 9% nickel steel, it is of interest to consider the maximum local tensile stress available from the McMeeking analysis. This varies from 3453 to 4634 MPa based on work hardening exponents of 0.1 and 0.2 respectively (n is estimated at 0.14 even at −196ºC mentioned in Section 7.3). This speculative analysis supports the greater resistance to cleavage fracture of the 9% nickel steel over that of the 7% nickel steel.

For the fracture of specimens, as discussed in Chapter 4 of the fracture of SA-738 Gr. B steel, the nucleation and propagation of microcrack for cleavage fracture should satisfy the following three criteria: $\varepsilon_p \geq \varepsilon_{pc}$, $\sigma_m/\sigma_e \geq T_c$, and $\sigma_{yy} \geq \sigma_f$. The criteria above could not be met, and stress triaxiality could not prevent the pre-crack of the specimens from becoming blunted. At the cryogenic temperatures, σ_{yy} increased as the yield strength increased, and the applied load was increased further, lead to the initiation of cleavage fracture.

7.6 Fatigue Crack Growth Tests

The fatigue crack growth was monitored by D.C.P.D method in environmental chamber. The nitrogen flow inside the chamber slightly affected the voltage stability, and the affected P.D. values would be higher than the baseline voltage. The disturbance would occur in every 360-400 cycles, with a maximum increase of 6.5μV from peak baseline P.D. values. Most of the signals remain unaffected and they are still valid to calculate crack growth rate. The average value of measured striation lengths of da/dN are similar to the corresponded da/dN estimated by D.C.P.D. and suggests the reliability of D.C.P.D. method at cryogenic temperatures as low as −170ºC.

Striation distance reflects the fatigue crack growth rate, it is the crack growth after each cyclic

loading. Striation distance measured from those SEM images matches well with those predicted da/dN from D.C.P.D method at different test temperatures. The appearance of tear ridges enhances the roughness of fatigue crack propagation region. The fracture surfaces of these specimens failed by monotonic loading after fatigue crack propagation are mainly micro-void coalescence, and there are some cleavage facets on one 7% nickel steel specimen tested at −163ºC. The maximum stress intensity factor at the fatigue crack end is ~60MPam$^{1/2}$.

For 7% nickel steel, −170ºC and −163ºC are within the transition region according to Charpy test results, and room temperature is corresponded to its upper shelf temperature. As the results shown, the fatigue crack growth rate within the Paris regime for 7% and 9% nickel steel drops as the test temperature decreases. According to C. L. Walters [161], ferritic steels would have a fatigue ductile-brittle transition (FDBT) phenomenon, with an increase of fatigue crack growth rate as temperatures decrease, but 7% nickel steel did not exhibit transition behaviour in region II at −170 and −163ºC. It could be caused by the increase of yield stress at lower temperatures, the plastic crack tip opening displacement (CTOD) [162] as well as the size of the plastic zone at the crack tip decreases [35, 124, 163]. Other mechanisms which can enhance fatigue resistance include crack closure effect on the near-threshold fatigue crack propagation [164, 165], deformation-induced phase transformation [166, 167], and thermally activated theory based on dislocation dynamic concept [167-169]. Cleavage would be hard to occur during fatigue crack propagation due to the small increment of the crack tip growth and very small driving force. If there is a FDBT for 7% nickel steel, this temperature would be lower than its DBTT. As the maximum stress intensity factor K is in region II, and it does not get any cleavage facets forming, and thus there is no increase to fatigue crack growth rate. According to fracture toughness results of 7% nickel steel, specimens would not cleave without ductile crack growth, and it explains the failure mode of these specimens after a certain amount of fatigue crack

growth is ductile failure.

7.7 Splitting Observed in Fractography of 7% Nickel Steel

It is observed that fracture surfaces of tensile, Charpy, and fracture toughness specimens of 7% nickel steel show splitting, and these splits propagate perpendicular to the main crack surface and parallel to the longitudinal plane of steel plate. The splits appeared on tensile specimens tested at −196 to −130ºC, Charpy specimens tested at −196 and −140ºC, fracture stress specimens tested at −196ºC, and fracture toughness specimens tested at −196 to −163ºC. The mode of main fracture surfaces could be either cleavage or ductile fracture, but by referring to the fractography of Charpy specimens, lower temperatures should be more preferred for the occurrence of splitting, and the density of splitting also increases with the decreasing temperature.

Splitting phenomenon is related to the anisotropic microstructure of material, such as elongated grains caused by hot rolling below the austenite recrystallisation temperature and grain boundary embrittlement as the result of the formation of precipitates (i.e., carbides and nitrides) during tempering [170]. Apart from any anisotropic microstructure, stress conditions are the necessary factor to cause splitting. Specimens deformed in constrained plane-strain conditions (triaxial tensile stress), and the stresses emerged from this constrained zone could be two to three times higher than yield stress [171]. During necking of tensile specimens, this rigid zone is located in the centre of the necking area, and there is a uniform axial stress together with a hydrostatic tensile component [172]. At the surface of neck, the hydrostatic component could be zero, and reaches a maximum in centre. If there is a weak plane in material, splitting could be initiated from centre and developed to surface of specimens. For 7% nickel steel specimens, differences between tensile strengths and yield strengths are not too big, necking is therefore

premature and intense. The weak plane would experience strong tangential and radial stresses and lead to splitting. The reasons for specimens without splitting are due to sufficient uniform ductility caused by lack of strong stress condition [129].

For notched specimens such as CVN specimens tested at −196 to −140ºC (Figure 6.25), fracture stress specimens tested at −196ºC (Figure 6.44), and fracture toughness specimens tested at −163ºC (Figure 6.55), −170ºC (Figure 6.57), and −196ºC (Figure 6.61), one or more splits could be observed from the fracture surfaces of these specimens. This could be explained that when specimens are loaded, a plastic zone is formed at the notch, and contraction in thickness direction is constrained. When a crack starts to grow, the plastic zone size would also increase and spread through the thickness of the specimens. A triaxial stress state is formed in these notched specimens, which satisfies the emerging condition of splitting.

Splitting should be correlated to test temperature, for CVN specimens tested from −196 to −80ºC, splitting could only be observed from specimens tested in the range from −196 to −140ºC, which include the lower shelf and ductile-to-brittle transition region, and this could be explained with the yield stress of specimens at lower temperatures.

CHAPTER 8: 7% AND 9% NICKEL STEELS: CONCLUSIONS

1. The differences in alloying element contents especially nickel between 7% and 9% nickel steel result in differences in microstructure, low-temperature mechanical properties in tensile tests, Charpy V-notch tests, fracture toughness tests, as well as their failure mechanisms. The microstructure of 7% and 9% nickel steels are mainly tempered martensite, and EBSD results have confirmed that the majority of grain boundaries for both nickel steels are high-angle grain boundaries. Retained austenite could only be observed for 9% nickel steel with a content of 4%. 9% nickel steel has smaller prior-austenite grain size according to EBSD analysis, which may further promote its low-temperature toughness.
2. The yield stress and tensile strength of 7% nickel steel decreased with increasing test temperature, and specimens tested below −170ºC also exhibited Lüders elongations. Total elongation to failure of 7% nickel steel was independent with test temperature, while the work hardening exponent of 7% nickel steel had a weak positive correlation with test temperature. The work hardening exponents are from 0.03 to 0.06 in the temperature range of −196 to −130ºC.
3. In tensile tests, the fractography of 7% nickel steel specimens are mainly micro-void coalescence, with longitudinal splits on fracture surfaces. One specimen tested at −196ºC showed some cleavage facets on its fragments. The better ductility of 9% nickel steel than 7% nickel steel is due to its higher total elongation and work hardening exponent. It also has a lower and larger yield stress/tensile strength ratio at temperatures as low as −196ºC. Specimens failed by micro-void coalescence alone for 9% nickel steel.
4. Charpy results of 7% nickel steel exhibited ductile-to-brittle transition behaviour at the temperature range from −170 to −140ºC, and the ductile-to-brittle transition temperature defined by a than-curve is −165ºC. The lower shelf energies were from 38 to 55J, while the

upper shelf energies were in the range of 233 to 238J. The fracture surfaces of specimens were changed from 84% of crystallinity at lower shelf temperatures to 100% ductile area at upper shelf temperatures. Fractography of specimens tested at the range from −196 to −140ºC showed a mixed mode of micro-void coalescence and transgranular cleavage fracture, and as the test temperature increased, the fraction of crystallinity decreased.

5. Slow blunt notch testing of 7% nickel steel showed nonlinearity at −196ºC, and the values of stress intensification R, σ_{nom}/σ_y, L/L_{GY} exceed the FEM analysis. The value of its local cleavage fracture stress thus has to be greater than 2756MPa. The fractography of fracture surfaces are mainly transgranular cleavage, with micro-void coalescence located between the cleavage facets.
6. The fracture toughness tests on 7% nickel steel SENB specimens at −196, −170 and −163ºC did not break into halves even after transgranular cleavage. Stable ductile crack growth extension from 0.03 to 0.2 mm was observed for bend specimens (W = 7mm) tested at −196ºC. Ductile crack growth extension from 1.0 to 1.9 mm was observed for bend specimens (W = 10mm) tested at −170 and −163ºC. K_{Jc} values of SENB specimens with W = 7 mm tested at −196ºC are in the range of 214 to 291MPam$^{1/2}$, while K_{Jc} values of SENB specimens with W = 32mm tested at −170 and −163ºC are in the range of 547 to 726 MPam$^{1/2}$. K_{Jc} increased with increasing test temperature, and the variations in K_{Jc} results of specimens tested at −163ºC should be due to the interruption of stable crack growth by cleavage at extensions between 1.1 and 1.9mm. K_{Jc} values are measured as 568 and 726 MPam$^{1/2}$ respectively. From the maximum local tensile stress predicted by FEM in these sharp crack tests, the value of local cleavage fracture stress for 7% nickel steel is deduced to lie between 2765 to 3501 MPa, and for 9% nickel steel, it is deduced to lie between 3453 to 4634 MPa.

7. The fatigue crack growth rates of 7% and 9% nickel steels in region II are similar both at room temperature and −163ºC. Fatigue crack growth resistance in this region increased as the test temperature decreased. All da/dN versus ΔK plots have similar gradient and thus similar m values, from 2.2 to 2.8. There was no fatigue ductile-to-brittle transition occurred at these test temperatures, and if there is a fatigue ductile-to-brittle transition temperature, it must be lower than −170ºC.
8. No cleavage fracture could be observed from fatigue crack growth regions.
9. The fatigue striation spacings from different temperatures/ΔK were measured, and these values are comparable to the predicted fatigue crack growth rate by the D.C.P.C method, which suggests the reliability of the D.C.P.D method at cryogenic temperatures as low as −170ºC.
10. One of the design criteria for 7% nickel steel suggest they should exhibit fully ductile behaviour at −163ºC. However, the material exhibits a ductile-to-brittle transition behaviour in Charpy impact tests at the temperature range of −170 to −140ºC, and variations in fracture toughness results at −163ºC. However, it still has high values of K_{Jc} and shows a good low-temperature toughness by comparing to the requirements within ASTM A553/553M.

Future Work

The phenomenon of splitting and fragmentation occurred in 7% nickel steel tensile specimens make it interesting to further investigate the how the orientation of specimens affect the mechanical properties. Therefore, some additional specimens could be machined with the notch in ST-L direction.

All fracture toughness specimens from both nickel steels cleaved after ductile crack growth passed maximum load. Effects of test piece size at such temperatures should be investigated.

Retained austenite was detected by EBSD analysis for 9% nickel steel only in this preliminary study. Further analysis using transmission electron microscopy and higher resolution XRD is required.

Fatigue crack growth in region II at lower temperatures than −170ºC could be tested to find out if there is a “fatigue ductile-to-brittle transition” temperature for 7% nickel steel.

References

1. ASME, *Boiler and pressure vessel code. Section II, Part A, SA-738/SA-738M Specification for pressure vessel plates, heat treated, carbon-manganese-silicon steel, for moderate and lower temperature service*. 2001, ASME.
2. ASTM, *Standard specification for pressure vessel plates, alloy steel, quenched and tempered 7%, 8%, and 9% Nickel*. 2022, ASTM International: West Conshohocken.
3. Knott, J. F., *Micro-mechanisms of fracture and the fracture toughness of engineering alloys*, in *Advances in Research on the Strength and Fracture of Materials*. 1978, Elsevier. p. 61-92.
4. Iricibar, R., IeRoy, G., and Embury, J. D., *Relationship of strain hardening and damage in ductile fracture.* Metal Science, 1980. **14**(8-9): p. 337-343.
5. Argon, A. S., Im, J., Safoglu, R., *Cavity formation from inclusions in ductile fracture.* Metallurgical Transactions A, 1975. **6**: p. 825-837.
6. Brown, L. M., Stobbs, W. M., *The work-hardening of copper-silica v. equilibrium plastic relaxation by secondary dislocations.* Philosophical Magazine, 1976. **34**(3): p. 351-372.
7. Rice, J. R., Tracey, D. M., *On the ductile enlargement of voids in triaxial stress fields∗.* Journal of the Mechanics and Physics of Solids, 1969. **17**(3): p. 201-217.
8. Thomason, P. G., *Ductile Fracutre of Metals*. 1990, Oxford, UK: Pergamon Press.
9. Griffith, A. A., *The phenomena of rupture and flow in solids*. Philosophical Transactions of the Royal Society of London,. A. Mathematical and Physical Sciences Vol.221, no. 587. 1920.
10. Orowan, E., *Fracture and Strength of Solids.* Reports in Progress in Physics, 1948. **Vol. XII**: p. 185.
11. Irwin, G. R., *Fracture Dynamics.* Fracture of Metals, American Society for Metals, 1948: p. 147-166.
12. Low, J. R., *The relation of microstructure to brittle fracture.* Relation of Properties to Microstructure, 1954. **ASM**: p. 163-179.
13. Zener, C., *Fracturing of Metals.* Cleverlands, OH, 1948. **ASM**: p. 3-31.
14. Stroh, A. N., *The formation of cracks as a result of plastic flow.* Proceedings of the Royal Society of London, 1954. **A223**: p. 404-414.
15. Cottrell, A. H., *Theory of brittle fracture in steel and similar metals.* Transactions of the Metallurgical Society of AIME, 1958. **212**: p. 192-203.
16. McMahon, C. J., Cohen, M., *Initiation of cleavage in polycrystalline iron.* Acta Metallurgica, 1965. **13**(6): p. 591-604.
17. Smith, E., *Cleavage fracture in mild steel.* The International Journal of Fracture Mechanics, 1968. **4**(2): p. 131-145.
18. Curry, D. A., and Knott, J. F., *The relationship between fracture toughness and microstructure in the cleavage fracture of mild steel.* Metal Science, 1976. **10**: p. 1-6.
19. Orowan, E., *Notch brittleness and the strength of metals. Transactions.* Institute of Engineers of the Ship Builders in Scotland, 1945. **89**: p. 165-215.
20. Green, A. P., and Hundy, B. B., *Initial plastic yielding in notch bend tests.* Journal of Mechanics and Physics of Solids, 1956. **4**: p. 128-144.
21. Knott, J. F., *Some effects of hydrostatic tension on the fracture behaviour of mild steel.* Journal of the Iron and Steel Institute, 1966. **204**: p. 104-111.

22. Westergaard, H. M., *Bearing pressures and cracks: Bearing pressures through a slightly waved surface or through a nearly flat part of a cylinder, and related problems of cracks.* Journal of Applied Mechanics, 1939. **6**: A49-A53.
23. Ritchie, R. O., Knott, J. F., Rice, J. R., *On the relationship between critical tensile stress and fracture toughness in mild steel.* Journal of the Mechanics and Physics of Solids, 1973. **21**(6): p. 395-410.
24. Rice, J. R., Johnson, M. A., *The role of large crack tip geometry changes in plane strain fracture*. Inelastic Behaviour of Solids. 1969, Division of Engineering: Brown University. 641-672.
25. Griffith, J. R., Owen, D. R. J., *An elastic-plastic stress analysis for a notched bar in plane strain bending.* Journal of Mechanics and Physics of Solids, 1971. **19**: p. 419-431.
26. Curry, D. A., Knott, J. F., *Effects of microstructure on cleavage fracture stress in steel.* Metal Science, 1978. **12**(11): p. 511-514.
27. Curry, D. A., Knott, J. F., *Effect of microstructure on cleavage fracture toughness of quenched and tempered steels.* Metal Science, 1979. **13**(6): p. 341-345.
28. Bowen, P., and Knott, J. F., *Cleavage fracture of A 533 B pressure vessel steel in martensitic condition.* Metal Science, 1984. **18**(5): p. 225-235.
29. Wang, G. Z., Liu, Y. G., Chen, J. H., *Investigation of cleavage fracture initiation in notched specimens of a C-Mn steel with carbides and inclusions.* Materials Science and Engineering: A, 2004. **369**(1-2): p. 181-191.
30. Beremin, F. M., *Cavity formation from inclusions in ductile fracture of A508 steel.* Metallurgical Transactions A, 1981. **12**: p. 723-731.
31. Linaza, M. A., Rodriguez-Ibabe, J. M., and Urcola, J. J., *Determination of the energetic parameters controlling cleavage fracture initiation in steels.* Fatigue & Fracture of Engineering Materials & Structures, 1997. **20**(5): p. 619-632.
32. San Martin, J. I., Rodriguez-Ibabe, J. M., *Determination of energetic parameters controlling cleavage fracture in a Ti-V microalloyed ferrite-pearlite steel.* Scripta Materialia, 1999. **40**(4): p. 459-464.
33. Pineau, A., Benzerga, A. A., Pardoen, T., *Failure of metals I: brittle and ductile fracture.* Acta Materialia, 2016. **107**: p. 424-483.
34. Wells, A. A. *Unstable crack propagation in metals: cleavage and fast fracture*. in *Proceedings of the crack propagation symposium*. 1961.
35. Dugdale, D. S., *Yielding of steel sheets containing slits.* Journal of the Mechanics and Physics of Solids, 1960. **8**(2): p. 100-104.
36. Barenblatt, G. I., *The mathematical theory of equilibrium cracks in brittle fracture.* Advances in Applied Mechanics, 1962. **7**: p. 55-129.
37. Rice, J. R., *A path independent integral and the approximate analysis of strain concentration by notches and cracks.* Journal of Applied Mechanics, 1968. **35**: p. 379-386.
38. Petch, N. J., *The cleavage strength of polycrystals.* J. Iron Steel Inst., 1953. **174**: p. 25-28.
39. Heslop, J., Petch, N. J., *LXXXVIII. The stress to move a free dislocation in alpha iron.* Philosophical Magazine, 1956. **1**(9): p. 866-873.
40. Mundheri, M. A., Soulat, P., Pineau, A., *Irradiation embrittlement of a low alloy steel interpreted in terms of a local approach of cleavage fracture.* Fatigue & Fracture of Engineering Materials & Structures, 1989. **12**: p. 19-30.

41. Knott, J. F., *The transition from fibrous fracture to cleavage fracture.* International Journal of Pressure Vessels and Piping, 1995. **64**(3): p. 225-234.
42. Wallin, K., *The scatter in KIC-results.* Engineering Fracture Mechanics, 1984. **19**(6): p. 1085-1093.
43. Merkle, J., Wallin, K., McCabe, D., *Technical Basis for an ASTM standard on determining the reference temperature, T0, for ferritic steels in the transition range*, NUREG/CR-5504, Editor. 1998, US Nuclear Regulatory Commission.
44. Kirk, M. T., *The technical basis for application of the master curve to the assessment of nuclear reactor pressure vessel integrity.* United States Nuclear Regulatory Commission, ADAMS ML093540004, 2009.
45. Council, W. R., *PVRC Recommendations on Toughness Requirements for Ferritic MaterialsWRC Bulletin 175*, in *WRC Bulletin 175*. 1972.
46. ASTM, *Standard test method for conducting drop-weight test to determine nil-ductility transition temperature of ferritic steels*, in *Annual Book of ASTM Standards*. 1998, ASTM International: West Conshohocken, PA.
47. Landes, J. D., and Shaffer, D. H., *Statistical characterization of fracture in the transition region.* ASTM International, 1980: p. 368-382.
48. Heerens, J., Read, D. T., Cornec, A., and Schwalbe, K. H., *Interpretation of fracture toughness in the ductile-to-brittle transition region by fractographical observations.* Defect Assessment in Components—Fundamentals and Applications, 1991: p. 659-678.
49. Wallin, K., Saario, T., and Törrönen, K., *Statistical model for carbide induced brittle fracture in steel.* Metal Science, 1984. **18**(1): p. 13-16.
50. Van Der Sluys, W. A., and Miglin, M. T., *Resutls of MPC/JSPS cooperative testing program in the brittle-to-ductile transition region.* Fracture Mechanics, ASTM STP 1207, ASTM International, West Conshohocken, PA, 1994.
51. Wallin, K., *Fracture toughness transition curve shape for ferritic structural steels*, in *Fracture of engineering materials and structures*. 1991, Springer. p. 83-88.
52. Sattari-Far, I., and Wallin, K., *Application of master curve methodology for structural integrity assessments of nuclear components*. 2005: Statens Kärnkraftinspektion.
53. Yoon, K. K., Hall, J. B., Sluys, W. A., Higuchi, M., Iida, K., *Japanese fracture toughness data analysis using the master curve method.* ASME-PUBLICATIONS-PVP, 2001. **423**: p. 167-178.
54. Meshii, T., *Failure of the ASTM E 1921 master curve to characterize the fracture toughness temperature dependence of ferritic steel and successful application of the stress distribution T-scaling method.* Theoretical and Applied Fracture Mechanics, 2019. **100**: p. 354-361.
55. Yang, J., Wang, W. W., Qiu, S. Z., Tian, W. X., Su, G. H., Wu, Y. W., *Simulation and analysis on 10-in. cold leg small break loca for ap1000.* . Annals of Nuclear Energy, 2012. **46**: p. 81-89.
56. Schulz, T. L., *Westinghouse AP1000 advanced passive plant.* Nuclear Engineering and Design, 2006. **236**: p. 1547-1557.
57. Hung, Z. Y., Ferng, Y. M., Hsu, W. S., Pei, B. S., Chen, Y. S., *Analysis of AP1000 containment passive cooling system during a loss-of-coolant accident.* Annals of Nuclear Energy, 2015. **85**: p. 717-724.
58. ASME Boiler and Pressure Vessel Committee, *ASME boiler and pressure vessel code an international code*. 2007, Shanghai Scientific and Technological Literature Press: Shanghai. p. 132.

59. ASME Boiler and Pressure Vessel Committee, 2015, The American Society of Mechanical Engineers: USA. p. 1174-1175.
60. Zhang, Y. L., Hui, H., Zhou, Z., & Cong, X. C., *Study on fracture toughness evaluation method of SA738Gr.B steel heat affected zone in ductile-brittle transition region.* Journal of Nuclear Science and Technology, 2019. **56**(6): p. 503-512.
61. Lin, M., Hansen, S. S., Nelson, T. D., & Focht, R. B., *Effects of composition and heat treatment on the toughness of ASTM A508 Grade 3 class 1 material for pressure vessels.* ASTM Special Technical Publication, 1997. **1259**: p. 33-55.
62. Branco, R., Berto, F., *High-strength low-alloy steels.* Metals, 2021. **11**(7): p. 1000.
63. Totten, G. E., Howes, M. A. H., *Steel heat treatment handbook*. 1997, New York, USA: Marcel Dekker.
64. Carvil, J., *Engineering materials*, in *Mechanical Engineer's Data Handbook*. 1993, Butterworth-Heinemann. p. 218-266.
65. Singh, R., *Stresses, shrinkage, and distortion in weldments*, in *Applied Welding Engineering* R. Singh, Editor. 2016, Butterworth-Heinemann. p. 201-238.
66. Irvine, K. J., and Pickering, F. B., *Low-carbon bainitic steels.* Journal of the Iron and Steel Institute, 1957. **184**(12): p. 292-309.
67. Ohtsubo, H., Araki, K., Moriya, Y., *Development of SA-738 Gr. B high strength steel plate with excellent toughness for power generating plants*, in *JFE Technical Report*. 2012. p. 50-55.
68. Irvine, K. J., and Pickering, F. B., *Physical properties of martensite and bainite*, in *Special Report 93*. 1965, The Iron and Steel Institute. p. 110.
69. Jha, A. K., Prasad, B. K., Modi, O. P., Das, S., & Yegneswaran, A. H., *Correlating microstructural features and mechanical properties with abrasion resistance of a high strength low alloy steel.* Wear, 2003. **254**(1-2): p. 120-128.
70. Grange, R. A., Hribal, C. R., Porter, L. F., *Hardness of tempered martensite in carbon and low-alloy steels.* Metallurgical Transactions A, 1977. **8A**(11): p. 1775-1785.
71. Tan, Y. H., Chang, D. E., Dong, X. C., He, Y. H., Hu, S. Q., *New observation of martensitic morphology and substructure using transmission electron microscopy.* Metallurgical Transactions A, 1992. **23**: p. 1413-1421.
72. Owen, W. S., *The effect of silicon on the kinetics of tempering.* Transactions of the American Society for Metals, 1954. **46**: p. 812-829.
73. Keh, A. S., Leslie, W. C., *Recent observations on quench-aging and strain-aging of iron and steel.* Materials Science Research, 1963: p. 208-250.
74. Davenport, E. S., and Bain, E. C., *Transformation of austenite at constant subcritical temperatures.* Metallurgical Transactions A, 1970. **1**(12): p. 3503-3530.
75. Bhadeshia, H. K. D. H., Honeycombe, R. W. K., *Steels : Microstructure and Properties*. 2017.
76. Habraken, L., *Some special aspects of the bainitic structure*, in *Physikalisch-Technischer Teil*, G. Möllenstedt, Niehrs, H., Ruska, E., Editor. 1960, Springer: Berlin.
77. Li, Y., Zhang, S., Zhao, C., Song, M., and Jiang, Z., *Effects of high-temperature tempering on mechanical properties and microstructure of SA738 Gr.B steel.* Metals, 2020. **10**(9): p. 1207.
78. Liu, H. B., Zhang, H. Q., Li, J. F., *Toughness of SA738Gr.B steel used for nuclear containment vessel.* International Journal of Pressure Vessels and Piping, 2018. **168**: p. 200-209.

79. Wang, Y. Q., Ning, D., Wang, Y. D., Ge, H. H., and Li, H., *Study on mechanical properties at different test temperatures of SA-738 Gr.B plate in two states*, in *The 9th Global Conference on Materials Science and Engineering (CMSE 2020)*. 2021, Journal of Physics, Conference Series.
80. Ma, Y., Ran, G., Chen, N., Lei, P., Shen, Q., *Investigation of mechanical properties and proton irradiation behaviors of SA-738 Gr.B steel used as reactor containment.* Nuclear Materials and Energy, 2016. **8**: p. 18-22.
81. Zinkle, S. J., Was, G. S., *Materials challenges in nuclear energy.* Acta Materialia, 2013. **61**(3): p. 735-758.
82. Collins, C., Patel, D. A., Tarlowski, J., *Developments in LNG storage: overview of LNG storage tanks*, in *LNG 2000*. 2000, M W Kellogg Ltd.
83. Morrison, D. M., *Composite Structure Provides LNG & LPG Storage Solution*, in *American Gas Association Distrubution and Transmission Conference*. 1985: Boston, MA.
84. Kern, A., Schriever, U., Stumpfe, J., *Development of 9% nickel steel for LNG applications.* Steel Research International, 2007. **78**(3): p. 189-194.
85. Krauss, G., *Steels : processing, structure, and performance*. 2015: A. S. M. International.
86. Kinney, C. C., Pytlewski, K. R., Khachaturyan, A. G., and Morris, J. W. Jr., *The microstructure of lath martensite in quenched 9Ni steel.* Acta Materialia, 2014. **69**: p. 372-385.
87. Frear, D., Morris, J. W., *A study of the effect of precipitated austenite on the fracture of a ferritic cryogenic steel.* Metallurgical and Materials Transactions A-Physical Metallurgy and Materials Science, 1986. **17**: p. 243-252.
88. Fultz, B., Kim, J. I., Kim, Y. H., Morris, J. W., *The chemical composition of precipitated austenite in 9Ni steel.* Metallurgical and Materials Transactions A-Physical Metallurgy and Materials Science, 1986. **17**: p. 967-972.
89. Morito, S., Oh-Ishi, K., Hono, K., Ohba, T., *Carbon enrichment in retained austenite films in low carbon lath martensite steel.* ISIJ International, 2011. **51**(7): p. 1200-1202.
90. Xiong, X. C., Chen, B., Huang, M. X., Wang, J. F., Wang, L., *The effect of morphology on the stability of retained austenite in a quenched and partitioned steel.* Scripta Materialia, 2013. **68**(5): p. 321-324.
91. Sandvik, B. P. J., Nevalainen, H. P., *Structure property relationships in commercial low-alloy bainitic-austenitic steel with high strength, ductility, and toughness.* Metals Technology, 1981. **8**(1): p. 213-220.
92. Strife, J. R., Passoja, D. E., *The effect of heat treatment on microstructure and cryogenic fracture properties in 5Ni and 9Ni steel.* Metallurgical Transactions A, 1980. **11**: p. 1341-1350.
93. Wang, M., Liu, Z. Y., Li, C. G., *Correlations of Ni contnts, formation of reversed austenite and toughness for Ni-containing cryogenic steels.* Acta Metallurgica Sinica, 2017. **30**(3).
94. Khodir, S., Shibayanagi, T., Takahashi, M., Abdel-Aleem, H., Ikeuchi, K., *Microstructural evolution and mechanical properties of high strength 3-9% Ni-steel alloys weld metals produced by electron beam welding.* Materials & Design, 2014. **60**: p. 391-400.
95. Morris, J. W. Jr., *On the ductile-brittle transition in lath martensitic steel.* ISIJ International, 2011. **51**(10): p. 1569-1575.

96. Marshall, R. F., Heheman, R. F., and Troiano, A. R., *The charateristics of 9% nickel low carbon steels.* Transactions of the American Society for Metals, 1962. **55**: p. 135.
97. Sarno, D. A., Havens, F. E., and Bowley, D. L., *Unpublished research presented at 1970 Materials Engineering Congress*. 1970, ARMCO Steel Corporation: Middletown, OH. .
98. Judge, V. K., Speer, J. G., Clarke, K. D., Findley, K. O., Clarke, A. J., *Rapid thermal processing to enhance steel toughness*, in *Scientific Reports*. 2018.
99. Zhang, Y., Shimizu, K., Kusumoto, K., Hara, H., Higuchi, C., *Influence of Ni addition on erosive wear characteristics of multi-component white cast iron at elevated temperature.* Wear, 2017. **376**: p. 452-457.
100. Kang, B. Y., Kim, H. J., and Hwang, S. K., *Effect of Mn and Ni on the variation of the microstructure and mechanical properties of low-carbon weld metals.* ISIJ International, 2000. **40**(12): p. 1237-1245.
101. ASM Handbook, *Fatigue and Fracture*, ed. A. International. Vol. 18. 1996, Materials Park, OH.
102. Schwartz, L. H., *Final Report to AISI on Project 66-32*. 1976, Dept. of Mat. Sci. and Eng., Northwestern University: Evanston.
103. Song, C. H., Yu, H., Lu, J., Zhou, T., Yang, S. F., *Stress partitioning among ferrite, martensite and retained austenite of a TRIP-assisted multiphase steel: an in-situ high-energy X-ray diffraction study.* Materails Science and Engineering A, 2018. **726**: p. 1-9.
104. Kim, K. J., Schwartz, L. H., *On the effects of intercritical tempering on the impact energy of Fe–9Ni–0.1C.* Materials Science and Engineering, 1978. **33**: p. 5-20.
105. Zhou, Q., Qian, L., Tan, J., Meng, J. Y., Zhang, F. C., *Inconsistent effects of mechanical stability of retained austenite on ductility and toughness of transformation-induced plasticity steels.* Materials Science and Engineering: A, 2013. **578**: p. 370-376.
106. Richman, R. H., Landgraf, R. W., *Some effects of retained austenite on the fatigue resistance of carburized steel.* Metallurgical Transactions A, 1975. **6**: p. 955-964.
107. Cao, H., Luo, X., Zhan, G., Liu, S., *Effect of intercritical quenching on the microstructure and cryogenic mechanical properties of a 7 Pct Ni steel.* Metallurgical and Materials Transactions A, 2017. **48**: p. 4403-4410.
108. Jain, D., Isheim, D., Zhang, X. J., Ghosh, D., Seidman, D. N., *Thermally stable Ni-rich austenite formed utilizing multistep intercritical heat treatment in a low-carbon 10 Wt Pct Ni martensitic steel.* Metallurgical and Materials Transactions A, 2017. **48**: p. 3642-3654.
109. Fultz, B., Kim, J. I., Kim, Y. H., Fior, G. O., Morris, J. W., *The stability of precipitated austenite and the toughness of 9Ni steel.* Metallurgical Transactions A, 1985. **16**: p. 2237-2249.
110. Pampillo, C. A., and Paxton, H. W., Metallurgical Transaction, 1972. **3**: p. 2895.
111. Hwang, S. K., Jin, S., and Morris, J. W. Jr., Metallurgical Transaction A, 1975. **6A**: p. 2015.
112. *Metallurgical properties of ARMCO Cryogenic 5 steel*, A.S. Corporation, Editor. 1971: Middletown, OH.
113. Syn, C. K., Morris, J. W., Jin, S., *Cryogenic fracture toughness of 9Ni steel enhanced through grain refinement.* Metallurgical and Materials Transactions A, 1976. **7**(12): p. 1827-1832.

114. Kim, J. I., Syn, C. K., Morris, J. W., *Microstructural sources of toughness in QLT-treated 5.5Ni cryogenic steel.* Metallurgical and Materials Transactions A, 1983. **14**(1): p. 93-103.
115. Kim, J. I., Morris, J. W., *On the scavenging effect of precipiated austenite in a low carbon Fe-5.5Ni alloy.* Metallurgical and Materials Transactions A, 1980. **11**(8): p. 1401-1406.
116. Wu, S. J., Sun, G. J., Ma, Q. S., Shen, Q. Y., Xu, L., *Influence of QLT treatment on microstructure and mechanical properties of a high nickel steel.* Journal of Materials Processing Technology, 2012. **213**(1): p. 120-128.
117. Podder, A. S., Bhadeshia, H. K. D. H., *Thermal stability of austenite retained in bainitic steels.* Materials Science and Engineering A, 2010. **527**(7-8): p. 2121-2128.
118. ASTM, *Standard test methods for tension testing of metallic materials*. 2016, ASTM International: West Conshohocken.
119. ASTM, *Standard test methods for notched bar impact testing of metallic materials*. 2016, ASTM International: West Conshohocken.
120. ASTM, *Standard test method for measurement of fracture toughness*. 2017, ASTM International: West Conshohocken.
121. ASTM, *Standard test method for linear-elastic plane-strain fracture toughness of metallic materials*. 2020, ASTM International: West Coshohocken.
122. ASTM, *Standard test method for determination of reference temperature, T0, for ferritic steels in the transition range*. 2018, ASTM International: West Conshohocken.
123. Xu, W., *Characterisation of Micro-Mechanisms of Cleavage Fracture in SA738 Gr. B Steel*, in *Department of Metallugy and Materials*. 2023, The University of Birmingham.
124. Irwin, G. R., *Plastic zone near a crack tip and fracture toughness*, in *Sagamore Ordnance Mater. Conf.* 1960. p. IV63-IV78.
125. McMeeking, R. M., *Finite deformation analysis of crack-tip opening in elastic-plastic materials and implications for fracture.* Journal of the Mechanics and Physics of Solids, 1977. **25**(5): p. 357-381.
126. Cottrell, A. H., Bilby, B. A., *Dislocation theory of yielding and strain ageing of iron.* Proceedings of the Physical Society. Section A, 1949. **62**(1): p. 49-62.
127. Hallai, J. F., Kyriades, S., *On the effect of Lüders bands on the bending of steel tubes. Part IÖ Experiments.* International Journal of Solids and Structures, 2011. **48**(24): p. 3275-3284.
128. Butler, J. F., *Lüders front propagation in low carbon steels.* Journal of the Mechanics and Physics of Solids, 1962. **10**(4): p. 313-318.
129. Dieter, G. E., *Mechanical Property*. 3rd ed. 1986, McGraw-Hill, New York, NY.
130. Baker, T. J., Kavishe, F. P. L., Wilson, J., *Effect of non-metallic inclusions on cleavage fracture.* Materials Science and Technology, 1986. **2**(6): p. 576-582.
131. Zhang, F., *Study on the impact properties of SA-738 Gr.B welded by SMAW*. 2022, Journal of Physics.
132. Druce, S., Gage, G., Jordan, G., *Effect of ageing on properties of pressure vessel steels.* Acta Metallurgica, 1986. **34**: p. 641-652.
133. Chaouadi, R., Gérard, R., *Development of a method for extracting fracture toughness from instrumented Charpy impact tests in the ductile and transition regimes.* Theoretical and Applied Fracture Mechanics, 2021. **115**.

134. Nakanishi, D., Kawabata, T., Aihara, S., *Effect of dispersed retained γ-Fe on brittle crack arrest toughness in 9% Ni steel in cryogenic temperatures.* Materials Science and Engineering: A, 2018. **723**: p. 238-246.
135. Landes, J. D., *Effect of size, thickness and geometry on fracture toughness in the transition*. 1992: GKSS-Forschungszentrum GeesthachtGmbH.
136. Berveiller, M., Zaoui, A., *An extension of the self-consistent scheme to plastically-flowing polycrystals.* Journal of Mechanics and Physics of Solids, 1979. **26**: p. 325-344.
137. Chen, J. H., Cao, R., *Micromechanism of cleavage fracture of metals : a comprehensive microphysical model for cleavage cracking in metals*. 2015.
138. Chen, J. H., Wang, Q., Wang, G. Z., Li, Z., *Fracture behavior at crack tip- a new framework for cleavage mechanism of steel.* Acta Materialia, 2003. **51**(7): p. 1841-1855.
139. Chen, J. H., Li, G., Cao, R., Fang, X. Y., *Micromechanism of cleavage fracture at the lower shelf of the transition temperature in a C-Mn steel.* Materials Science and Engineering A, 2010. **527**: p. 5044-5054.
140. Dodds, R. H., Ming, T., Anderson, T. L., *Numerical modelling of ductile tearing effects on cleavage fracture toughness, constraint effects in fracture theory and applications.* ASTM Special Technical Publication, 1995. **1244**: p. 103-133.
141. O'Dowd, N. P., Shih, C. F., Dosss, R. H., *The role of geometry and crack growth on constraint and implication for ductile/brittle fracture.* ASTM STP, 1994. **1224**: p. 134-159.
142. Ostby, E., Thaulow, C., Zkang, Z.L., *Numerical simulations of specimen size and mismatch effects in ductile crack growth-Part I: Tearing resistance and crack growth paths.* Engineering Fracture Mechanics, 2007. **74**: p. 1770-1792.
143. Bowen, P., Druce, S. G., and Knott, J. F., *Effects of microstructure on cleavage fracture in pressure vessel steel.* Acta Metallurgica, 1986. **34**(6): p. 1121-1131.
144. Zhang, Y.L., Hui, H., Zhang, J. B., Zhou, Z. Q., Hu, X., Cong, X., *Prediction of fracture toughness of SA738Gr.B steel in the ductile-brittle transition using master curve method and bimodal master curve method.* International Journal of Pressure Vessels and Piping, 2020. **182**: p. 104033.
145. Ohmura, T., Hara, T., Tsuzaki, K., Nakatsu, H., & Tamura, Y., *Mechanical characterization of secondary-hardening martensitic steel using nanoindentation.* Journal of Materials Research, 2004. **19**(1): p. 79-84.
146. Brownrigg, A., *The effect of austenite grain size on the strength of low carbon martensite.* Scripta Materialia, 1973. **7**: p. 1139-1142.
147. Han, S. Y., Shin, S. Y., Lee, S., Kim, N. J., Bae, J. H., & Kim, K., *Effects of cooling conditions on tensile and charpy impact properties of API X80 linepipe steels.* Metallurgical and Materials Transactions A, 2010. **41**: p. 329-340.
148. Qiao, Y., *Modelling of resistance curve of high-angle grain boundary in Fe-3 wt. % Si alloy.* Materials Science and Engineering: A, 2003. **361**(1-2): p. 350-357.
149. Hwang, B., Kim, Y. G., Lee, S., Kim, Y. M., Kim, N. J., & Yoo, J. Y., *Effective grain size and charpy impact properties of high-toughness X70 pipeline steels.* Metallurgical and Materials Transactions A, 2005. **36**: p. 2107-2114.
150. Yang, Z., Liu, Z., He, X., Qiao, S., and Xie, C., *Effect of microstructure on the impact toughness and temper embrittlement of SA508Gr.4N steel for advanced pressure vessel materials*, in *Scientific Reports*. 2018. p. 207.

151. Kalish, D., Kulin, S. A., *Thermomechanical treatments applied to ultra-high strength steels*. 1964.
152. Coldren, C. L., Chu, P. T., *In situ pipeline heat generation*, 6712209, Editor. 1969, EDB-83-017798: United States.
153. Jaoul, B., *Consolidation des polycristaux de fer et hypothèses sur l'origine du palier des courbes de traction.* Journal of the Mechanics and Physics of Solids, 1961. **9**(2): p. 69-90.
154. Tsuchida, N., Tomota, Y., Nagai, K., Fukaura, K., *A simple relationship between Lüders elongation and work-hardening rate at lower yield stress.* Scripta Materialia, 2006. **54**(1): p. 57-60.
155. Zhou, T., Yu, H., Wang, S., *Microstructural characterization and mechanical properties across thickness of ultra-heavy steel plate.* Steel Research International, 2017. **88**(12).
156. Guo, K., Pan, T., Zhang, N., Meng, L., Luo, X., Chai, F., *Effect of microstructural evolution on the mechanical properties of Ni-Cr-Mo ultra-heavy steel plate.* Materials (Basel), 2023. **16**(4).
157. Rancel, L., Gómez, M., Medina, S. F., Gutierrez, I., *Measurement of bainite packet size and its influence on cleavage fracture in a medium carbon bainitic steel.* Materails Science and Engineering A, 2011. **530**: p. 21-27.
158. Mao, G., Cayron, C., Cao, R., Logé, R., Chen, J., *The relationship between low-temperature toughness and secondary crack in low-carbon bainitic weld metals.* Materials Characterization, 2018. **145**: p. 516-526.
159. Lee, S. G., Sohn, S. S., Kim, B., Kim, W. G., Um, K. K., Lee, S., *Effects of martensite-austenite constituent on crack initiation and propagation in inter-critical heat-affected zone of high-strength low-alloy (HSLA) steel.* Materails Science and Engineering A, 2018. **715**: p. 332-339.
160. Iron and Steel Institute, *Metallurgical Developments in Carbon Steels*, ed. British Iron and Steel Research Association. Vol. 81. 1963, Carbon Steels Committee: Iron and Steel Institute. 95.
161. Walters, C. L., *The effect of low temperatures on the fatigue of high-strength structural grade steels.* Procedia materials science, 2014. **3**: p. 209-214.
162. Borges, M. F., Antunes, F. V., Prates, P., Branco, R., Liveira, M. C., *Effect of yield stress on fatigue crack growth.* Frattura ed Integrità Strutturale, 2019. **13**(50): p. 9-19.
163. Park, H. B., Kim, K. M., Lee, B. W., *Plastic zone size in fatigue cracking.* International Journal of Pressure Vessels and Piping, 1996. **68**(3): p. 279-285.
164. Jeong, D. H., Lee, S. G., Jang, W. K., Choi, J. K., Kim, Y. J., Kim, S., *Cryogenic S-N fatigue and fatigue crack propagation behaviors of high manganese austenitic steels.* Metallurgical and Materials Transactions A-Physical Metallurgy and Materials Science, 2013. **44**(10): p. 4601-4612.
165. Cheng, X., Fisher, J. W., Prask, H. J., Gnäupel-Herold, T., Yen, B. T., Roy, S., *Residual stress modification by post-weld treatment and its beneficial effect on fatigue strength of welded structures.* International Journal of Fatigue, 2003. **25**(9-11): p. 1259-1269.
166. Mei, Z., Morris, J. W. Jr., *Influence of deformation-induced martensite on fatigue crack propagation in 304-type steels.* Metallurgical Transactions A, 1990. **21**: p. 3137-3152.
167. Lawson, L., Chen, E. Y., Meshii, M., *Near-threshold fatigue: a review.* International Journal of Fatigue, 1999. **21**: p. S15-S34.

168. Liao, X. W., Wang, Y. Q., Qian, X. D., Shi, Y. J., *Fatigue crack propagation for Q345qD bridge steel and its butt welds at low temperatures.* Fatigue & Fracture of Engineering Materials & Structures, 2018. **41**(3): p. 675-687.
169. Park, D. Y., Liang, J., *Effects of temperature on fatigue crack growth rates of a low-carbon pipe steel in the ductile and ductile-to-brittle transition regions.* Journal of Pipeline Science and Engineering, 2023. **3**(4): p. 100139.
170. Yan, W., Sha, W., Zhu, L., Wang, W., Shan, Y. Y., Yang, K., *Delamination fracture related to tempering in a high-strength low-alloy steel.* Metallurgical and Materials Transactions A, 2010. **41**: p. 159-171.
171. Yan, W., Shan, Y. Y., Yang, K., *Influence of TiN inclusions on the cleavage fracture behavior of low-carbon microalloyed steels.* Metallurgical and Materials Transactions A, 2007. **38**: p. 1211-1222.
172. Bridgman, P.W., *Studies in large plastic flow and fracture: with special emphasis on the effects of hydrostatic pressure*. 1964: Harvard University Press.

Figure 1.1

Stress Field ahead of the Main Crack Front in a Ductile Material

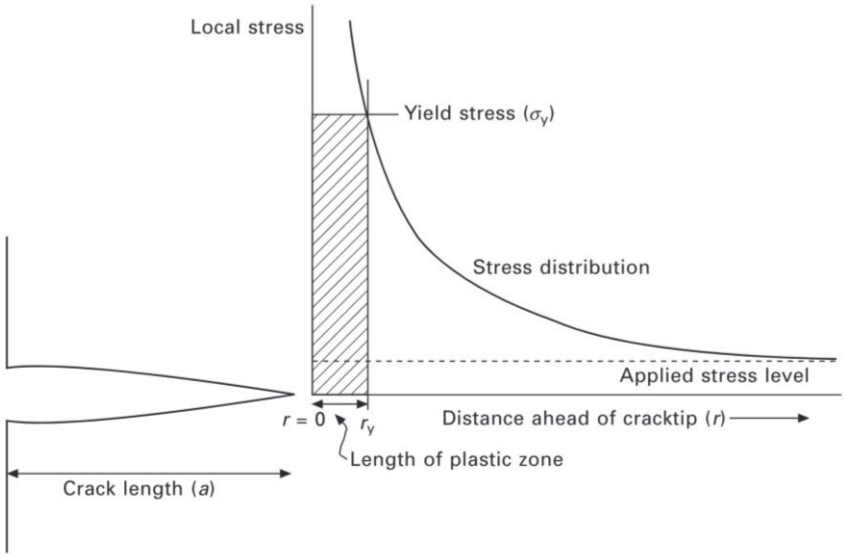

Figure 1.2

Grain Size Effects on Fracture Stress and Yield Stress

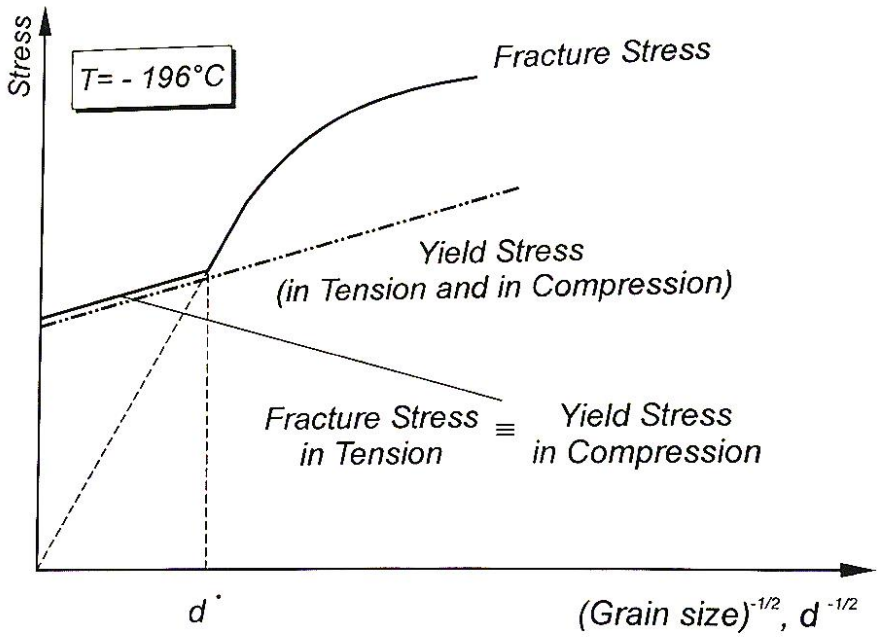

Figure 1.3

Zener's Model for Cleavage Microcrack Formation [13]

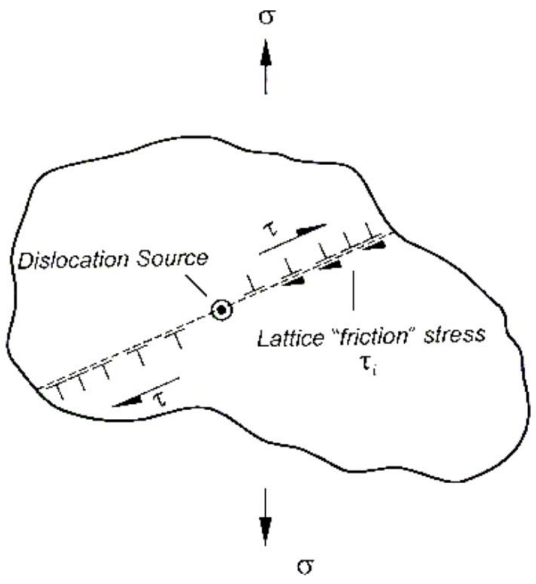

Figure 1.4

Stroh's Model for Cleavage Fracture [14]

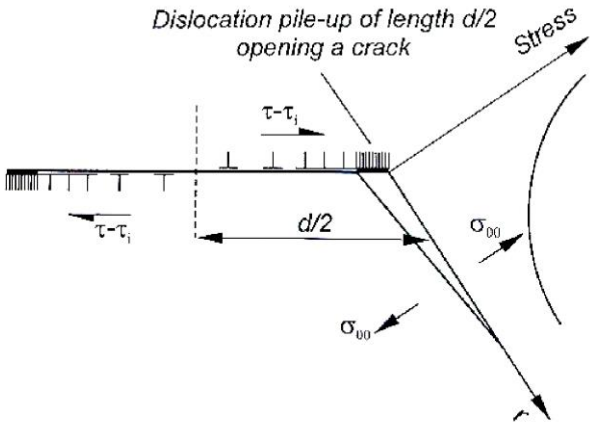

Figure 1.5

Cottrell's Model for Cleavage Fracture [15]

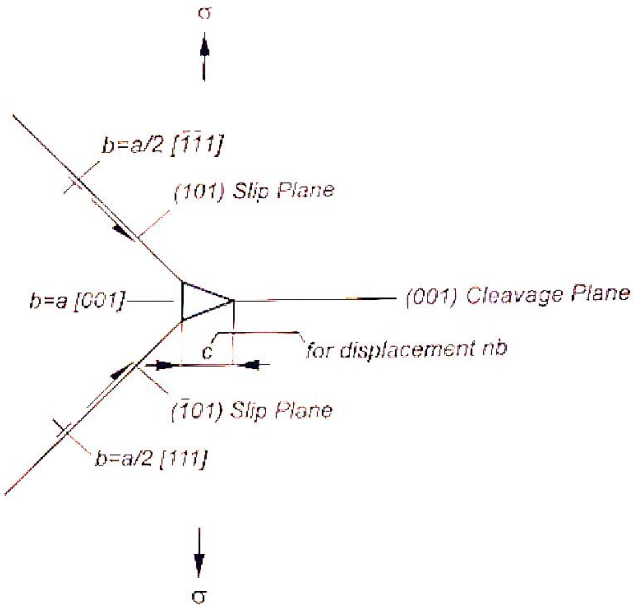

Figure 1.6

Smith Model for Cleavage Fracture [17]

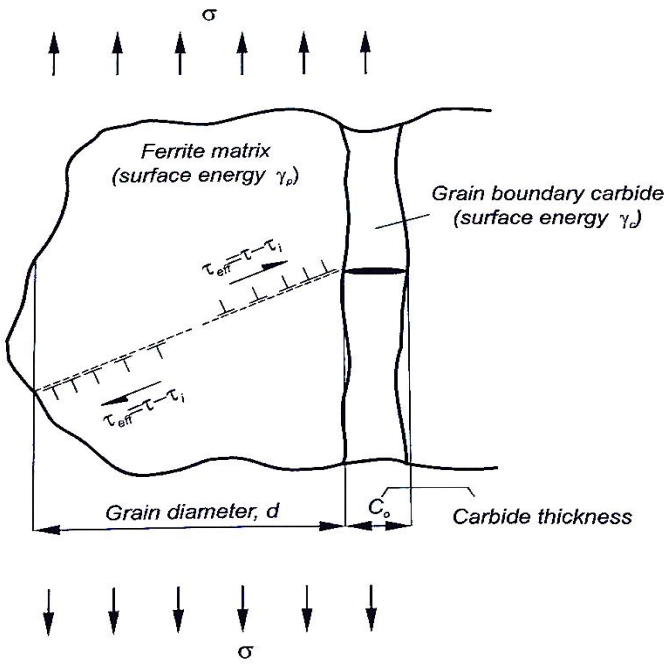

Figure 1.7

Containment Structure of Pressurised Water Reactor AP1000 [56]

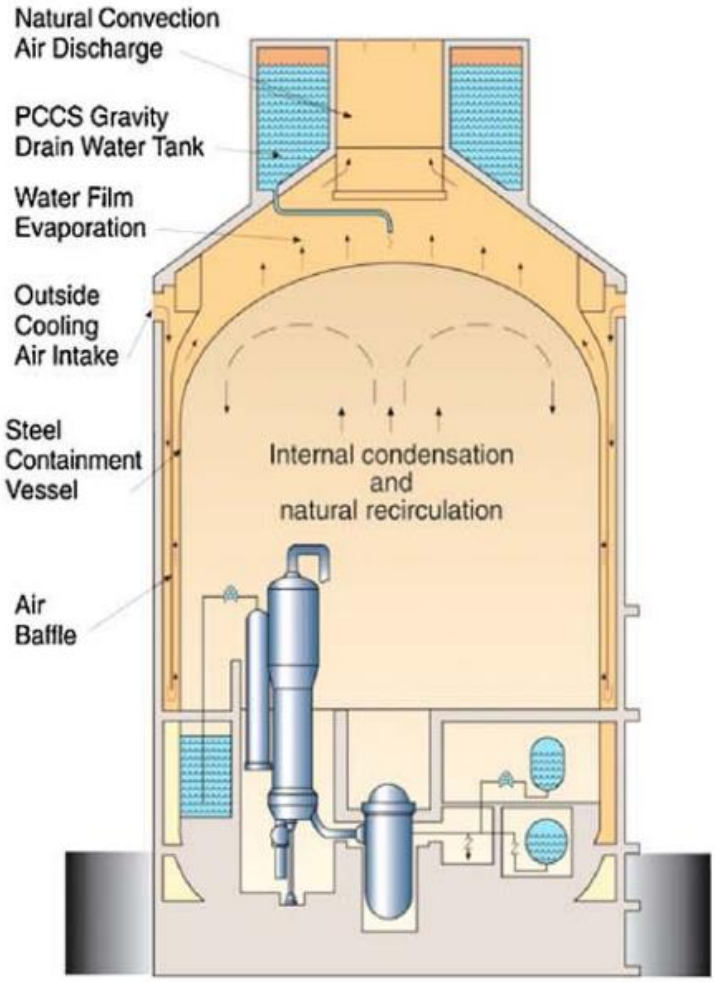

Table 2.1

Chemical Composition of SA-738 Gr. B Steel

Element [wt%]	C	Si	Mn	P	S	Cr+Ni+Cu	Mo	V+Nb	CE*
Baowu 55mm	0.088	0.18	1.47	0.003	0.0002	0.37	0.19	0.063	0.40
ASME Requirements	≤0.20	0.15-0.55	0.90-1.50	≤0.030	≤0.030	≤1.25	≤0.30	≤0.08	≤0.48

*Carbon equivalent (CE) = C + Mn/6 + (Cr + Mo + V)/5 + (Ni + Cu)/15

Table 2.2

Heat Treatment Conditions for HT1 and HT2

Batch No.	Heat Treatment Condition
HT1	900℃/2h WQ + 630℃/3h
HT2	900℃/2h WQ + 630℃/3h + 620℃/15h

Table 2.3

Chemical Composition of 9% Nickel Steel Produced by Baowu Steel

Element [wt%]	C	Si	Mn	P	S	Al	Ni
20mm	0.037	0.205	0.599	0.0036	0.0002	0.032	9.688

Table 2.4

Chemical Composition of 7% Nickel Steel Produced by Baowu Steel

Element [wt%]	C	Si	Mn	P	S	Al	Ni	Mo	Cr	N [ppm]
20mm	0.051	0.01	0.65	0.004	0.0035	0.029	7.14	0.064	0.39	37

Figure 2.1

SA-738 Gr. B Steel Plate Orientation

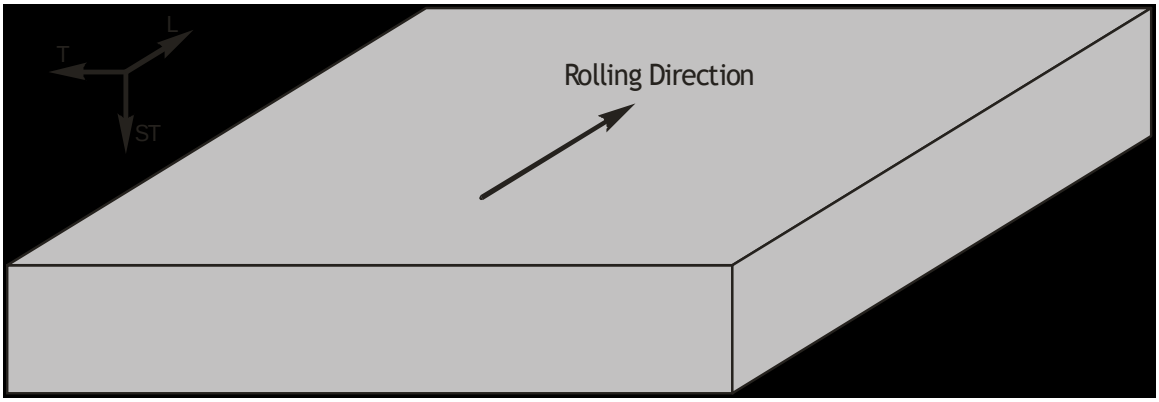

L: longitudinal Direction; T: Transverse Direction; ST: Short Transverse Direction

Figure 2.2

Test Specimen Locations on SA-738 Gr. B Steel Plate

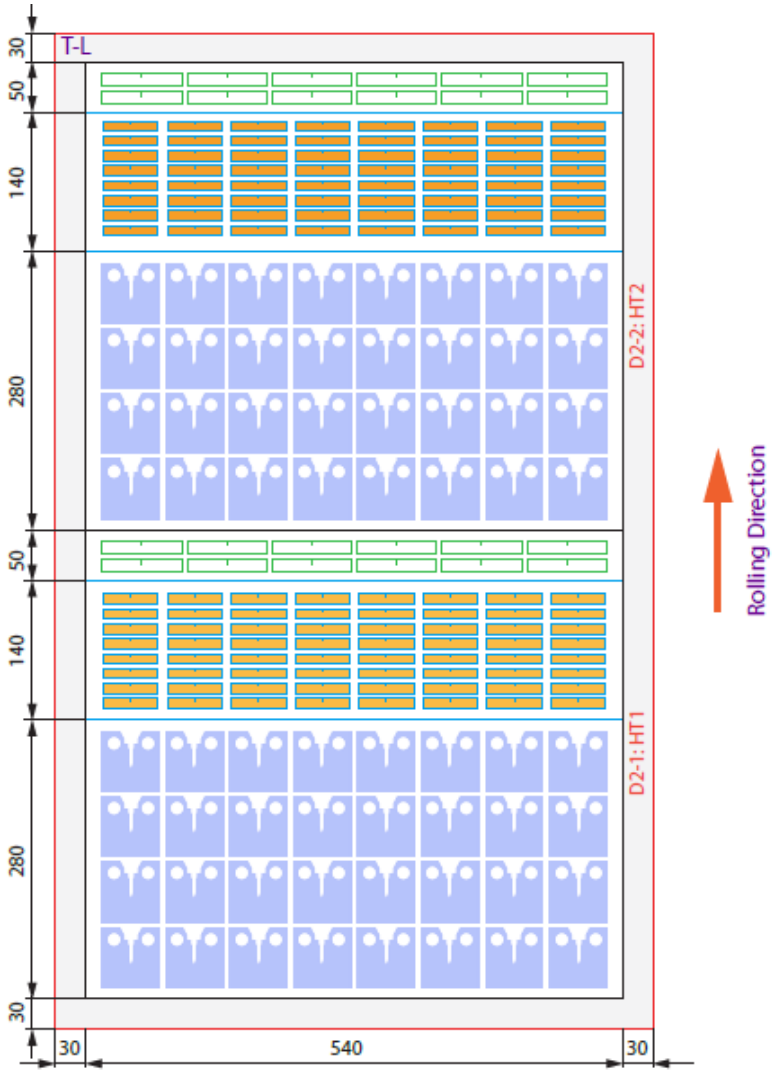

Figure 2.3

Specimen Sampling Scheme for 9% and 7% Nickel Steel

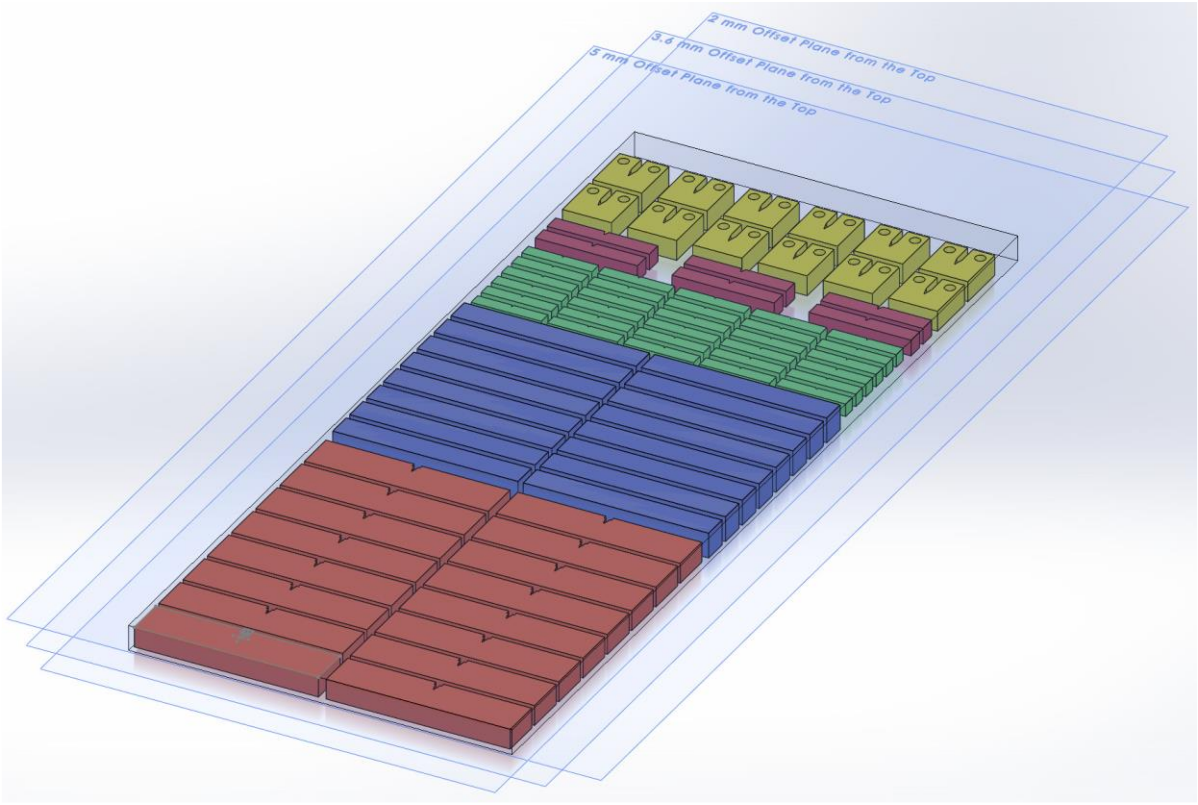

Figure 2.4

Tensile Specimen Locations and Orientation

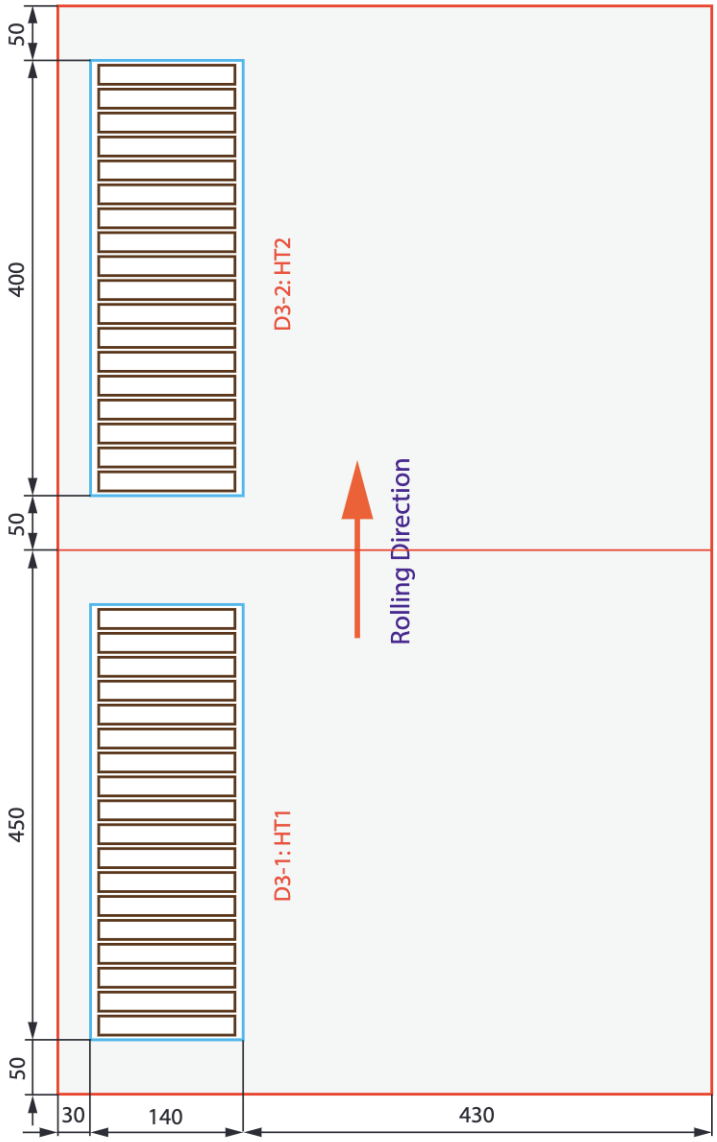

Figure 2.5

Tensile Specimen Design

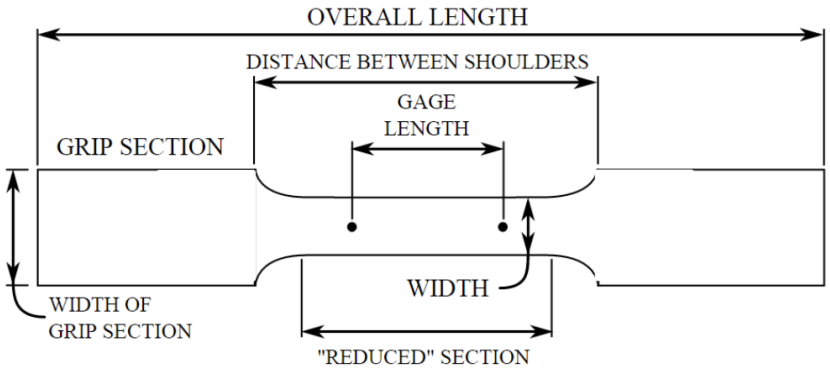

Figure 2.6

Design of Charpy Test Specimen

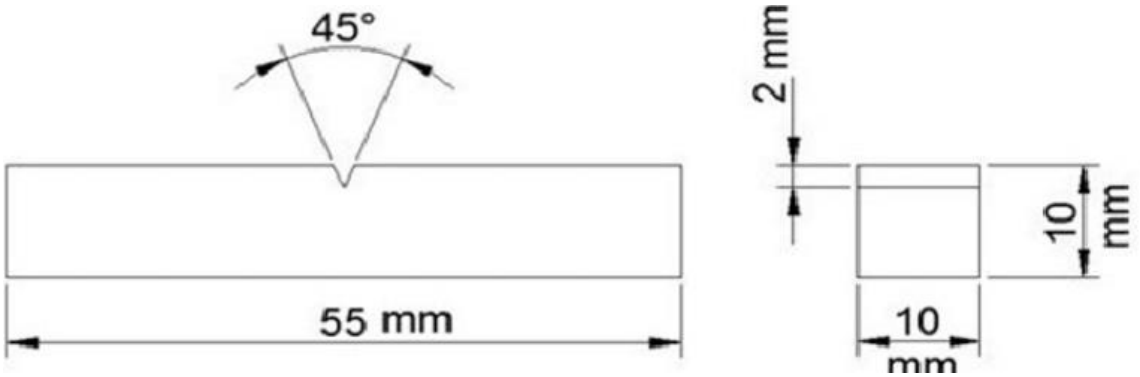

Figure 2.7

Machined Charpy Specimen

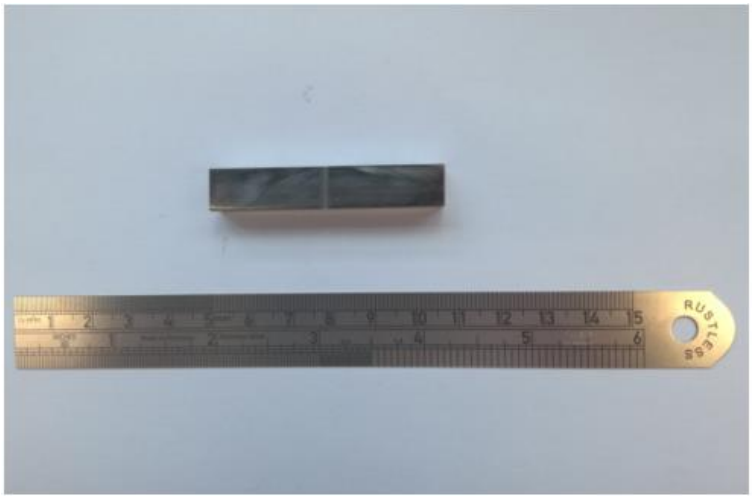

Figure 2.8

Designed Dimensions for Fracture Stress Specimens

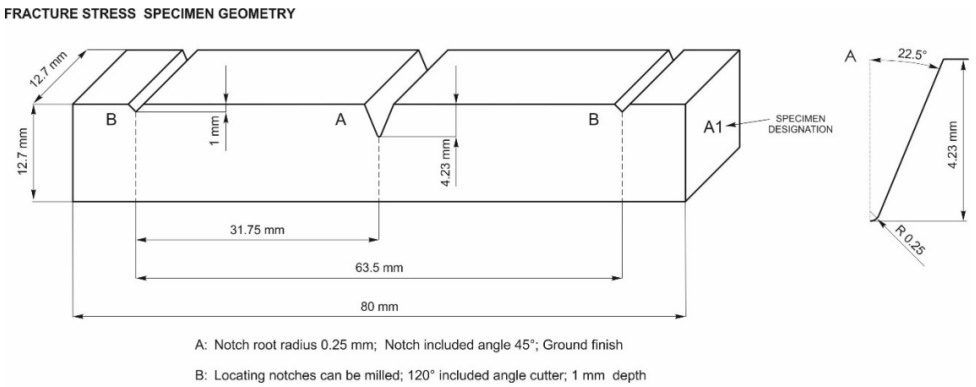

Figure 2.9

As-Received 7%Ni Steel Fracture Stress Specimens

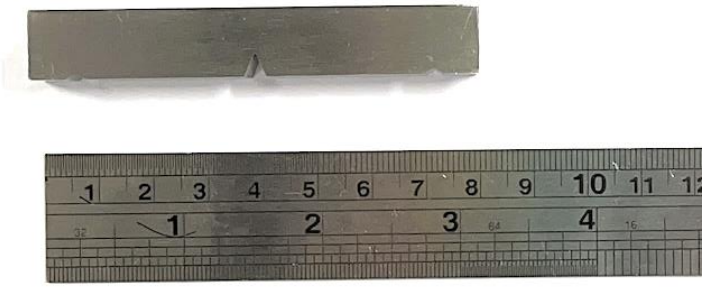

Figure 2.10

Illustration of Four-Point Bending Fracture Stress Testing

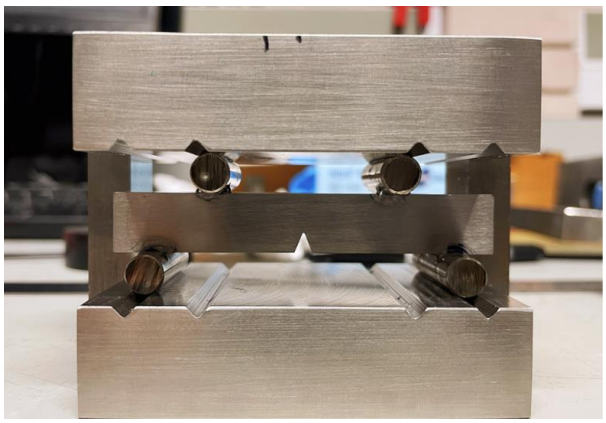

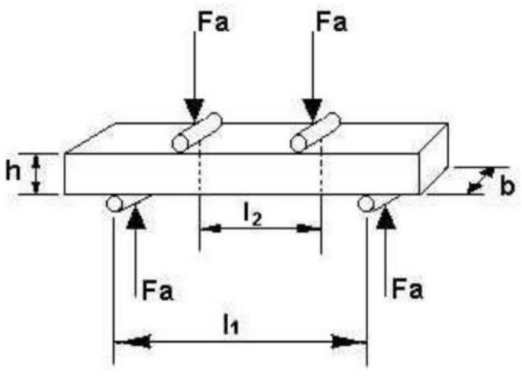

Figure 2.11

Experimental Setup for Fracture Stress Tests at -196ºC

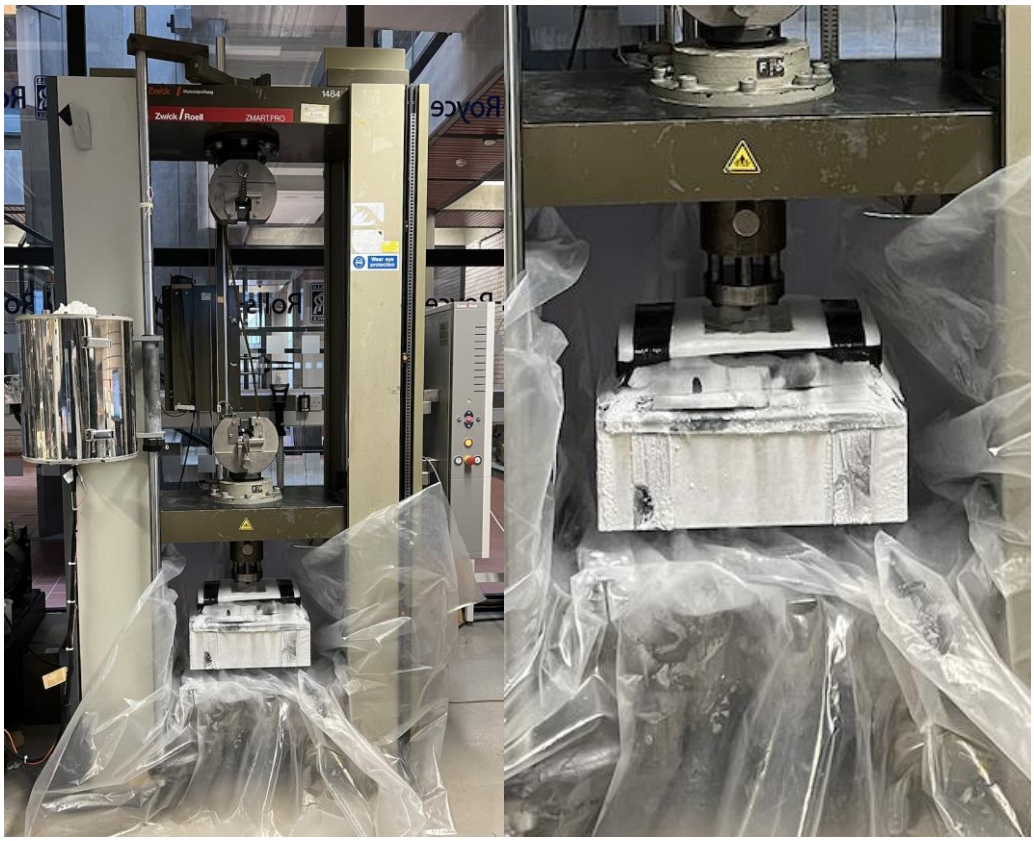

Figure 2.12

Relationship Between Stress Intensification Factor R, Applied Load L/L_{GY}, and Nominal Stress σ_{nom}/σ_y

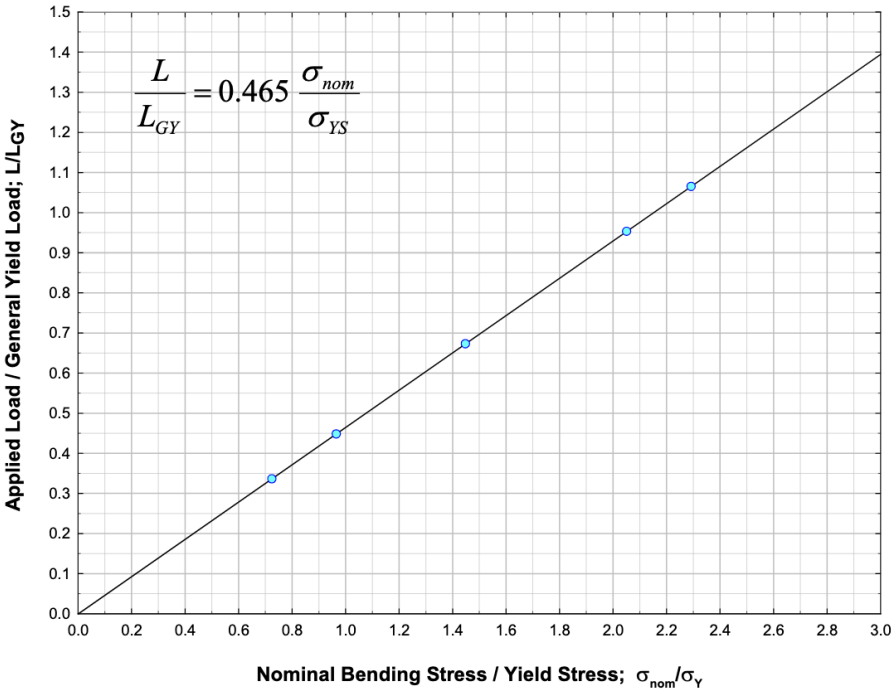

Figure 2.13

Stress Intensification Factor R vs. Nominal Bending Stress/Yield Stress

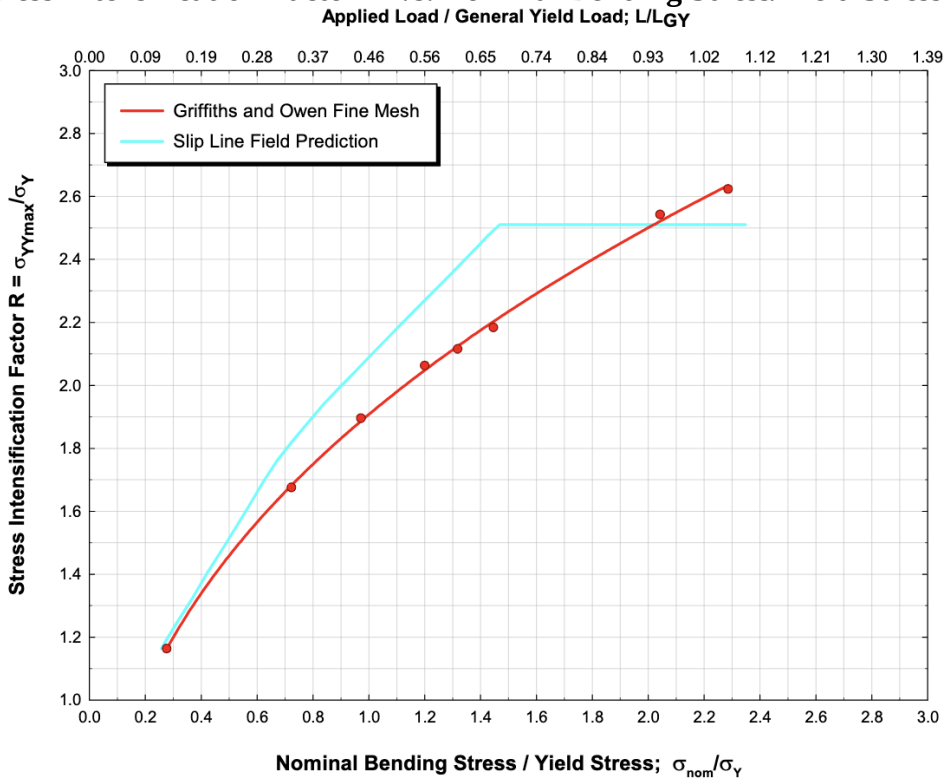

Figure 2.14

The Variation of the Maximum Principal Stress Below the Notch Root at Various Loads [25]

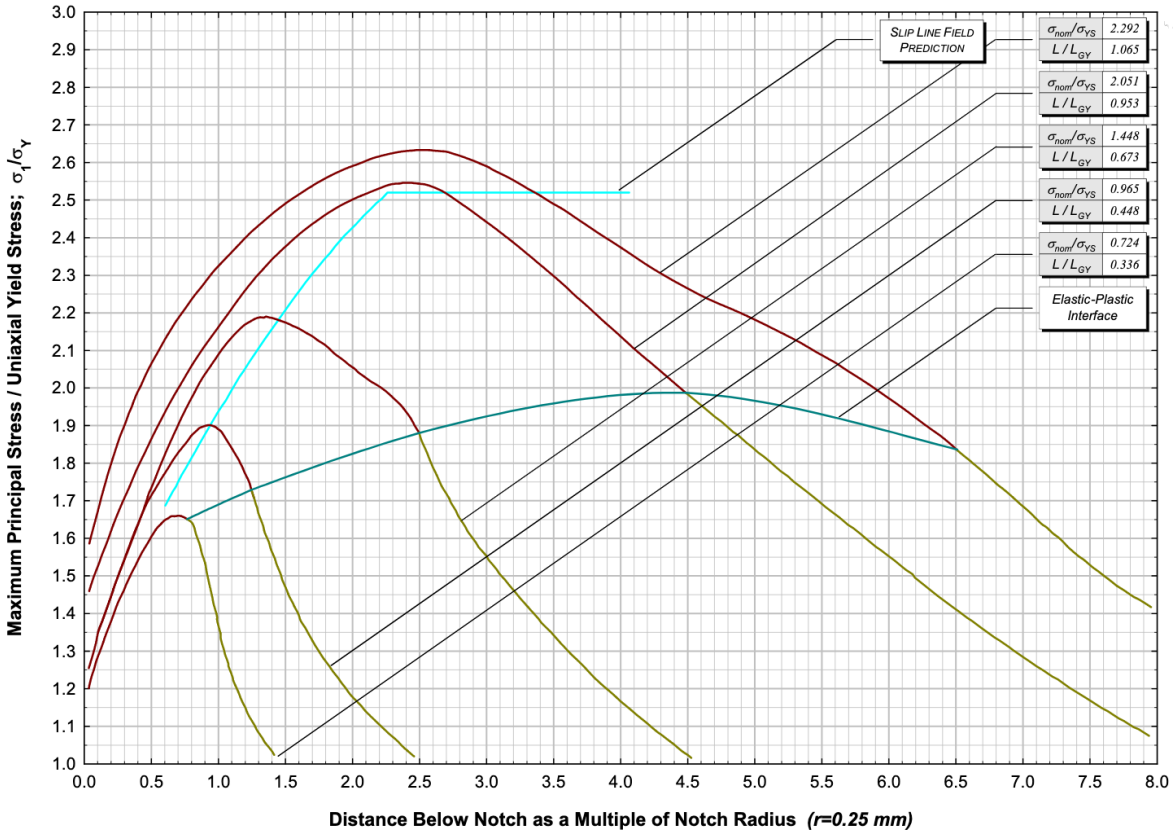

Figure 2.15

Designed Dimensions of Compact Tension Specimen for Fracture Toughness Test

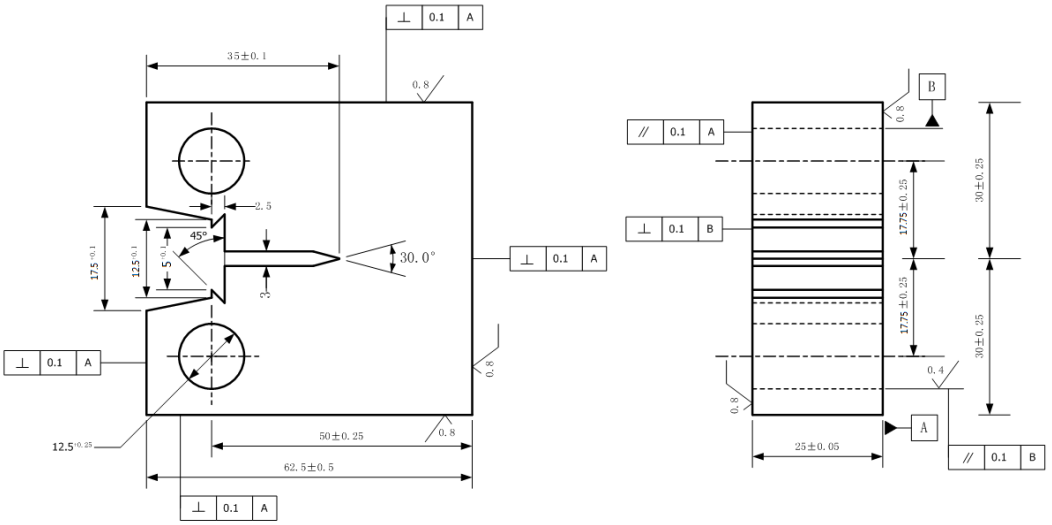

Figure 2.16

Machined Compact Tension Specimen

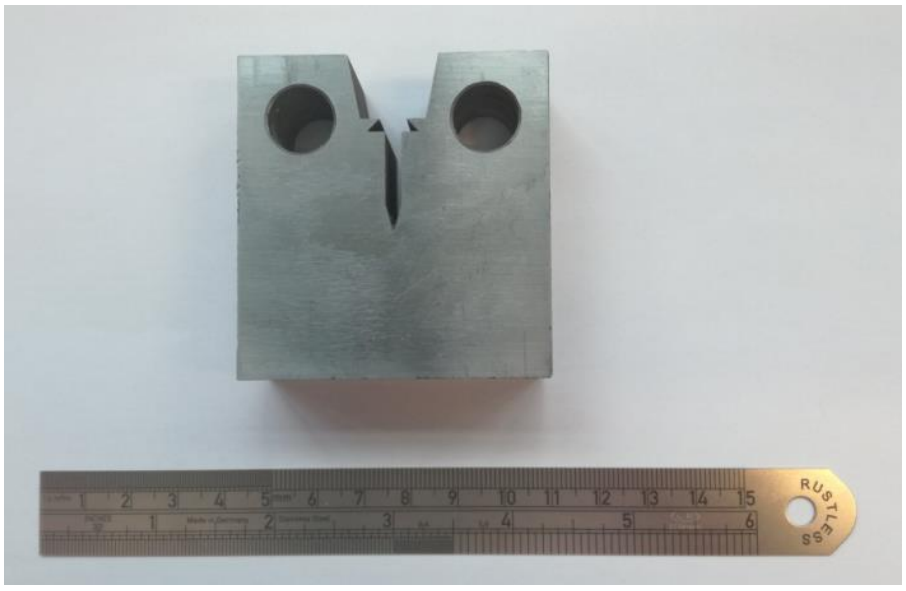

Figure 2.17

Amsler Vibrophore Machine for Fatigue Pre-cracking

Figure 2.18

C(T) Fracture Toughness Specimen in Environmental Chamber with Clip Gauge attached

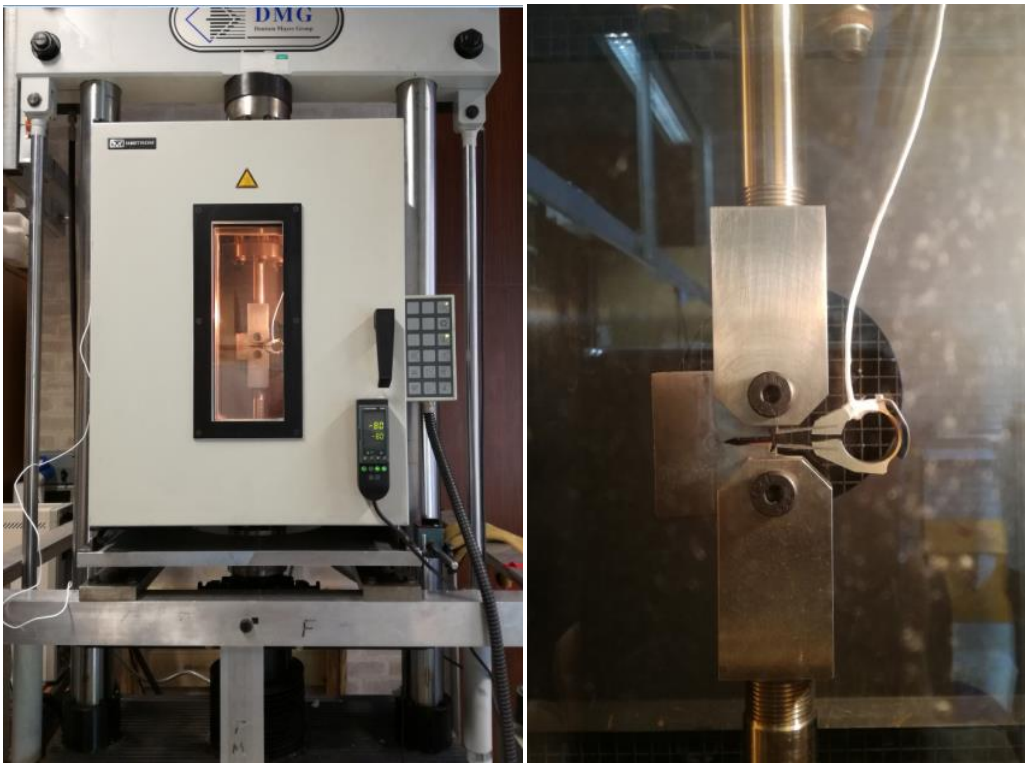

Figure 2.19

Designed Geometry of SENB Specimen for Fracture Toughness Tests

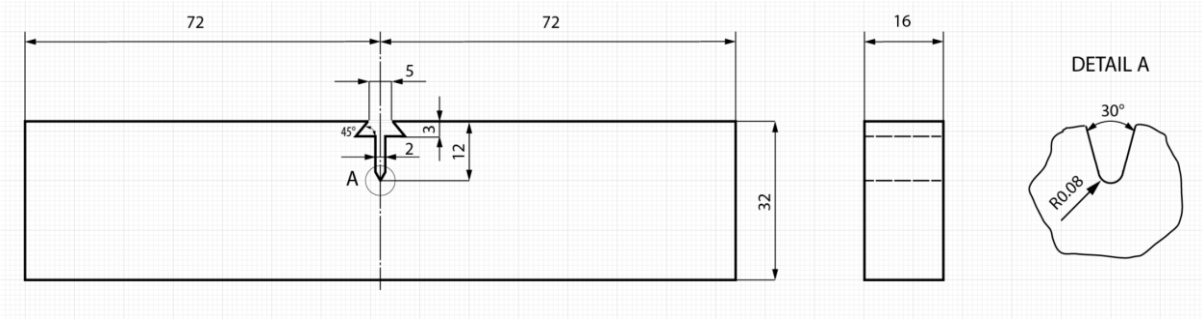

Figure 2.20

SENB Fracture Toughness Specimen in Environmental Chamber with Clip Gauge attached

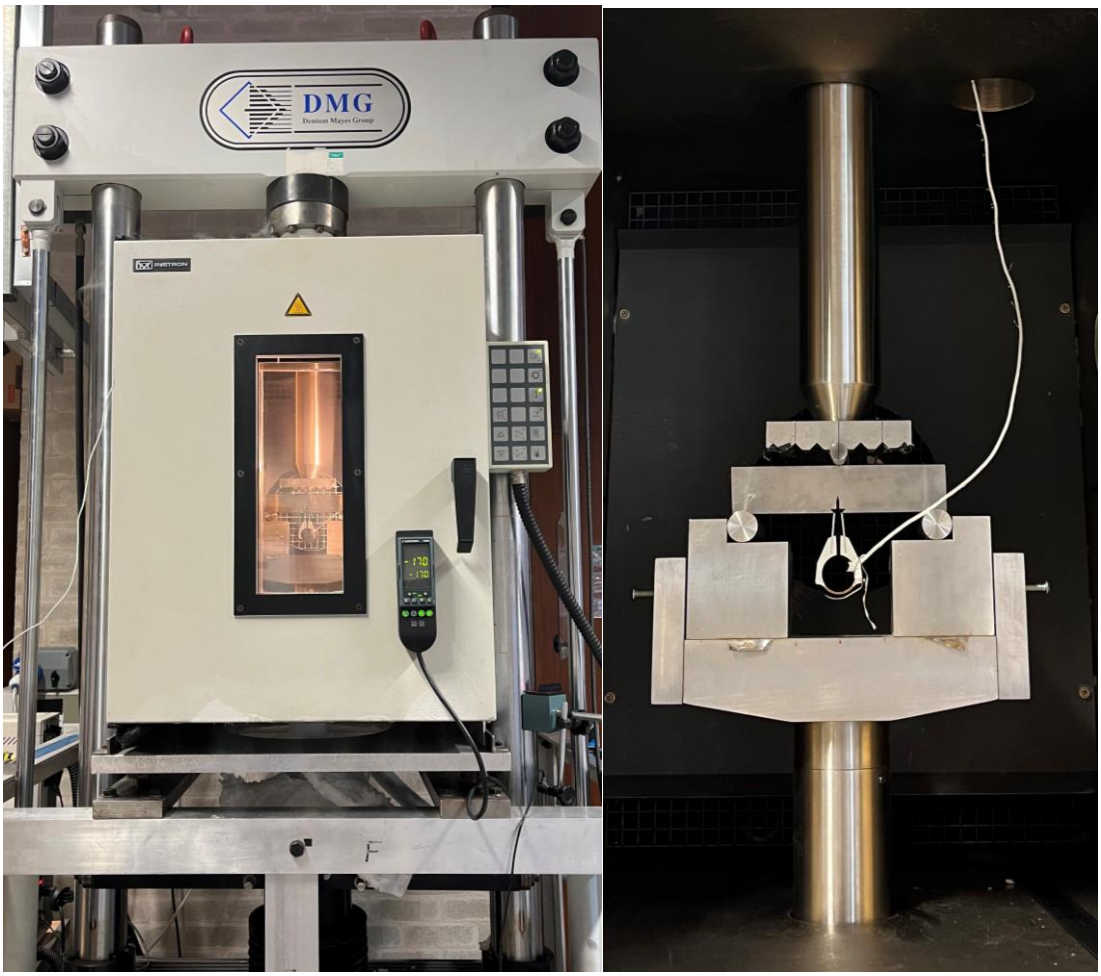

Figure 2.21

Designed Geometry of Small SENB Specimen for Fatigue Crack Growth Tests

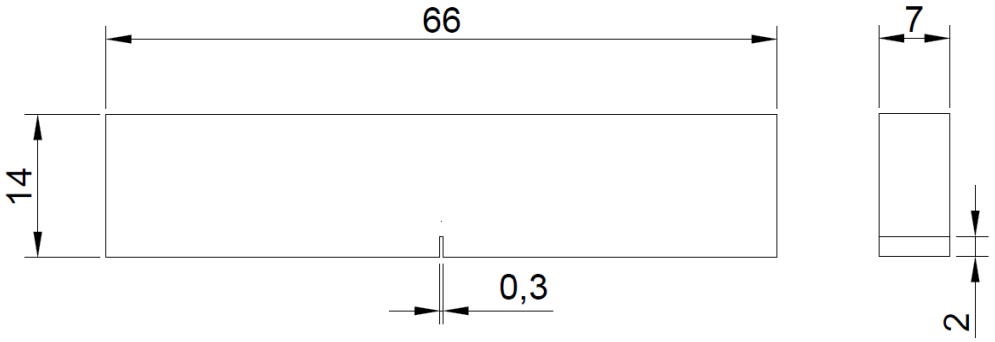

Figure 2.22

Experimental Setup for Three-Point Bending Fatigue Crack Growth Tests

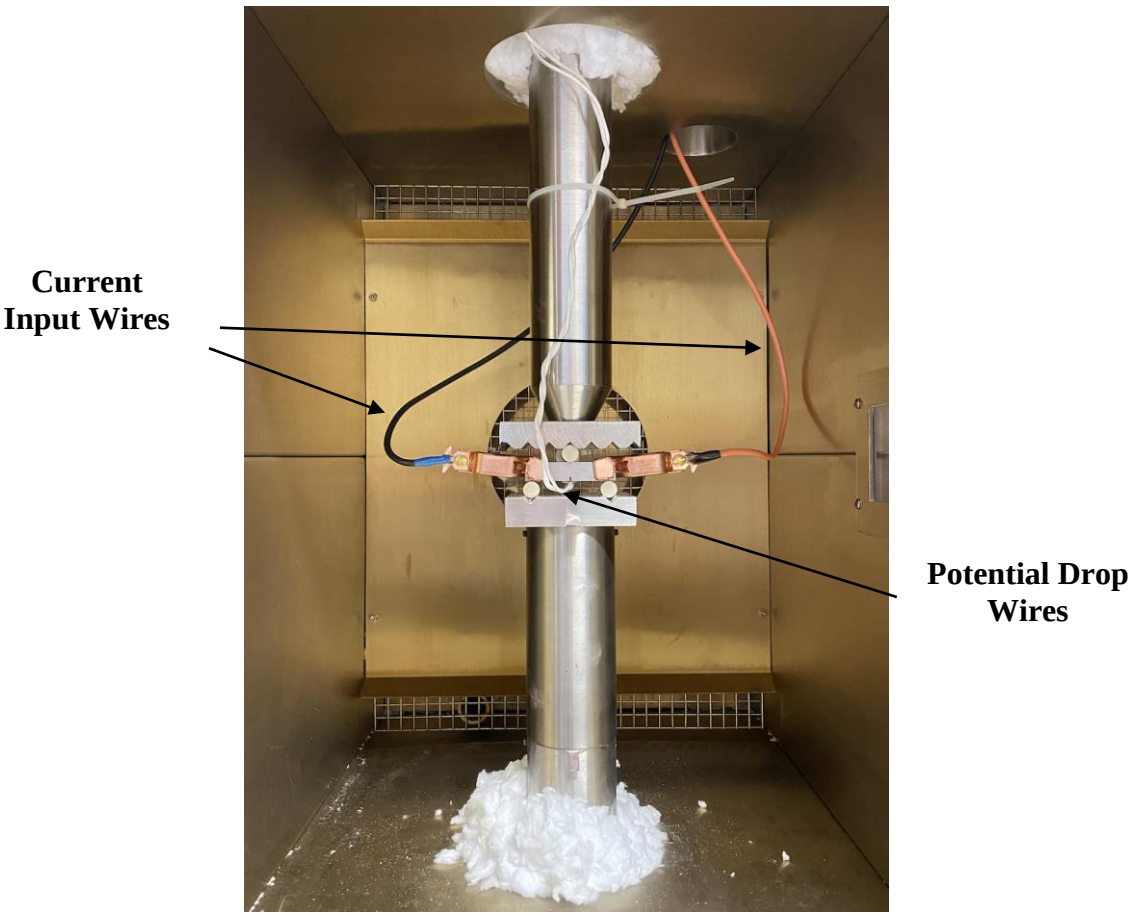

Table 3.1

Measured Diameters of HT1 Tensile Specimens

Specimen Nr.	Temperature [°C]	d_1 [mm]	d_2 [mm]	d_3 [mm]	$d_{average}$ [mm]	Area [mm^2]
HT1-01	-196	9.94	9.96	9.94	9.95	77.70
HT1-02		9.92	9.97	9.92	9.94	77.55
HT1-03		9.96	9.95	9.93	9.95	77.70
HT1-04	-170	9.92	9.90	9.92	9.91	77.18
HT1-06	-140	9.95	9.93	9.93	9.94	77.55
HT1-08		9.95	9.95	9.95	9.95	77.76
HT1-09	-120	10.03	9.98	9.99	10.00	78.54
HT1-10		9.95	9.95	9.95	9.95	77.76
HT1-11	-100	9.95	9.95	9.96	9.95	77.81
HT1-12		9.93	9.92	9.93	9.93	77.39
HT1-13	-80	9.93	9.93	9.93	9.93	77.44
HT1-14		9.91	9.91	9.91	9.91	77.13
HT1-15	-60	9.93	9.93	9.93	9.93	77.44
HT1-16		9.93	9.91	9.92	9.92	77.29

Table 3.2

Measured Diameters of HT2 Tensile Specimens

Specimen Nr.	Temperature [°C]	d_1 [mm]	d_2 [mm]	d_3 [mm]	$d_{average}$ [mm]	Area [mm^2]
HT2-01	-196	10.03	9.99	10.02	10.01	78.75
HT2-02		9.99	9.99	10.01	10.00	78.49
HT2-03		9.98	9.98	9.99	9.98	78.28
HT2-04	-170	9.99	9.98	10.02	10.00	78.49
HT2-06	-140	9.99	10.01	10.00	10.00	78.54
HT2-08		9.98	9.98	9.99	9.98	78.28
HT2-09	-120	9.99	10.01	9.99	10.00	78.49
HT2-10		9.98	9.99	9.98	9.98	78.28
HT2-11	-100	9.99	9.99	10.00	9.99	78.44
HT2-12		10.01	10.03	9.99	10.01	78.70
HT2-13	-80	9.98	9.98	9.98	9.98	78.23
HT2-14		9.98	9.98	9.98	9.98	78.23
HT2-15	-60	10.01	10.02	10.02	10.02	78.80
HT2-16		10.01	10.00	9.99	10.00	78.54

Table 3.3

Upper and Lower Yield Stress, Tensile Strength, Lüders Elongation, Work Hardening Exponent n of HT1 and HT2 tested from -196 to -60°C

Specimen Nr.	Temp.	Upper Yield Stress [MPam$^{1/2}$]		Lower Yield Stress [MPam$^{1/2}$]		Tensile Strength [MPam$^{1/2}$]		Lüders Elongation [%]		Work Hardening Exponent n	
	[°C]	HT1	HT2	HT1	HT2	HT1	HT2	HT1	HT2	HT1	HT2
1	-196	1003	954	921	934	952	951	7	5	0.02	0.01
2		1001	1000	931	927	954	941	9	9	0.01	0.01
3		1001	1008	933	921	951	949	9	7	0.01	0.03
4	-170	890	892	791	785	844	829	5	5	0.04	0.04
6	-140	792	739	717	706	772	767	5	5	0.04	0.04
8		785	750	711	695	783	769	5	5	0.05	0.06
9	-120	743	703	676	646	733	723	4	3	0.04	0.06
10		728	694	636	628	736	721	3	3	0.08	0.08
11	-100	690	646	633	607	702	693	3	3	0.06	0.05
12		662	653	612	588	704	692	3	2	0.08	0.09
13	-80	602	617	577	567	678	664	2	3	0.08	0.06
14		642	593	581	567	673	663	2	2	0.08	0.08
15	-60	622	576	566	528	653	641	2	2	0.08	0.11
16		586	562	558	537	655	639	2	2	0.09	0.08

Table 3.4

Test Temperatures and Absorbed Impact Energy for HT1 and HT2

Test Temperature [℃]	Specimen No.	Absorbed Impact Energy [J]		Test Temperature [℃]	Specimen No.	Absorbed Impact Energy [J]	
		HT1	HT2			HT1	HT2
-196	1	2.4	2.2	-90	40	299.0	247.5
	2	2.9	2.4		41	298.5	180.0
	3	2.0	2.0		42	200.0	89.7
-120	7	5.0	5.0	-80	13	299.0	23.0
	8	5.0	5.5		14	236.0	258.5
	9	5.0	6.0		15	298.5	250.0
	52	7.5	8.5		19	297.0	241.0
	53	7.5	5.0		20	297.0	203.0
	54	5.0	5.0		21	246.0	212.0
-100	10	26.0	12.5		25	299.0	261.0
	11	15.0	7.5		26	273.0	278.0
	12	10.5	19.0		27	13.0	298.5
	16	8.5	36.0	-70	34	298.5	298.5
	17	15.0	12.2		35	298.5	240.0
	18	8.0	23.0		36	283.5	233.0
	37	102.0	14.0		43	298.5	229.5
	38	19.5	9.5		44	258.0	298.5
	39	11.5	20.0		45	272.5	298.5
	46	6.0	8.0	-60	22	297.5	297.0
	47	3.0	10.0		23	297.0	297.0
	48	7.5	6.0		24	297.0	297.0
-90	4	298.0	192.0		31	299.0	299.0
	5	56.5	159.0		32	299.0	299.0
	6	25.0	8.5		33	298.5	237.0
	28	12.0	12.0	-40	49	298.5	299.0
	29	12.0	9.5		50	298.5	299.0
	30	267.0	32.0		51	298.2	299.0

Table 3.5

Lateral Expansion, Shear Lip Extension, %Cleavage Area, and Ductile Length of Charpy Impact Specimens of HT1 and HT2 tested from -196 to -90ºC

Temperature [ºC]	Sample no.	Lateral Expansion [mm]		Shear Lip Expansion [mm]		%Cleavage Area		Ductile Length [mm]	
		HT1	HT2	HT1	HT2	HT1	HT2	HT1	HT2
-196	1	0.14	0.00	0.00	0.00	100.00	100.00	0.00	0.00
	2	0.12	0.15	0.00	0.00	100.00	100.00	0.00	0.06
	3	0.14	0.08	0.00	0.00	100.00	100.00	0.00	0.00
-120	7	0.12	0.18	0.00	0.00	99.10	99.43	0.00	0.00
	8	0.12	0.10	0.00	0.00	99.29	100.00	0.00	0.00
	9	0.14	0.10	0.00	0.00	98.37	99.87	0.06	0.00
	52	0.23	0.13	0.00	0.00	98.69	97.54	0.01	0.00
	53	0.15	0.13	0.00	0.00	99.22	99.45	0.00	0.02
	54	0.17	0.15	0.00	0.00	98.05	99.92	0.04	0.00
-100	10	0.37	0.17	0.19	0.21	92.95	94.60	0.29	0.11
	11	0.25	0.27	0.20	0.16	94.80	95.63	0.11	0.00
	12	0.35	0.22	0.13	0.29	97.01	93.35	0.28	0.00
	16	0.16	0.47	0.18	0.42	95.07	96.91	0.19	0.27
	17	0.27	0.18	0.22	0.22	95.90	96.90	0.19	0.08
	18	0.17	0.15	0.17	0.14	96.50	95.36	0.04	0.14
	37	2.12	0.18	2.72	0.17	42.33	96.59	3.87	0.17
	38	0.31	0.15	0.19	0.21	91.92	97.33	0.27	0.05
	39	0.22	0.32	0.00	0.23	94.85	95.24	0.16	0.32
	46	0.14	0.25	0.00	0.00	99.92	99.44	0.01	0.02
	47	0.08	0.17	0.00	0.16	98.12	96.21	0.00	0.14
	48	0.20	0.27	0.00	0.00	98.69	99.83	0.00	0.04
-90	4	2.54	2.04	2.49	2.30	0.00	44.47	5.77	4.17
	5	0.72	1.74	0.00	2.29	83.48	62.52	0.52	3.11
	6	0.27	0.32	0.22	0.00	91.52	94.77	0.42	0.10
	28	0.23	0.30	0.00	0.00	91.93	93.47	0.09	0.14
	29	0.25	0.10	0.00	0.00	91.79	90.98	0.14	0.04
	30	2.23	0.29	2.31	0.27	18.21	92.27	5.23	0.36
	40	2.15	2.42	3.06	2.59	0.00	23.37	6.55	5.21
	41	1.98	0.14	3.19	0.22	4.00	94.82	6.77	0.19
	42	0.65	1.14	0.35	0.68	86.02	78.96	0.59	1.38

Table 3.6

Lateral Expansion, Shear Lip Extension, %Cleavage Area, and Ductile Length of Charpy Impact Specimens of HT1 and HT2 tested from -80 to -40ºC

Temperature [ºC]	Sample no.	Lateral Expansion [mm]		Shear Lip Expansion [mm]		%Cleavage Area		Ductile Length [mm]	
		HT1	HT2	HT1	HT2	HT1	HT2	HT1	HT2
-80	13	2.30	0.35	2.66	0.25	0.00	94.10	6.62	0.27
	14	2.53	2.08	2.02	2.33	26.21	22.03	4.53	5.27
	15	2.20	2.21	3.35	2.73	0.00	20.63	6.70	5.25
	19	2.50	2.26	2.98	2.49	0.00	25.15	6.41	4.91
	20	2.26	2.40	3.23	2.10	0.00	35.02	6.52	4.03
	21	2.32	2.45	2.09	2.28	20.97	30.29	4.64	4.75
	25	2.28	2.13	2.91	2.92	6.10	18.38	6.58	5.36
	26	2.04	2.22	2.11	2.13	15.39	52.01	5.22	3.33
	27	0.26	2.35	0.31	3.37	90.40	0.00	0.20	6.82
-70	34	1.79	2.24	2.91	2.91	0.00	0.00	6.73	6.87
	35	2.28	2.40	2.79	2.67	0.00	28.19	6.45	4.72
	36	2.19	2.21	1.95	2.21	14.76	27.95	5.48	4.56
	43	2.25	2.53	3.61	2.26	0.00	26.99	6.72	4.84
	44	1.92	2.12	1.91	3.23	20.09	7.20	4.85	6.54
	45	2.04	2.47	2.12	3.38	19.62	0.00	4.91	6.67
-60	22	2.28	2.33	2.95	2.73	0.00	0.00	6.61	6.57
	23	2.36	2.36	2.96	2.87	0.00	0.00	6.72	6.62
	24	2.53	2.44	3.14	2.70	0.00	0.00	6.37	6.55
	31	2.35	2.33	3.34	2.63	0.00	0.00	6.89	6.40
	32	2.44	2.43	3.26	2.63	0.00	22.12	6.59	4.90
	33	2.21	2.10	3.12	2.86	0.00	0.00	6.71	6.48
-40	49	2.25	2.46	3.46	3.05	0.00	0.00	6.60	7.08
	50	2.39	2.36	3.46	3.22	0.00	0.00	6.80	7.12
	51	2.36	2.30	3.66	3.29	0.00	0.00	6.40	6.78

Table 3.7

Fracture Toughness Results for Compact Tension Specimens tested from -170 to -80°C

Temperature	Specimen	P_{max}	P_Q	P_{max}/P_Q	K_Q	$2.5(K_Q/\sigma_y)^2$	Validity
[°C]	Number	[kN]	[kN]		[MPam$^{1/2}$]	[mm]	As K_{Ic}
-170	HT1-06	25.70	25.70	1.00	42.6	7.25	valid
	HT1-12	30.18	28.43	1.06	52.0	10.78	valid
	HT2-15	21.45	21.45	1.00	40.6	6.67	valid
	HT2-17	27.47	27.47	1.00	46.8	8.90	valid
-120	HT1-16	37.00	37.00	1.00	66.0	25.26	invalid
	HT1-20	31.16	31.16	1.00	54.9	17.50	valid
	HT1-21	65.93	52.12	1.26	94.4	51.64	invalid
	HT1-22	47.82	47.82	1.00	86.7	43.57	invalid
	HT1-23	31.09	31.09	1.00	55.4	17.83	valid
	HT1-24	44.42	44.42	1.00	80.0	37.15	invalid
	HT2-05	37.99	37.99	1.00	69.6	29.83	invalid
	HT2-06	45.22	45.22	1.00	79.5	38.91	invalid
	HT2-07	44.63	44.63	1.00	78.4	37.85	invalid
	HT2-08	49.43	49.43	1.00	87.0	46.62	invalid
	HT2-19	43.35	43.35	1.00	77.2	36.67	invalid
	HT2-22	43.08	38.52	1.12	66.3	27.07	invalid
-100	HT1-01	77.36	47.38	1.63	87.1	48.82	invalid
	HT1-07	67.30	43.44	1.55	77.9	39.02	invalid
	HT1-18	63.07	36.56	1.73	64.7	26.90	valid
	HT1-25	52.09	48.55	1.07	86.4	48.02	invalid
	HT1-26	67.67	45.63	1.48	81.1	42.30	invalid
	HT1-27	54.00	44.25	1.22	79.5	40.66	invalid
	HT2-01	68.78	46.84	1.47	83.2	47.65	invalid
	HT2-02	33.74	33.74	1.00	58.6	23.66	valid
	HT2-03	54.94	47.18	1.16	82.8	47.19	invalid
	HT2-04	55.62	48.93	1.14	84.8	49.54	invalid
	HT2-09	46.25	44.60	1.04	82.0	46.25	invalid
	HT2-21	74.55	36.25	2.06	63.1	27.42	invalid
-80	HT1-17	70.06	40.13	1.75	70.9	37.49	invalid
	HT2-24	74.63	58.33	1.28	99.9	77.40	invalid
	HT2-25	72.36	45.96	1.57	82.7	53.14	invalid

Table 3.8

Fracture Toughness Results for SENB Specimens tested at -196°C

Specimen No.	Span Width [mm]	a_0 [mm]	P_{max} [N]	a/W	K_{Ic} [MPam$^{1/2}$]
HT1LT-4	40	4.59	3624	0.46	34.0
HT1LT-5		4.47	3977	0.45	36.0
HT1LT-6		4.63	3830	0.46	36.4
HT1TL-D		4.51	4620	0.45	42.3
HT1TL-E		4.31	5500	0.43	47.6
HT1TL-F		4.52	3564	0.45	32.8

Table 3.9

K_{Jc} Results of C(T) Specimens of SA-738 Gr.B Steel tested from -120 to -80°C

Temperature	Specimen	K_Q	K_{Jc}	CTOD	Average K_{Jc}	$K_{Jclimit}$
[°C]	Number	[MPam$^{1/2}$]	[MPam$^{1/2}$]	[μm]	[MPam$^{1/2}$]	[MPam$^{1/2}$]
-120	HT1-16	66.0	66.0	15.2	75.9	350.0
	HT1-20	54.9	55.7	10.9		
	HT1-21	94.4	106.9	39.9		
	HT1-22	86.7	89.7	28.2		
	HT1-23	55.4	55.6	10.8		
	HT1-24	80.0	81.7	23.4		
	HT2-05	69.6	70.1	17.6	78.9	346.7
	HT2-06	79.5	81.7	23.9		
	HT2-07	78.4	80.7	23.3		
	HT2-08	87.0	91.4	29.9		
	HT2-19	77.2	78.8	22.2		
	HT2-22	66.3	70.4	17.7		
-100	HT1-01	87.1	211.7	164.3	117.0	339.6
	HT1-07	77.9	109.1	43.6		
	HT1-18	64.7	89.2	29.1		
	HT1-25	86.4	92.8	31.6		
	HT1-26	81.1	110.6	44.8		
	HT1-27	79.5	88.3	28.6		
	HT2-01	83.2	115.7	50.2	96.5	334.5
	HT2-02	58.6	59.6	13.3		
	HT2-03	82.8	91.1	31.1		
	HT2-04	84.8	93.2	32.6		
	HT2-09	82.0	86.3	27.9		
	HT2-21	63.1	133.3	66.6		
-80	HT1-17	70.9	120.6	56.2	120.6	325.9
	HT2-24	99.9	147.6	86.1	163.4	325.3
	HT2-25	82.7	179.2	120.4		

Table 3.10

Fracture Toughness Fractography Results for specimens tested at -196 and -170°C

Temperature [°C]	Specimen Nr.	X_0 [µm]	Inclusion Size [µm]	Facet Area [µm^2]	Facet Size [µm]	γ_p [Jm^{-2}]	CTOD [µm]	Element
-196	HT1LT-4	73.5	1.70	794	50	10.0	3.24	Mg, Al, Ca, Ti; O, S
	HT1LT-5	24.1	1.44	1329	64	13.0	3.66	Ti; S
	HT1LT-6	79.5	3.33	1149	53	20.3	3.71	Mg, Al, Ca, Ti, Nb; O,S
	HT1TL-D	43.3	1.90	1360	80	15.6	5.05	Al; S
	HT1TL-E	28.1	1.16	791	42	11.7	6.46	Mg, Al, Ca, Ti, Nb; S
	HT1TL-F	21.3	1.47	1136	60	13.1	3.03	Mg, Al, Ca, Ti; O, S
-170	HT1-06	48.6	0.93	1456	79	5.6	5.43	Mg, Al, Ca, Ti; O, S
	HT1-12	220.8	NA	1206	63	NA	8.07	NA
	HT2-15	6.1	NA	1429	65	NA	5.00	NA
	HT2-17	28.6	1.15	1546	66	8.5	6.66	Ca, Ti

Table 3.11

R/b Values and Resulting Local Failure Stress calculated according to McMeeking FEM Analysis (n = 0)

Test Temperature [°C]	Specimen Number	CTOD [μm]	X_0 [μm]	R/b	σ_y [MPa]	$\sigma_{\theta\theta}/\sigma_y$	σ_{max} [MPa]	$\sigma_{\theta\theta}$ [MPa]	$\sigma_{\theta\theta}/\sigma_{max}$	Plastic Zone Size r_y [μm]
-196	HT1LT-4	3.24	73.5	22.7	928	2.2	2811	2069	0.74	131
	HT1LT-5	3.66	24.1	6.60		2.8		2560	0.91	179
	HT1LT-6	3.71	79.5	21.4		2.3		2102	0.75	217
	HT1TL-D	5.05	43.3	8.6		2.6		2442	0.87	331
	HT1TL-E	6.46	28.1	4.4		2.9		2699	0.96	419
	HT1TL-F	3.03	21.3	7.0		2.7		2539	0.90	199
-170	HT1-06	5.43	48.6	9.00	791	2.6	2396	2091	0.87	461
	HT1-12	8.07	220.8	27.3		2.2		1716	0.72	687
	HT2-15	5.00	6.1	1.2	785	2.6	2378	2029	0.85	425
	HT2-17	6.66	28.6	4.3		3.0		2315	0.97	566

Figure 3.1

Microstructure of HT1 and HT2 Specimens under Optical Microscope

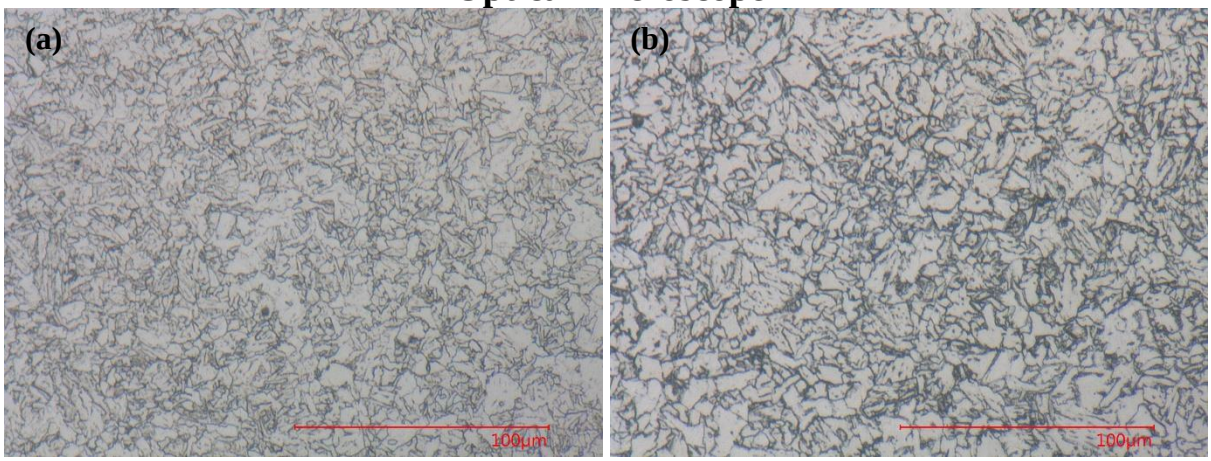

HT1: 3.1(a); HT2: 3.1(b).

Figure 3.2

Microstructure of HT1 and HT2 Specimens under SEM

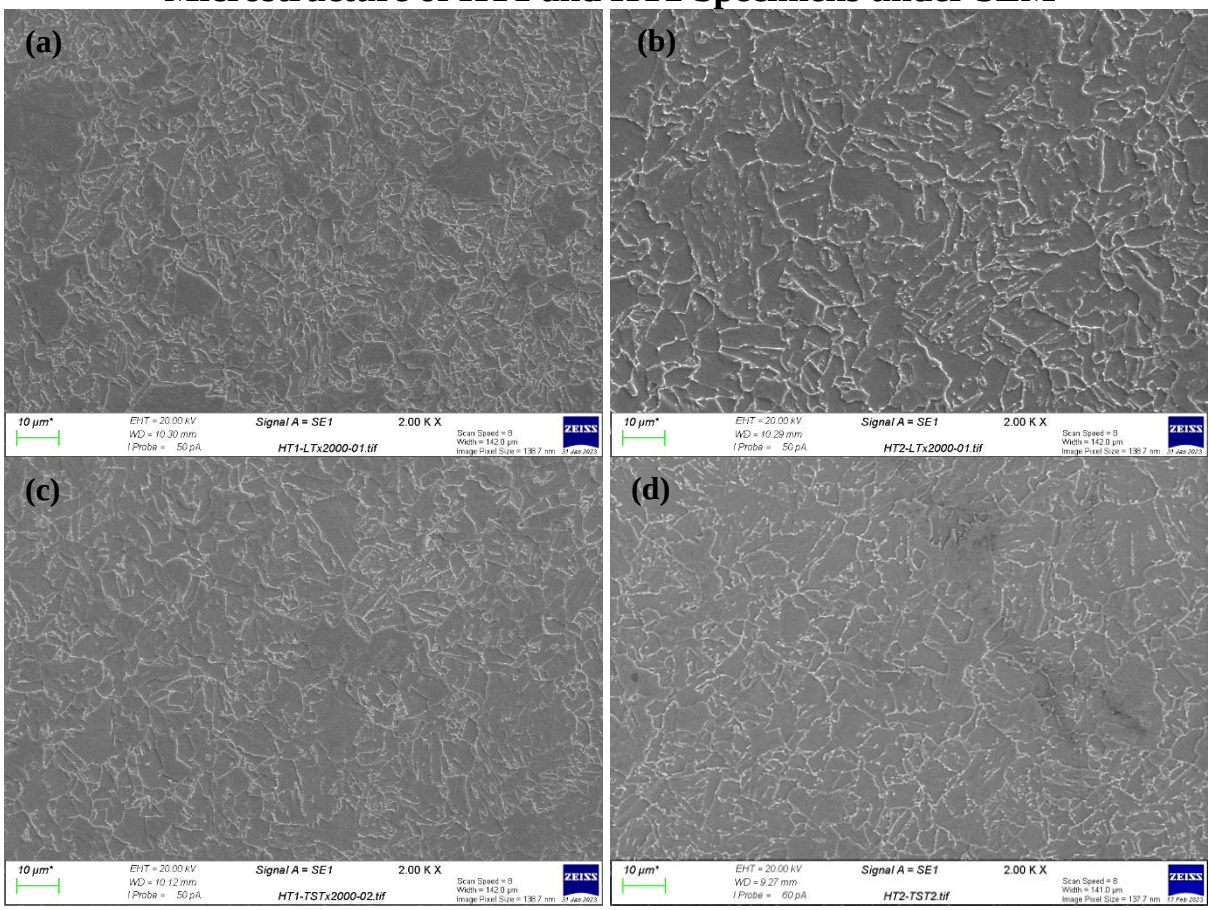

HT1**(a, c)** and HT2**(b, d).** Magnification = 2000. (a)(b): microstructure on **longitudinal** section; (c)(d): microstructure on **transverse** section.

Figure 3.3

Microstructure of HT1 and HT2 Specimens under SEM with Magnification of 5000

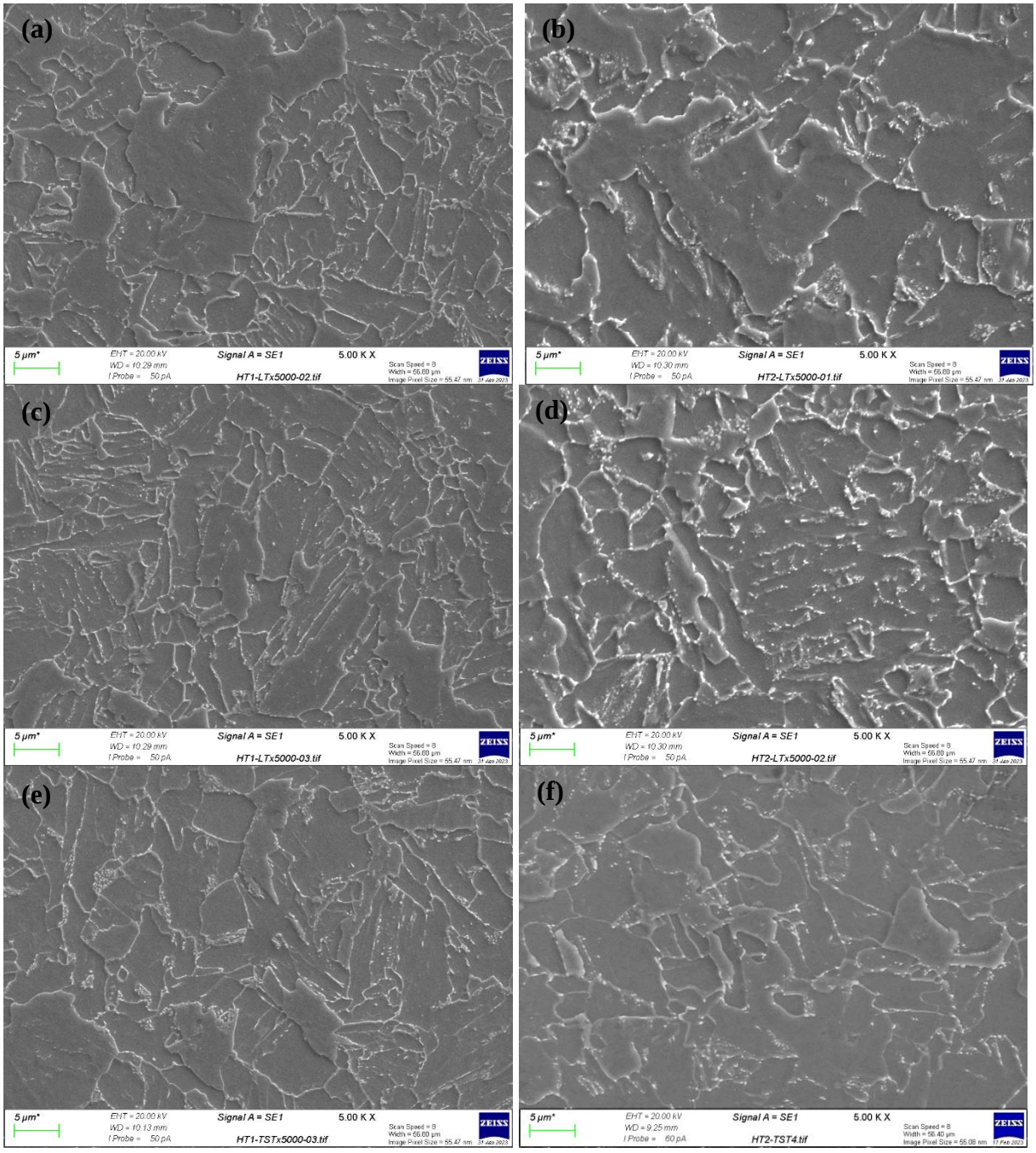

HT1 (**a, c, e**) and HT2 (**b, d, f**) specimens under SEM with magnification of 5000. **(**a) (b) (c) (d): microstructure of **longitudinal** section; (e) (f): microstructure of **transverse** section.

Figure 3.4

Microstructure of HT1 and HT2 Specimens under SEM with Magnification of 10000

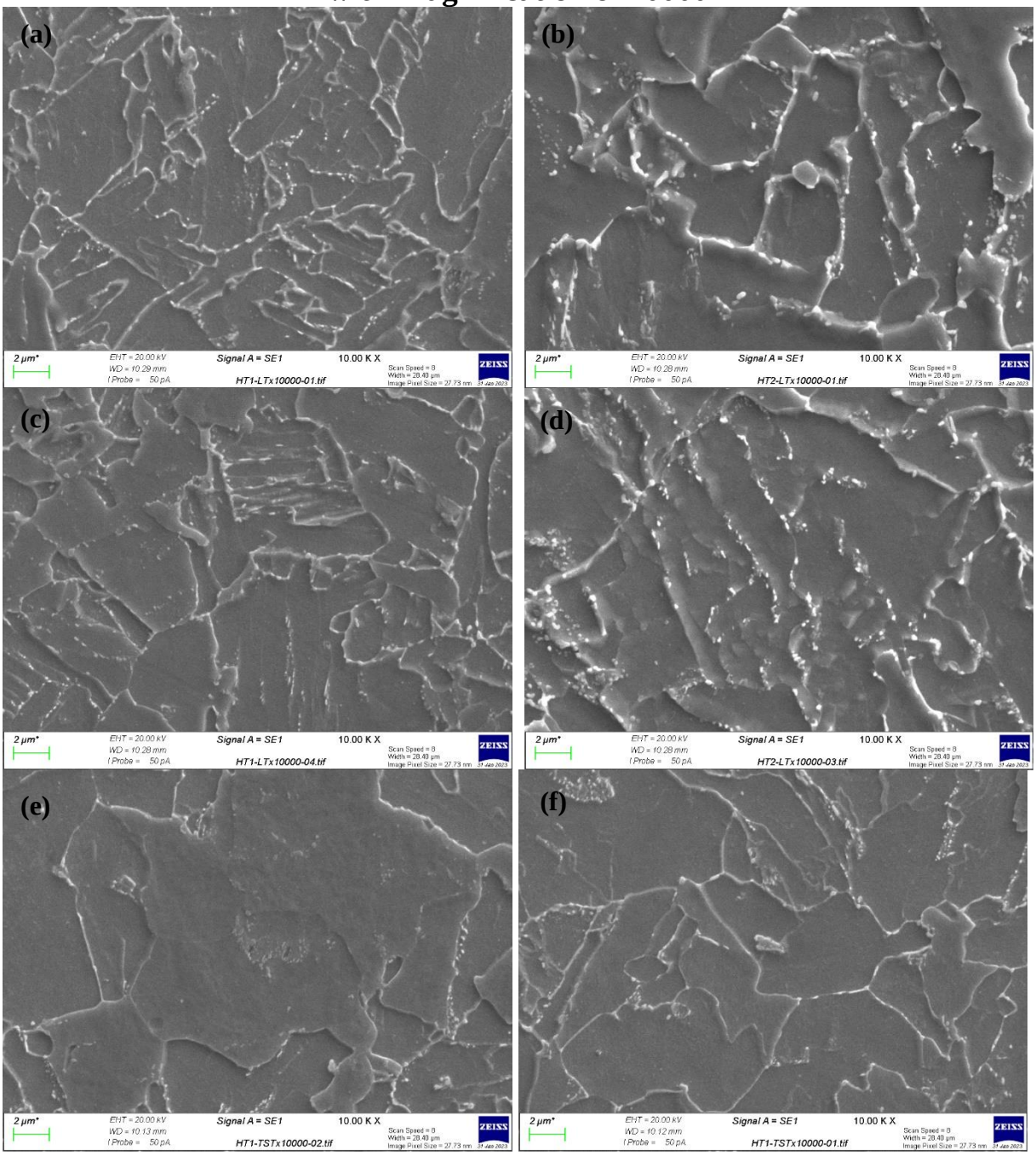

Microstructure of HT1 (a, c, e, f) and HT2 (b, d) specimens under SEM with magnification of 10000. (a-d): microstructure on longitudinal section; (e) (f): microstructure on transverse section.

Figure 3.5

Inclusion Size Distribution Analysis of HT1 and HT2

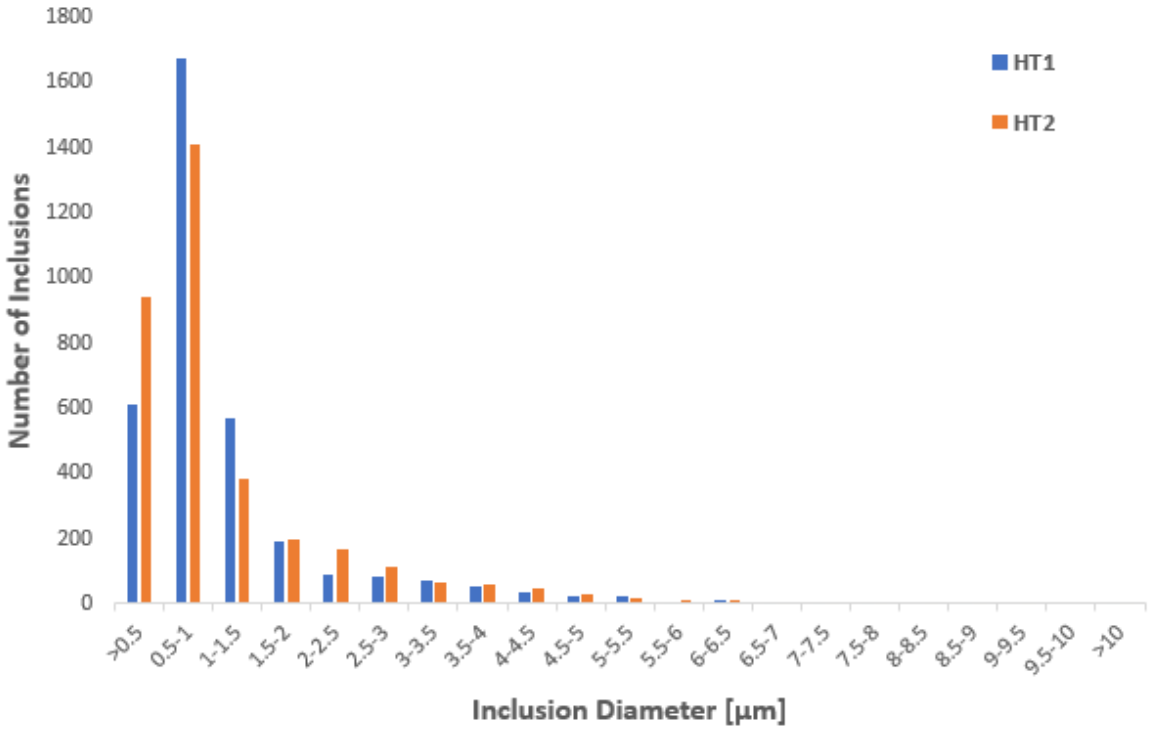

Figure 3.6

Stroke-Controlled Engineering Stress-Strain Curves

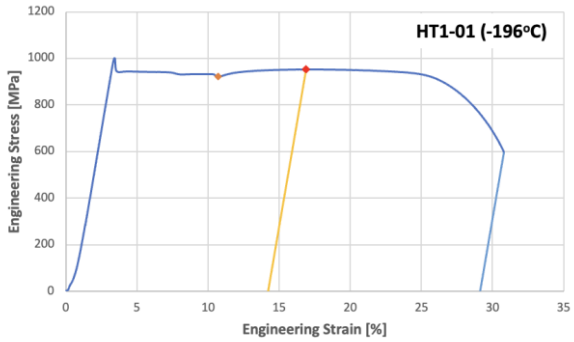

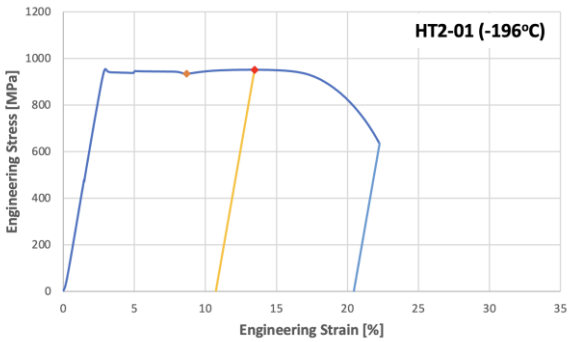

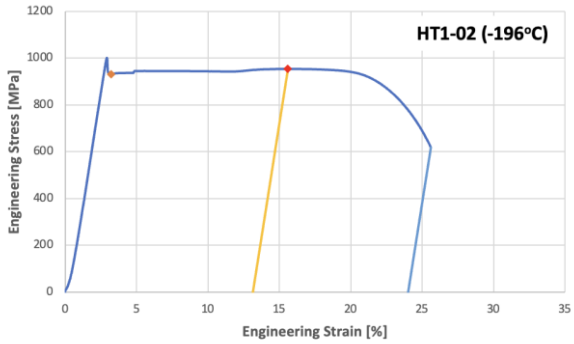

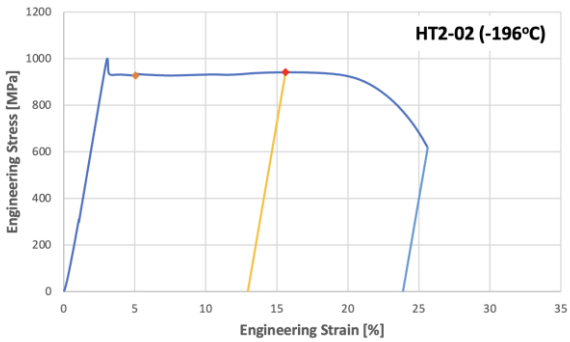

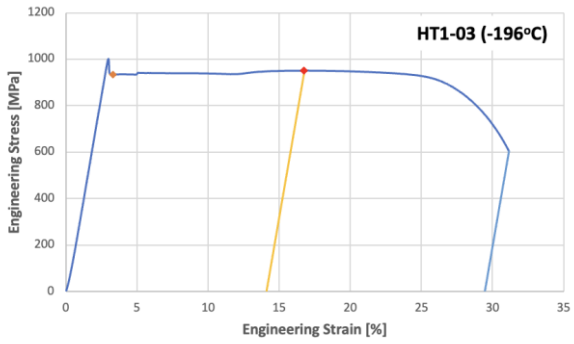

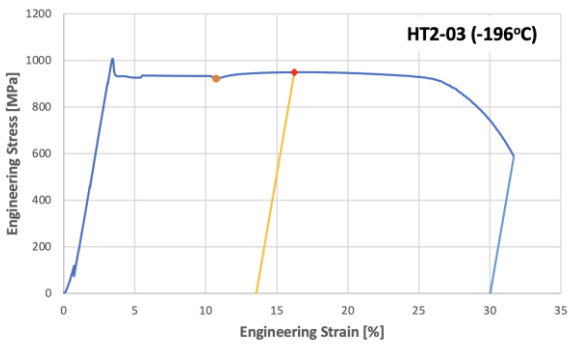

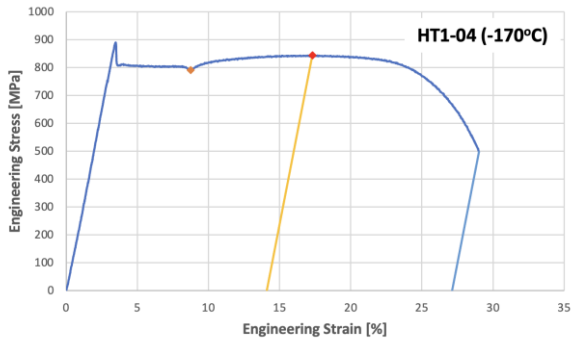

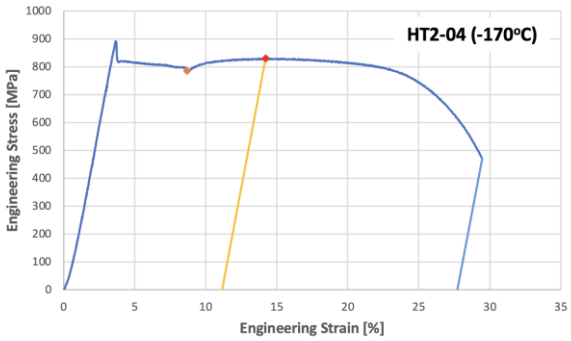

Figure 3.6

Stroke-Controlled Engineering Stress-Strain Curves

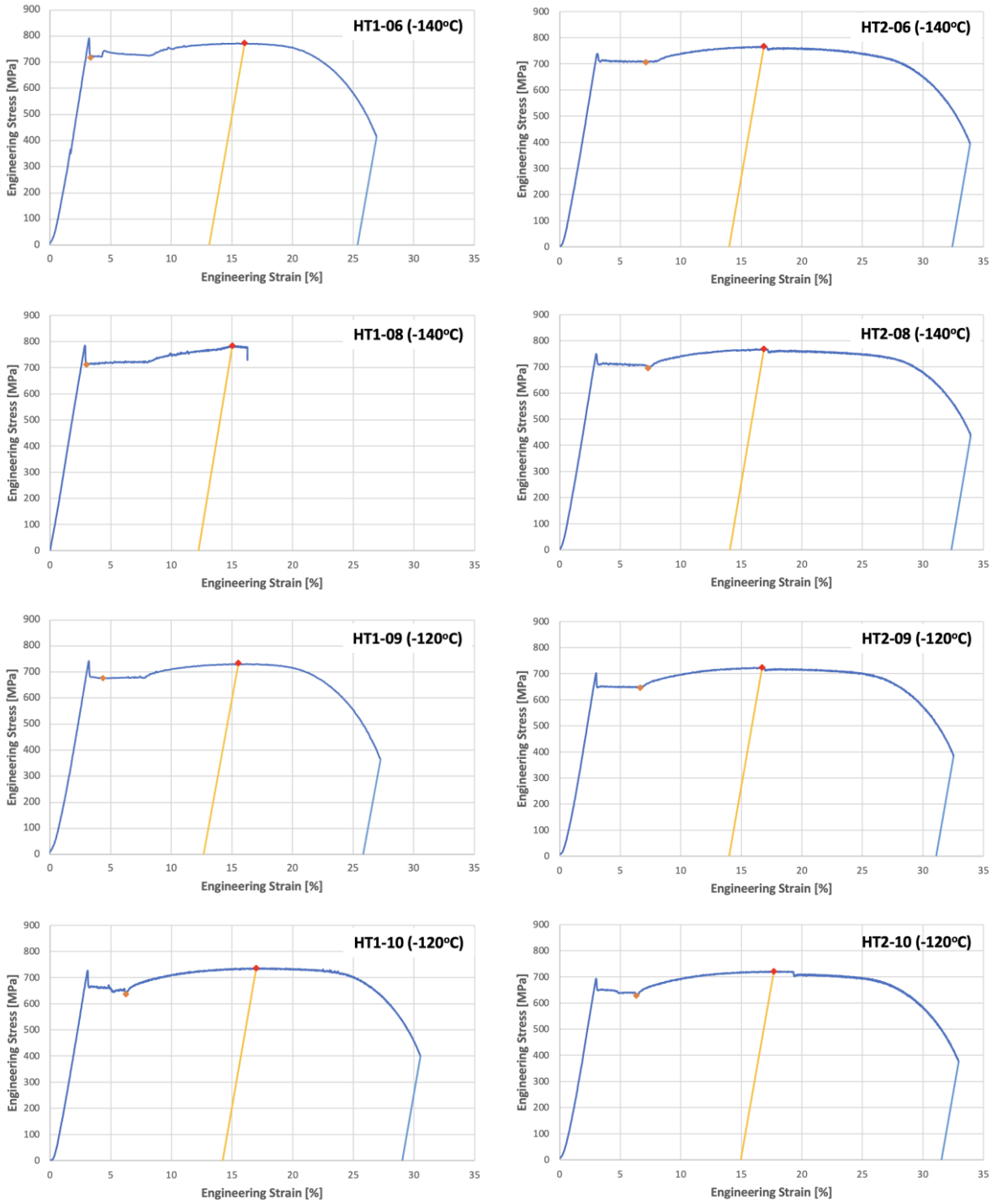

Figure 3.6

Stroke-Controlled Engineering Stress-Strain Curves

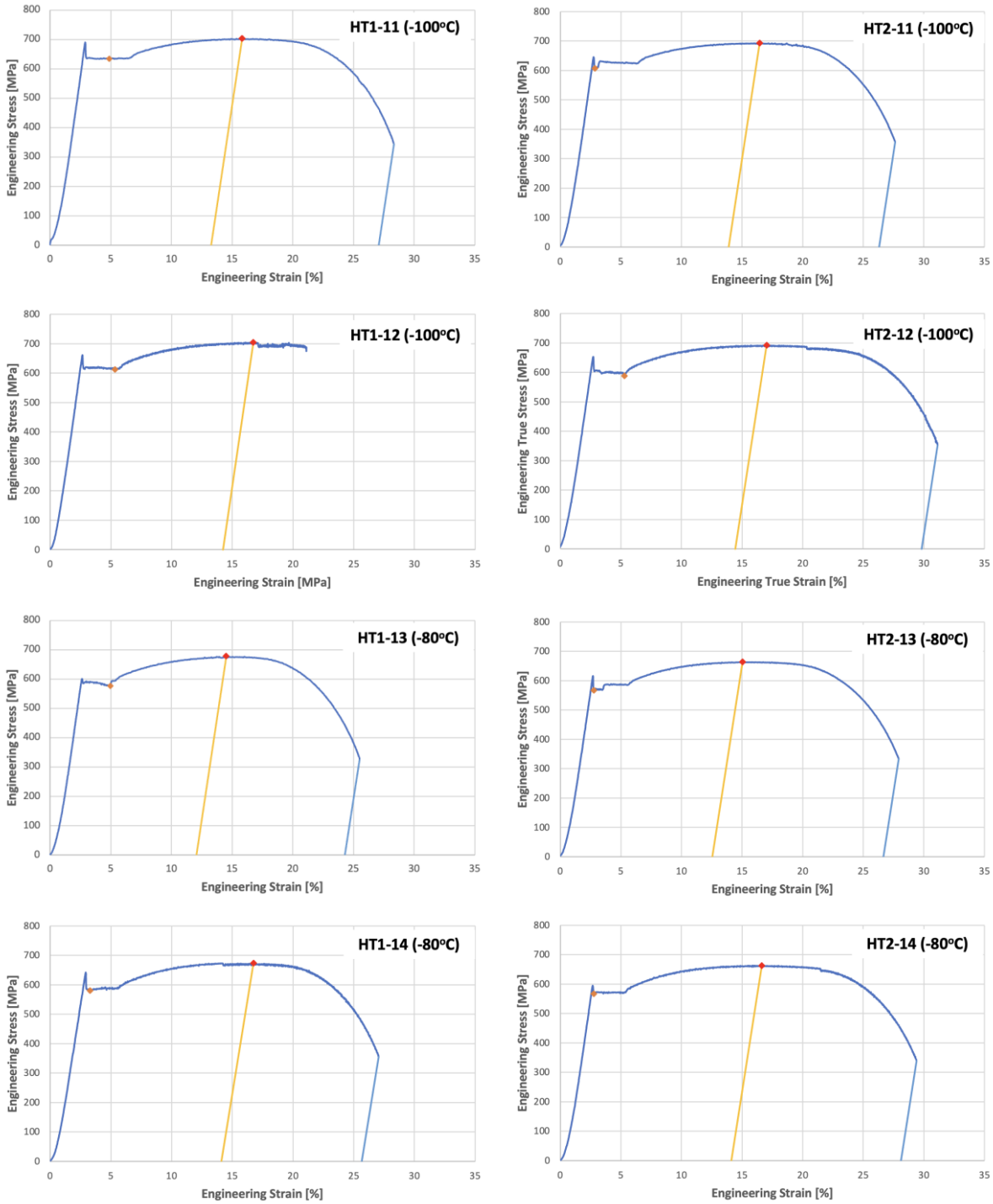

Figure 3.6

Stroke-Controlled Engineering Stress-Strain Curves

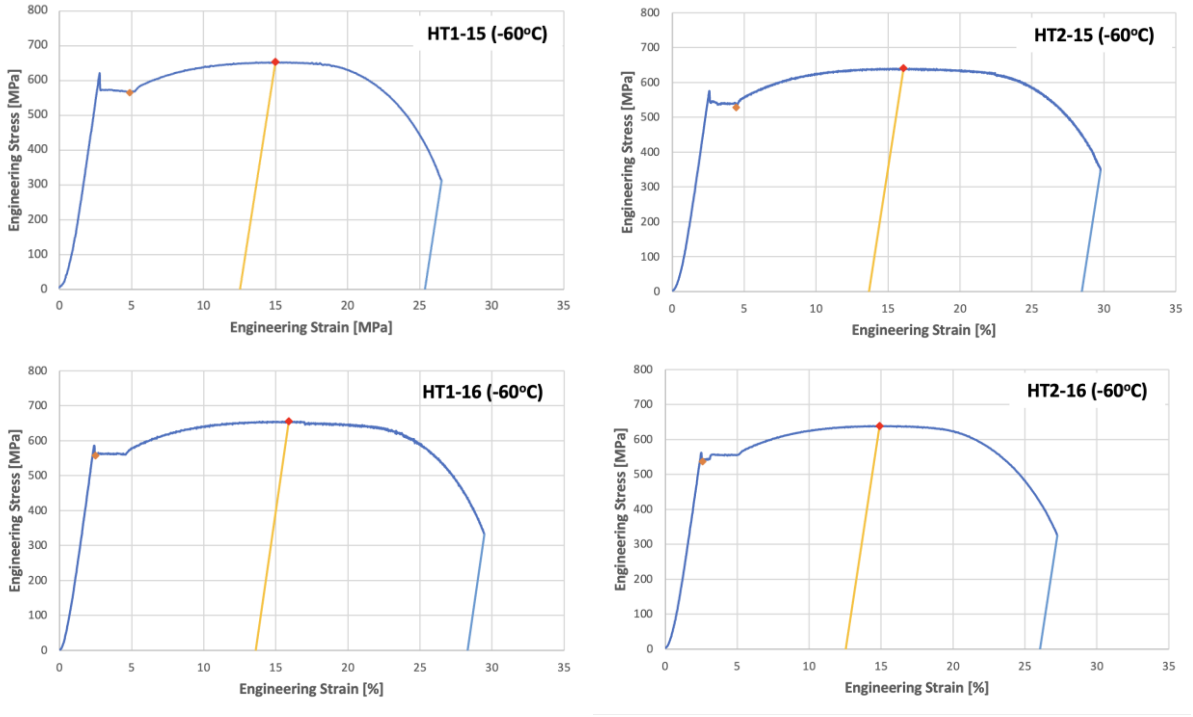

Figure 3.7

Extensometer-Attached Engineering Stress-Strain Curves

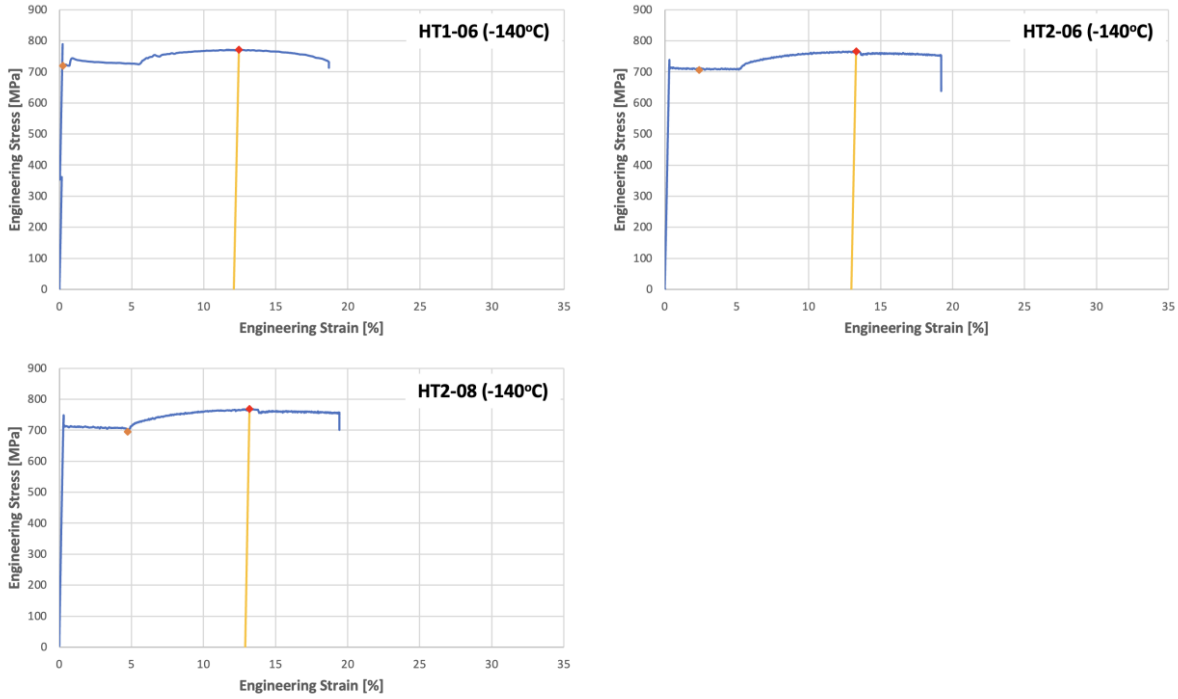

Figure 3.7

Extensometer-Attached Engineering Stress-Strain Curves

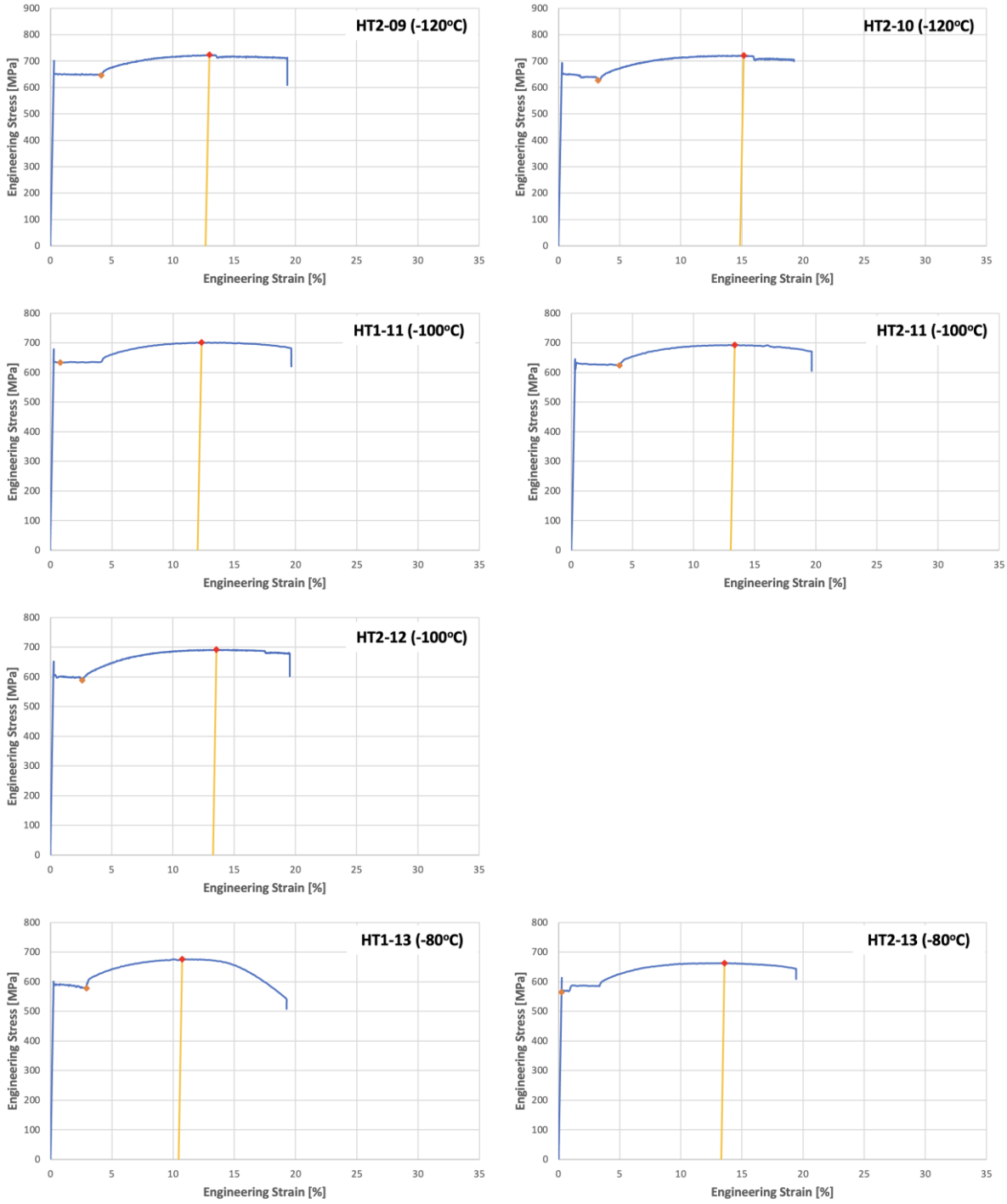

Figure 3.7

Extensometer-Attached Engineering Stress-Strain Curves

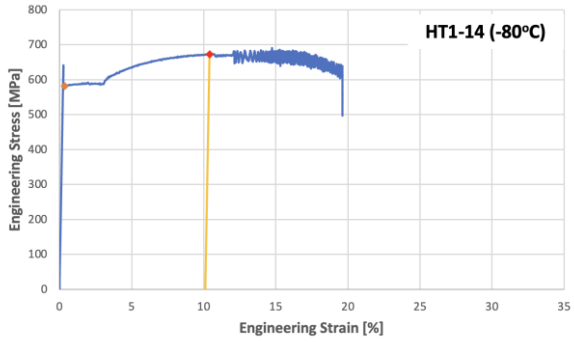

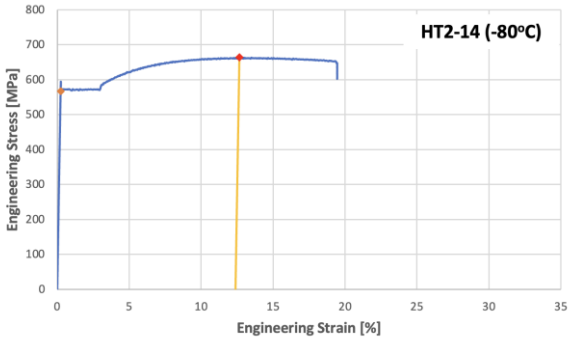

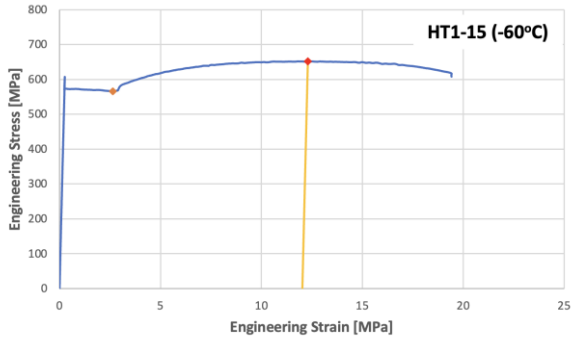

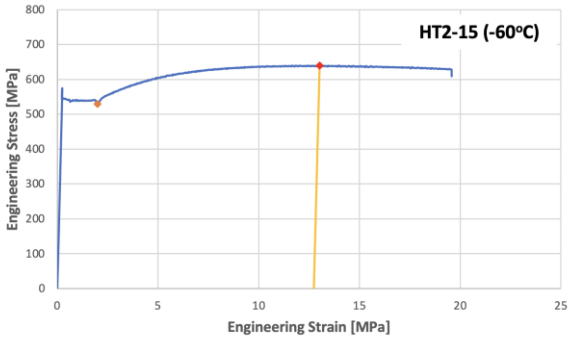

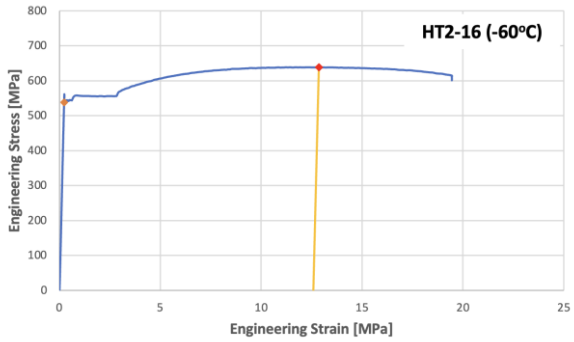

Figure 3.8

True Stress-Strain Curves

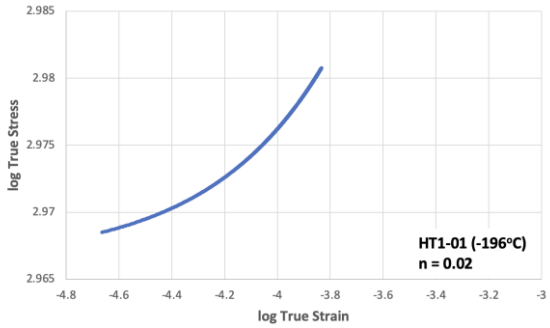

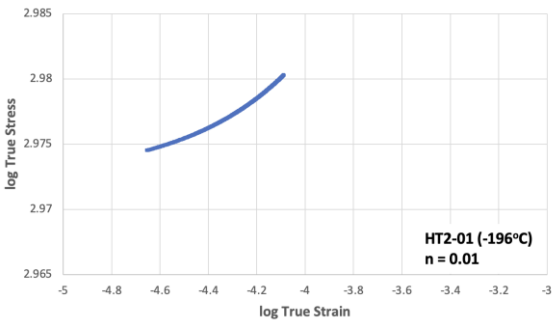

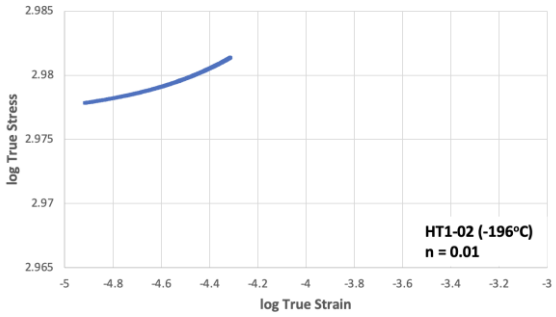

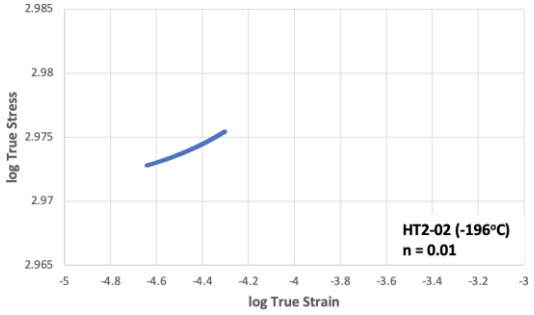

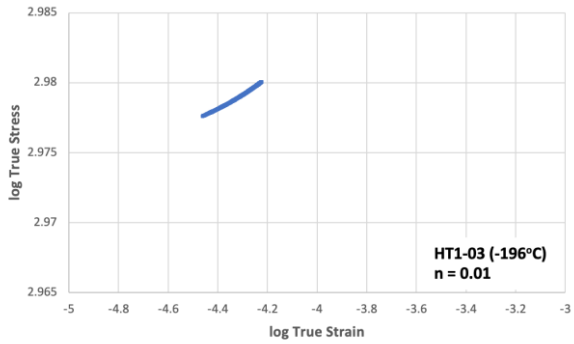

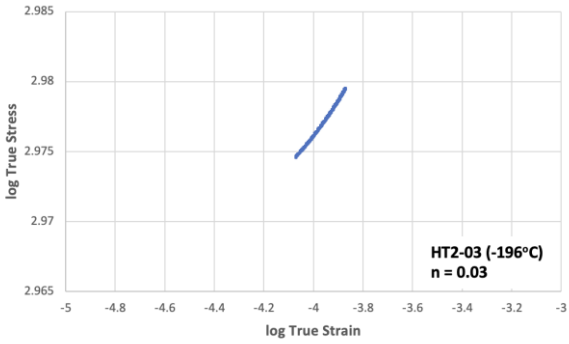

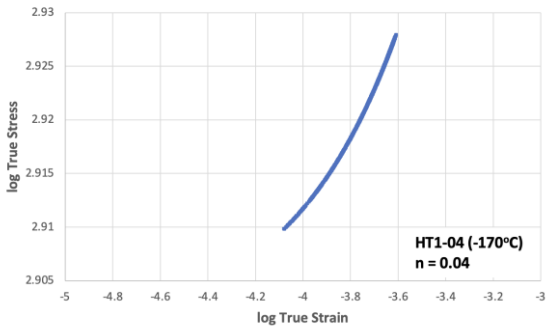

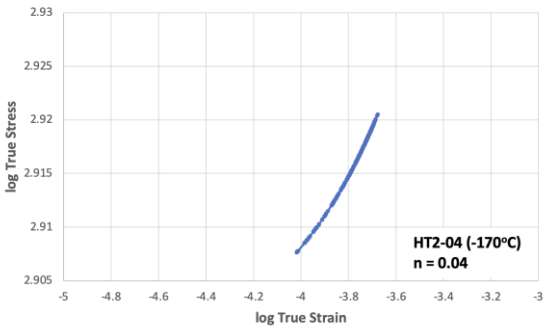

Figure 3.8

True Stress-Strain Curves

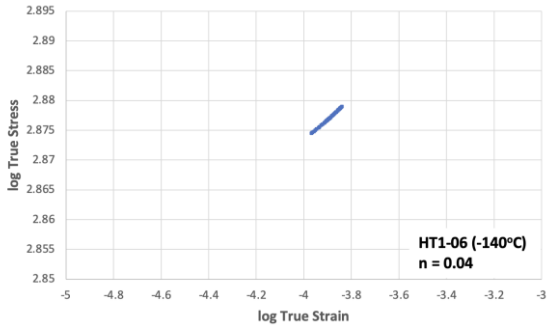

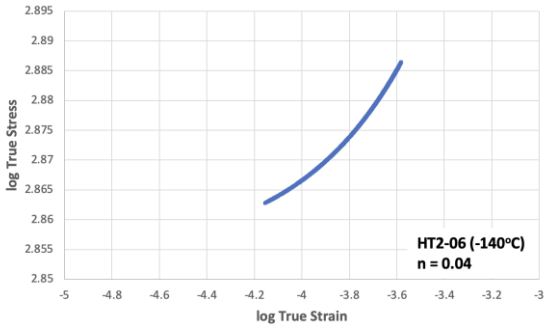

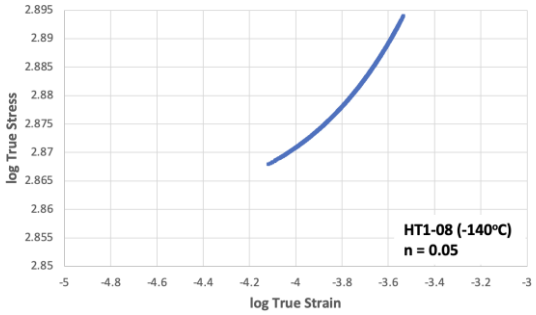

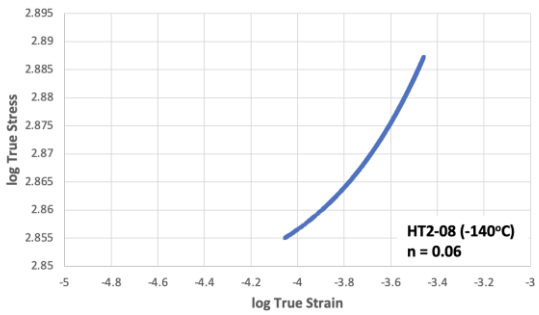

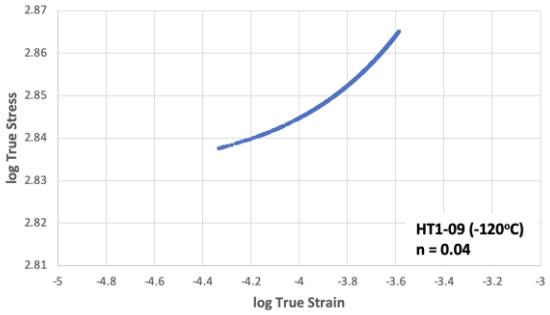

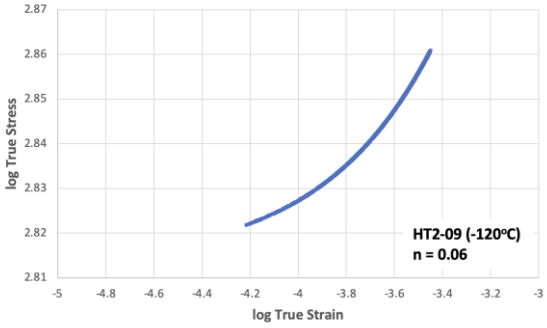

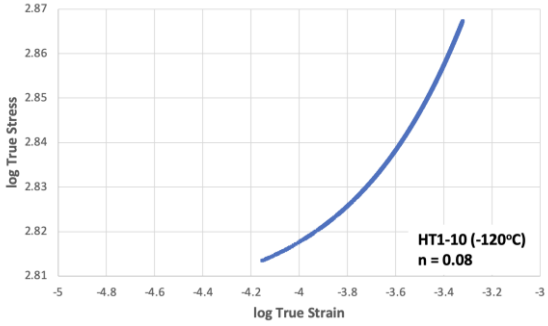

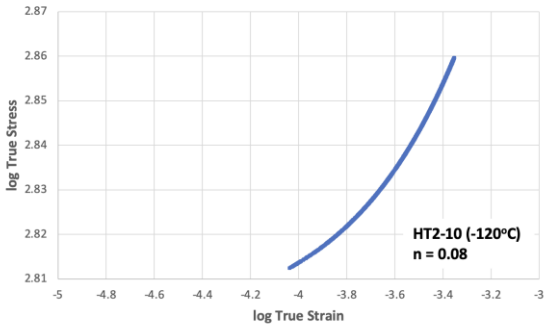

Figure 3.8

True Stress-Strain Curves

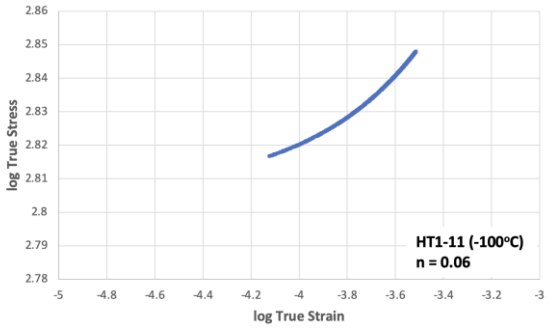

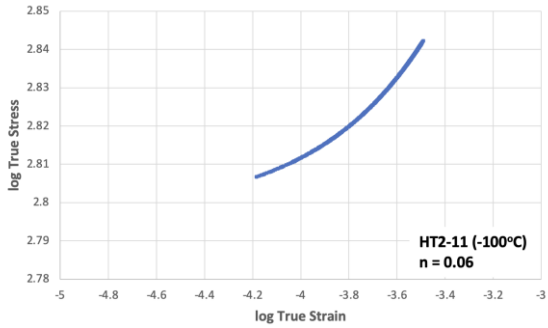

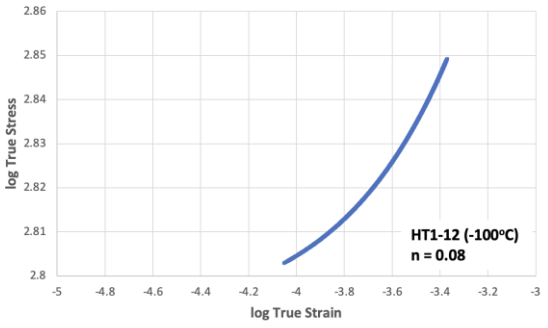

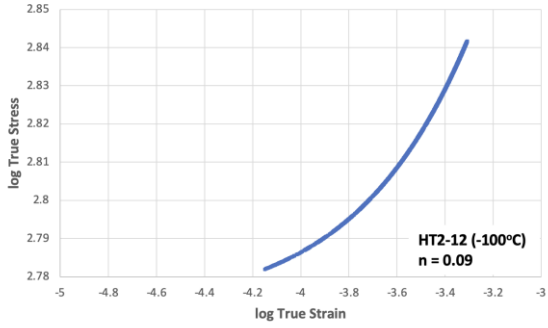

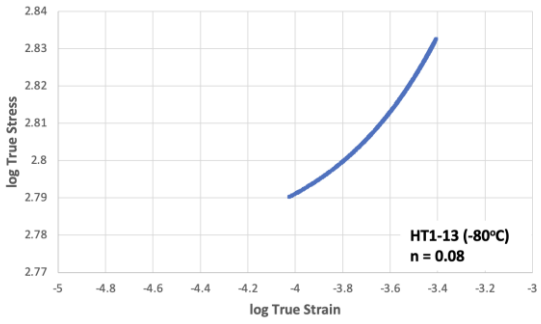

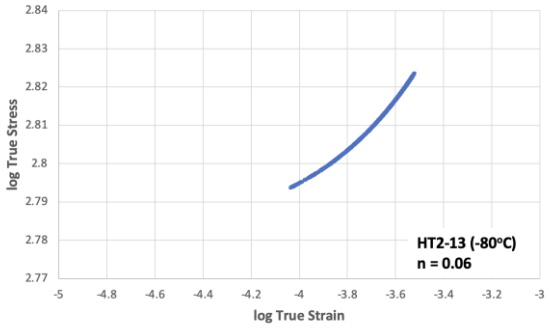

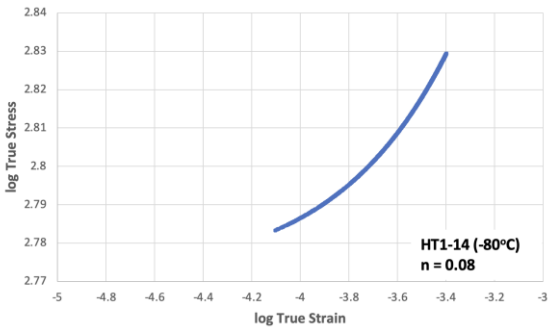

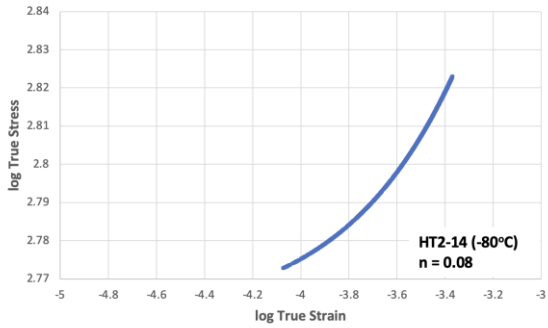

Figure 3.8

True Stress-Strain Curves

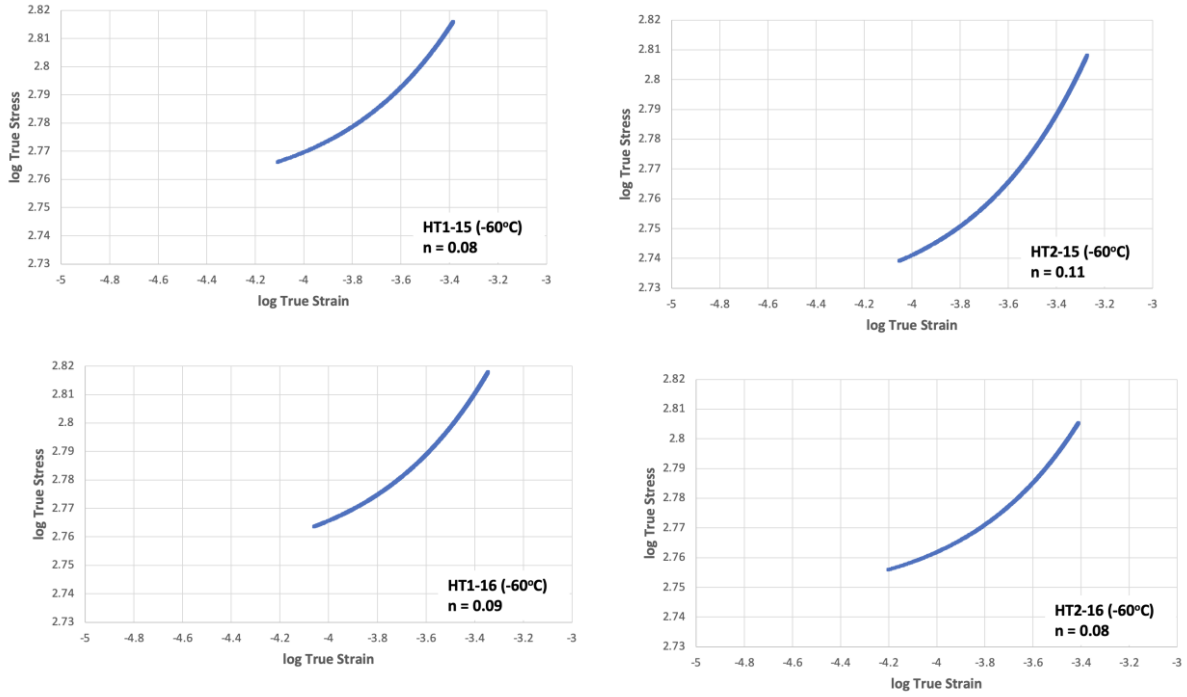

Figure 3.9

Yield Stress, Tensile Strength versus Test Temperature of HT1 and HT2 from -196 to -60°C

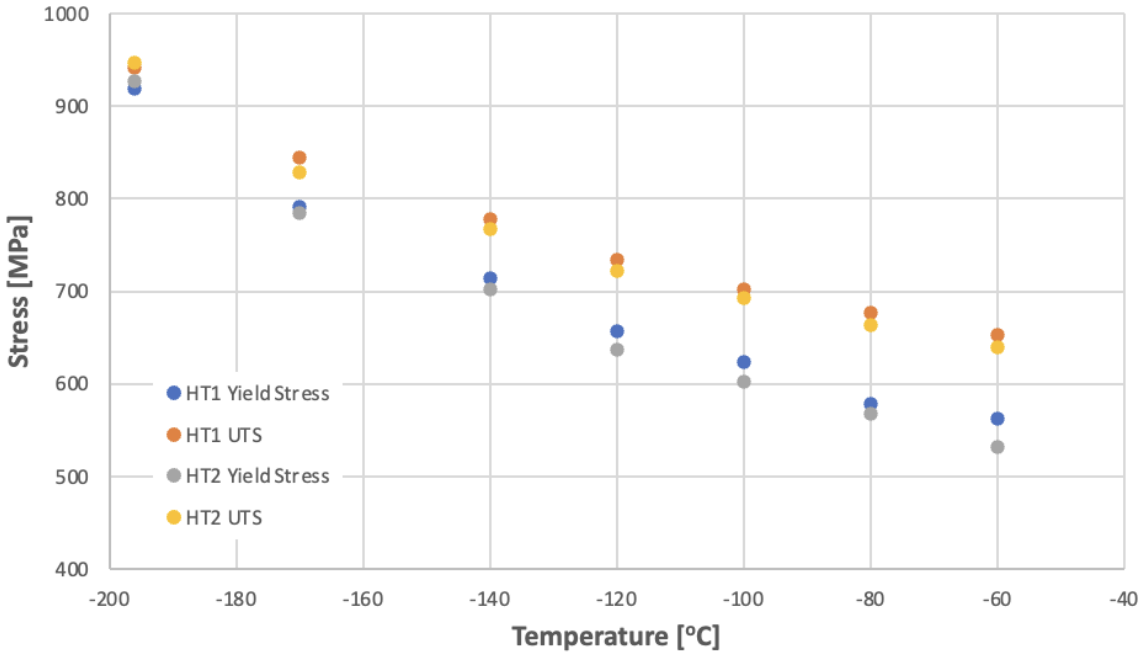

Figure 3.10

Fractography of Tensile Specimen HT1-02 tested at -196ºC

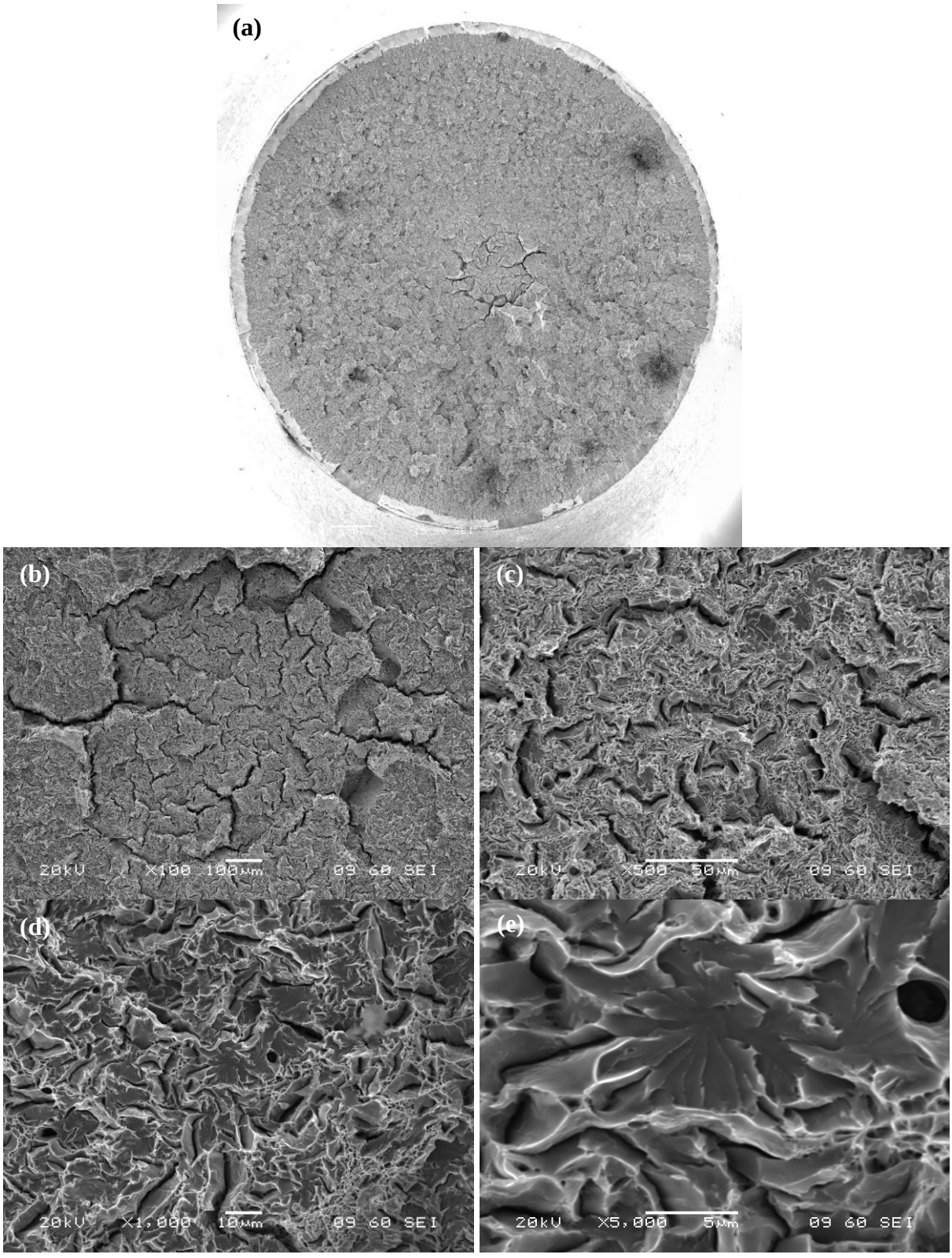

(a): total fracture surface; **(b), (c), (d), (e):** central fibrous region of HT1-02 in increased magnification sequences.

Figure 3.10

EDX Analysis of Selected Regions of HT1-02

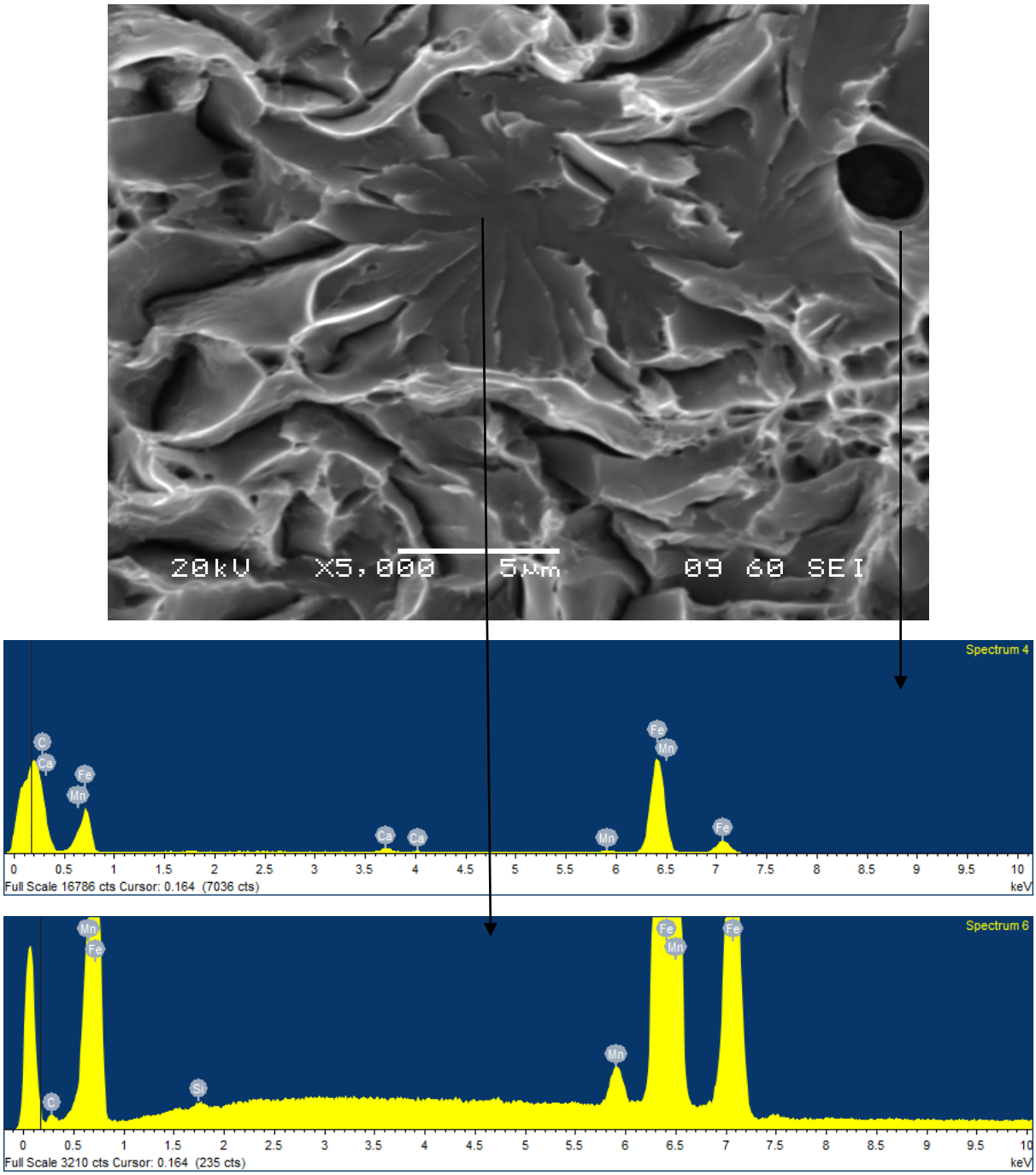

Figure 3.11

Fractography of Tensile Specimen HT2-02 tested at -196ºC

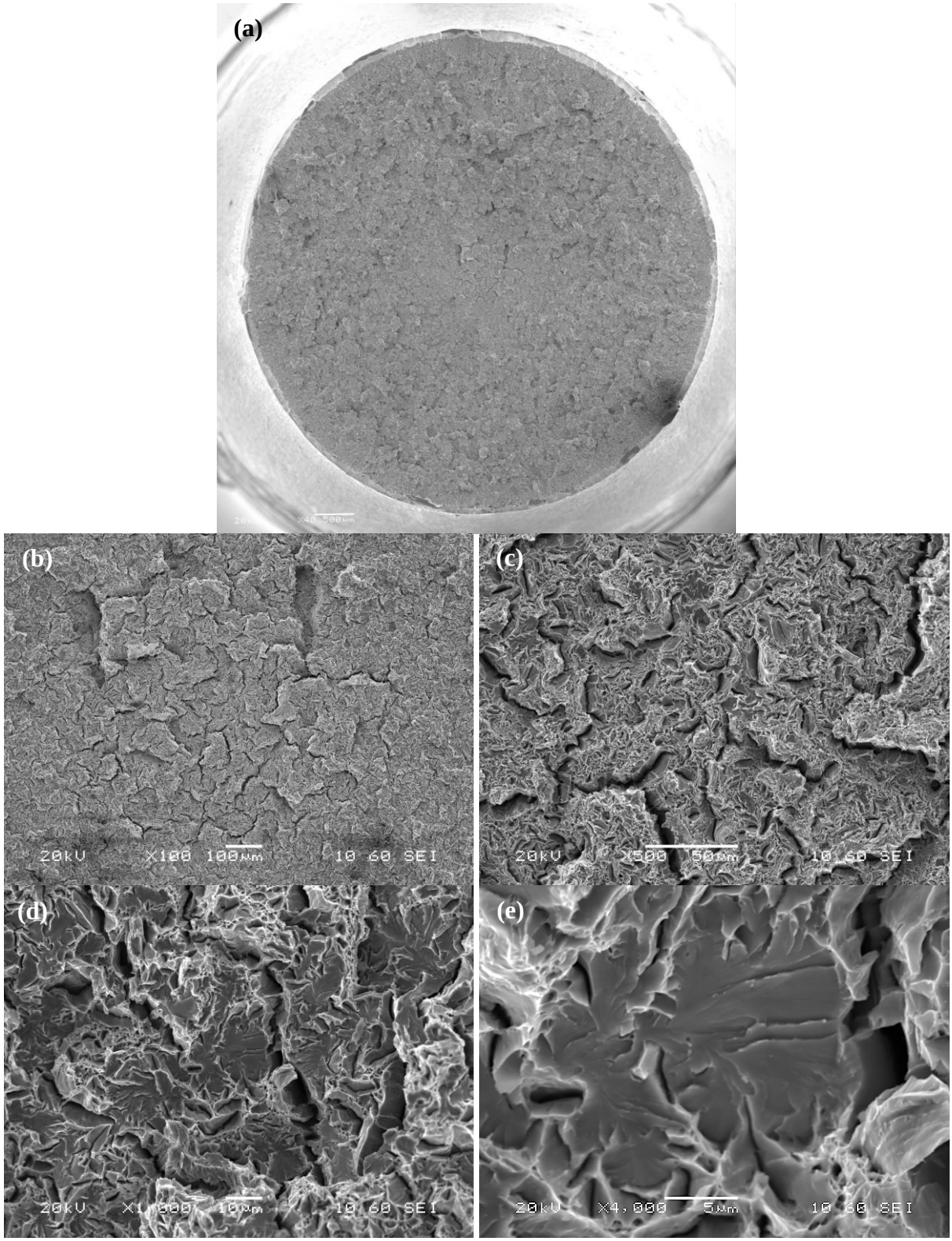

(a): Total fracture surface; **(b), (c), (d), (e):** central fibrous region of HT2-02 in increased magnification sequences.

Figure 3.11(e)

EDX Analysis of Selected Regions of HT2-02

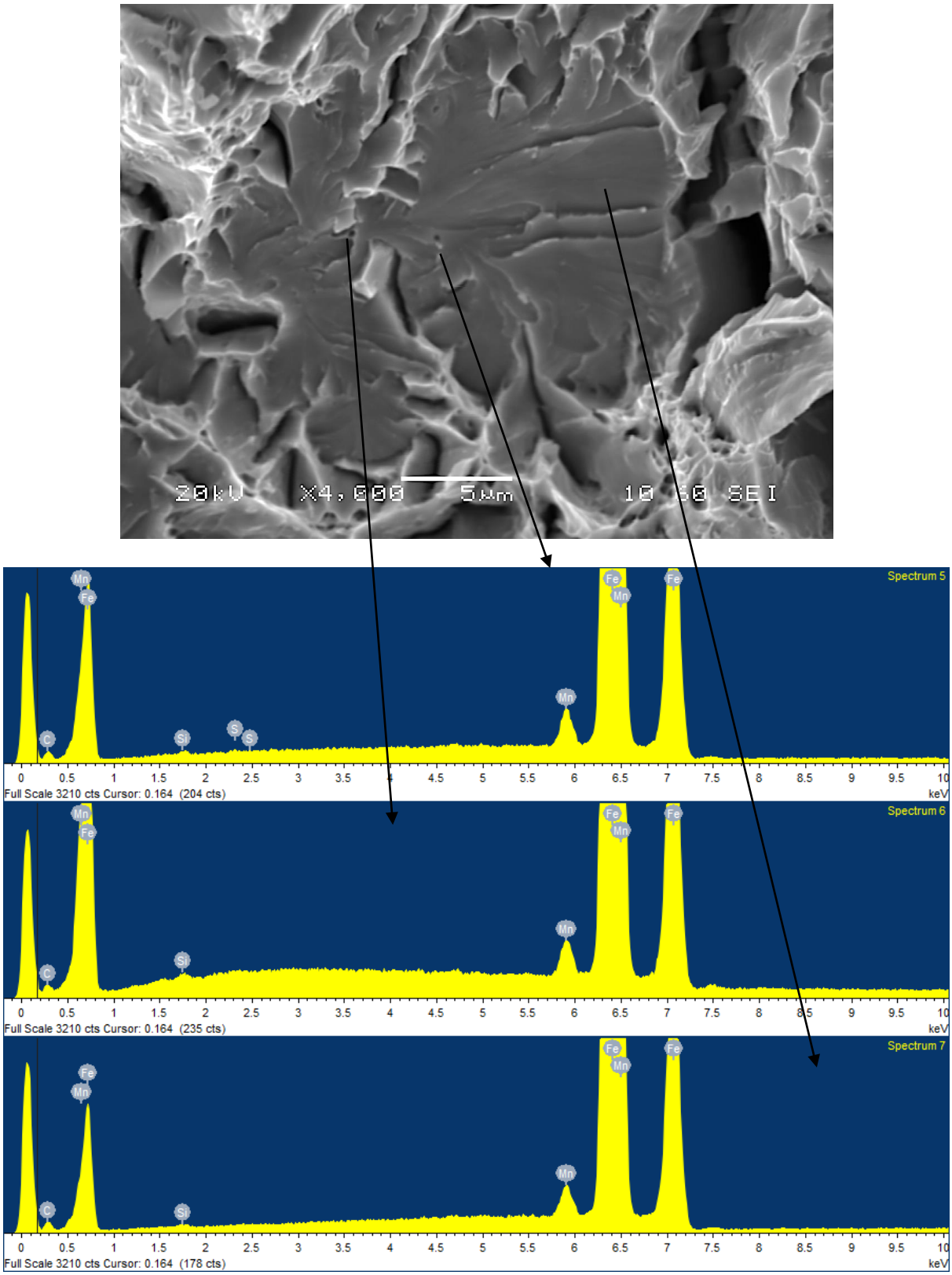

Figure 3.12

Fractography of Tensile Specimen HT1-10 tested at -120ºC

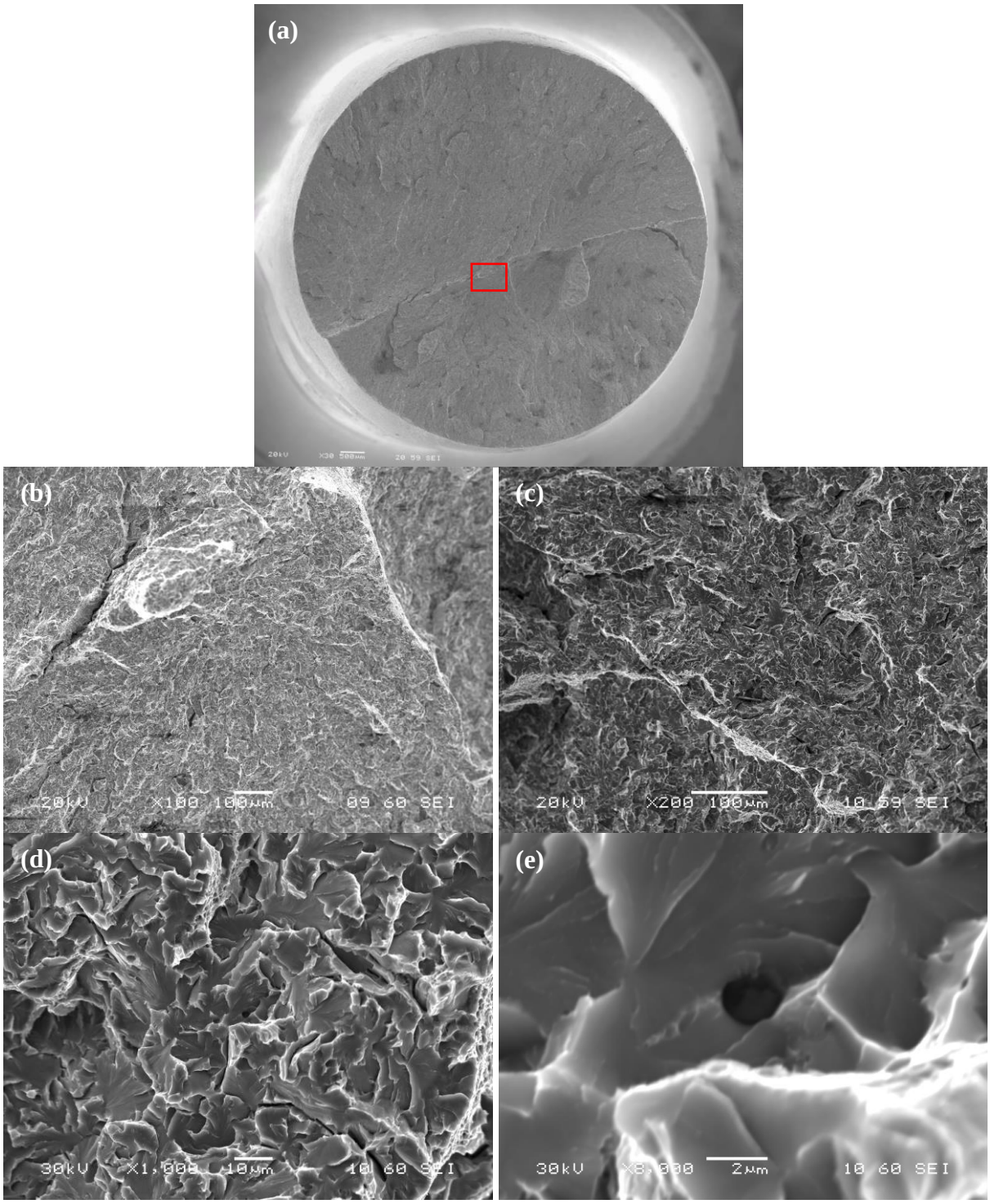

(a): Total fractography of tensile specimen HT1-10.
(b), (c), (d), (e): central fibrous region of HT1-10 in increased magnification sequences.

Figure 3.12(f)

EDX Analysis of Inclusion from HT1-10

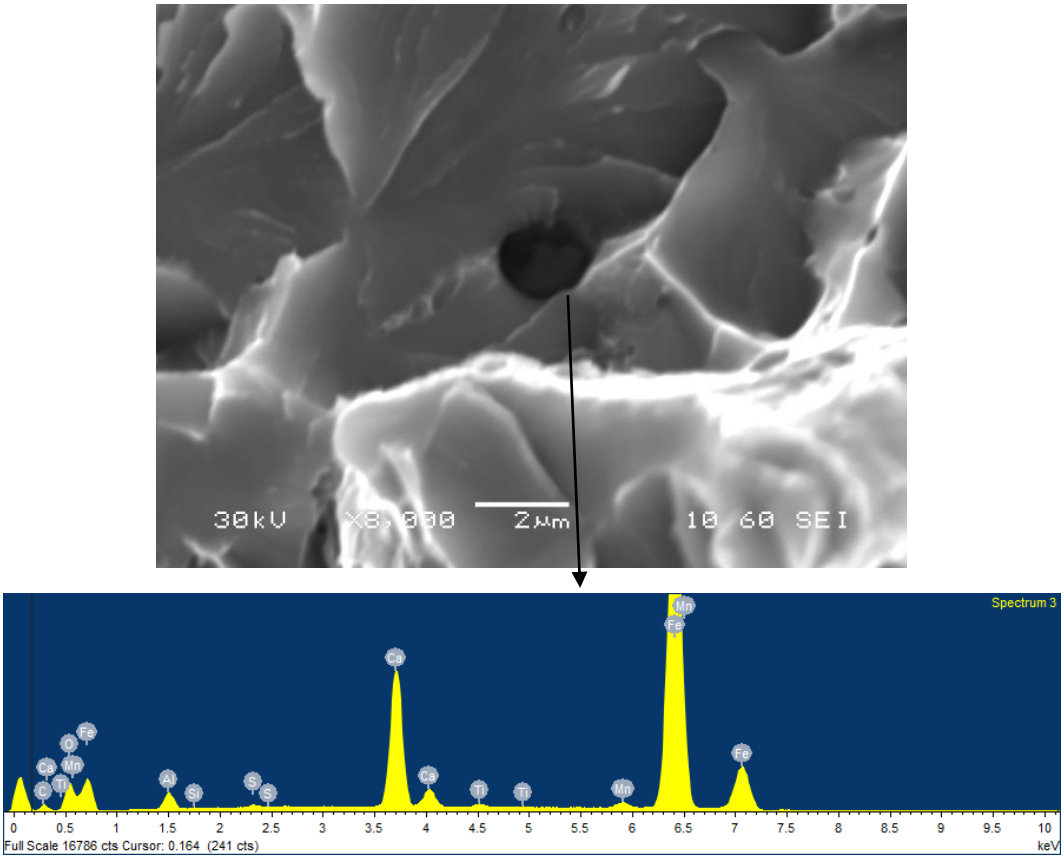

Figure 3.13

Charpy Fracture Surfaces

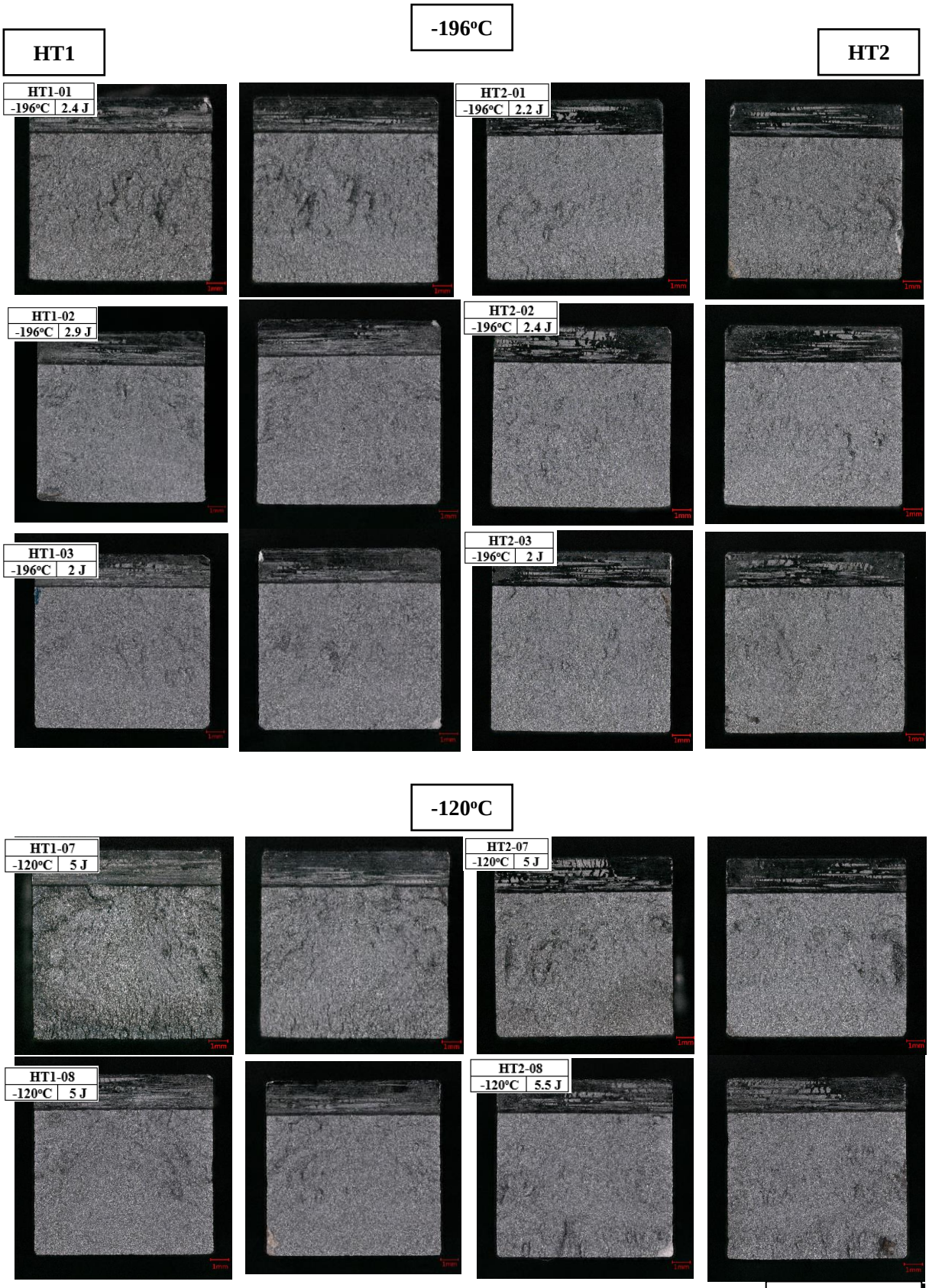

Figure 3.13

Charpy Fracture Surfaces

-120°C

HT1 | **HT2**

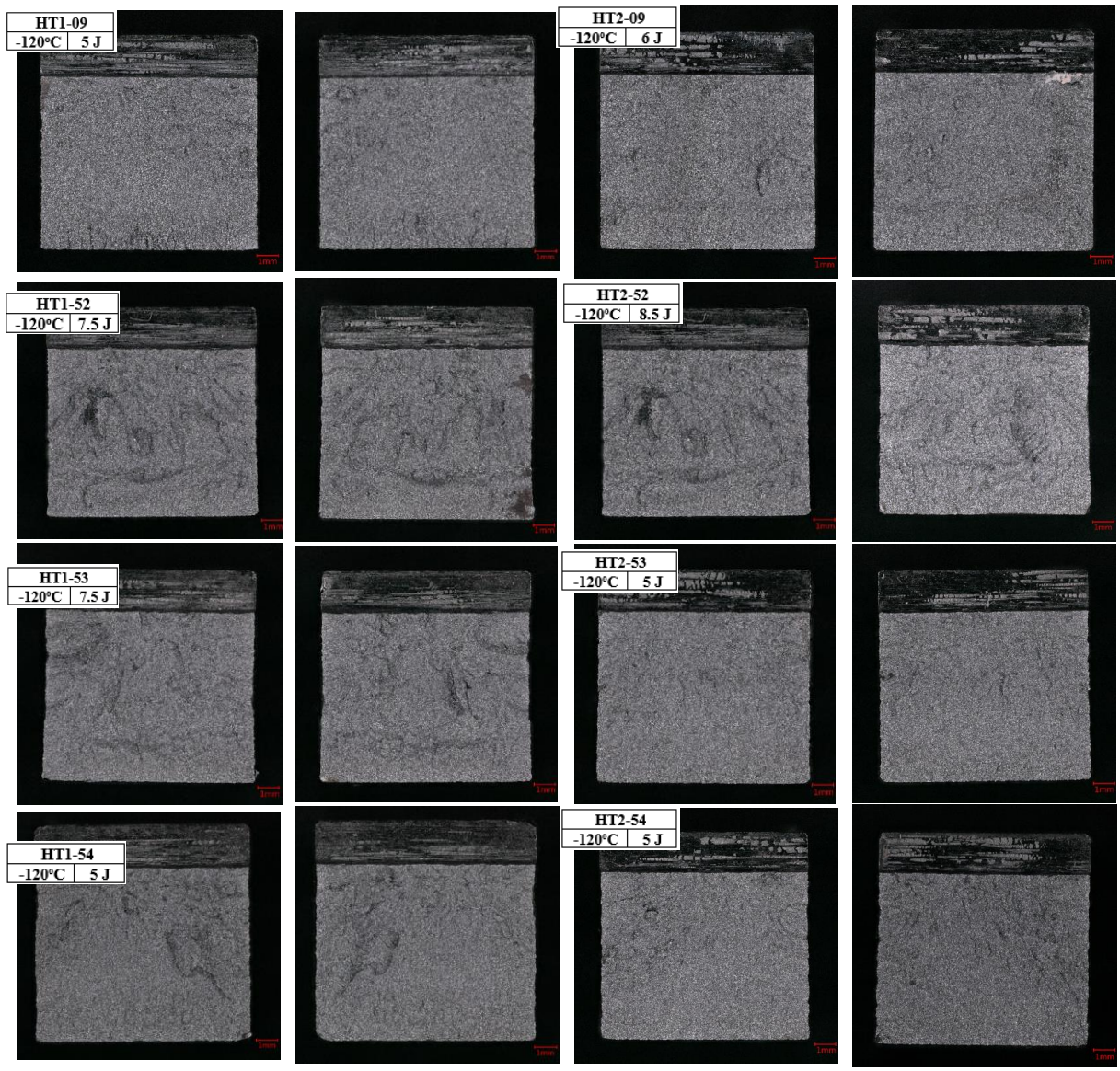

Figure 3.13

Charpy Fracture Surfaces

-100°C

HT1 **HT2**

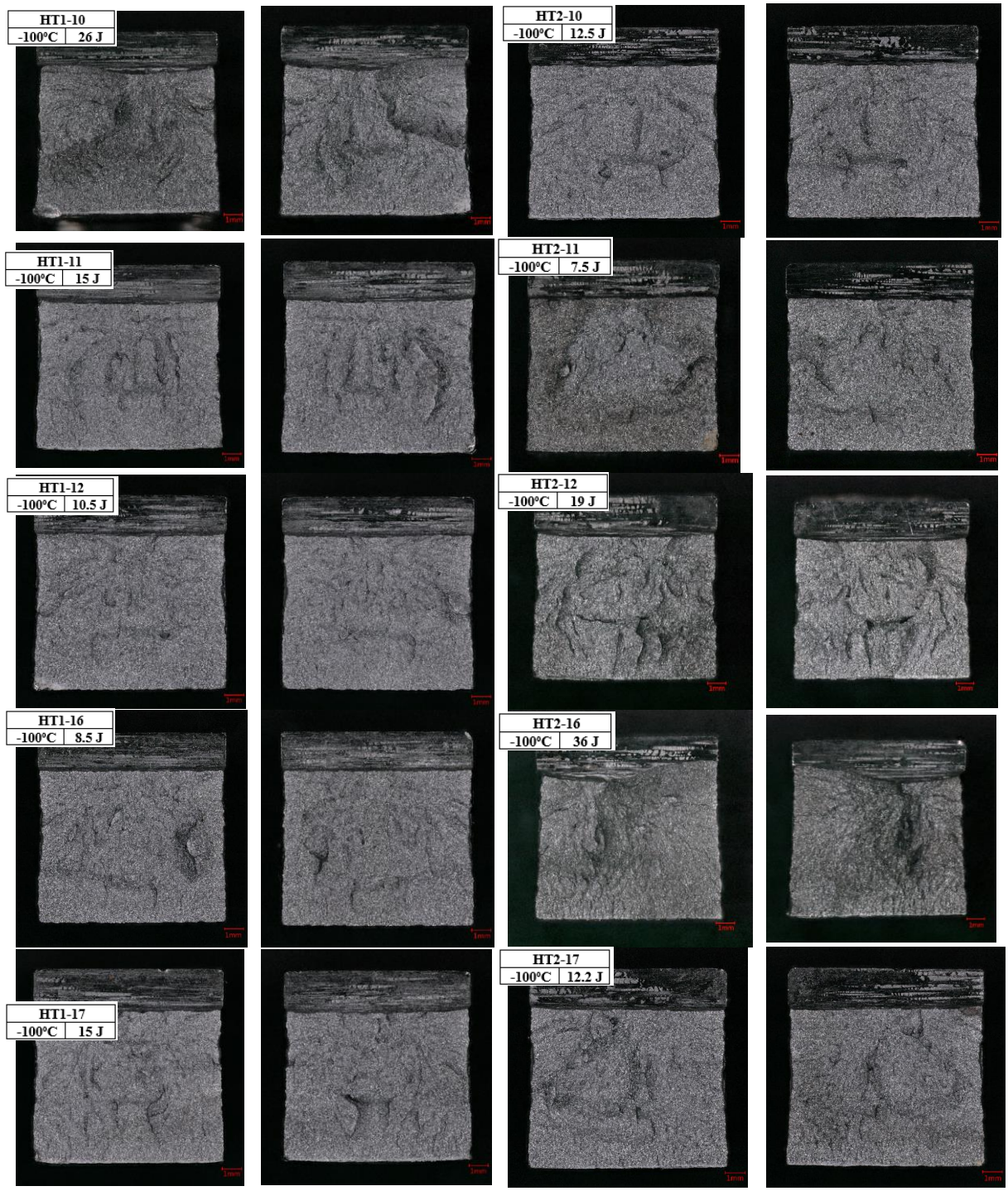

Figure 3.13

Charpy Fracture Surfaces

-100°C

HT1 **HT2**

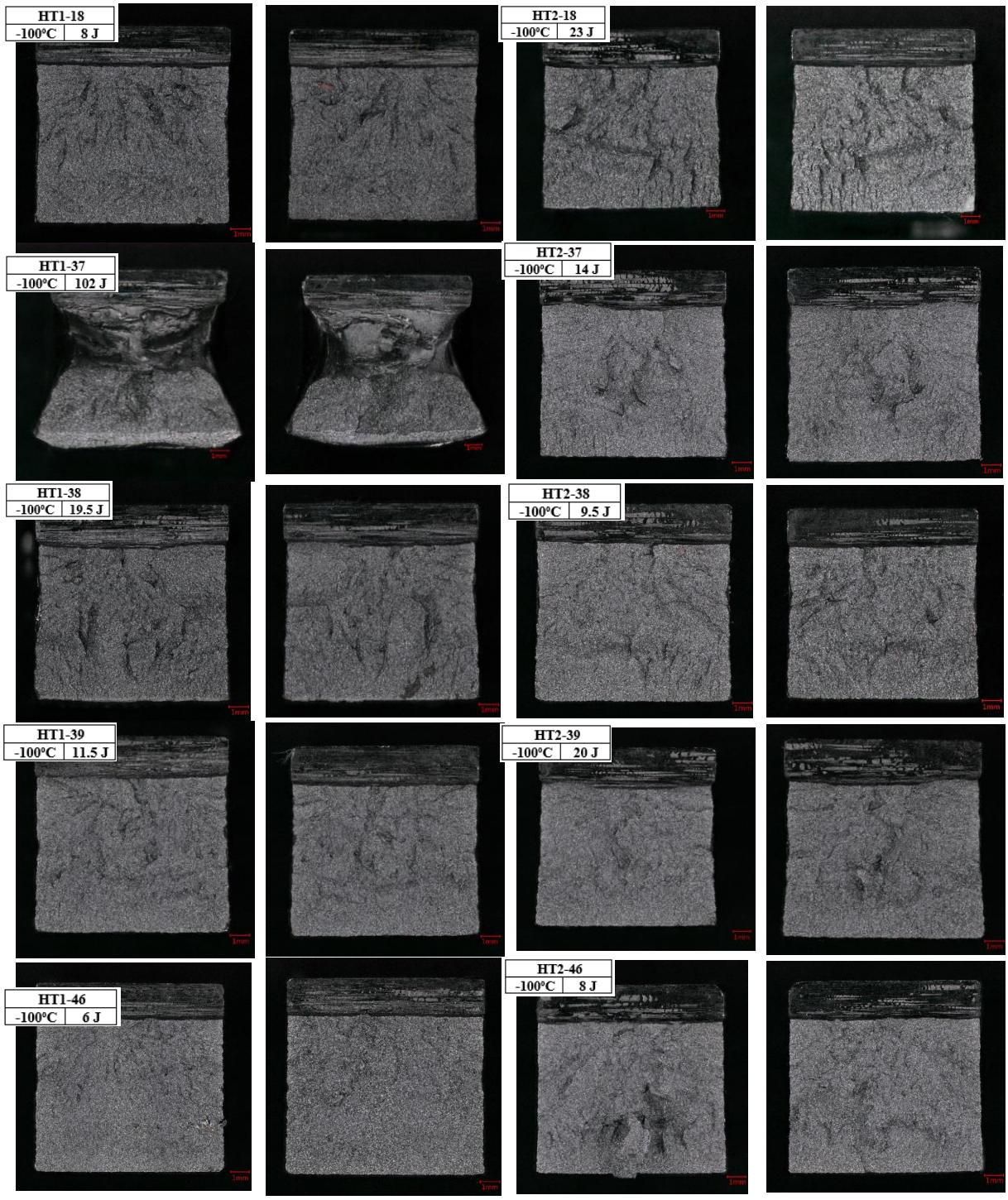

Figure 3.13

Charpy Fracture Surfaces

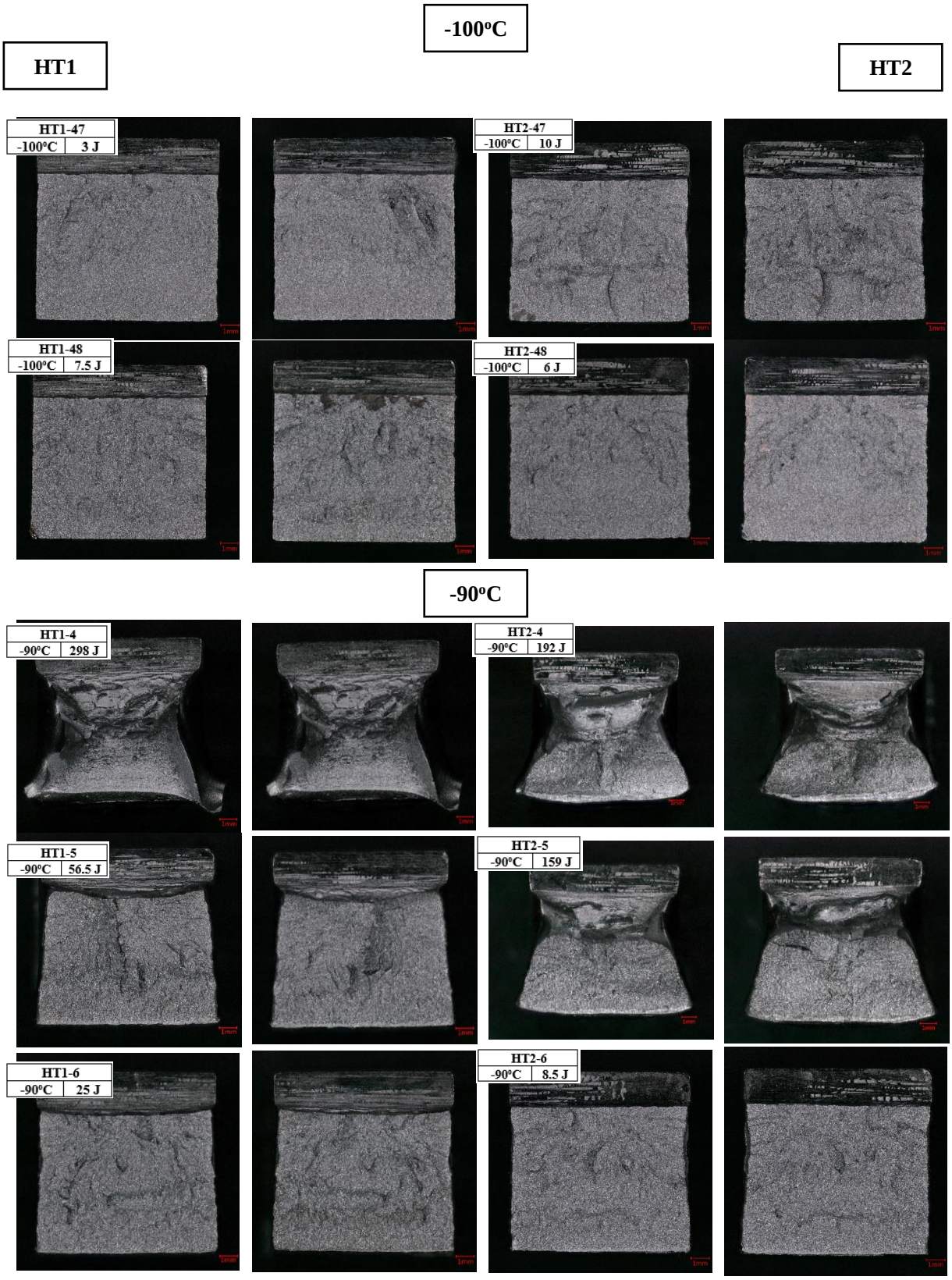

Figure 3.13

Charpy Fracture Surfaces

-90ºC

HT1 **HT2**

Figure 3.13

Charpy Fracture Surfaces

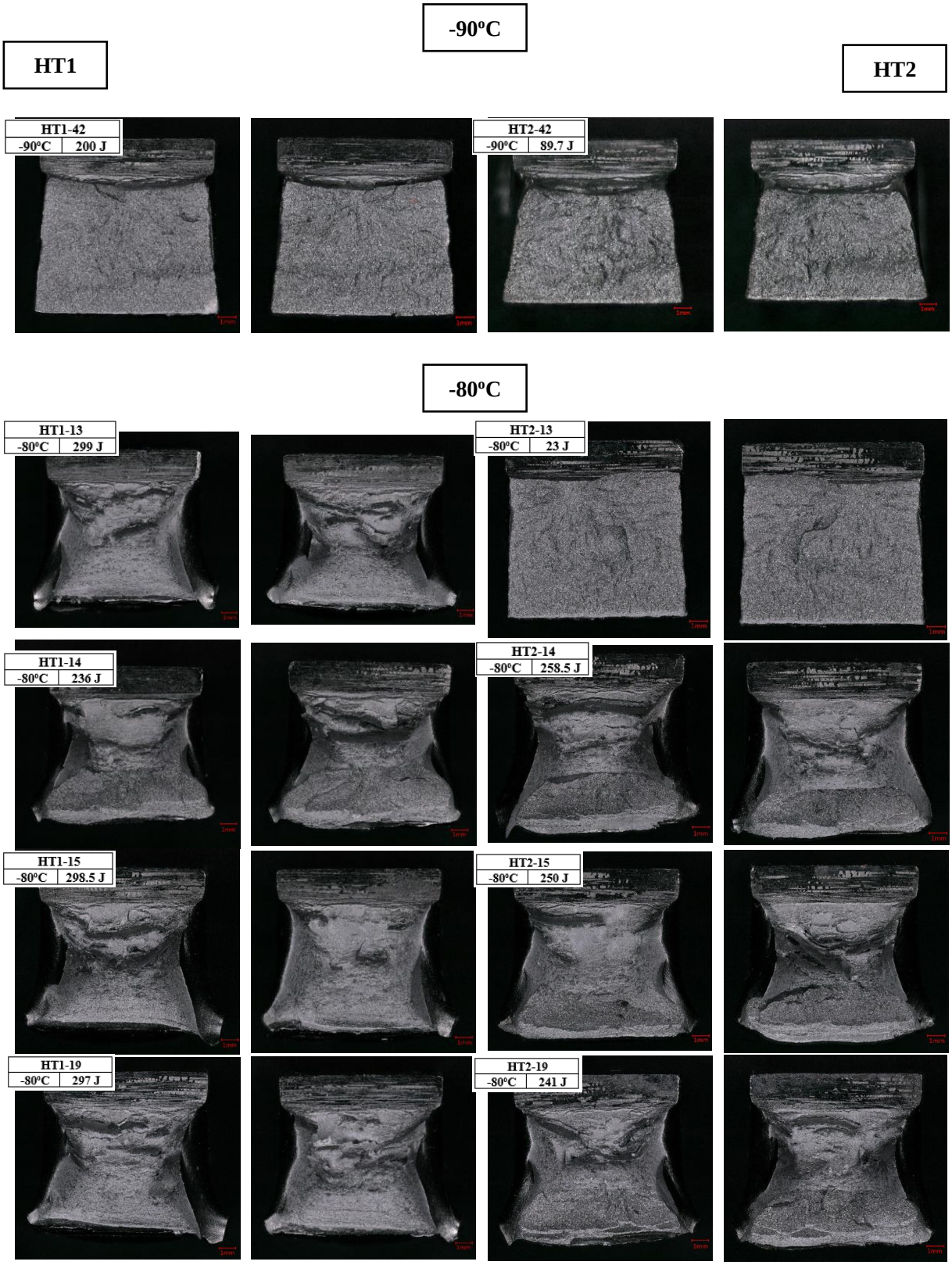

Figure 3.13

Charpy Fracture Surfaces

-80°C

HT1 **HT2**

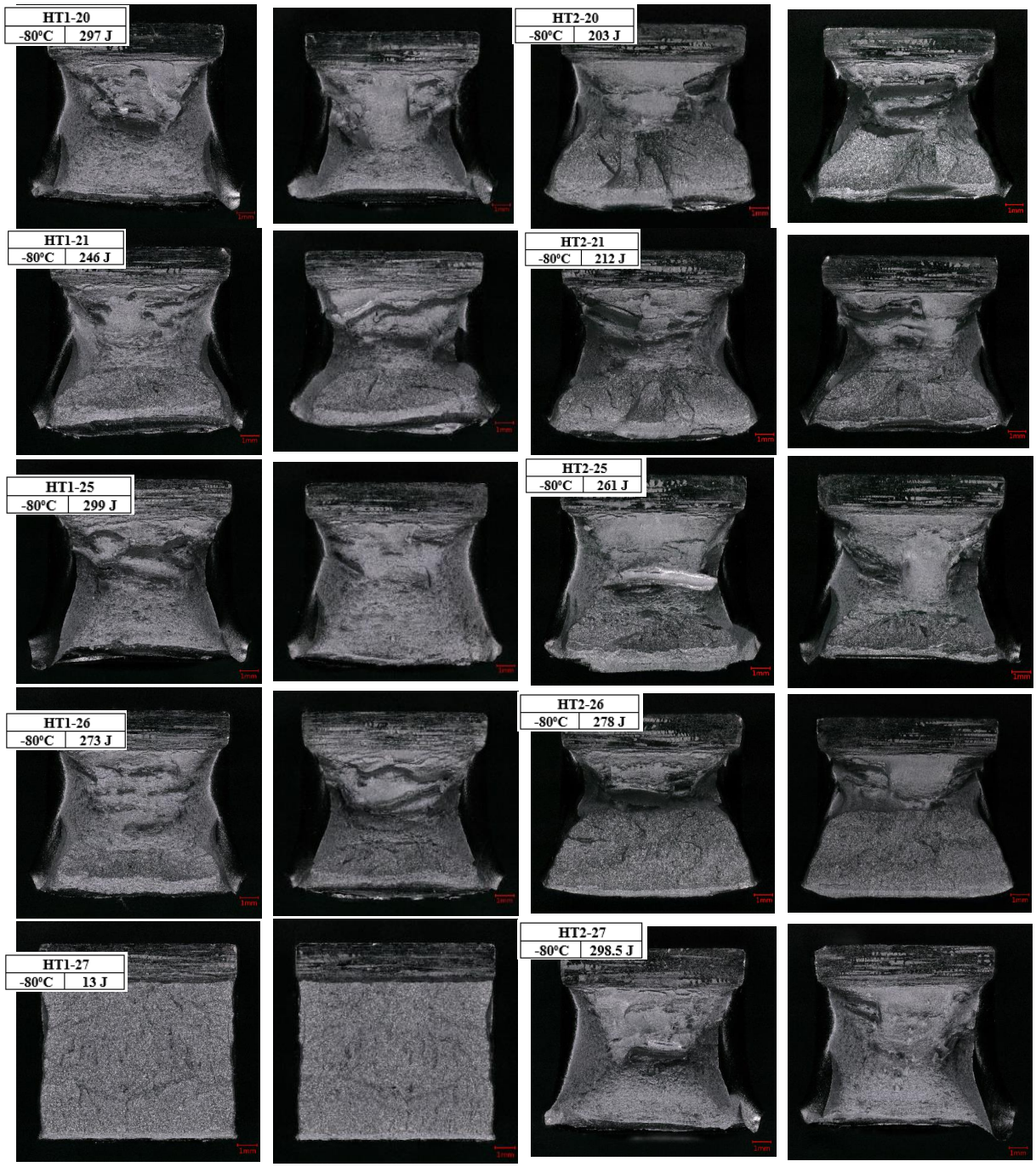

Figure 3.13

Charpy Fracture Surfaces

-70°C

HT1 **HT2**

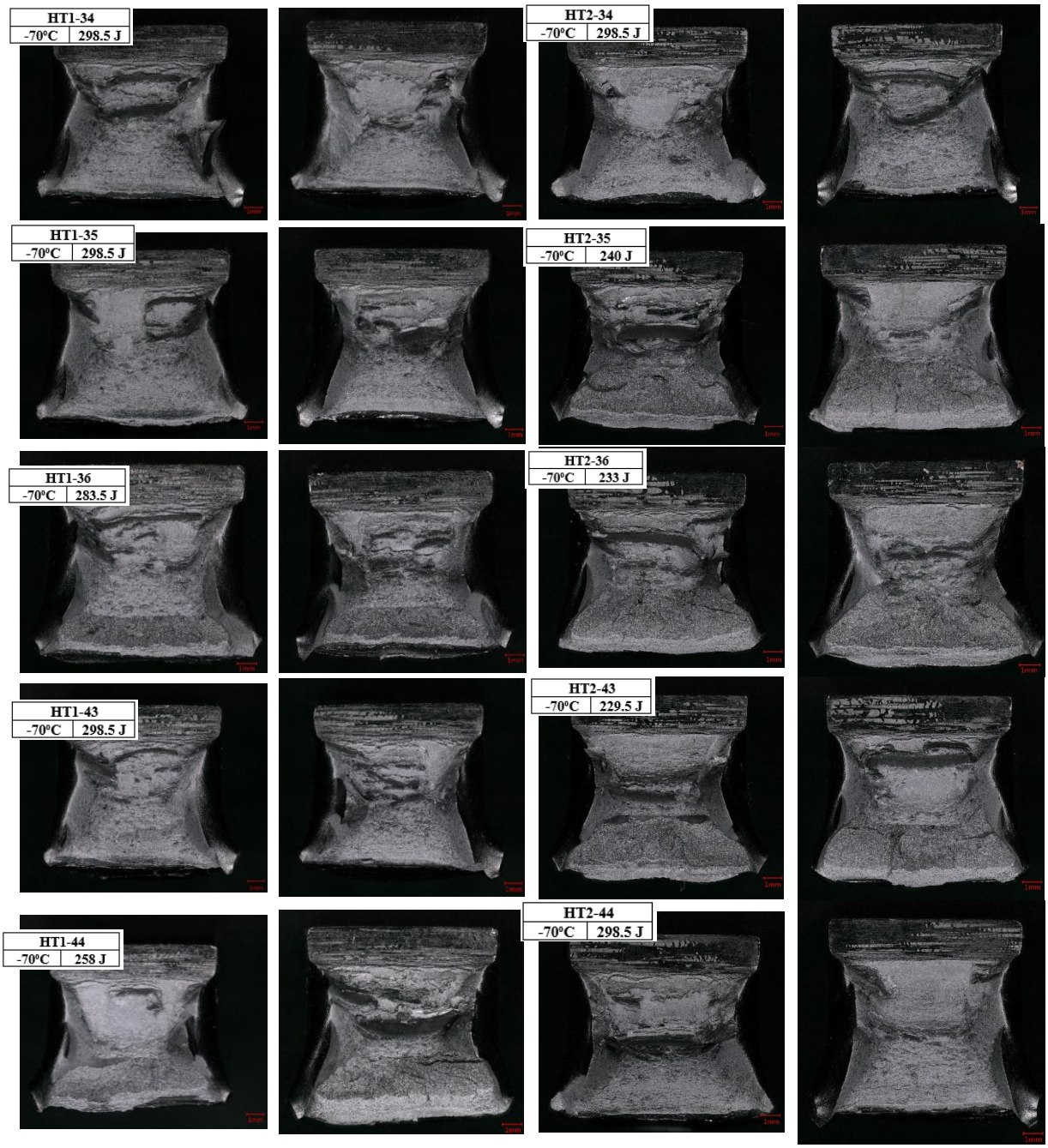

Figure 3.13

Charpy Fracture Surfaces

-70ºC

HT1 **HT2**

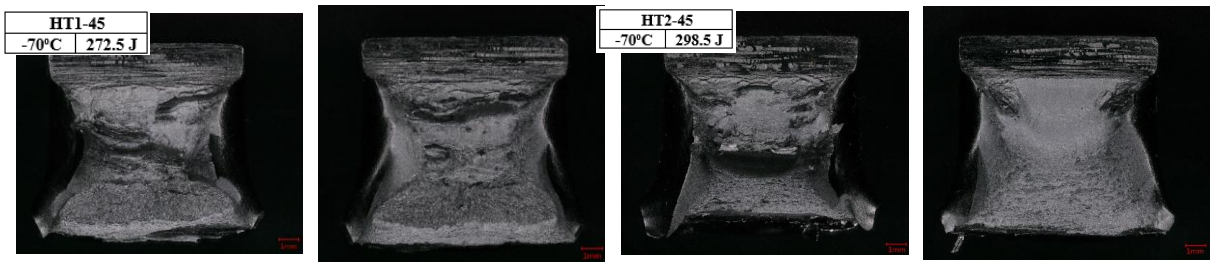

-60ºC

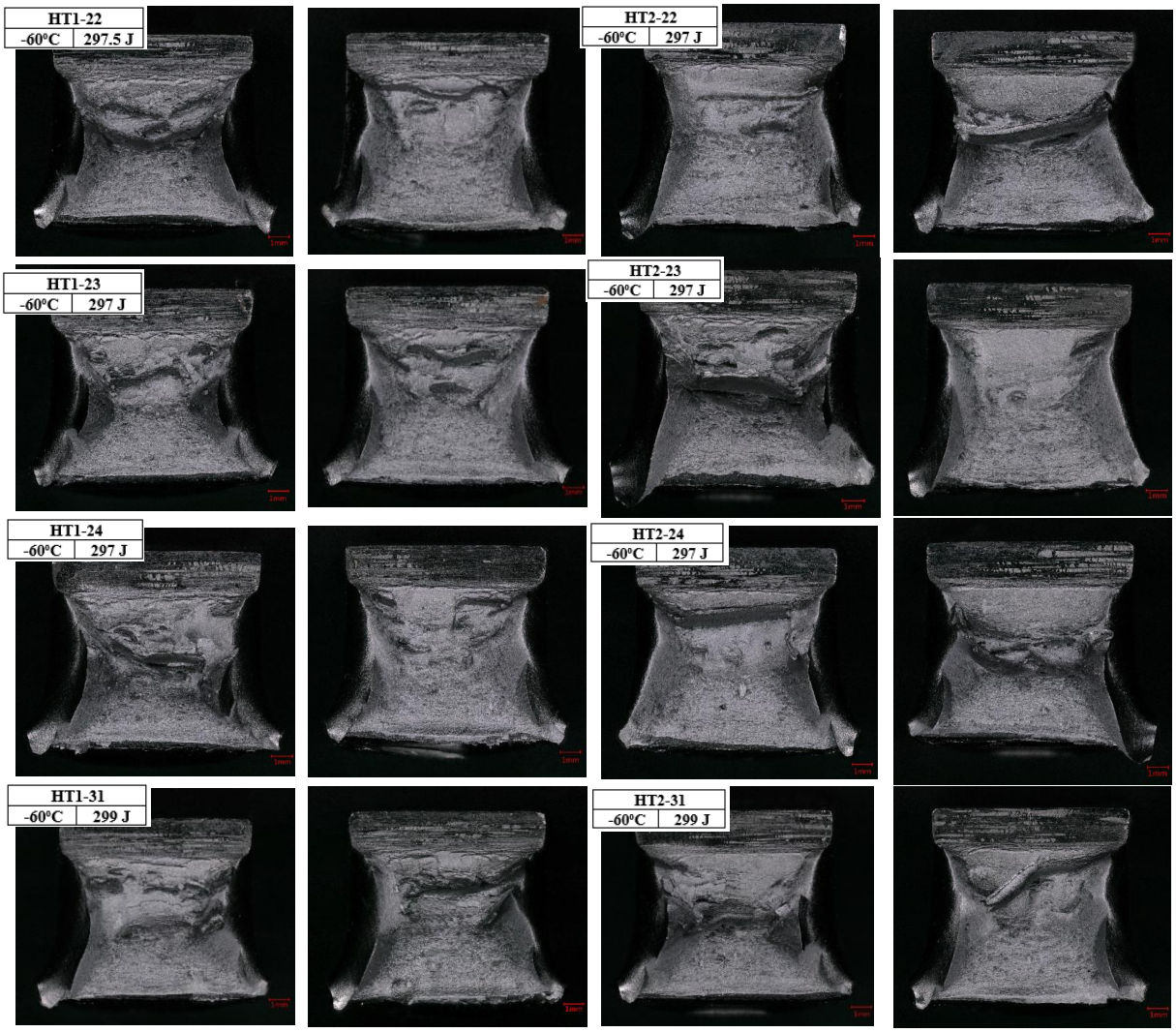

Figure 3.13

Charpy Fracture Surfaces

-60ºC

HT1 **HT2**

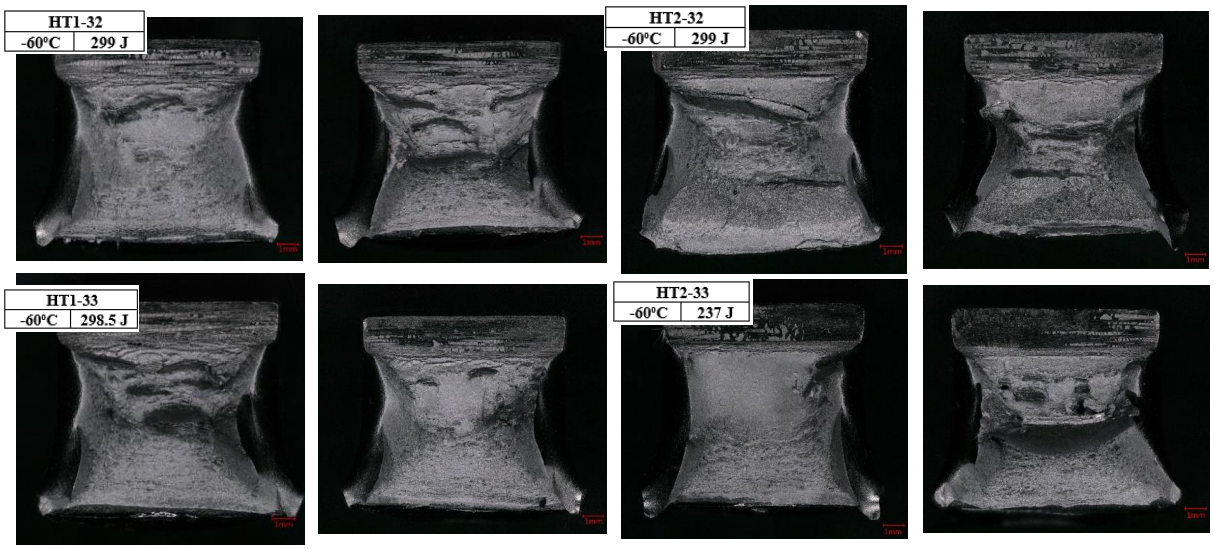

-40ºC

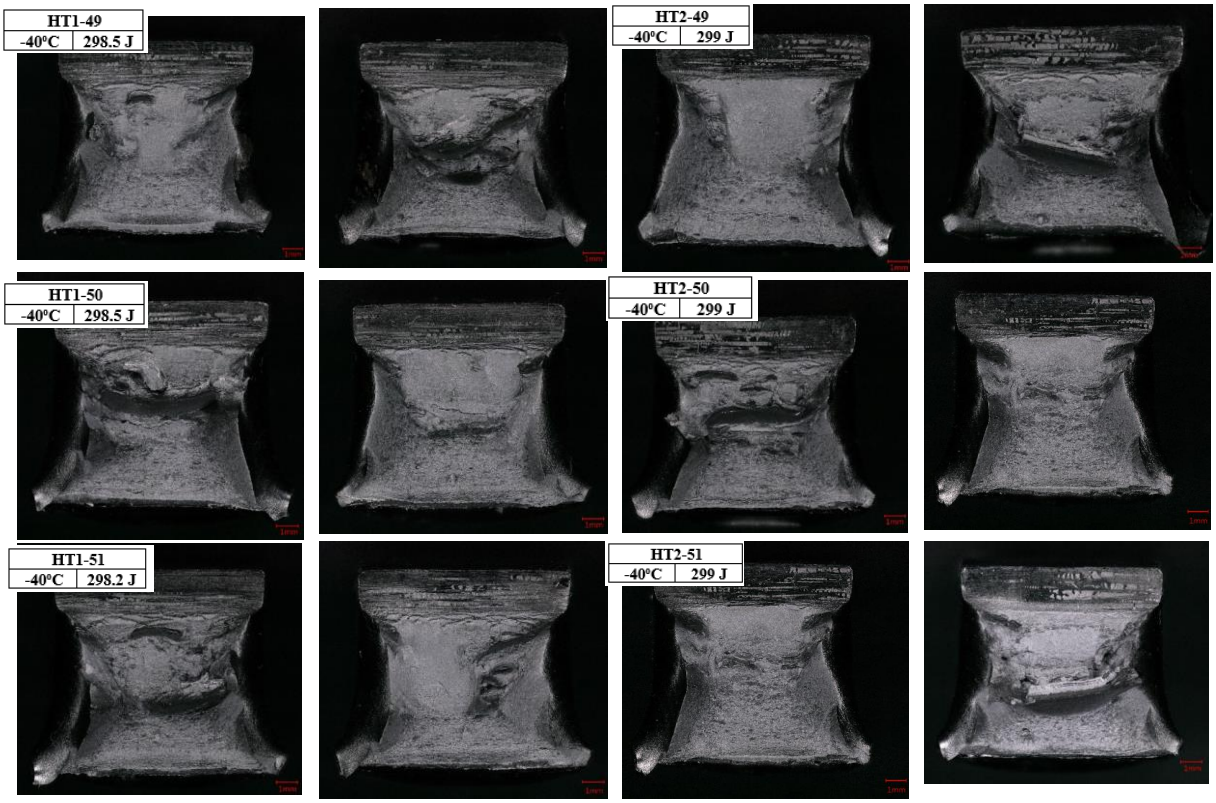

Figure 3.14

Absorbed Impact Energy Versus Temperature Plot with Tanh fit Curve for HT1

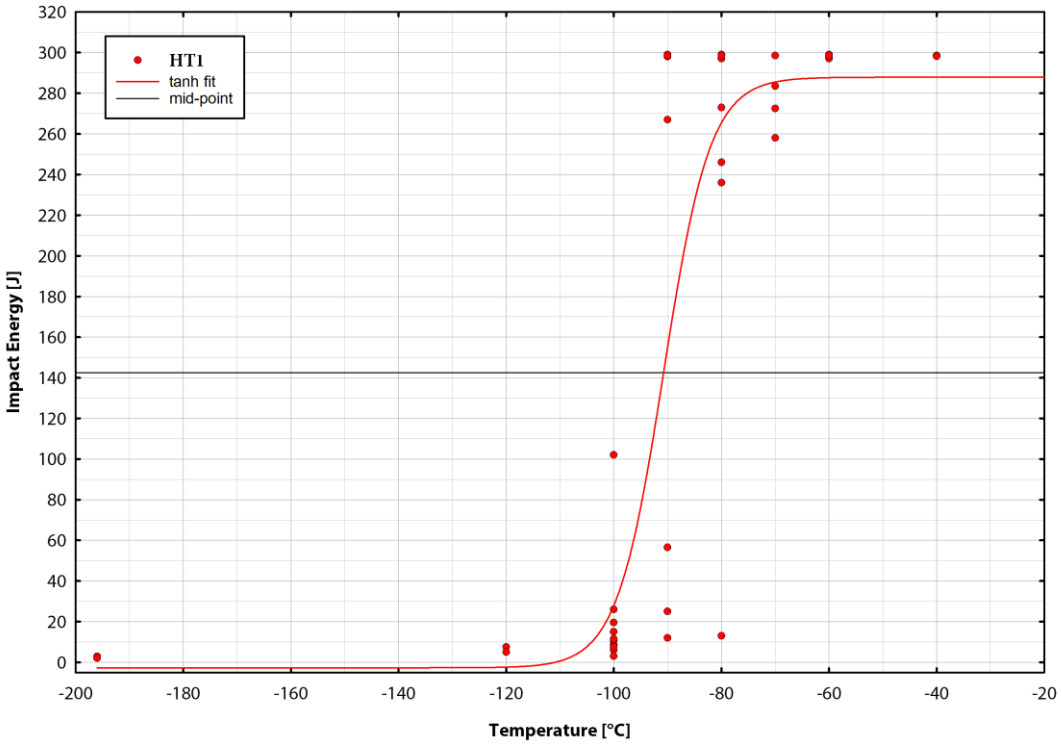

Figure 3.15

Absorbed Impact Energy versus Temperature Plot with Tanh-fit Curve for HT2

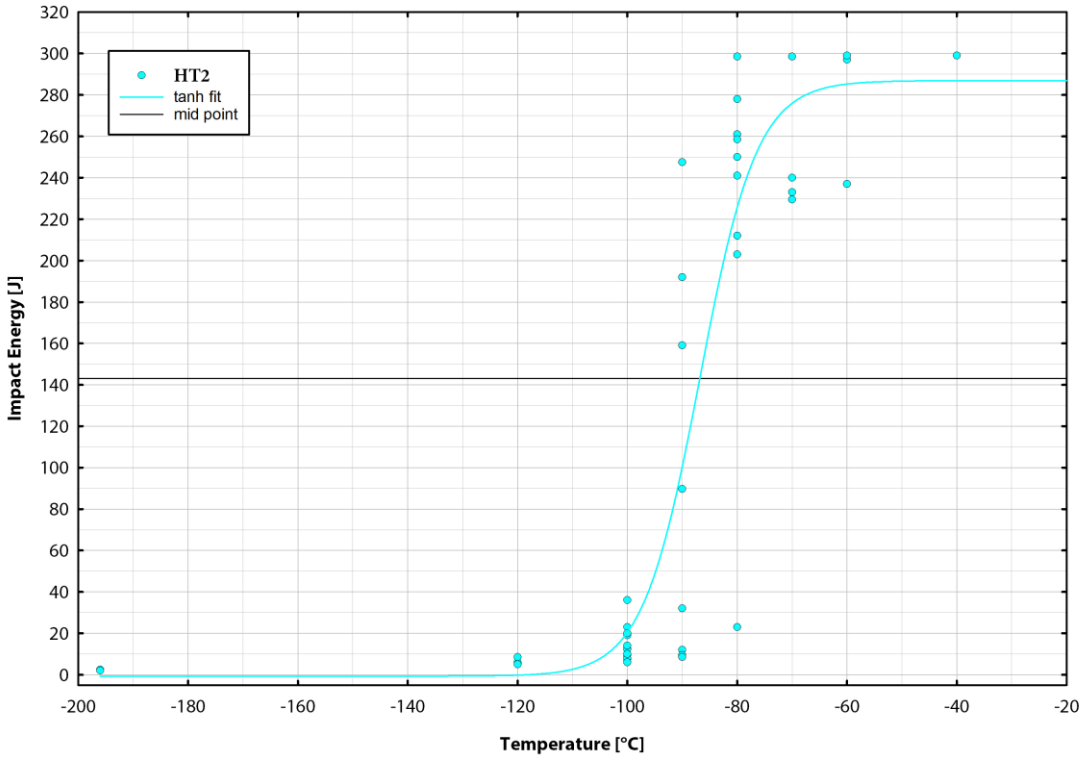

Figure 3.16

Absorbed Impact Energy versus Temperature Plots for HT1 and HT2

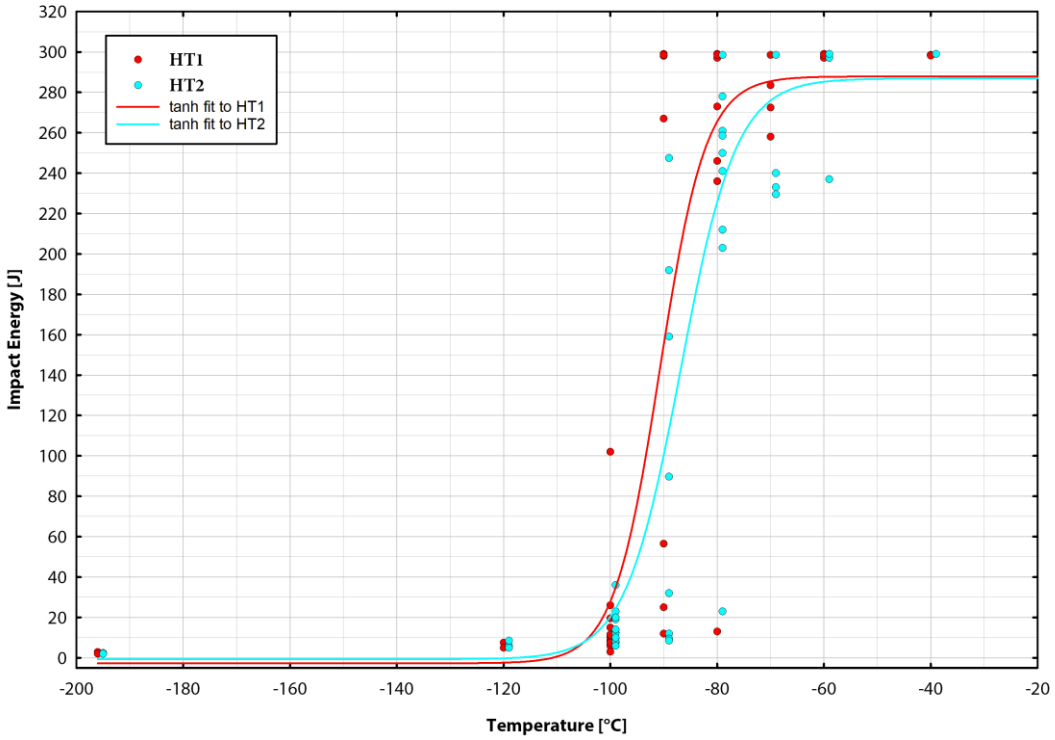

Figure 3.17

Absorbed Impact Energy versus Temperature Plots of HT1 and HT2 based on Baowu's Results

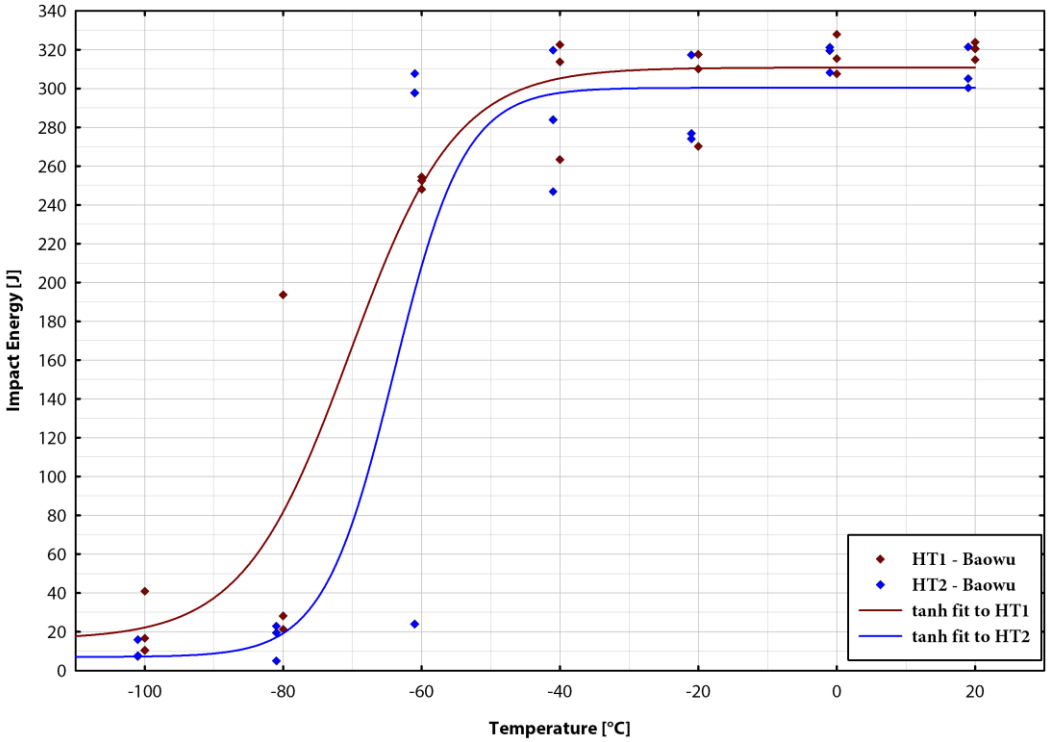

Figure 3.18

Absorbed Impact Energy versus %Cleavage Area of HT1

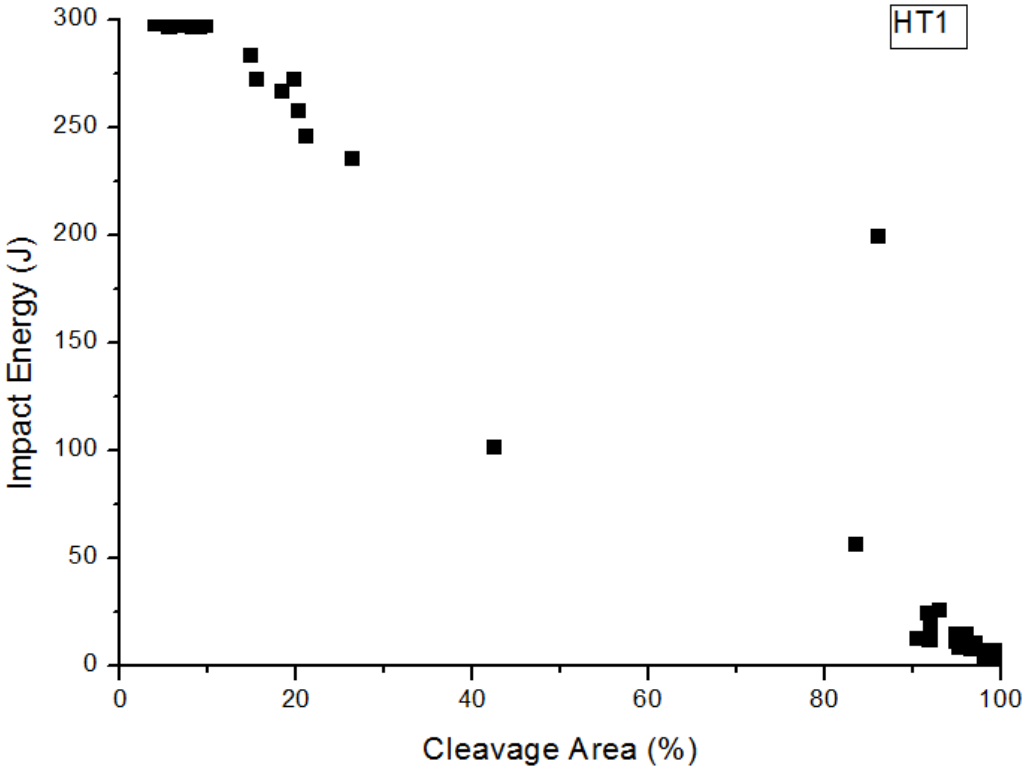

Figure 3.19

Absorbed Impact Energy versus %Cleavage Area of HT2

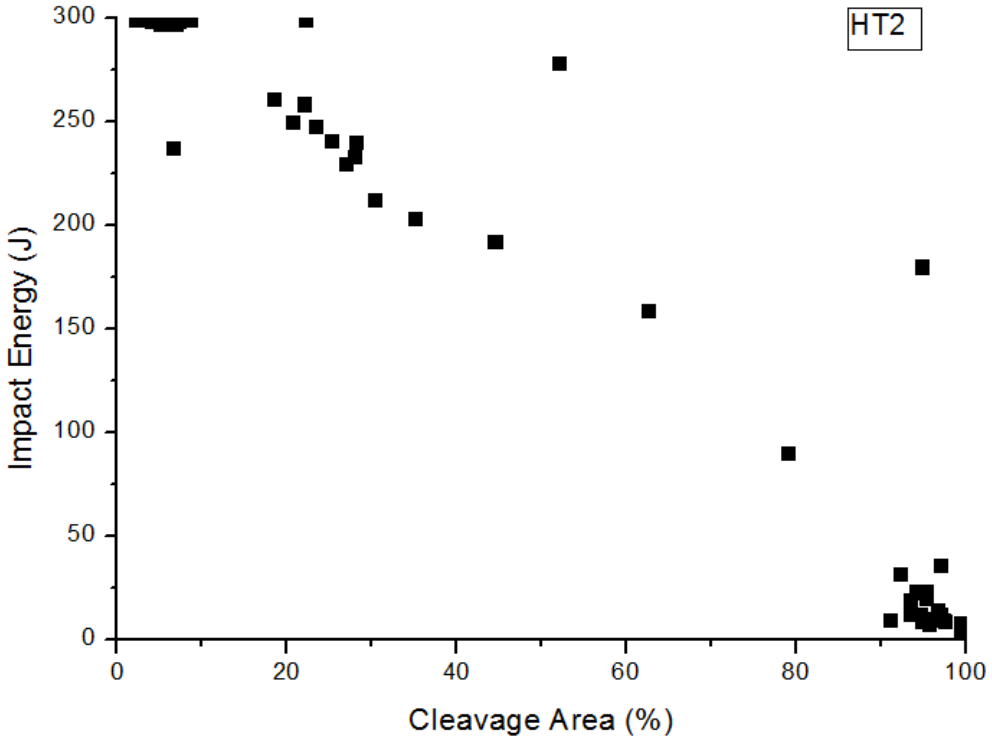

Figure 3.20

Absorbed Impact Energy versus %Cleavage Area of HT1 and HT2

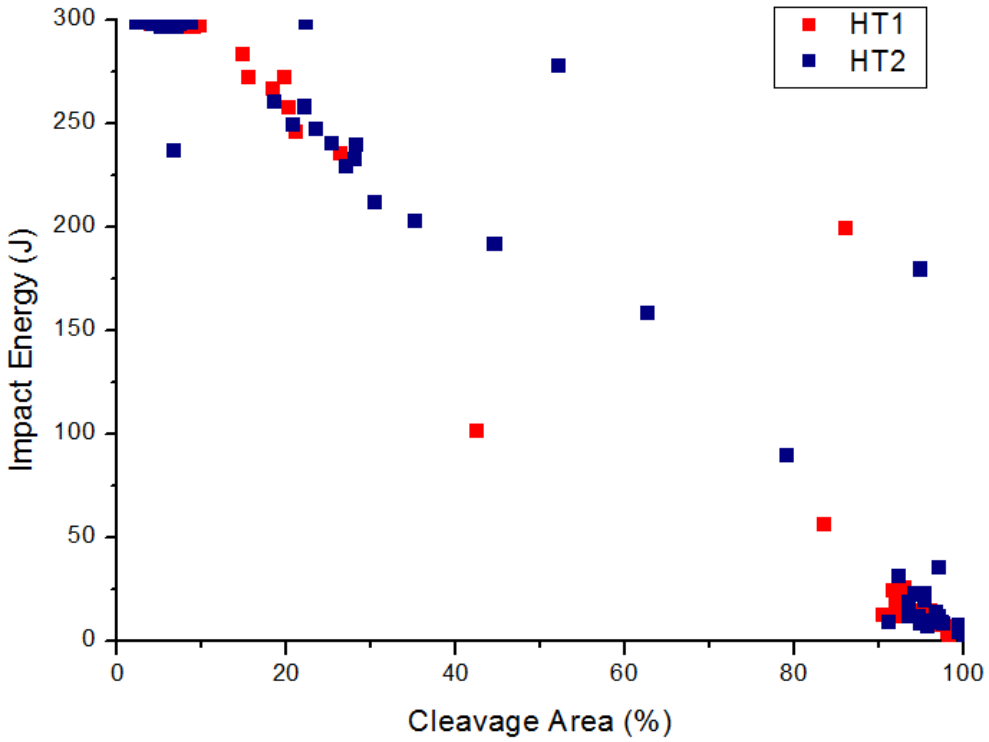

Figure 3.21

Absorbed Impact Energy versus Lateral Expansion of HT1

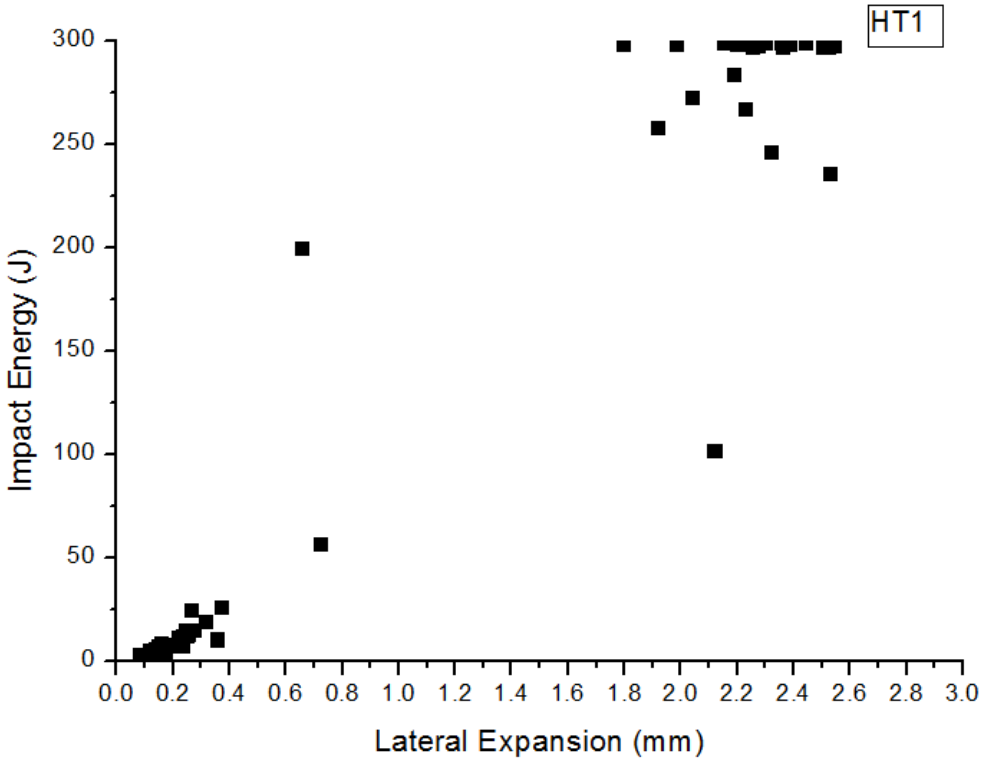

Figure 3.22

Absorbed Impact Energy versus Lateral Expansion of HT2

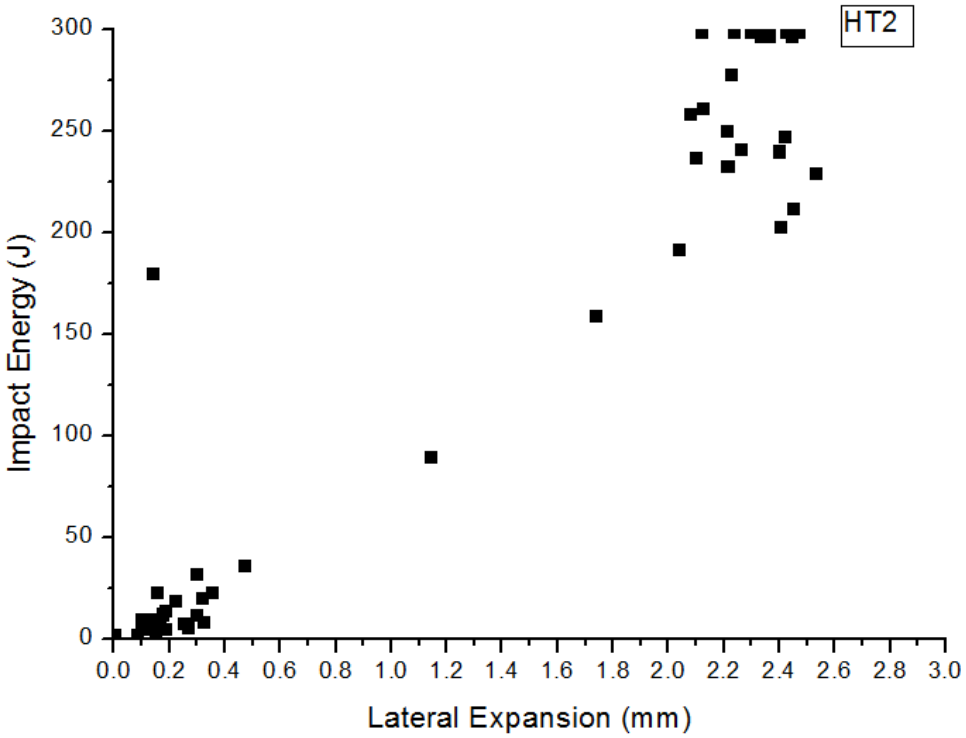

Figure 3.23

Absorbed Impact Energy versus Lateral Expansion of HT1 and HT2

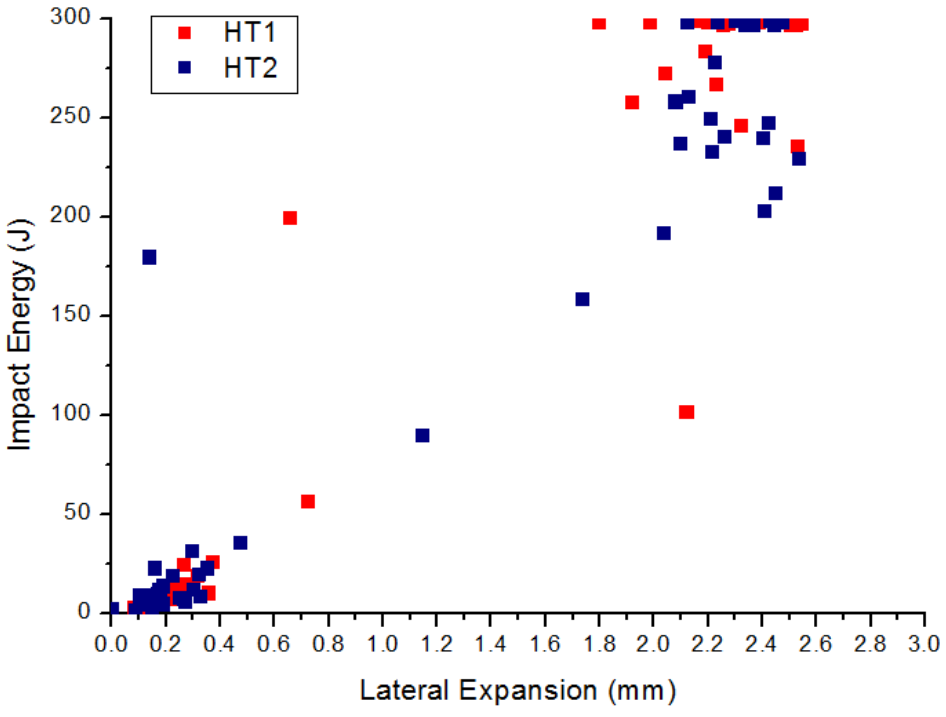

Figure 3.24

Absorbed Impact Energy versus Ductile Thumbnail Extension of HT1

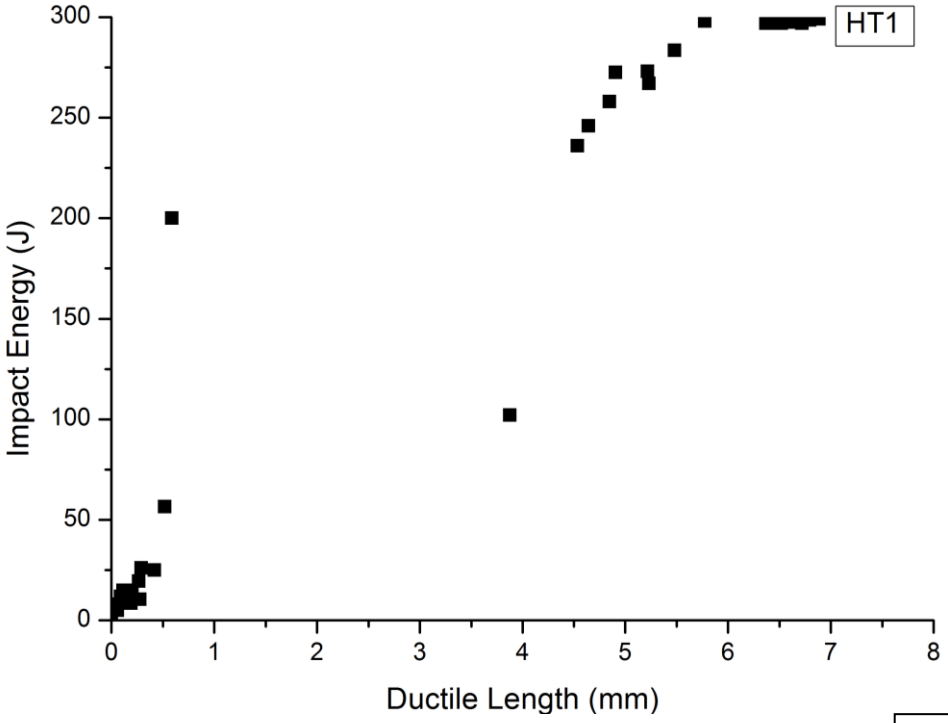

Figure 3.25

Absorbed Impact Energy versus Ductile Thumbnail Extension of HT2

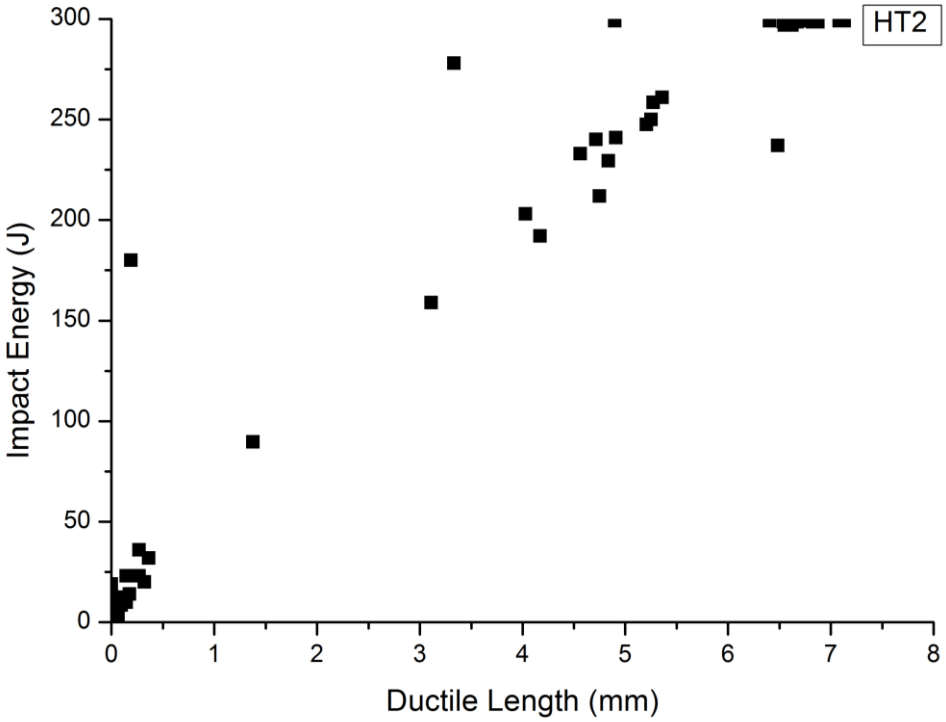

Figure 3.26

Absorbed Impact Energy versus Ductile Thumbnail Extension of HT1 and HT2

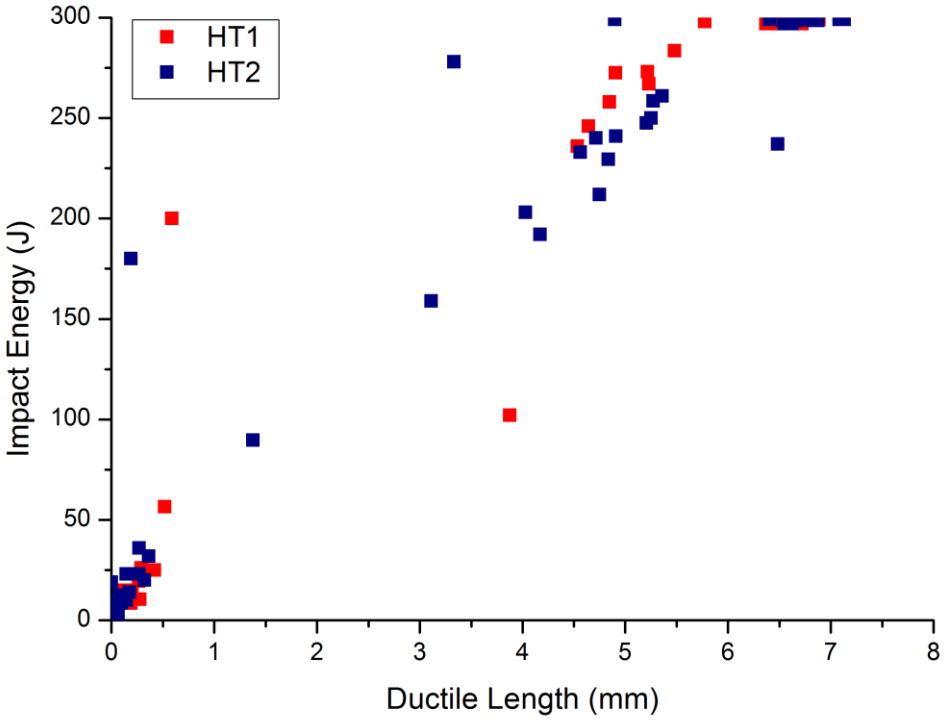

Figure 3.27

C(T) Specimen Load-Displacement Curves

-170°C

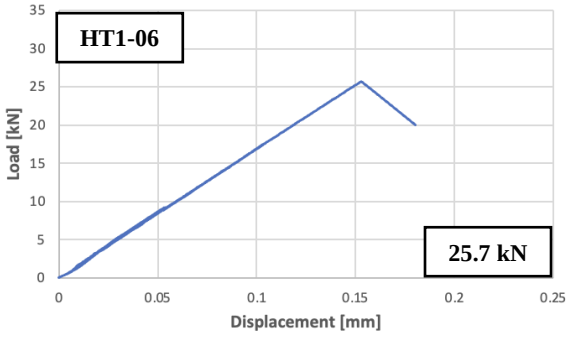

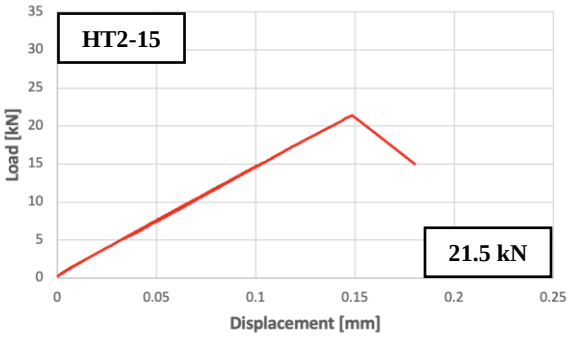

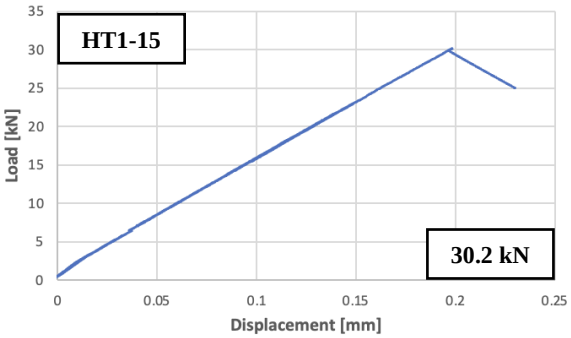

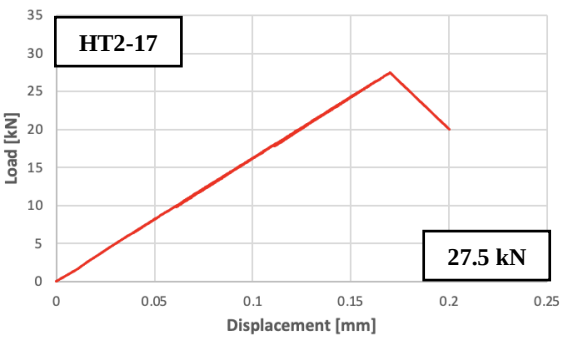

-120°C

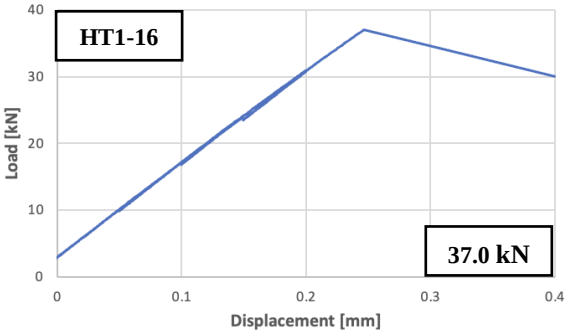

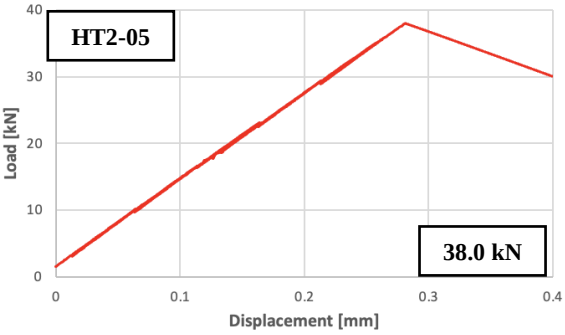

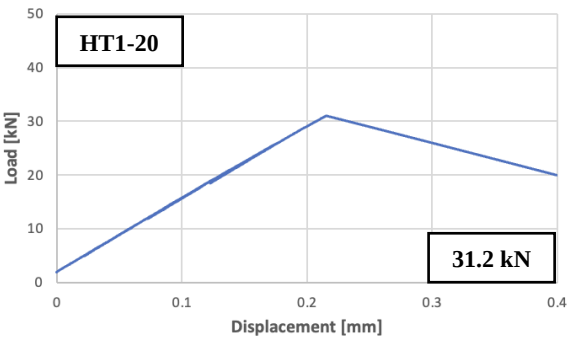

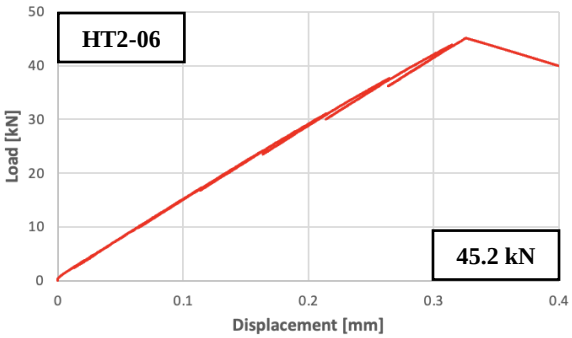

Figure 3.27

C(T) Specimen Load-Displacement Curves

-120°C

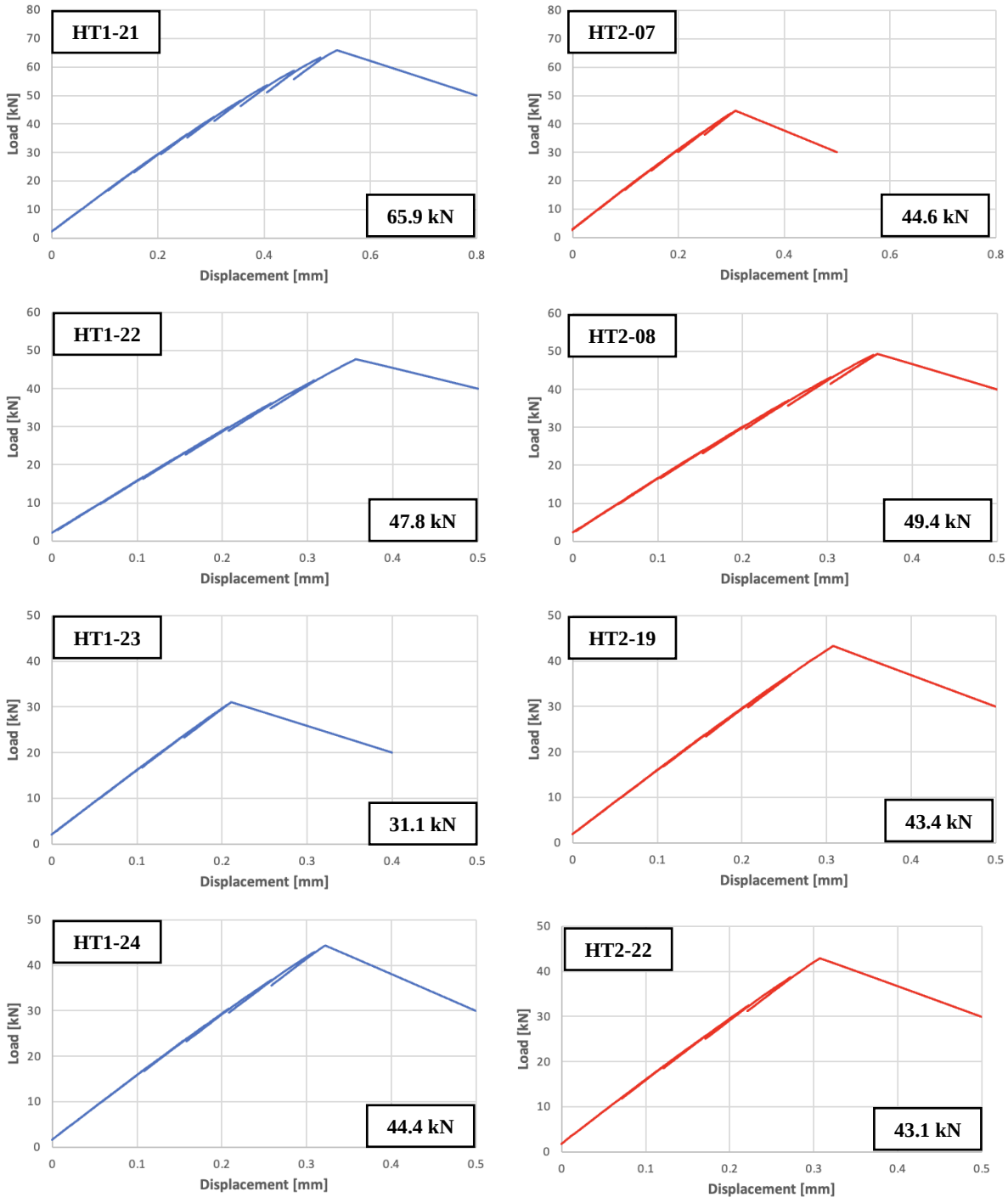

Figure 3.27

C(T) Specimen Load-Displacement Curves

-100ºC

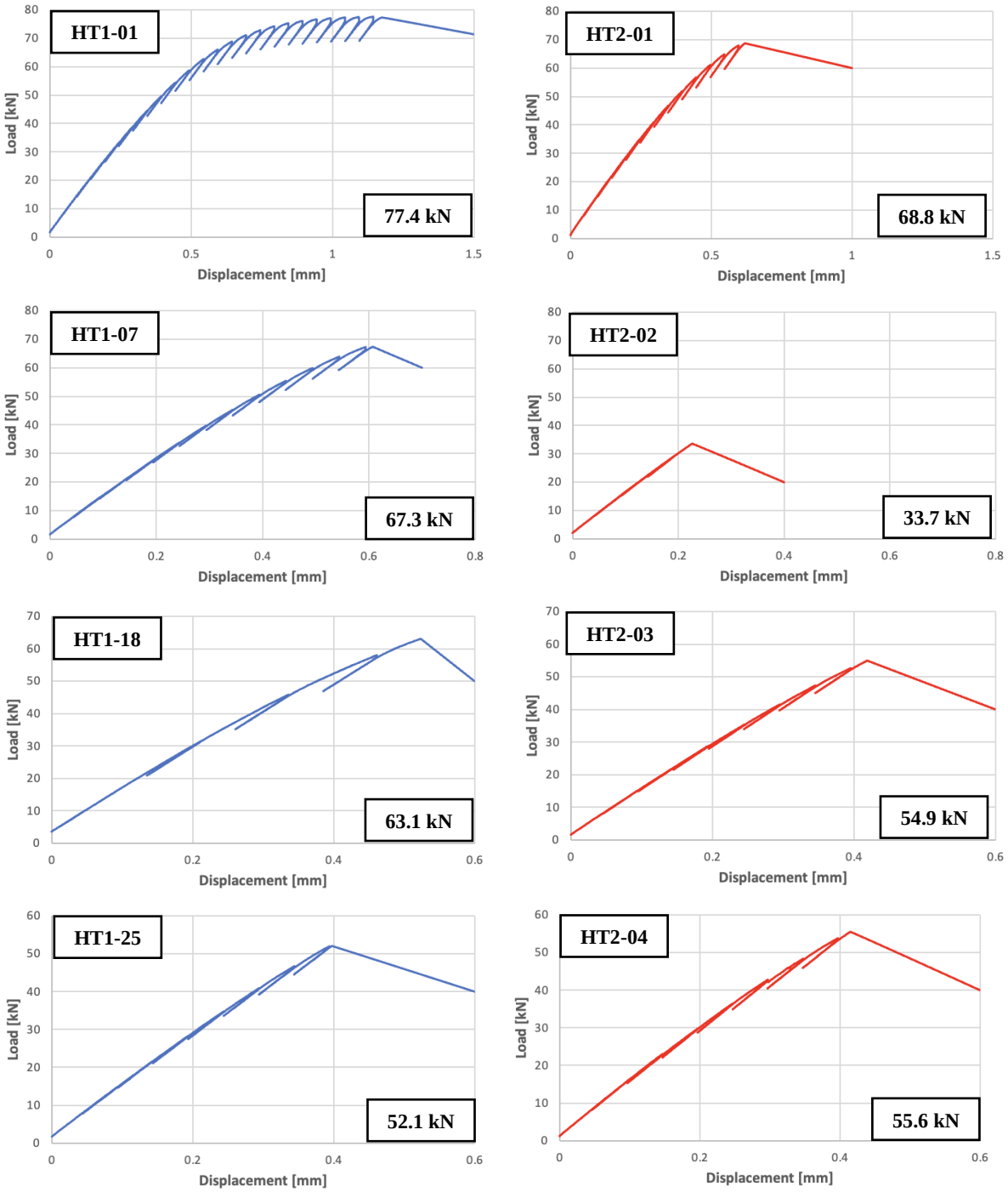

Figure 3.27

C(T) Specimen Load-Displacement Curves

-100ºC

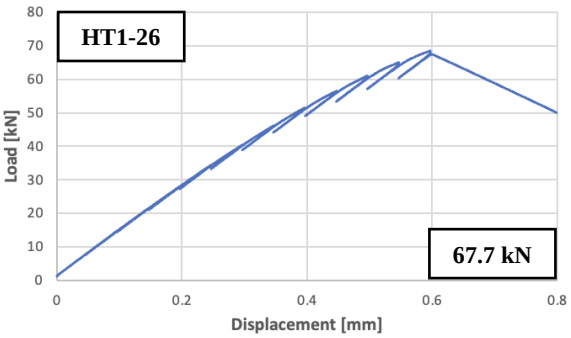

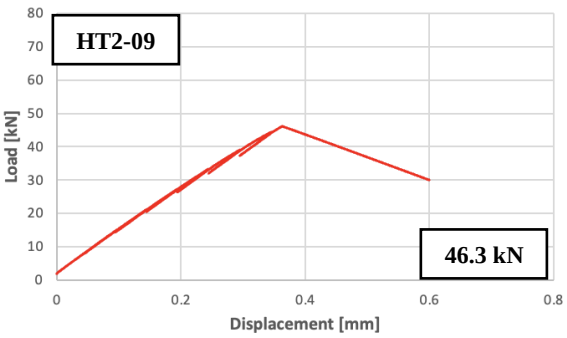

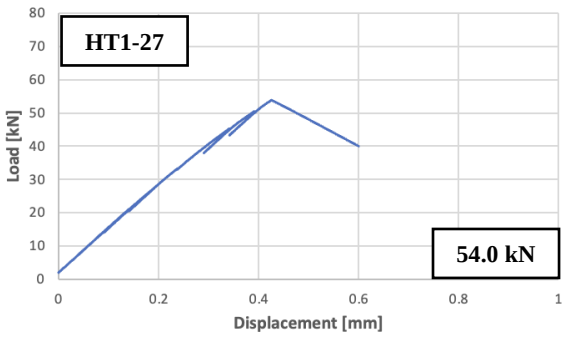

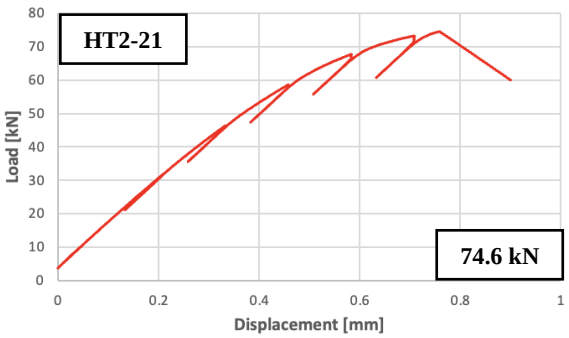

-80ºC

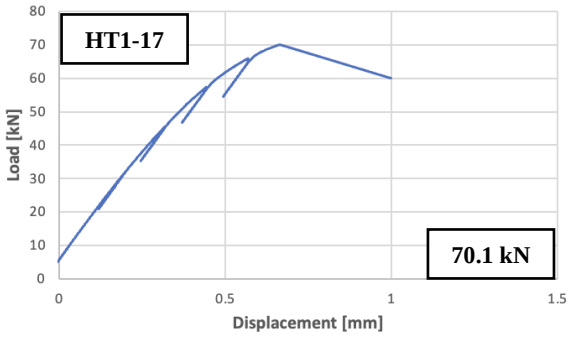

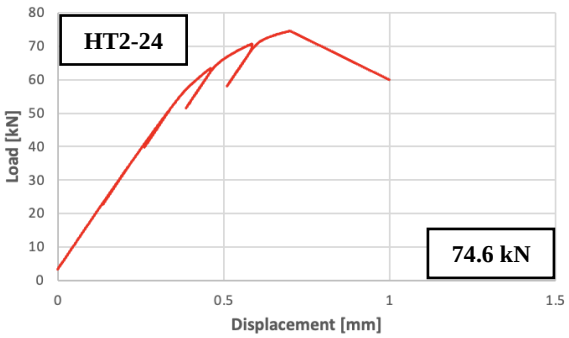

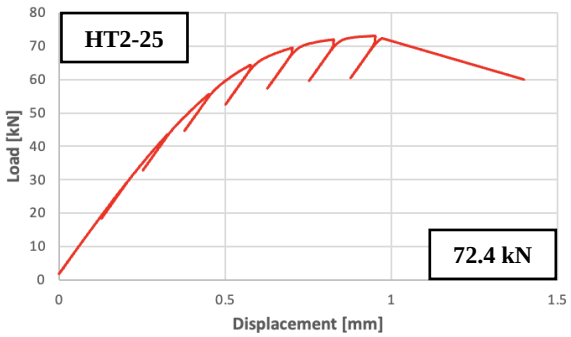

Figure 3.28

SENB Specimen Load-Displacement Curves at -196ºC

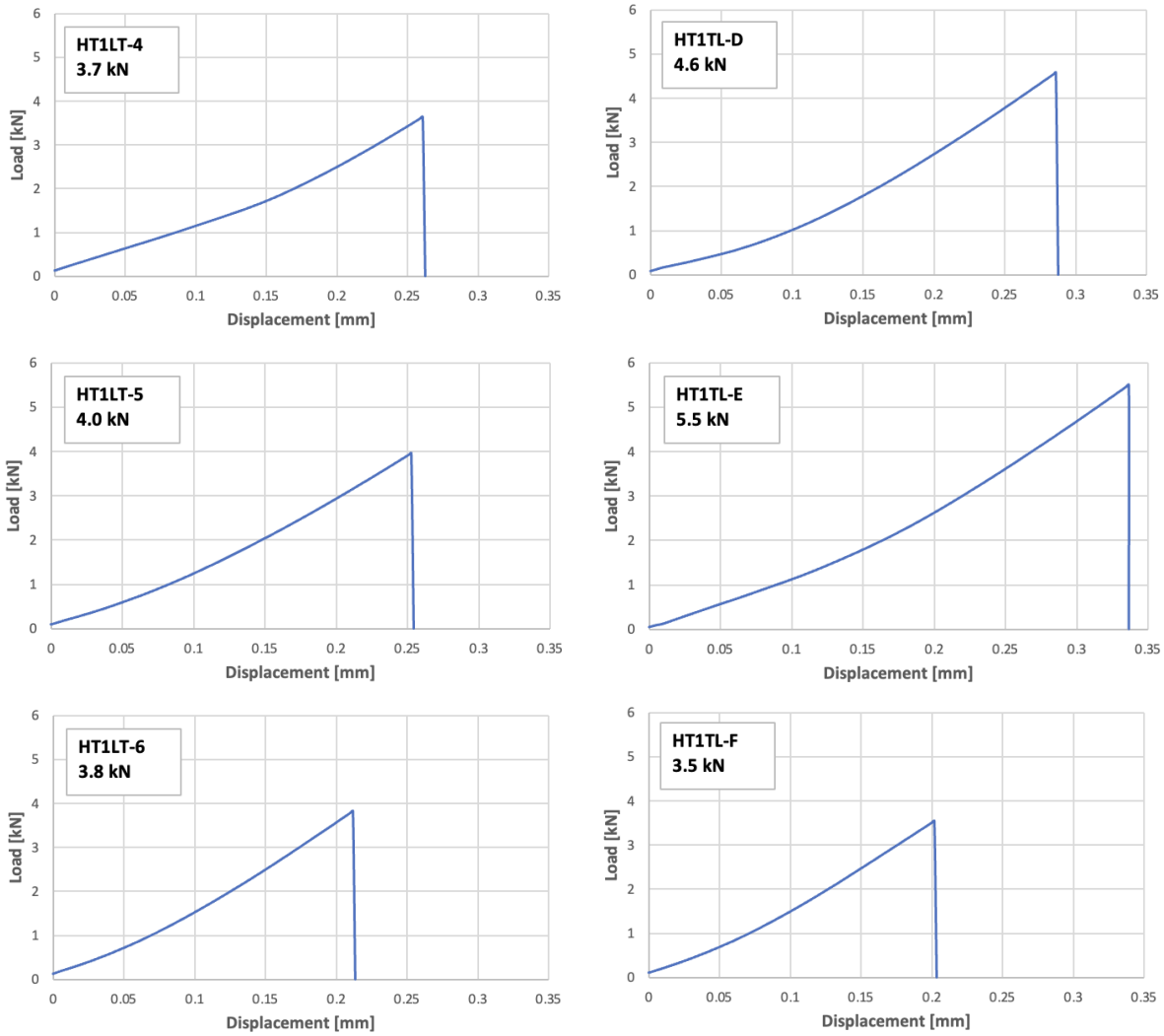

*HT1TL-F was loaded to 2kN during cooling process.

Figure 3.29

K_{Ic} of HT1, HT2 and HT1LT/TL versus Test Temperatures

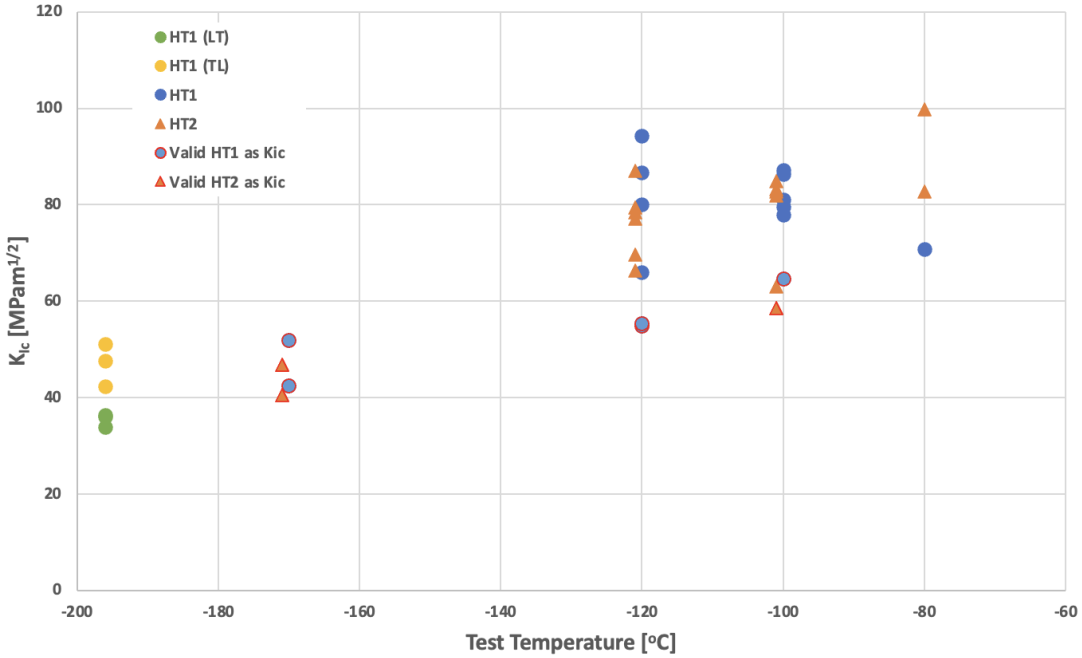

Figure 3.30

K_{Jc} of HT1, HT2 and HT1LT/TL versus Test Temperatures

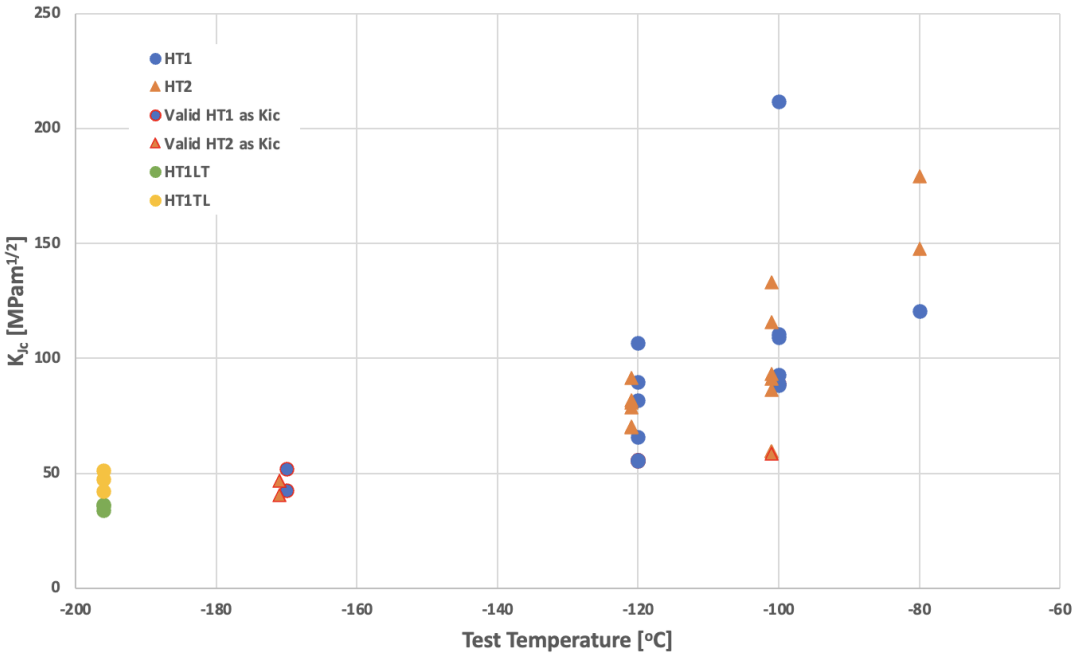

Figure 3.31

Master Curves with 95% and 5% Tolerance Bounds based on Single Temperature Analysis at -120ºC for HT1 and HT2

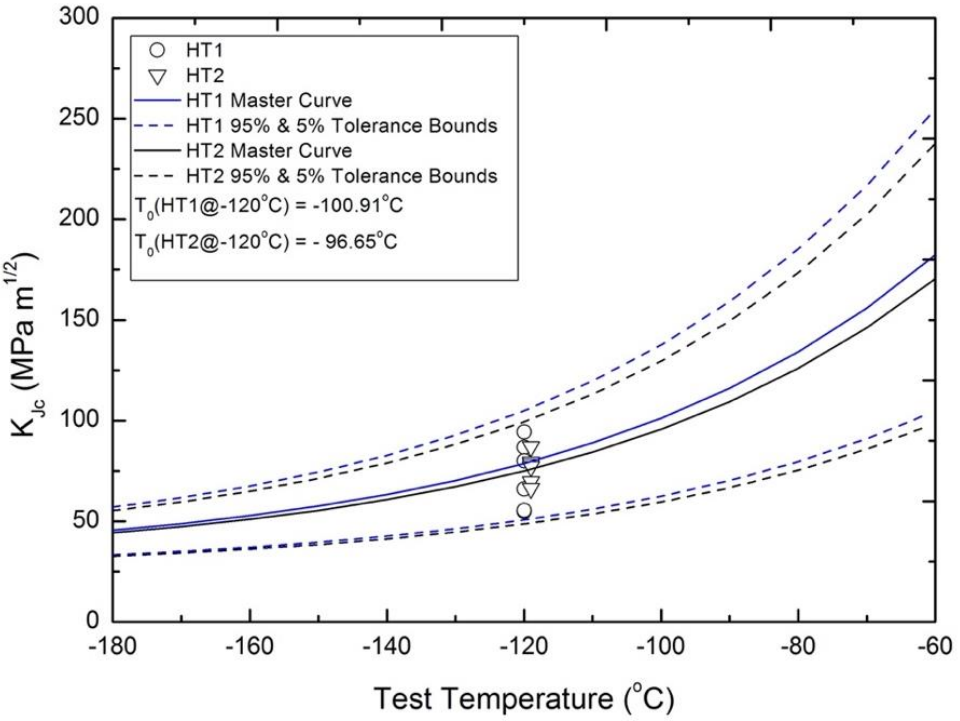

Figure 3.32

Master Curves with 95% and 5% Tolerance Bounds based on Single Temperature Analysis at -100ºC for HT1 and HT2

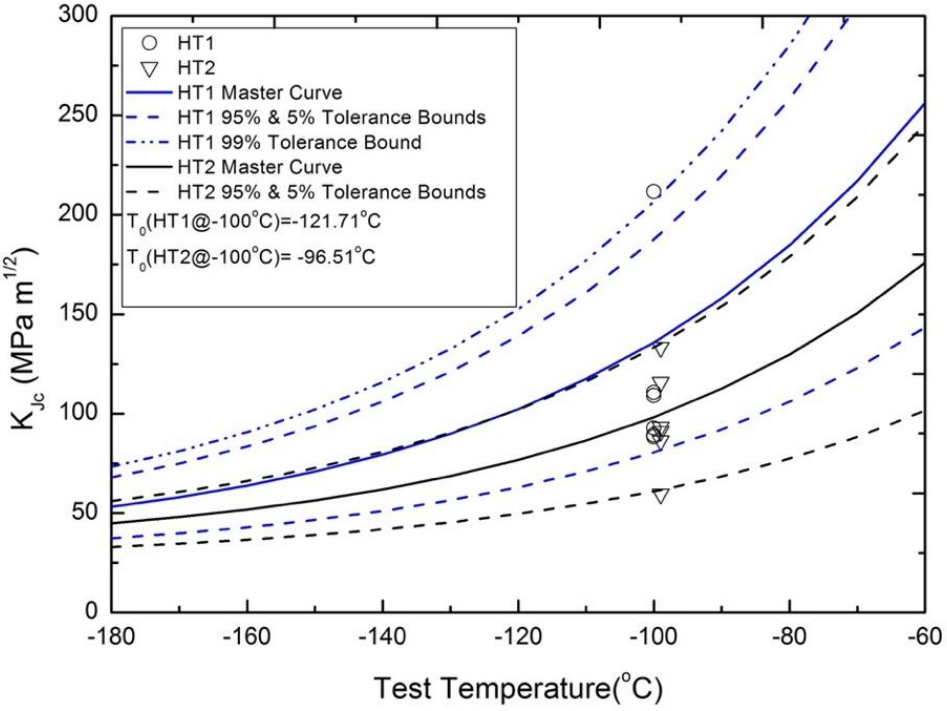

Figure 3.33

Master Curves with Tolerance Bounds based on Results of -120, -100, and -80ºC for HT1 and HT2

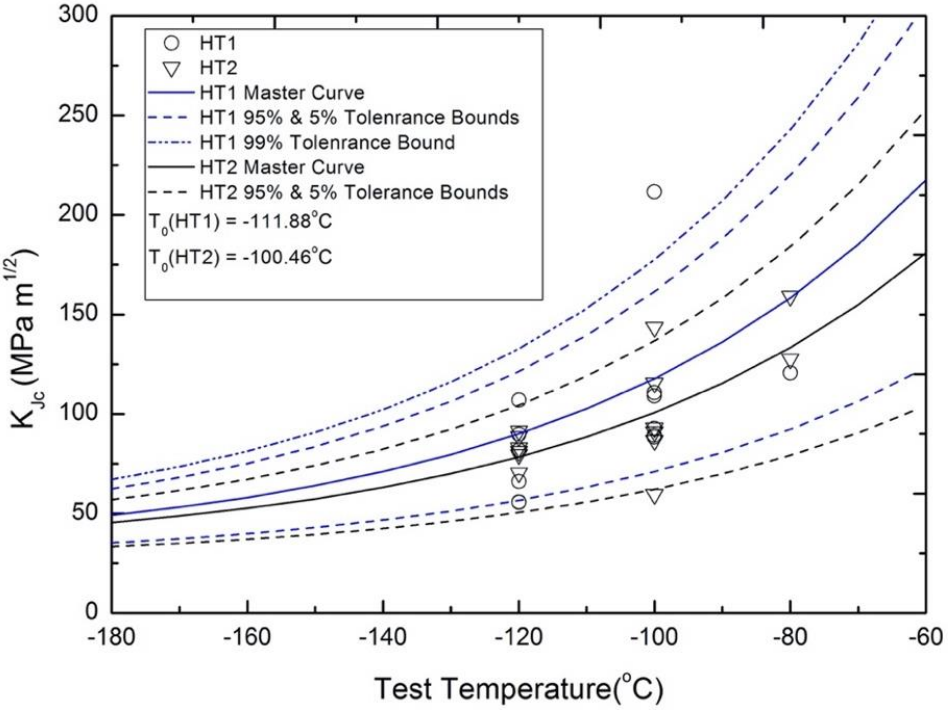

Figure 3.34

Master Curves with Tolerance Bounds based on Results of -120, -100, and -80ºC for HT1 and HT2 without HT1-01

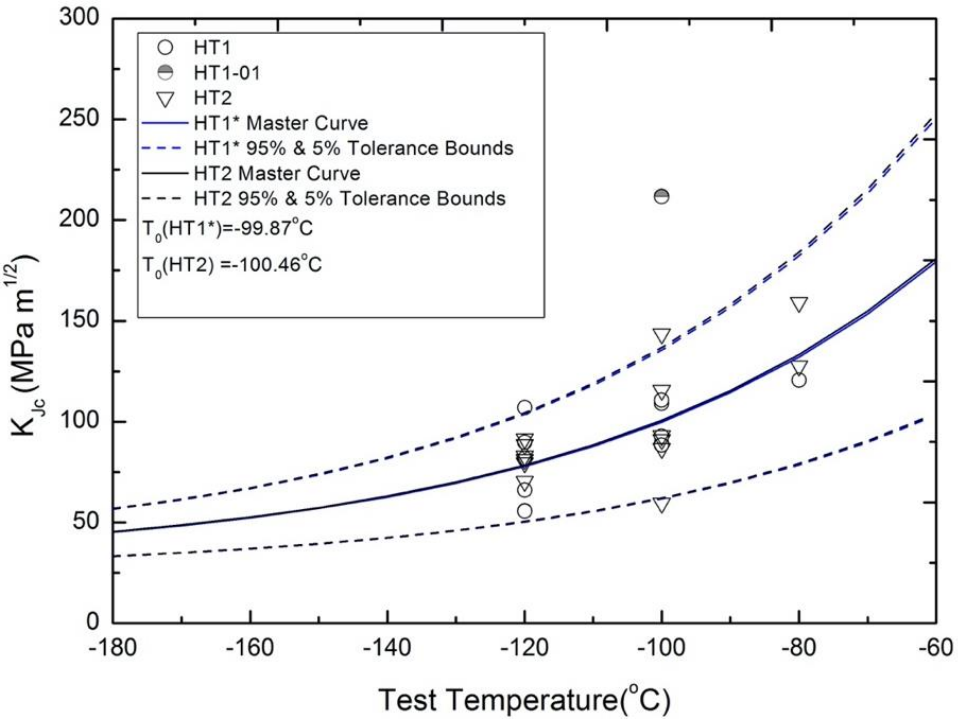

Figure 3.35

Master Curve with Tolerance Bounds at -120, -100, and -80ºC for Combining Results of HT1 and HT2

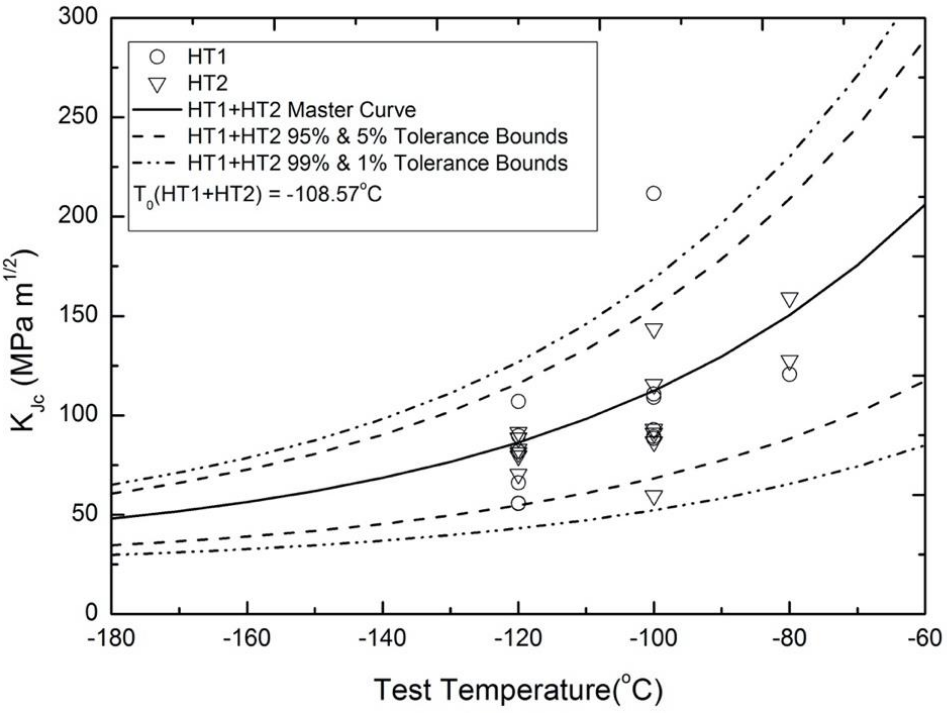

Figure 3.36

Master Curve with Tolerance Bounds at -120, -100, and -80ºC for Combining Results of HT1 and HT2 without HT1-01

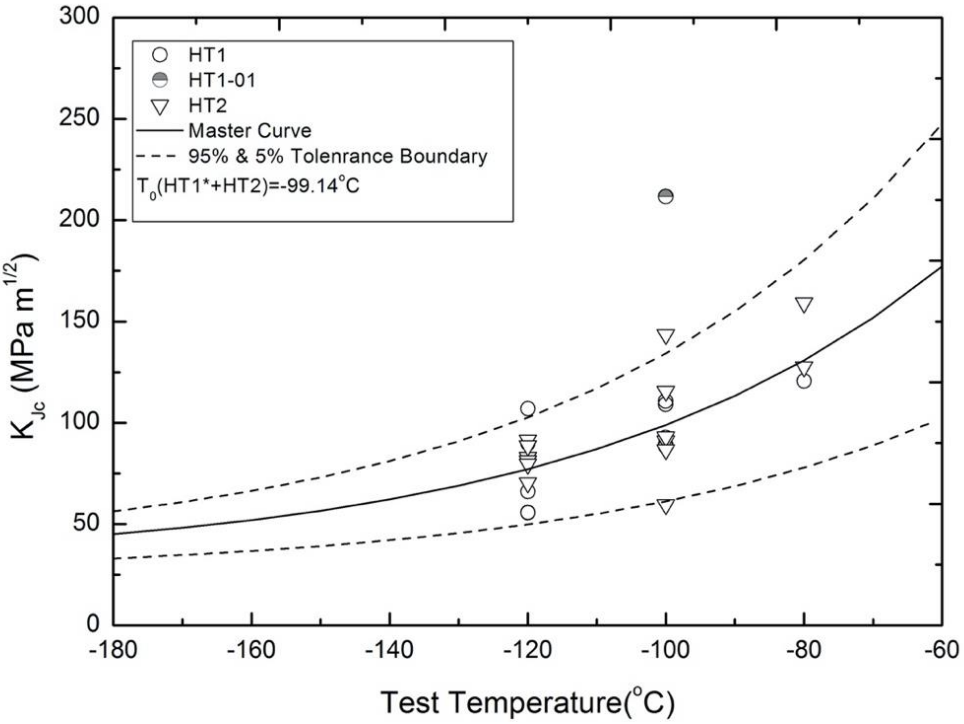

Figure 3.37

Data tested at -120, -100 and -80ºC plotted in Weibull Coordinates

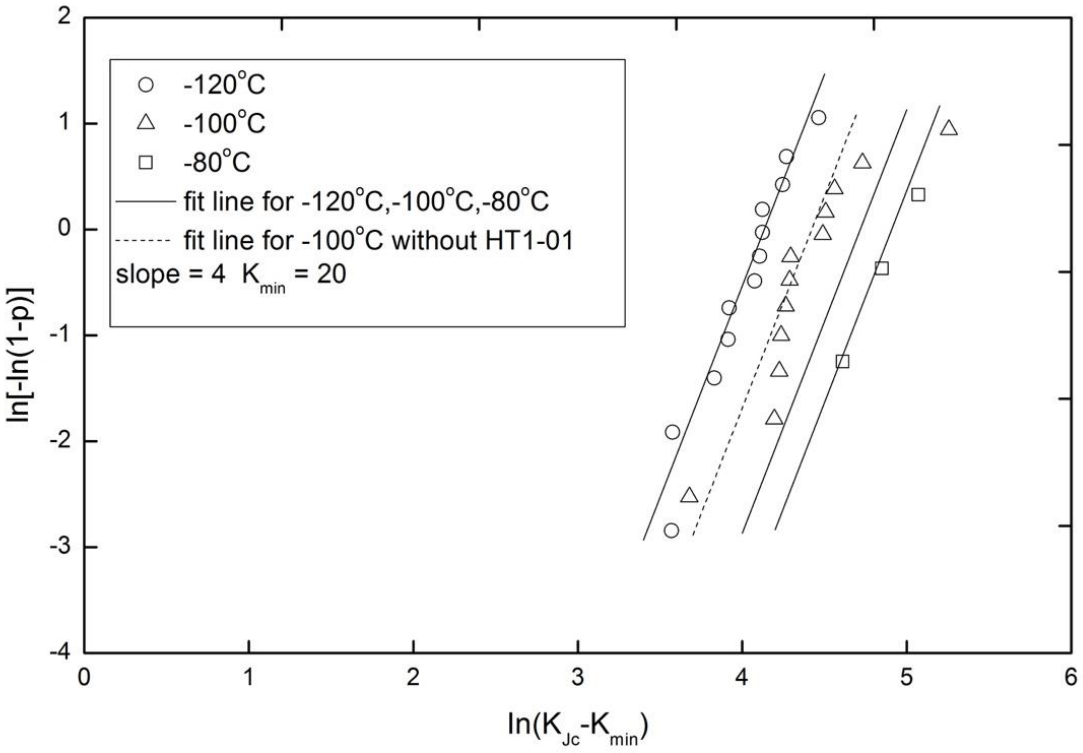

HT1-01 A

Figure 3.38

Fractography of Fracture Toughness Specimen HT1-01 tested at -100°C

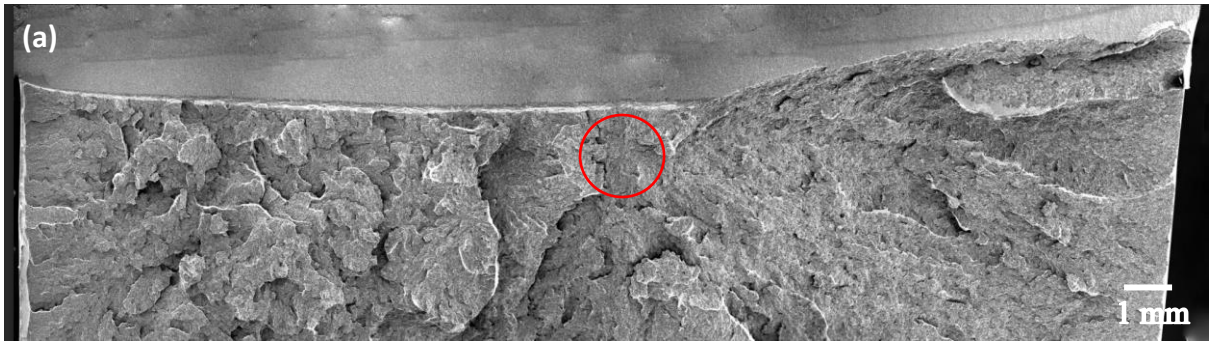

(a): Fracture surface after fatigue precrack. The possible initiation site is circled in red.

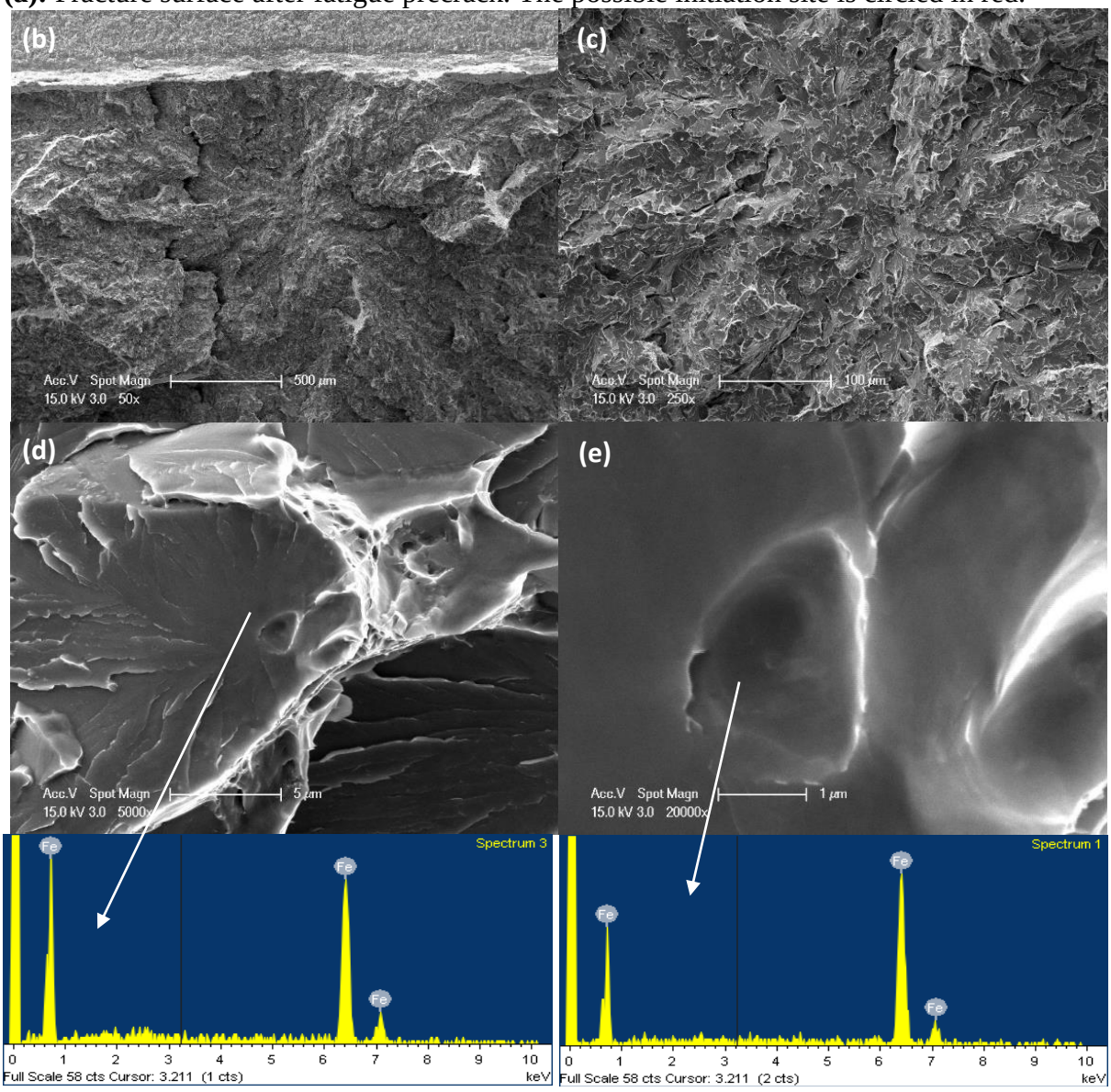

(b), (c), (d), (e): details of circled site in magnification sequence; (f), (g): EDX results of matrix and possible initiation site.

HT1-01 B

Figure 3.38

Fractography of Fracture Toughness Specimen HT1-01 tested at -100ºC

(f), (g), (h), (i): detail of circled site in magnification sequence on **opposite** side of HT1-01.

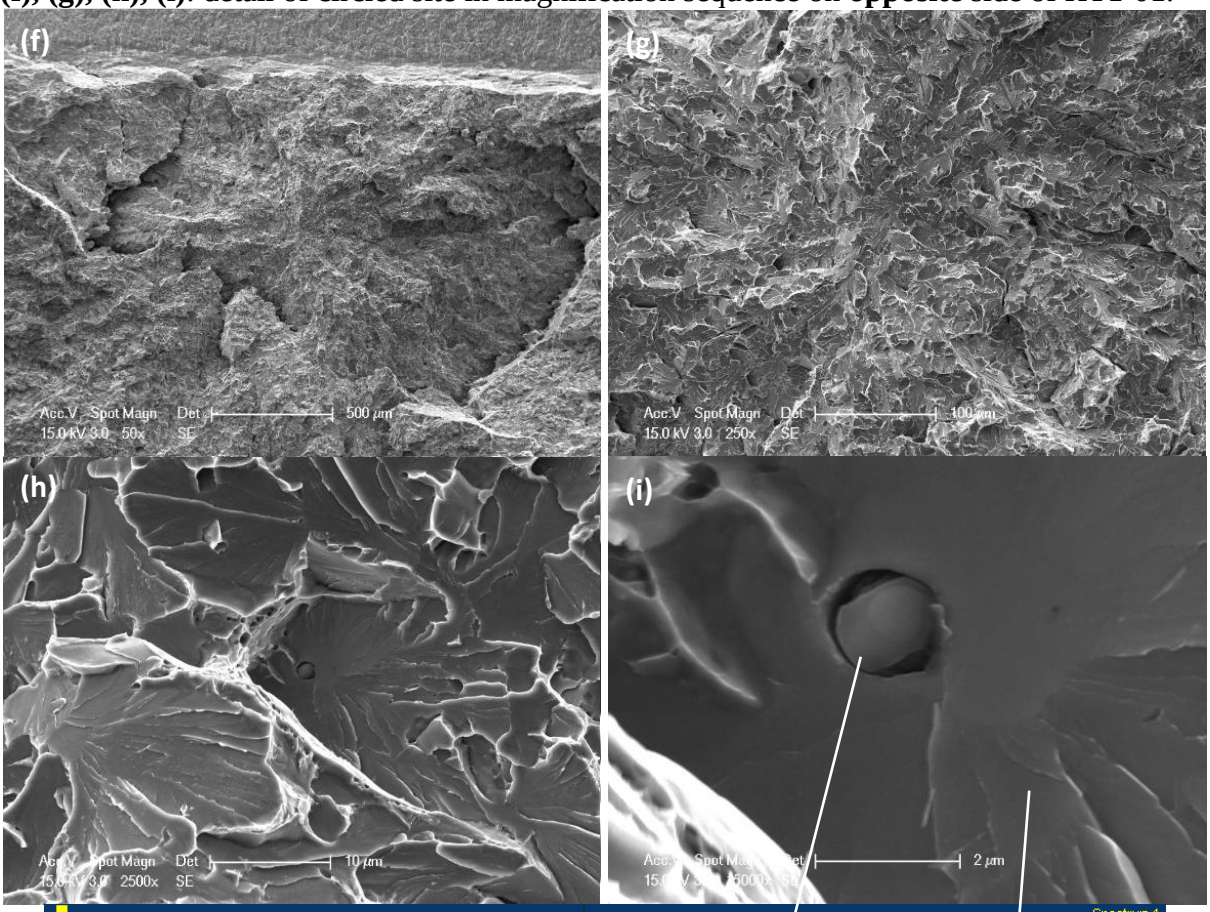

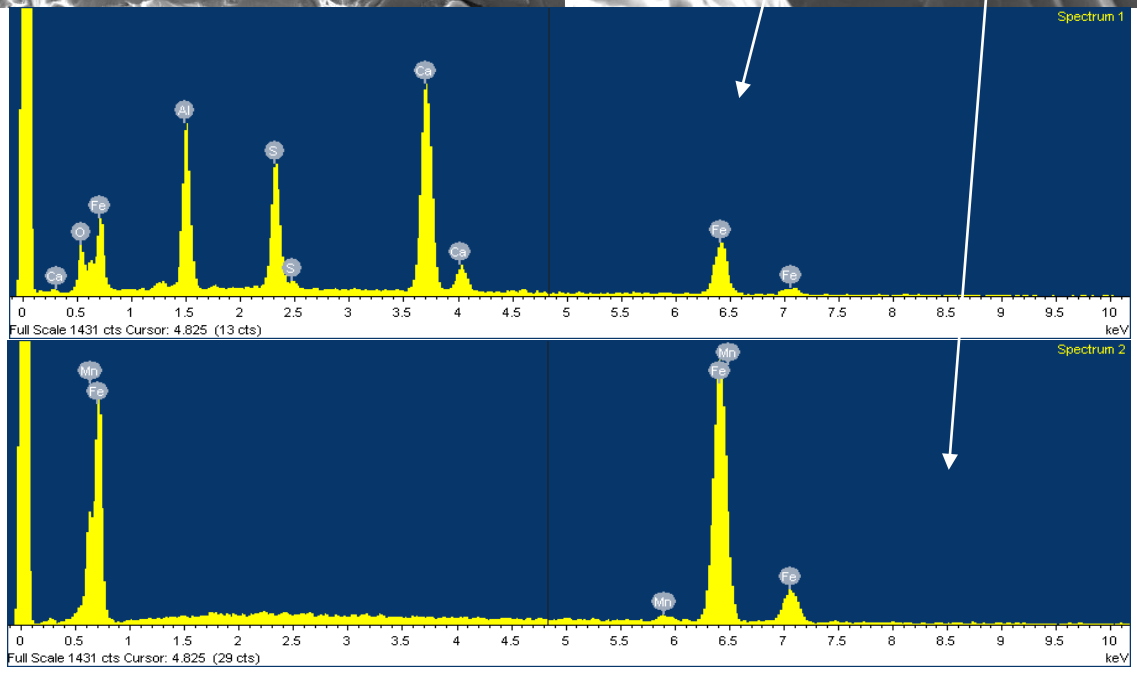

Figure 3.39

HT1-01 Crack Side Path under Optical Microscope (a) and SEM (b) (c)

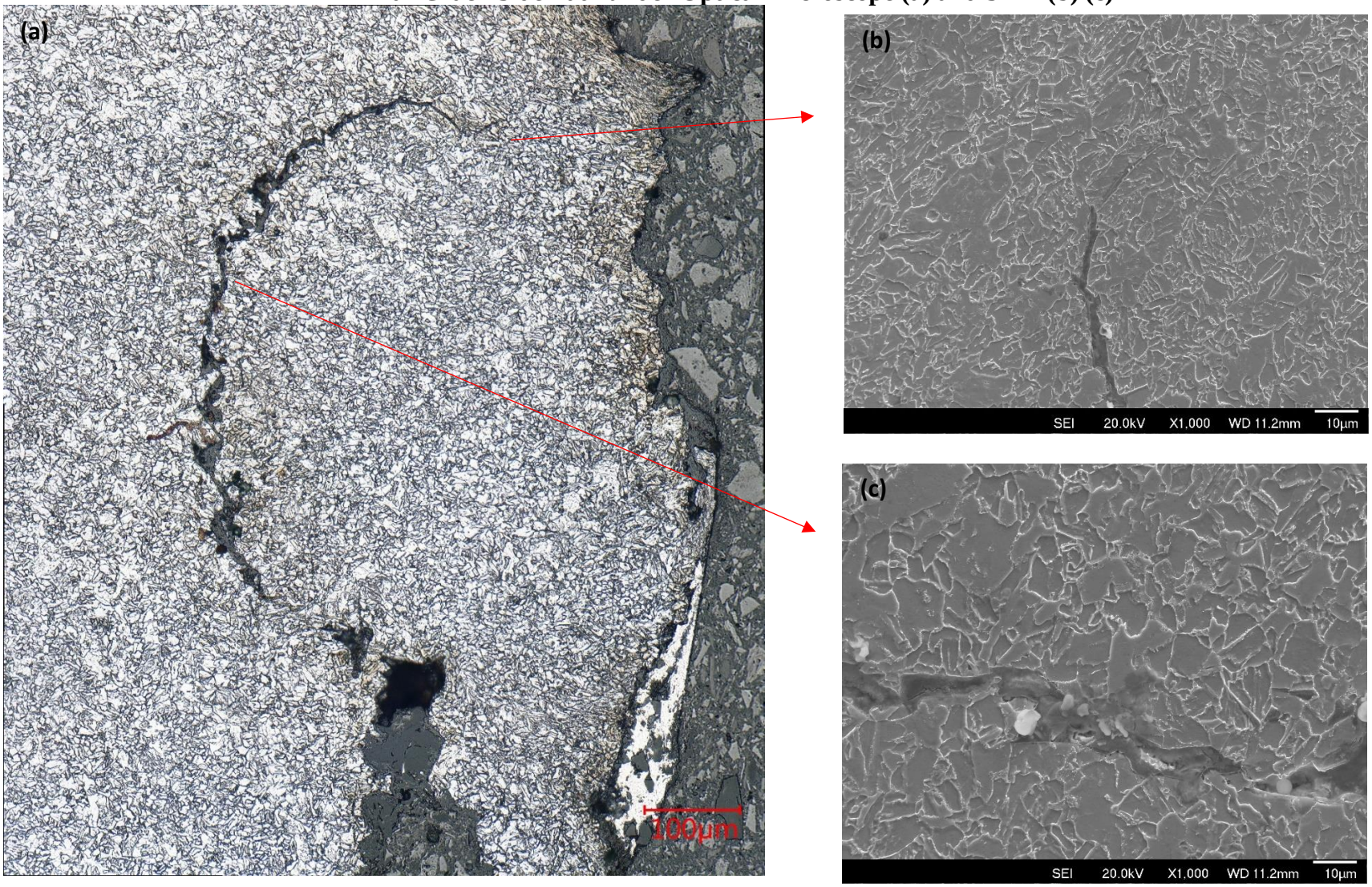

Figure 3.40

McMeeking Plot of Stress and Plastic Strain around the Blunted Notch (n = 0) [124]

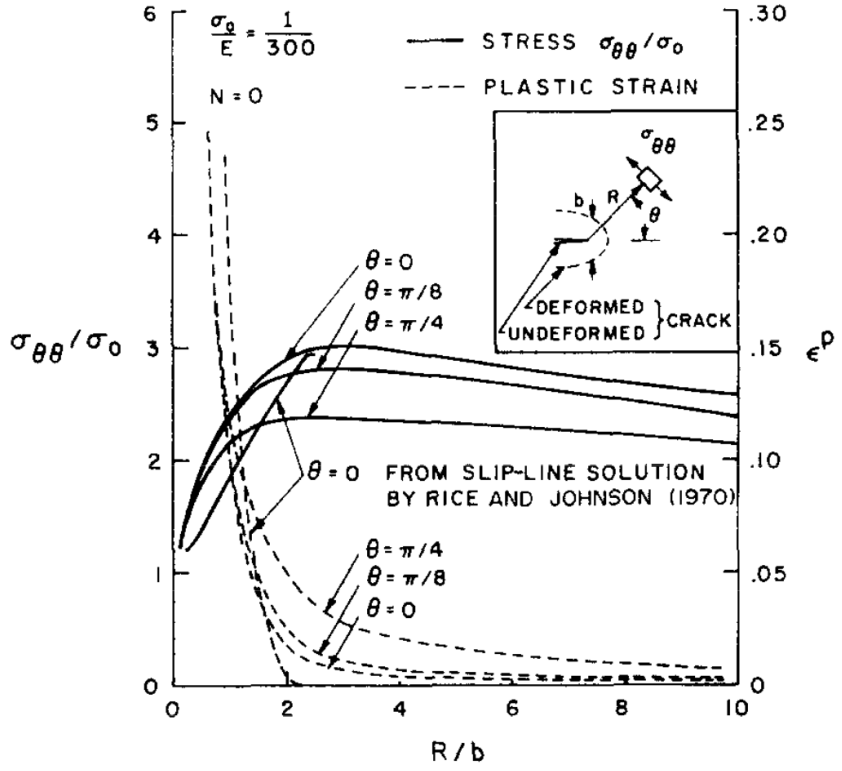

Figure 3.41

McMeeking Plot of Stress and Plastic Strain around the Blunted Notch (n = 0.1) [124]

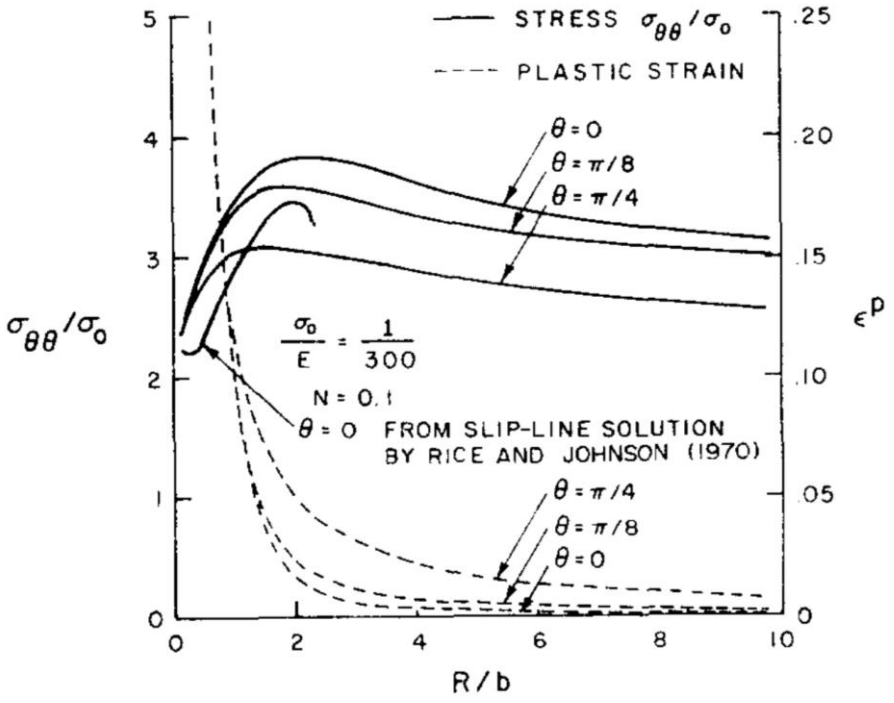

Figure 3.42

K_{Ic} Values versus Fracture distance X_0 of Fracture Toughness Specimens tested at -196 and -170°C

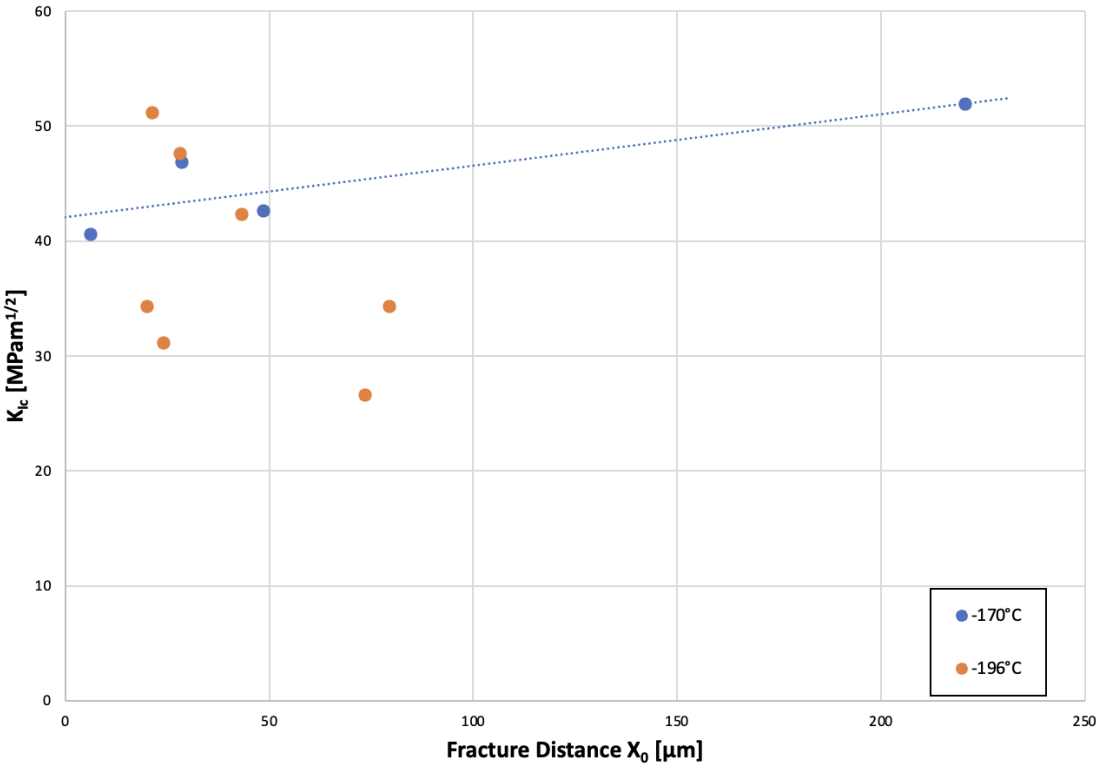

Figure 3.43

Local Cleavage Stress versus Fracture distance X_0 of Fracture Toughness Specimens tested at -196 and -170°C (n = 0)

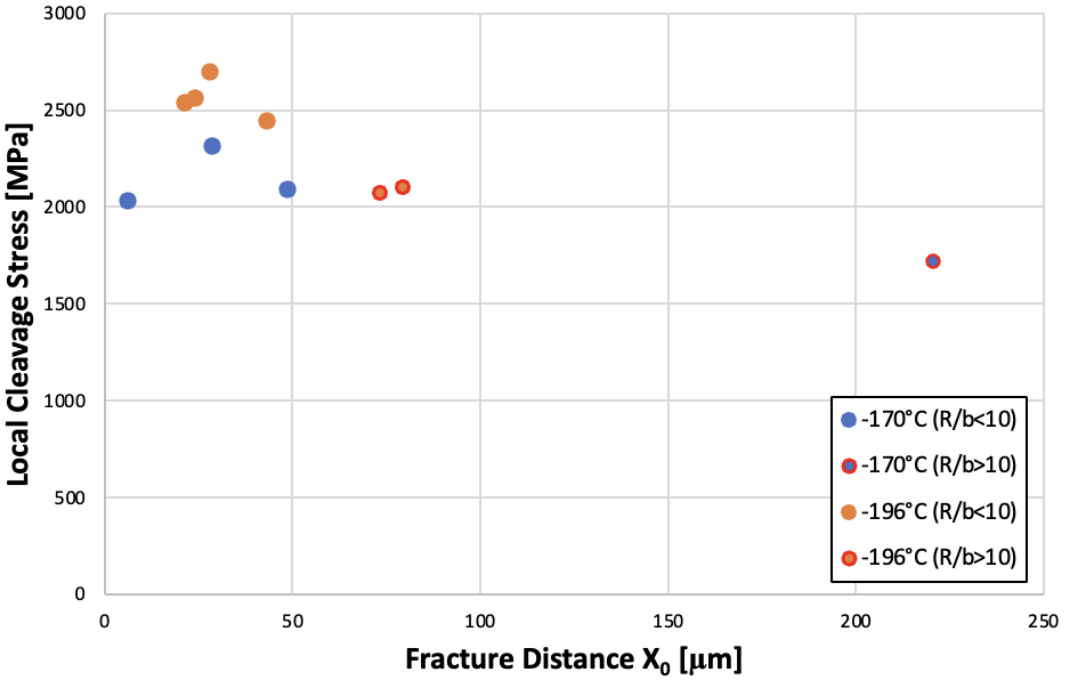

Figure 3.44

Local Cleavage Stress versus Maximum Principal Stress (McMeeking) of Fracture Toughness Specimens tested at -196 and -170°C (n = 0)

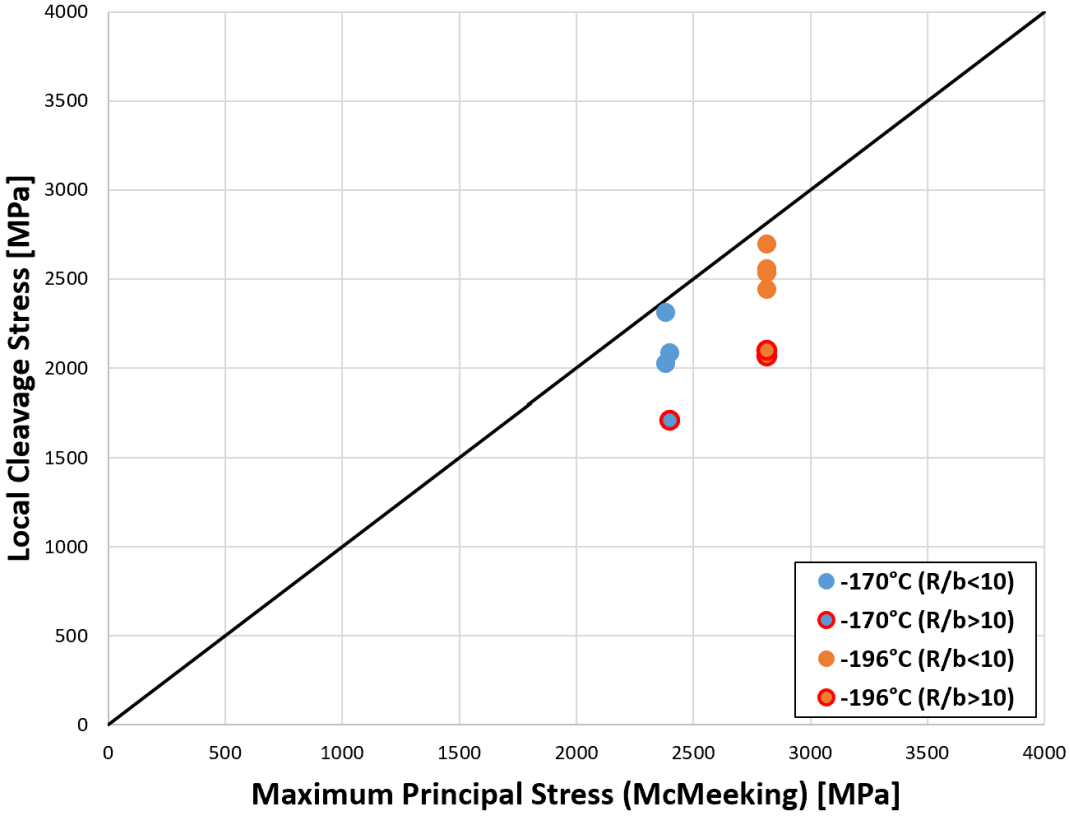

Figure 3.45

Local Cleavage Stress of Fracture Toughness Specimens tested at -196 and -170°C versus Test Temperatures (n = 0)

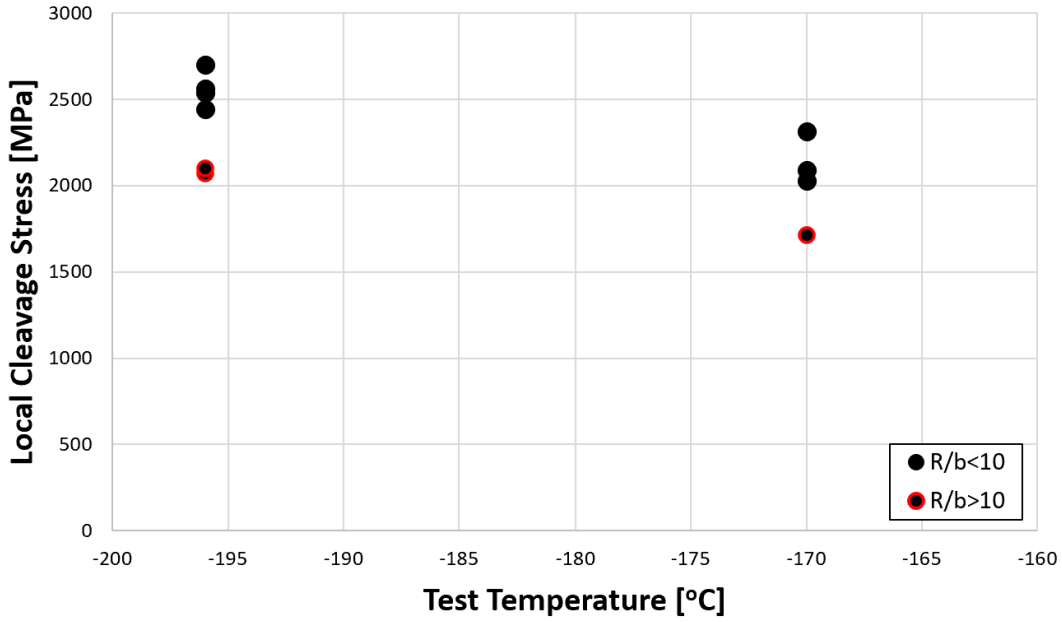

Figure 3.46

Local Cleavage Stress versus Reciprocal Square Root of Inclusion Diameter (0.93 to 3.33µm found from Cleavage Initiation Site (n = 0)

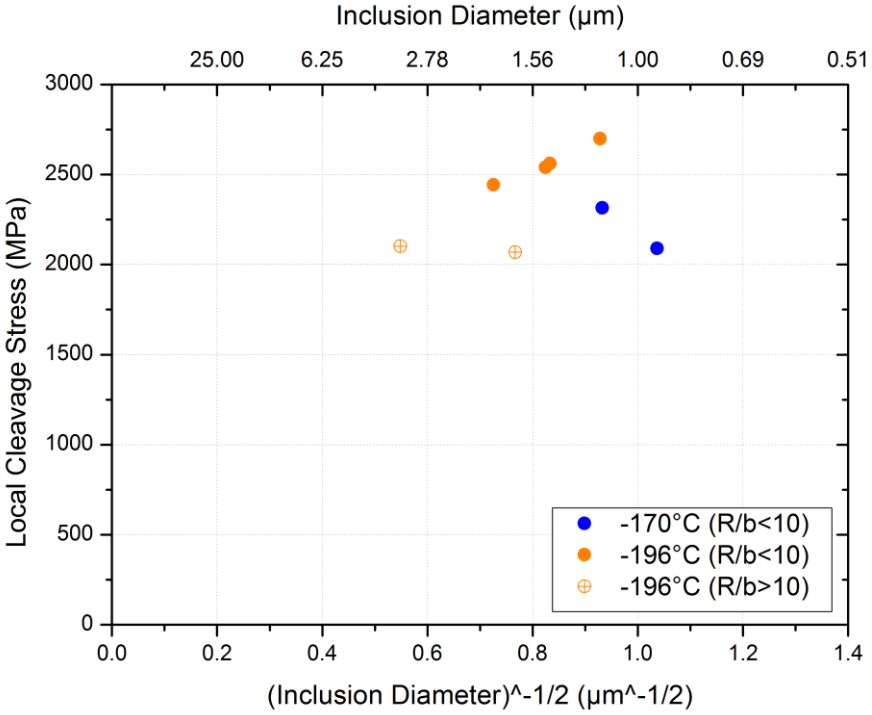

*Estimated γ_p through the modified Griffith equation ranging from 5.6 to 20.3 Jm^{-2}.

Figure 3.47

Local Cleavage Stress versus Reciprocal Square Root of Facet Diameter (42 to 80 µm) found from Cleavage Initiation Sites (n = 0)

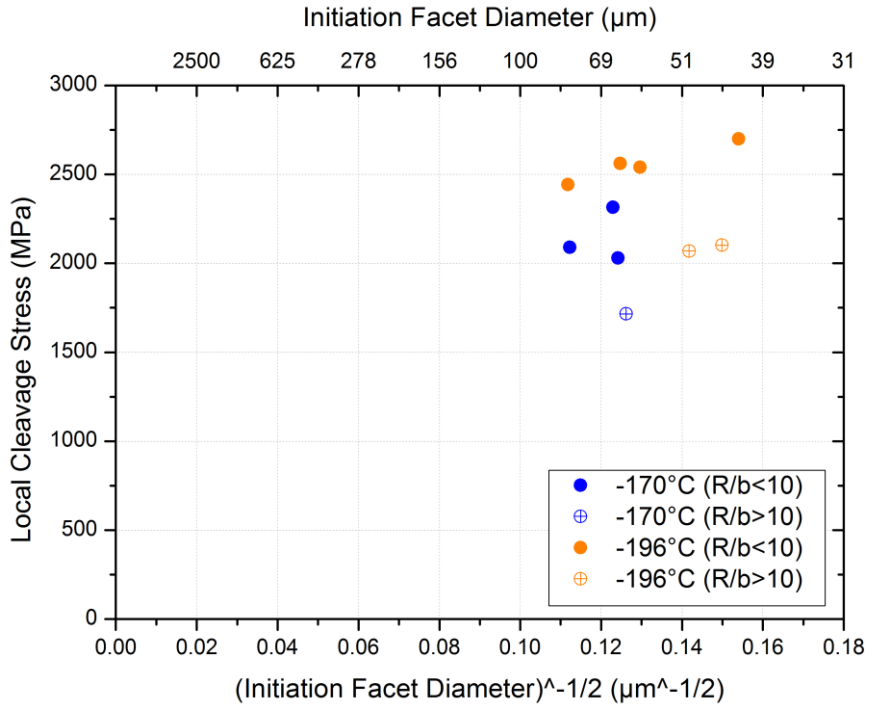

Figure 3.48

Local Cleavage Stress versus Fracture Distance of Sharp-Cracked Specimens (McMeeking FEM Analysis) tested at -196 to -80°C and Blunt-Notched Specimens (Griffiths FEM Analysis) tested at -196°C and -170°C

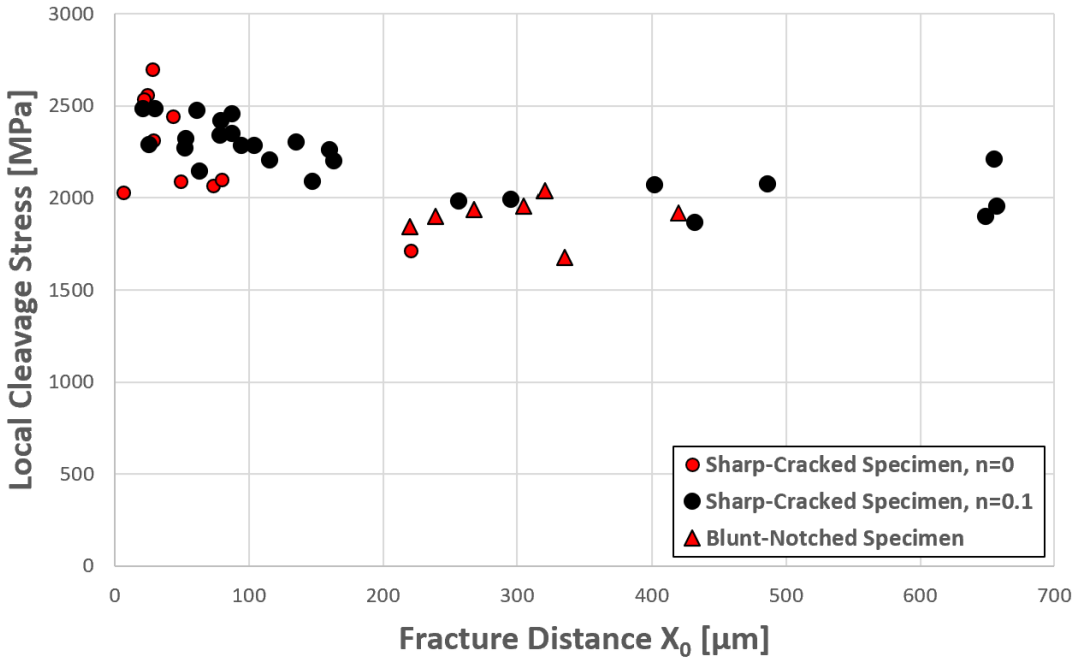

Figure 3.49

Local Cleavage Stress versus Test Temperature of Sharp-Cracked Specimens (McMeeking FEM Analysis) tested at -196 to -80°C and Blunt-Notched Specimens (Griffiths FEM Analysis) tested at -196°C and -170°C

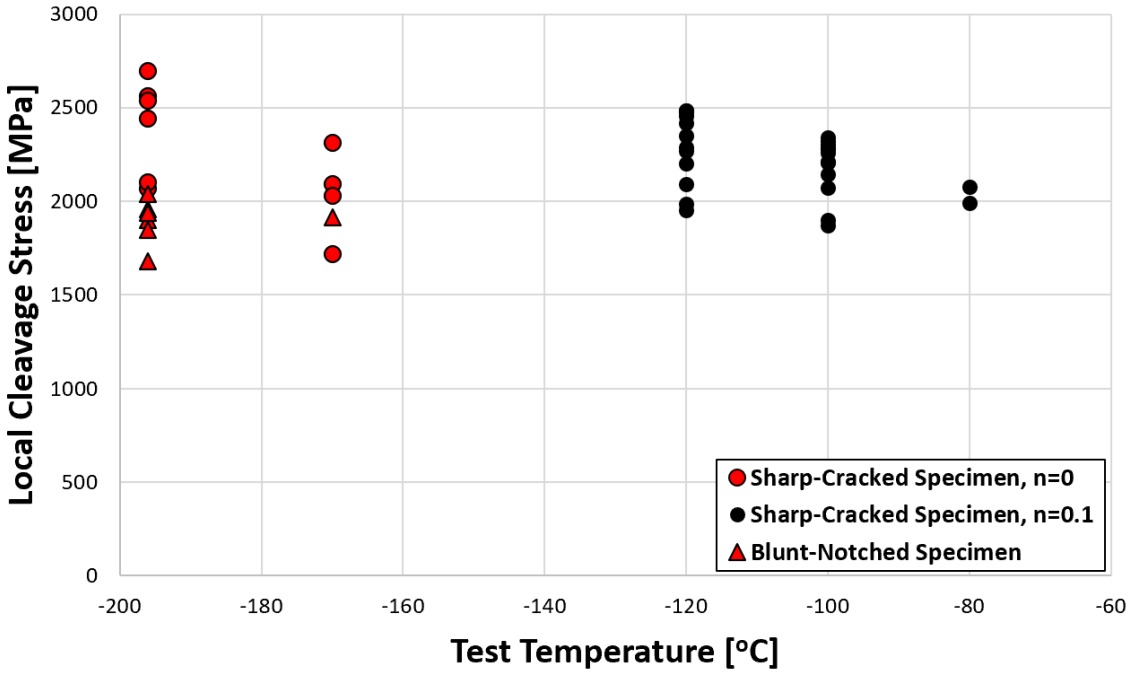

Figure 3.50

Local Cleavage Stress versus Maximum Principal Stress of Sharp-Cracked Specimens (McMeeking FEM Analysis) tested at -196 to -80°C and Blunt-Notched Specimens (Griffiths FEM Analysis) tested at -196°C and -170°C

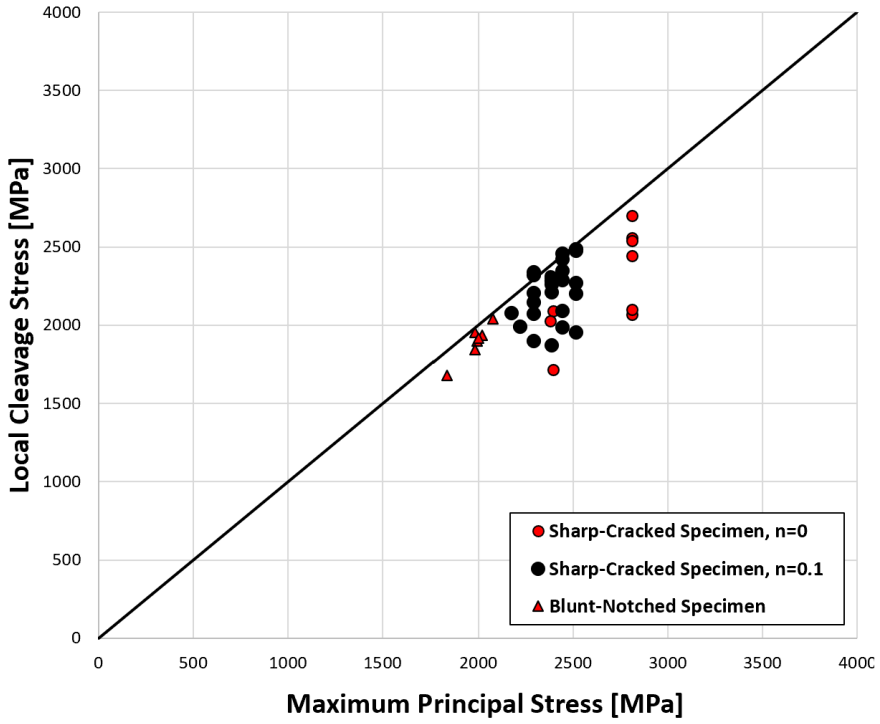

Figure 3.51

Local Cleavage Stress versus Reciprocal of Square Root of Inclusion Diameter of Sharp-Cracked Specimens (McMeeking FEM Analysis) tested at -196 to -80°C and Blunt-Notched Specimens (Griffiths FEM Analysis) tested at -196°C and -170°C

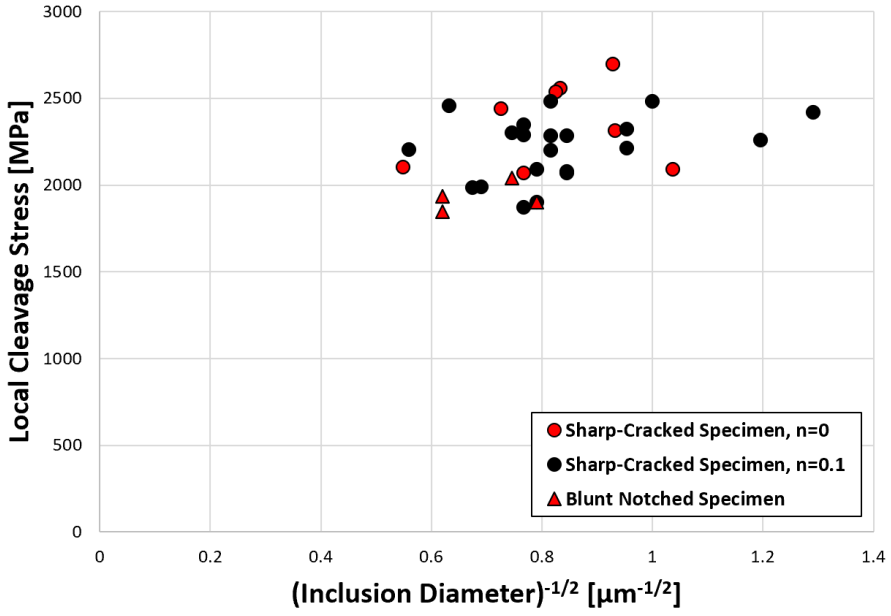

HT1-06

Figure 3.52

Fractography of Fracture Toughness Specimen HT1-06 tested at -170°C

(a): Fracture surface of HT1-06 after fatigue precrack. The possible initiation site is circled in red.

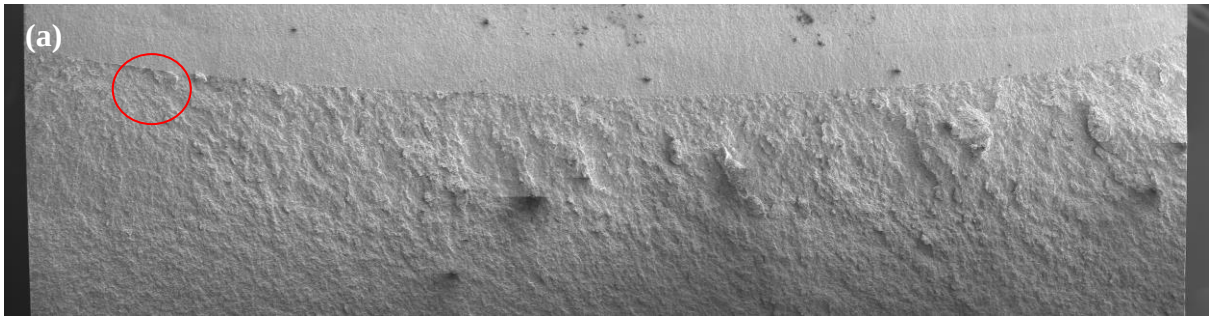

(b), (c), (d), (e): detail of circled site in magnification sequence.

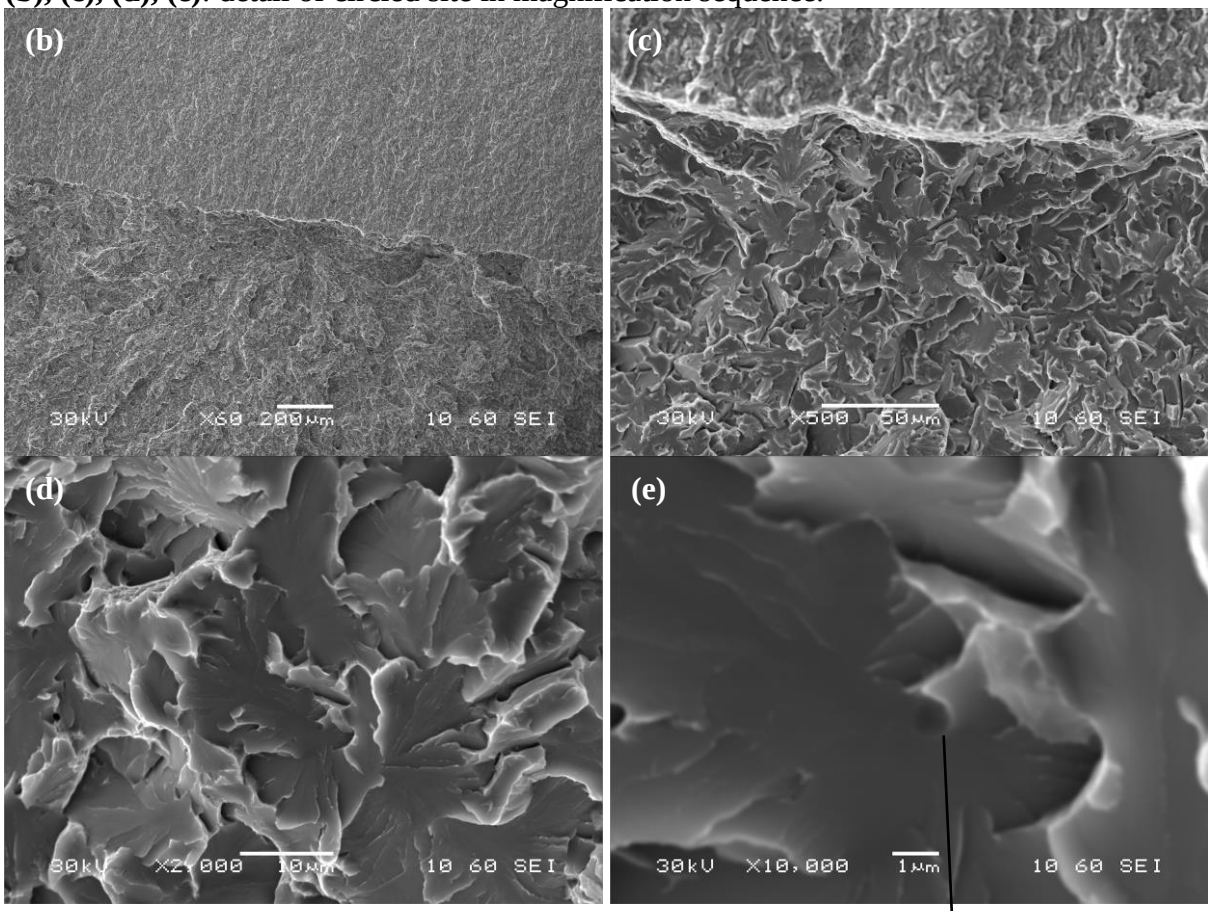

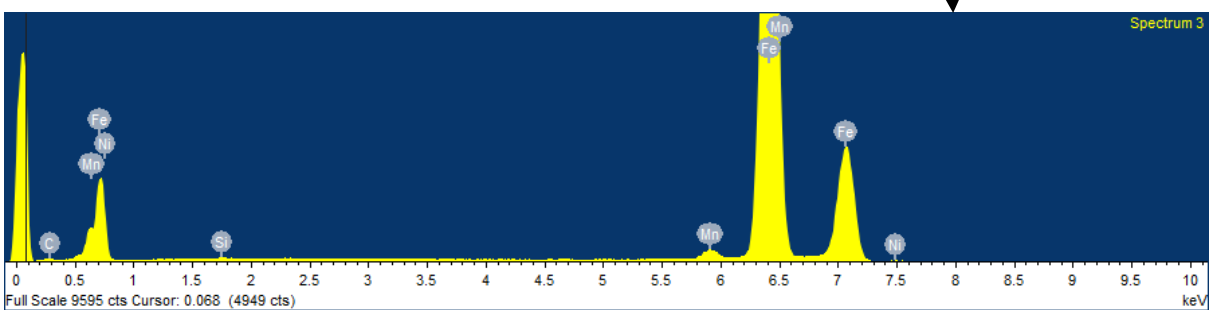

HT1-06

Figure 3.52

Fractography of Fracture Toughness Specimen HT1-06 tested at -170°C

(f), (g), (h), (i): detail of circled site in magnification sequence on **opposite** side.

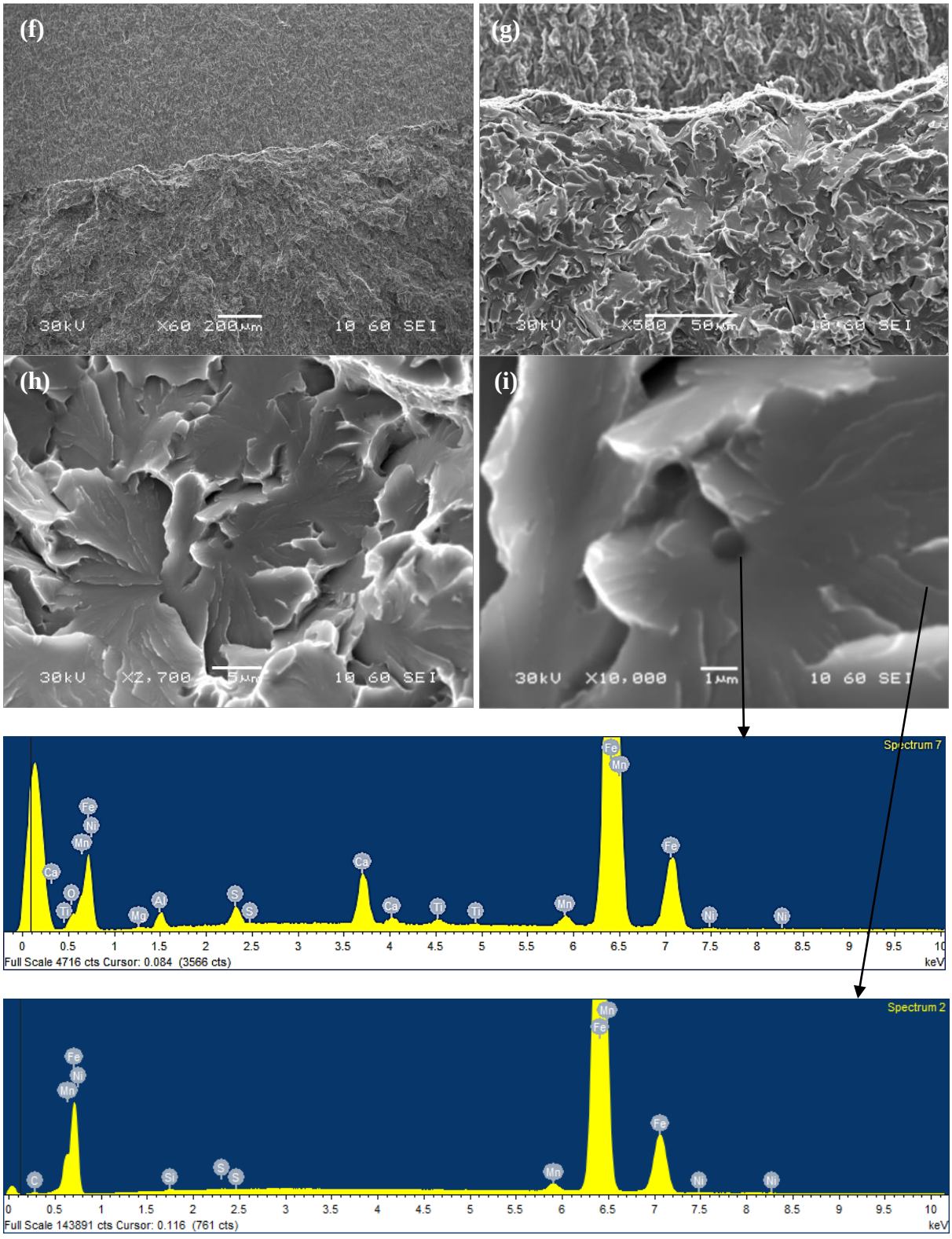

HT1-12

Figure 3.53

Fractography of Fracture Toughness Specimen HT1-12 tested at -170°C

(a): Fracture surface after fatigue precracking. The possible initiation site is circled in red.

(b), (c), (d), (e): detail of circled site in magnification sequence.

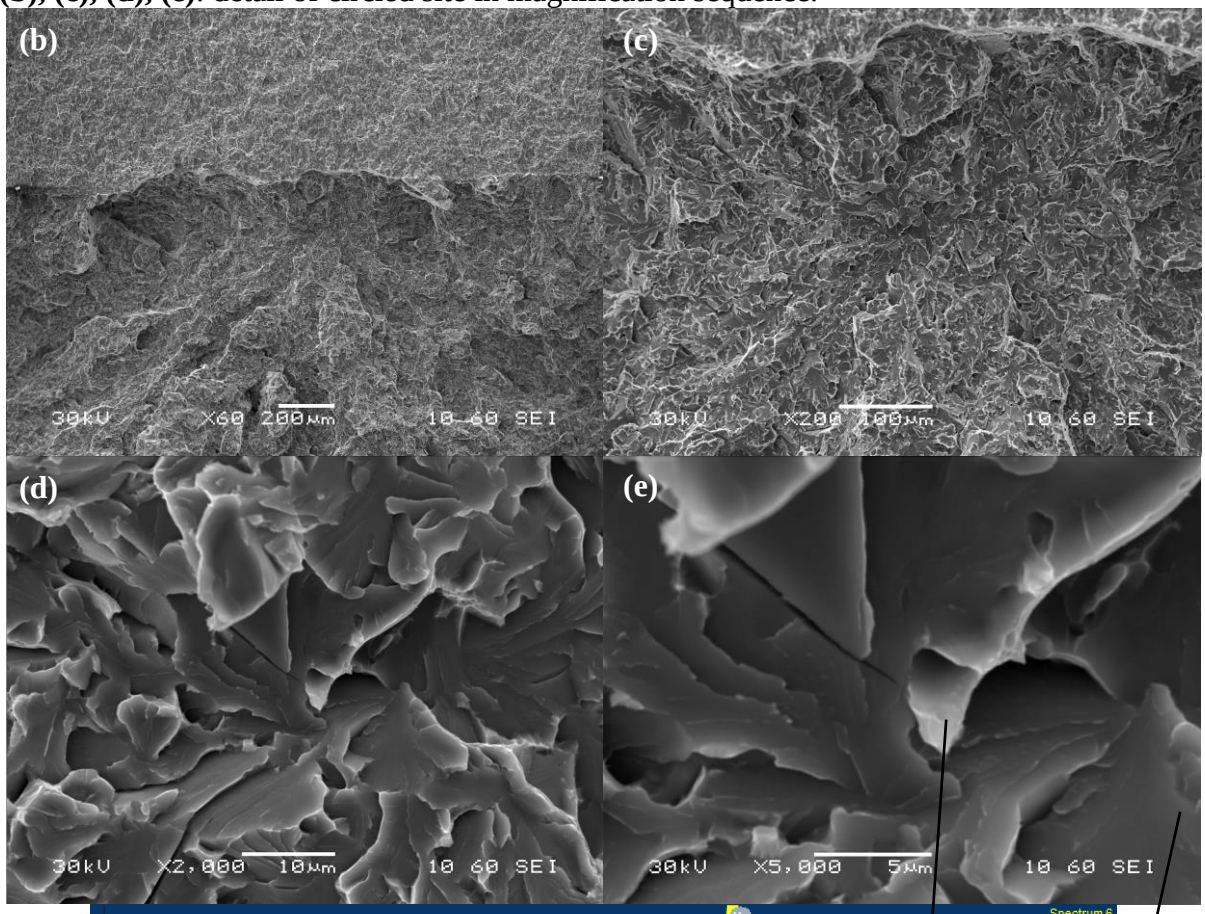

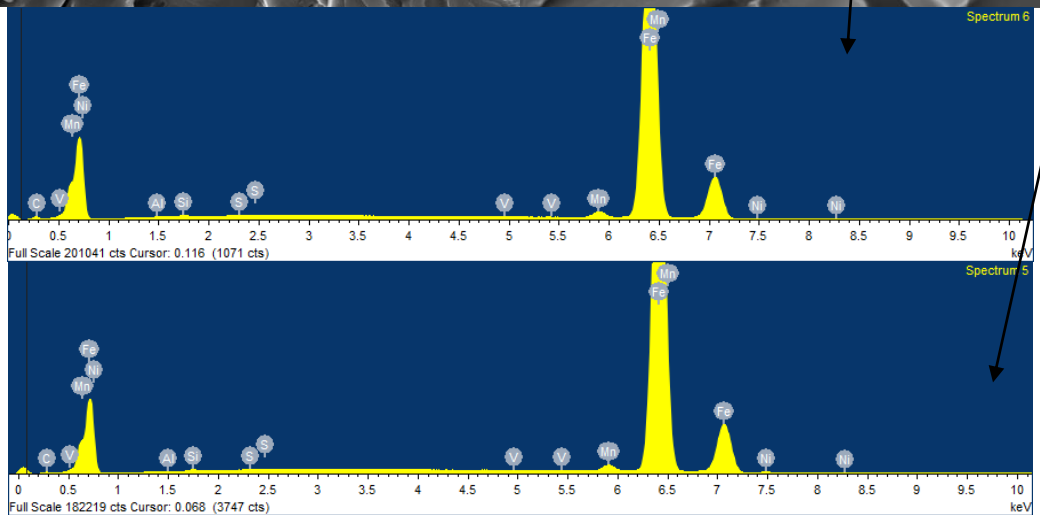

HT1-12

Figure 3.53

Fractography of Fracture Toughness Specimen HT1-12 tested at -170°C

(f), (g), (h), (i): detail of circled site in magnification sequence on opposite side.

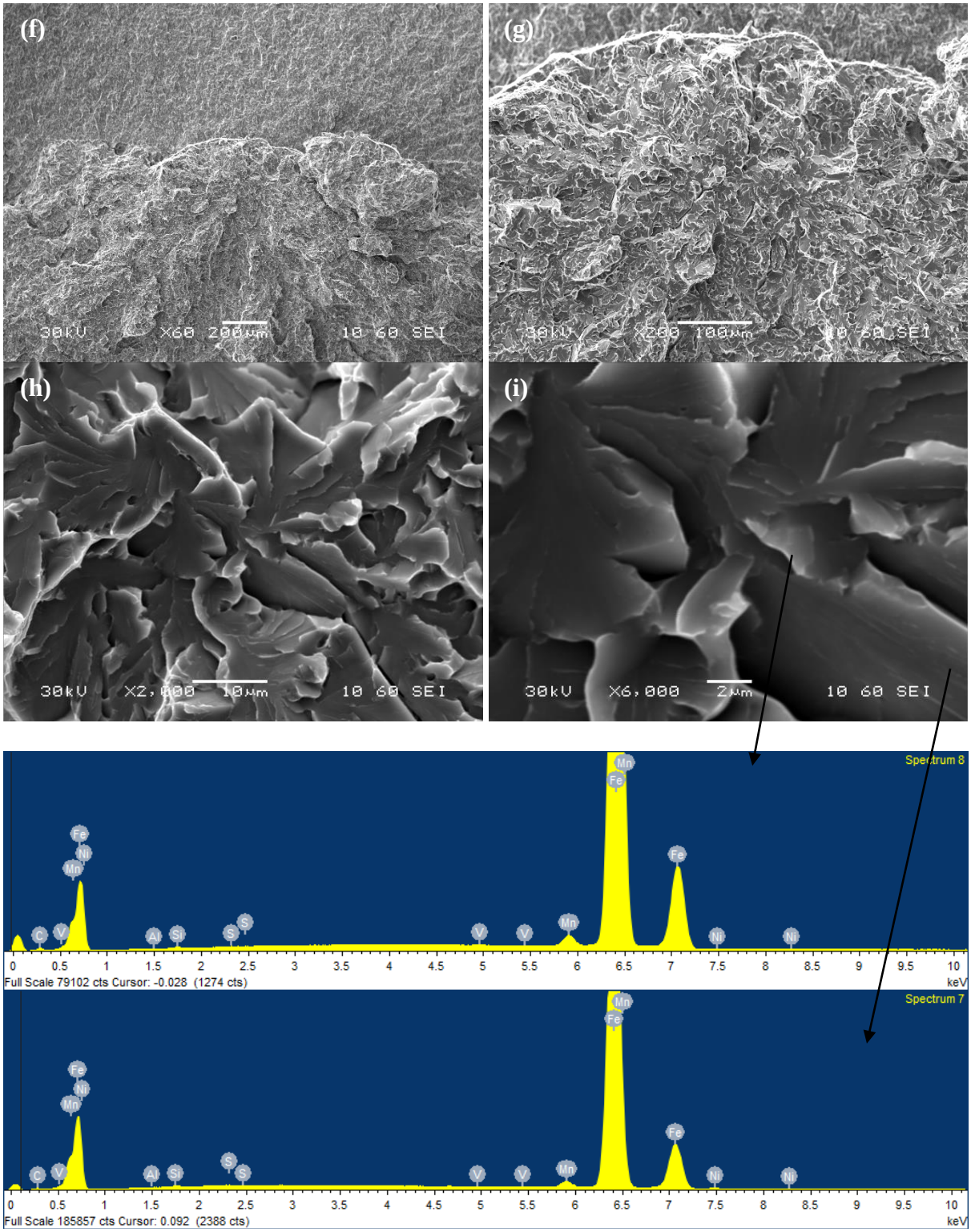

HT2-15

Figure 3.54

Fractography of Fracture Toughness Specimen HT2-15 tested at -170ºC

(a): Fracture surface after fatigue precracking. The possible initiation site is circled in red.

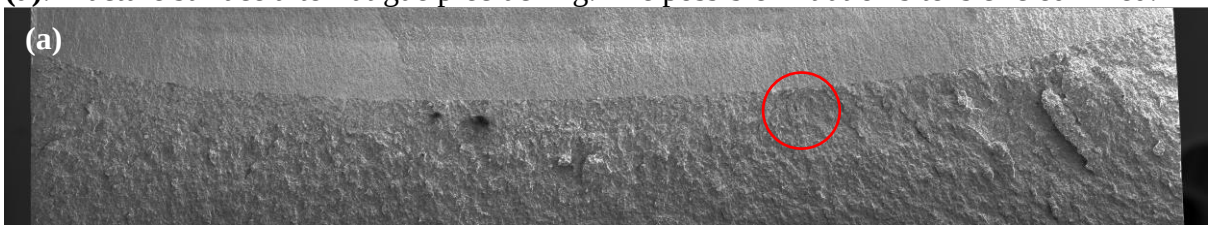

(b), (c), (d), (e): detail of circled site in magnification sequence.

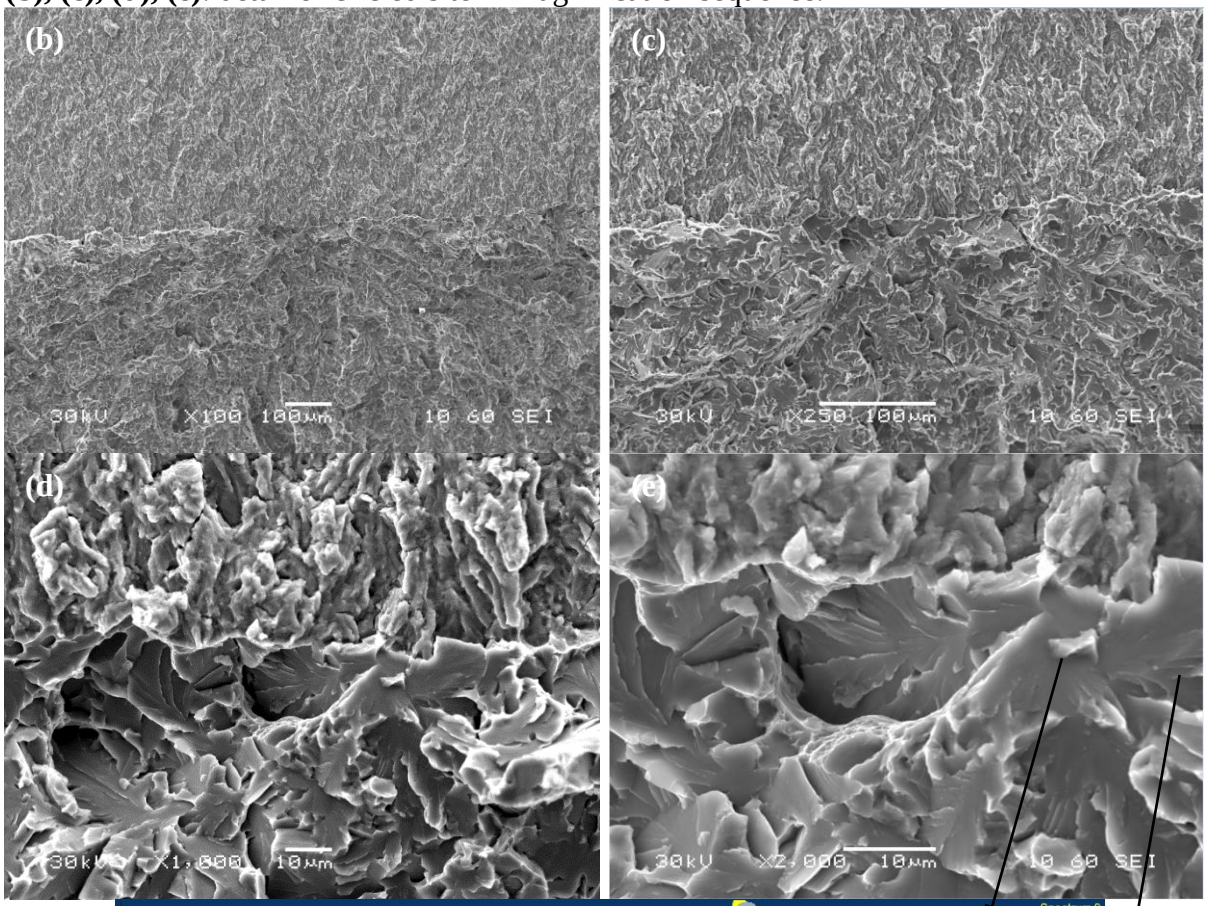

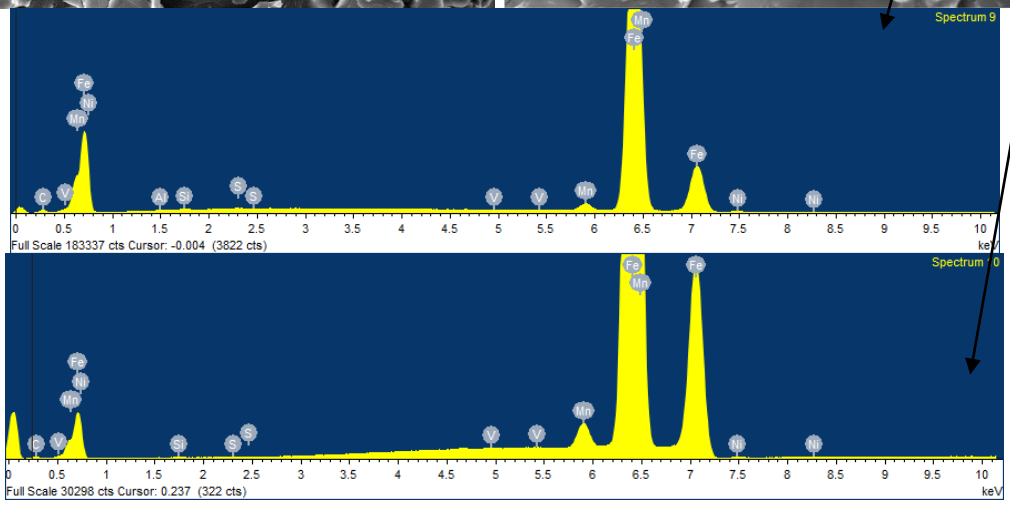

HT2-15

Figure 3.54

Fractography of Fracture Toughness Specimen HT2-15 tested at -170°C

(f), (g), (h), (i): detail of circled site in magnification sequence on opposite side.

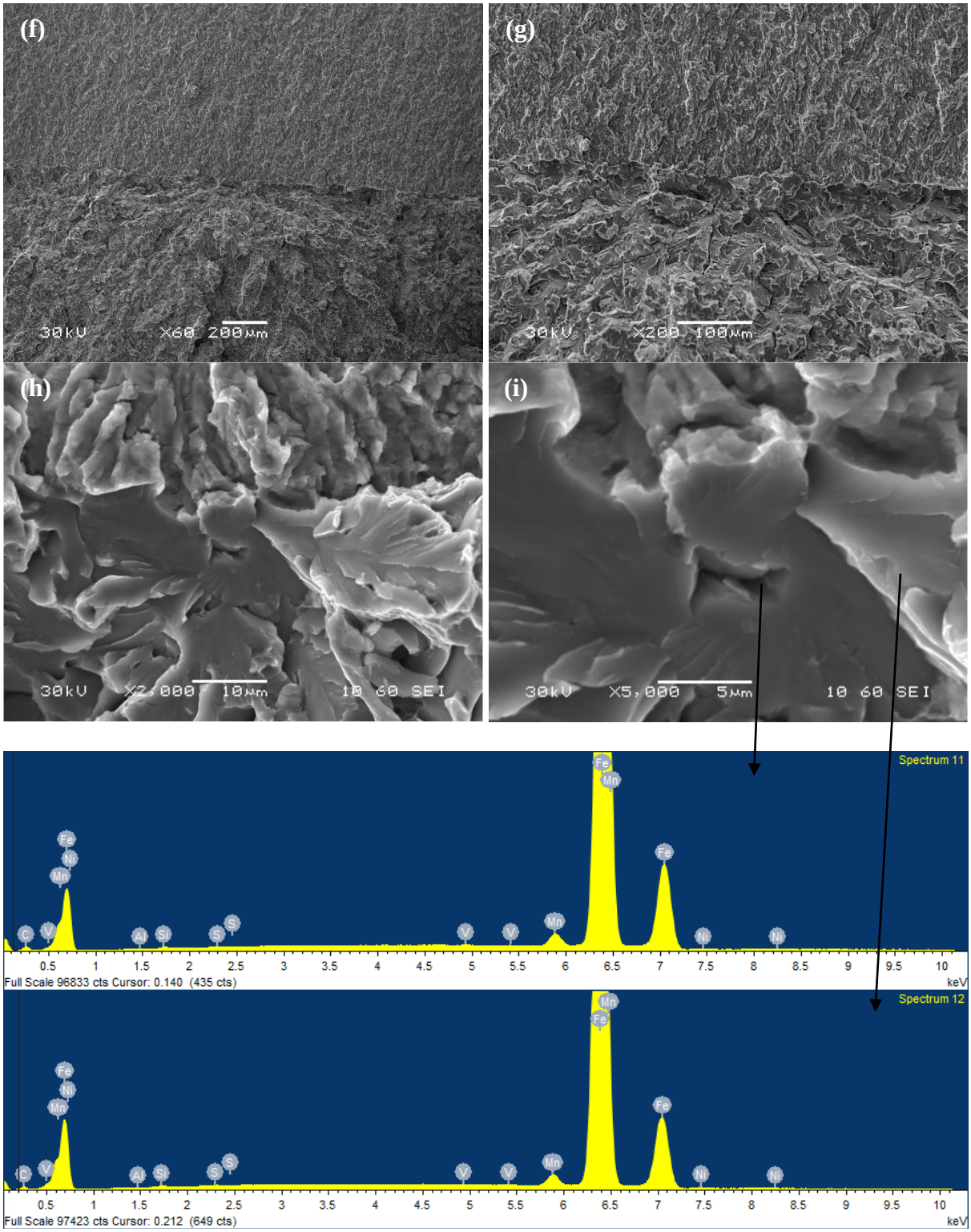

HT2-17

Figure 3.55

Fractography of Fracture Toughness Specimen HT2-17 tested at -170ºC

(a): Fracture surface after fatigue precracking. The possible initiation site is circled in red.

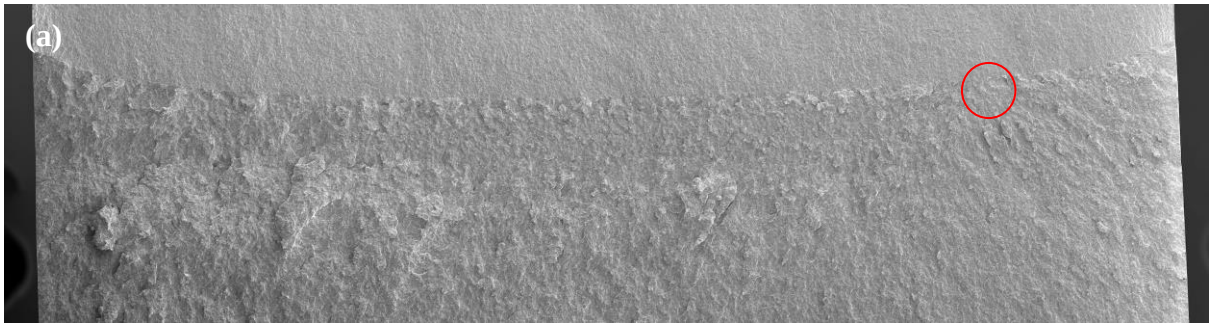

(b), (c), (d), (e): detail of circled site in magnification sequence.

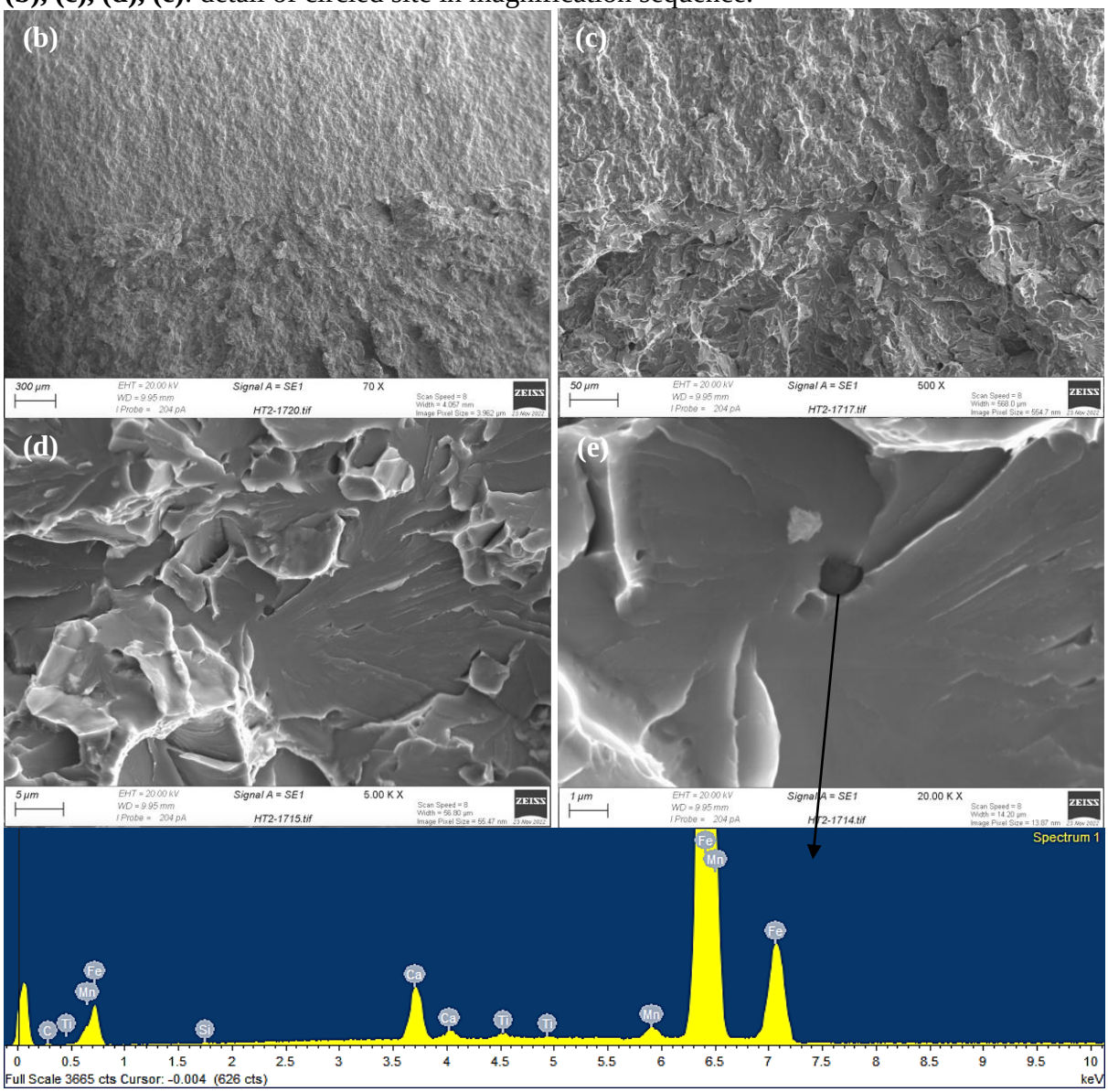

HT2-17

Figure 3.55

Fractography of Fracture Toughness Specimen HT2-17 tested at -170°C

(f), (g), (h), (i): detail of circled site in magnification sequence on opposite side.

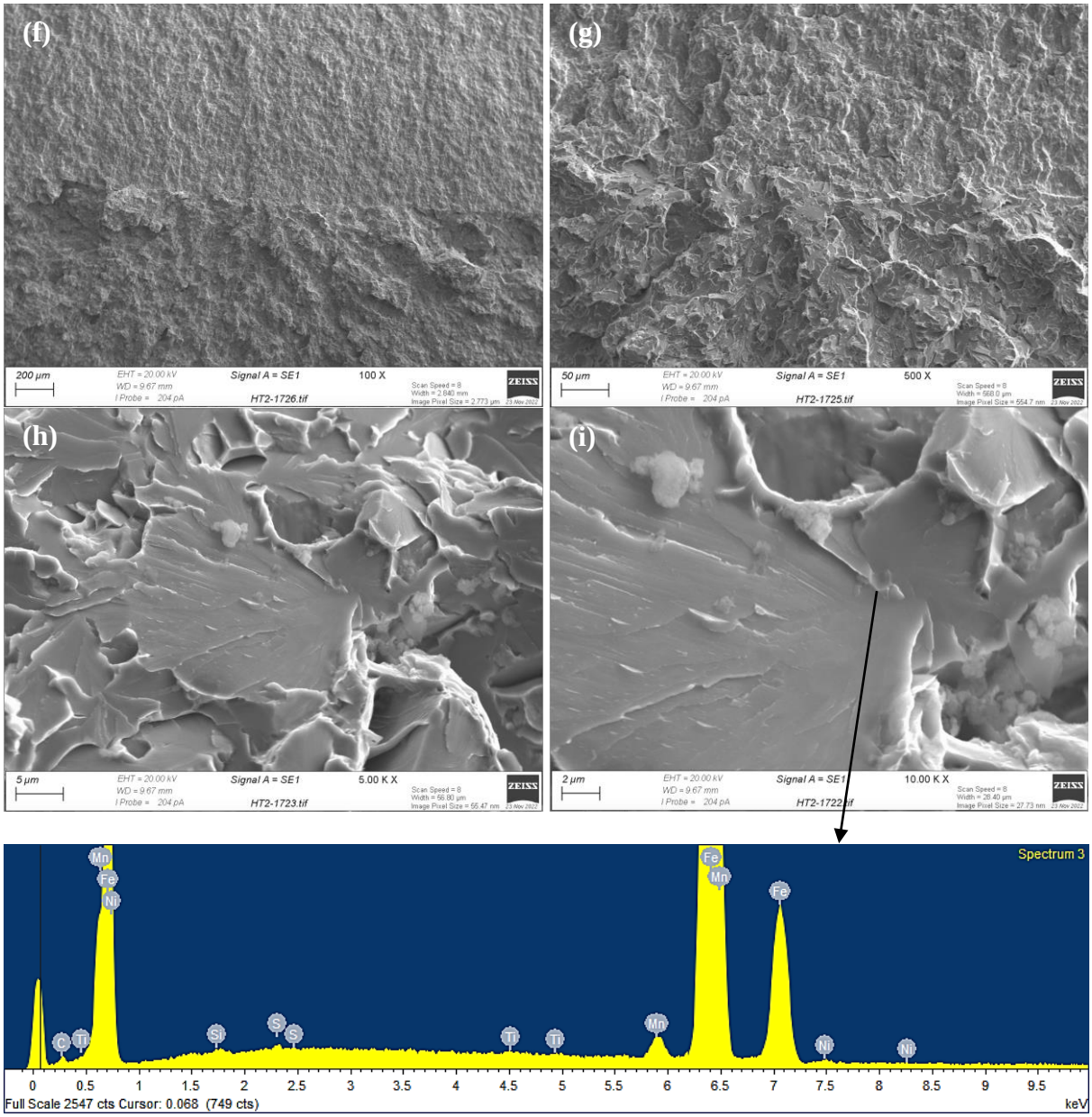

HT1LT-4

Figure 3.56

Fractography of Fracture Toughness Specimen HT1LT-4 tested at -196ºC

(a): Fracture surface after fatigue precracking. The possible initiation site is circled in red.

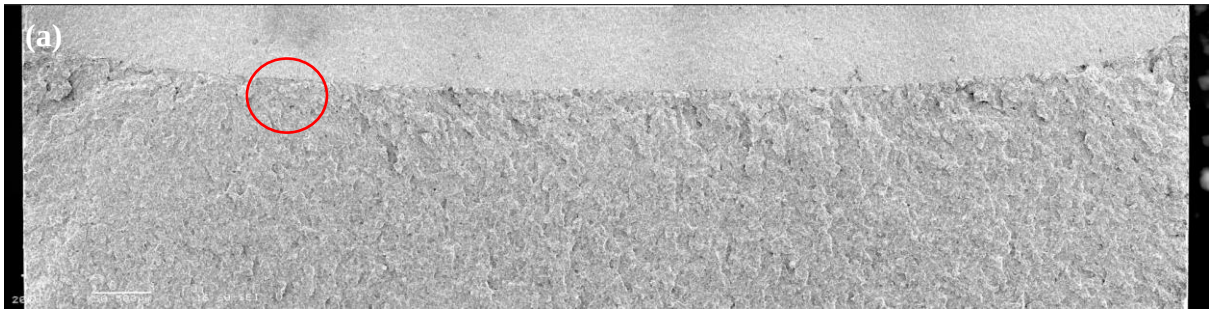

(b), (c), (d), (e): detail of circled site in magnification sequence.

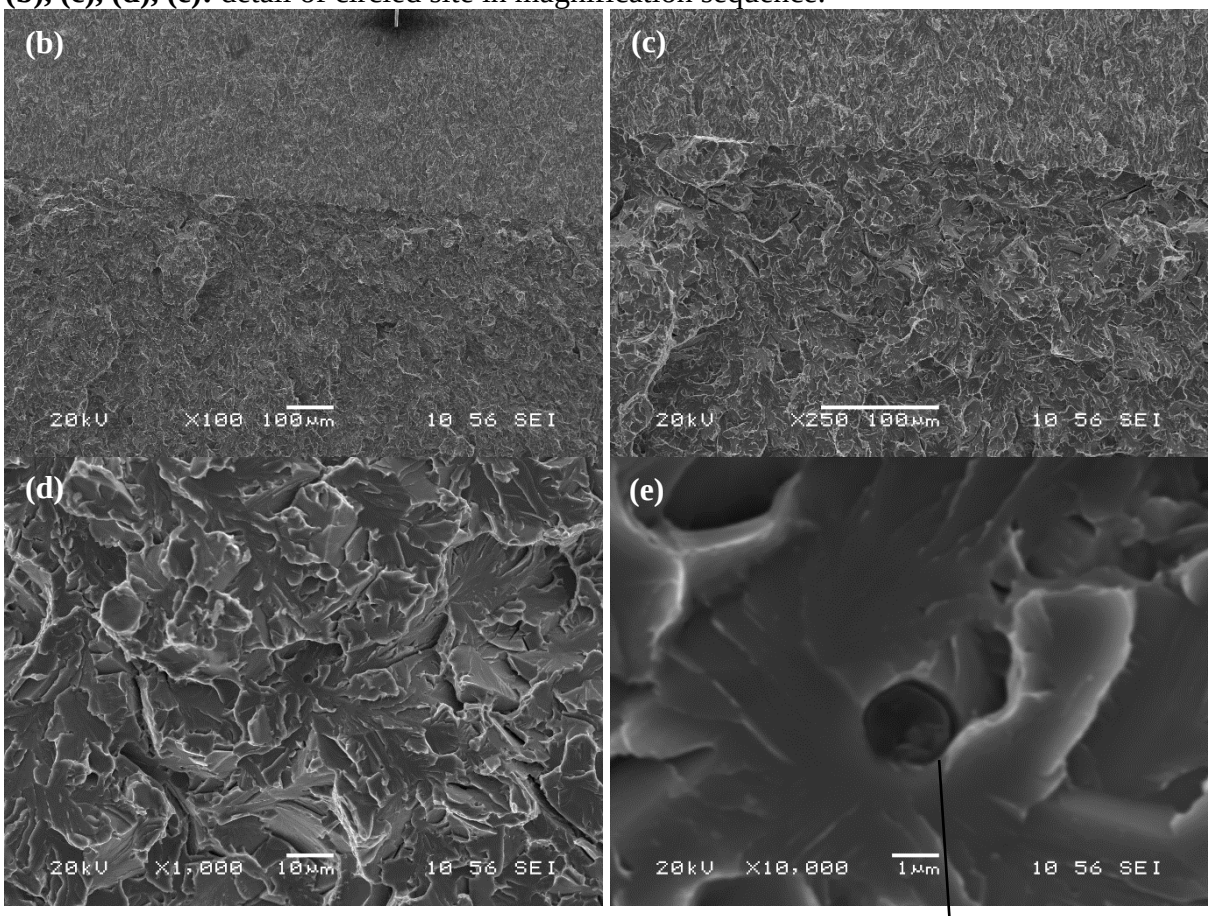

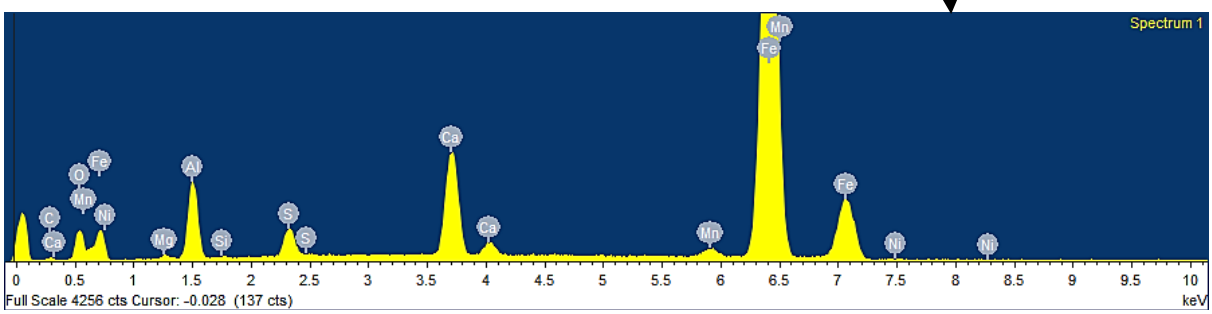

HT1LT-4

Figure 3.56

Fractography of Fracture Toughness Specimen HT1LT-4 tested at -196ºC

(f), (g), (h), (i): detail of circled site in magnification sequence on opposite side.

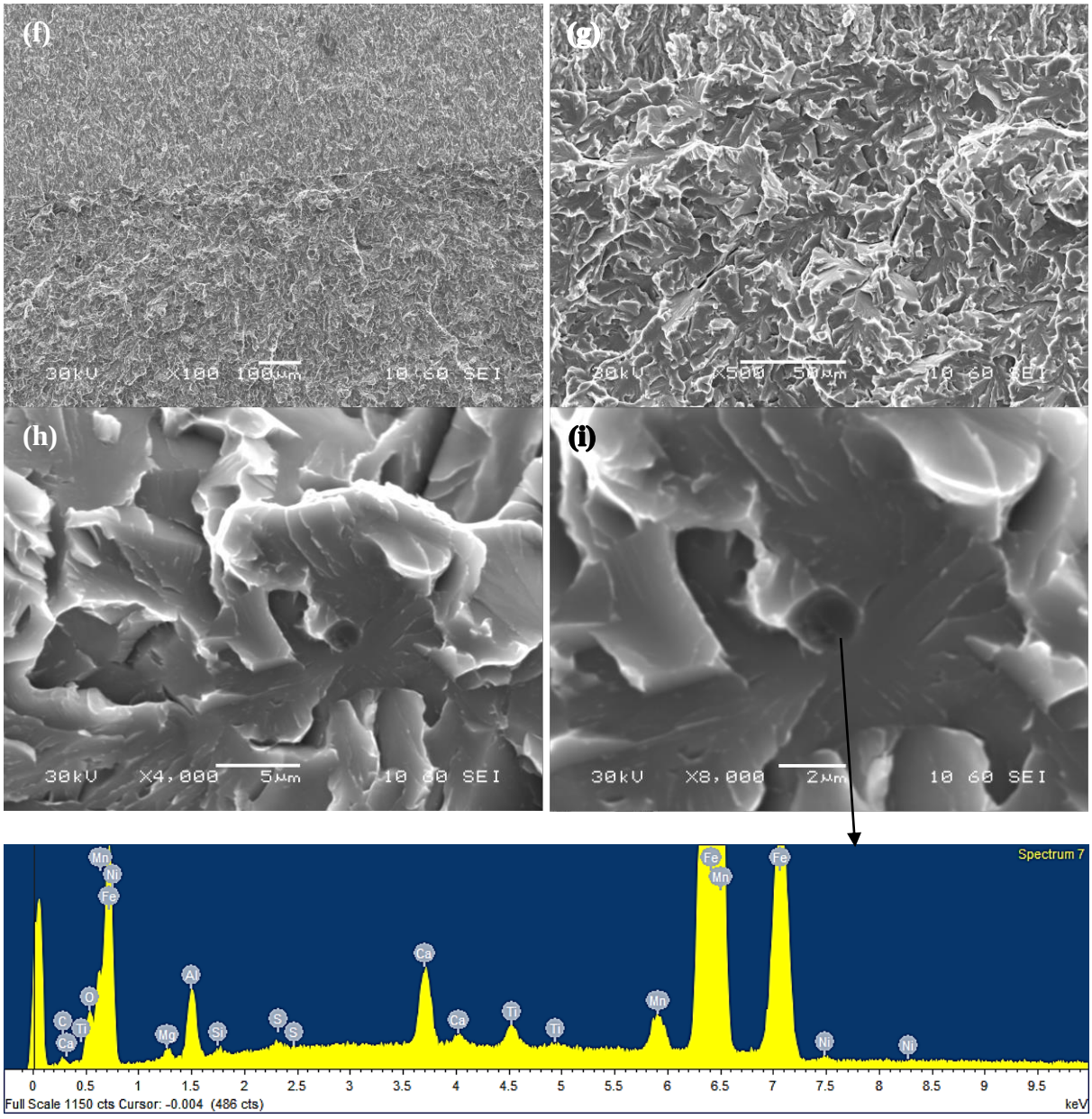

HT1LT-5

Figure 3.57

Fractography of Fracture Toughness Specimen HT1LT-5 tested at -196ºC

(a): Fracture surface after fatigue precracking. The possible initiation site is circled in red.

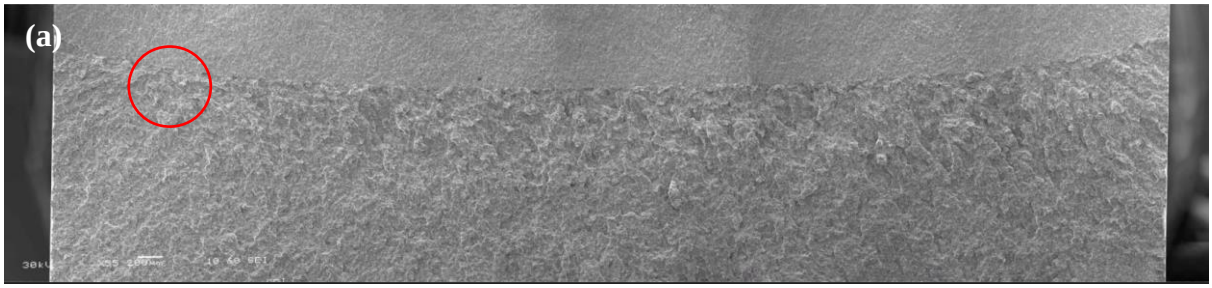

(b), (c), (d), (e): detail of circled site in magnification sequence.

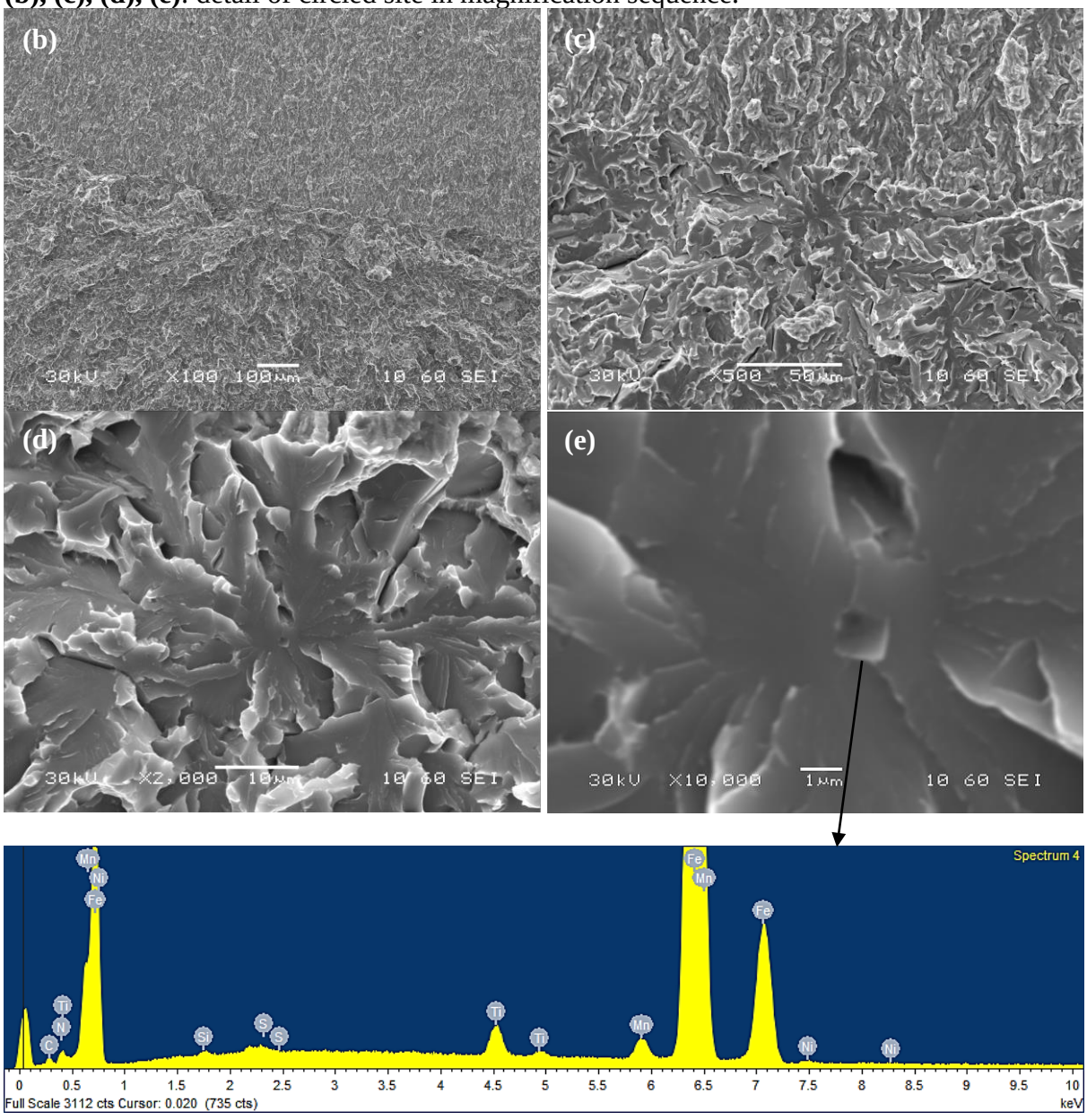

HT1LT-5

Figure 3.57

Fractography of Fracture Toughness Specimen HT1LT-5 tested at -196ºC

(f), (g), (h), (i): detail of circled site in magnification sequence on opposite side.

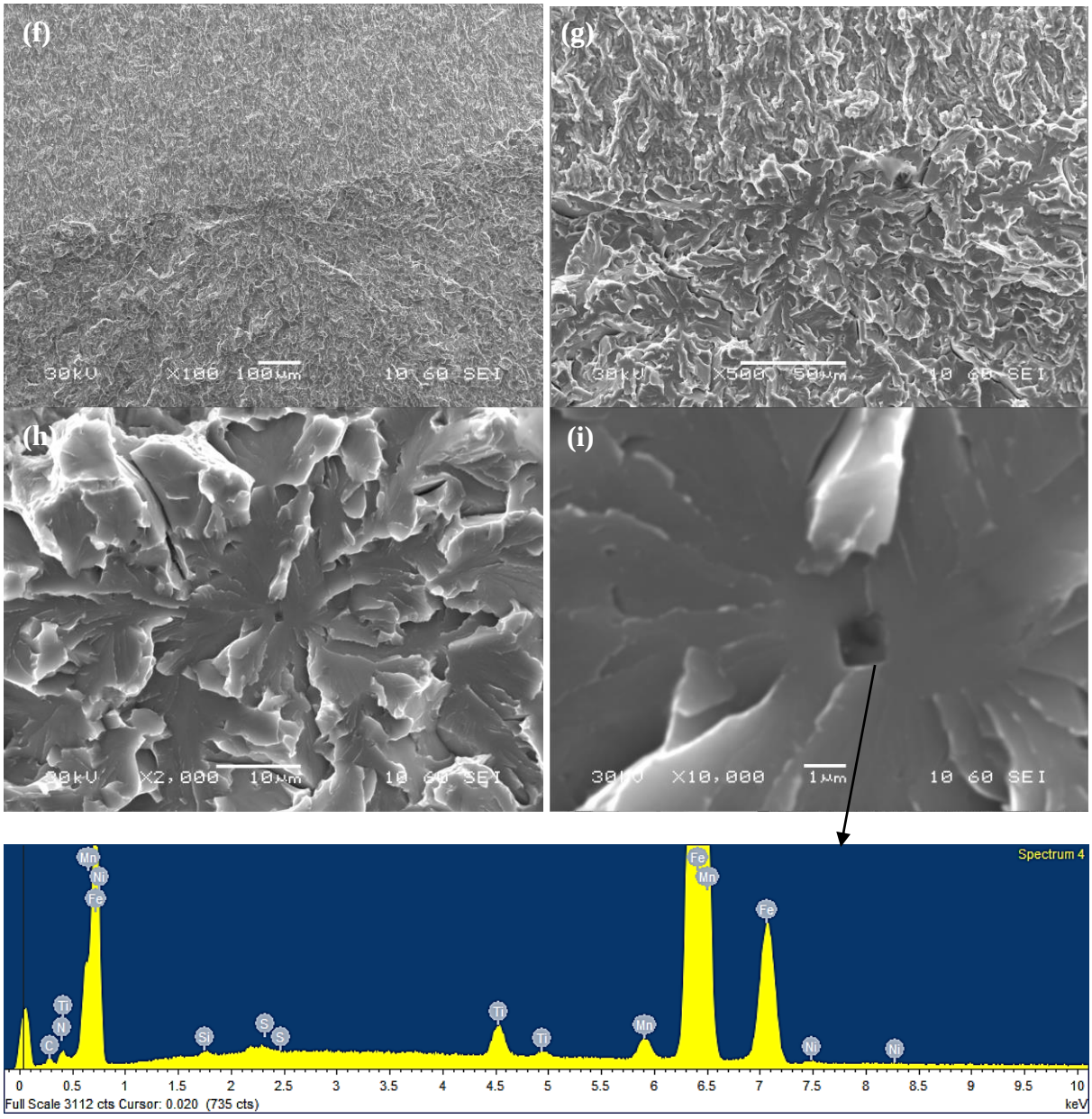

HT1LT-6

Figure 3.58

Fractography of Fracture Toughness Specimen HT1LT-6 tested at -196ºC

(a): Fracture surface after fatigue precracking. The possible initiation site is circled in red.

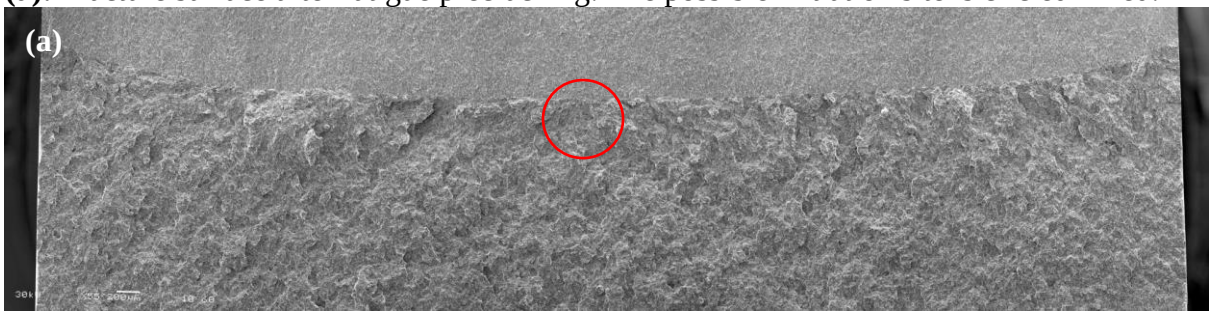

(b), (c), (d), (e): detail of circled site in magnification sequence.

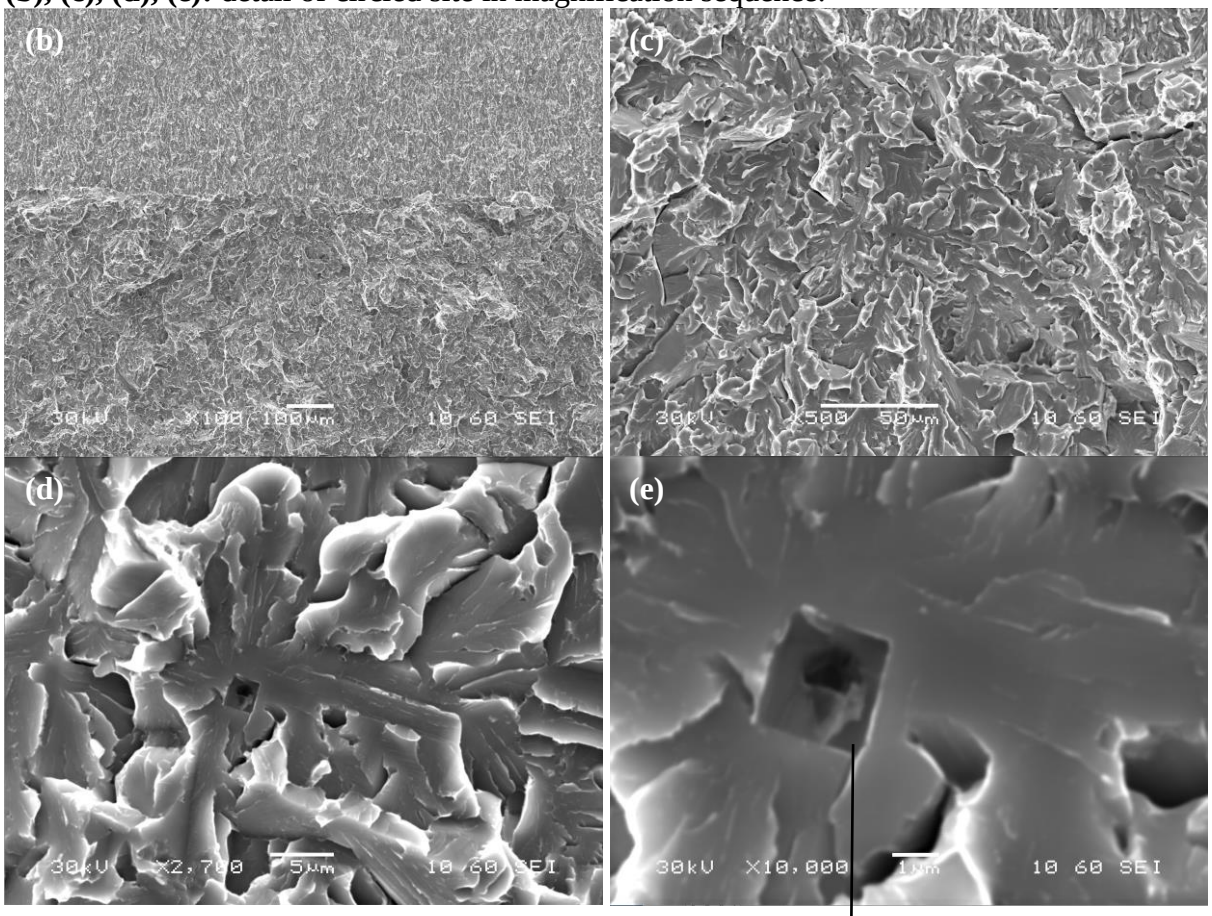

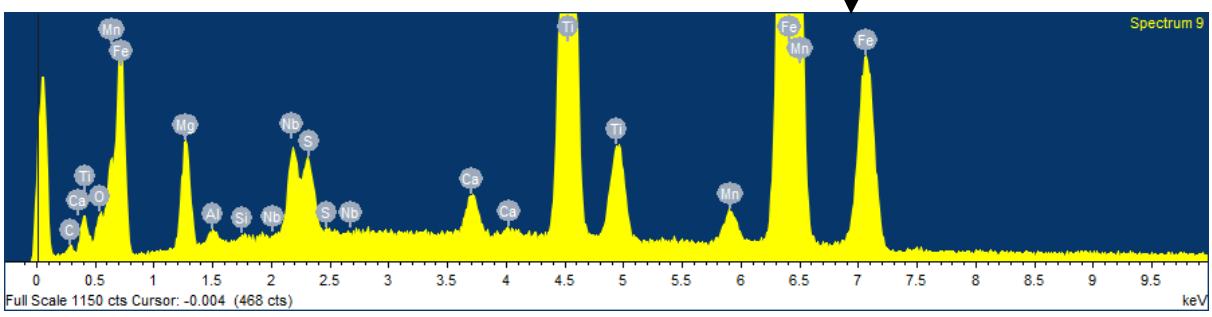

HT1LT-6

Figure 3.58

Fractography of Fracture Toughness Specimen HT1LT-6 tested at -196ºC

(f), (g), (h), (i): detail of circled site in magnification sequence on opposite side.

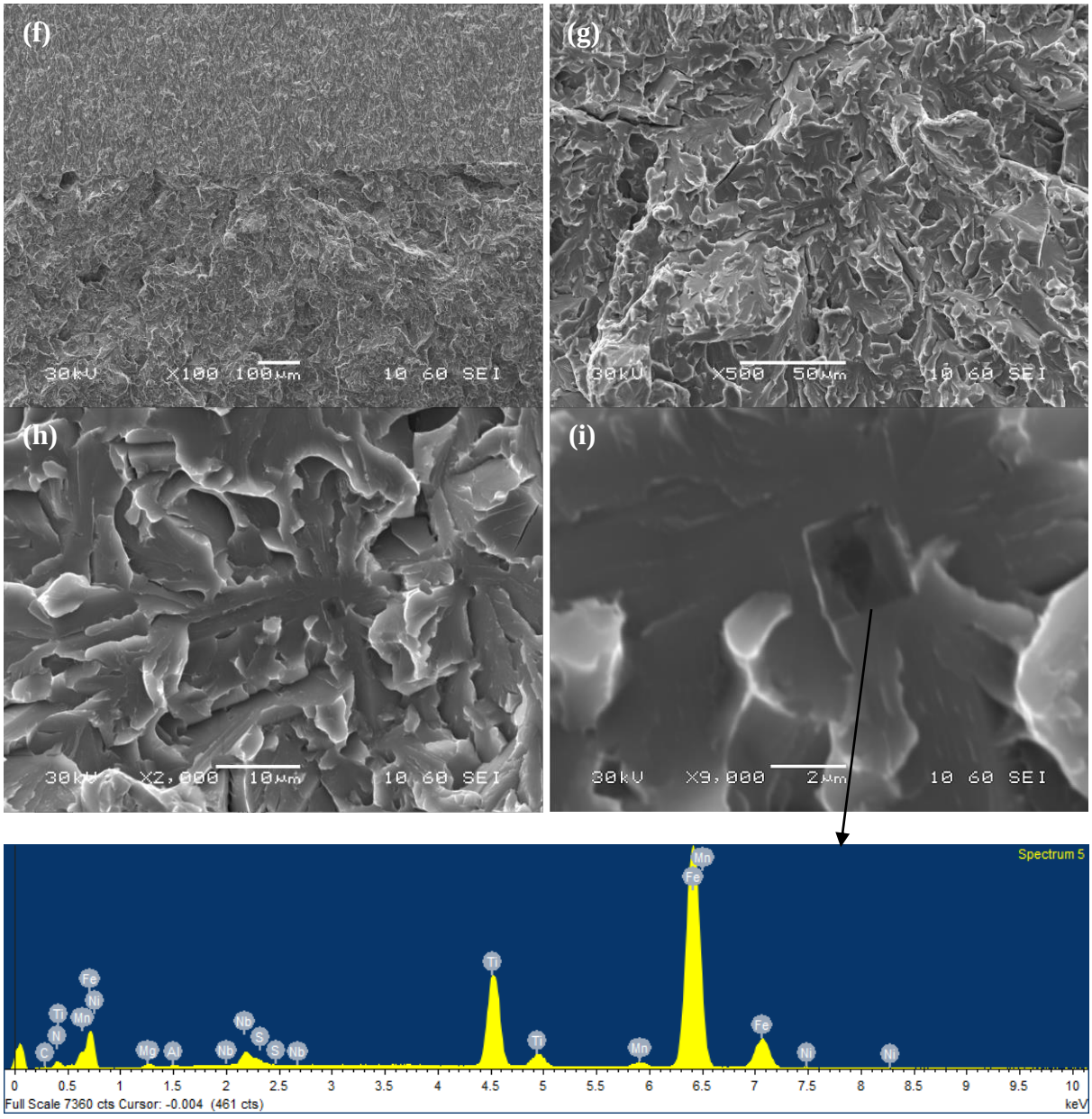

HT1TL-D

Figure 3.59

Fractography of Fracture Toughness Specimen HT1TL-D tested at -196ºC

(a): Fracture surface after fatigue precracking. The possible initiation site is circled in red.

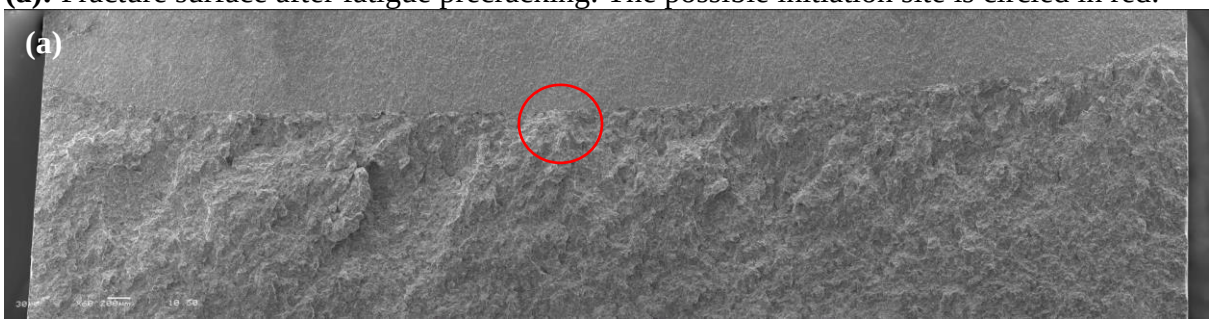

(b), (c), (d), (e): detail of circled site in magnification sequence.

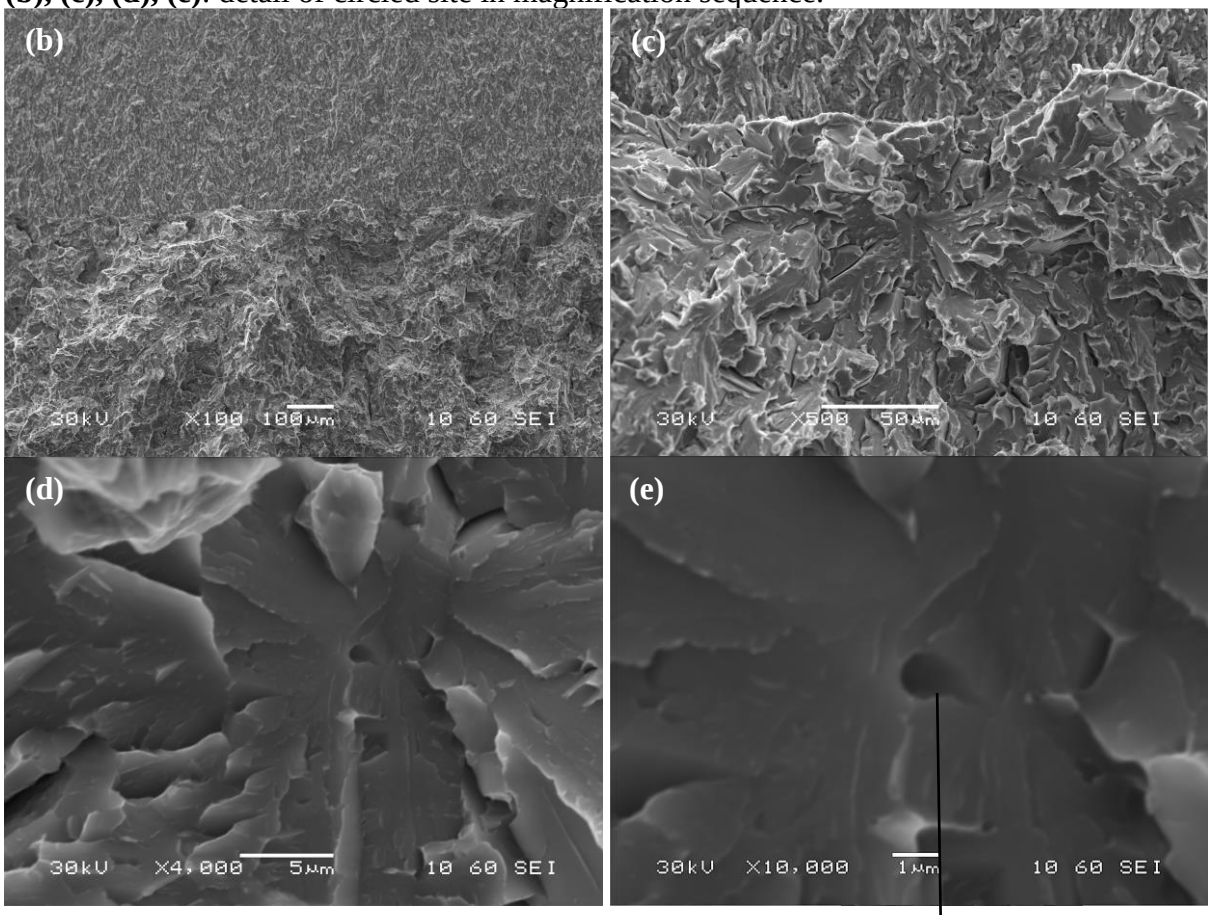

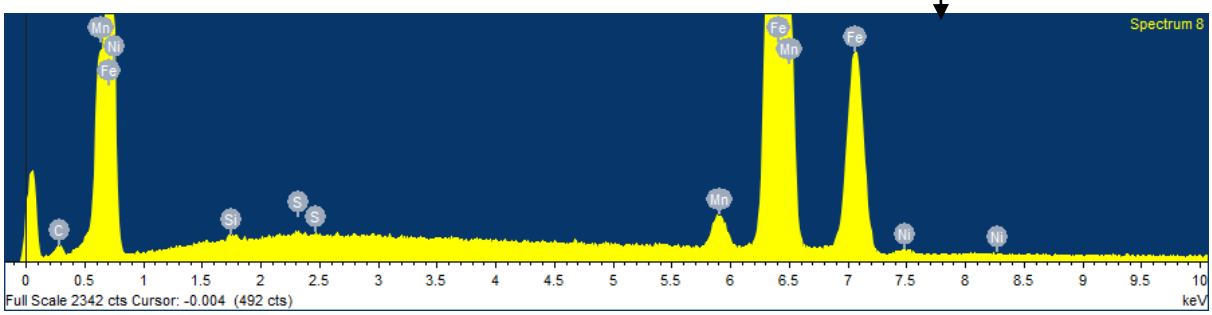

HT1TL-D

Figure 3.59

Fractography of Fracture Toughness Specimen HT1TL-D tested at -196ºC

(f), (g), (h), (i): detail of circled site in magnification sequence on **opposite side.**

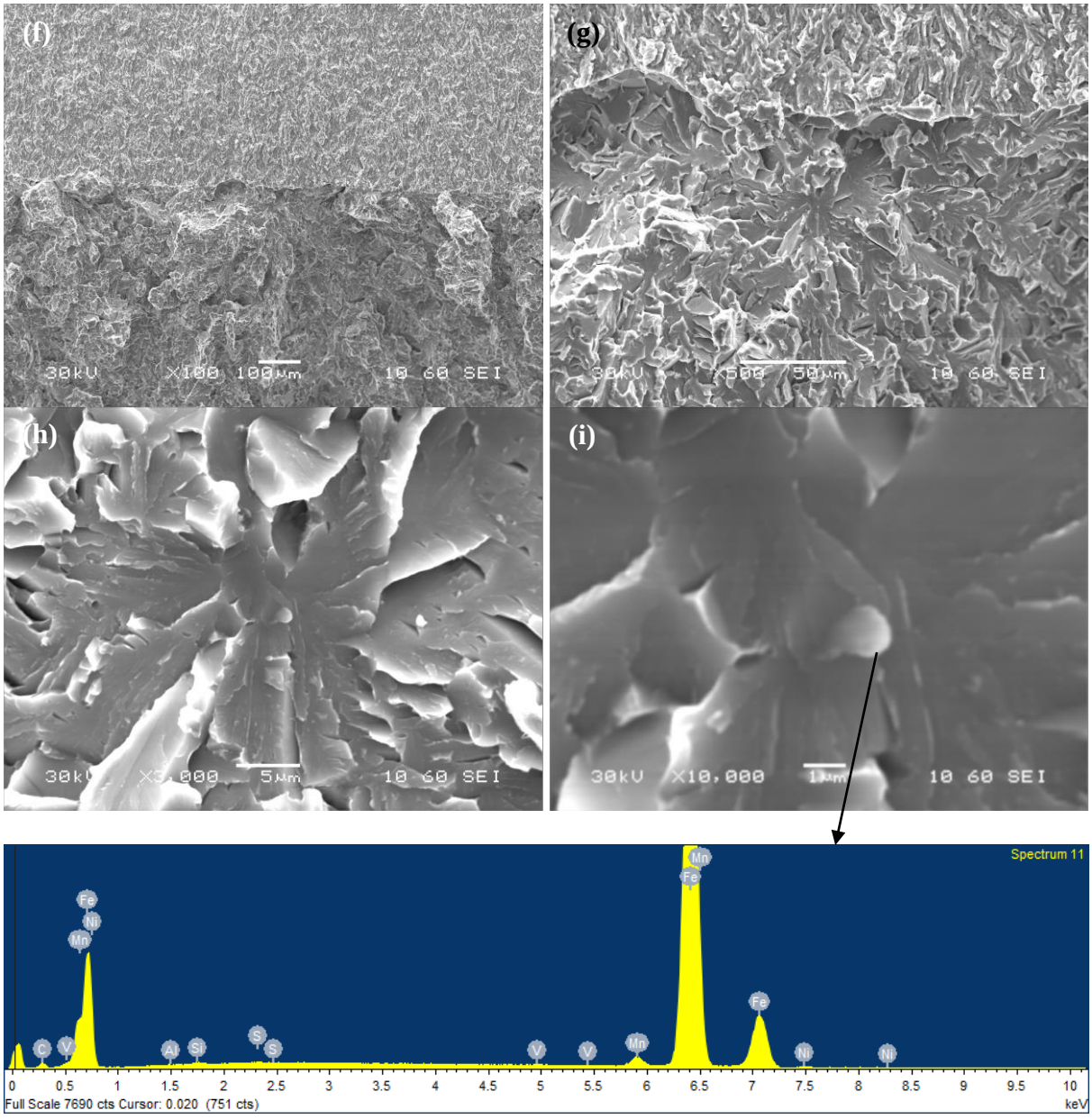

HT1TL-E

Figure 3.60

Fractography of Fracture Toughness Specimen HT1TL-E tested at -196ºC

(a): Fracture surface after fatigue precracking. The possible initiation site is circled in red.

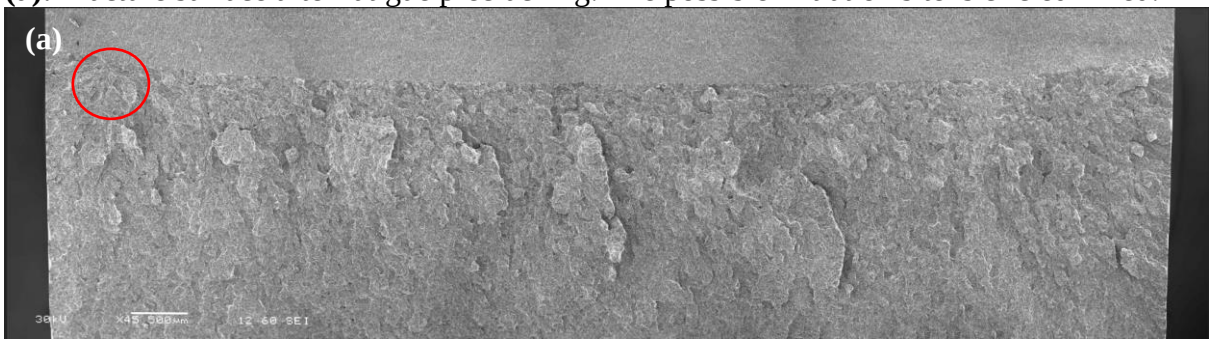

(b), (c), (d), (e): detail of circled site in magnification sequence.

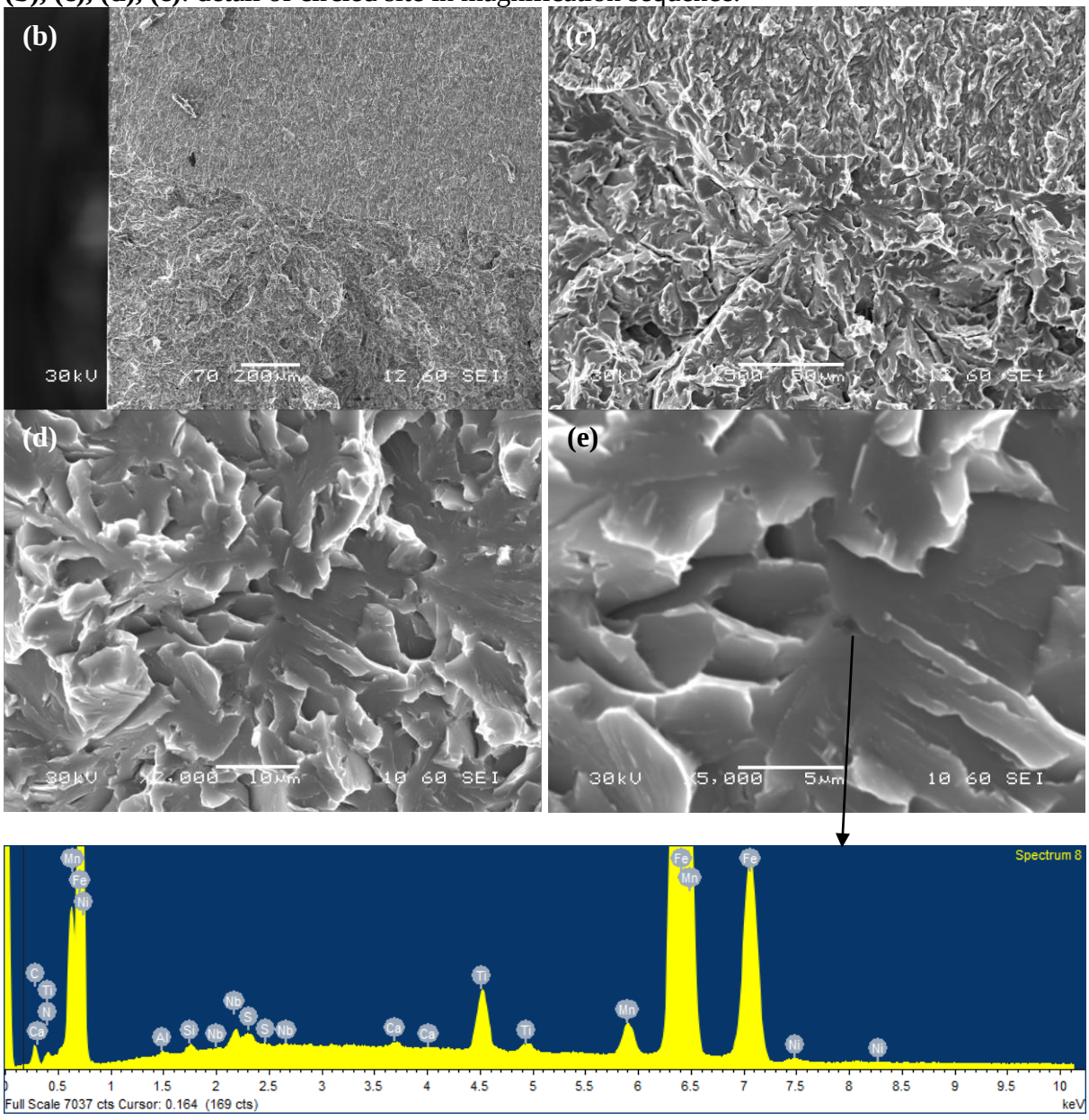

HT1TL-E

Figure 3.60

Fractography of Fracture Toughness Specimen HT1TL-E tested at -196ºC

(f), (g), (h), (i): detail of circled site in magnification sequence on **opposite** side.

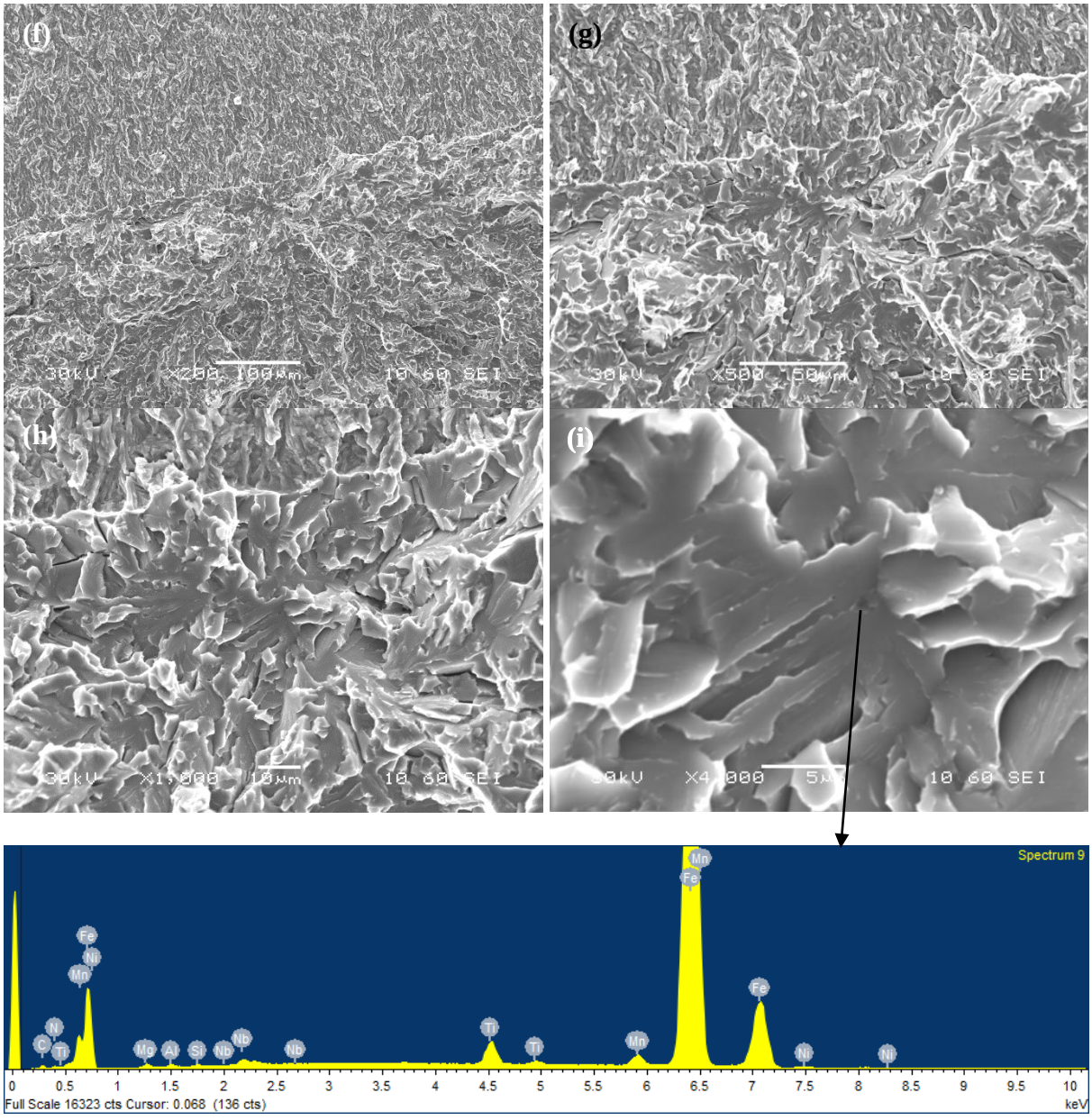

HT1TL-F

Figure 3.61

Fractography of Fracture Toughness Specimen HT1TL-F tested at -196ºC

(a): Fracture surface after fatigue precracking. The possible initiation sites are circled in red.

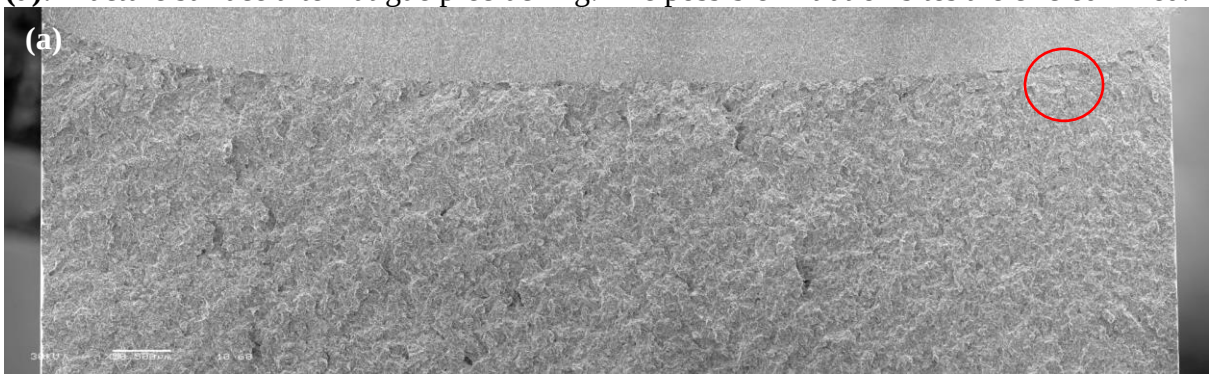

(b), (c), (d), (e): detail of circled site in magnification sequence.

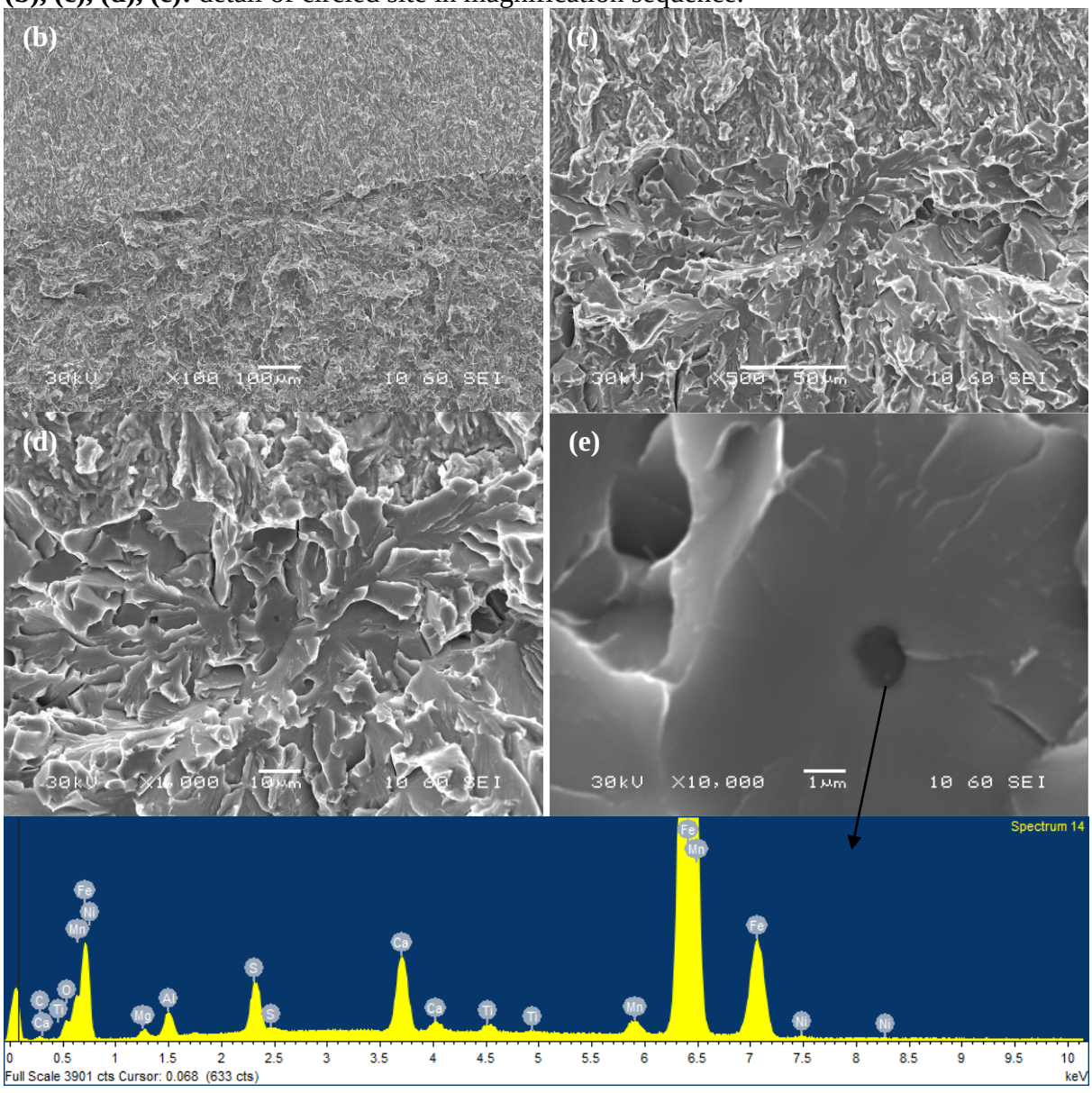

HT1TL-F

Figure 3.61

Fractography of Fracture Toughness Specimen HT1TL-F tested at -196ºC

(f), (g), (h), (i): detail of site 2 in magnification sequence on opposite side.

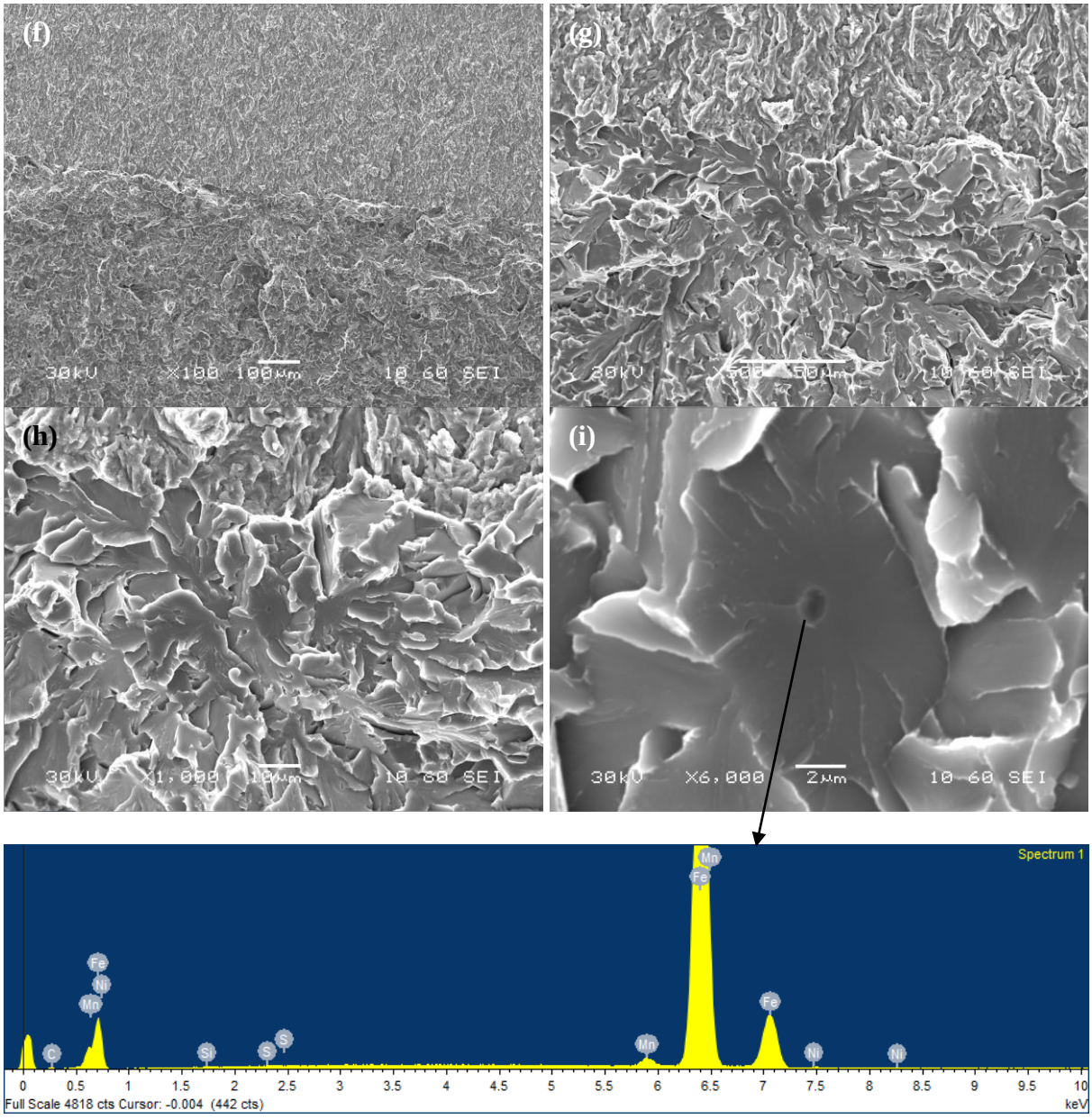

Table 6.1

Hardness Values Along the Thickness of 9% Ni Steel SENB Sample

Test Point No.	Hardness [HV5]				
1	256	256	255	262	251
2	263	251	253	253	268
3	256	256	252	254	254
4	250	250	255	258	258
5	258	259	256	259	254
6	254	255	248	251	251
7	258	255	253	256	257
8	254	253	247	243	248
9	255	251	259	254	253
10	254	251	251	257	254
11	256	248	252	246	257
12	254	252	258	259	249

Table 6.2

Hardness Values Along the Thickness of 7% Ni Steel SENB Sample

Test Point No.	Hardness [HV5]				
1	223	225	226	234	230
2	229	230	228	221	232
3	231	233	228	231	223
4	229	229	223	224	230
5	223	221	232	228	229
6	227	224	231	225	231
7	222	227	232	229	228
8	231	228	227	231	223
9	231	227	230	222	229
10	230	227	234	216	229

Table 6.3

7%Ni Steel Tensile Specimen Dimensions

Specimen Identification	Test Temperature	d_1	d_2	d_3	d	S
	[°C]	[mm]	[mm]	[mm]	[mm]	[mm^2]
7Ni-5	-130	10.01	10.02	9.97	10.00	78.54
7Ni-6		10.00	9.98	10.02	10.00	78.54
7Ni-3	-150	10.01	10.00	10.03	10.01	78.75
7Ni-4		9.98	9.99	10.03	10.00	78.54
7Ni-1	-170	9.99	9.97	9.98	9.98	78.23
7Ni-2		10.01	9.98	10.03	10.01	78.64
7Ni-9	-196	9.99	10.02	9.98	10.00	78.49
7Ni-10		10.00	10.00	9.98	9.99	78.44

Table 6.4

7% Ni Steel Tensile Testing Results

Specimen Identification	Test Temperature	Upper Yield Stress	Lower Yield Stress	Ultimate Tensile Strength	Total Plastic Strain	Work Hardening Exponent n
	[ºC]	[MPa]	[MPa]	[MPa]	[%]	
7Ni-5	-130	898	879	932	19.3	0.06
7Ni-6		900	879	932	19.3	0.06
7Ni-3	-150	929	910	962	19.7	0.04
7Ni-4		941	916	970	19.9	0.06
7Ni-1	-170	997	971	1016	18.8	0.03
7Ni-2		967	940	990	19.3	0.03
7Ni-9	-196	1068	1049	1089	19.7	0.04
7Ni-10		1076	1054	1098	21.0	0.05

Table 6.5

9% Ni Steel Tensile Testing Results

Specimen Identification	Test Temperature	Yield Stress (0.2% Offset)	Ultimate Tensile Strength	Total Plastic Strain
	[ºC]	[MPa]	[MPa]	[%]
9Ni-9	-130	811	1006	23.2
9Ni-10		812	1012	25.3
9Ni-11	-150	846	1051	23.7
9Ni-12		846	1017	23.0
9Ni-13	-170	904	1095	23.4
9Ni-14		897	1066	21.8
9Ni-1	-196	961	1166	25.0
9Ni-2		958	1166	25.1

Table 6.6

The Absorbed Energy, Lateral Expansion, and %Cleavage Area of 7% Ni Steel Charpy Impact Testing

Specimen Nr.	Temperature	Impact Energy	Lateral Expansion	%Cleavage Area
	[ºC]	[J]	[mm]	
7Ni-CVN-1	-196	38	0.49	78.86
7Ni-CVN-2		55	0.60	73.45
7Ni-CVN-3		44	0.40	84.43
7Ni-CVN-13	-180	62	0.55	71.77
7Ni-CVN-8	-170	72	0.80	56.20
7Ni-CVN-10		123	1.30	43.23
7Ni-CVN-14		78	0.92	56.80
7Ni-CVN-9	-160	186	2.03	18.45
7Ni-CVN-15		186	2.05	17.69
7Ni-CVN-7	-150	180	2.14	23.47
7Ni-CVN-12	-140	223	2.24	3.55
7Ni-CVN-11	-130	235	2.07	0
7Ni-CVN-5	-100	233	2.14	0
7Ni-CVN-6		238	2.64	0
7Ni-CVN-4	-80	233	2.24	0

Table 6.7

7%Ni Steel Blunt Notch Specimen Test Results

Specimen Nr.	**Temperature**	**Yield Stress**	**Maximum Load**	**Nominal Stress**	**σ_{nom}/σ_y**	**L/L_{GY}**	**Stress Intensification**	**Max Principal Stress**
	[^oC]	[MPa]	[kN]	[MPa]	(max 2.292)	(max 1.065)	$R=\sigma_{yy}^{max}/\sigma_y$ (max 2.62)	σ_{yy}^{max}[MPa]
7Ni-FS-2	-196	1052	101.65	4251	4.04	1.84	3.30	>2756
7Ni-FS-3			102.59	4290	4.08	1.90	3.31	>2756

Table 6.8

Fracture Toughness for 7% Ni Steel SENB Specimens (W = 32mm) Tested at -170 and -163ºC

Specimen Code	Test Temperature	a_0	a_f	Δa	a_0/W	a_f/W	P_{max}	P_Q	K_Q	K_{Jc}	J_c	CTOD
	[ºC]	[mm]	[mm]	[mm]			[kN]	[kN]	[MPa×m$^{1/2}$]	[MPa×m$^{1/2}$]	[kJ/m^2]	[mm]
SENB1	-163	13.92	14.97	1.05	0.44	0.47	53.78	28.69	96.6	568	1314.6	0.90
SENB2		14.71	16.61	1.90	0.46	0.52	50.74	26.24	103.8	726	2194.7	1.46
SENB3	-170	14.06	15.12	1.06	0.44	0.47	54.04	26.09	89.1	547	1205.7	0.84
SENB4		14.58	15.49	0.91	0.46	0.48	51.98	25.14	89.0	549	1210.8	0.84

Table 6.9

Fracture Toughness for Small 7% Ni Steel SENB Specimens (W = 7mm) Tested at -196ºC

Specimen Code	a_0	a_f	Δa	a_0/W	a_f/W	P_{max}	P_Q	K_Q	K_{Jc}	J_c	CTOD
	[mm]	[mm]	[mm]			[kN]	[kN]	[MPa×m$^{1/2}$]	[MPa×m$^{1/2}$]	[kJ/m^2]	[mm]
7Ni-LT-1	3.40	3.43	0.03	0.49	0.49	5.02	4.03	76.1	213.5	197.5	0.11
7Ni-LT-2	3.25	3.29	0.04	0.46	0.47	5.66	4.33	76.8	260.7	294.4	0.16
7Ni-TL-3	3.06	3.26	0.20	0.44	0.47	6.13	4.39	77.0	291.3	367.7	0.21
7Ni-TL-4	3.26	3.31	0.05	0.47	0.47	5.52	4.45	79.6	277.8	334.3	0.19

Figure 6.10

Fatigue Crack Growth Specimens at -170°C and -163°C and Paris Region Constant (c and m) derived from 9% and 7%Ni Steel

Test Temperature [°C]	**Specimen Number**	***C*** mm/cycle	***m***
RT	9Ni-FCGS-4	1.9×10^{-8}	2.5
	7Ni-FCGS-3	9.2×10^{-9}	2.6
	7Ni-FCGS-4	1.4×10^{-8}	2.4
-163	9Ni-FCGS-1	4.1×10^{-9}	2.8
	7Ni-FCGS-1	4.5×10^{-9}	2.8
-170	7Ni-FCGS-2	4.0×10^{-8}	2.2
	7Ni-FCGS-4	1.5×10^{-8}	2.4

Figure 6.1

Microstructure of 9%Ni (a) and 7%Ni (b) Steels under Optical Microscope

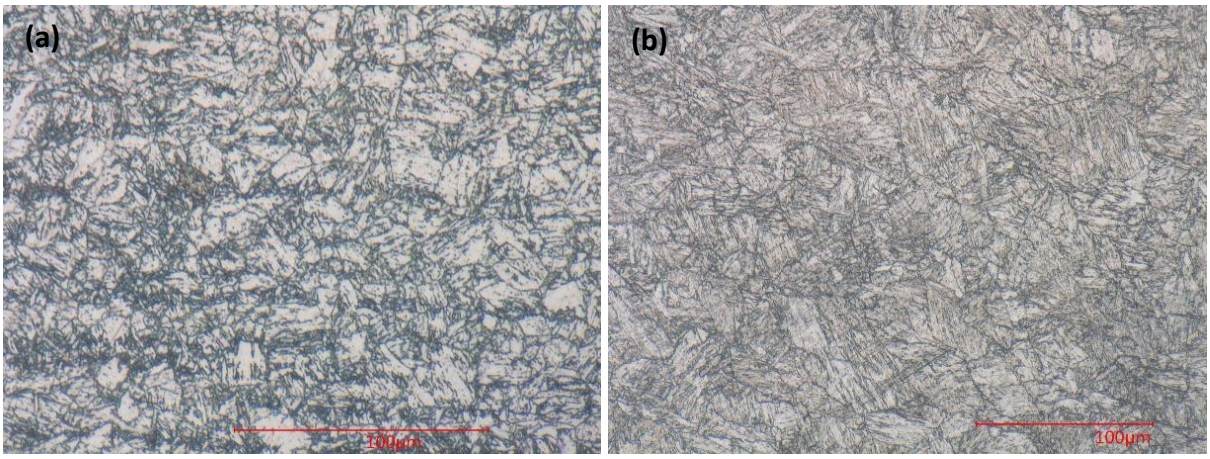

Figure 6.2

Microstructure of 9%Ni and 7%Ni Steels under SEM

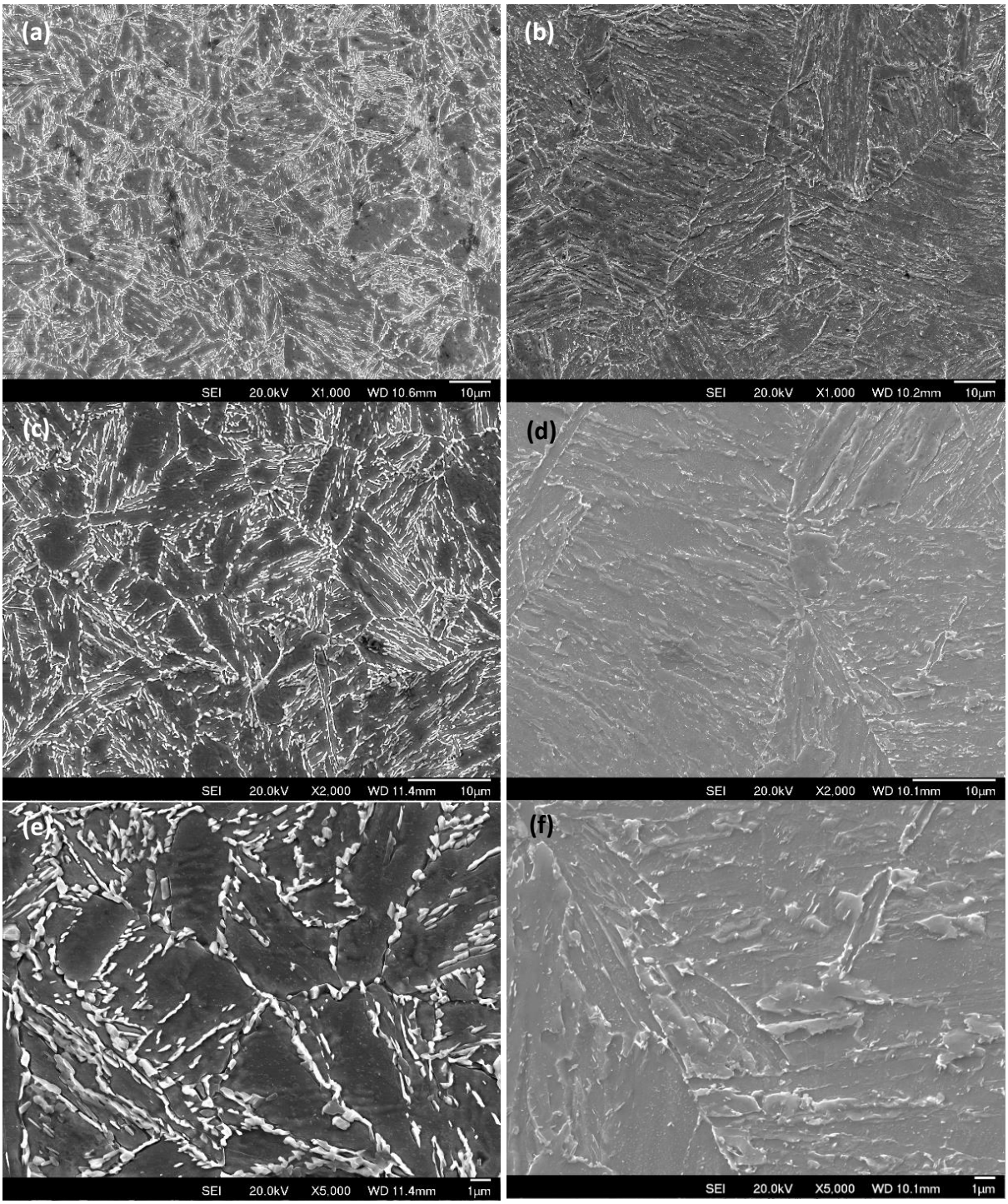

Microstructure of 9% (Figure 6.2a, c, e) and 7% (Figure 6.2b, d, e) Nickel Steel under SEM in magnification sequences.

Figure 6.3

EBSD Results of 7% and 9% Nickel Steels

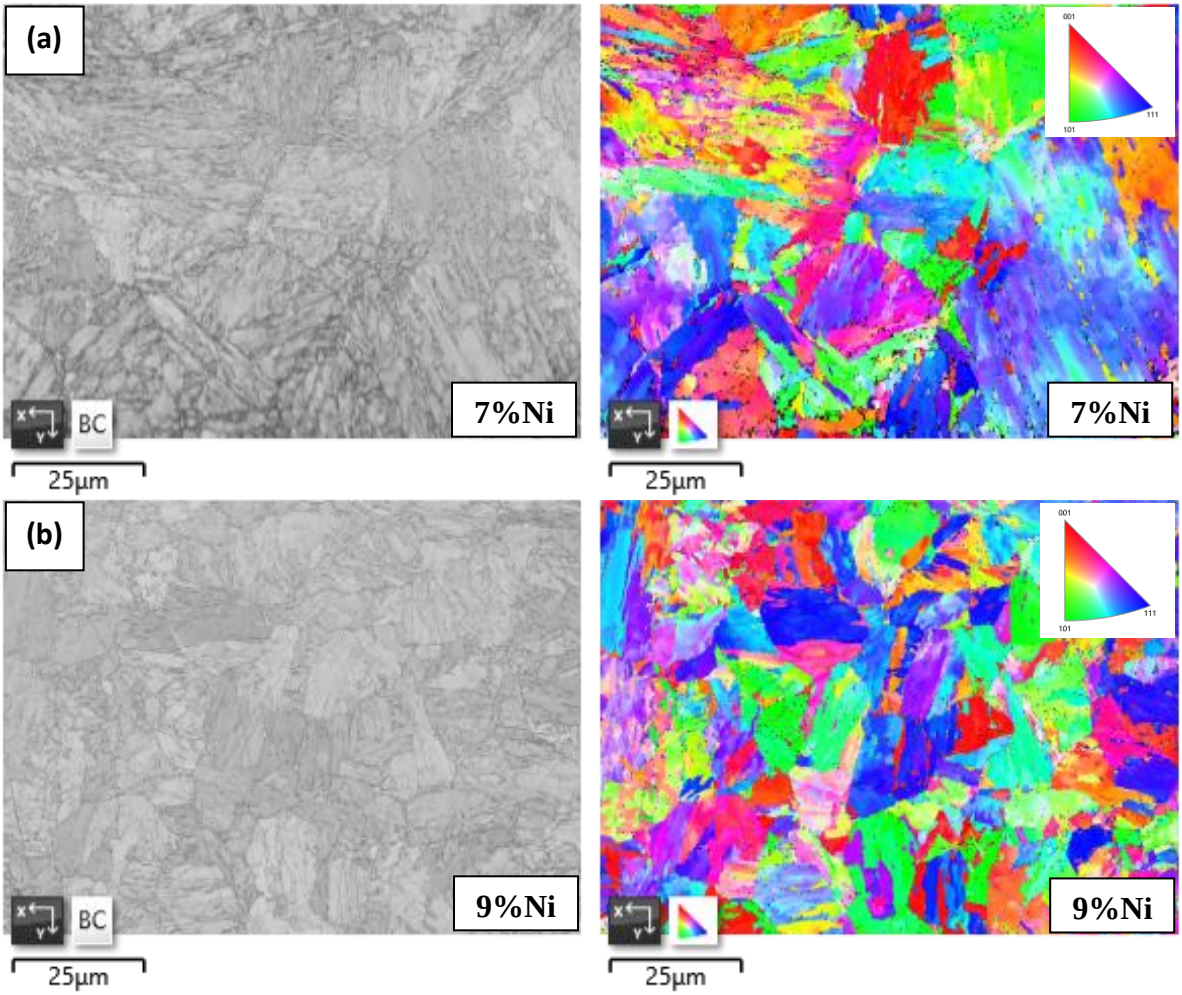

SEM micrographs and EBSD maps of (a) 7% Ni Steel; (b) 9% Ni Steel.

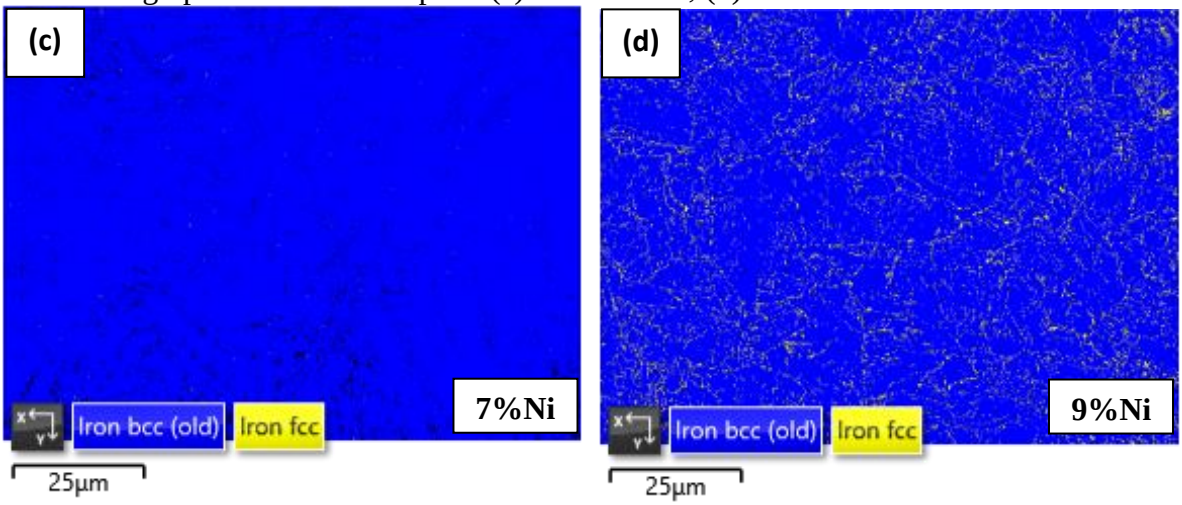

Phase distribution of (c) 7% Ni Steel; (d) 9% Ni Steel. Blue: BCC; yellow: FCC.

Figure 6.4

Misorientation Angle of 9% Ni Steel by EBSD Analysis

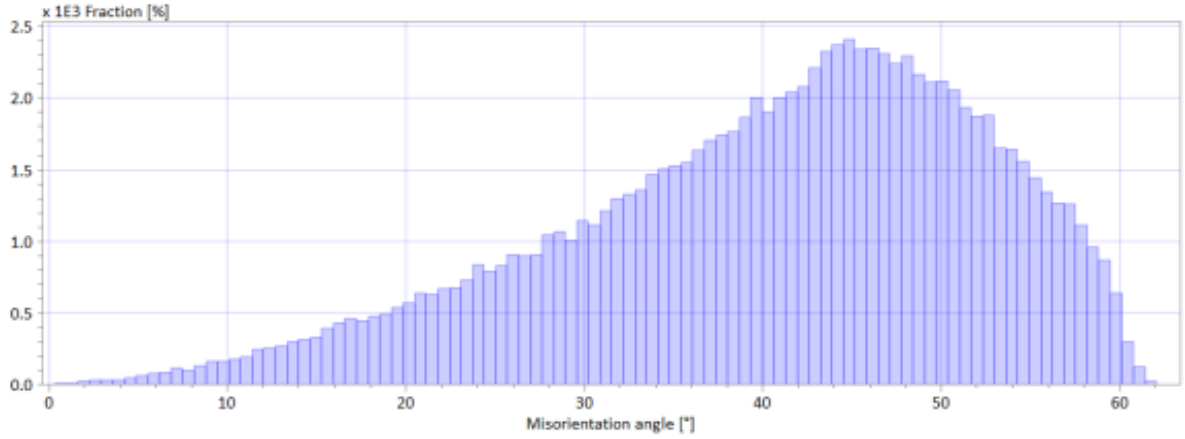

Figure 6.5

Misorientation Angle of 7% Ni Steel by EBSD Analysis

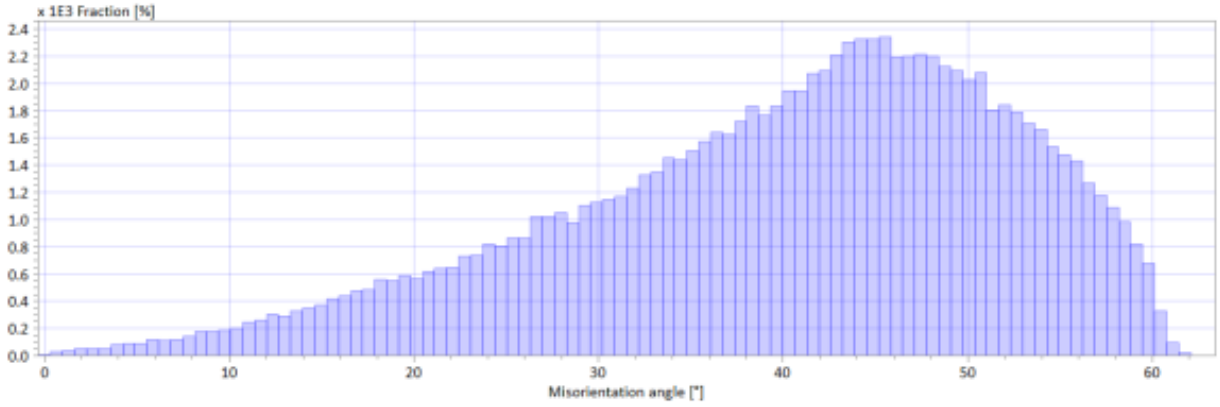

Figure 6.6

Inclusion Size Distribution of 9% and 7% Nickel Steels

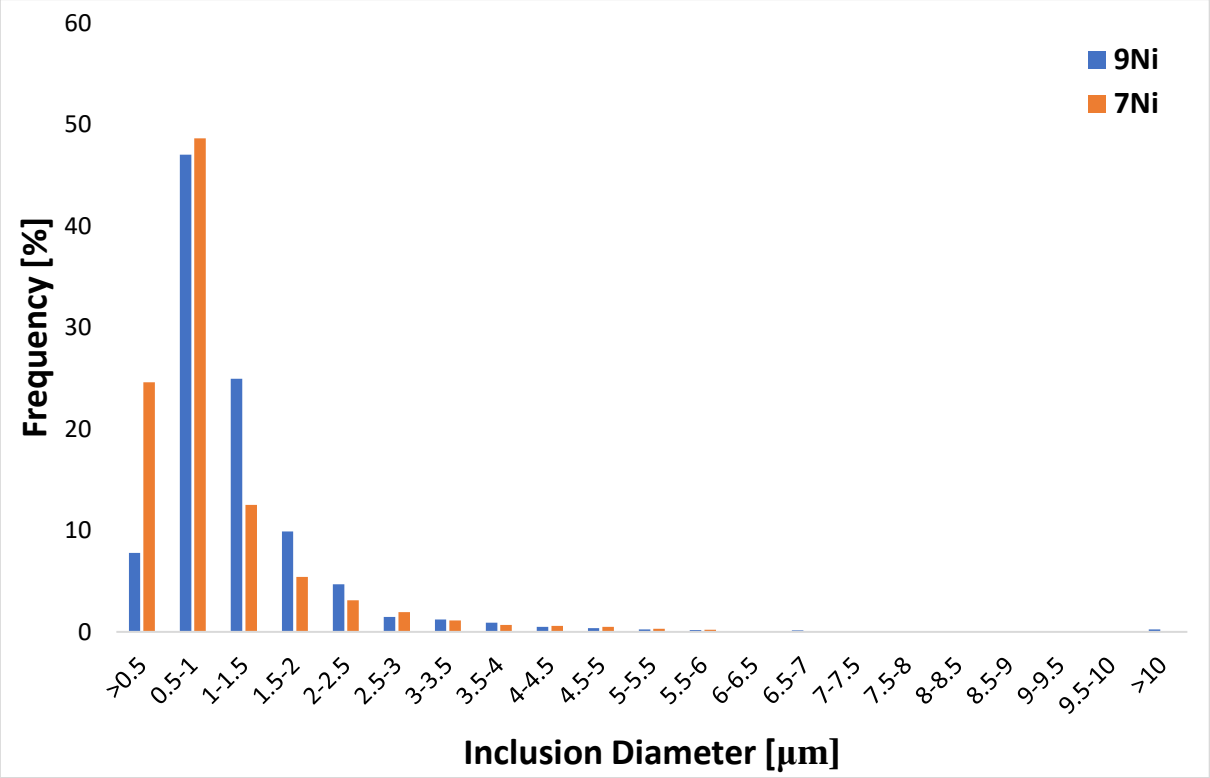

Figure 6.7

Through-Thickness Hardness Profile of 9% Ni Steel in Transverse Direction

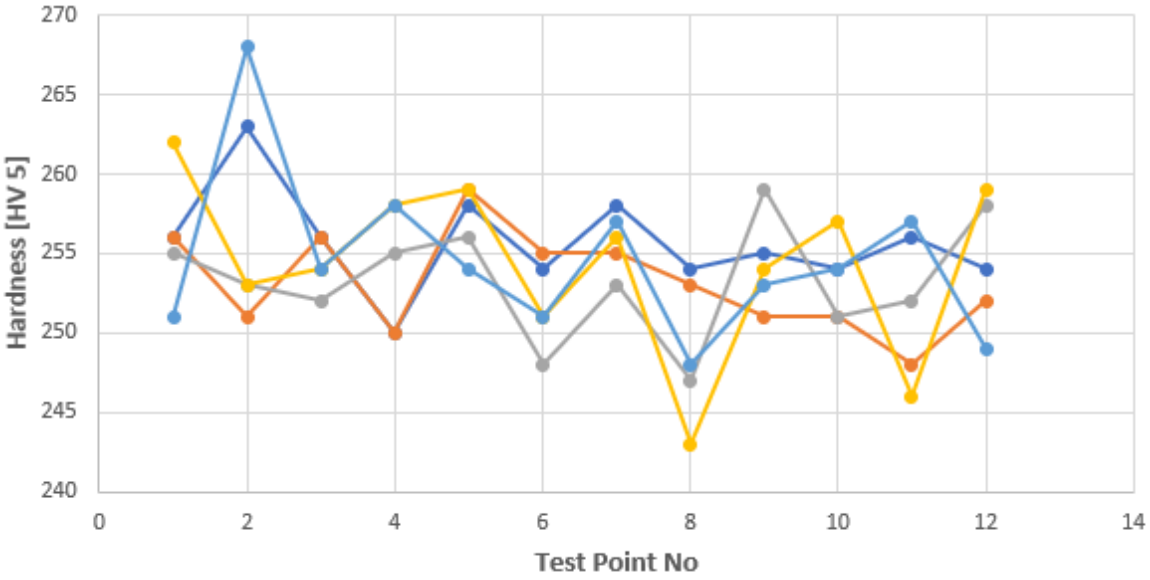

Figure 6.8

Through-Thickness Hardness Profile of 7%Ni Steel in Transverse Direction.

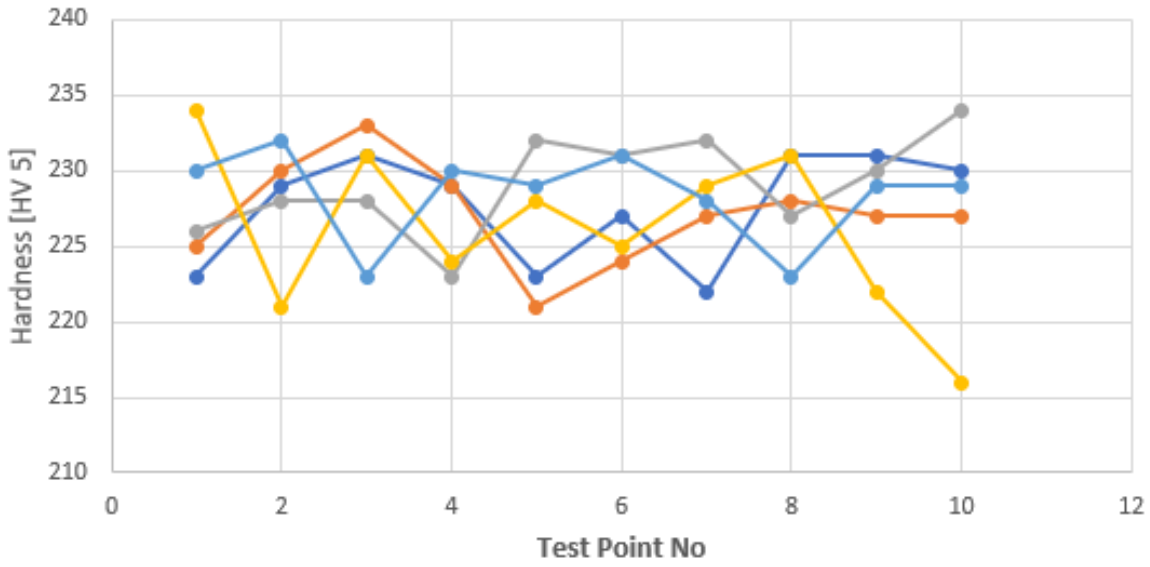

Figure 6.9

Side View of Fractured 7% Ni Steel Tensile Specimens

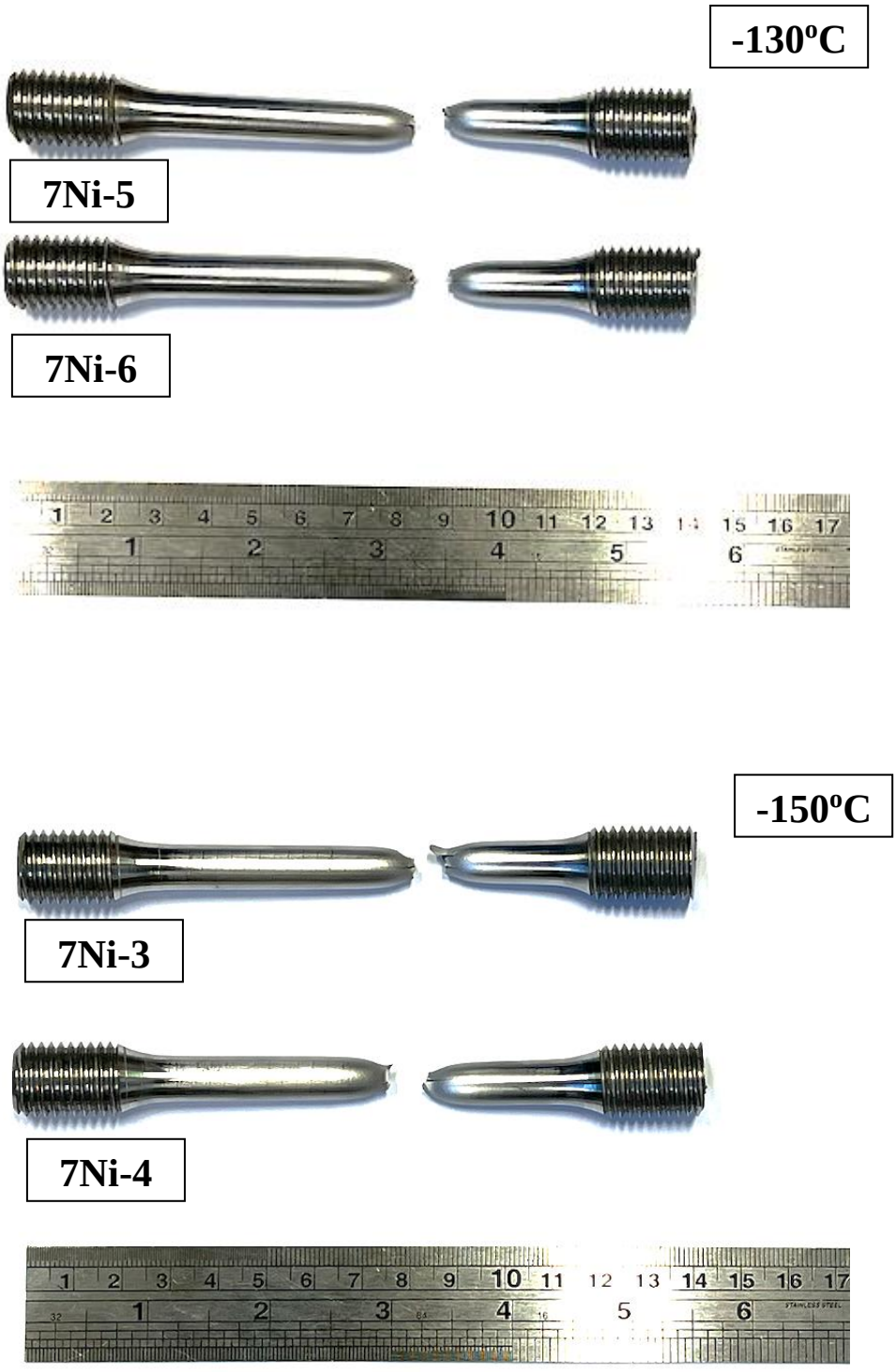

Figure 6.9

Side View of Fractured 7% Ni Steel Tensile Specimens

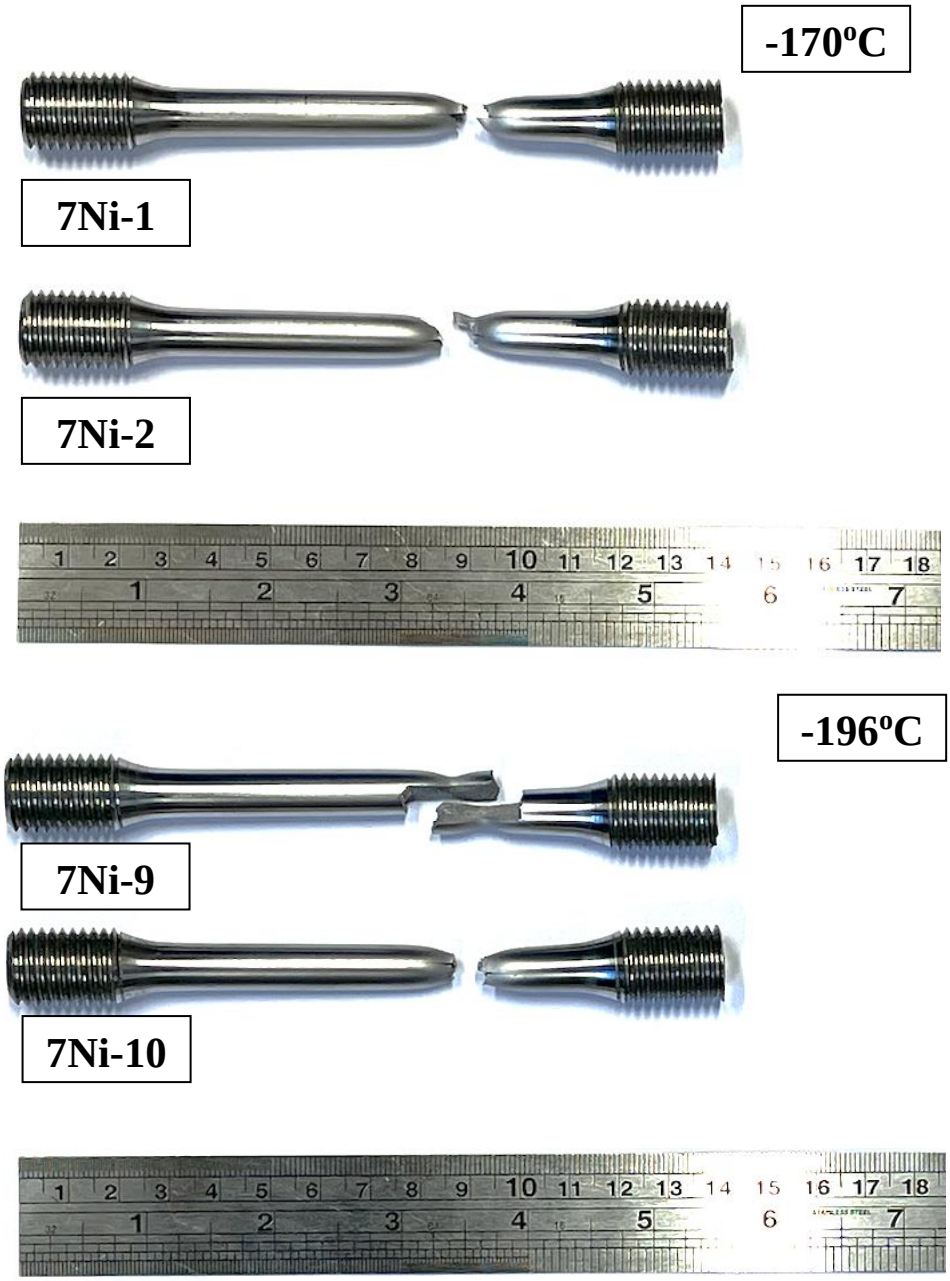

Figure 6.10

Side View of Tensile Specimen 7Ni-9 at -196ºC

Figure 6.11

Side View of Fractured 9% Ni Steel Tensile Specimens

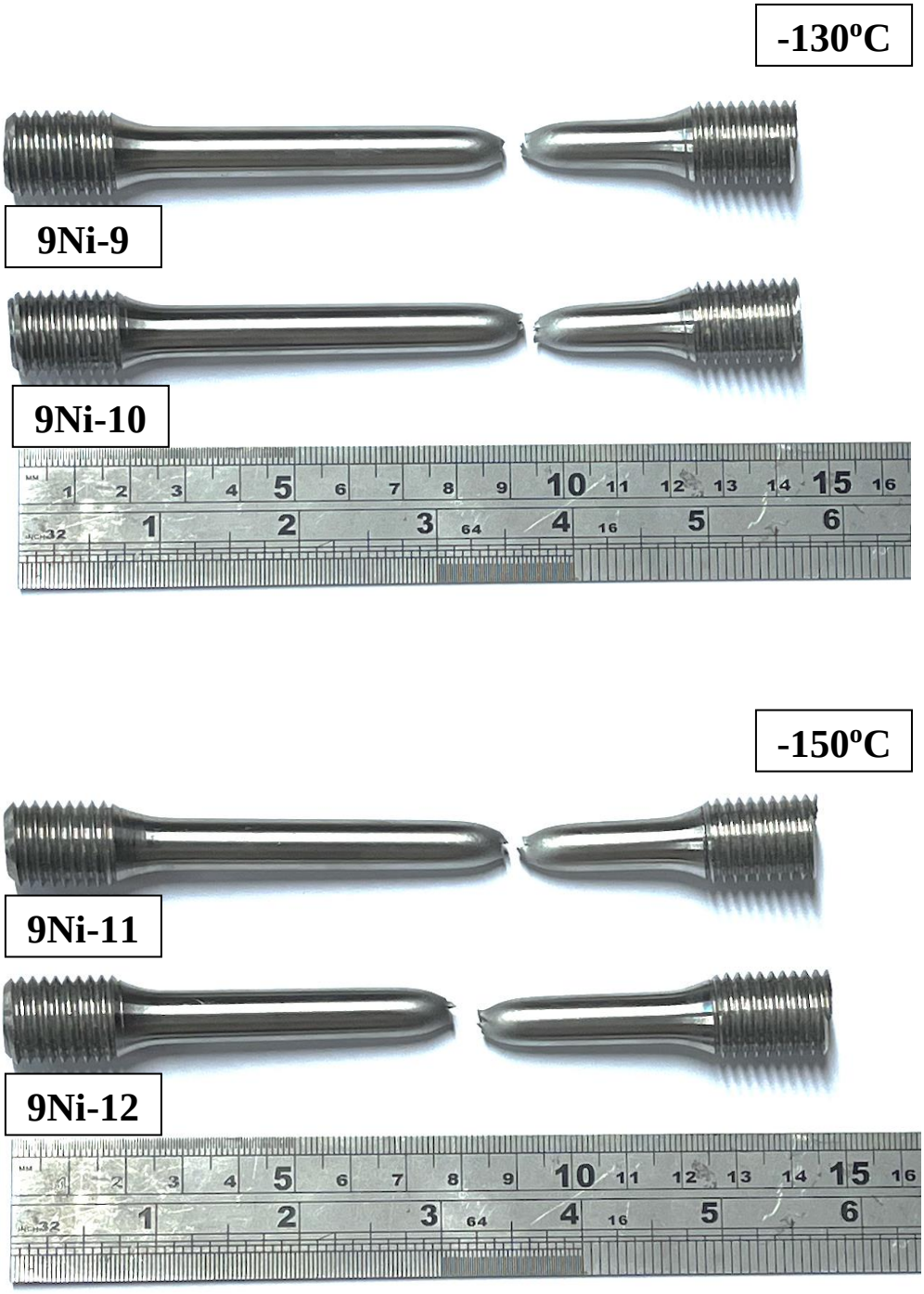

Figure 6.11

Side View of Fractured 9% Ni Steel Tensile Specimens

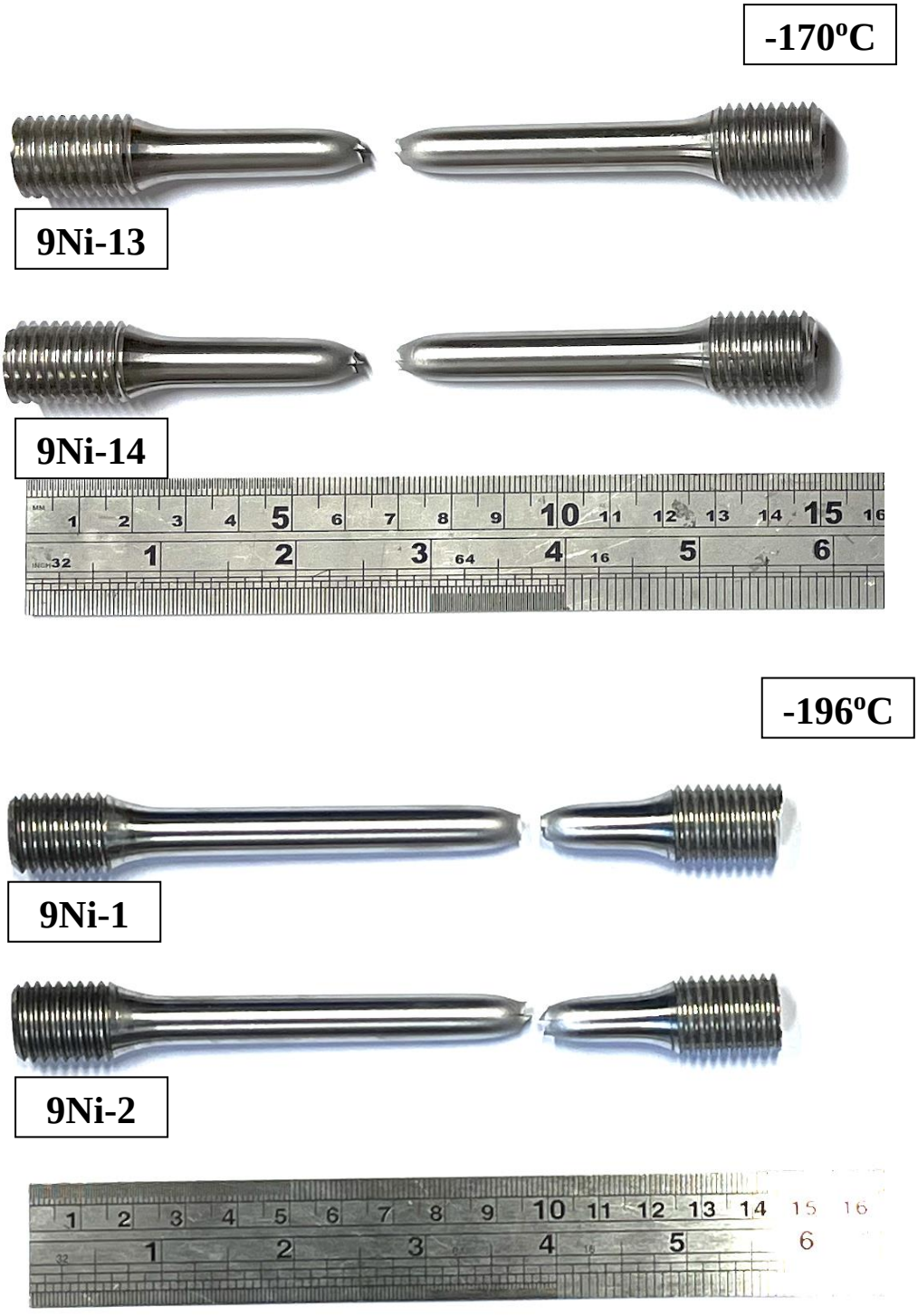

Figure 6.12

Engineering Stress-Strain Curves of 7% Ni Steel

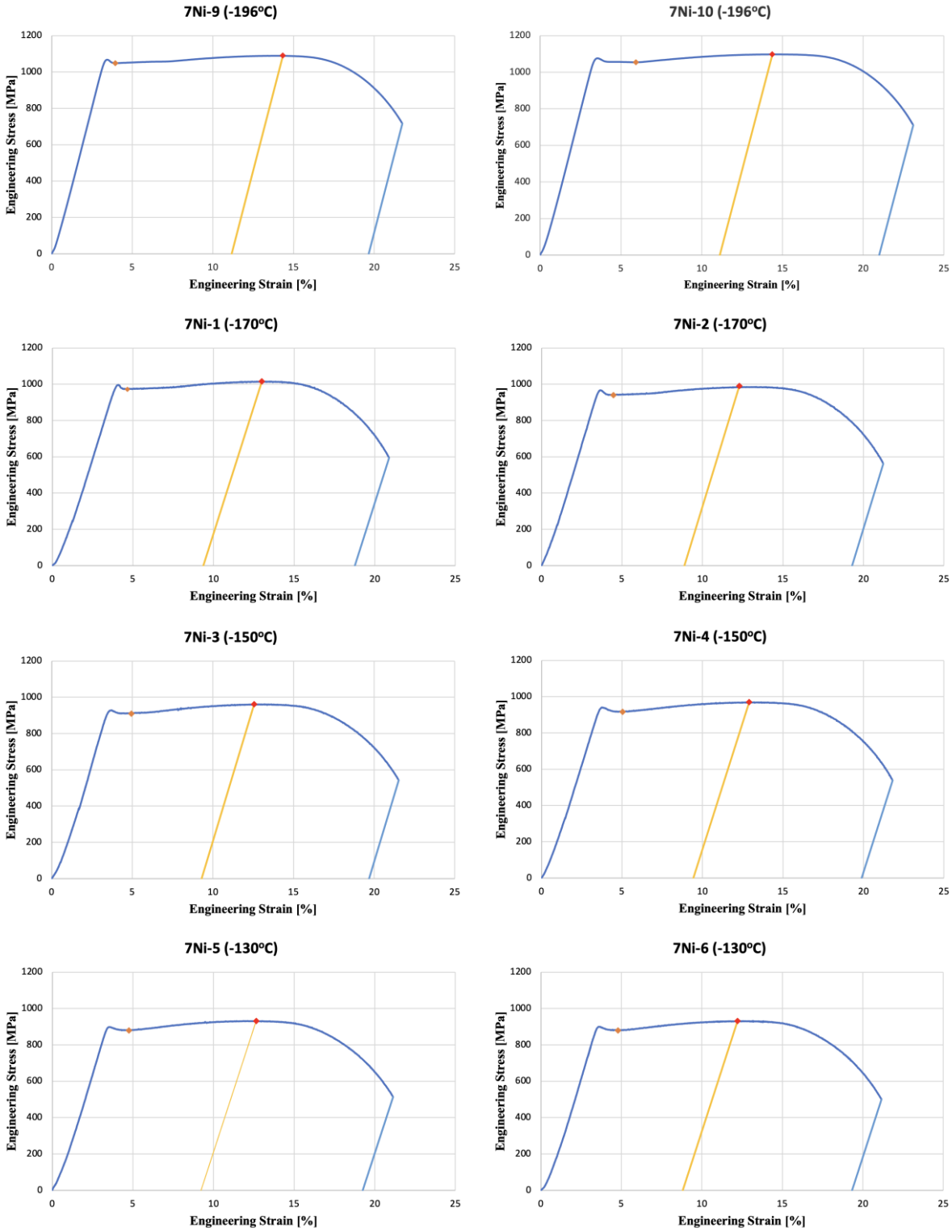

Figure 6.13

Engineering Stress-Strain Curves of 7% Ni Steel with Extensometer from -170 to -130°C

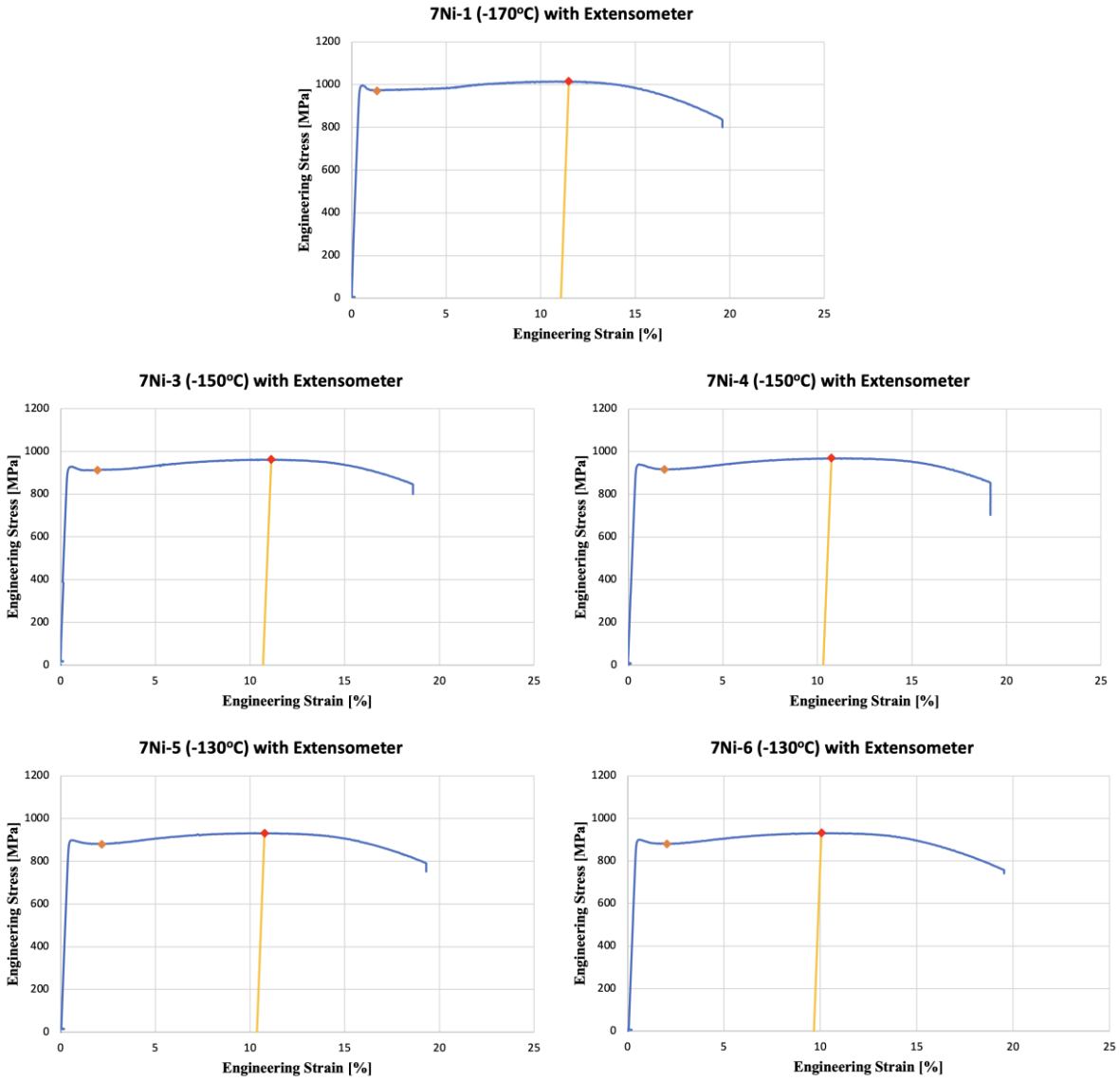

Figure 6.14

True Stress-Strain Curves in Uniform Elongation Region of 7% Ni Steel without Extensometer

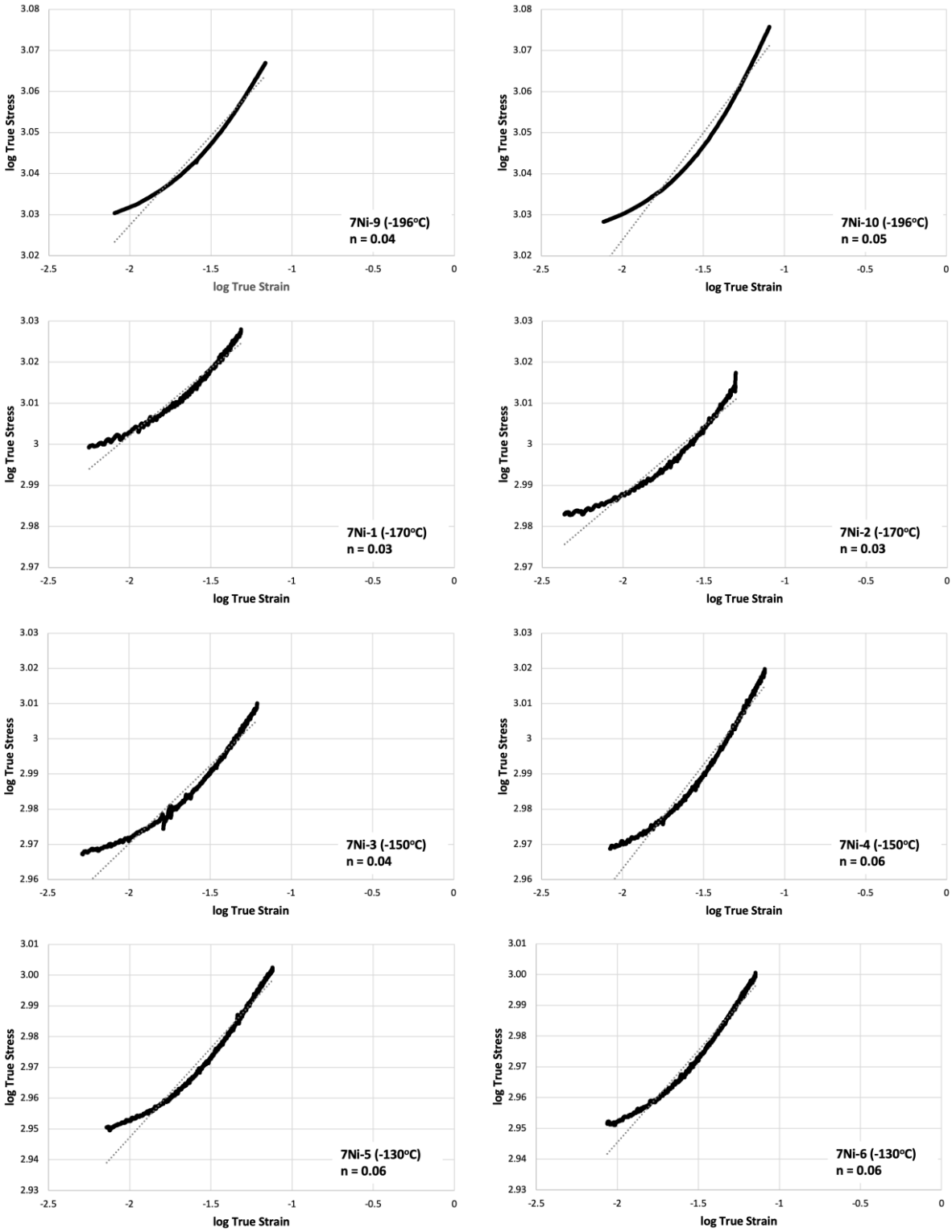

Figure 6.15

True Stress-Strain Curves in Uniform Elongation Region of 7% Ni Steel with Extensometer

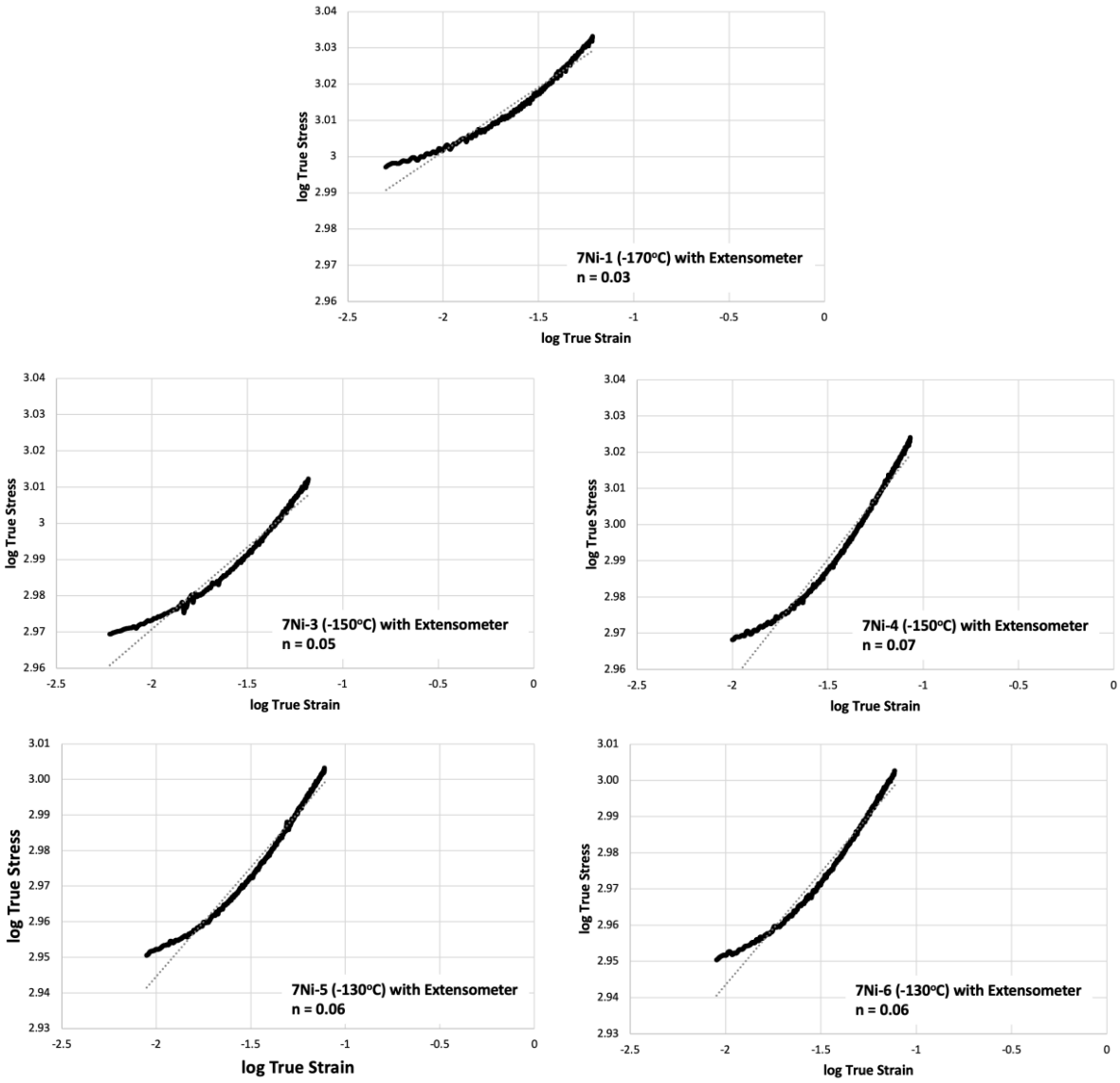

Figure 6.16

Engineering and True Stress-Strain Curves in Uniform Elongation Region for 9% Ni Steel tested at -196°C

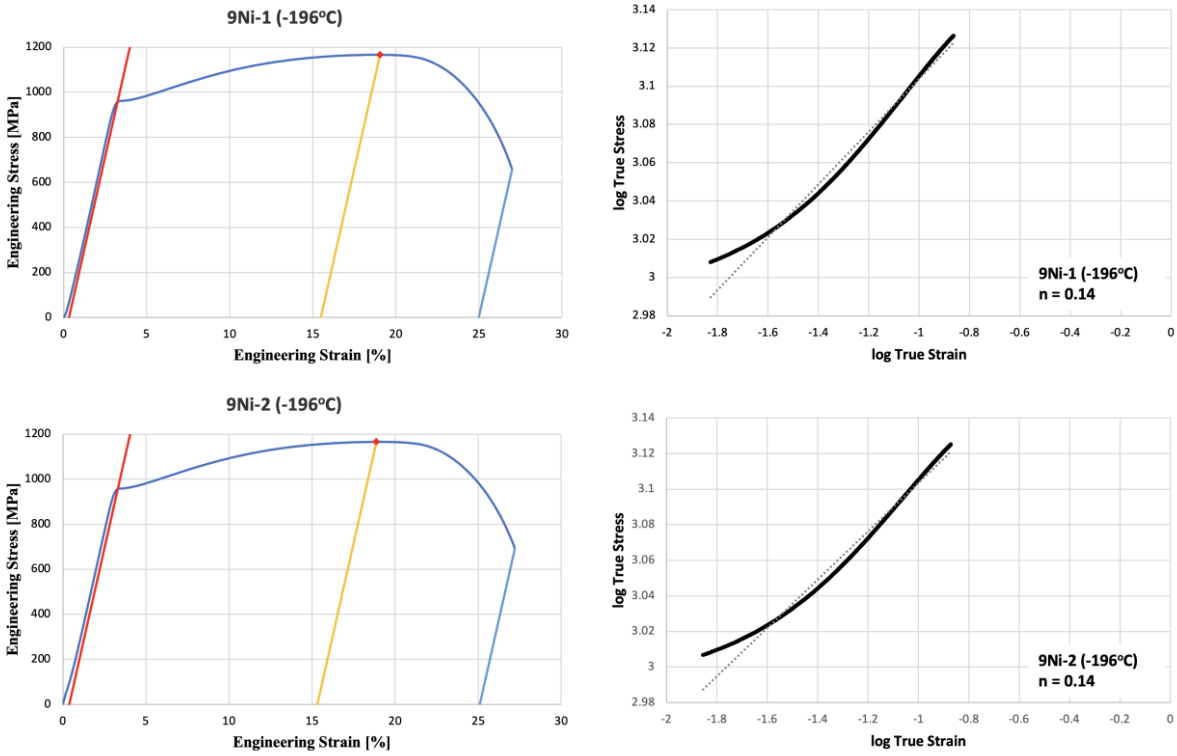

Figure 6.17

Yield Stress and Ultimate Tensile Strength from -196 to -130ºC

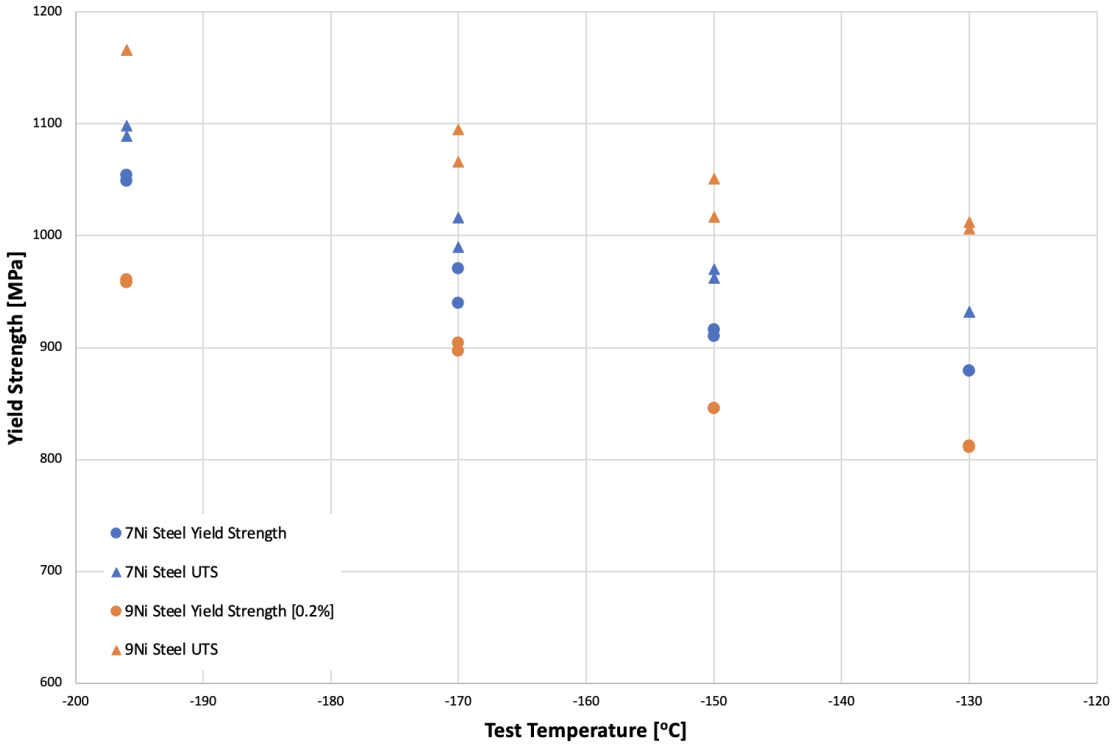

Figure 6.18

Fractography of 7%Ni Steel Tensile Specimens

7Ni-5

-130 °C

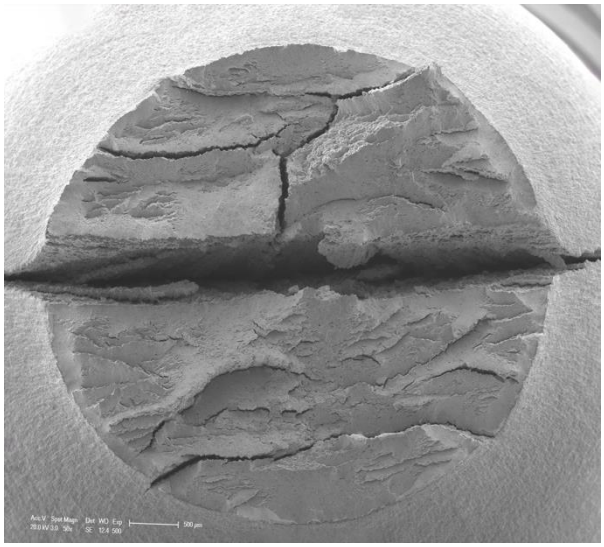

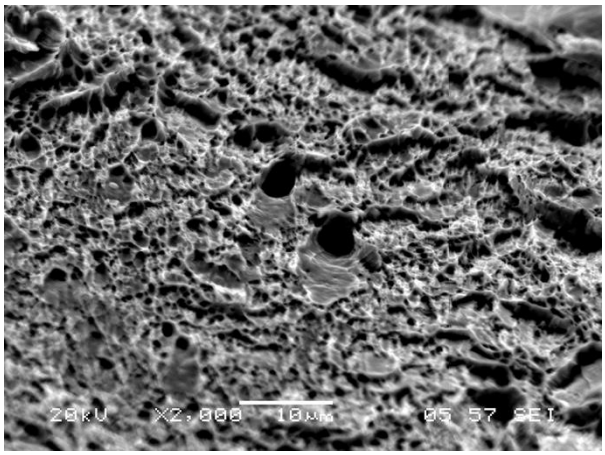

7Ni-4

-150 °C

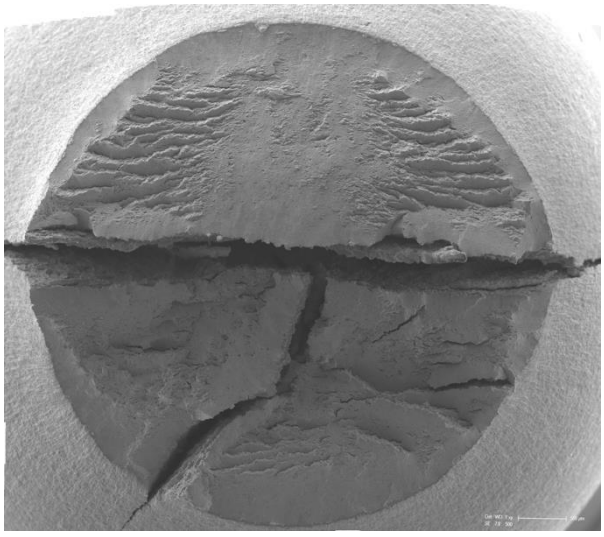

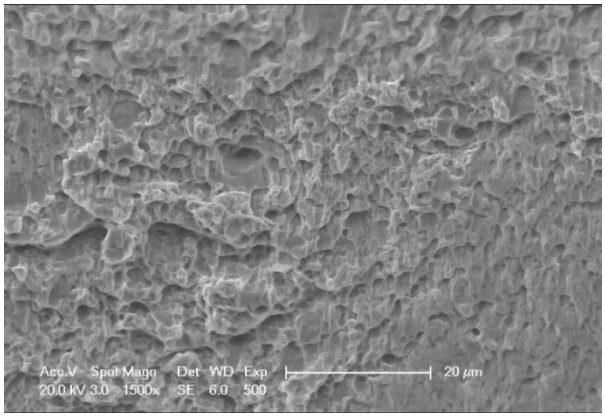

Figure 6.18

Fractography of 7%Ni Steel Tensile Specimens

7Ni-1

-170 °C

7Ni-10

-196 °C

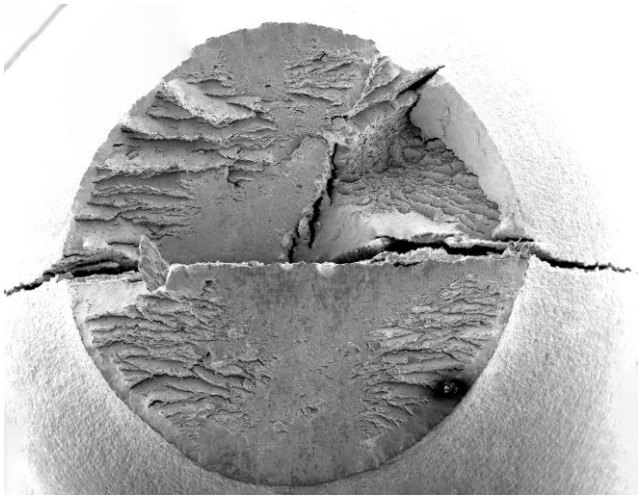

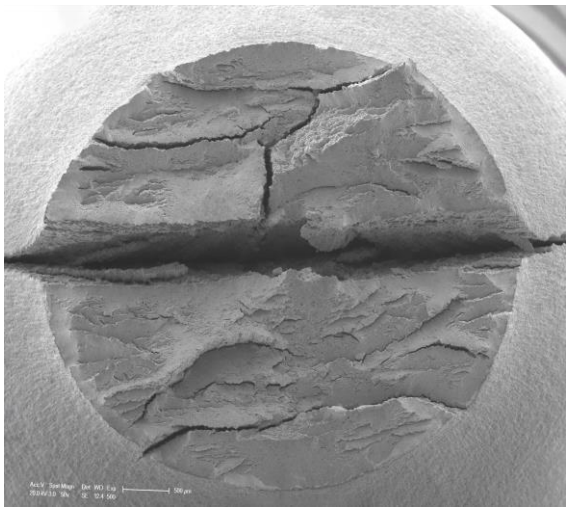

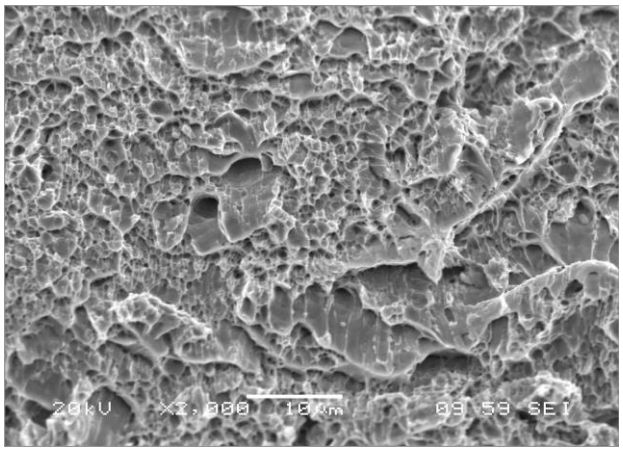

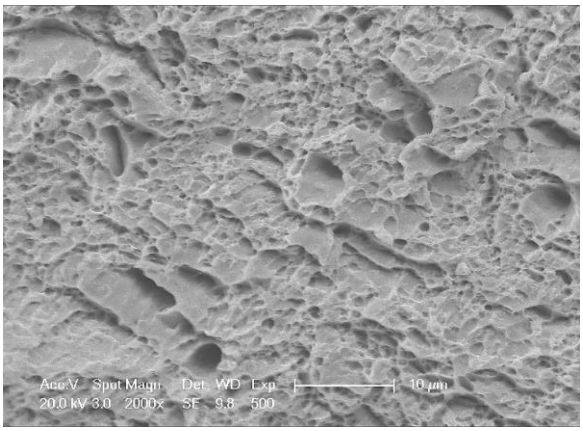

7Ni-9

-196 °C

Fractography of 7%Ni Steel Tensile Specimen Tested at -196ºC

Figure 6.19a

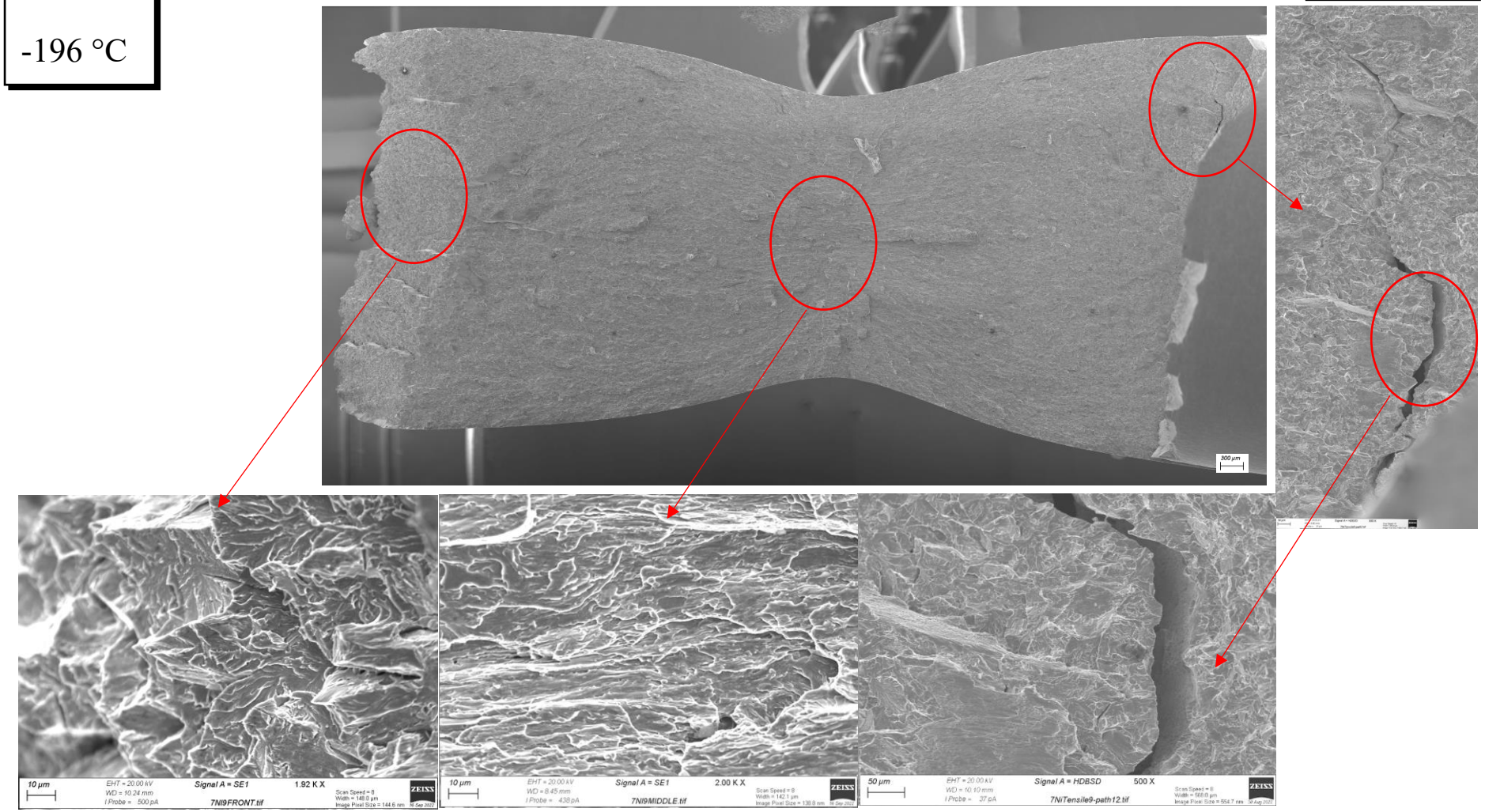

7Ni-9

-196 °C

Fractography of 7%Ni Steel Tensile Specimen Tested at -196ºC

Figure 6.19b

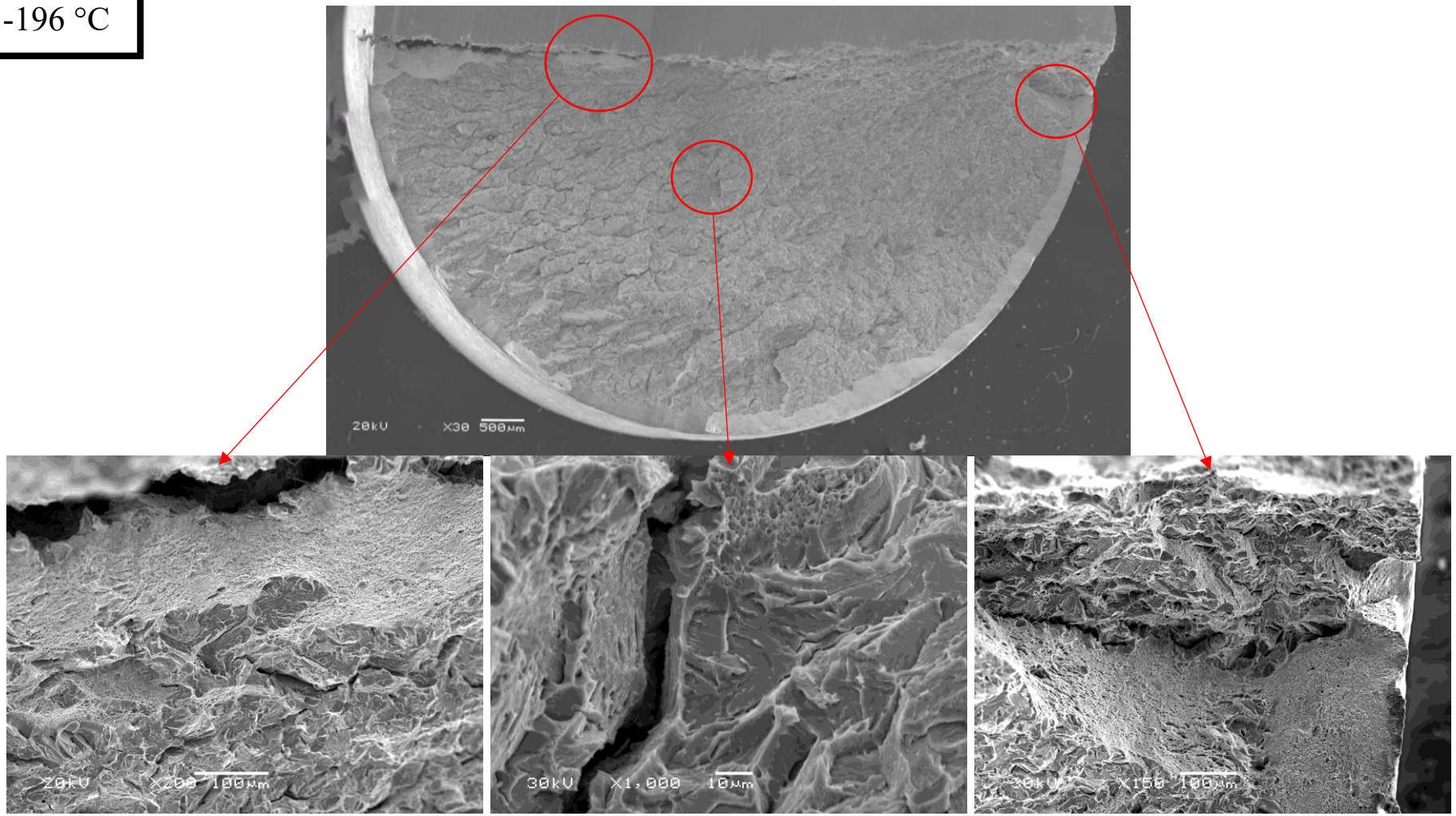

9Ni-1

-196 °C

Figure 6.20

Fractography of 9%Ni Steel Tensile Specimen Tested at -196ºC

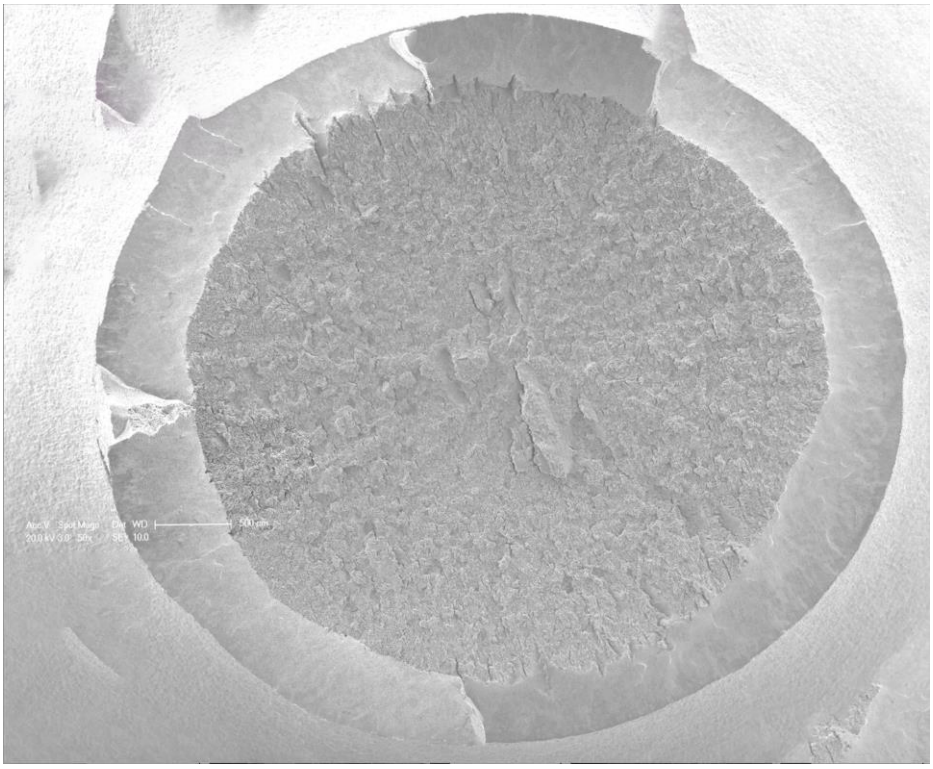

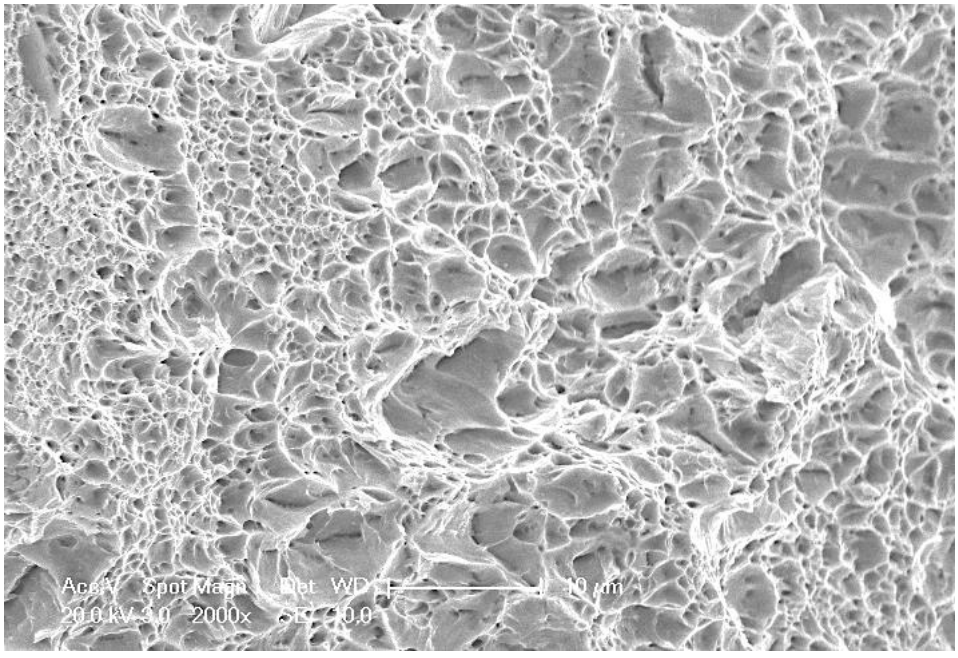

Figure 6.21

Fracture Surfaces of 7%Ni Steel CVN Specimens tested from -196 to -80ºC

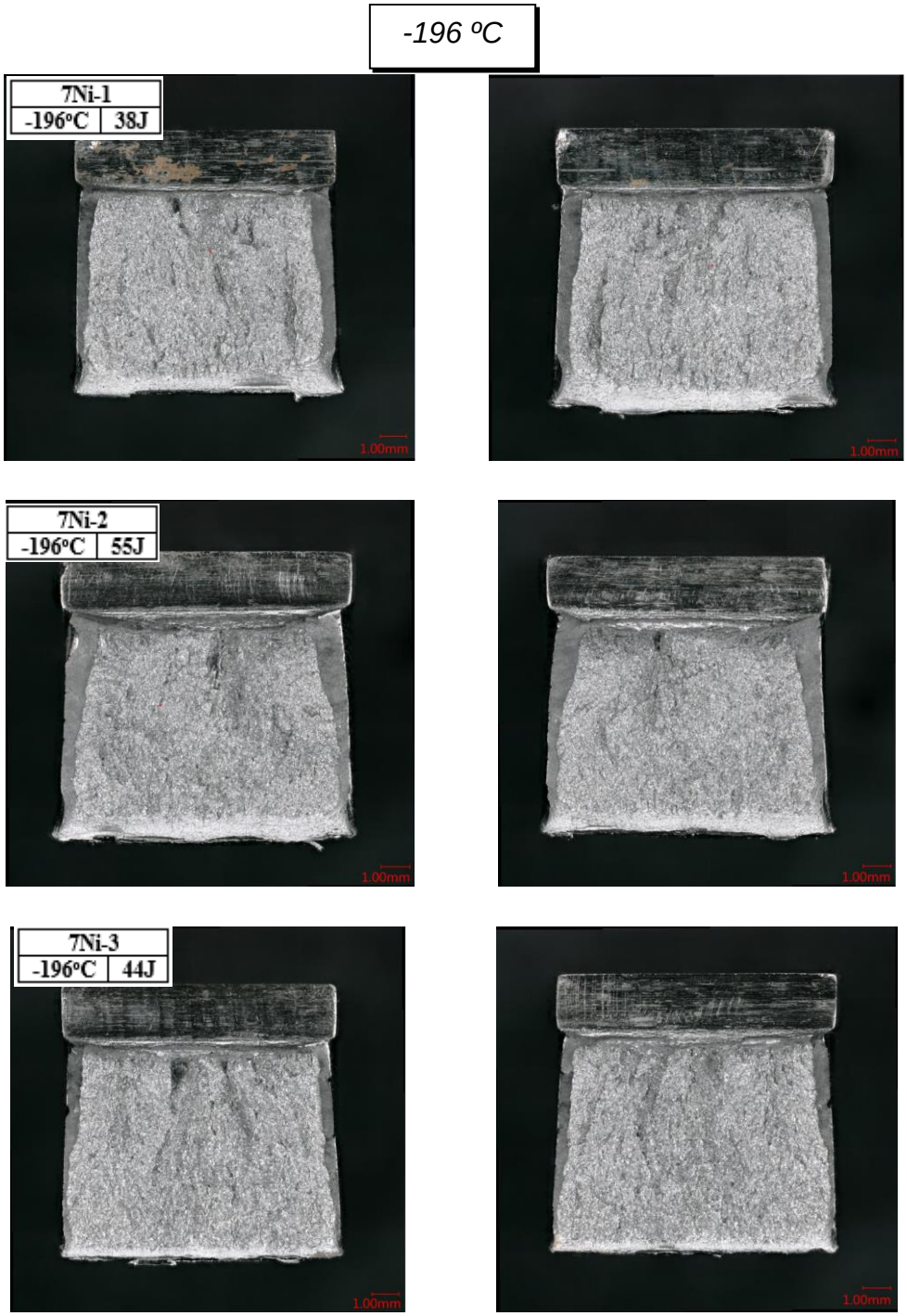

Figure 6.21

Fracture Surfaces of 7%Ni Steel CVN Specimens tested from -196 to -80ºC

-180 ºC

-170 ºC

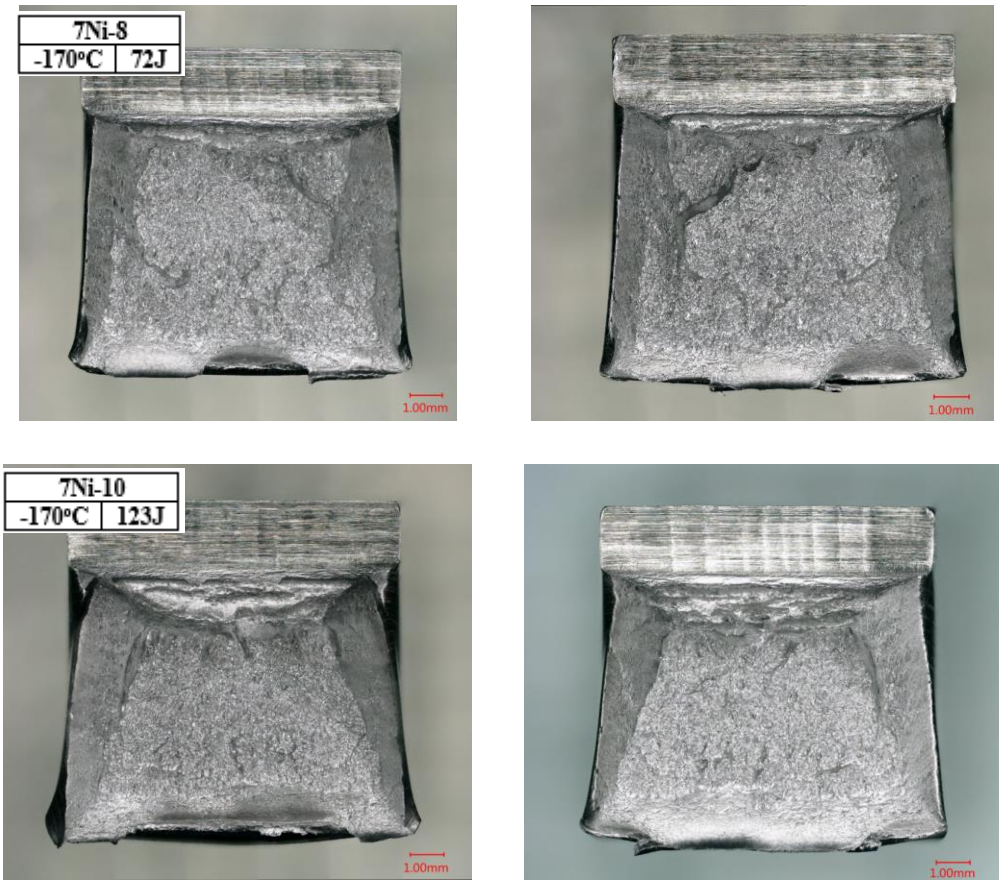

Figure 6.21

Fracture Surfaces of 7%Ni Steel CVN Specimens tested from -196 to -80ºC

-170 ºC

-160 ºC

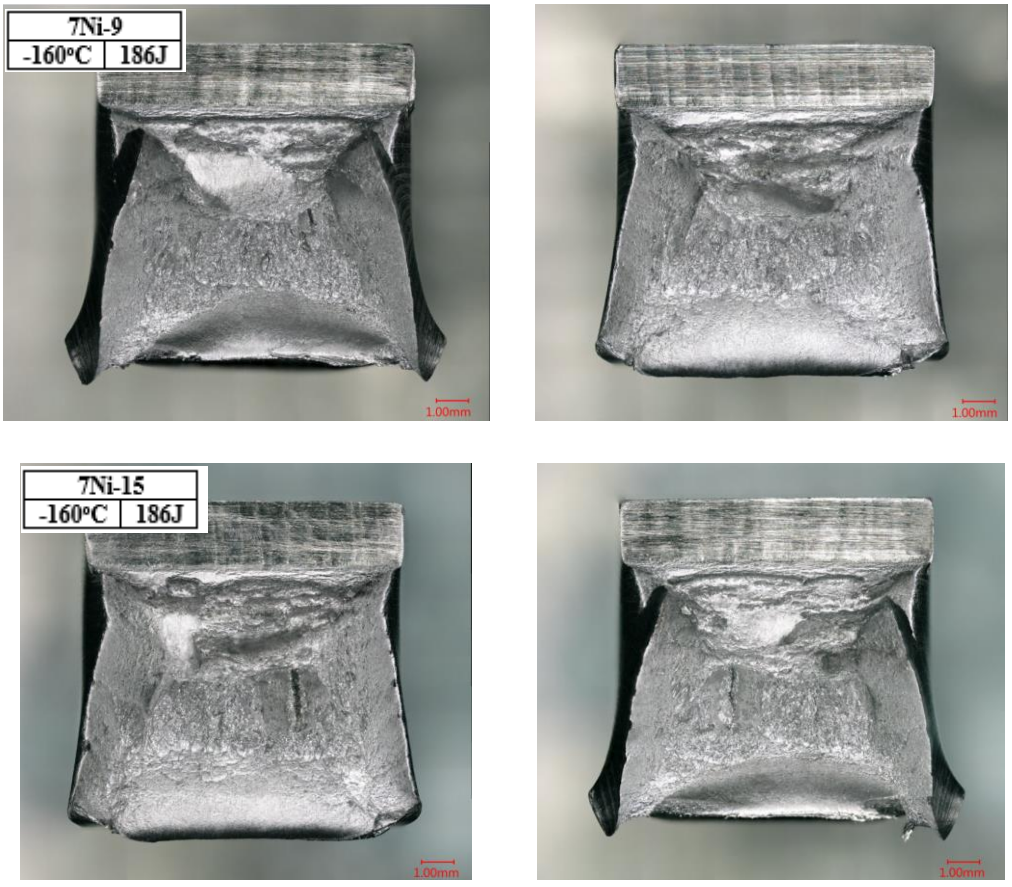

Figure 6.21

Fracture Surfaces of 7%Ni Steel CVN Specimens tested from -196 to -80ºC

-150 ºC

-140 ºC

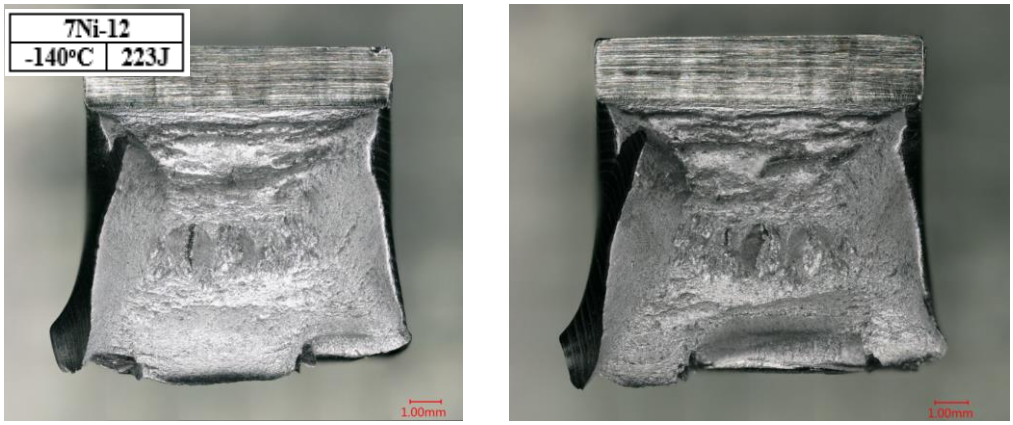

-130 ºC

Figure 6.21

Fracture Surfaces of 7%Ni Steel CVN Specimens tested from -196 to -80ºC

-100 ºC

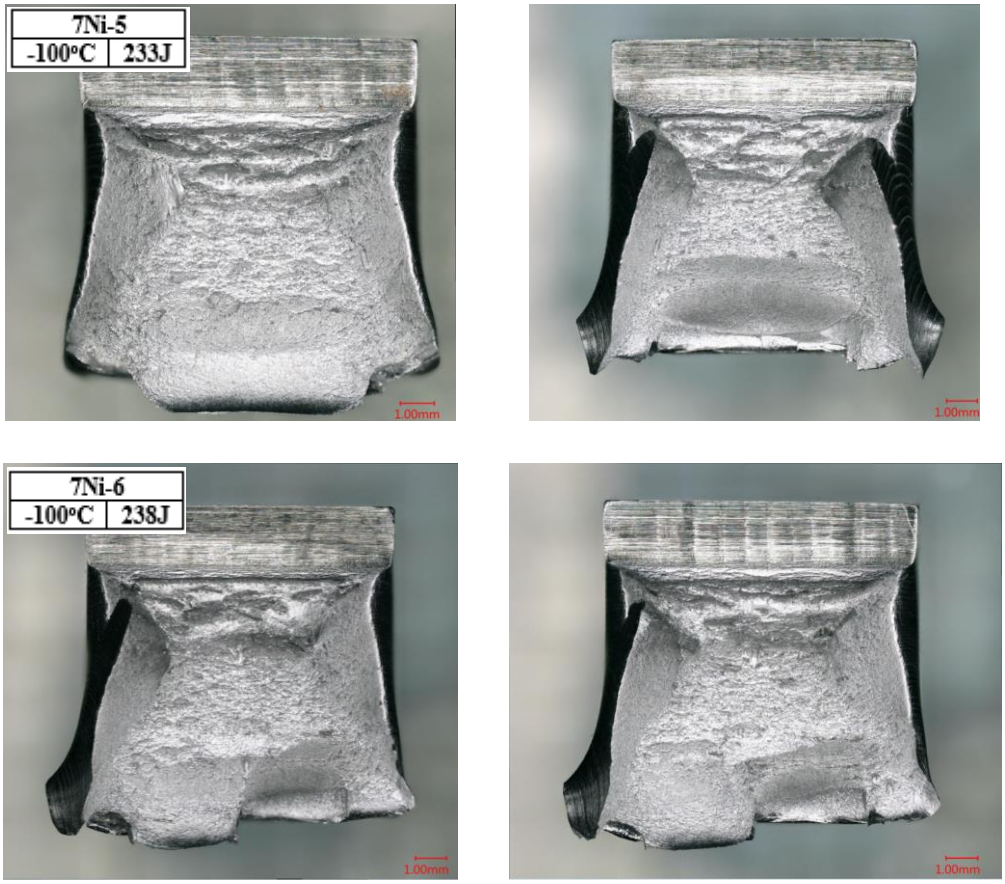

-80 ºC

Figure 6.22

Impact Energy vs. Test Temperatures of 7%Ni Steel with Than-fit Curve

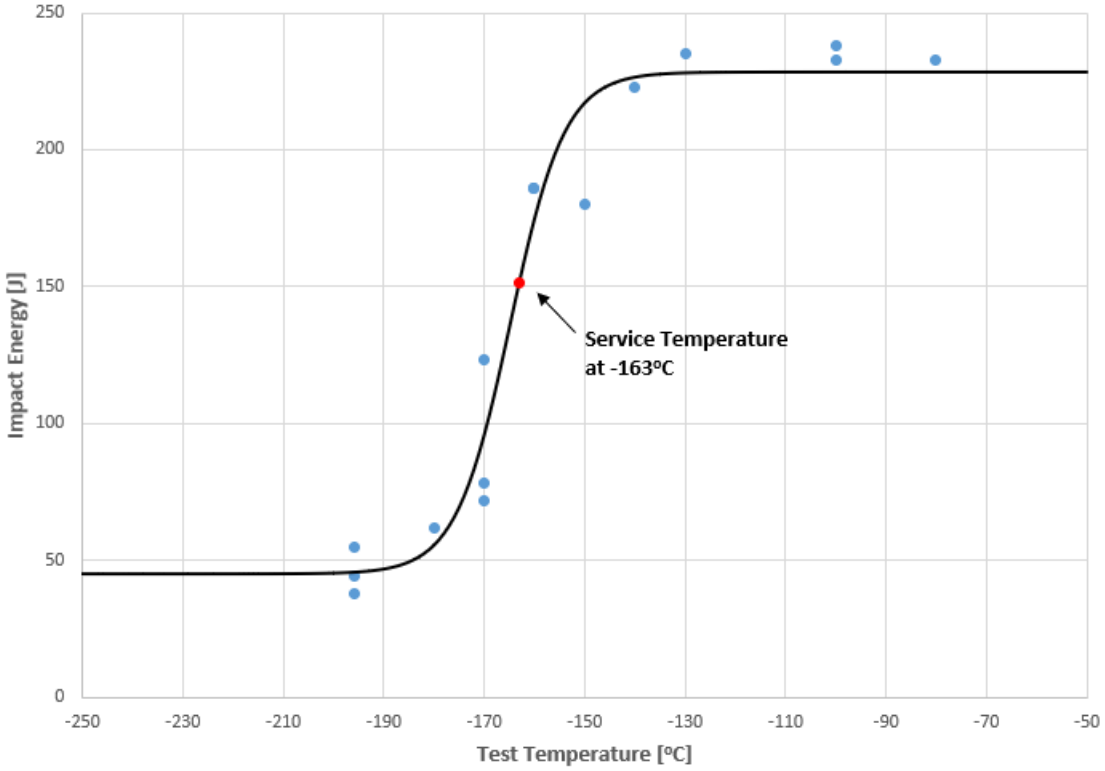

Figure 6.23

Relationship Between Absorbed Impact Energy and Lateral Expansion

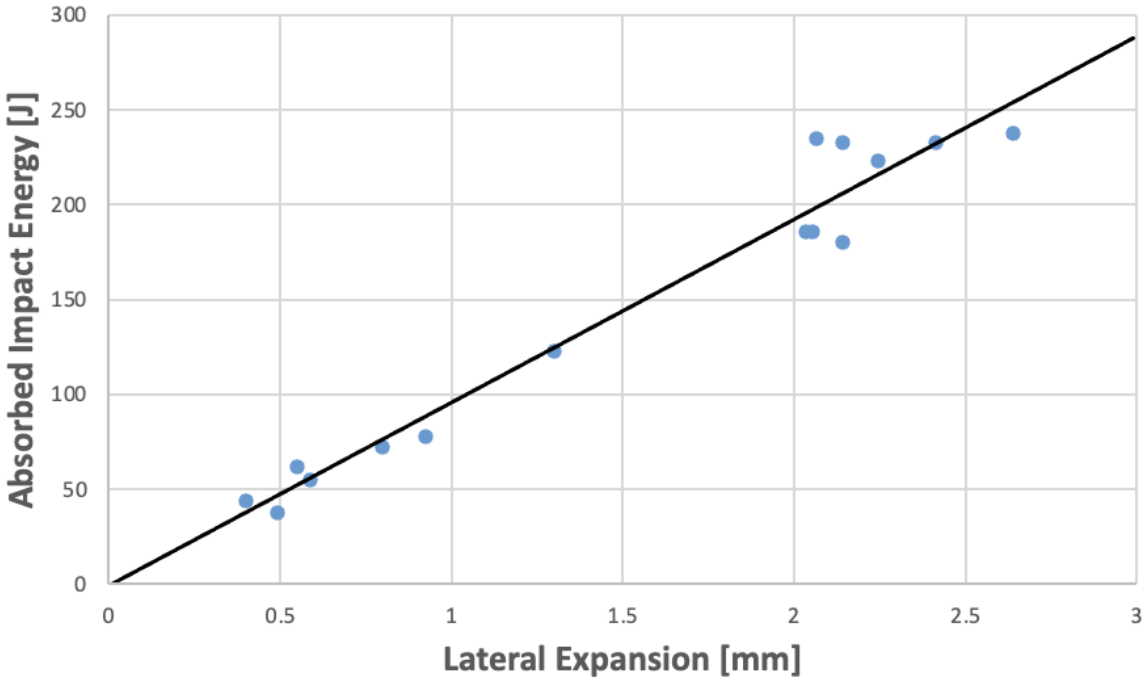

Figure 6.24

Relationship Between Absorbed Impact Energy and %Cleavage Area

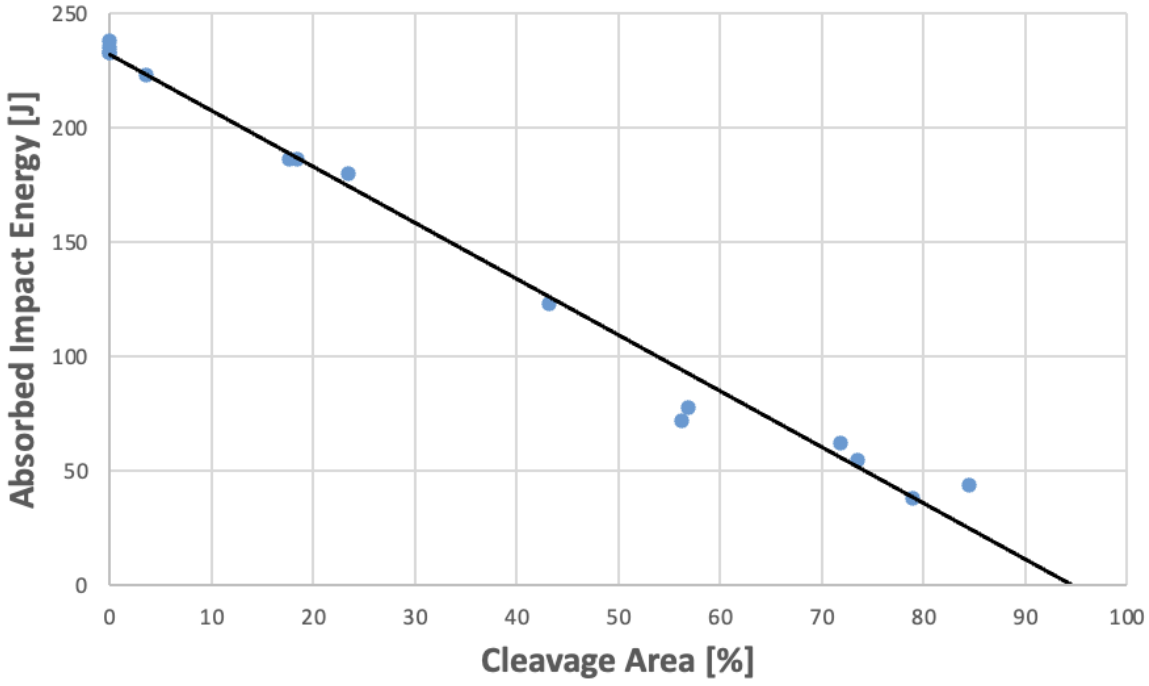

Figure 6.25

Fracture Surface of 7%Ni Steel CVN Specimens

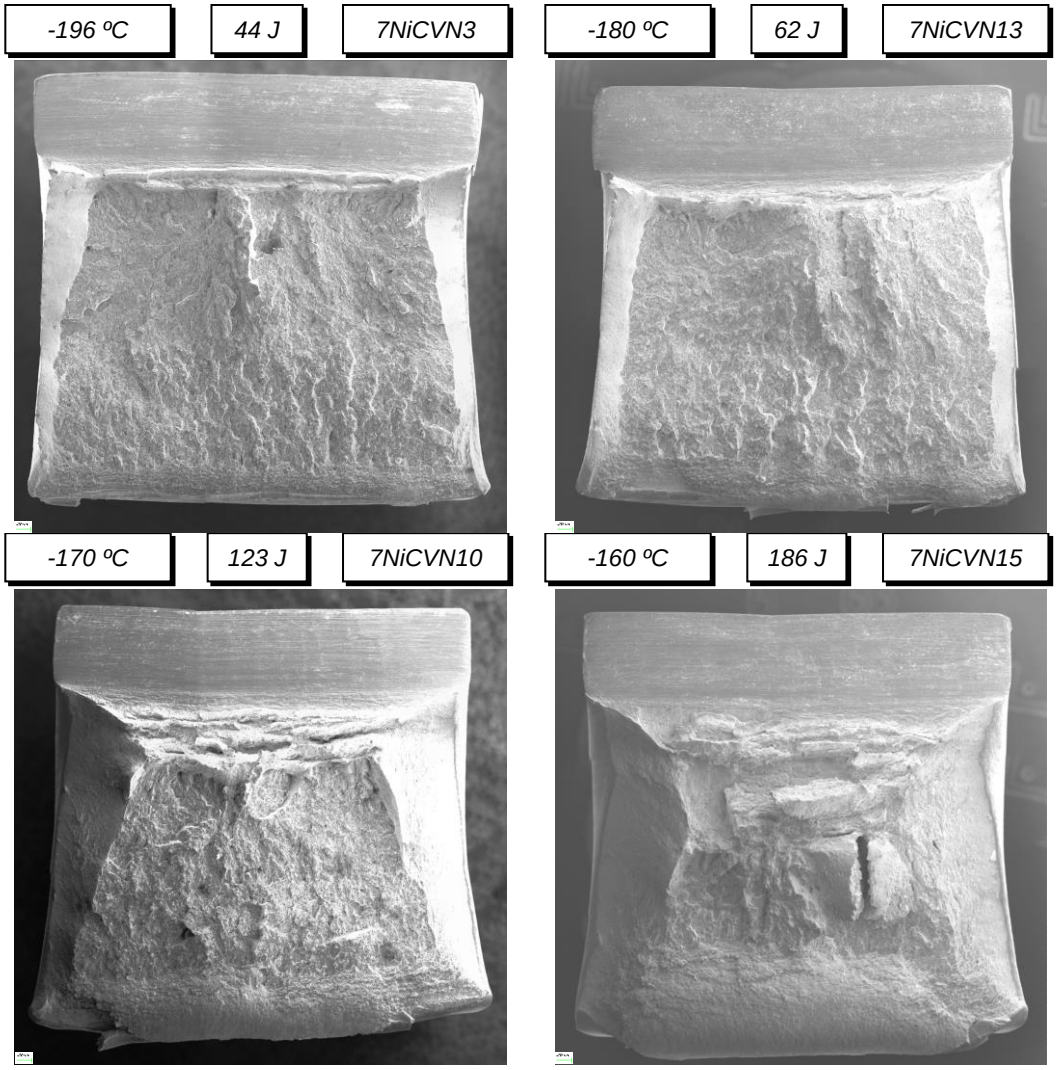

Figure 6.25

Fracture Surface of 7%Ni Steel CVN Specimens

-150 ºC | 180 J | 7NiCVN7

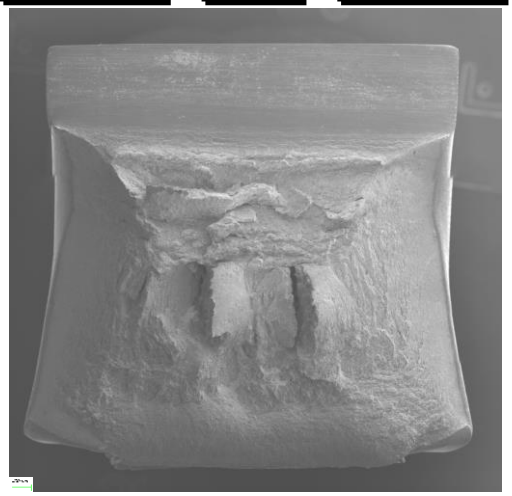

-140 ºC | 223 J | 7NiCVN12

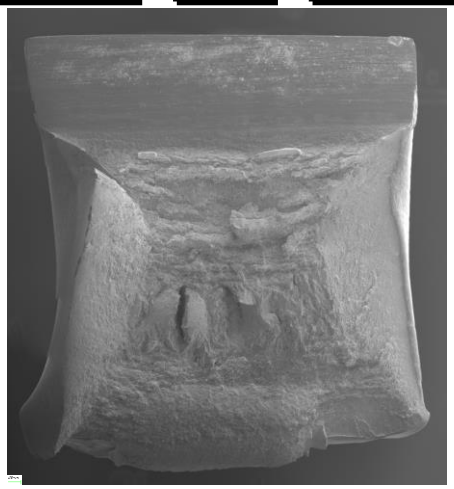

-130 ºC | 235 J | 7NiCVN11

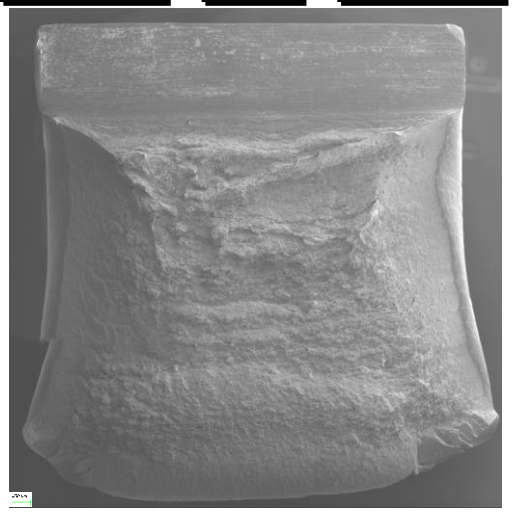

-100 ºC | 238 J | 7NiCVN6

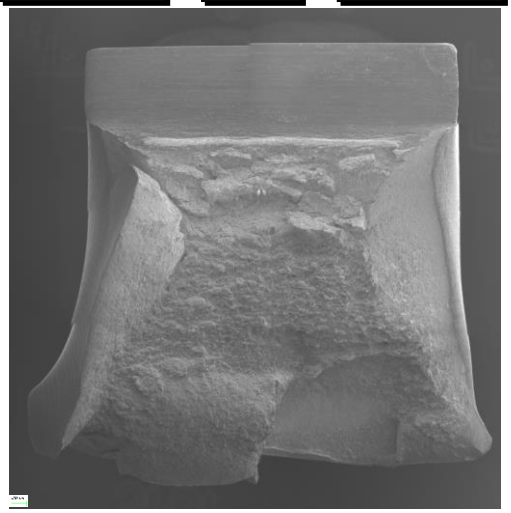

-80 ºC | 233 J | 7NiCVN4

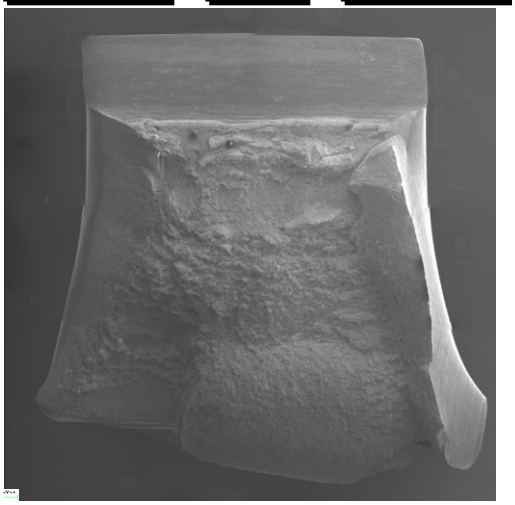

7Ni-CVN1

-196 °C

Figure 6.26a

38 J

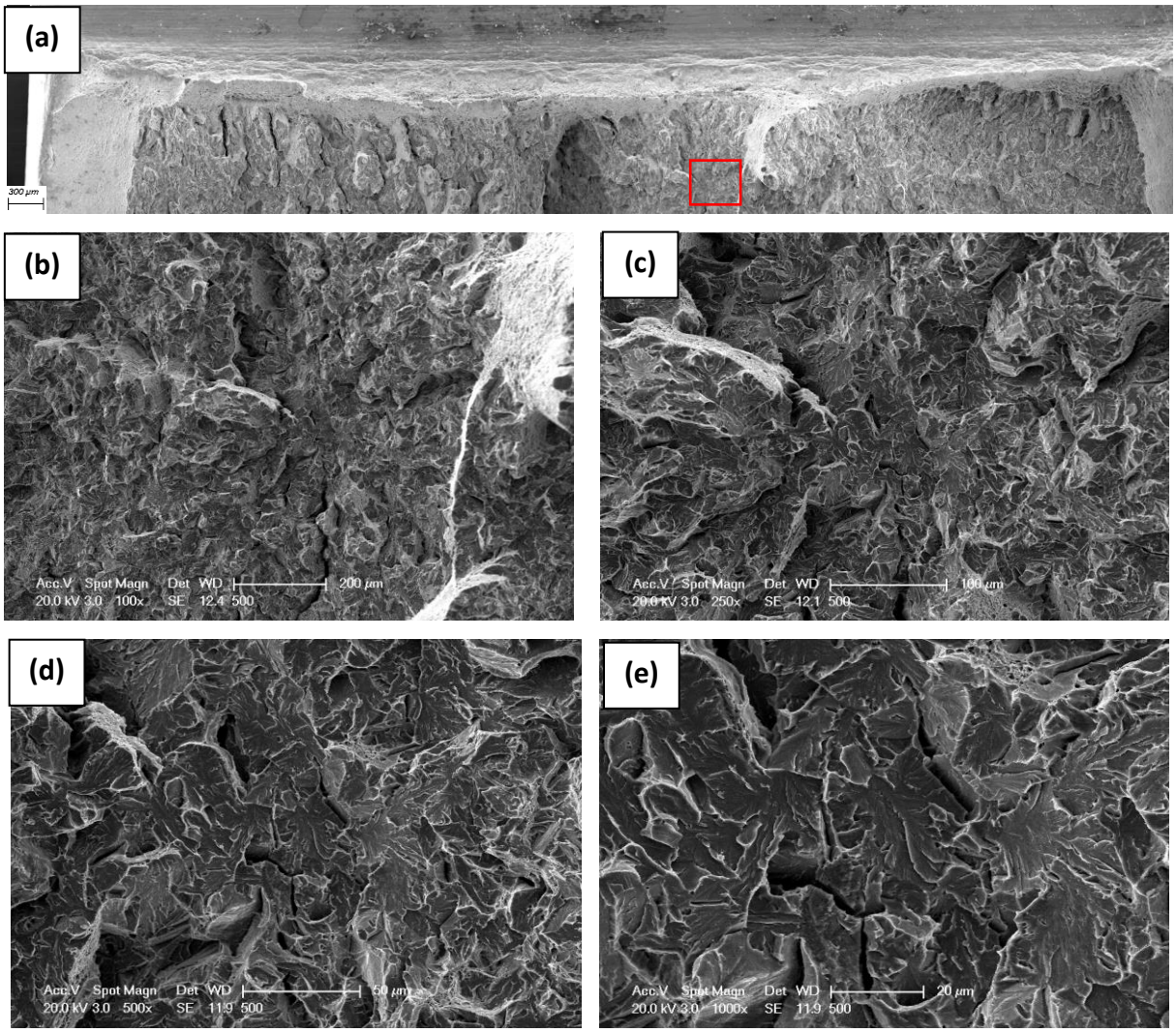

(a): Possible initiation site is circled in red; **(b), (c), (d), (e)**: detail of circled site in magnification sequence.

7Ni-CVN1

-196 °C

Figure 6.26b

38 J

(f), (g), (h), (i): detail of circled site in magnification sequence on **opposite side.**

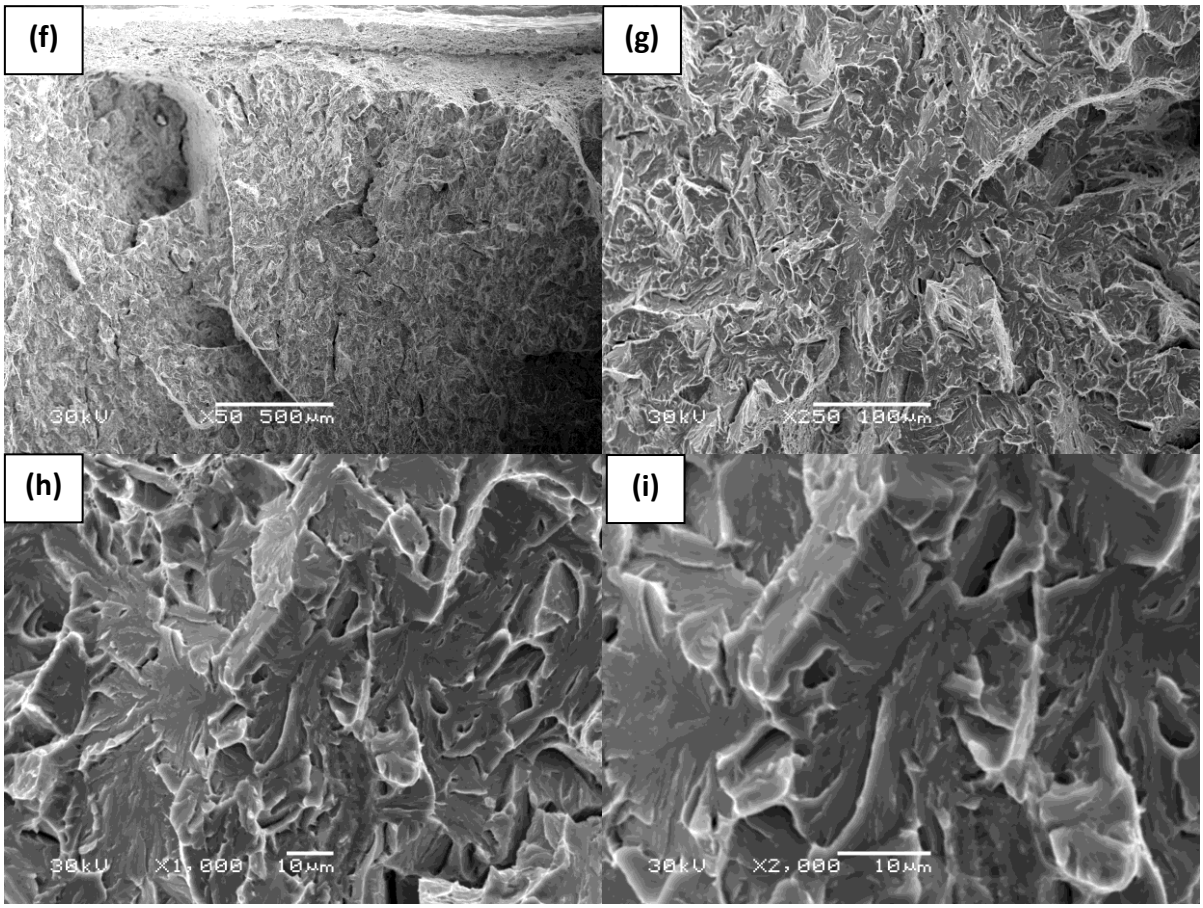

7Ni-CVN2

-196 °C

Figure 6.27a

55 J

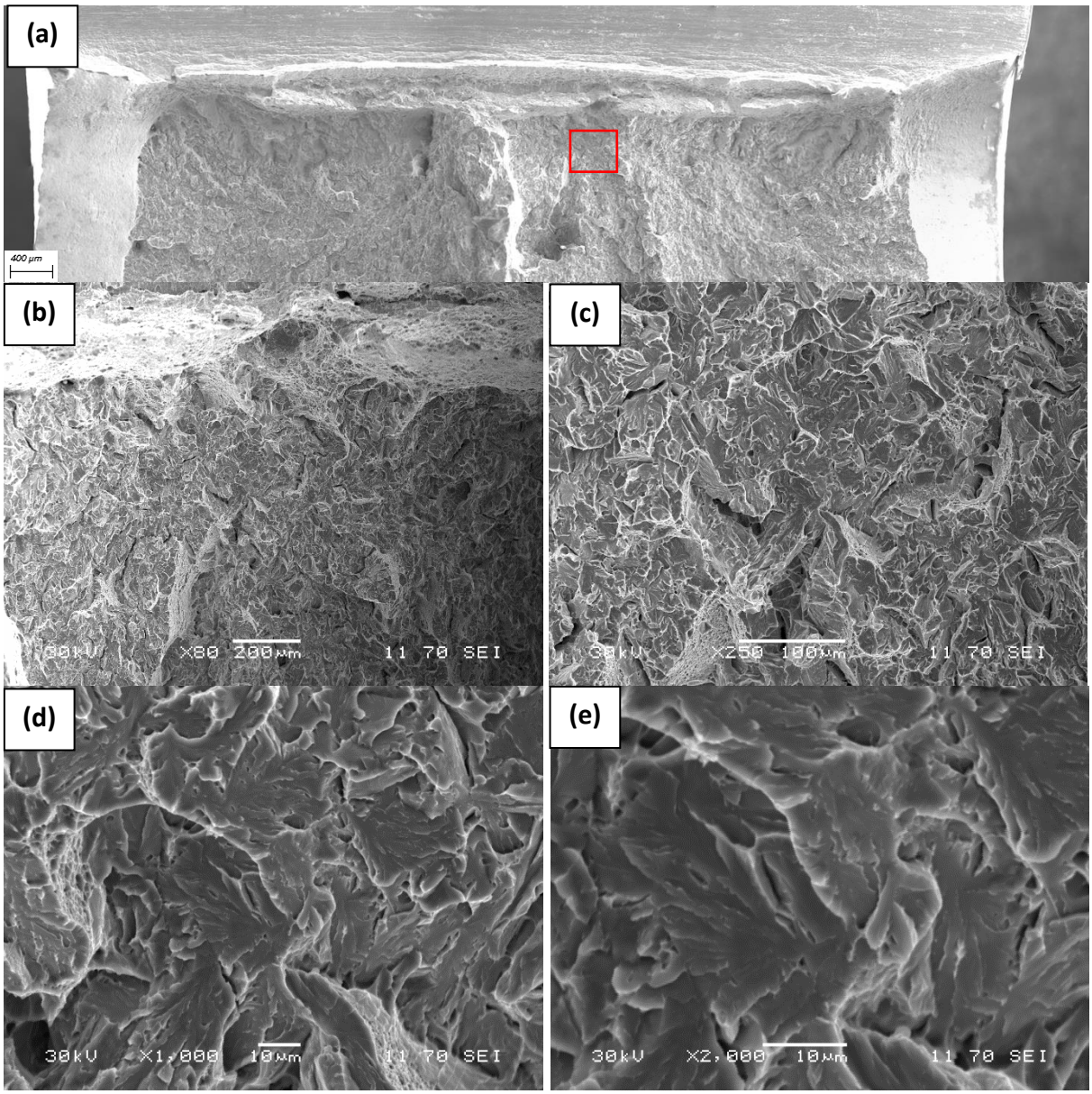

(a): Possible initiation site is circled in red; **(b), (c), (d), (e)**: detail of circled site in magnification sequence.

7Ni-CVN2

-196 °C

Figure 6.27b

55 J

(f), (g), (h), (i): detail of circled site in magnification sequence on **opposite side.**

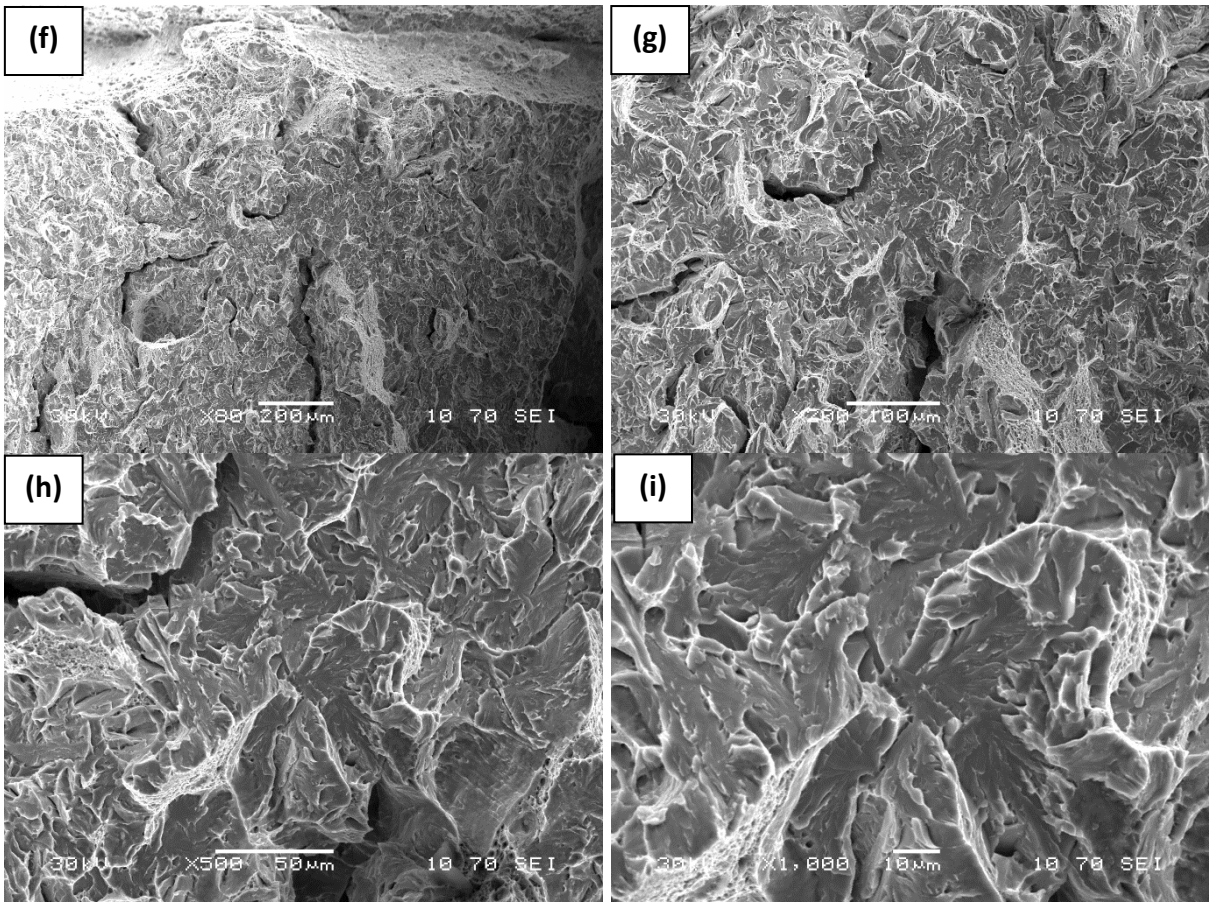

7Ni-CVN3

-196 °C

Figure 6.28

44 J

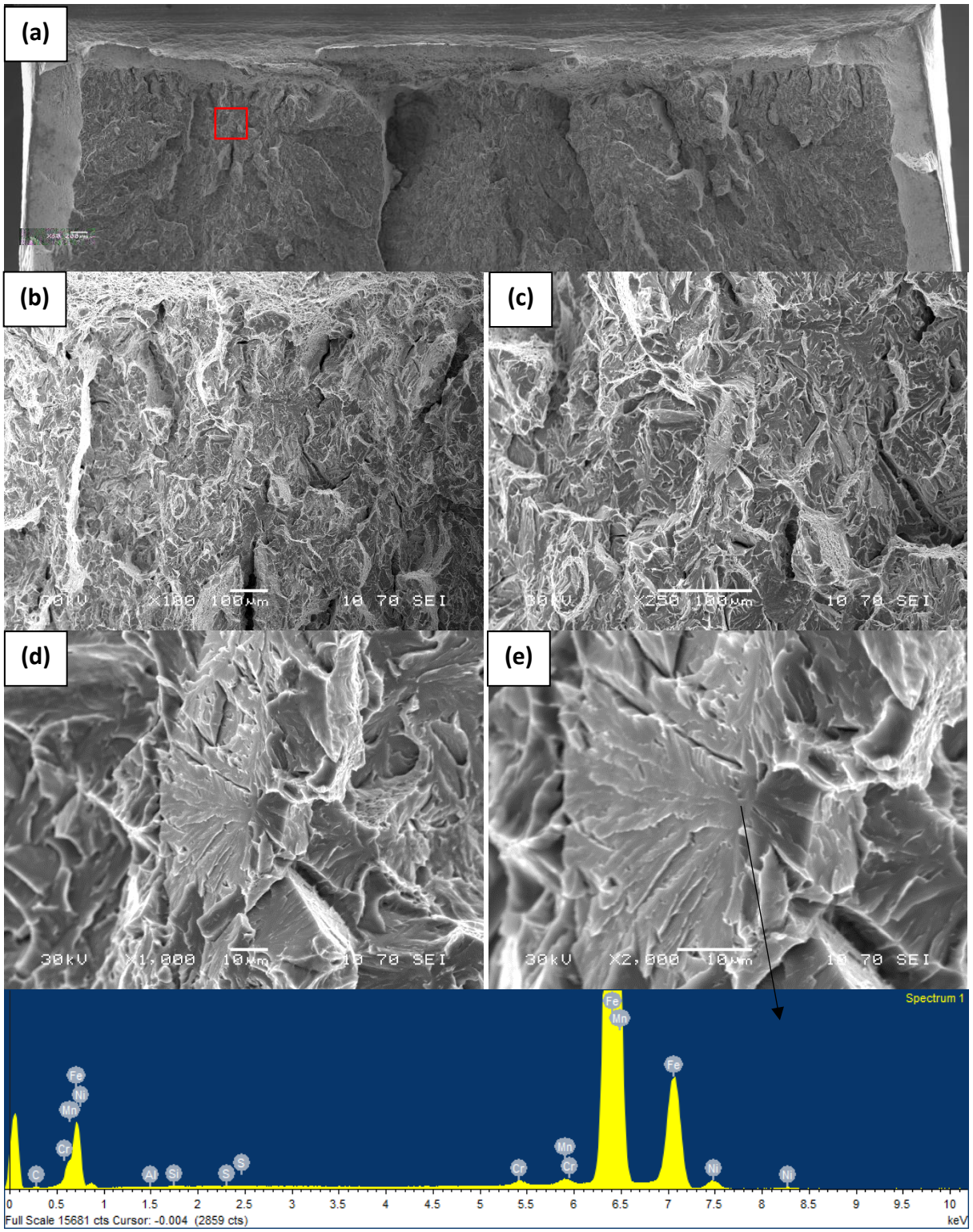

(a): Possible initiation site is circled in red; **(b), (c), (d), (e)**: detail of circled site in magnification sequence.

7Ni-CVN13

-180 °C

Figure 6.29a

62 J

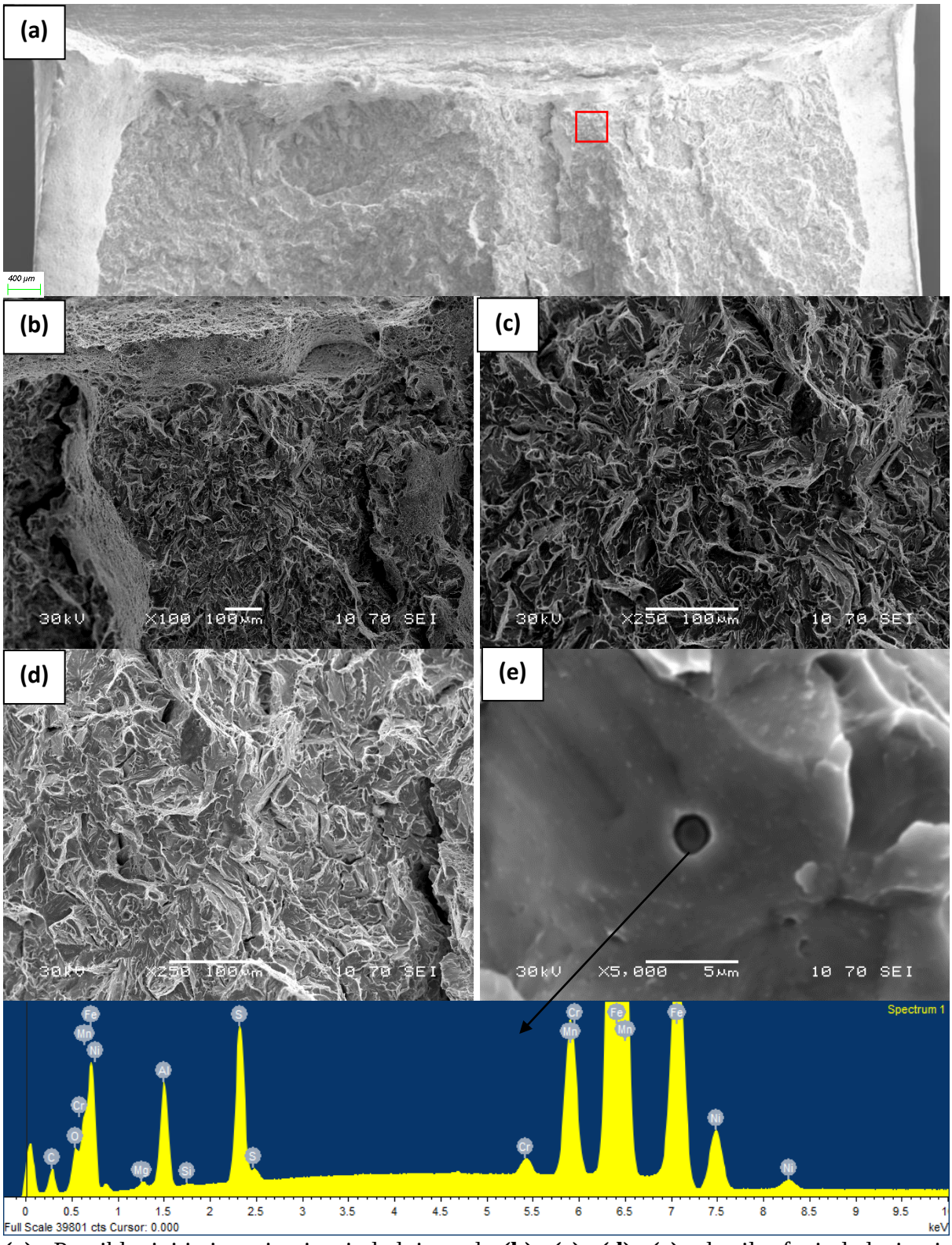

(a): Possible initiation site is circled in red; **(b), (c), (d), (e)**: detail of circled site in magnification sequence.

7Ni-CVN13

-180 °C

Figure 6.29b

62 J

(f), (g), (h), (i): detail of circled site in magnification sequence on **opposite side.**

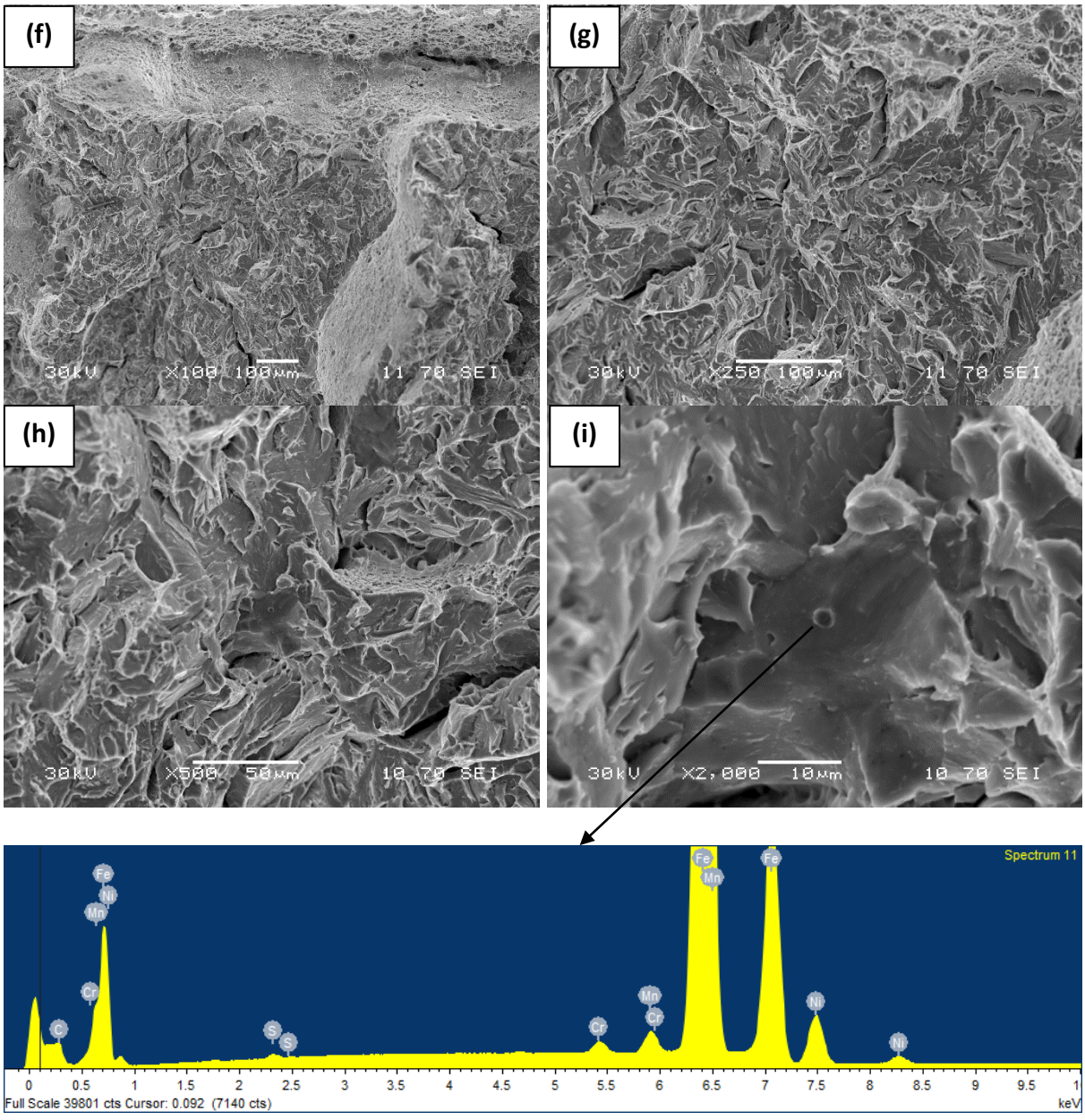

7Ni-CVN14

-170 °C

Figure 6.30a

78 J

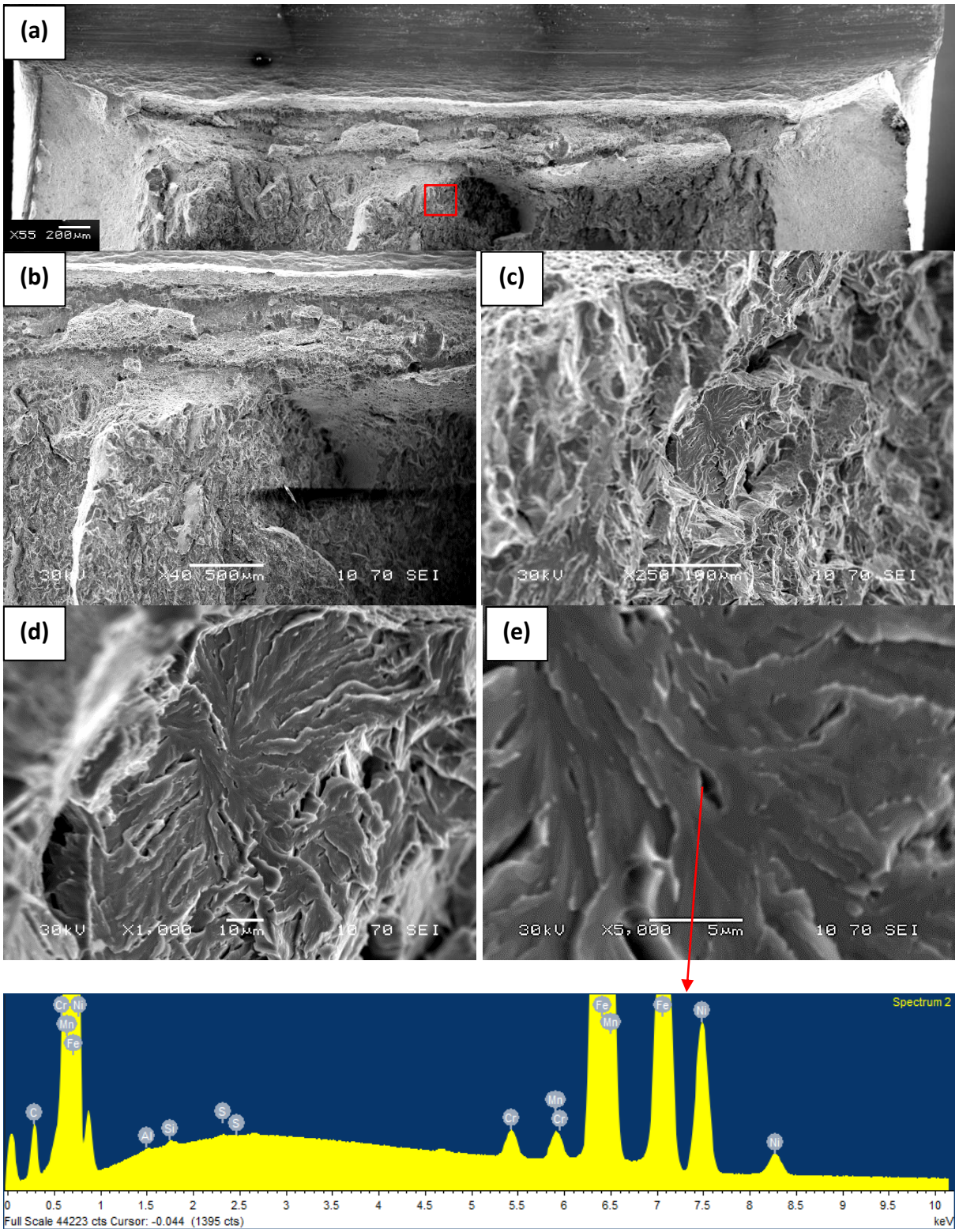

(a): Possible initiation site is circled in red; **(b), (c), (d), (e)**: detail of circled site in magnification sequence.

7Ni-CVN14

-170 °C

Figure 6.30b

78 J

(f), (g), (h), (i): detail of circled site in magnification sequence on **opposite side.**

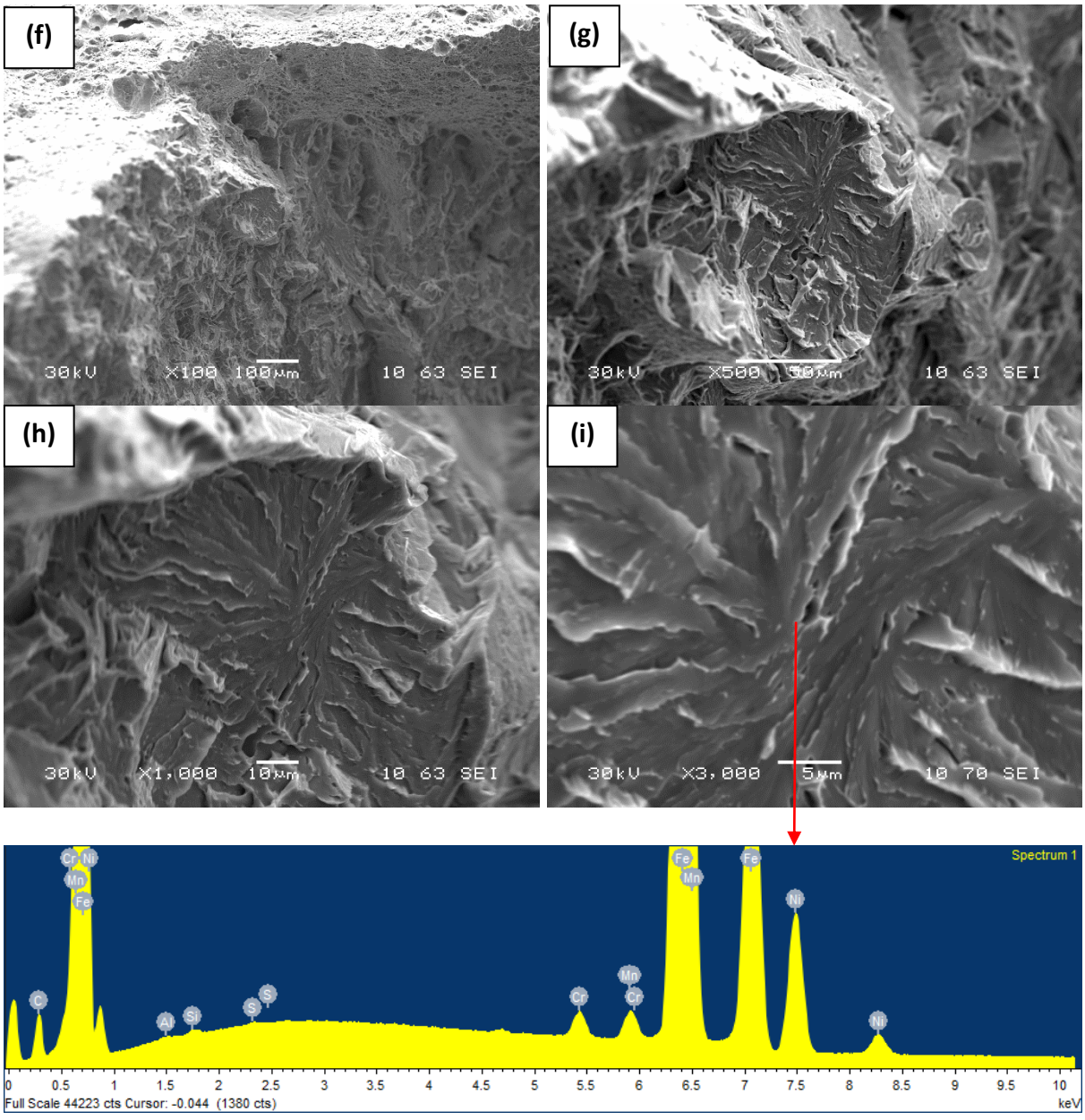

Figure 6.31

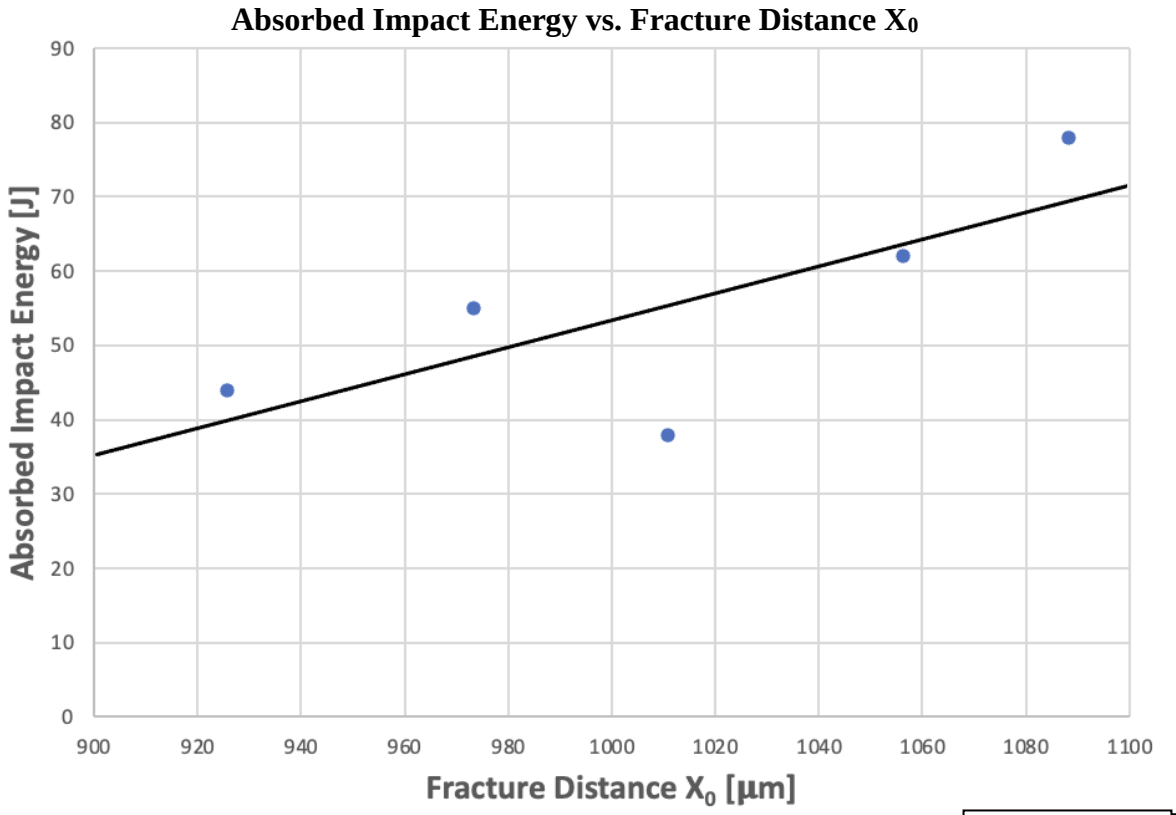

Figure 6.32

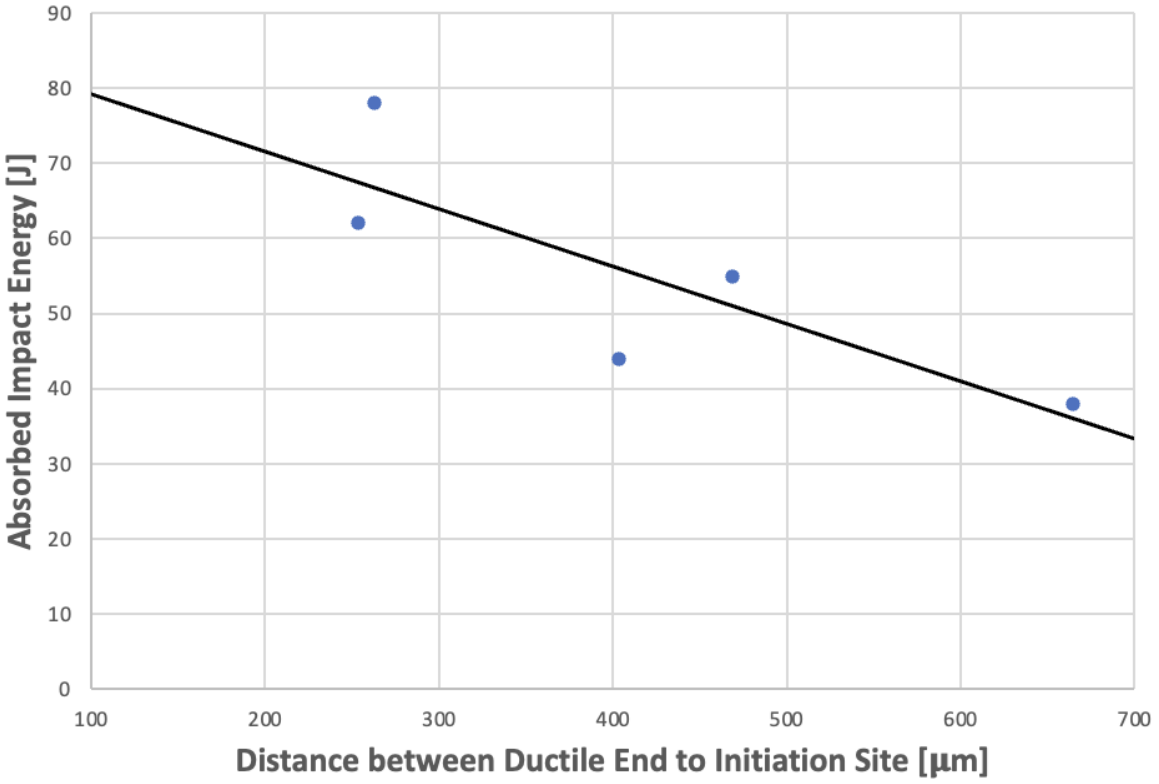

7Ni-CVN3

-196 °C

Figure 6.33

44 J

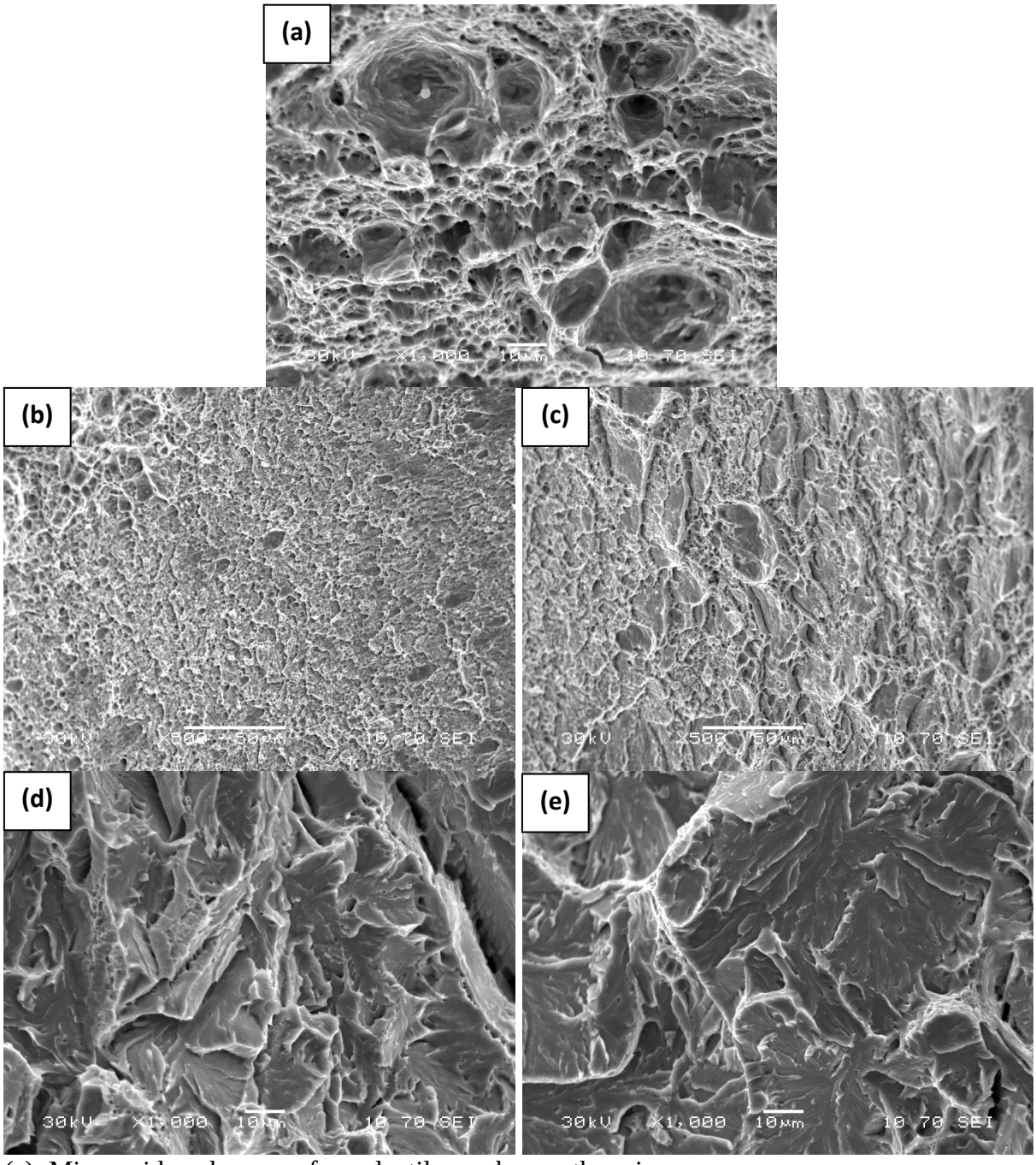

(a): Microvoid coalescence from ductile crack growth region
(b): Microvoid coalescence from left shear lip
(c): Microvoid coalescence from right shear lip
(d): Cleavage facets from middle of the sample
(e): Cleavage facets near the bottom of the sample

7Ni-CVN13

-180 °C

Figure 6.34

62 J

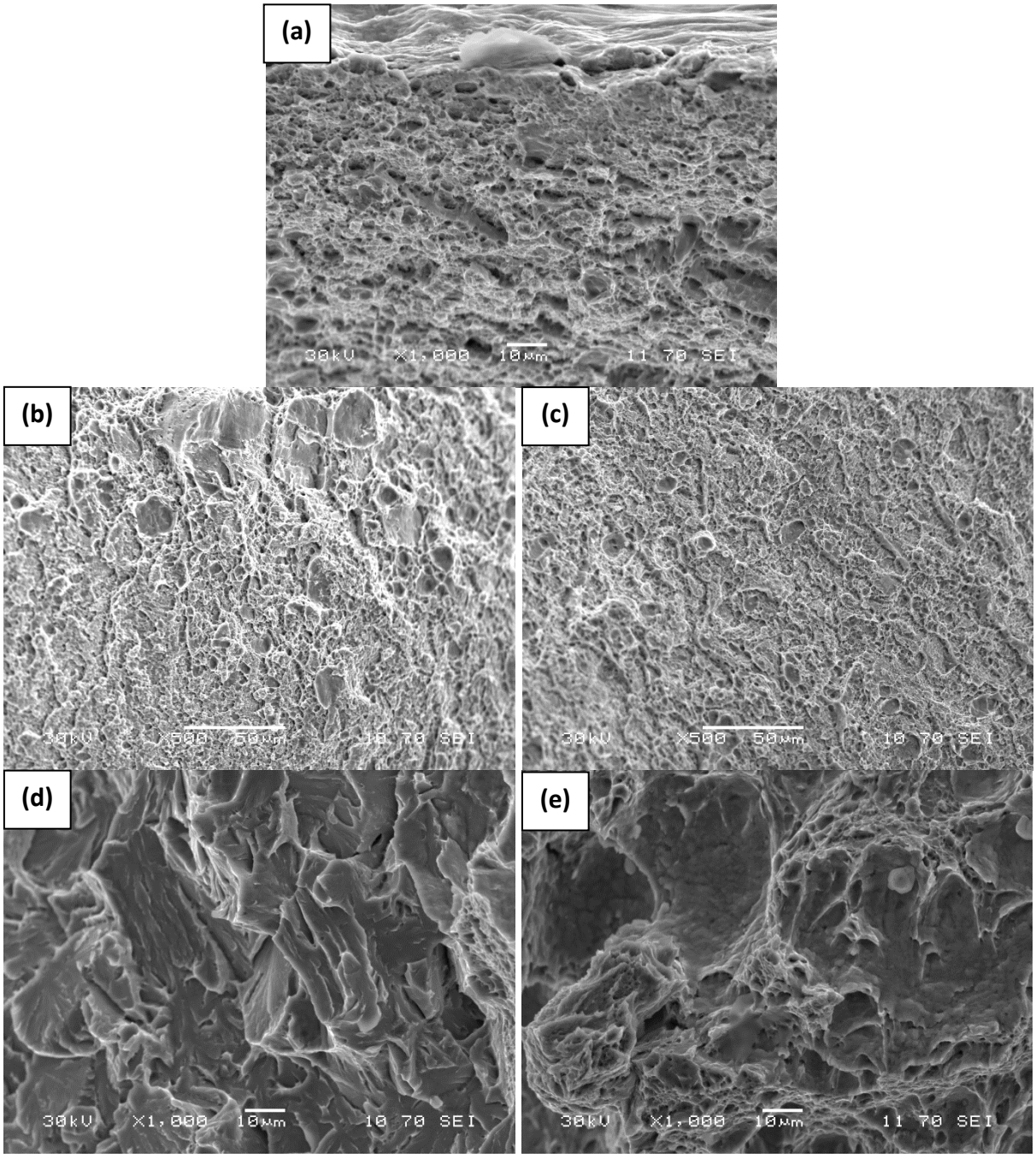

(a): Microvoid coalescence from ductile crack growth region
(b): Microvoid coalescence from left shear lip
(c): Microvoid coalescence from right shear lip
(d): Cleavage facets from middle of the sample
(e): Microvoid coalescence from the bottom of the sample

7Ni-CVN8

-170 °C

Figure 6.35

72 J

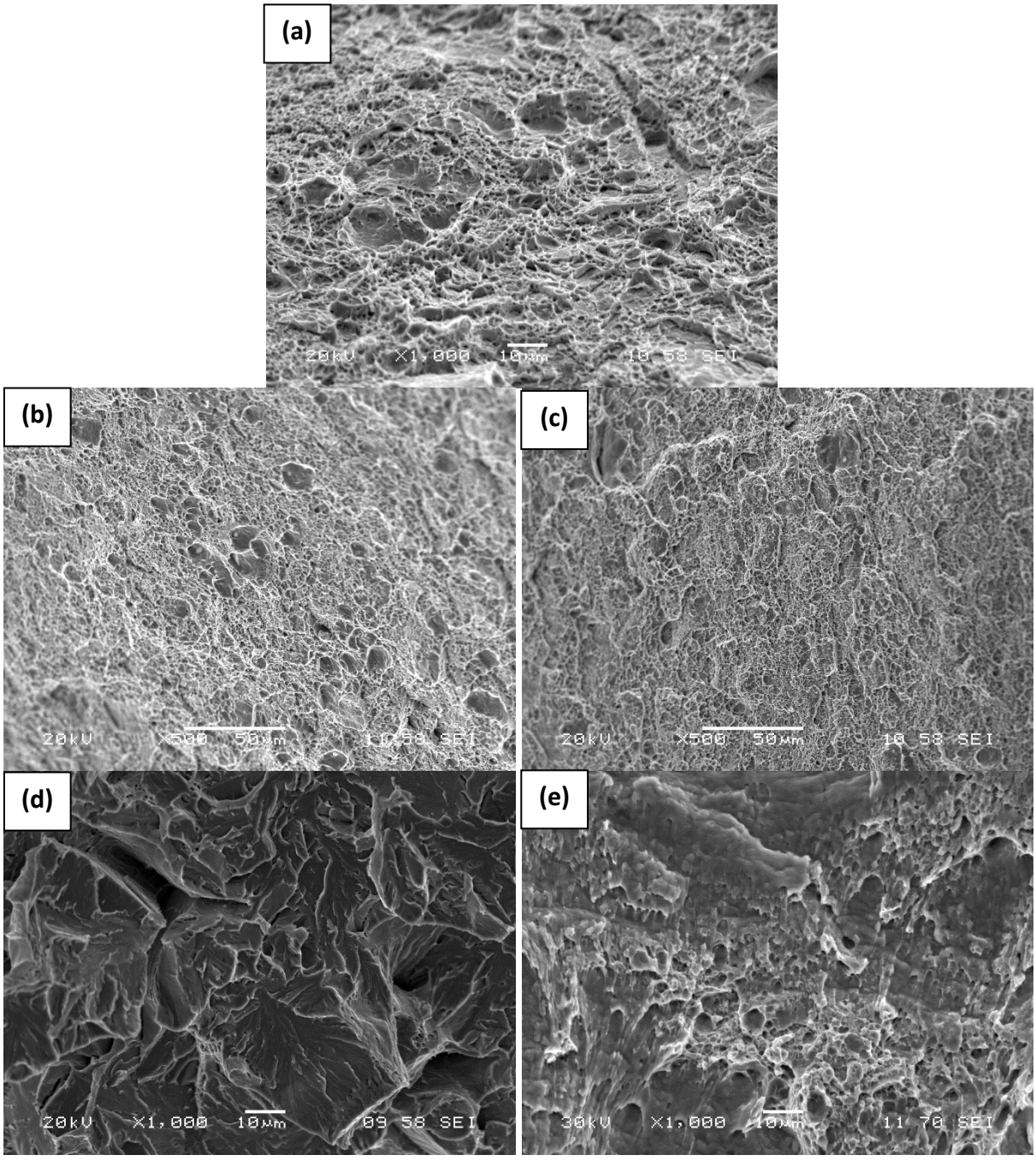

(a): Microvoid coalescence from ductile crack growth region
(b): Microvoid coalescence from left shear lip
(c): Microvoid coalescence from right shear lip
(d): Cleavage facets from middle of the sample
(e): Microvoid coalescence from the bottom of the sample

7Ni-CVN10

-170 °C

Figure 6.36

123 J

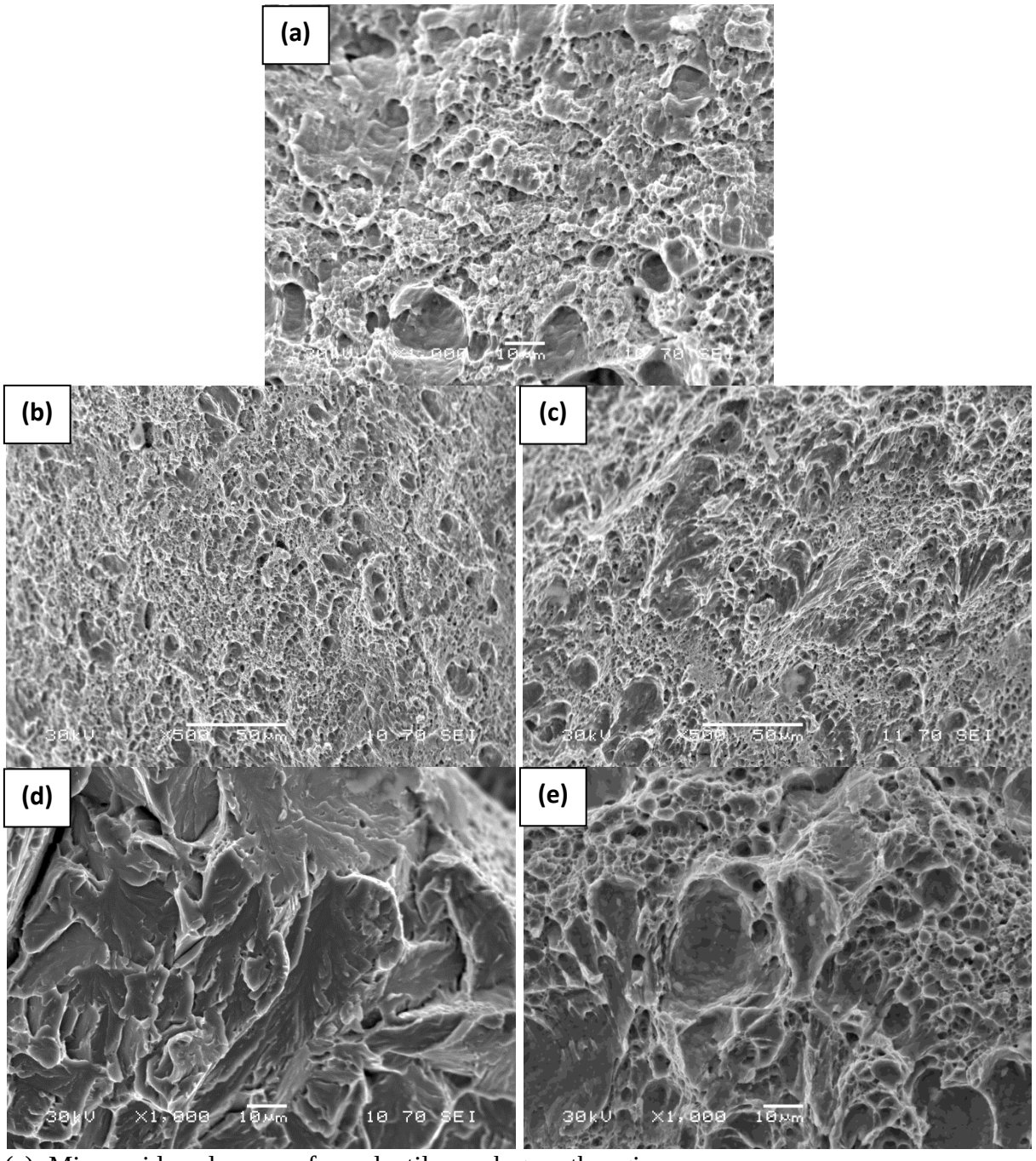

(a): Microvoid coalescence from ductile crack growth region
(b): Microvoid coalescence from left shear lip
(c): Microvoid coalescence from right shear lip
(d): Cleavage facets from middle of the sample
(e): Microvoid coalescence from the bottom of the sample

7Ni-CVN15

-160 °C

Figure 6.37

186 J

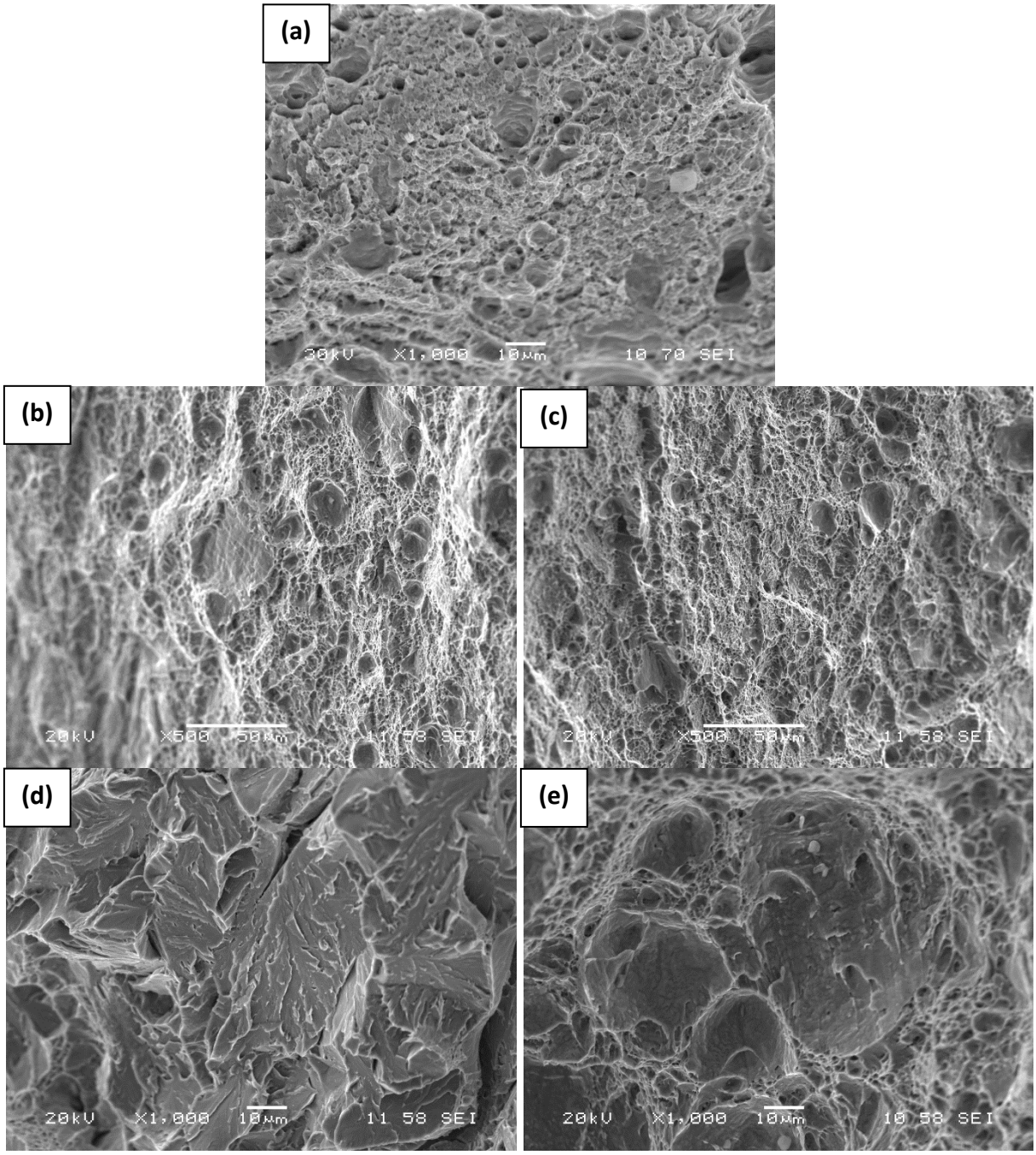

(a): Microvoid coalescence from ductile crack growth region
(b): Microvoid coalescence from left shear lip
(c): Microvoid coalescence from right shear lip
(d): Cleavage facets from middle of the sample
(e): Microvoid coalescence from middle of the sample

7Ni-CVN7

-150 °C

Figure 6.38

180 J

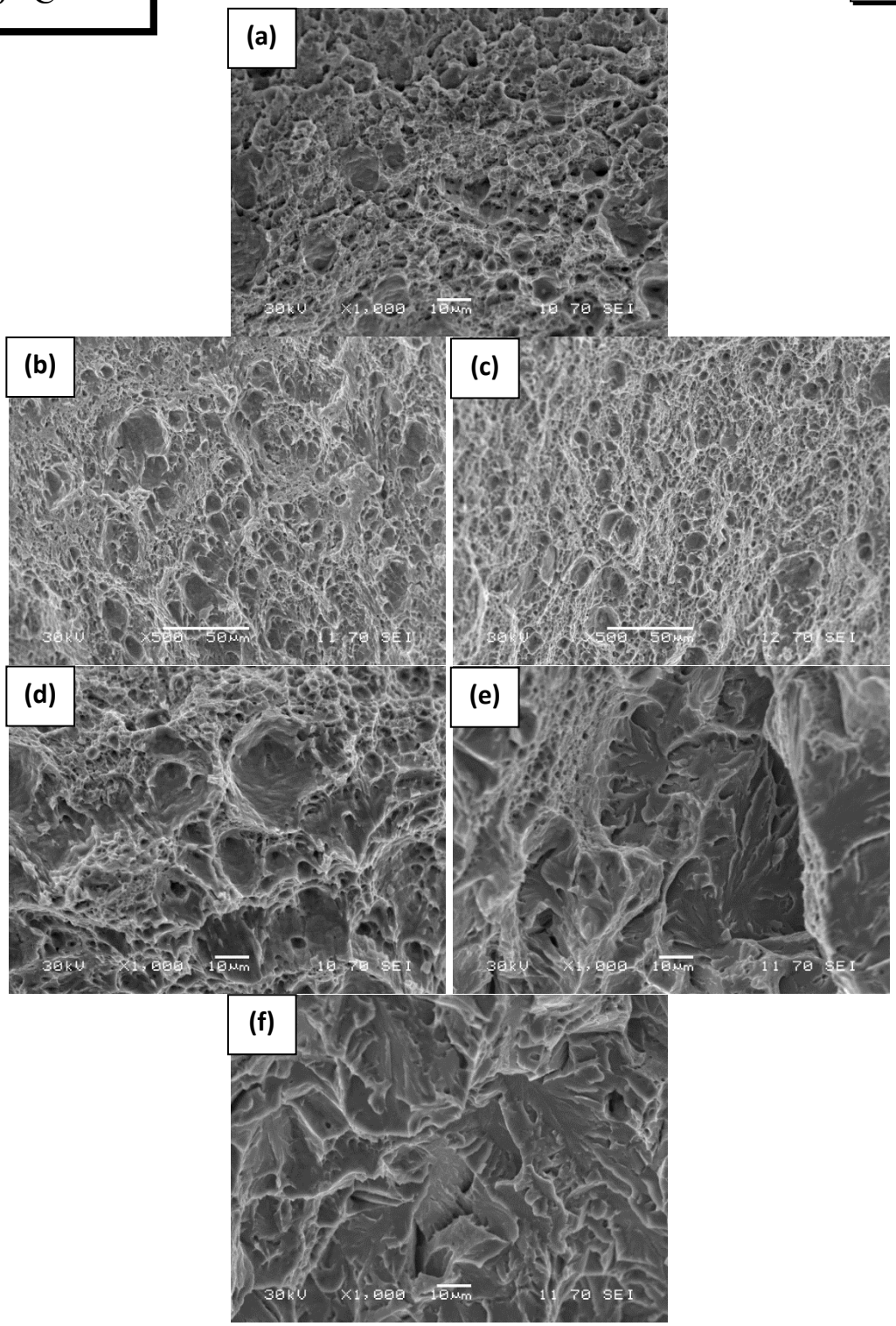

(a): Microvoid coalescence from ductile crack growth region
(b)(c): Microvoid coalescence from left and right shear lip
(d): Microvoid coalescence from middle of the sample
(e): Cleavage facets from middle of the sample
(f): Cleavage facets from bottom of the sample

7Ni-CVN12

-140 °C

Figure 6.39

223 J

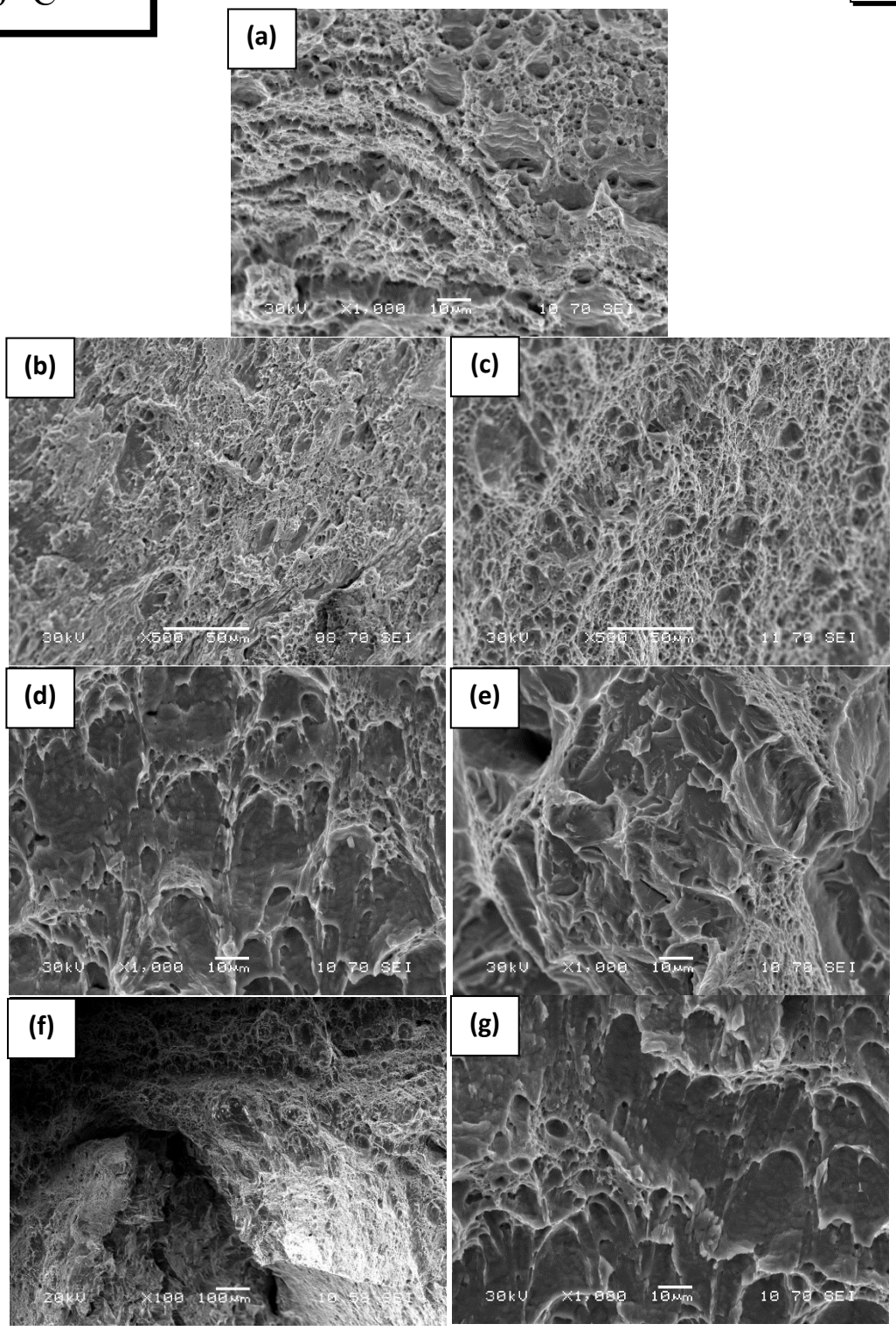

(a): Microvoid coalescence from ductile crack growth region
(b) (c): Microvoid coalescence from left and right shear lip
(d) (e): Microvoid coalescence and cleavage facets from middle of the sample respectively.
(f): Detail of split, and cleavage facets inside split and microvoid coalescence around split.
(g): Microvoid coalescence from bottom of the sample

7Ni-CVN11

-130 °C

Figure 6.40

235 J

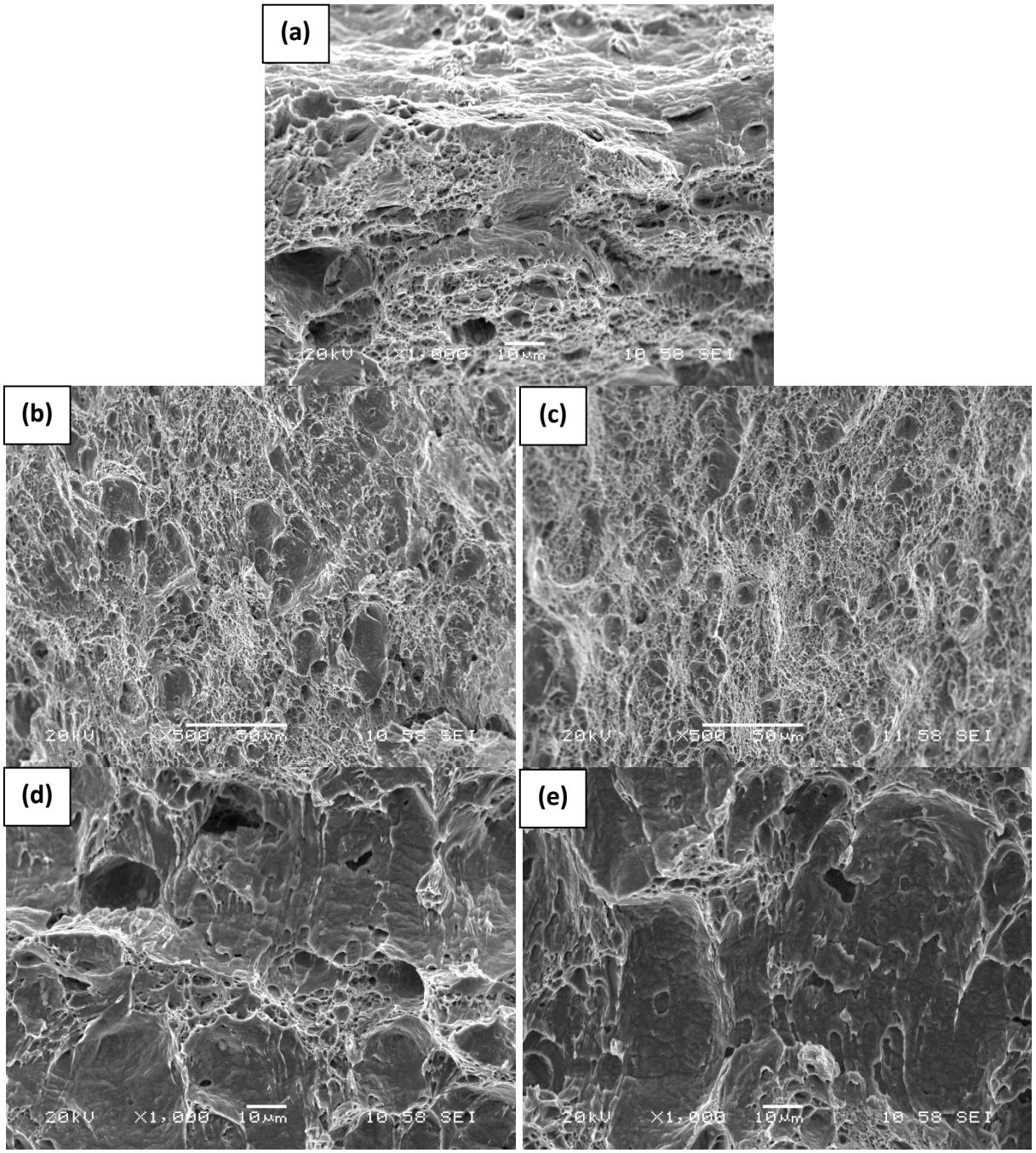

(a): Microvoid coalescence from ductile crack growth region
(b): Microvoid coalescence from left shear lip
(c): Microvoid coalescence from right shear lip
(d): Microvoid coalescence from middle of the sample
(e): Microvoid coalescence from bottom of the sample

7Ni-CVN4

-80 °C

Figure 6.41

233 J

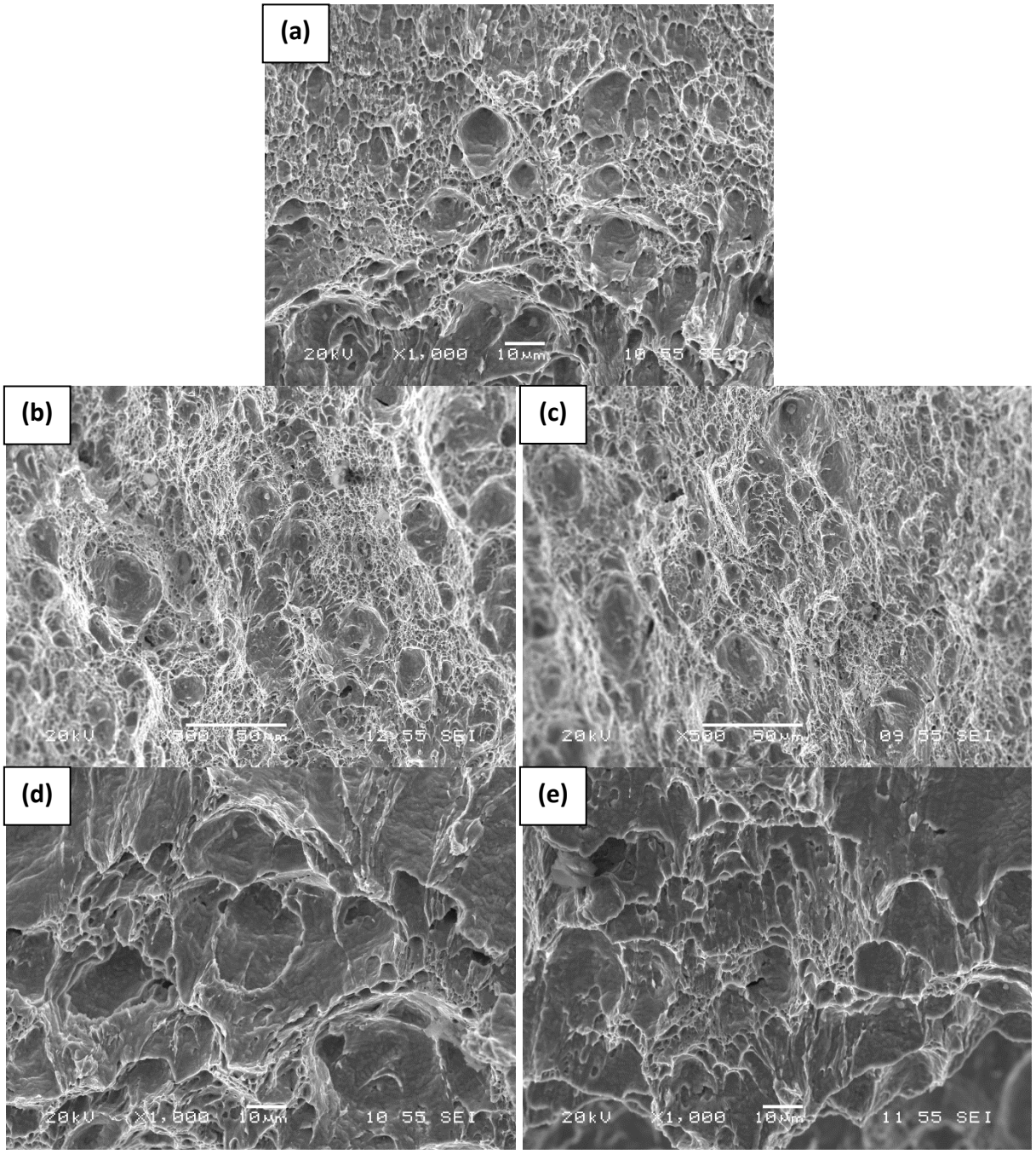

(a): Microvoid coalescence from ductile crack growth region
(b): Microvoid coalescence from left shear lip
(c): Microvoid coalescence from right shear lip
(d): Microvoid coalescence from middle of the sample
(e): Microvoid coalescence from bottom of the sample

Figure 6.42

EDX Mapping of the Inclusion from 7Ni-CVN13 tested at -180ºC

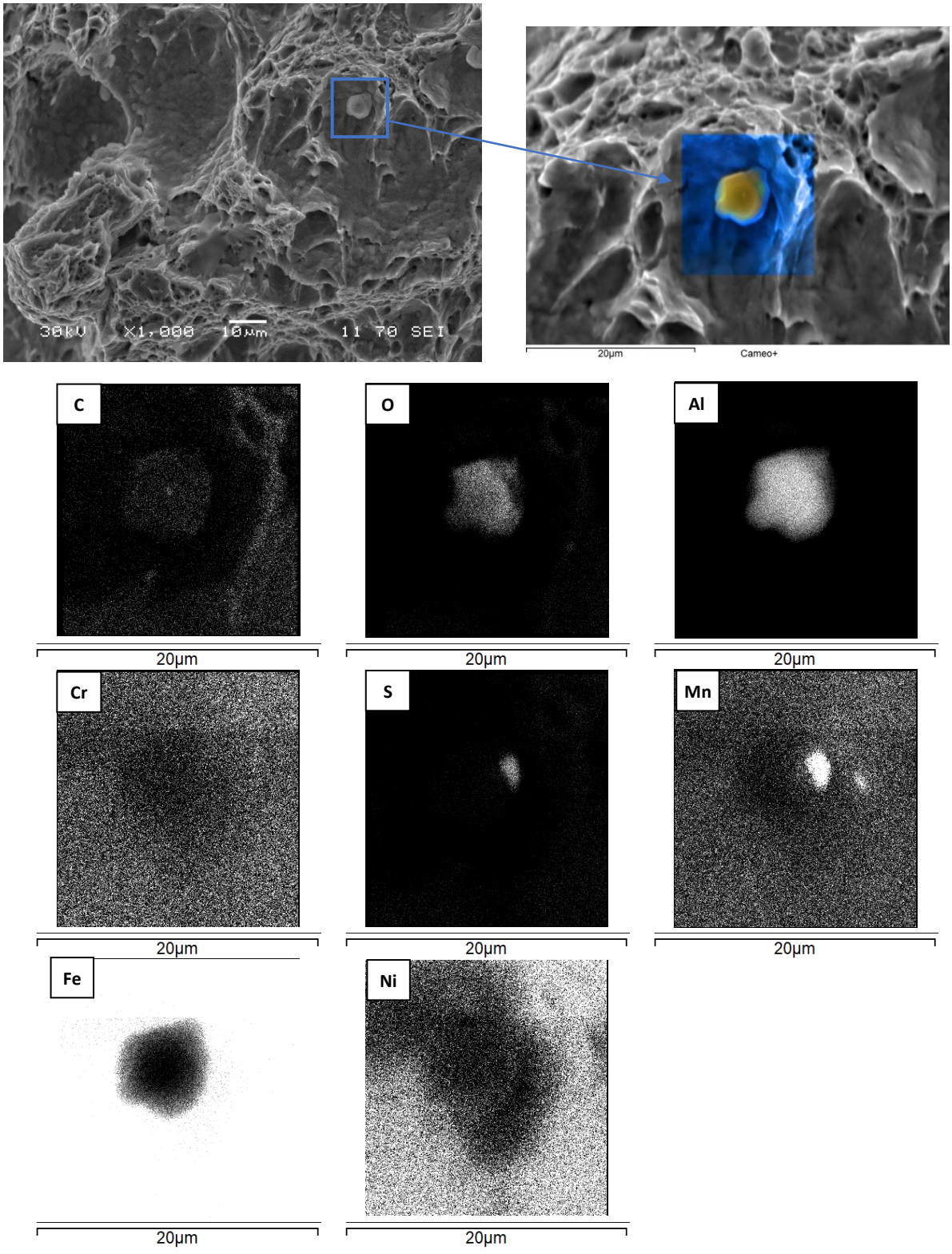

Figure 6.43

Broken Halves of 7%Ni Steel Fracture Stress Specimens tested at -196ºC

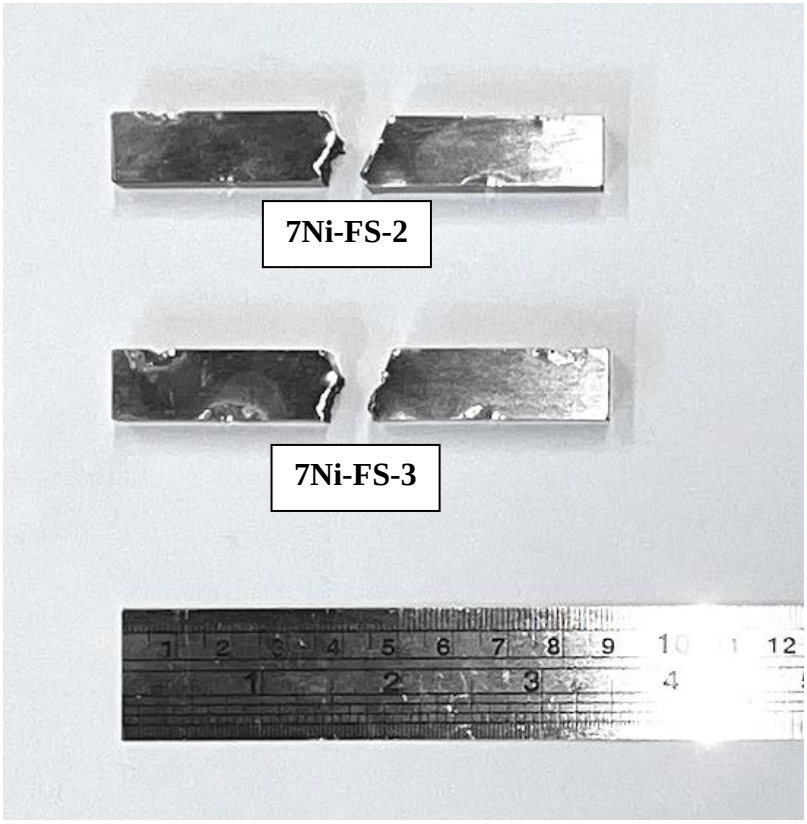

Figure 6.44

Broken Halves of Fracture Stress Specimens tested at -196ºC

7Ni-FS-2

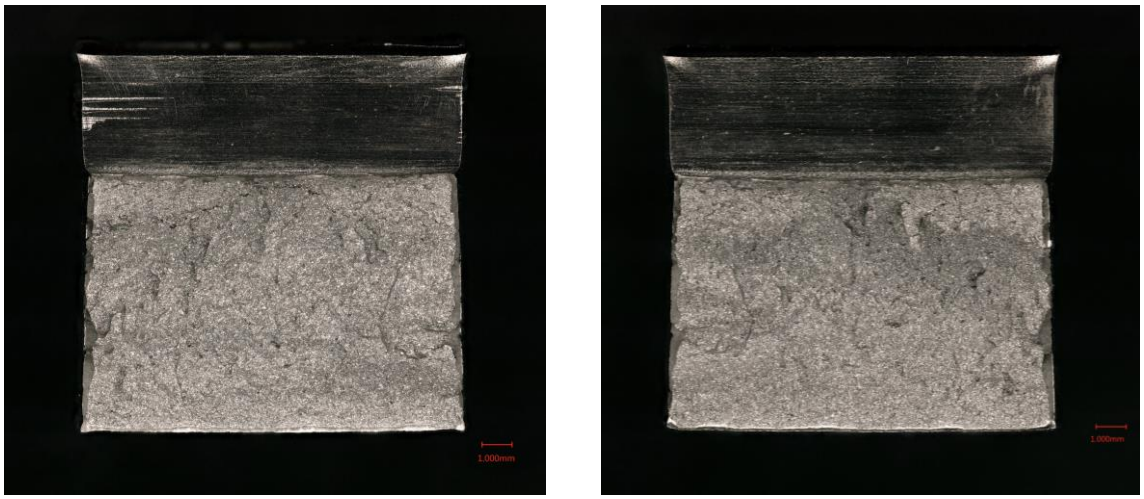

7Ni-FS-3

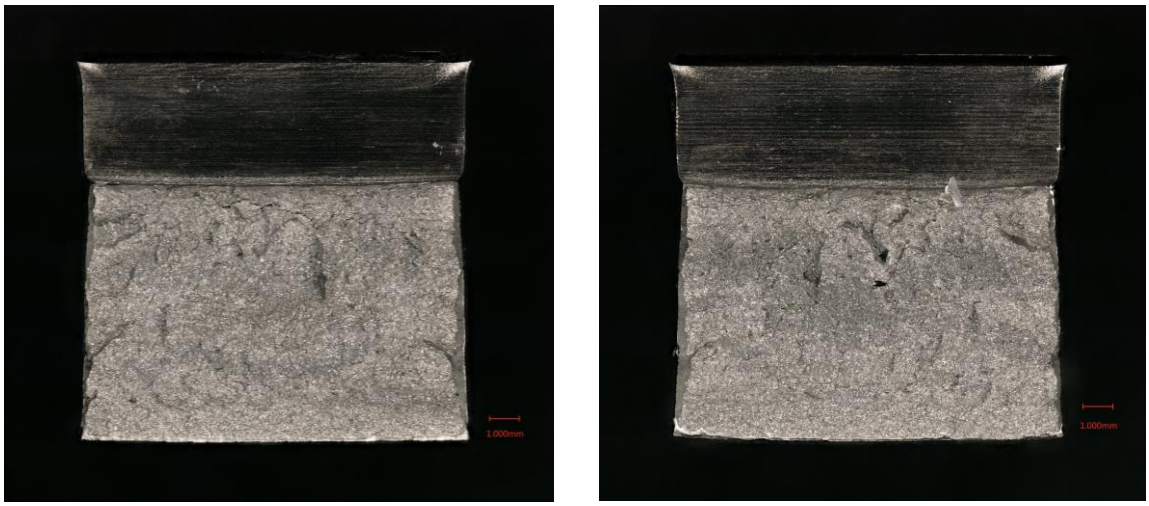

Figure 6.45

Load-Displacement Curves of Fracture Stress Testing at -196ºC

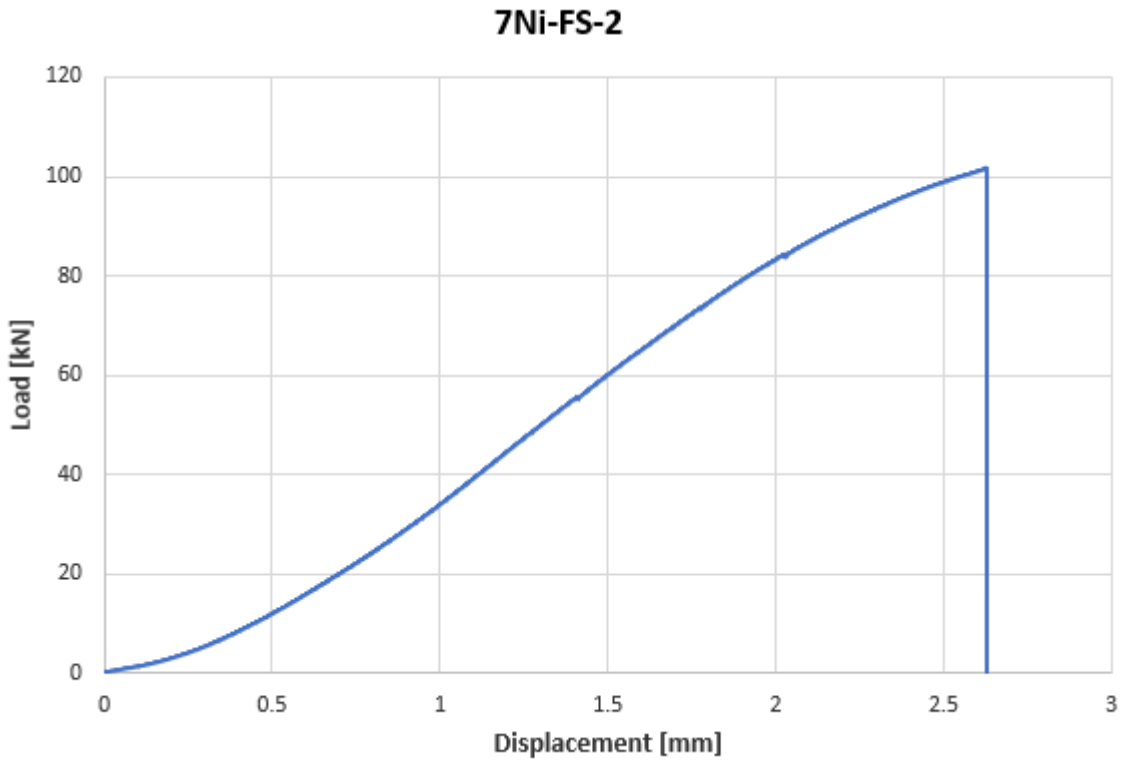

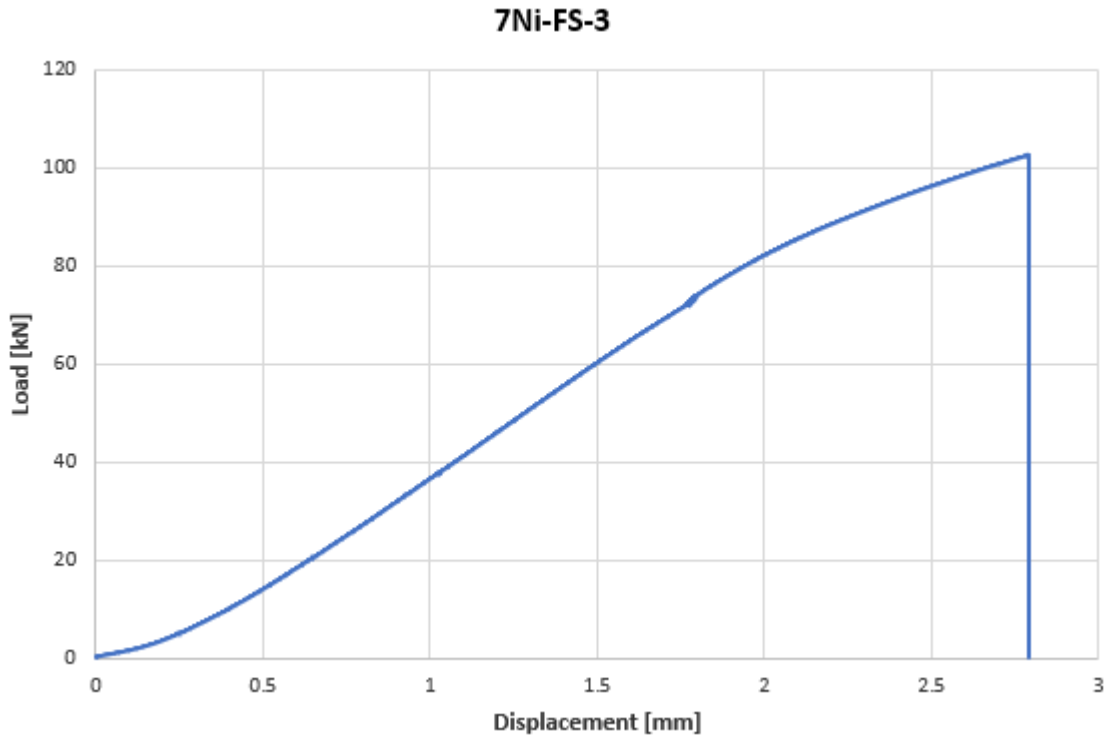

7Ni-FS2

-196 °C

Figure 6.46a

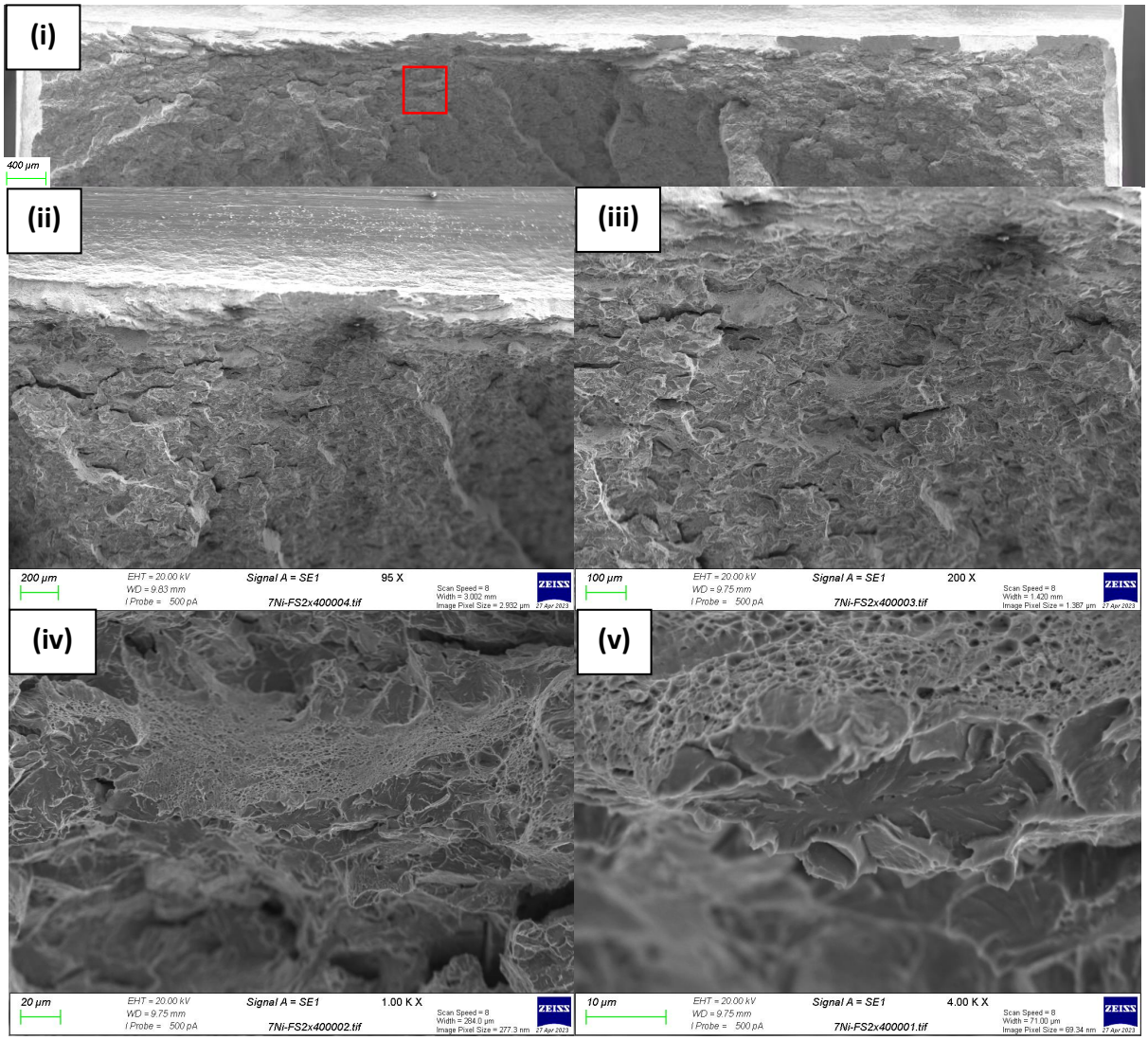

(i): ductile crack growth at the onset of notch root followed with cleaving.
(ii), (iii), (iv), (v): detail of framed site in magnification sequence.

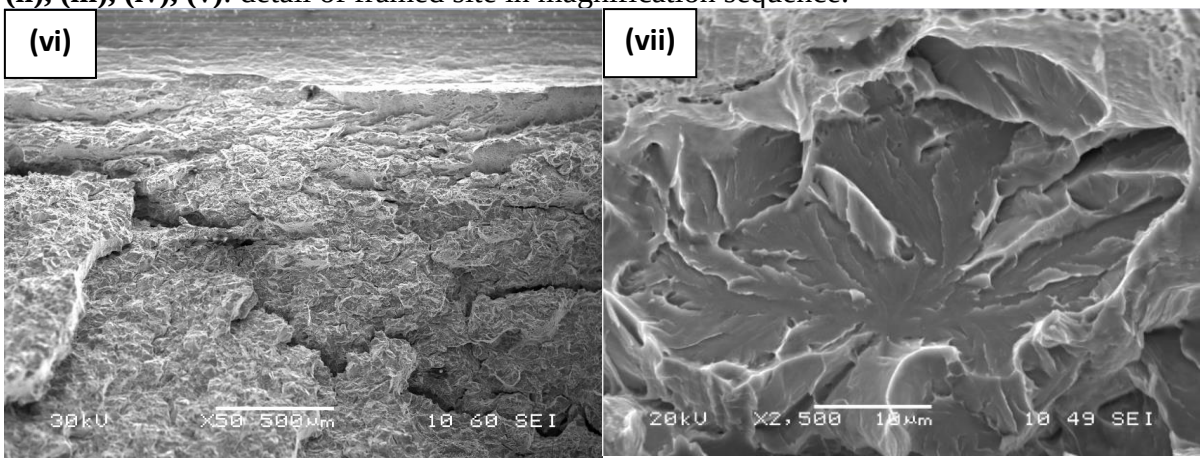

(vi), (vii): opposite side of the framed site in magnification sequence.

7Ni-FS2

-196 °C

Figure 6.46b

7Ni Fracture Stress Fractography

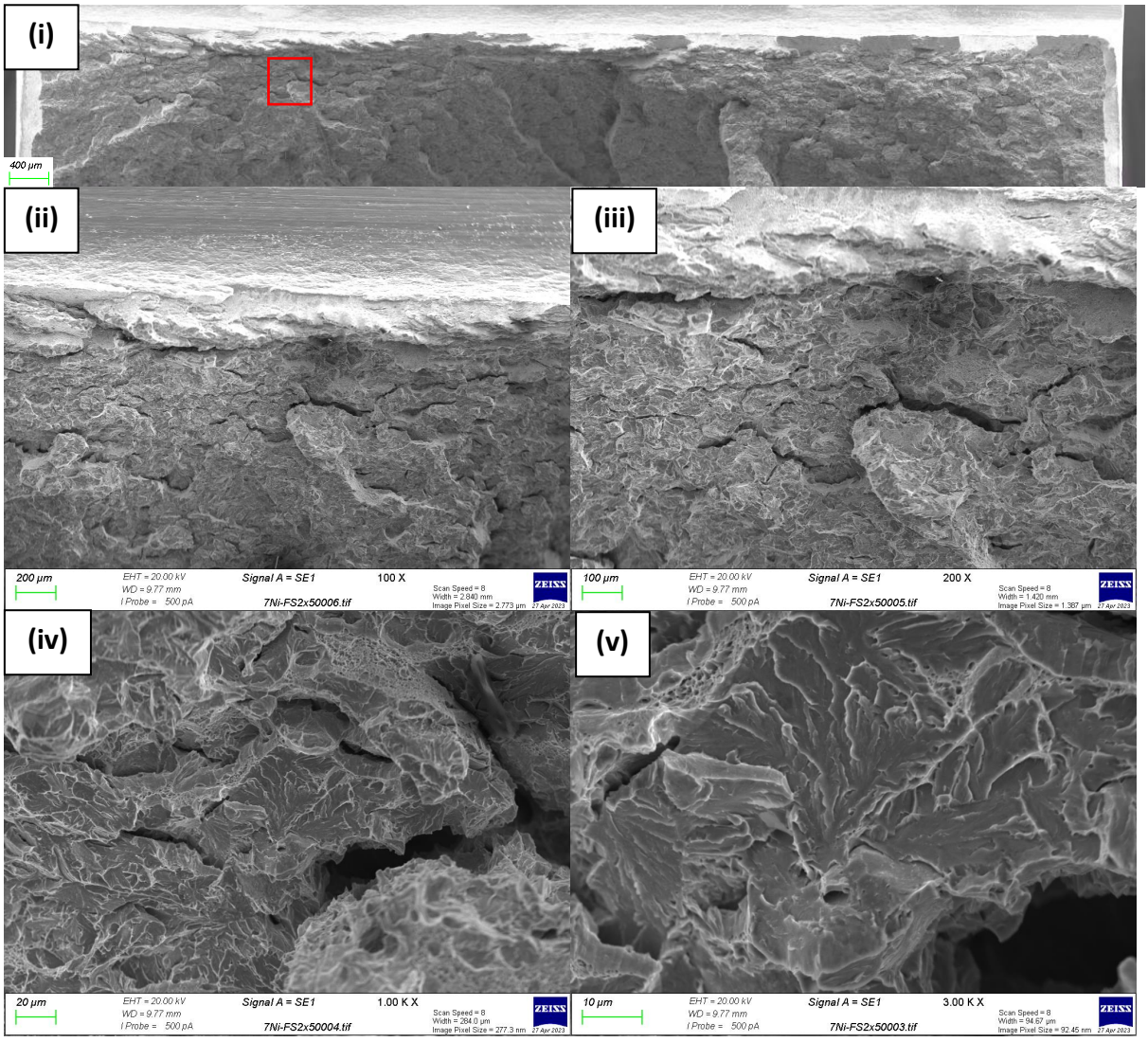

(i): ductile crack growth at the onset of notch root followed with cleaving.
(ii), (iii), (iv), (v): detail of framed site in magnification sequence.

7Ni-FS3

-196 °C

Figure 6.47a

7Ni Fracture Stress Fractography

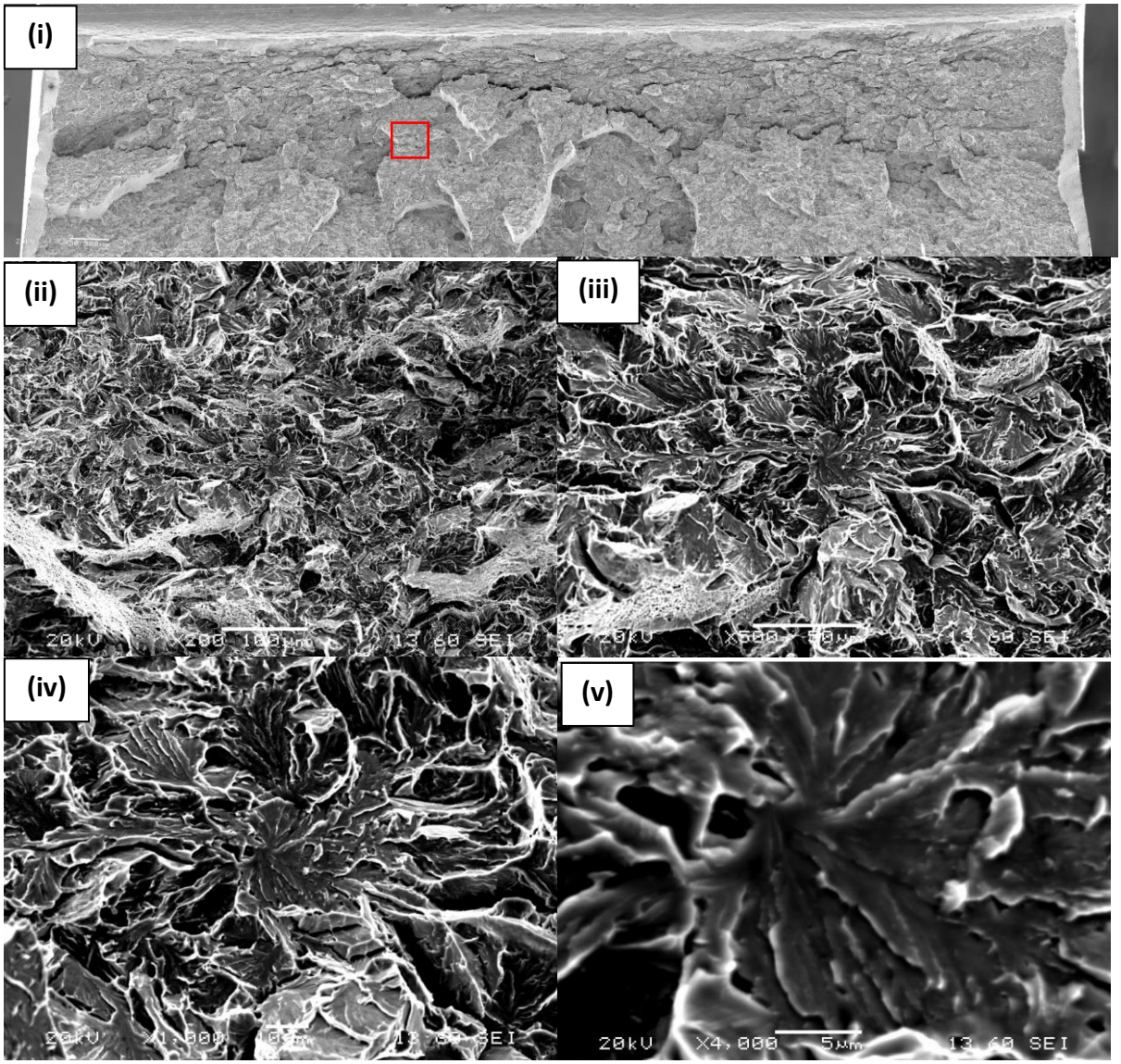

(i): ductile crack growth at the onset of notch root followed with cleaving.
(ii), (iii), (iv), (v): detail of framed site in magnification sequence.

7Ni-FS3

-196 °C

Figure 6.47b

7Ni Fracture Stress Fractography

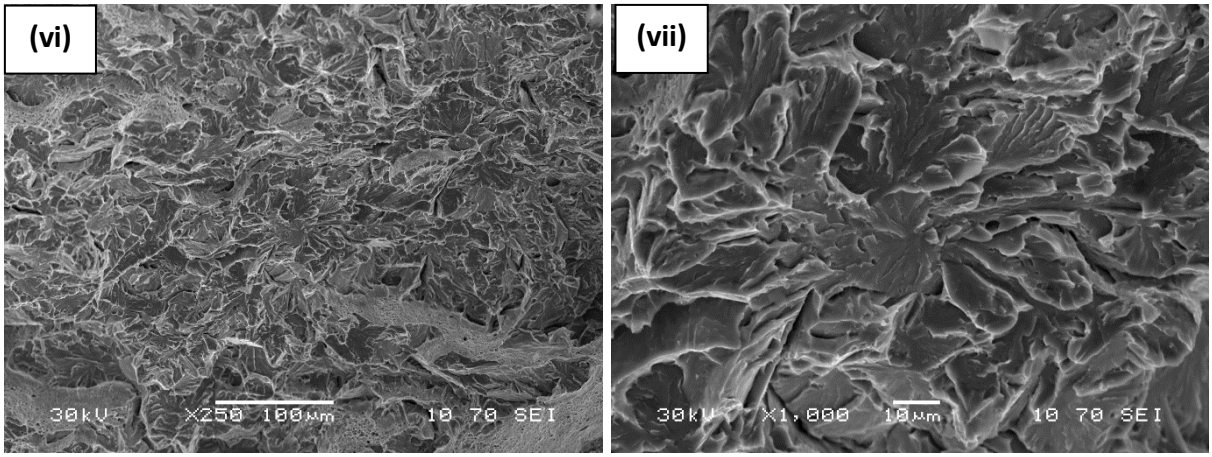

(vi), (vii): opposite side of the framed site in magnification sequence.

7Ni-FS3

-196 °C

Figure 6.48a

7Ni Fracture Stress Inclusion

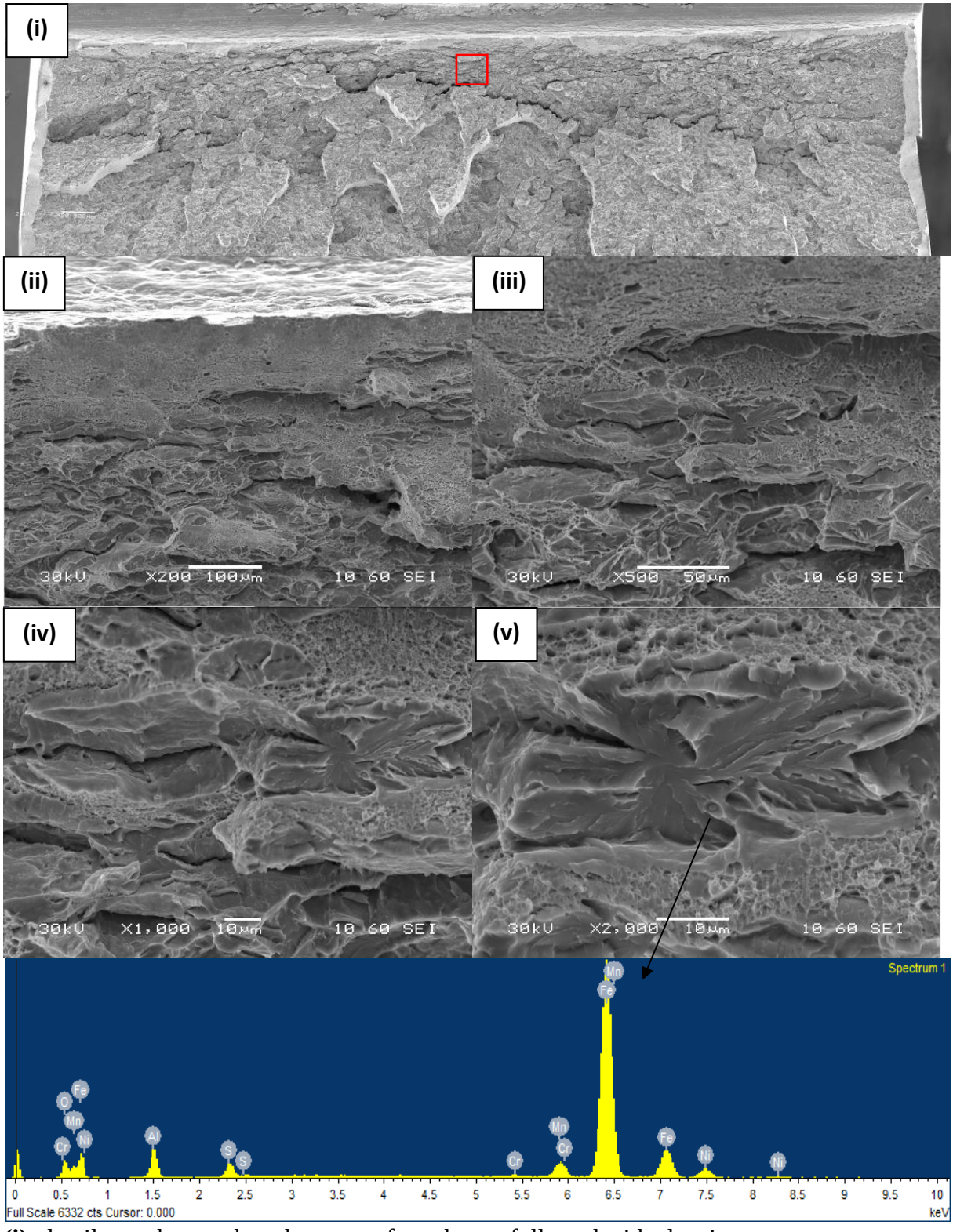

(i): ductile crack growth at the onset of notch root followed with cleaving.
(ii), (iii), (iv), (v): detail of framed site in magnification sequence.

7Ni-FS3

-196 °C

Figure 6.48b

(vi): opposite side of the framed site in detail.

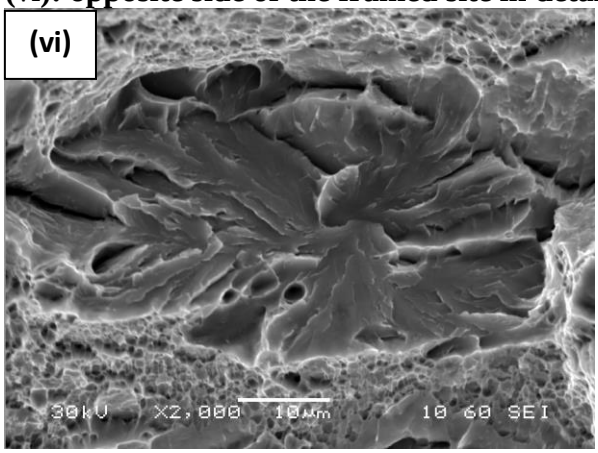

Figure 6.49

Fracture Surfaces of SENB Specimens

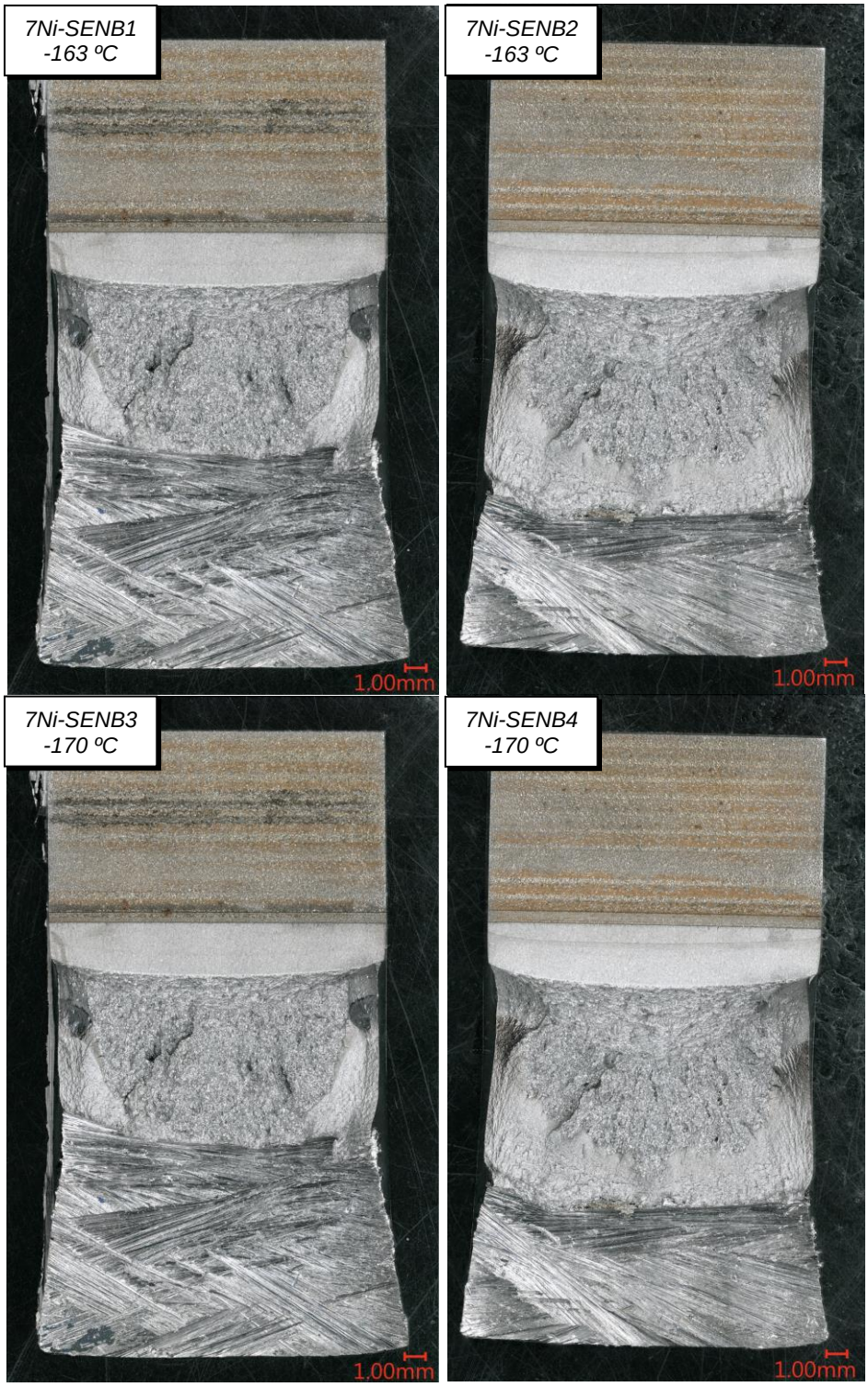

Figure 6.50

Crack Extension Measurement under Optical Microscope

7Ni-SENB1 -163ºC

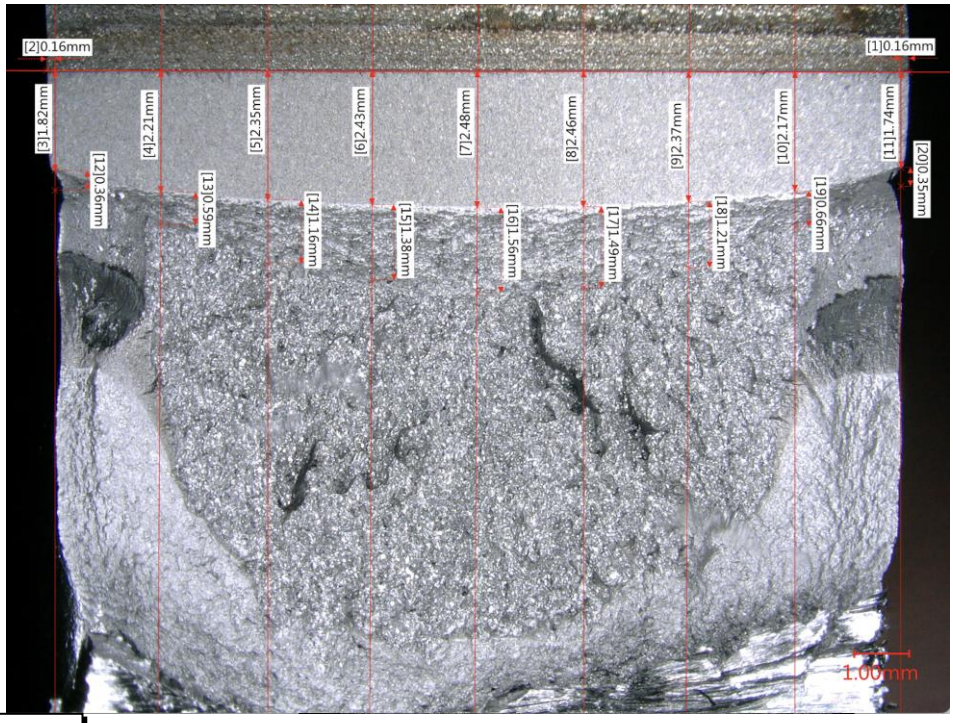

7Ni-SENB2 -163ºC

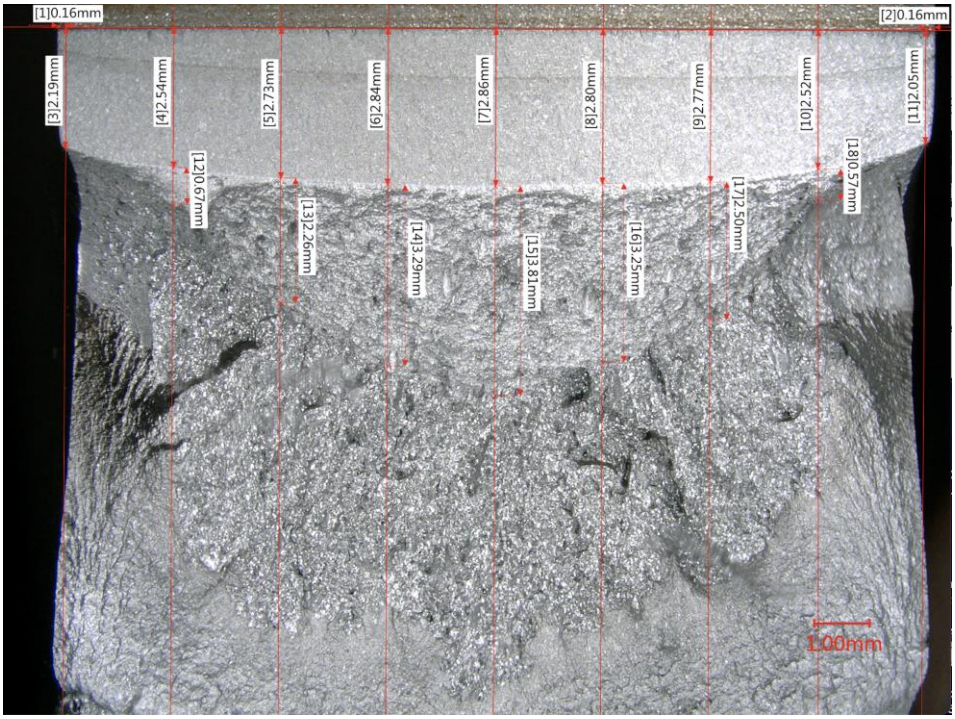

Figure 6.50

Crack Extension Measurement under Optical Microscope

7Ni-SENB3 -170ºC

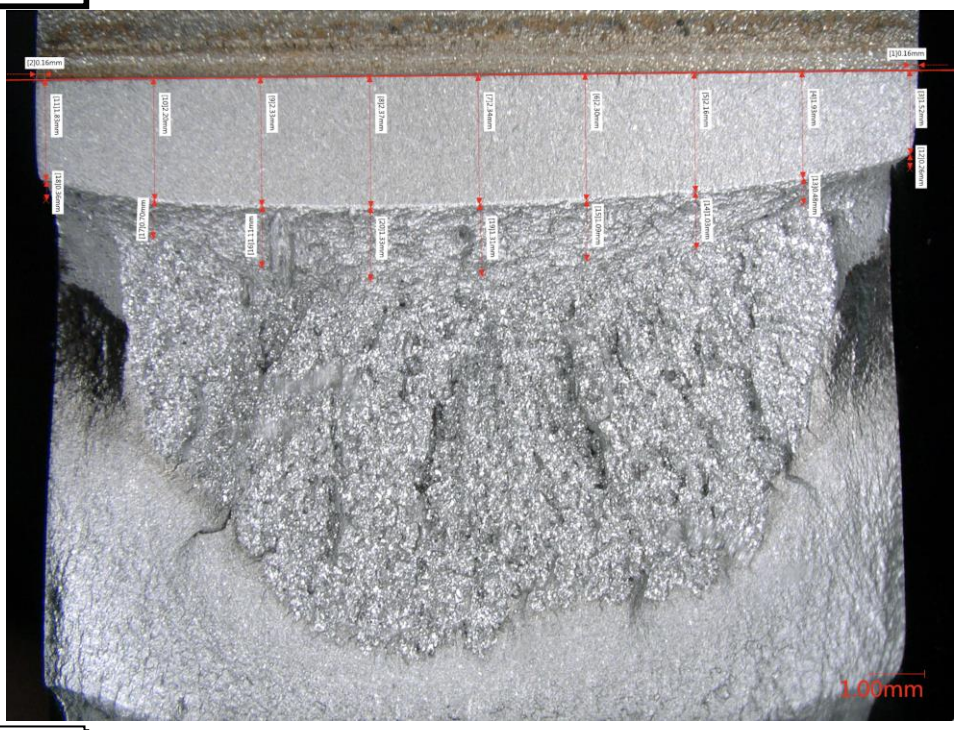

7Ni-SENB4 -170ºC

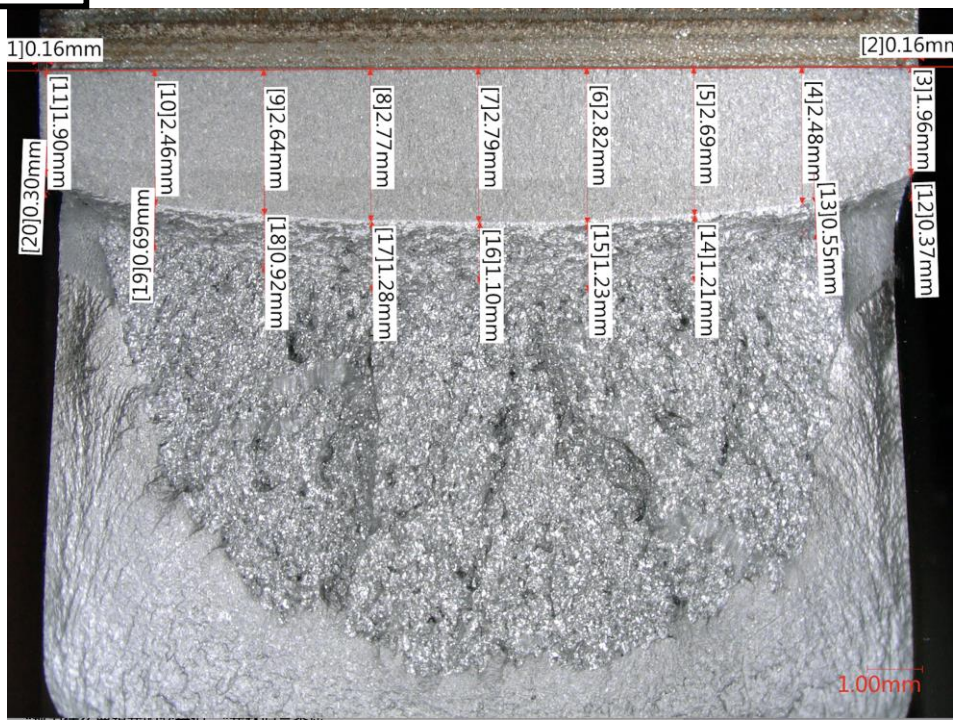

Figure 6.51

Load-Displacement Curves for Fracture Toughness Tests at -163ºC

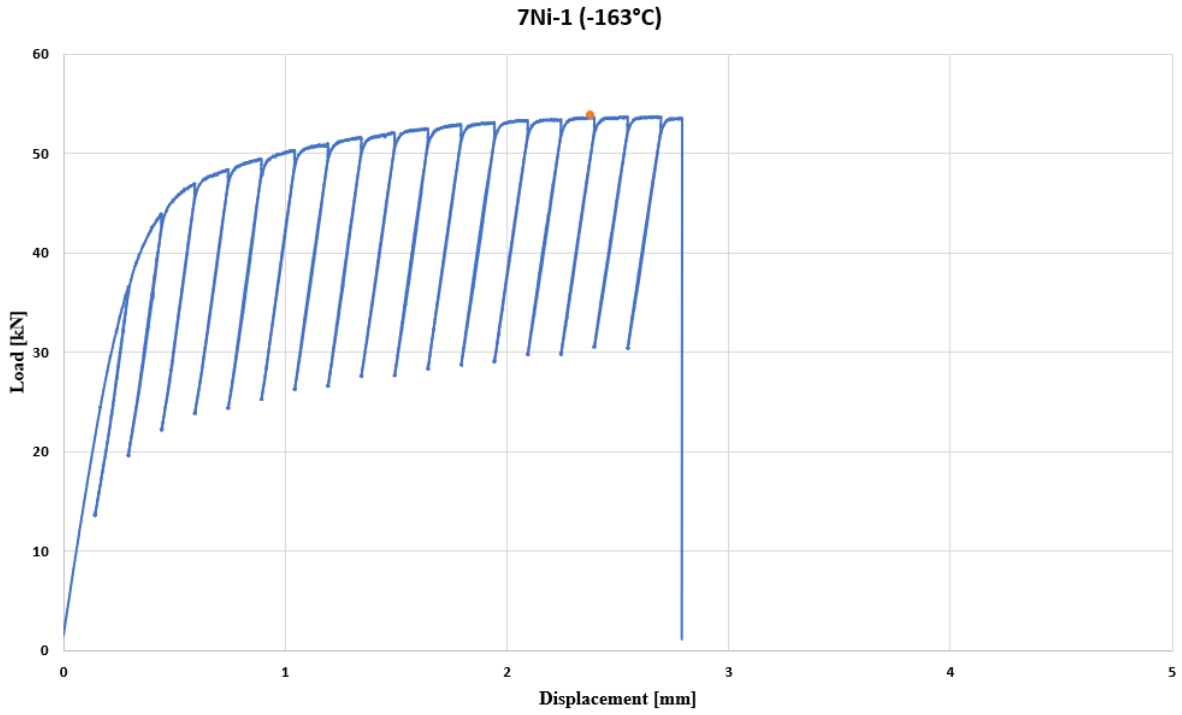

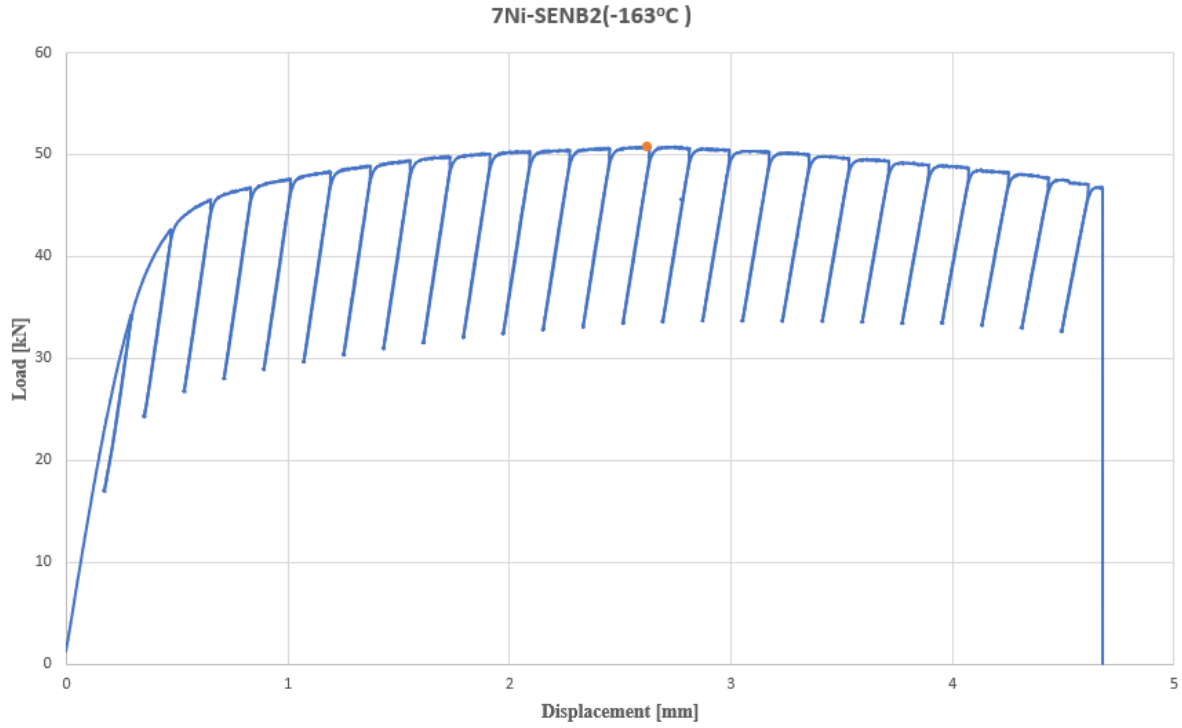

Figure 6.51

Load-Displacement Curves for Fracture Toughness Tests at -170ºC

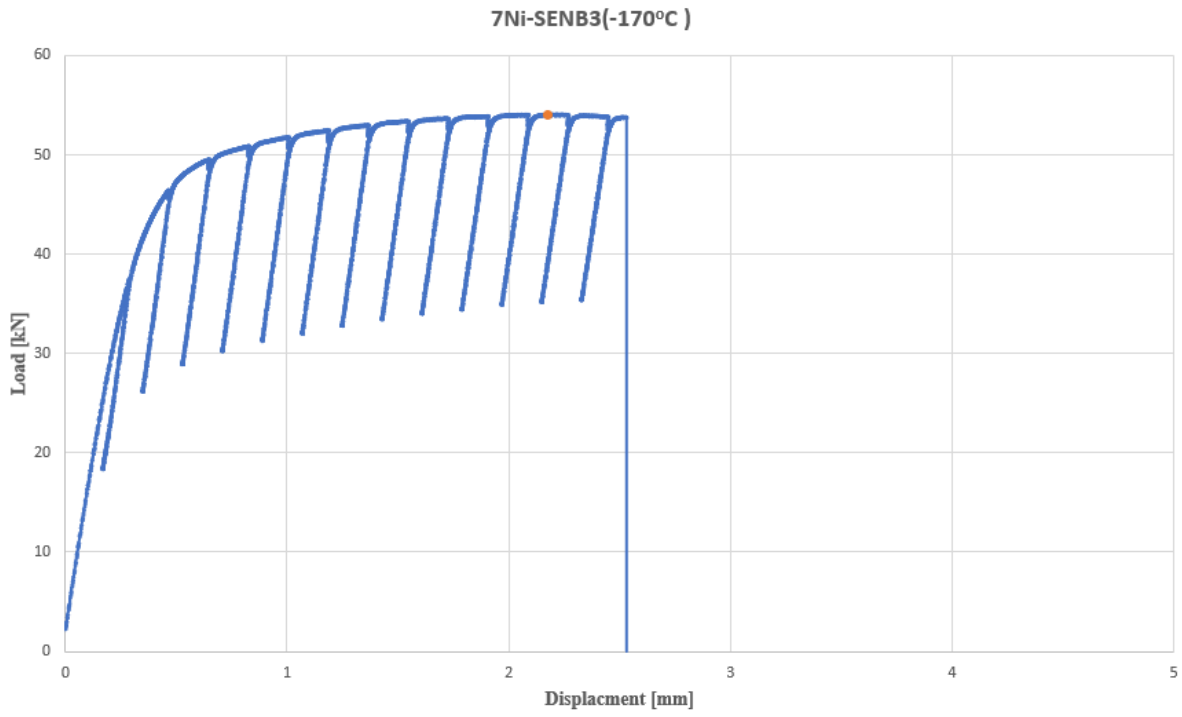

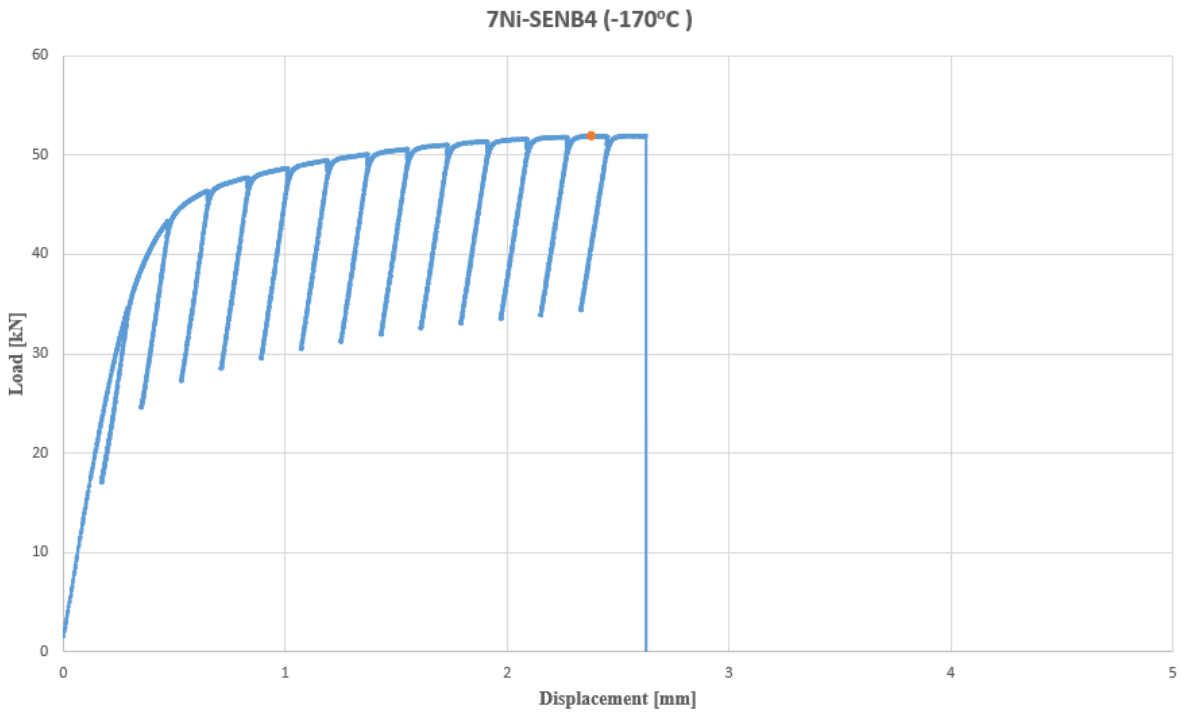

Figure 6.52

Fracture Surface of Small 7% Ni Steel SENB Specimens (W = 7mm) tested at -196°C

7Ni-LT-1

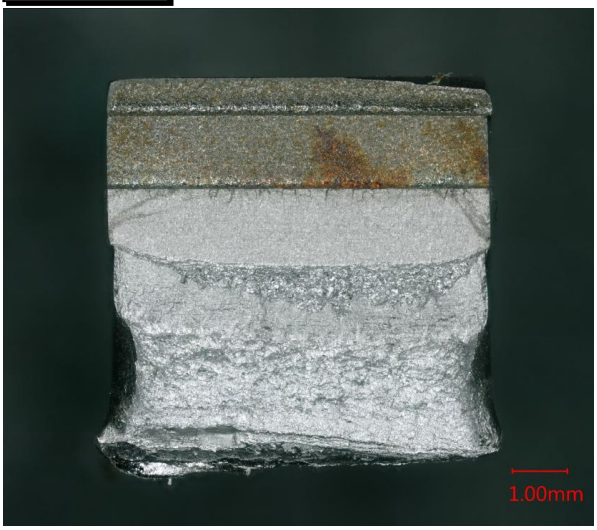

7Ni-LT-2

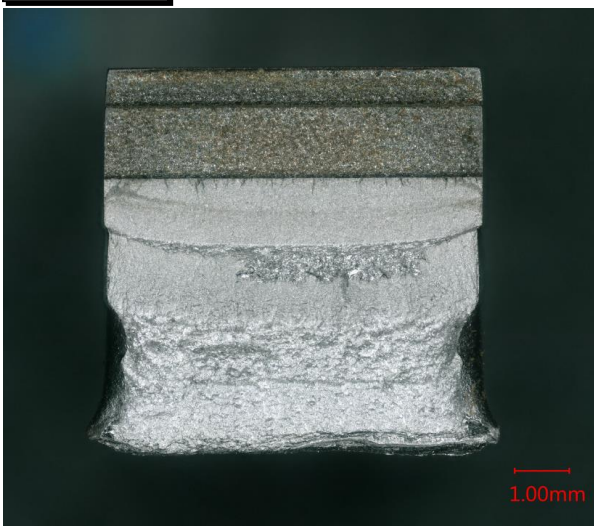

7Ni-TL-3

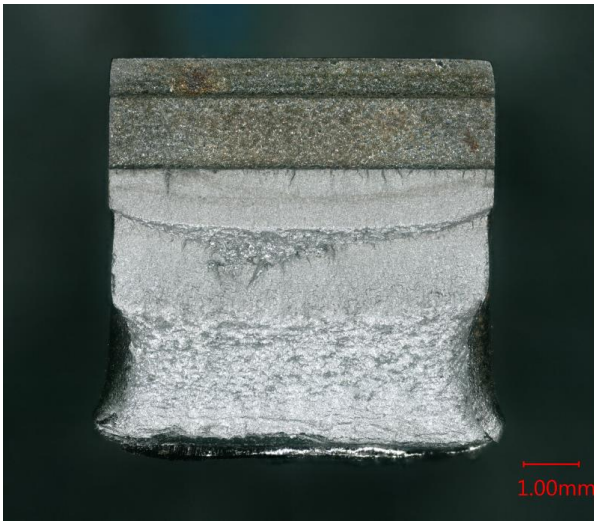

7Ni-TL-4

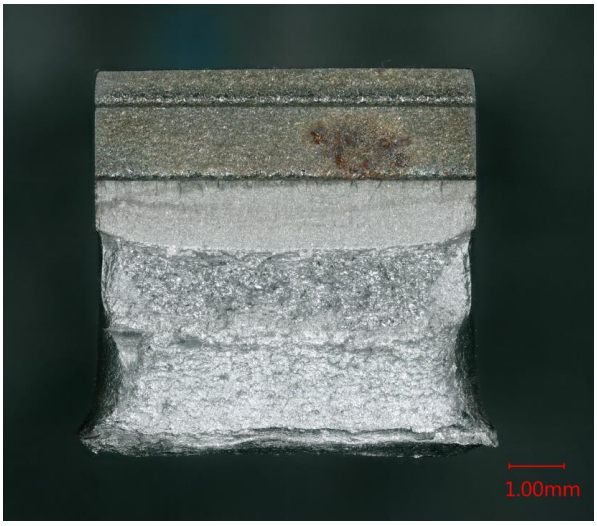

Figure 6.53

Load-Load Line Displacement Curves for Fracture Toughness Tests at -196ºC

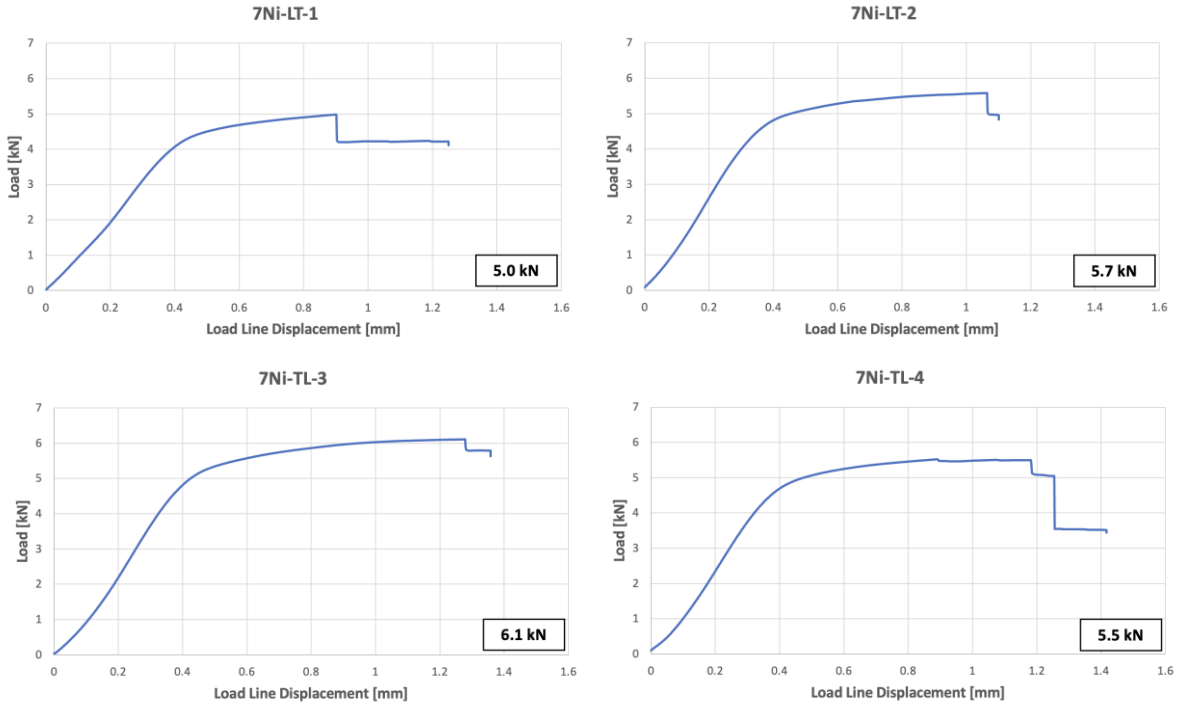

Figure 6.54

K_Q and K_{Jc} of 7%Ni Steel tested at -196, -170 and -163°C

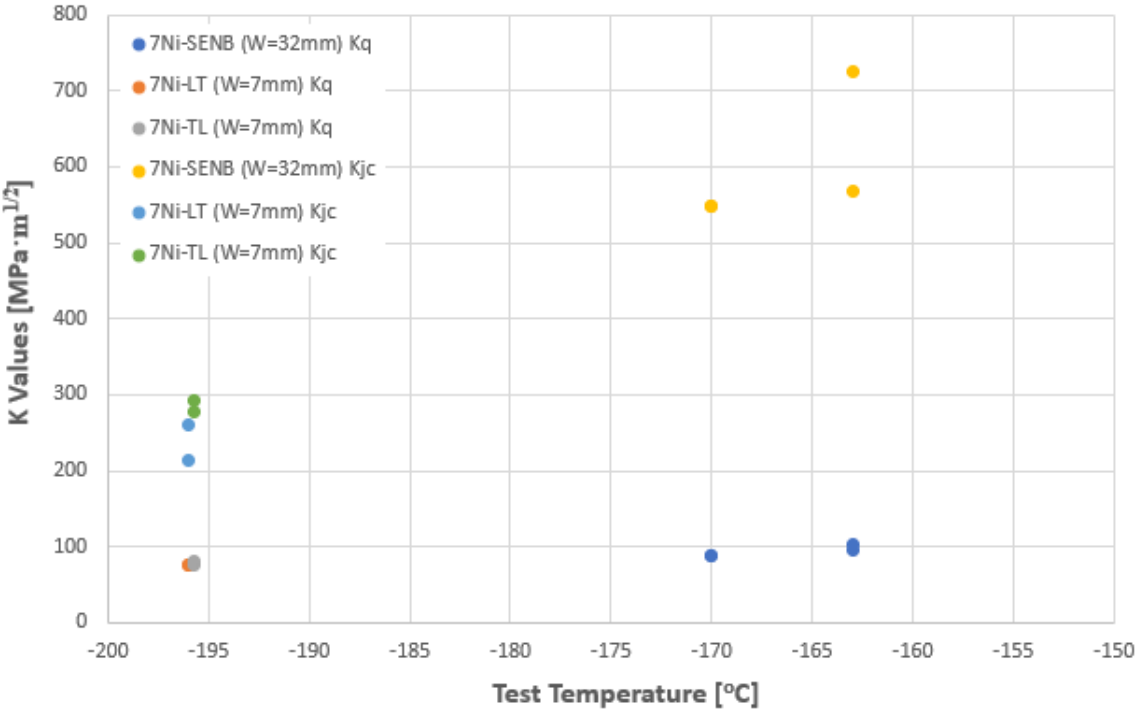

7Ni-SENB1

-163 °C

Figure 6.55

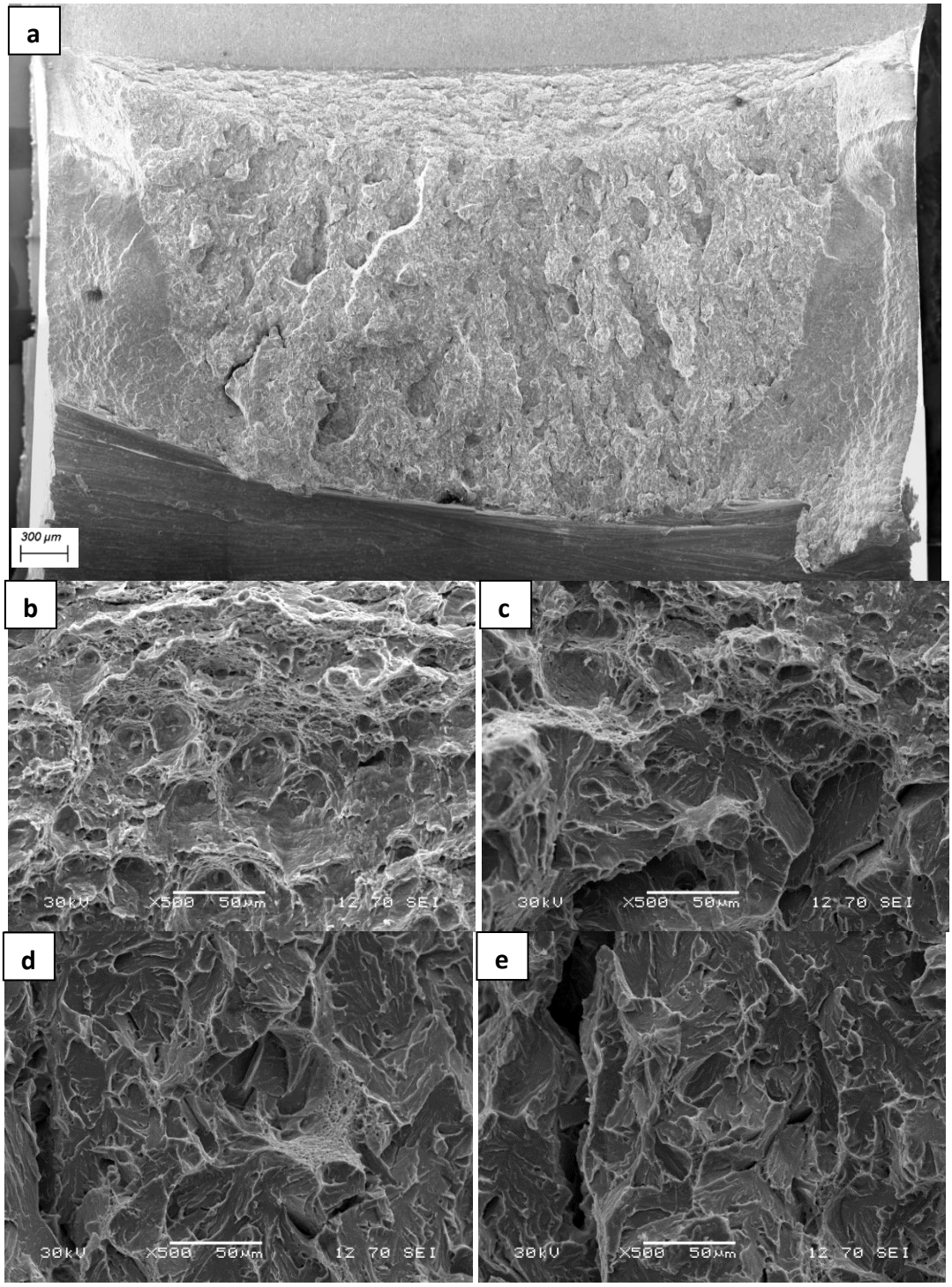

(a) Total fracture surface of 7Ni-SENB1 tested at -163ºC.
(b) Microvoid coalescence at stable crack growth region.
(c) Mixed microvoid coalescence and cleavage facets at onset of stable crack growth region.
(d) Cleavage facets in the middle of the fracture surface.
(e) Cleavage facets at the bottom of fracture surface.

7Ni-SENB2
-163 °C

Figure 6.56

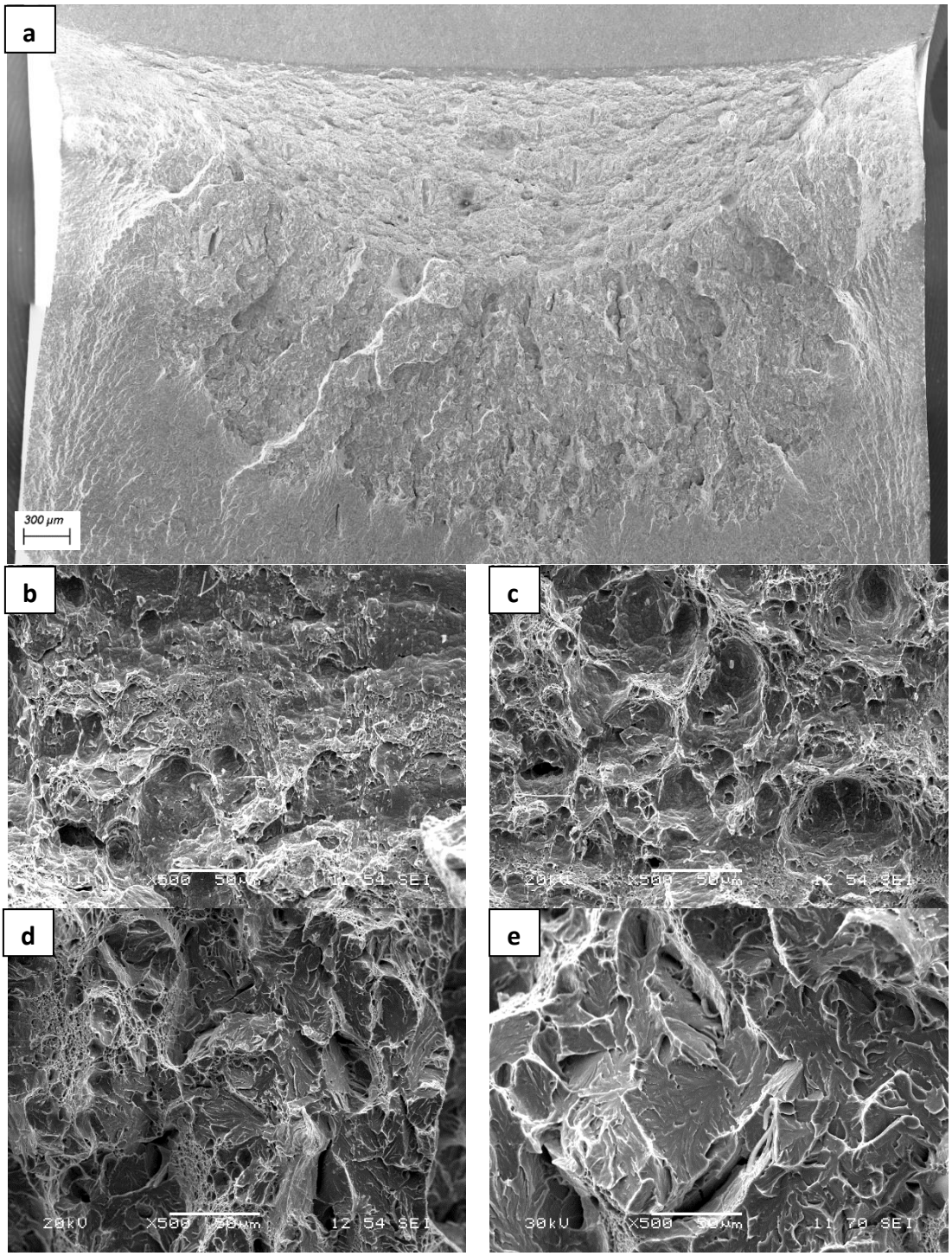

(a) Total fracture surface of 7Ni-SENB2 tested at -163ºC.
(b) Microvoid coalescence near precrack end
(c) Detail of microvoid coalescence at stable crack growth region
(d) Mixed microvoid coalescence and cleavage facets
(e) Cleavage facets at the bottom of the fracture surface

7Ni-SENB3

-170 °C

Figure 6.57

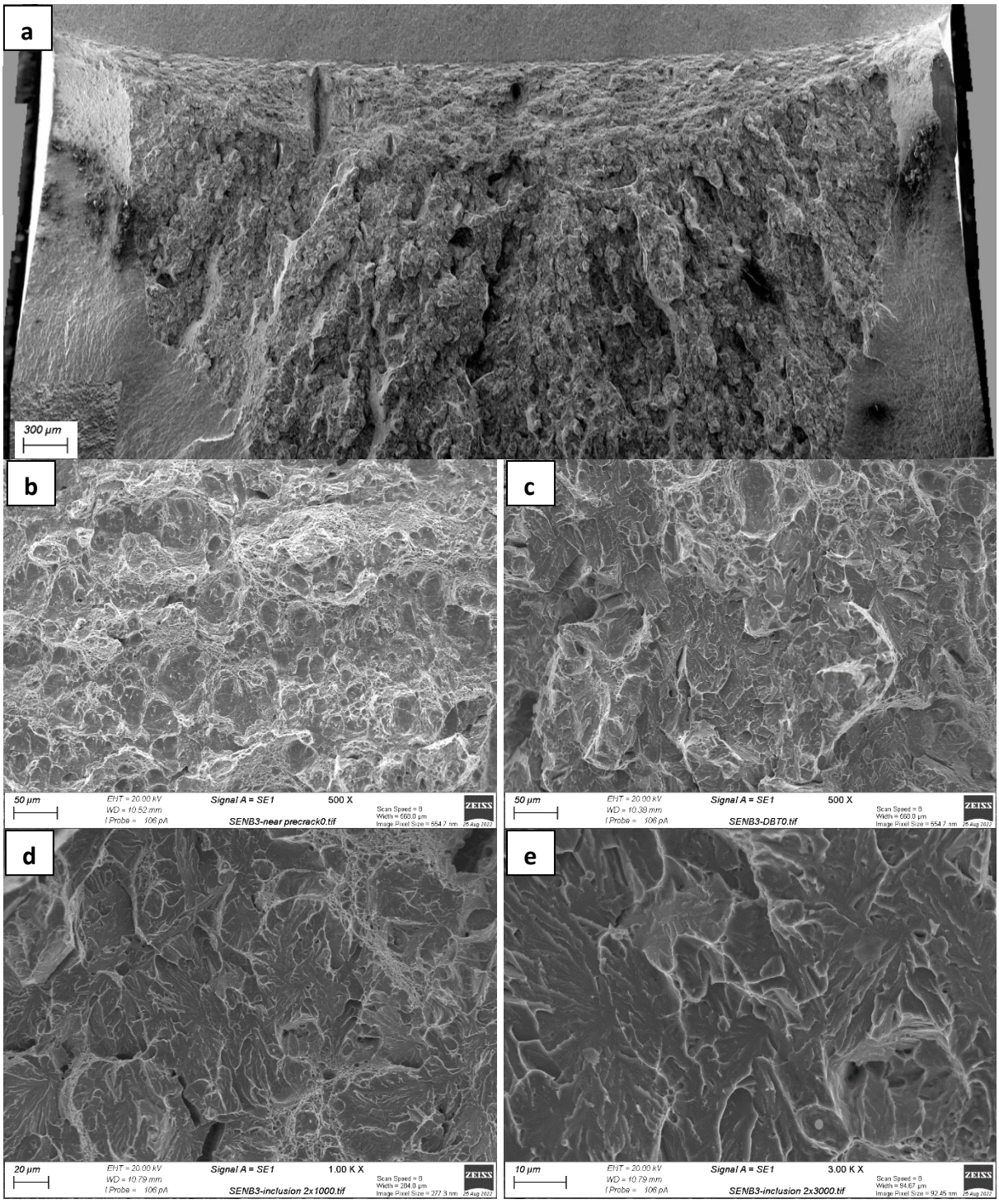

(a) Total fracture surface of 7Ni-SENB3 tested at -163ºC
(b) Microvoid coalescence near precrack end
(c) Cleavage facets at onset of stable crack growth region
(d) Mixed microvoid coalescence and cleavage facets
(e) Cleavage facets at the bottom of the fracture surface

7Ni-SENB4

-170 °C

Figure 6.58

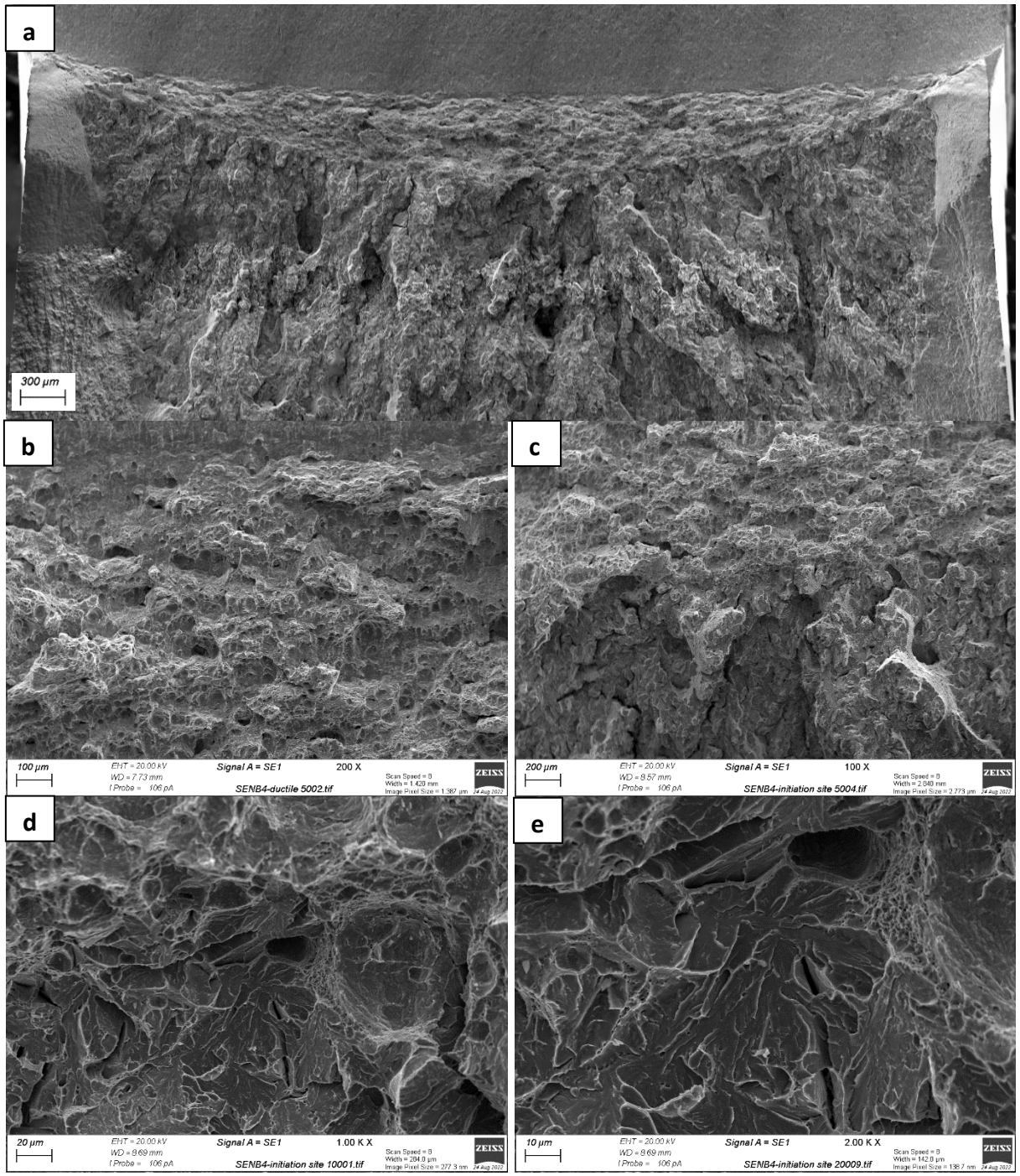

(a) Total fracture surface of 7Ni-SENB4 tested at -163^{o}C
(b) Microvoid coalescence near precrack end
(c) Microvoid coalescence at stable crack growth region
(d) Mixed microvoid coalescence and cleavage facets
(e) Detail of cleavage facets in (d)

7Ni-SENB2

-163 °C

Figure 6.59

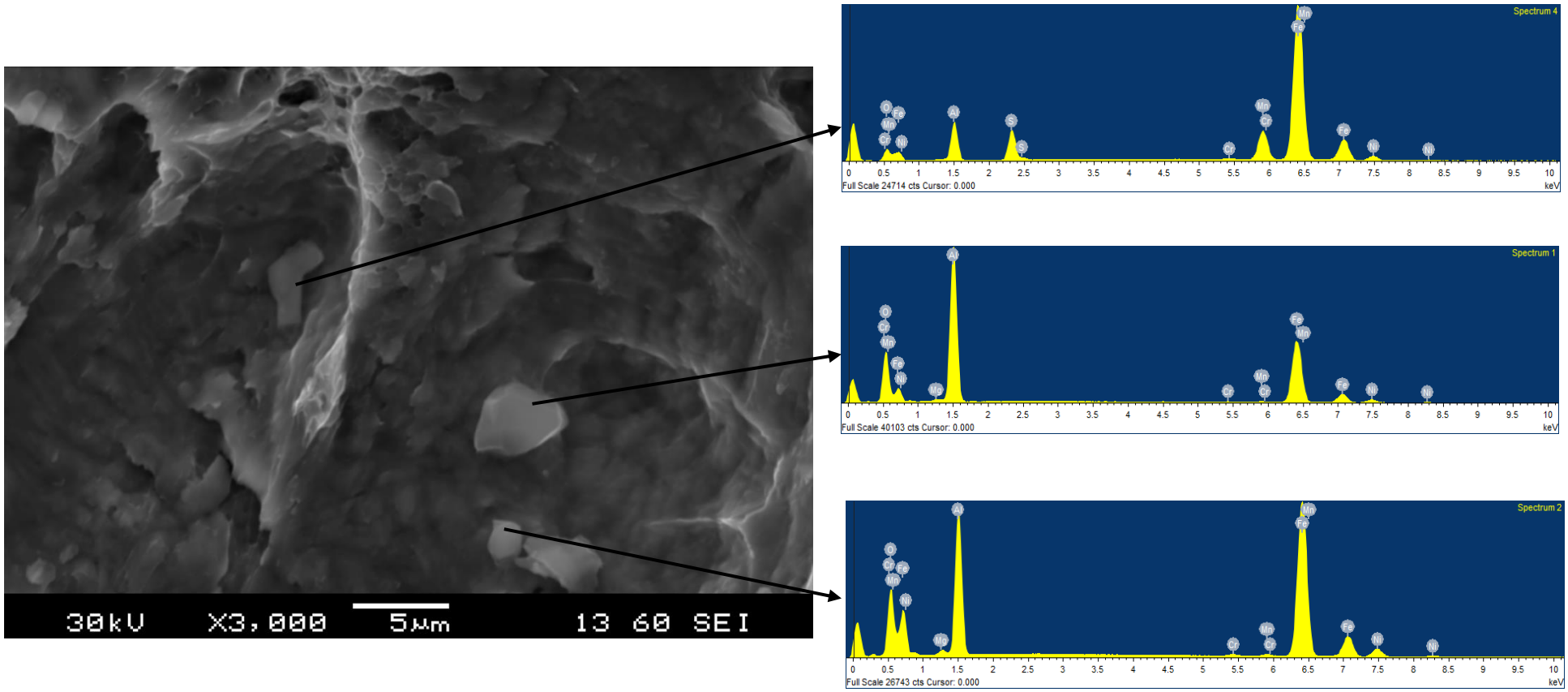

7Ni-SENB2

-163 °C

Figure 6.60

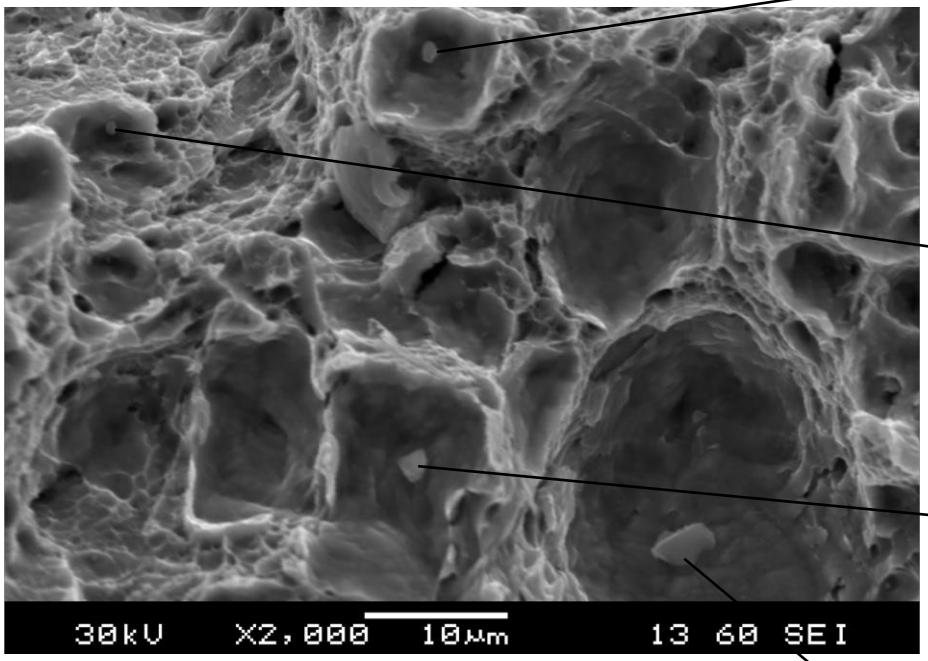

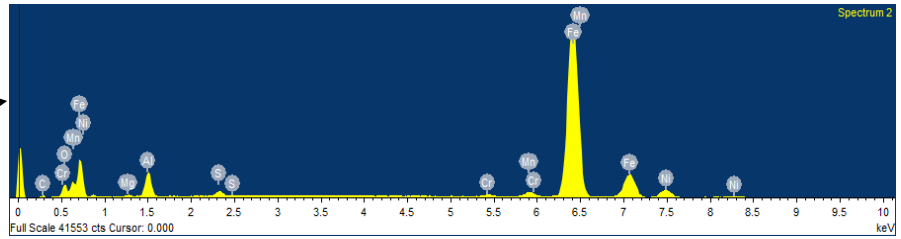

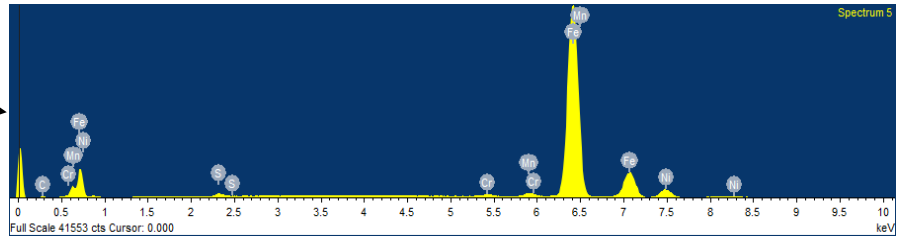

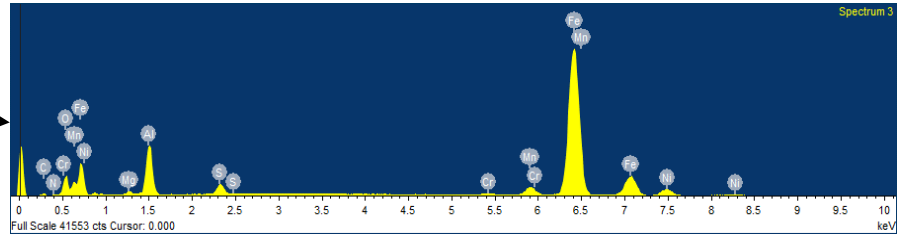

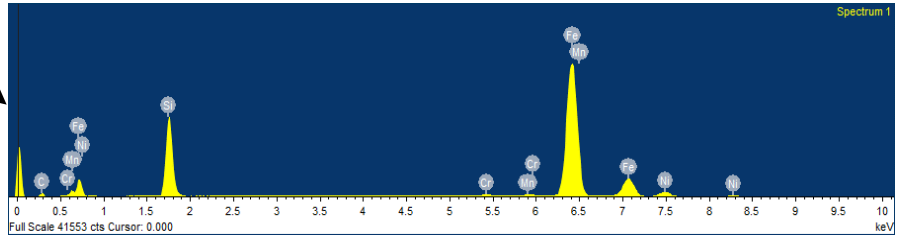

7Ni-LT-1
-196 °C

Figure 6.61

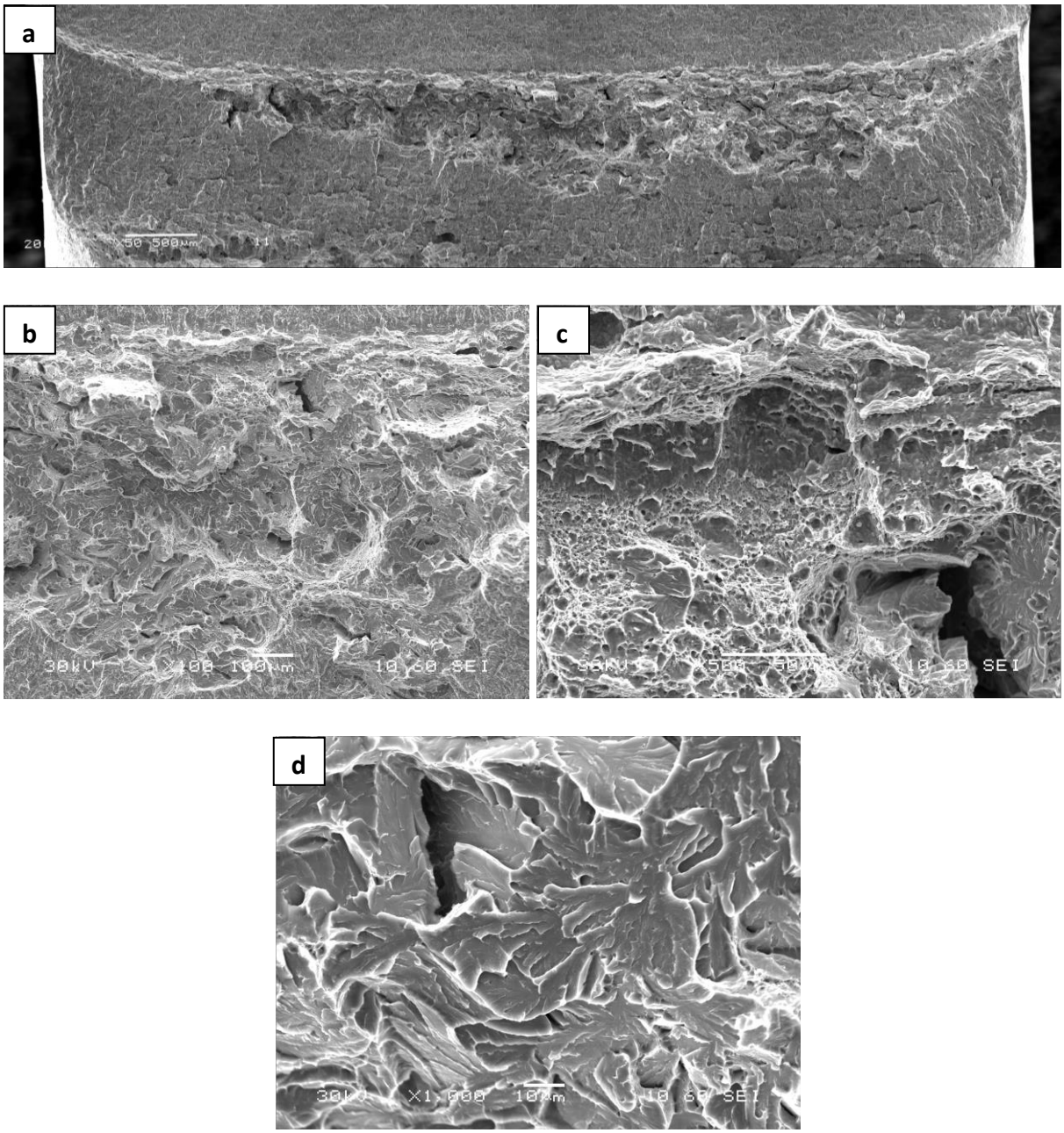

(a): Total fracture surface.
(b): Ductile crack growth and cleavage area.
(c): Detail of microvoid coalescence below fatigue precrack.
(d): Detail of cleavage facets.

7Ni-LT-2
-196 °C

Figure 6.62

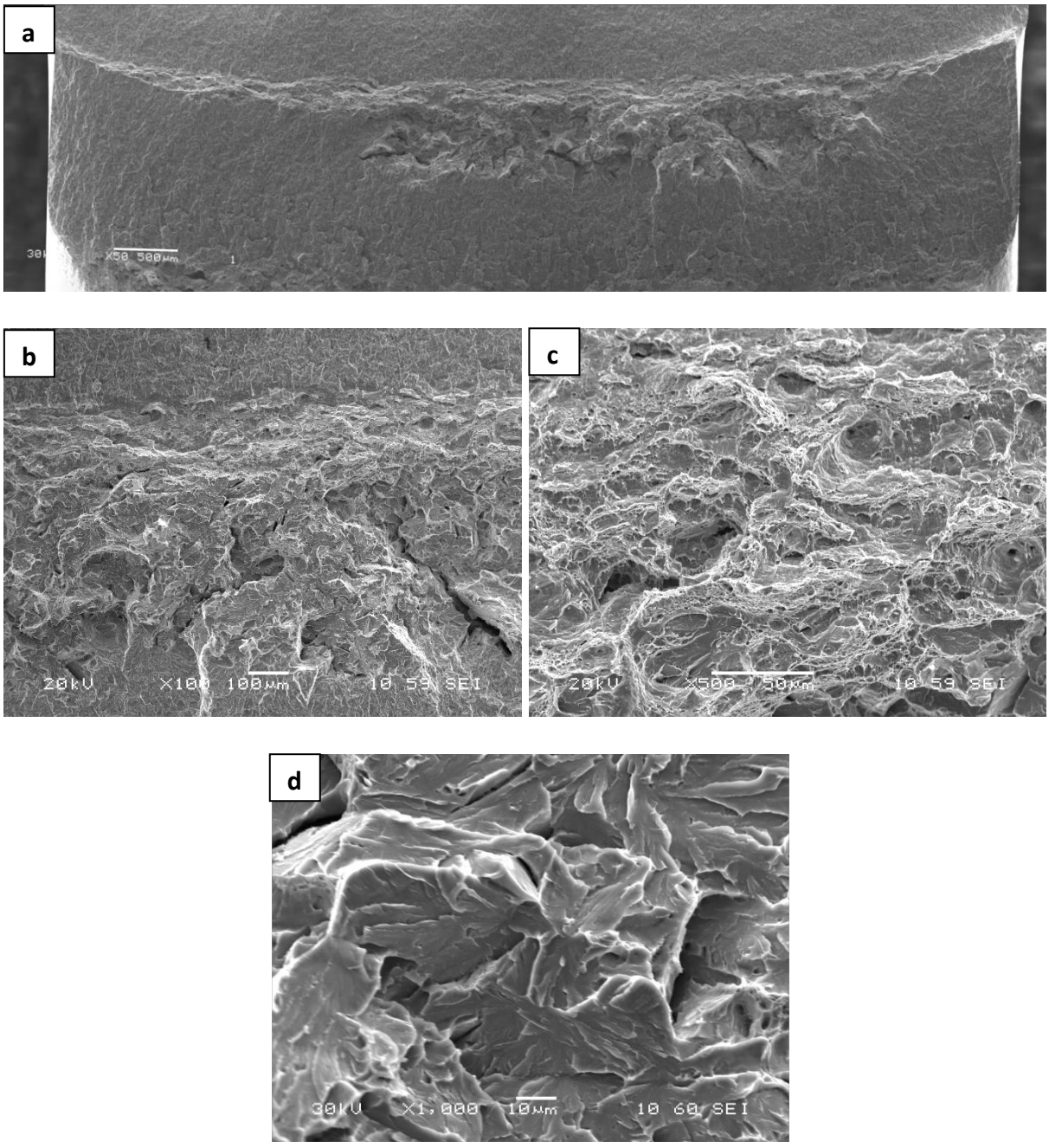

(a): Total fracture surface.
(b): Ductile crack growth and cleavage area.
(c): Detail of microvoid coalescence below fatigue precrack.
(d): Detail of cleavage facets.

7Ni-TL-3
-196 °C

Figure 6.63

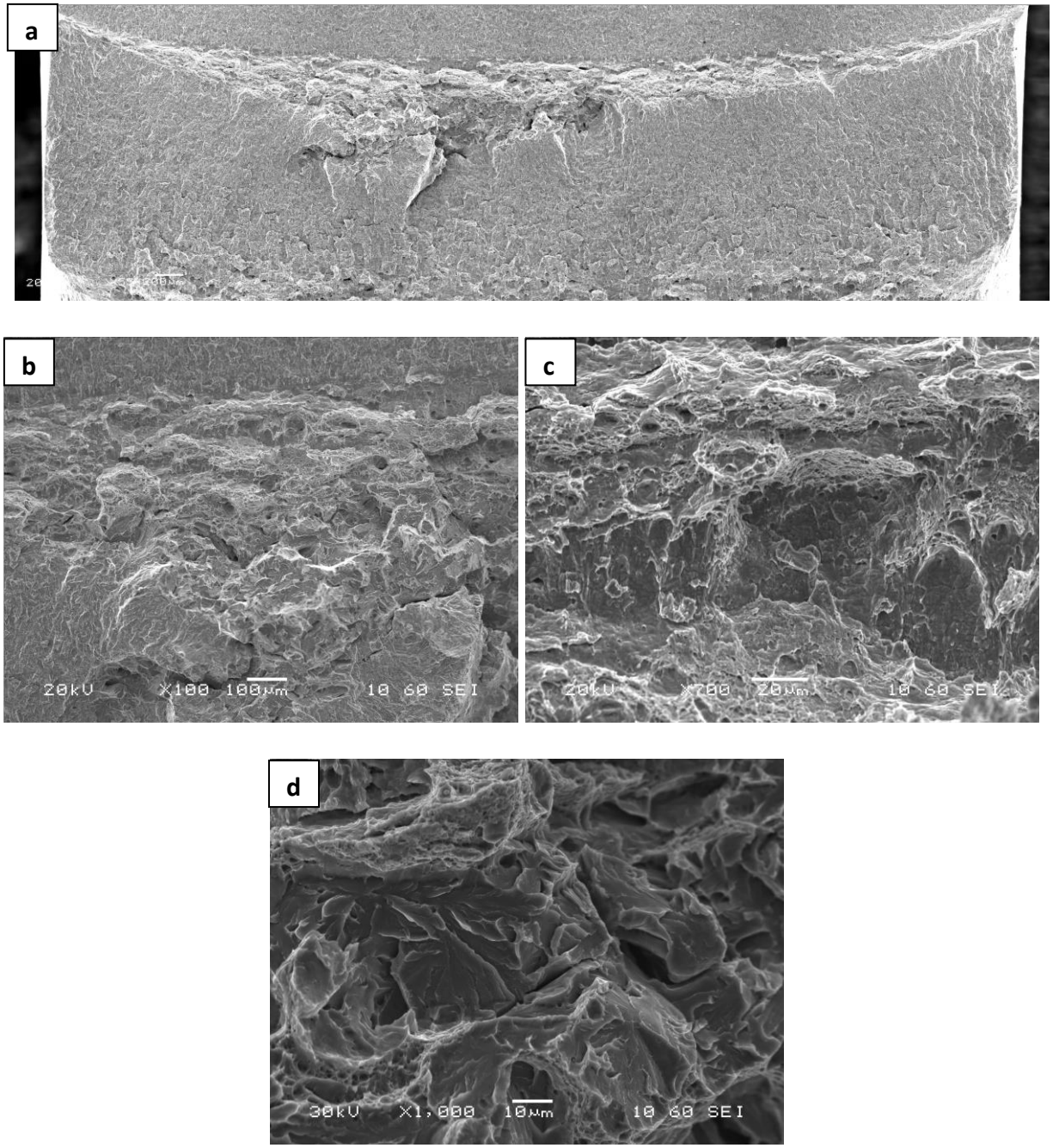

(a): Total fracture surface.
(b): Ductile crack growth and cleavage area.
(c): Detail of microvoid coalescence below fatigue precrack.
(d): Detail of cleavage facets.

7Ni-TL-4
-196 °C

Figure 6.64

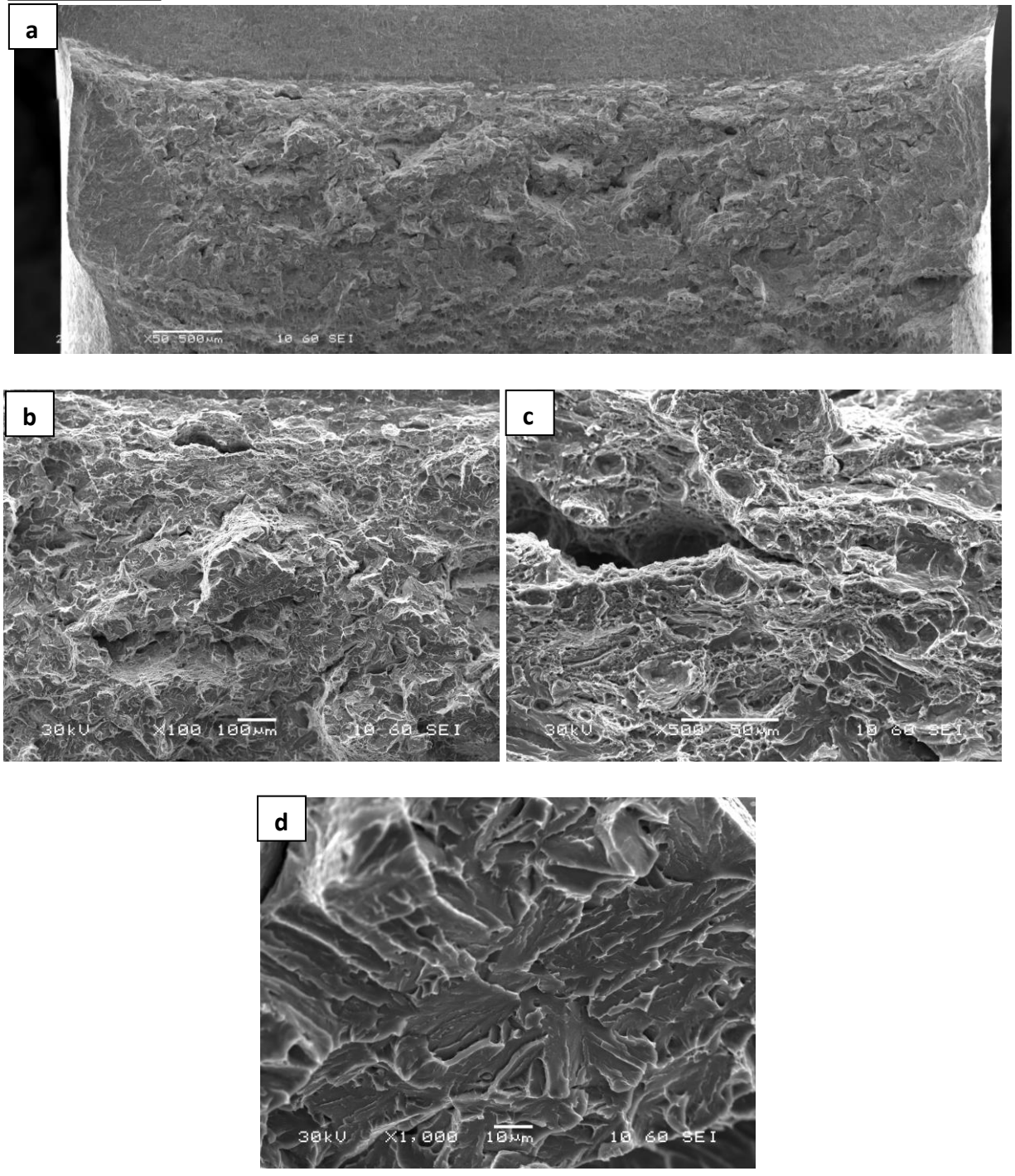

(a): Total fracture surface.
(b): Ductile crack growth and cleavage area.
(c): Detail of microvoid coalescence below fatigue precrack.
(d): Detail of cleavage facets.

Figure 6.65

Fatigue Crack Growth Rate of 9% and 7% Nickel Steel at Different Temperatures

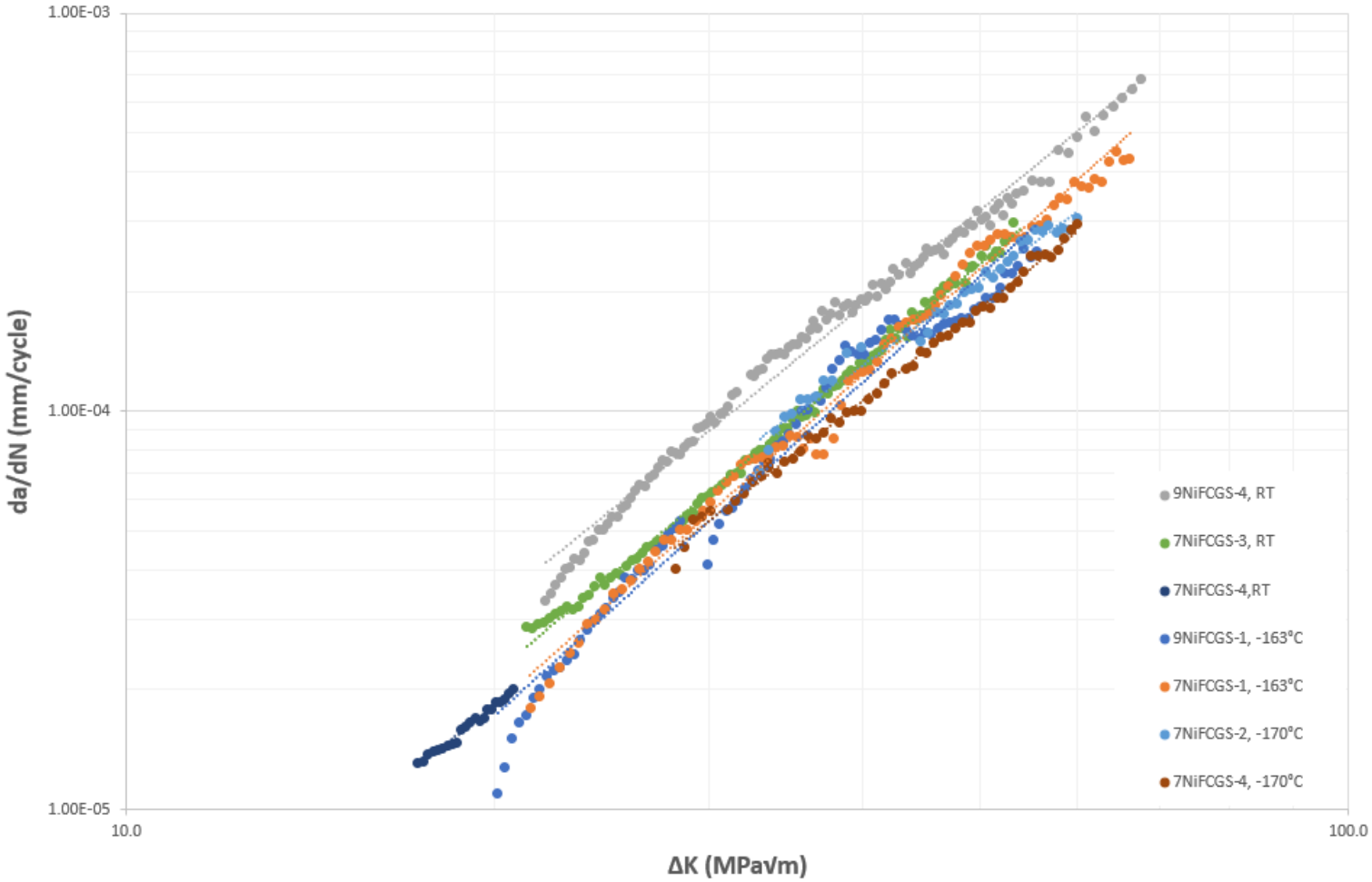

Figure 6.66

7Ni-FCGS2

Fatigue Striations at Paris Regime

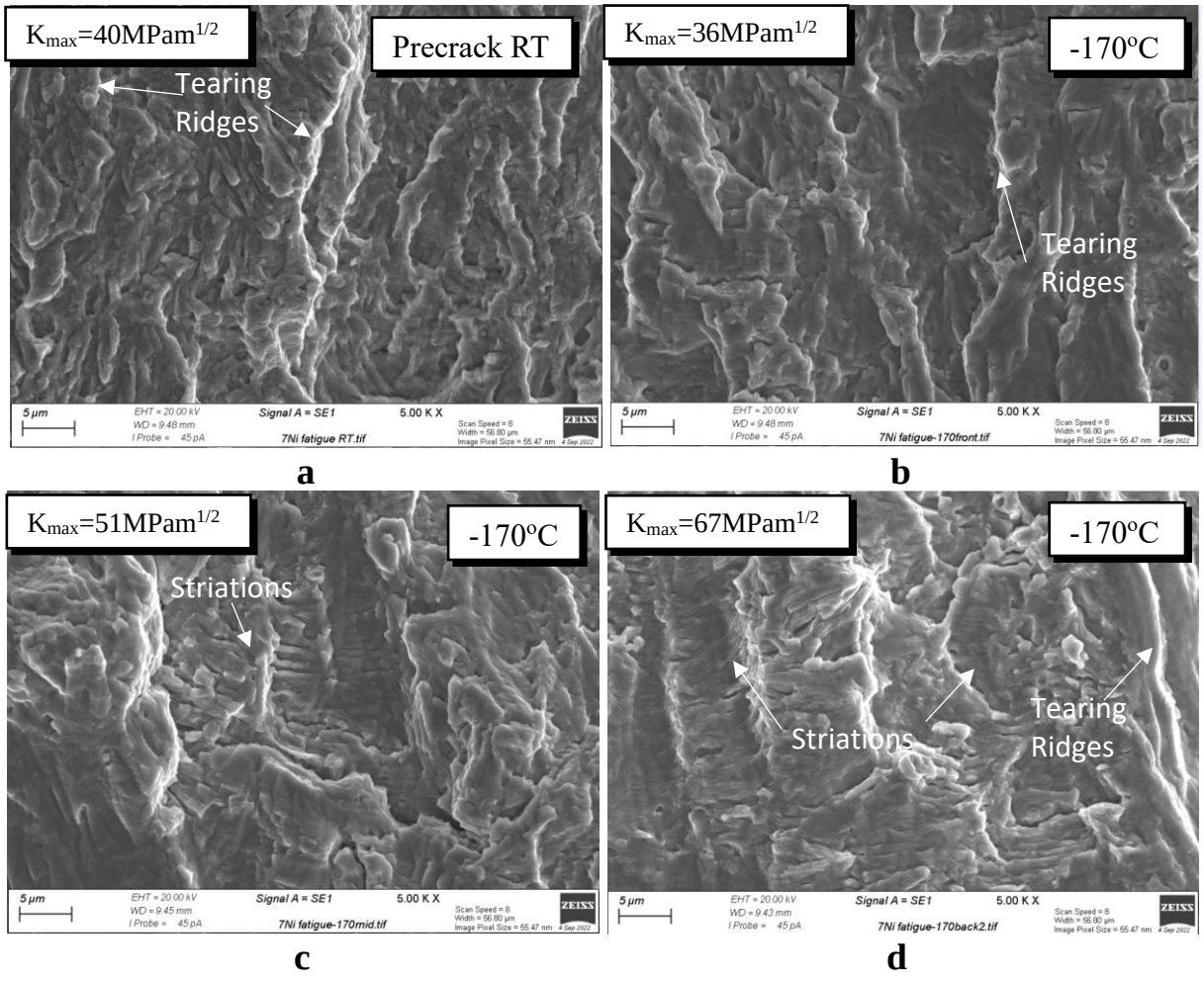

a **b**

c **d**

Figure 6.67

9Ni Steel Fatigue Fracture Surface at -163ºC

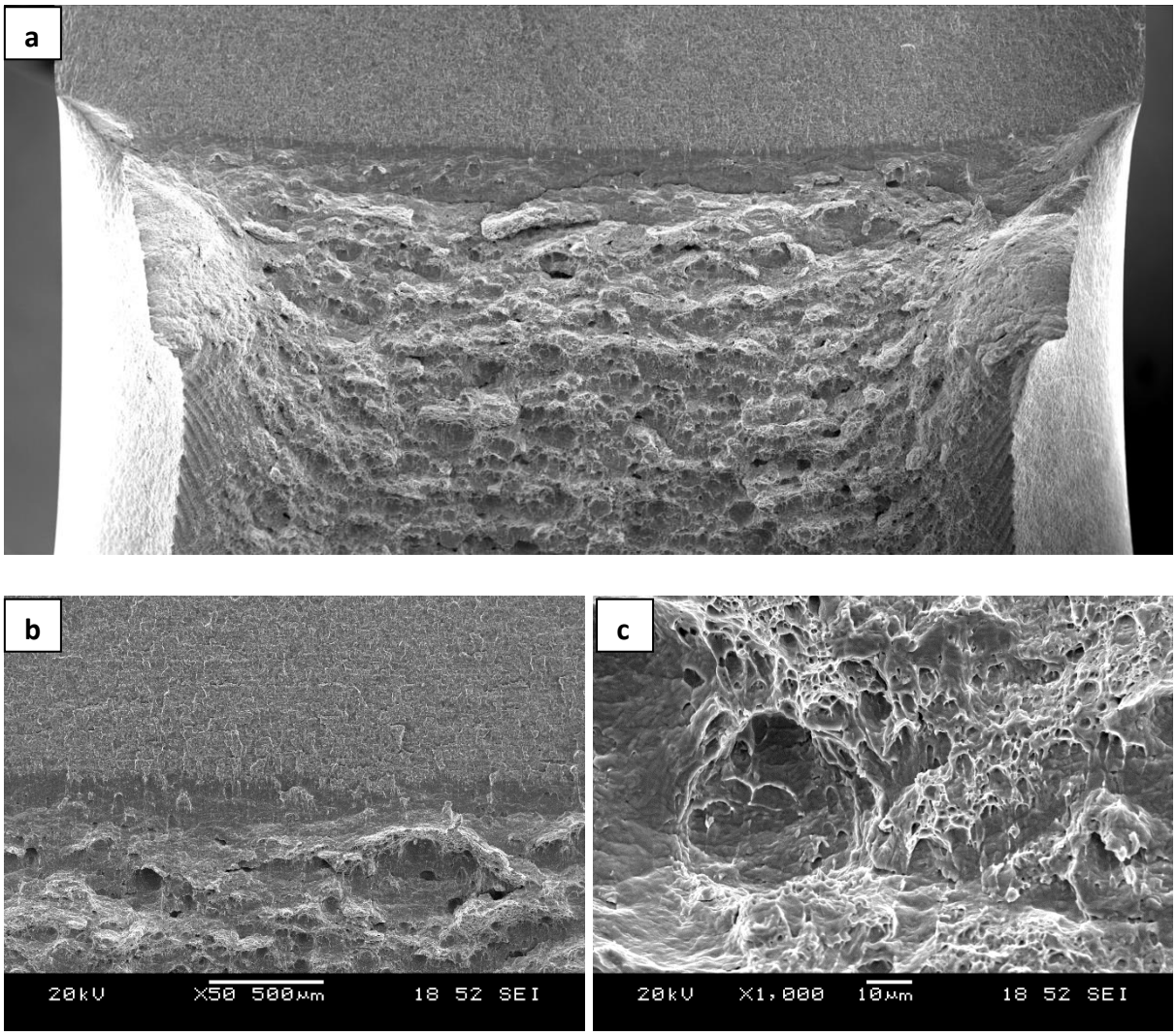

(a): Total fracture surface.
(b): Microvoid coalescence near fatigue crack end.
(c): Detail of microvoid coalescence.

Figure 6.68

7%Ni Steel Fatigue Fracture Surface at -163ºC

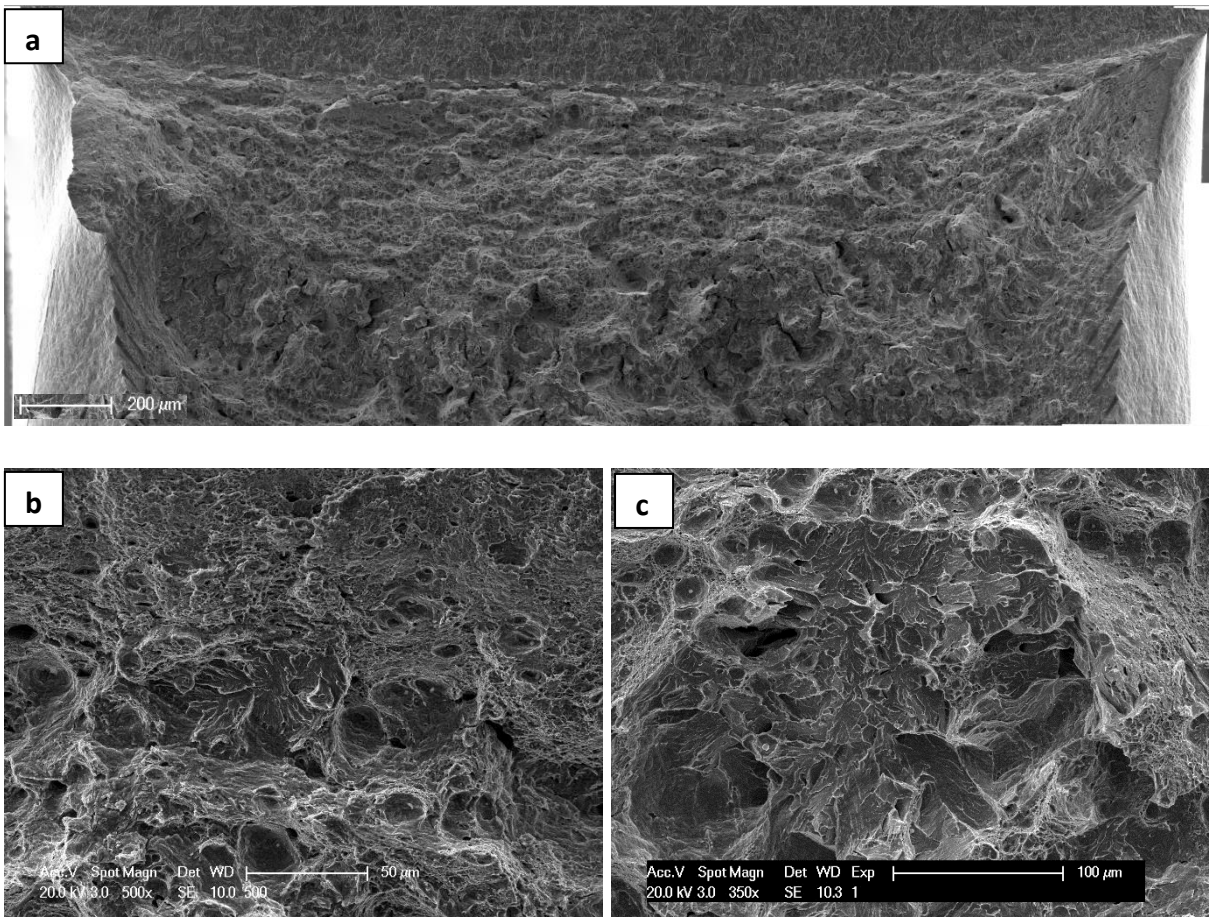

(a): Total fracture surface.
(b): Microvoid coalescence with cleavage facet.
(c): Cleavage facets close to fracture.

Figure 6.69

7%Ni Steel Fatigue Fracture Surface at -170ºC

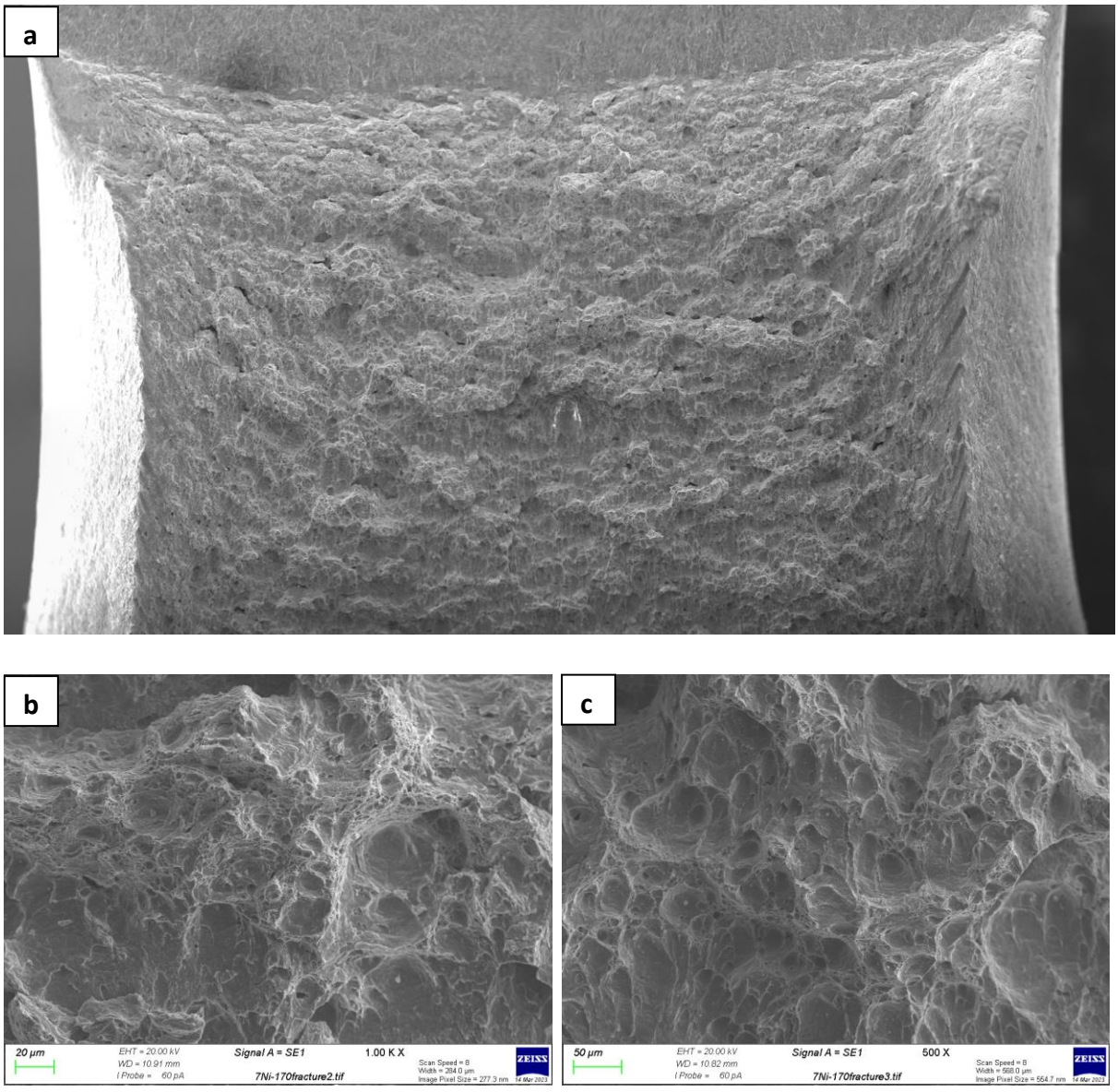

(a): Total fracture surface.
(b), (c): Microvoid coalescence on fracture surface.